UNUSUAL SUBDUCTION PROCESSES

EDITED BY: Vlad Constantin Manea, Marina Manea, Min Chen,
Jeroen Van Hunen and Matthias Konrad-Schmolke

PUBLISHED IN: Frontiers in Earth Science

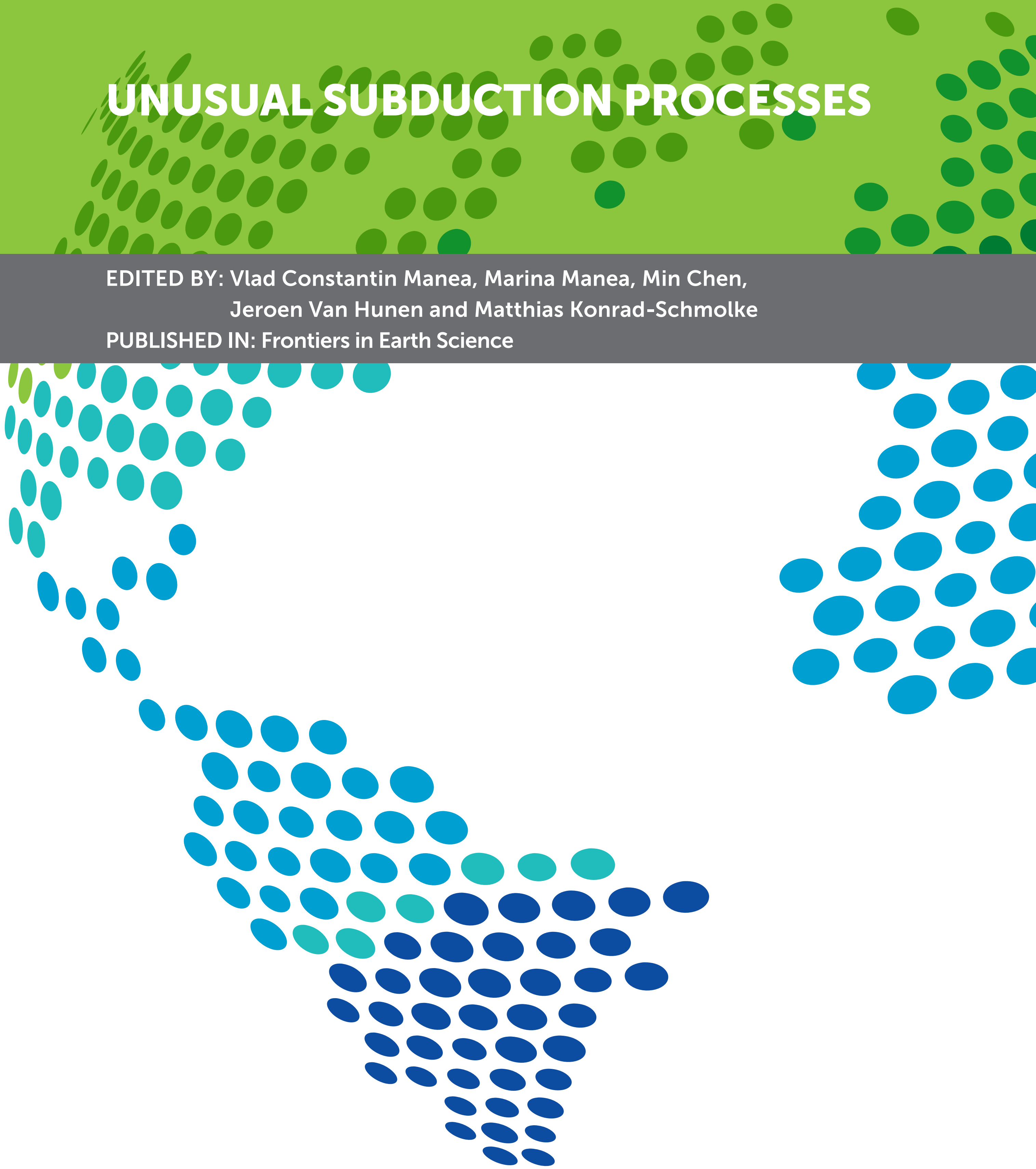

frontiers Research Topics

ISSN 1664-8714
ISBN 978-2-88966-265-4
DOI 10.3389/978-2-88966-265-4

About Frontiers

Frontiers is more than just an open-access publisher of scholarly articles: it is a pioneering approach to the world of academia, radically improving the way scholarly research is managed. The grand vision of Frontiers is a world where all people have an equal opportunity to seek, share and generate knowledge. Frontiers provides immediate and permanent online open access to all its publications, but this alone is not enough to realize our grand goals.

Frontiers Journal Series

The Frontiers Journal Series is a multi-tier and interdisciplinary set of open-access, online journals, promising a paradigm shift from the current review, selection and dissemination processes in academic publishing. All Frontiers journals are driven by researchers for researchers; therefore, they constitute a service to the scholarly community. At the same time, the Frontiers Journal Series operates on a revolutionary invention, the tiered publishing system, initially addressing specific communities of scholars, and gradually climbing up to broader public understanding, thus serving the interests of the lay society, too.

Dedication to Quality

Each Frontiers article is a landmark of the highest quality, thanks to genuinely collaborative interactions between authors and review editors, who include some of the world's best academicians. Research must be certified by peers before entering a stream of knowledge that may eventually reach the public - and shape society; therefore, Frontiers only applies the most rigorous and unbiased reviews.
Frontiers revolutionizes research publishing by freely delivering the most outstanding research, evaluated with no bias from both the academic and social point of view. By applying the most advanced information technologies, Frontiers is catapulting scholarly publishing into a new generation.

What are Frontiers Research Topics?

Frontiers Research Topics are very popular trademarks of the Frontiers Journals Series: they are collections of at least ten articles, all centered on a particular subject. With their unique mix of varied contributions from Original Research to Review Articles, Frontiers Research Topics unify the most influential researchers, the latest key findings and historical advances in a hot research area! Find out more on how to host your own Frontiers Research Topic or contribute to one as an author by contacting the Frontiers Editorial Office: researchtopics@frontiersin.org

UNUSUAL SUBDUCTION PROCESSES

Topic Editors:
Vlad Constantin Manea, National Autonomous University of Mexico, Mexico
Marina Manea, National Autonomous University of Mexico, Mexico
Min Chen, Michigan State University, United States
Jeroen Van Hunen, Durham University, United Kingdom
Matthias Konrad-Schmolke, University of Gothenburg, Sweden

Citation: Manea, V. C., Manea, M., Chen, M., Van Hunen, J., Konrad-Schmolke, M., eds. (2020). Unusual Subduction Processes. Lausanne: Frontiers Media SA.
doi: 10.3389/978-2-88966-265-4

Table of Contents

frontiers in Earth Science

EDITORIAL
published: 21 October 2020
doi: 10.3389/feart.2020.607697

Editorial: Unusual Subduction Processes

Vlad Constantin Manea[1,2]*, *Marina Manea*[1,3], *Min Chen*[4], *Jeroen van Hunen*[5] *and* *Matthias Konrad-Schmolke*[6]

[1] *Computational Geodynamics Laboratory, Centro de Geociencias, Universidad Nacional Autónoma de México, Mexico City, Mexico,* [2] *Research Institute of the University of Bucharest–iCUB, University of Bucharest, Bucharest, Romania,* [3] *Astronomical Institute of the Romanian Academy, Bucharest, Romania,* [4] *Michigan State University, East Lansing, MI, United States,* [5] *Durham University, Durham, United Kingdom,* [6] *University of Gothenburg, Gothenburg, Sweden*

Keywords: ***subduction zones*, intermediate-depth seismicity, geochemistry, flat slab subduction, numeric modeling**

Editorial on the Research Topic

Unusual Subduction Processes

Subduction zones display arguably the most complex geodynamic setting on Earth, which driven the Earth's interior dynamics and shaped the Earth's surface since the onset of plate tectonics. Processes within subduction zones comprise large earthquakes and volcanic eruptions, generation of continental crust, ore formation as well as long-term element exchange between atmosphere, hydrosphere and the Earth's interior, all of which are of fundamental societal, economic and scientific interest. Despite significant progress in our understanding of the bulk of subduction zones, many regions with unusual tectonic characteristics continue to be a challenge, as they do not always straightforwardly fit into the plate tectonic paradigm. Key questions remain regarding the complex dynamics associated with subduction zones. Addressing these problems is essential if we want to understand the role of subduction in the Earth's distant past or future, or if we want to reduce the significant natural hazards associated with plate subduction. It has become increasingly clear that significant progress can only be made through multidisciplinary research that combines new hypotheses, observations, and modeling. The set of 10 papers in this special Research Topic on the "Unusual Subduction Processes" aims to provide a multidisciplinary framework for future research efforts.

Flat slab subduction is one of the most unusual subduction geometries that challenge our view on how subduction is the key driver behind plate tectonics. Using numerical modeling, Schellart shows that only wide subduction zones (>6,000 km) have a predisposition to a shallow dip angle in the central part, where ultimately slab flattening can occur after a prolonged period of subduction (>80–110 Myr).

Unusual slab behavior at the interface between the upper and lower mantle illustrates that this mantle transition zone remains enigmatic. Employing numerical modeling, Grima et al. show that a slab orphaning regime, where the slab tip detaches at 660 km depth and is abandoned by its parent slab, provides a dynamic link between the stagnation and penetration regimes. Similarly, Tsucida and Kameyama demonstrate numerically that the descent of stagnant slabs at 660 km depth is controlled by the specific history of trench retreat. Acceleration of trench retreat favors the formation of horizontally-lying slabs at the base of the transition zone, whereas deceleration enhances the collapse of stagnant slabs into the lower mantle. Slab detachment dynamics is investigated in detail by Thielmann and Schmalholz who demonstrate that the slab break-off is mainly controlled by grain damage, but in the later stages thermal weakening becomes dominating. Connecting the two processes induces a thermomechanical chain effect resulting in more efficient slab detachment.

The interaction between mid-ocean ridges and subduction zones represents another complex process that produces major changes in arc-related magmatic activity and creating a unique

Edited and reviewed by:
Derek Keir,
University of Southampton,
United Kingdom

****Correspondence:***
Vlad Constantin Manea
vlad@geociencias.unam.mx

Specialty section:
This article was submitted to
Structural Geology and Tectonics,
a section of the journal
Frontiers in Earth Science

Received: *17 September 2020*
Accepted: *24 September 2020*
Published: *21 October 2020*

Citation:
Manea VC, Manea M, Chen M, van Hunen J and Konrad-Schmolke M (2020) Editorial: Unusual Subduction Processes.
Front. Earth Sci. 8:607697.
doi: 10.3389/feart.2020.607697

geological signature on overriding plates. Iannelli et al. combine new isotopic geochemical data with seismic tomography to track such tectonic changes that affected the Andean margin from Latest Cretaceous to early Miocene times. The magmatic arc isotopic composition records reveal time-space variations of a partially enriched mantle source which reflect the existence of a slab window that migrated southward along the Southern Central Andes until Eocene times. The common view about how subduction zones work is challenged by Leeman who used the atypical Cascades volcanic arc as a test site that is broader than usual, with significant basaltic volcanism located in frontal and back arc regions. Using thermobarometry of the most primitive basalts Leeman underpins the unusual relationships between depth and composition that yield conflicting views regarding melt generation.

Another important process observed in subduction zones along continental margins characterized by slab edges is mantle tearing, or delamination, which is accommodated by subduction-transform edge propagator faults. Negredo et al. investigate numerically the necessary conditions to trigger such continental mantle delamination associated with a seismically imaged subduction-transform edge propagator fault under the central Betic orogen at the northern edge of the Gibraltar arc subduction. They found a combination of specific conditions favoring slow or rapid continental delamination, as a strong density contrast between the orogenic and a thinned back-arc lithosphere, as well as a thick and mechanically weak lower crust along the continental margin. Understanding such mechanics of continental lithosphere in the context of mantle dripping is also of paramount importance to understand tectonic processes throughout Earth's history. Gunawardana et al. investigate numerically the lithospheric yield stress for conditions appropriate to the early-to-mid Archean Earth. Their results indicate that lithospheric yield stress values of less than 100 MPa can generate crustal trondhjemite-granodiorite volumes that indicate the dominance of lithospheric dripping in Archean.

Seismicity associated with subduction zones can also reveal key processes that occur at different depth ranges. Wagner et al. show that subduction zones with thick oceanic crust have little seismicity at intermediate depths, whereas adjacent regions with normal oceanic crust are characterized by intense seismicity at similar depths. Based on this particular distribution of intermediate depth seismicity, Wagner et al. advance a new provocative hypothesis. For subduction regions with normal thickness oceanic crust the intraslab seismicity is caused by mantle dehydration reactions, whereas areas characterized by unusual thick oceanic crust seismicity is almost absent due to the inability to seawater to penetrate and hydrate the lithospheric mantle before arrival at the trench.

Subduction zones may not only be affected by unusual thicknesses of the incoming oceanic crust, but also by atypical forearc dynamics. Using continuous GPS records gathered over a time span of more than a decade in the Guerrero region in Mexico, Kazachkina et al. reveal an active ~650 km long shear zone parallel to the Middle America trench. This left-lateral shear zone delimits a wide forearc sliver that moves over the subducting Cocos plate at a rate of 3–6 mm/yr with respect to the North America plate. The long-term effects of such sliver on the subduction dynamics for the unusually shallow Mexican flat slab are yet to be quantified.

We hope that the reader will find this Research Topic collection of papers a useful reference for future research on subduction zones and related processes.

AUTHOR CONTRIBUTIONS

VM, MM, MC, JvH, and MK edited the Research Topic of Unusual Subduction Processes. VM wrote the manuscript, and MM, MC, JH, and MK provided comments and suggestions, and revised the manuscript.

FUNDING

This work was partially supported by a grant of the Romanian Ministry of National Education and Scientific Research, RDI Program for Space Technology and Advanced Research (STAR), Romania, as well as by the Research Institute of the University of Bucharest–ICUB, University of Bucharest.

frontiers in Earth Science

ORIGINAL RESEARCH
published: 19 February 2020
doi: 10.3389/feart.2020.00026

Control of Subduction Zone Age and Size on Flat Slab Subduction

*Wouter Pieter Schellart**†

Department of Earth Sciences, Vrije Universiteit Amsterdam, Amsterdam, Netherlands

Flat slab subduction is an enigmatic style of subduction where the slab attains a horizontal orientation for up to several hundred kilometers below the base of the overriding plate. It has been linked to the subduction of buoyant aseismic ridges or plateaus, but the spatial correlation is problematic, as there are subducting aseismic ridges and plateaus that do not produce a flat slab, most notably in the Western Pacific, and there are flat slabs without an aseismic ridge or plateau. In this paper an alternative hypothesis is investigated which poses that flat slab subduction is associated with subduction zones that are both old (active for a long time) and wide (large trench-parallel extent). A global subduction zone compilation is presented showing that flat slabs preferentially occur at old (>∼80–100 Myr) and wide (≥∼6000 km) subduction zones. This is explained by the tendency for wide subduction zones to decrease their dip angle in the uppermost mantle with progressive time, especially in the center. A set of numerical subduction models confirms this behavior, showing that only the central parts of wide slabs progressively reduce their slab dip, such that slab flattening, and ultimately flat slab subduction, can occur. The models further show that a progressive decrease in slab dip angle for wide slabs leads to increased vertical deviatoric tensional stresses at the top surface of the slab (mantle wedge suction), facilitating flat slab subduction, while narrow slabs retain steep dip angles and low vertical deviatoric tensional stresses. The results provide a potential explanation why present-day flat slabs only occur in the Eastern Pacific, as only here subduction zones were old and wide enough to initiate flat slab subduction, and why Laramide flat slab subduction and South China flat slab subduction were possible in the geological past.

Keywords: subduction, flat slab, suction, mantle wedge, slab dip, geodynamics, numerical model, aseismic ridge

Edited by:
Jeroen Van Hunen,
Durham University, United Kingdom

Reviewed by:
Claire Currie,
University of Alberta, Canada
Bernhard Maximilian Steinberger,
German Research Centre
for Geosciences, Helmholtz Centre
Potsdam, Germany

****Correspondence:***
Wouter Pieter Schellart
w.p.schellart@vu.nl

†ORCID:
Wouter Pieter Schellart
orcid.org/0000-0002-9802-0143

Specialty section:
This article was submitted to
Solid Earth Geophysics,
a section of the journal
Frontiers in Earth Science

Received: *16 October 2019*
Accepted: *27 January 2020*
Published: *19 February 2020*

Citation:
Schellart WP (2020) Control
of Subduction Zone Age and Size on
Flat Slab Subduction.
Front. Earth Sci. 8:26.
doi: 10.3389/feart.2020.00026

INTRODUCTION

The cross-sectional geometry of upper mantle slabs varies considerably on Earth, with variations in slab dip angle, bending curvature and potential deflection of the slab in the mantle transition zone (e.g., Jarrard, 1986; Lallemand et al., 2005). For most active subduction zones on Earth, the uppermost ∼200 km of the slab is defined by one convex-upward slab hinge located close to the trench (**Figures 1A,B**) (e.g., Kuril-Kamchatka, Izu-Bonin-Mariana, Sunda, Tonga-Kermadec-Hikurangi, New Hebrides). Some subduction segments, however, show two or three slab hinges in the uppermost 200 km. The former generally has a very gentle, convex upward, slab hinge near the trench and a second, more pronounced, convex upward hinge several hundred kilometers downdip, with a very low angle slab segment in between (**Figure 1C**) (e.g., Alaska, Nankai, Cascadia). The latter, with three slab hinges, has one convex-upward hinge near the trench, one concave upward hinge that marks the start of a flat slab segment dipping ≤10°, and one convex-upward hinge that marks the end of the flat slab segment (**Figure 1D**). It is this subduction geometry, with three slab hinges that is most enigmatic and that is the subject of this study. In this contribution, only the subduction geometry with three slab hinges will be referred to as flat slab subduction. There are only a few current cases of such flat slab subduction, including central Chile, southern Peru, central Peru and Mexico, as has been discussed recently (Manea et al., 2017) and as can be seen in global slab models (e.g., Hayes et al., 2012). Several examples have also been proposed for the geological past, such as western North America, Central Andes and South China (Henderson et al., 1984; Li and Li, 2007; Ramos and Folguera, 2009).

The origin of flat slab subduction remains enigmatic. Previous work proposed that flat slabs occur through subduction of buoyant ridges or plateaus such as the Juan Fernandez Ridge and Nazca Ridge at the South American subduction zone (e.g., Pilger, 1981; Gutscher et al., 2000; van Hunen et al., 2002). But the spatial correlation between ridge/plateau subduction and flat slab subduction has many exceptions, with regions of aseismic ridge subduction lacking flat slab subduction (e.g., Tonga with Louisville Ridge, New Hebrides with d'Entrecasteaux Ridge, Mariana with Marcus-Necker Ridge, Kamchatka with Emperor Ridge) and some flat slab subduction segments lacking an aseismic ridge/plateau (e.g., Mexico) (Skinner and Clayton, 2011, 2013; Manea et al., 2017). Others have proposed that flat slab subduction might result from forced trench retreat (e.g., van Hunen et al., 2004; Schepers et al., 2017), strong suction forces in the mantle wedge (e.g., Tovish et al., 1978), or slab-plume interaction (e.g., Betts et al., 2009). The latter mechanism has not generally been applied to Cenozoic examples of flat slab subduction, and recent geodynamic models of slab-plume interaction for present-day Earth-like settings indicate that plumes generally do not affect slab geometry as their upward buoyancy flux can be more than two orders of magnitude smaller than the downward slab buoyancy flux (Mériaux et al., 2016). Wedge suction forces are generally considered to play a role in enhancing flat slab subduction (Tovish et al., 1978; van Hunen et al., 2004), but the question is, what might enhance wedge suction? A number of recent modeling works indicate that a relatively thick or far-field cratonic overriding plate will enhance wedge suction and thus facilitate flat slab subduction (Manea et al., 2012; O'Driscoll et al., 2012; Taramón et al., 2015). Forced trench retreat can also reproduce flat slab subduction in geodynamic models (van Hunen et al., 2004), but this forcing is generally externally imposed (mostly as a velocity boundary condition on the overriding plate) and so the question remains what the source of this forcing is and if sufficient forcing can arise in a buoyancy-driven geodynamic environment in nature (and model).

A number of relatively recent works argue that flat slab subduction requires a combination of physical ingredients. Proposed combinations include forced trench retreat and enhanced suction due to a thick cratonic overriding plate (Manea et al., 2012), buoyant plateau subduction with forced trench and plate motion (Liu and Currie, 2016), buoyant ridge/plateau subduction, enhanced suction, young oceanic plate subduction, and forced trench and plate motion (Hu et al., 2016), or ridge/plateau subduction, suction and forced trench retreat (van Hunen et al., 2004; Antonijevic et al., 2015).

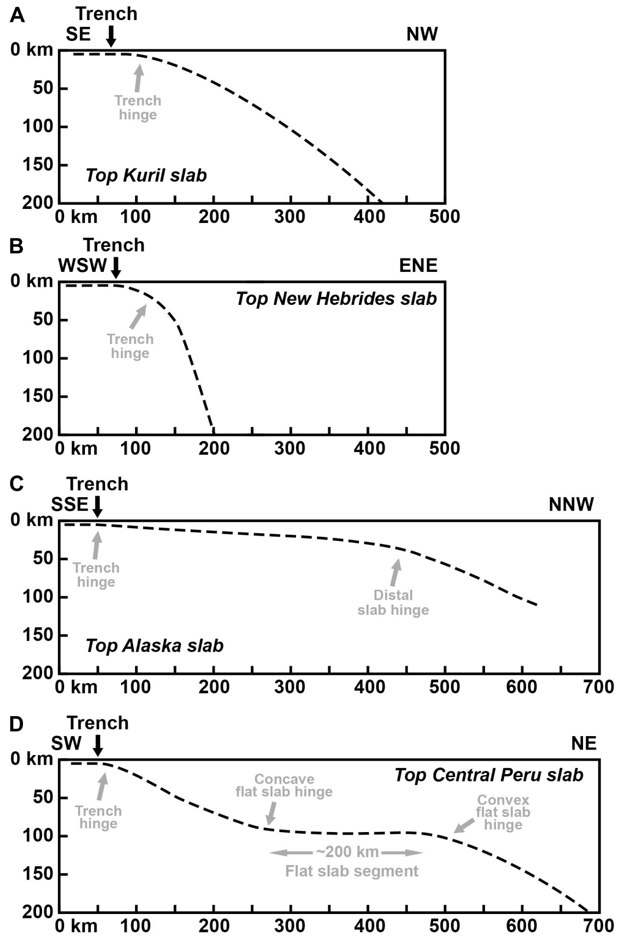

FIGURE 1 | Variability in geometry and dip angle of the uppermost ~200 km of slabs in nature, as shown by four examples. **(A)** The southern Kuril slab segment as an example of normal subduction with one convex-upward slab hinge and a normal slab dip angle [geometry derived from Slab1.0 model (Hayes et al., 2012)]. **(B)** The southern New Hebrides slab segment as an example of normal subduction with one convex-upward slab hinge and a steep slab dip angle [geometry from Slab1.0 model (Hayes et al., 2012)]. **(C)** The Alaska slab segment as an example of unusual subduction with two convex-upward slab hinges and a low-dip-angle slab segment in between [geometry derived from Ohta et al. (2006)]. **(D)** The Central Peru slab segment as an example of unusual subduction with two convex-upward slab hinges (trench hinge and convex flat slab hinge) and one concave upward slab hinge (concave flat slab hinge) in between [geometry derived from Phillips and Clayton (2014)]. A (sub)horizontal slab segment is located between the concave and convex flat slab hinges. It is only this slab geometry with three hinges that is referred to as flat slab subduction in this work and that is the focus of this study. Note that all images show the geometry of the top of the slab.

Here I build on these earlier findings and investigate the hypothesis that flat slab subduction (with three slab hinges as in **Figure 1D**) preferentially occurs at old subduction zones (those that have been active for a long time) that are very wide (large trench-parallel extent), because long-term subduction facilitates lower mantle slab penetration, which – through deep-mantle return flow – forces trenchward overriding plate motion, overriding plate thickening, upper mantle slab dip reduction and trench retreat (Schellart, 2017), with trench retreat being slow due to the wide-slab setting (Schellart et al., 2007), while wide-slab subduction enhances wedge suction, especially in the center (Dvorkin et al., 1993). A compilation from geological data of subduction zones in nature is presented, as well as results from buoyancy-driven geodynamic subduction models, that both provide support for the hypothesis that subduction zone width and age play an important role in flat slab subduction.

MATERIALS AND METHODS

Data Sources for Subduction Zones in Nature

A major compilation of subduction zone age and size of the active subduction zones on Earth has been constructed, either with or without flat slab subduction, as well as a number of subduction settings from the geological past for which flat slab subduction has been reported (**Figure 2**). The data sources that have been used are listed in **Tables 1**, **2**, and consist of previous works on the geological and tectonic evolution of subduction zones. **Table 1** lists those subduction zones that have a present-day flat slab or a flat slab in the geological past as defined in **Figure 1D** in the paper (i.e., a subduction zone with a trench hinge and two flat slab hinges). **Table 2** lists those subduction zones that have no reported flat slab and subduction segments of relatively large subduction zones for which that particular segment itself currently has no flat slab. For both tables, slab widths are listed. For **Table 1** these are the slab widths during (or close to) subduction zone formation and the slab widths at the time when flat slab subduction commenced. For **Table 2** these are the slab widths during (or close to) subduction zone formation and the present-day slab widths. All the present-day slab widths have been derived from Schellart et al. (2007). For slab width values during the geological past, a variety of published plate tectonic reconstructions have been used. Both tables also list the age of the subduction zone (the time of subduction initiation), while **Table 1** also lists the time of flat slab inception and the subduction zone age at the time of flat slab inception. Details and justifications for data selection and uncertainties associated with the data are listed in the **Appendix**.

Numerical Modeling Method

The hypothesis that flat slab subduction occurs for old and wide subduction zones is tested with geodynamic models of long-lived, buoyancy-driven, progressive subduction in which slab width is varied. The models use the *Underworld* numerical modeling code (Stegman et al., 2006; Moresi et al., 2007) and the model approach is the same as discussed in Schellart (2017). The models are run non-dimensionally and are later scaled to natural values. The reader is referred to the earlier works for

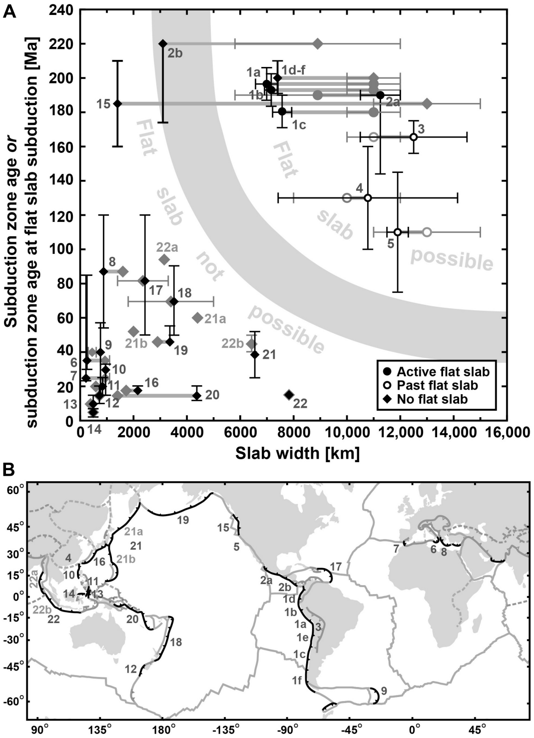

FIGURE 2 | (A) Diagram showing the dependence of flat slab subduction in nature on slab width (trench-parallel extent) and subduction zone age. Diamonds represent subduction zones/segments without a flat slab. Filled circles and white circles with an outline represent subduction zones with a present-day flat slab and flat slab in the geological past, respectively. For the black circles and white circles with black outline subduction zone age and slab width represent the age and width at the time of flat slab inception. For the black diamonds subduction zone age and slab width represents their age and width at present. For the gray circles, white circles with a gray outline and gray diamonds slab width represents the width at subduction initiation. See **Appendix** and **Tables 1**, **2** for data choices, justification and uncertainties. Black bars and gray bars are not error bars but indicate range of age estimates and slab width estimates, where data point location represents the average or the best estimate (see **Appendix** and **Tables 1**, **2**). Thick horizontal gray lines connect subduction initiation data point with present-day subduction zone data point (diamonds) or flat slab subduction initiation data point (circles) of the same subduction zone (segment). Subduction zone data points: 1–South America with 1a–Southern Peru segment (Nazca ridge), 1b–Central Peru segment, 1c–Central Chile segment (Juan Fernandez ridge), 1d–Colombia segment, 1e–Northern Chile segment, 1f–Southern Chile segment; 2–Mexico-Central America with 2a–Mexico segment, 2b–Central America segment; 3–South America (Central Andes segment); 4–South China; 5–Farallon (Laramide segment); 6–Calabria; 7–Gibraltar; 8–Hellenic; 9–Scotia; 10–Manila; 11–Sangihe; 12–Puysegur; 13–Halmahera; 14–North Sulawesi; 15–Cascadia; 16–Nankai-Ryukyu; 17–Lesser Antilles-Puerto Rico; 18–Tonga-Kermadec-Hikurangi; 19–Aleutians-Alaska; 20–Melanesia (New Britain-San Cristobal-New Hebrides); 21–Northwest Pacific (Kamchatka-Kuril-Japan-Izu-Bonin-Mariana) with 21a–Kamchatka-Kuril-Japan segment, 21b–Izu-Bonin-Mariana segment; 22–Sunda (Burma-Andaman-Sumatra-Java-Banda) with 22a–Burma-Andaman segment, 22b–Burma-Andaman-Sumatra-Java segment. The light gray zone indicates the approximate location of the boundary separating the domains where flat slab subduction is not possible (lower left) and possible (upper right). Note that for the individual subduction zone segments (1a-f and 2a-b) the entire width of the slab that these segments form part of has been plotted. **(B)** Map showing the location of those subduction zones and segments plotted in panel **(A)**.

TABLE 1 | Subduction zones with a flat slab.

Subduction zone	Number in Figure 2	Slab width (average) at flat slab initiation* [km]	Slab width (min.-max.) at flat slab initiation [km]	Distance to closest slab edge at flat slab initiation^ [km]	Slab width during/close to subduction zone formation [km]	Subduction zone age (best estimate/average)† [Ma]	Subduction zone age (min.-max.) [Ma]	Time of flat slab inception [Ma]	Subduction zone age at flat slab initiation‡ [Ma]
With present-day flat slab									
South America (Southern Peru)§	1a	6992(1,2)	6571–7413	2200	11,000 ± 1000(2)	200 (be)	191–210(3–6)	4(7)	196
South America (Central Peru)@	1b	7162(1,2)	6911–7413	1400	11,000 ± 1000(2)	200 (be)	191–210(3–6)	8(7)	192
South America (Central Chile)¶	1c	7570(1,2)	7212–7928	2400	11,000 ± 1000(2)	200 (be)	191–210(3–6)	20(8)	180
Mexico-Central America (Mexico)#	2a	11,250(9,10)	10,500–12,000	2100	∼5800(6) or 11,000 ± 1000(2)	220 (be)	174–201(11) or 220(12)	30–25(13–15)	190
With past flat slab									
South America (Central Andes)&	3	12,500(9,10)	10,500–14,500	3800	11,000 ± 1000(2)	200 (be)	191–210(3–6)	35(16)	165
South China+	4	10,784(17)	7421–14,146	3000	10,000 ± 2000(17)	360 (av)	330–390(17,18)	230(19)	130
Farallon%	5	11,900(9,10)	11,500–12,300	1700–2700	13,000 ± 2000(2)	185 (av)	160–210(20,21)	85–65(22–24)	100–120

*Slab width is based on the average of the estimated minimum and maximum slab width at the time of inception of flat slab subduction. It is derived from tectonic reconstructions presented in Gordon and Jurdy (1986); Collins (2003), Schellart et al. (2007, 2010), Domeier and Torsvik (2014) and Seton et al. (2012). ^Trench-parallel distance from flat slab segment to closest lateral slab edge at the time of flat slab inception. †Subduction zone age (time of subduction zone initiation) based on the best estimate (be) or average (av) of the estimated minimum and maximum age. ‡Age of the subduction zone at the time of inception of flat slab subduction. §Southern Peru flat slab spatially correlated with the subducting Nazca Ridge (Pilger, 1981; Gutscher et al., 2000). @Central Peru flat slab possibly related to subduction of the Inca plateau (Gutscher et al., 2000). ¶Central Chile flat slab spatially correlated with the subducting Juan Fernandez Ridge (Pilger, 1981; Gutscher et al., 2000). #Mexican flat slab, not spatially associated with any ridge or plateau (Skinner and Clayton, 2011). Note that a flat slab subduction initiation age of 30–25 Ma is chosen, based on the timing of migration of arc magmatism from the Sierra Madre del Sur to the Trans-Mexican Volcanic Belt (Ferrari et al., 1999; Morán-Zenteno et al., 1999; Kim et al., 2010), and not a younger initiation age of 16–9 Ma proposed more recently (Manea et al., 2017). A consequence of adopting the older age is that the slab width then includes the South American segment and Mexico-Central America segment (and possibly the Baja California segment), because the Nazca and Cocos plates still formed one single plate until ∼23 Ma (Lonsdale, 2005). &Central Andes (southern Peru-northernmost Chile) flat slab in the latest Eocene-Oligocene (Ramos and Folguera, 2009). +South China flat slab in the Middle Triassic-Early Jurassic (Li and Li, 2007). %Farallon flat slab in western North America, thought to be responsible for the Laramide orogeny and eastward migration of the magmatic arc (Dickinson and Snyder, 1978; Henderson et al., 1984). The numbers in between the brackets refer to the following references: [1]Schellart et al. (2007), [2]Seton et al. (2012), [3]Coira et al. (1982), [4]Vásquez et al. (2011), [5]Scheuber et al. (1994), [6]van der Meer et al. (2018), [7]Rosenbaum et al. (2005), [8]Kay and Abbruzzi (1996), [9]Schellart et al. (2010), [10]Gordon and Jurdy (1986), [11]Centeno-García (2017), [12]Boschman et al. (2018), [13]Kim et al. (2010), [14]Morán-Zenteno et al. (1999), [15]Ferrari et al. (1999), [16]Ramos and Folguera (2009), [17]Domeier and Torsvik (2014), [18]Collins (2003), [19]Li and Li (2007), [20]Burchfiel and Davis (1975), [21]DeCelles (2004), [22]Henderson et al. (1984), [23]Liu et al. (2010), [24]Copeland et al. (2017).

TABLE 2 | Active subduction zones and active subduction zone segments without a flat slab.

Subduction zone	Number in Figure 2	Present-day slab width* [km]	Slab width during/close to subduction zone formation [km]	Subduction zone age (best estimate/average) [Ma]	Subduction zone age (lower limit) [Ma]	Subduction zone age (upper limit) [Ma]
Subduction zones						
Calabria	6	300	800(1) or 1100(2,3)	35 (be)	30(2,3)	85(1)
Gibraltar	7	250	800(1) or 1100(2,3)	25 (be)	23(4)	85(1)
Hellenic	8	900	1600(5)	87 (av)	54(6)	120(7)
Scotia	9	800	∼300(8) or ∼600(9)	50(9,10) (be)	15^(11)	57(8)
Manila	10	1000	∼1000(12)	30(12) (be)	15(13)	33(13)
Sangihe	11	850	600(14)	20 (av)	15(14)	25(14)
Puysegur	12	750	750(15)	15 (av)	10(16)	20(15)
Halmahera	13	500	400(14)	10(14) (be)	7(14)	15(14)
North Sulawesi	14	500	500(17)	5(14) (be)	2(14)	7(14)
Cascadia	15	1400	13,000 ± 2000(18)	185 (av)	160(19)	210(20)
Nankai-Ryukyu	16	2200	∼1600(12)	18(12) (be)		20(17)
Lesser Antilles-Puerto Rico	17	2450	∼1400(21) or 3300(22)	85 (av)	50(21)	120(22)
Tonga-Kermadec-Hikurangi	18	3550	∼1800(23) or ∼5000(15)	70 (av)	50(23)	90(15,24)
Aleutians-Alaska	19	3400	2900(25)	46(26)		55(25)
Melanesia†	20	4400	1400(15)	15(17) (be)	12(24)	15(17,15)
Northwest Pacific‡	21	6550		39 (av)	25(30)	52(29)
Kamchatka-Japan segment	21a		4400(27)	60(27) (be)		
Izu-Mariana segment	21b		∼2000(28)	52(29) (be)	48(31)	52(29)
Sunda	22	7850		15 (be)		
Burma-Andaman (Bu-Ad)	22a		3150	94?(32) (be)		
Bu-Ad + Sumatra-Java (Su-Jv)	22b		3150 + 3300	45(14) (av)	40(14)	50(14)
Bu-Ad-Su-Jv + Banda	22		6450 + 1400	15(33) (be)		
Subduction zone segments						
South America						
Colombia	1d	7400	11,000 ± 1000(18)	200(34−36,10) (be)	191(35)	210(35)
Northern Chile	1e	7400	11,000 ± 1000(18)	200(34−36,10) (be)	191(35)	210(35)
Southern Chile	1f	7400	11,000 ± 1000(18)	200(34−36,10) (be)	191(35)	210(35)
Mexico-Central America						
Central America	2b	3100	5800(10)/11,000 ± 1000(18)	220 (be)	174–201(37)	220(38)

*The numbers in between the brackets refer to the following references: [1]van Hinsbergen et al. (2014), [2]Séranne (1999), [3]Rosenbaum et al. (2002), [4]Lonergan and White (1997), [5]Wortel and Spakman (2000), [6]Dilek and Sandvol (2009), [7]van Hinsbergen et al. (2005), [8]Vérard et al. (2012), [9]Eagles and Jokat (2014), [10]van der Meer et al. (2018), [11]Larter et al. (2003), [12]Lallemand et al. (2001), [13]Li et al. (2014), [14]Hall (2012), [15]Schellart et al. (2006), [16]LeBrun et al. (2003), [17]Hall (2002), [18]Seton et al. (2012), [19]Burchfiel and Davis (1975), [20]DeCelles (2004), [21]Boschman et al. (2014), [22]Pindell et al. (2006), [23]Meffre et al. (2012), [24]Schellart and Spakman (2012), [25]Scholl et al. (1986), [26]Jicha et al. (2006), [27]Schellart et al. (2003), [28]Deschamps and Lallemand (2002), [29]Ishizuka et al. (2011), [30]Sdrolias et al. (2004), [31]Arculus et al. (2015), [32]Sarma et al. (2010), [33]Spakman and Hall (2010), [34]Coira et al. (1982), [35]Vásquez et al. (2011), [36]Scheuber et al. (1994), [37]Centeno-García (2017), [38]Boschman et al. (2018). *All present-day slab widths (trench-parallel extent) are from Schellart et al. (2007). ^Minimum based on the age of the oldest part of Scotia backarc basin (East Scotia Sea) bordering the active Scotia arc. †Melanesia: New Britain-San Cristobal-New Hebrides. ‡Northwest Pacific: Kamchatka-Kuril-Japan-Izu-Bonin-Mariana.*

details on the numerical method and approach. The model set-up involves buoyancy-driven subduction of a higher-density, viscously stratified, subducting plate below an overriding plate into a lower density, lower viscosity, stratified mantle that extends down to the core-mantle boundary (**Figure 3**). Each model has free-slip conditions along all its boundaries and starts with a short, 206-km-long slab perturbation dipping at 29° that triggers buoyancy-driven subduction. The model domain is 10,000 km long and 2900 km deep. Four models are presented that are all exactly the same except for their subduction zone width (W) and box width (BW): a narrow slab model (W600 with $W = 600$ km, $BW = 4000$ km), an intermediate-width slab model (W2000 with $W = 2000$ km, $BW = 6000$ km), a wide slab model (W6000 with $W = 6000$ km, $BW = 12{,}000$ km), and a very wide slab model (W-infinite, a model with a 2D spatial set-up, so W = infinite, BW = infinite). The models do not contain lateral side plates, assuming that the transform faults along the sides of the plates are very weak. Furthermore, the trailing edges of the plates are free, mimicking spreading ridges, offering minimal resistance to lateral motion, following earlier works on free subduction (e.g., Kincaid and Olson, 1987; Chen et al., 2016).

The subducting plate has a homogeneous density that is 60 kg/m^3 higher than that of the sub-lithospheric mantle, and is viscously stratified into three layers, including a viscoplastic top layer with a von Mises rheology to allow for decoupling of the subducting plate from the top surface, a high-viscosity Newtonian central layer and a low-viscosity Newtonian bottom layer (**Figure 3**). The effective viscosity averaged over the

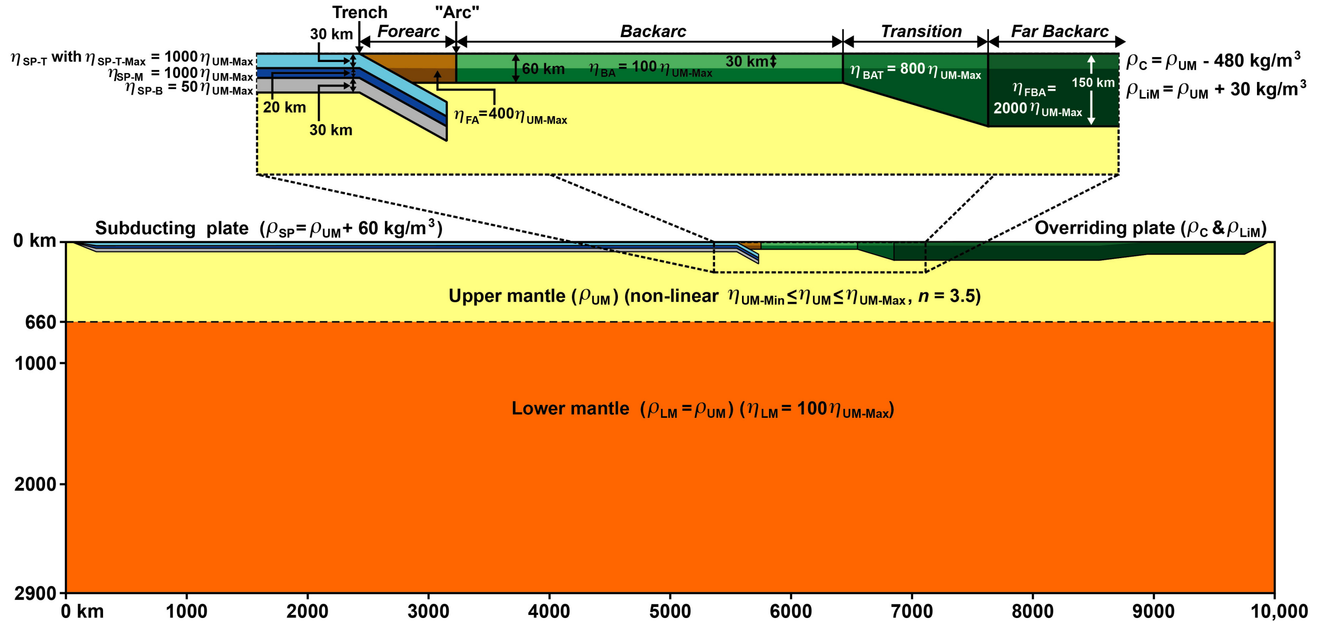

FIGURE 3 | Cross-section through the center of the numerical domain showing the model set-up to investigate buoyancy-driven time-evolving subduction in a very large domain with a layered whole mantle reservoir. The four models reported in the paper are all the same in cross-section but differ in trench-parallel extent with a different box width (*BW*) and slab width (*W*): the narrow slab model with *BW* = 4000 km and *W* = 600 km; the intermediate-width slab model with *BW* = 6000 km and *W* = 2000 km; the wide slab model with *BW* = 12,000 km and *W* = 6000 km; and the very wide slab model with *BW* = infinite and *W* = infinite (2D model set-up). The geodynamic models include a layered negatively buoyant subducting plate with three layers with different viscosity (top, middle and bottom) and a layered overriding plate with two layers with the same viscosity but different density (crustal layer and lithospheric mantle layer). η_{SP-T} = subducting plate top layer viscosity, $\eta_{SP-T-Max}$ = subducting plate top layer maximum viscosity, η_{SP-M} = subducting plate middle layer viscosity, η_{SP-B} = subducting plate bottom layer viscosity, η_{FA} = forearc viscosity, η_{BA} = backarc viscosity, η_{BAT} = backarc transition zone viscosity, η_{FBA} = far backarc viscosity, η_{UM} = sub-lithospheric upper mantle viscosity, η_{UM-Min} = minimum sub-lithospheric upper mantle viscosity, η_{UM-Max} = maximum sub-lithospheric upper mantle viscosity, η_{LM} = lower mantle viscosity, ρ_{UM} = sub-lithospheric upper mantle density, ρ_{LM} = lower mantle density, ρ_{SP} = subducting plate density, ρ_{C} = continental crustal density, and ρ_{LiM} = continental lithospheric mantle density. All the box boundaries have a free-slip condition.

thickness of the slab falls within the range 270–640η_{UM-Max} (with η_{UM-Max} being the maximum sub-lithospheric upper mantle viscosity), which is very comparable to viscosity estimates from earlier works, such as Ribe (2010) with an estimated slab/upper mantle viscosity ratio of 140–510, and Schellart (2008) with an estimated ratio of 100–700. The overriding plate has several lateral domains with each domain having a constant viscosity. It further has a vertical density stratification with a 30-km-thick top layer with a density that is 480 kg/m^3 less than that of the sub-lithospheric upper mantle, mimicking the density contrast between continental crust and sub-lithospheric upper mantle, while the density of the lithospheric mantle is 30 kg/m^3 higher, mimicking continental lithospheric mantle with a density that is moderately higher than that of the sub-lithospheric mantle.

The models include a sub-lithospheric upper mantle domain with a non-linear stress-dependent viscosity η_{UM} down to a depth of 660 km, with a stress exponent n = 3.5 (Mackwell et al., 1990), a minimum viscosity η_{UM-Min} and maximum viscosity η_{UM-Max}, such that $\eta_{UM-Min} = 0.1\ \eta_{UM-Max}$. The variation in sub-lithospheric upper mantle viscosity is therefore limited to one order of magnitude to facilitate reasonable convergence rates in the numerical calculations and to ensure that the scaled time of individual time steps does not drop significantly below the average scaled time. The dimensionalized $\eta_{UM-Min} = 5 \times 10^{19}$ Pa s and $\eta_{UM-Max} = 5 \times 10^{20}$ Pa s. Such values are within the estimated range of values for the sub-lithospheric upper mantle (10^{19}–10^{21} Pa s) in nature (Artyushkov, 1983; Ranalli, 1995). Note, however, that uncertainty in mantle viscosity values in nature directly affect dimensionalized velocity values in the models.

The 2240 km thick lower mantle domain has a Newtonian viscosity $\eta_{LM} = 100\ \eta_{UM-Max}$. As such, a minimum viscosity jump of a factor of 10^2 was applied between the upper and lower mantle. This viscosity step implementation represents all the effects of the 660 km discontinuity (viscosity changes, density changes, phase transitions) and captures the discontinuity's geodynamic essence through reducing the slab velocity in the lower mantle, as implied by earlier studies on mineral physics and phase transitions in the deep mantle (Torii and Yoshioka, 2007; Ganguly et al., 2009). The choice for this simple implementation is further supported by results from recent subduction modeling, which show that, unless a complete treatment of compositional layers and phase transitions is implemented, large-scale deformation of slabs is better approximated by a model with no phase transitions rather than including an incomplete approximation that over-predicts slab folding (Arredondo and Billen, 2016).

The isothermal conditions in the model, and thereby the absence of slab warming, will not affect the slab morphology, slab viscosity and slab-mantle density contrast in the upper mantle significantly due to the relatively rapid rate of subduction (up to 7.5 cm yr^{-1}) and the slow rate of conductive slab warming. Lower mantle slab warming is likely more significant, producing a weaker lower mantle slab, which would thereby likely result in stronger slab folding and tighter slab folds. However, the density contrast of the lower mantle folded slab pile is not significantly affected, because it sinks as a whole and includes the entrained mantle material enclosed within the folds. Considering that warming of the folded slab segment coincides with the cooling of the entrained ambient mantle in the folds (Schellart, 2017), the thermal buoyancy contrast between folded slab pile and ambient mantle does not diminish and disappear on a timescale representing the duration of the numerical models. Therefore, the driving mechanism of the lower mantle slab is not significantly affected.

The model resolution in cross-section is 512 (horizontal) × 192 (vertical) elements with 20 particles per element. A mesh refinement has been implemented such that a 3,000 km (length) by 290 km (depth) domain around the subduction zone has a maximum resolution with cells that are 9.8 km long and 7.6 km deep. This spatial refinement is required for properly resolving the subduction zone interface. The model resolution in the trench-parallel direction is 48 (W600), 80 (W2000), and 160 (W6000) elements. The models with a 3D spatial set-up were run on the Australian national supercomputer (Raijin) using 240–496 cores and individual models took between 3 months (W600) and more than 2 years (W6000) to complete, the latter model requiring more than 90 restarts to complete a total of more than 5000 time steps (with one time step scaling to, on average, ~0.04 Myr, so about 40,000 years). Considering the large amount of time and computational resources required to complete these models, it has not been possible to do an extensive parametric investigation other than investigating the influence of slab width. A detailed parametric study is beyond the scope of this work but is part of future studies using models with a 2D spatial set-up, in which the effect of various parameters and boundary conditions on flat slab subduction are investigated, including the subducting plate thickness, subducting plate viscosity, overriding plate viscosity, viscous stratification of the sub-lithospheric mantle, temperature-dependent viscosity and temperature-dependent density, as well as free-slip, no-slip and periodic boundary conditions.

The numerical models use Cartesian geometry. It could be conceived that the usage of (more realistic) spherical geometry would facilitate the formation of flat slabs, especially for wide slabs, because the reduction in spherical surface area with increasing depth requires a sinking slab to accommodate horizontal shortening strains and compressive stresses during progressive sinking, while the total required horizontal shortening increases linearly with slab width. The slab resistance to such strains and the associated in-plane stress arching would provide an additional lifting force to the slab that would promote slab flattening. However, the slab strain magnitude associated with the subduction of a spherical cap in spherical geometry (in contrast to a flat plate in Cartesian geometry which lacks such strain) is independent of the width of the slab, as it merely depends on the vertical sinking distance (with respect to the surface) and the radius of the sphere. Furthermore, it can be shown that strain rates in nature associated with such strains are relatively low. For example, if one considers a subducting plate that sinks from the surface down to 100 km depth at a vertical sinking rate of 5 cm/yr, this would amount to a trench-parallel shortening strain and strain rate of ~0.016 and $\sim 2.5 \times 10^{-16}\ \mathrm{s}^{-1}$, respectively, due to the decreased radial distance to the Earth's center and the associated reduction in trench-parallel line length. If we compare such a shortening strain rate with strain rates within subducting plates near the trench in nature resulting from plate convergence and bending, which reach values up to $\sim 10^{-14}\ \mathrm{s}^{-1}$ (e.g., Kreemer et al., 2003; Stadler et al., 2010), then it is clear that the trench-parallel strain rates are subordinate, being up to 40 times smaller than the convergence/bending related strain rates. Considering these relatively low trench-parallel strain rates in spherical geometry, implying low trench-parallel within-slab compressive stresses, it is here argued that the simplification of using Cartesian geometry does not have a significant effect on flat slab subduction formation and evolution.

RESULTS

Flat Slab Subduction Relation With Subduction Zone Age and Width in Nature

Figure 2 shows a compilation of the active subduction zones on Earth, either with or without flat slab subduction, and a number of subduction settings from the geological past for which flat slab subduction has been reported. Age since subduction initiation has been plotted against slab width. For those subduction zones without a flat slab (e.g., Scotia, Tonga-Kermadec-Hikurangi, Sunda, Nankai-Ryukyu, Aleutians-Alaska, Hellenic), their current age and width (their trench-parallel extent) have been plotted. Note again that, following the definition outlined in the introduction, Nankai, Alaska and Cascadia are not counted as flat slab settings because their uppermost slab geometry is not defined by three slab hinges (as in **Figure 1D** with one concave-upward hinge) but only by two convex-upward hinges (as in **Figure 1C**). For those subduction zones with a flat slab (as in **Figure 1D**), their age and width have been plotted as it was at the onset of flat slab subduction. For all zones, their width at or close to the time of subduction initiation has also been plotted. The data generally plot in two clusters: (1) One cluster that plots toward the bottom left where most subduction zones are relatively narrow and young (e.g., Scotia, Manila, North Sulawesi, Nankai-Ryukyu, Puysegur), some are older but narrow (e.g., Hellenic, Cascadia, Lesser Antilles-Puerto Rico) and some are wide but young (e.g., Melanesia, Sunda, Northwest Pacific); and (2) Another cluster that is located toward the top right where subduction zones are both old and wide (e.g., South America). Those subduction zones that plot in the first domain all lack flat slab subduction as defined in **Figure 1D** (but note that low angle subduction as in **Figure 1C** can occur). Those subduction zones that plot in the second domain in the upper right region do have one or more segments that are characterized by flat slab subduction (e.g., segments 1a–c) but also segments that are not (e.g., segments 1d–f).

Geodynamic Model Results

Geodynamic Model Evolution

The four models all show subduction through trenchward subducting plate motion and through trench retreat. The first 35–40 Myr of the model runs are characterized by upper mantle subduction, which are followed by whole mantle subduction as the deepest part of the slab sinks into the lower mantle. Each of the models shows a similar, relatively steep, slab geometry during upper mantle subduction (**Figure 4**). During whole mantle subduction the different models develop variability in slab geometry.

The minimum slab dip angle in the depth range 100–200 km is tracked to identify flat slab subduction. This minimum dip angle is comparable for the four experiments in the early subduction stage and of the order 60–70° (**Figure 5A**). Once the slab tip approaches the 660 km discontinuity at ∼35 Ma, the minimum dip angles for the different experiments start to diverge. All models show an overall, long-term, decrease in dip angle, but the magnitude of decrease depends on the slab width, with the largest decrease occurring for the widest slab. The narrow and intermediate-width slabs only show a moderate decrease in slab dip (with slab dip minima of 48 and 38°, respectively), while the wide and very wide slabs show a large decrease (with minima of 21 and 2°, respectively). For the wide slab model, slab flattening starts in a late stage at ∼171 Myr (**Figures 4C**, **5A**). Here, the start of slab flattening is defined as the onset of formation of the concave-upward slab hinge between ∼50–150 km depth in between the two convex-upward hinges. This slab flattening only occurs in the central part of the wide subduction zone (central ∼700 km) and does not occur in segments closer toward the lateral slab edges. Indeed, the local slab dip angle near the lateral slab edges is consistently steeper than in the center with observed differences in dip angle up to 27° toward the end of the model run (**Figure 5B**).

For the very wide slab model slab flattening starts at ∼134 Myr and flat slab subduction starts at ∼150 Myr, lasting ∼25 Myr (**Figures 4D**, **5**), although briefly interrupted by a ∼4 Myr period where the local dip angle exceeds 10°. Flat slab subduction is followed by approximately normal subduction with dip angles of ∼20–30° until the end of the model run at ∼185 Myr. Note again that flat slab subduction is defined as the moment when the flat slab segment downdip of the concave hinge has a dip angle ≤10°. Also note that time in the models depends on the scaling of viscosity and velocity. Average subduction rates in the models (3–4 cm/yr) are somewhat slower than the average present-day subduction rate on Earth (5.5 cm/yr, Schellart et al., 2007). If we scale the average subduction velocities in the models to those in nature (implying a $\eta_{UM-Max} = 2.7\text{–}3.6 \times 10^{20}$ Pa s in nature rather than $\eta_{UM-Max} = 5 \times 10^{20}$ Pa s, with all values falling

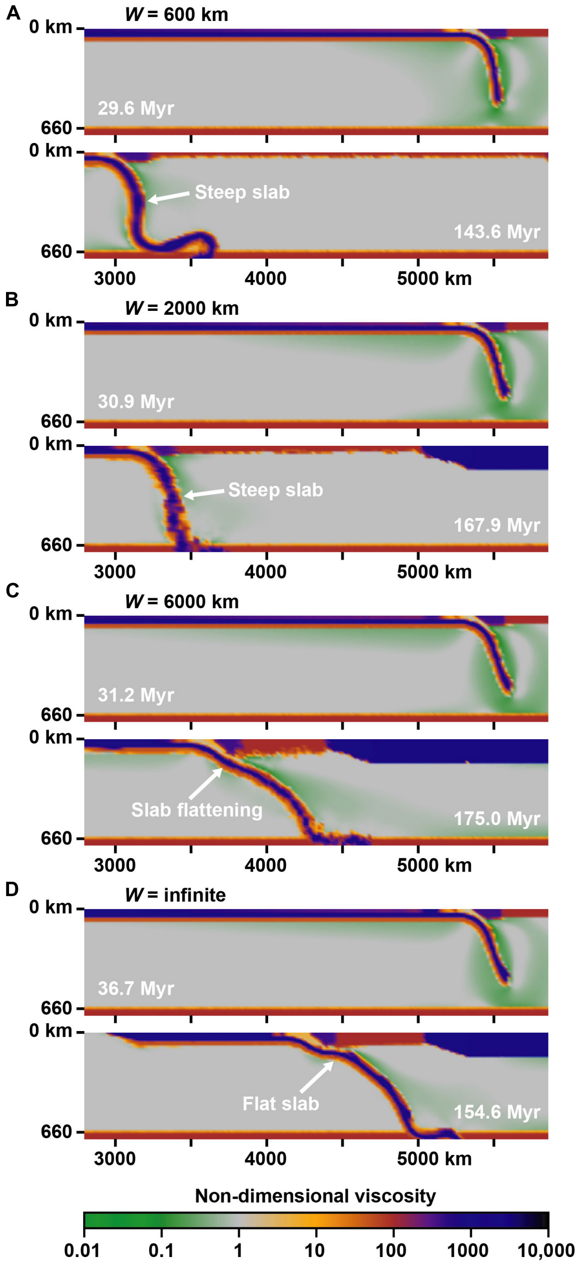

FIGURE 4 | Cross-sections through the center of four numerical subduction models with a different slab width showing two stages in the subduction process (early and late stage). **(A)** Narrow slab width model (*W* = 600 km) showing a steep upper mantle slab. **(B)** Intermediate-width slab model (*W* = 2000 km) showing a steep upper mantle slab. **(C)** Wide slab model (*W* = 6000 km) showing upper mantle slab flattening in a late stage of subduction. **(D)** Very wide slab model (*W* = infinite, 2D set-up) showing flat slab subduction in a late stage of the model evolution. Colors indicate the non-dimensional effective viscosity field. Note that the somewhat fuzzy-blocky appearance of the slab in the lower part of the upper mantle in the bottom panels of **(B,C)** is the result of the implemented spatial adaptive mesh, which gives a lower resolution in the lower part of the upper mantle compared to the upper part, and the many times that repopulation of cells with particles was required to avoid the occurrence of empty cells. The high number of repopulation exercises, in particular for *W* = 2000 and *W* = 6000, caused the boundaries between different particle fields to become progressively fuzzier.

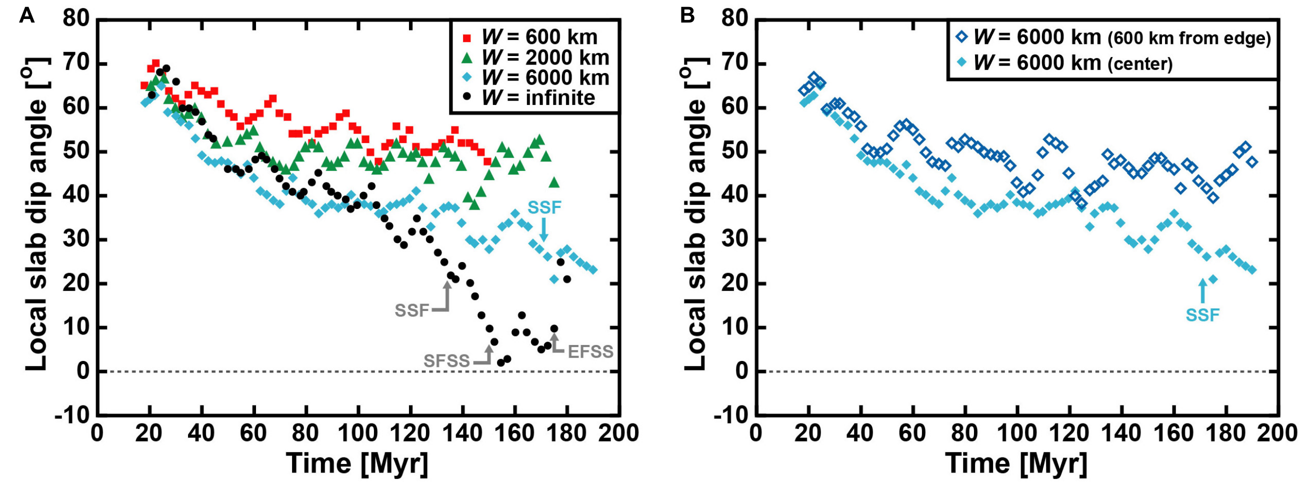

FIGURE 5 | Slab dip angle evolution of geodynamic models of progressive subduction in which the width (*W*) of the subduction zone is varied [narrow slab model with *W* = 600 km, intermediate-width slab model with *W* = 2000 km, wide slab model with *W* = 6000 km, and very wide slab model with *W* = infinite (2D set-up)]. The diagrams show the temporal evolution of the minimum slab dip angle for a local, 100-km-long, slab segment within the depth range 100–200 km to determine the flat slab subduction stage, which is defined as the time when the local slab dip is ≤10°. **(A)** Model results for the four different models for sections located in the center of the subduction zone. The narrow and intermediate-width slab models show no flat slab development. The wide slab model shows the onset of slab flattening in a late stage of the subduction process (~171 Myr), with the development of a concave-upward hinge in the slab at ~100–150 km depth. For the very wide slab model, the onset of slab flattening occurs earlier (~134 Myr) and flat slab subduction occurs in a late stage of subduction at 150–175 Myr with a brief intermittent period of ~4 Myr where the local slab dip exceeds 10°. **(B)** Model results of the wide slab model for one section located at 600 km from the nearest lateral slab edge and one section through the center of the subduction zone (3000 km from the lateral slab edges). The section near the lateral slab edge retains a relatively steep slab dip angle and shows no sign of slab flattening, in contrast to the central section. SSF-Start of slab flattening; SFSS-Start of flat slab subduction; EFSS-End of flat slab subduction.

within the natural range), then flat slab subduction in the very wide slab model would be reached earlier, at ~80–110 Myr rather than ~150 Myr. But note that stresses are not affected by any rescaling of velocities.

Stress in the Mantle Wedge and Sub-Slab Domain

The vertical deviatoric normal stress (σ_{YY}) in the mantle wedge and in the sub-slab domain has been plotted in **Figure 6** for models W600, W6000 and W-infinite. For all models it can be observed that σ_{YY} is mostly tensile in the mantle wedge near the top of the slab and compressive in the sub-slab domain near the base of the slab. Furthermore, σ_{YY} values are relatively small for the narrow slab model (**Figures 6A,B**), in particular in an advanced stage of subduction. Here, σ_{YY} is in the range −1.0 to 2.7 MPa at the slab top from the tip of the wedge down to 200 km depth and in the range −1.2 to 0.4 MPa at the base of the slab within the 100–200 km depth range. At an early stage of subduction σ_{YY} values are somewhat higher, with a maximum of ~4.0 MPa (tension) at the slab top and a minimum of about −1.9 MPa (compression) at the base of the slab.

For the very wide slab model, σ_{YY} values at an early subduction stage (**Figure 6G**) are comparable to those of the narrow slab model at the slab top with a maximum of ~4.0 MPa (tension), and are close to neutral (minimum of −0.2 MPa) at the base of the slab above 200 km depth. At an advanced subduction stage, however, σ_{YY} is generally much higher compared to the narrow slab model, with a maximum of ~7.5 MPa (tension) at the slab top and a minimum of about −2.0 MPa (compression) at the base (**Figure 6H**). For the wide slab model W6000, the stresses in the central section (**Figures 6E,F**) are comparable to those of W-infinite (**Figures 6G,H**), but the stresses in the section close to the lateral slab edge in a late stage of subduction (**Figure 6D**) are smaller.

DISCUSSION

Mechanism of Flat Slab Subduction in the Geodynamic Models

The major dip angle decrease for the wide and very wide slab models results from the large-scale whole mantle circulation they produce once the slabs enter the lower mantle. This flow drags the overriding plate trenchward, pushing the subduction hinge backward and forcing the overriding plate to thicken (Schellart, 2017) (forced hinge rollback or pushback, **Figures 4C,D**), while the slab itself resists rollback due to its great width (Schellart et al., 2007) and its partial anchoring in the lower mantle, thus attaining a progressively lower dip angle. The slab flattening that occurs in both models is facilitated by a relatively high effective suction force in the tip of the mantle wedge in a late stage of subduction. The very wide slab model with the 2D set-up, and thus an implied infinitely wide slab, develops the highest suction force in the tip that increases with time (**Figures 6G,H**), because lateral mantle inflow is absent, thereby facilitating flat slab formation. The wide slab model, despite its 6000 km width, allows for (minor) lateral mantle inflow around its lateral slab edges, reducing

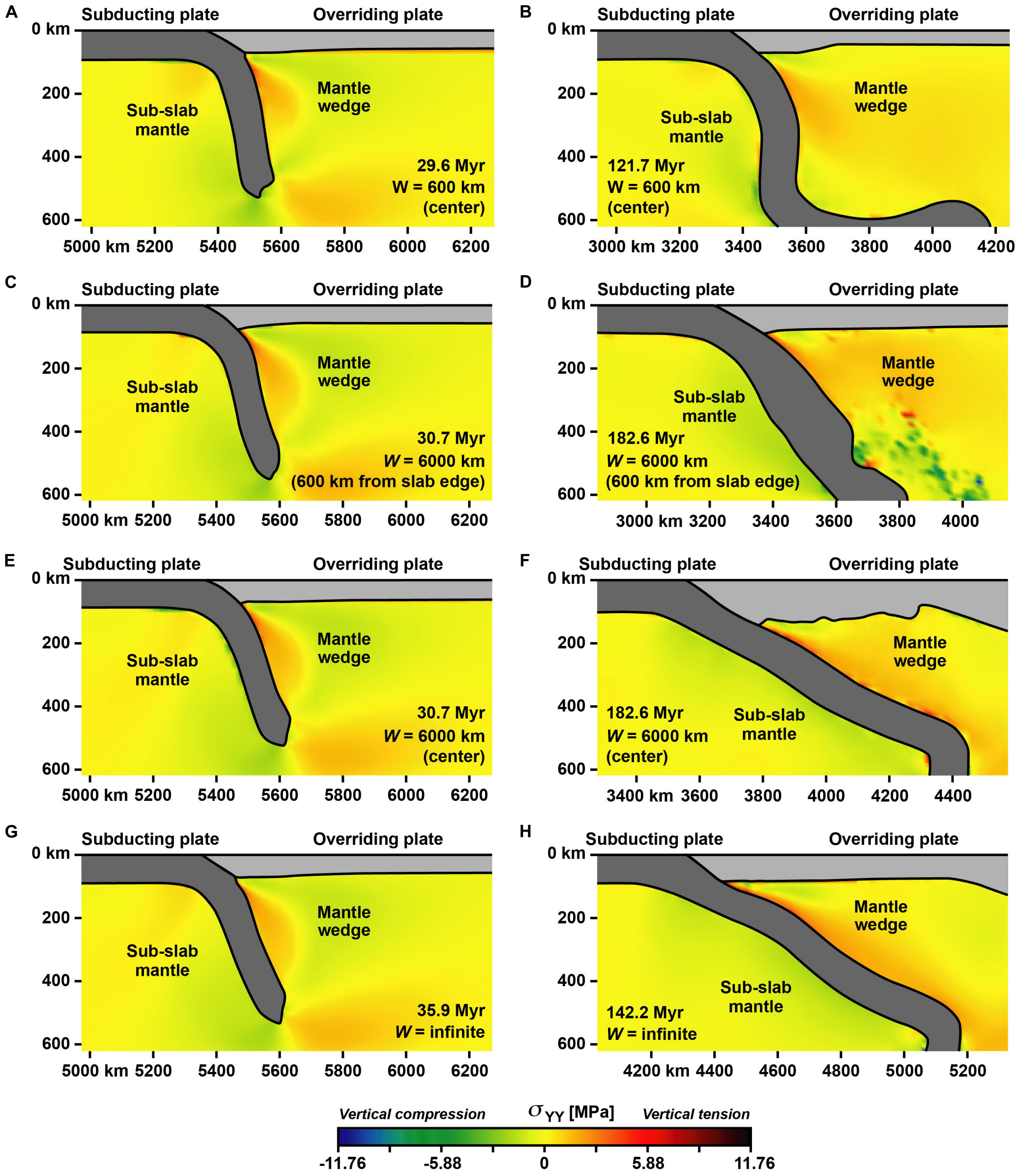

FIGURE 6 | Cross-sections through three numerical subduction models with a different slab width showing the vertical deviatoric normal stress (σ_{YY}) in the mantle wedge and sub-slab region at two stages during the subduction process (early and late stage). **(A,B)** Cross sections through the center of the narrow slab width model (*W* = 600 km) showing relatively low stresses at all times. **(C–F)** Wide slab model (*W* = 6000 km) with panels **C,D** for a section located 600 km from the closest lateral slab edge and panels **E,F** for a section located in the center of the subduction zone (3000 km from the lateral slab edges). Low stresses are observed in the early subduction stage **(C,E)**, intermediate stresses during a late stage near the lateral slab edge **(D)** and high stresses during a late stage in the center **(F)**. **(G,H)** Very wide slab model (*W* = infinite, 2D set-up) showing relatively low stresses in the early subduction stage **(G)** but high stresses in a late subduction stage **(H)**. Note that the short-wavelength structures in panel **(D)** (the dark green and red blobs at ~300–600 km depth in the mantle wedge and just below the base of the overriding plate) are formed by slab material from the lateral slab edge that has been advected into the mantle wedge by the rollback-induced toroidal upper mantle return flow. This toroidal flow, which is directed from the sub-slab and around the lateral slab edge into the mantle wedge (e.g., Schellart et al., 2007), has curved and sheared the slab edge into the mantle wedge and has also sheared off small fragments from the slab edge. Additionally, a consequence of the curvature is that the local trench orientation strikes at an oblique angle with respect to cross-section **(D)**. The slab edge material has a higher viscosity than the ambient upper mantle material and therefore shows higher deviatoric stresses than the ambient upper mantle material.

the wedge suction, and thus slab flattening develops more slowly (**Figure 5A**).

In case the slab is narrow or intermediate in width, slab rollback is directly driven by the negative buoyancy of the slab (slab-driven hinge rollback or pullback, **Figures 4A,B**) rather than being forced by the trenchward motion of the overriding plate, as is evident by the absence of overriding plate thickening but the presence of overriding plate thinning in these models. Rollback is facilitated by the presence of nearby lateral slab edges, which allow for efficient toroidal return flow from the sub-slab region toward the mantle wedge region (Dvorkin et al., 1993; Schellart et al., 2007), sustaining a relatively steep slab dip angle and lowering the suction in the mantle wedge. Indeed, σ_{YY} just above the top surface of the slab is significantly lower for a narrow slab (**Figure 6B**), which has two nearby lateral slab edges, than for the center of a wide slab (**Figure 6F**), which has two distant lateral slab edges, and for an infinitely wide slab (**Figure 6H**), which has no lateral slab edges. Furthermore, for trench segments of wide subduction zones located close to lateral slab edges, which only have one nearby lateral slab edge, σ_{YY} is intermediate to that of narrow slabs and wide slabs (**Figure 6**). What is more, the vertical slab lifting force (F_L) that results from σ_{YY} is about an order of magnitude larger for a very wide slab than for a narrow slab. For W600, this lifting force, calculated from the tip of the mantle wedge down to 200 km depth, is $\sim 1.5 \times 10^{11}$ N per meter trench length. Here, ~66% results from the vertical suction at the top of the slab, while ~34% results from vertical compressive stresses at the base of the slab. For the very wide slab model the vertical lifting force is $\sim 1.4 \times 10^{12}$ N per meter trench length, with ~76% resulting from the vertical suction at the slab top and ~24% from the vertical compressive stress at the base of the slab. F_L is also more significant for wide slabs when compared with the negative buoyancy force (F_{Bu}) of the same slab segment for which the lifting force has been calculated. For the very wide slab model $F_L/F_{Bu} = \sim 8.7\%$, while for the narrow slab model $F_L/F_{Bu} = \sim 1.7\%$.

The proposed important role of subduction zone size and age, and the proposed mechanism of slab-induced whole-mantle return flow in driving trenchward overriding plate motion, slab dip angle decrease and eventually slab flattening at wide subduction zones, can be reconciled with earlier modeling studies. Indeed, a number of earlier modeling works have advocated the important role of forced trench retreat (e.g., van Hunen et al., 2004; Manea et al., 2012), large wedge suction (e.g., Tovish et al., 1978; van Hunen et al., 2004; Manea et al., 2012; Rodríguez-González et al., 2012) and a thick overriding plate (e.g., Rodríguez-González et al., 2012) or far-field thick craton in the overriding plate (e.g., Manea et al., 2012; O'Driscoll et al., 2012; Taramón et al., 2015) in promoting flat slab subduction. The current work shows that, in a buoyancy-driven environment, forced trench retreat, large wedge suction and a thick overriding plate will develop in a wide subduction zone setting after a long period of subduction (of the order 100 Myr) once the slab tip has reached a significant depth in the lower mantle. The current work also shows that such features will not develop in a narrow or intermediate-width subduction zone setting, or close to lateral slab edges.

The mechanism for flat slab generation as proposed above requires a slab in nature to behave as a strong entity that is generally continuous from the surface to the lower mantle without major holes or tears in the upper mantle part of the slab. Indeed, it is generally thought that slab tearing can facilitate the collapse and removal of a flat slab (e.g., Hu and Liu, 2016; Schepers et al., 2017). For a strong and continuous slab, this requires natural slabs to have a greater viscosity than the ambient upper mantle, which is generally thought to be the case with slabs that are, on average, about 140–510 times (Ribe, 2010) or 100–700 times (Schellart, 2008) more viscous than the ambient mantle. The current models adopt comparable average viscosity ratios and slab deformation is accommodated through stretching, thickening, bending and buckling, not by slab tearing, thereby facilitating flat slab subduction. Another requirement is for slabs to be continuous from the surface down to the lower mantle, which is the case for a number of slabs in nature that include flat slab segments, as implied by mantle tomography studies. In particular, several tomography studies indicate that part of the Nazca slab subducting below South America continues down to ~2400 km (e.g., van der Meer et al., 2018), and that part of the Cocos slab subducting along the Mexico-Central America subduction zone continues down to ~2600–2800 km (e.g., Boschman et al., 2018).

Present-Day Flat Slabs in the Eastern Pacific

Flat slab subduction occurs in the Eastern Pacific in Peru, Central Chile, and Mexico and the proposed flat slab mechanism, involving a wide subduction zone ($\geq\sim$6000 km) and prolonged ($>\sim$80–110 Myr) subduction, applies to these examples (**Figure 2**). Indeed, they formed at the Farallon/South American subduction zone at a time when it had been active for a long period (since the Middle Triassic-Early Jurassic) (Burchfiel and Davis, 1975; Coira et al., 1982; Boschman et al., 2018) and when it was extremely wide (7000–13,000 km). The Altiplano flat slab that formed in the central Andes at ~35 Ma and terminated at ~25 Ma (Ramos and Folguera, 2009) can also be explained in this manner. Although the Mexico flat slab is currently part of an intermediate-width subduction zone (Mexico-Central America), at the time when this flat slab formed at 30–25 Ma, as implied by the inboard migration of arc magmatism (Ferrari et al., 1999; Morán-Zenteno et al., 1999; Kim et al., 2010), the subduction zone was very wide (~11,000 km) (**Table 1**).

There are also several subduction segments of the South American subduction zone and Mexico-Central America subduction zone that do not contain a flat slab, including the Colombia, Northern Chile, Southern Chile and Central America segments. This observation implies that an old and wide subduction zone is a requirement for flat slab subduction to occur, but it is not a guarantee that a flat slab will always be present. The observation is consistent with the geodynamic modeling results, which show that for the very wide slab model flat slab subduction is a transient phenomenon, for this model lasting some 25 Myr, and is preceded and succeeded by normal subduction. The transient nature of flat slab subduction is at least partly explained by the periodic folding of the slab at the 660 km discontinuity and the initiation of flat slab subduction is likely triggered by a new slab folding phase. Such folding is also responsible for the periodic dip angle changes (Schellart, 2017) that characterize each model (**Figure 5**). In nature, flat slab subduction at an old and wide subduction zone could also be triggered by a slab folding phase at the 660 km discontinuity, or it could be triggered by another process such as the initiation of subduction of an aseismic ridge or plateau.

Past Flat Slab Subduction

Latest Cretaceous-Early Cenozoic Flat Slab Subduction in Western North America

Flat slab subduction has been proposed for Western North America to explain the eastward migration of the magmatic arc and the eastward migration of the deformation front during cordilleran mountain building in the Late Cretaceous and Early Cenozoic (Henderson et al., 1984; DeCelles, 2004). Formation of the flat slab has been ascribed to the trenchward motion of the overriding North American plate and the subduction of aseismic ridges or oceanic plateaus (Henderson et al., 1984; Liu and Currie, 2016). The current work implies that flat slab subduction would not have been possible in the first place were it not for the extreme width (∼12,000 km) and longevity (∼110 Myr) of the subduction zone (**Figure 2**), and the large separation of the flat slab segment from lateral slab edges (**Table 1**).

Mid Triassic-Early Jurassic Flat Slab Subduction in South China

A model of flat slab subduction has been proposed to explain the broad intracontinental Mesozoic orogen in South China and the postorogenic magmatism in the region (Li and Li, 2007), with flat slab subduction starting in the mid Triassic (∼230 Ma) (Li and Li, 2007) along a subduction zone in the paleo Western Pacific. Reconstructions indicate that the subduction zone has been active since the mid Carboniferous (330 Ma) (Domeier and Torsvik, 2014) or Middle Devonian-Early Carboniferous (390–356 Ma) (Collins, 2003; Domeier and Torsvik, 2014). As such, the subduction zone had been active for 100–160 Myr when the flat slab developed along a subduction zone that was likely very wide (**Figure 2** and **Table 1**), which is consistent with the proposed mechanism.

Absence of Present-Day Flat Slabs in the Western Pacific and Elsewhere

The general absence of current flat slabs (i.e., with a slab geometry as in **Figure 1D**) in the Western Pacific, Indian Ocean, Atlantic Ocean, and Mediterranean can be explained by the lack of at least one of two crucial ingredients, namely subduction zone longevity and large slab width (**Figure 2**). There are three large subduction zones ($W \geq 4000$ km) in these regions, Sunda, Northwest Pacific and Melanesia (Schellart et al., 2007), but Sunda has been active only since the Middle Eocene (Hall, 2012), Northwest Pacific came into existence only after the Izu-Bonin-Mariana segment formed in the Early Eocene (Arculus et al., 2015), while Melanesia only formed in the Miocene (Hall, 2002; **Table 2**). Apart from these three subduction zones, the remaining ones in the Western Pacific, Atlantic, Indian Ocean and Mediterranean all have small or intermediate widths (Schellart et al., 2007). The lack of subduction zone longevity and/or large width did not allow for a significant decrease in slab dip angle (**Figure 5**) nor did it enhance suction forces (**Figures 6A–C,E**), thereby preventing subduction zones in these regions to form a flat slab. The lack of subduction zone longevity and/or large width also prevented those Western Pacific subduction zones subducting an aseismic ridge or plateau (e.g., d'Entrecasteaux Ridge at the New Hebrides subduction segment, Marcus-Necker Ridge at the Mariana-Bonin segment) to form a flat slab. This implies that buoyant ridge/plateau subduction is not sufficient on its own to cause flat slab subduction, in agreement with earlier work on Nazca Ridge subduction (Antonijevic et al., 2015). It is also consistent with recent geodynamic experiments of buoyancy-driven subduction with an aseismic ridge, indicating that subduction of a large ridge (e.g., Carnegie Ridge or Nazca Ridge) reduces the slab dip angle in the shallow part of the upper mantle by a mere ∼10° and does not produce flat slab subduction on its own (Flórez-Rodríguez et al., 2019).

CONCLUSION

The observational constraints (**Figure 2**) and models (**Figures 4–6**) imply that flat slab subduction dominantly initiates at wide subduction zones ($\geq \sim$6000 km) and only after a prolonged period of subduction ($\geq \sim$80–110 Myr). This finding is consistent with earlier works advocating the role of forced trench retreat, large wedge suction and a thick or cratonic overriding plate in promoting flat slab subduction (e.g., van Hunen et al., 2004; Manea et al., 2012, 2017; O'Driscoll et al., 2012; Rodríguez-González et al., 2012; Taramón et al., 2015; Schepers et al., 2017), because only in the center of wide subduction zones do forced trench retreat and overriding plate thickening develop in a late subduction stage, and is the effective wedge suction high. The conceptual model works for the proposed Laramide flat slab in western North America (Henderson et al., 1984; DeCelles, 2004), the Early Mesozoic South China flat slab (Li and Li, 2007), and the current flat slabs in the Eastern Pacific, as they developed at old and wide subduction zones (**Figure 2**). The finding can also explain the absence of present-day flat slabs in the Western Pacific, Indian Ocean, Atlantic Ocean and Mediterranean, because subduction zones here are either relatively young ($< \sim$80–110 Ma), less than ∼6000 km wide, or both. Subduction of a buoyant aseismic ridge or plateau in these regions will not induce flat slab subduction, as slabs in these regions will not have had sufficient time to reduce their dip angle at shallow depth and/or will not have a significant mantle wedge suction force due to the limited slab width. It thereby solves a longstanding debate on the lack of spatial correlation between ridge subduction and flat slab subduction in regions outside the Eastern Pacific.

DATA AVAILABILITY STATEMENT

All data and methods necessary to understand, evaluate, replicate, and build upon the reported research are presented in this article.

AUTHOR CONTRIBUTIONS

The author confirms being the sole contributor of this work and has approved it for publication.

FUNDING

This work has been funded by a Vici Fellowship (016.VICI.170.110) from the Dutch National Science Foundation (NWO), and has been supported by computational resources from the NCI National Facility in Australia through the National Computational Merit Allocation Scheme (project qk0).

ACKNOWLEDGMENTS

Discussions with and/or comments from Vincent Strak, Joao Duarte, Marc-Andre Gutscher, Douwe van Hinsbergen, Filipe Rosas, and Mélanie Gérault on subduction dynamics, subduction geology and flat slab subduction are greatly appreciated. I would like to thank the two reviewers for their constructive comments and suggestions, which have improved the contents and clarity of this paper. I would also like to thank Louis Moresi, Mirko Velic, Julian Giordani, John Mansour, and Owen Kaluza for technical support with, and development of, the Underworld code.

REFERENCES

Advokaat, E. L., Bongers, M. L. M., Rudyawan, A., BouDagher-Fadel, M. K., Langereis, C. G., and van Hinsbergen, D. J. J. (2018). Early Cretaceous origin of the Woyla arc (Sumatra, Indonesia) on the Australian plate. *Earth Planet. Sci. Lett.* 498, 348–361. doi: 10.1016/j.epsl.2018.07.001

Antonijevic, S. K., Wagner, L. S., Kumar, A., Beck, S. L., Long, M. D., Zandt, G., et al. (2015). The role of ridges in the formation and longevity of flat slabs. *Nature* 524, 212–215. doi: 10.1038/nature14648

Arculus, R. J., Ishizuka, O., Bogus, K. A., Gurnis, M., Hickey-Vargas, R., Aljahdali, M. H., et al. (2015). A record of spontaneous subduction initiation in the Izu–Bonin–Mariana arc. *Nat. Geosci.* 8, 728–733. doi: 10.1038/NGEO2515

Arredondo, K. M., and Billen, M. I. (2016). The effects of phase transitions and compositional layering in two-dimensional kinematic models of subduction. *J. Geodyn.* 100, 159–174. doi: 10.1016/j.jog.2016.05.009

Artyushkov, E. V. (1983). *Geodynamics*. Amsterdam: Elsevier.

Betts, P. G., Giles, D., Foden, J., Schaefer, B. F., Mark, G., Pankhurst, M. J., et al. (2009). Mesoproterozoic plume-modified orogenesis in eastern Precambrian Australia. *Tectonics* 28:TC3006. doi: 10.1029/2008TC002325

Boschman, L. M., van Hinsbergen, D. J. J., Kimbrough, D. L., Langereis, C. G., and Spakman, W. (2018). The dynamic history of 220 million years of subduction below Mexico: a correlation between slab geometry and overriding plate deformation based on geology, paleomagnetism, and seismic tomography. *Geochem. Geophys. Geosyst.* 19, 4649–4672. doi: 10.1029/2018GC007739

Boschman, L. M., van Hinsbergen, D. J. J., Torsvik, T. H., Spakman, W., and Pindell, J. L. (2014). Kinematic reconstruction of the Caribbean region since the Early Jurassic. *Earth Sci. Rev.* 138, 102–136. doi: 10.1016/j.earscirev.2014.08.007

Burchfiel, B. C., and Davis, G. A. (1975). Nature and controls of cordilleran orogenesis, western United States: extensions of an earlier synthesis. *Am. J. Sci.* 275, 363–396.

Burke, K. (1988). Tectonic evolution of the Caribbean. *Ann. Rev. Earth Planet. Sci.* 16, 201–230. doi: 10.1146/annurev.ea.16.050188.001221

Centeno-García, E. (2017). Mesozoic tectono-magmatic evolution of Mexico: an overview. *Ore Geol. Rev.* 81, 1035–1052. doi: 10.1016/j.oregeorev.2016.10.010

Chen, Y. W., Wu, J., and Suppe, J. (2019). Southward propagation of Nazca subduction along the Andes. *Nature* 565, 441–447. doi: 10.1038/s41586-018-0860-861

Chen, Z., Schellart, W. P., Strak, V., and Duarte, J. C. (2016). Does subduction-induced mantle flow drive backarc extension? *Earth Planet. Sci. Lett.* 441, 200–210. doi: 10.1016/j.epsl.2016.02.027

Coira, B., Davidson, J., Mpodozis, C., and Ramos, V. (1982). Tectonic and magmatic evolution of the Andes of northern Argentina and Chile. *Earth Sci. Rev.* 18, 303–332. doi: 10.1016/0012-8252(82)90042-3

Collins, W. J. (2003). Slab pull, mantle convection, and Pangaean assembly and dispersal. *Earth Planet. Sci. Lett.* 205, 225–237. doi: 10.1016/s0012-821x(02)01043-9

Copeland, P., Currie, C. A., Lawton, T. F., and Murphy, M. A. (2017). Location, location, location: the variable lifespan of the Laramide orogeny. *Geology* 45, 223–226. doi: 10.1130/G38810.1

DeCelles, P. G. (2004). Late Jurassic to Eocene evolution of the Cordilleran thrust belt and foreland basin system Western U.S.A. *Am. J. Sci.* 304, 105–168. doi: 10.2475/ajs.304.2.105

Deschamps, A., and Lallemand, S. (2002). The West Philippine Basin: an Eocene to early Oligocene back arc basin opened between two opposed subduction zones. *J. Geophys. Res.* 107:2322. doi: 10.1029/2001JB001706

Dickinson, W. R., and Snyder, W. S. (1978). Plate tectonics of the Laramide orogeny. *Geol. Soc. Am. Mem.* 151, 355–366. doi: 10.1130/mem151-p355

Dilek, Y., and Sandvol, E. (2009). "Seismic structure, crustal architecture and tectonic evolution of the Anatolian–African Plate Boundary and the Cenozoic Orogenic Belts in the Eastern Mediterranean Region," in *Ancient Orogens and Modern Analogues*, eds J. B. Murphy, J. D. Keppie, and A. J. Hynes (Bath: The Geological Society of London), 127–160. doi: 10.1144/SP327.8

Domeier, M., and Torsvik, T. H. (2014). Plate tectonics in the Late Paleozoic. *Geosci. Front.* 5, 303–350. doi: 10.1016/j.gsf.2014.01.002

Dvorkin, J., Nur, A., Mavko, G., and Ben-Avraham, Z. (1993). Narrow subducting slabs and the origin of backarc basins. *Tectonophysics* 227, 63–79. doi: 10.1016/0040-1951(93)90087-z

Eagles, G., and Jokat, W. (2014). Tectonic reconstructions for paleobathymetry in Drake Passage. *Tectonophysics* 611, 28–50. doi: 10.1016/j.tecto.2013.11.021

Ferrari, L., López-Martínez, M., Aguirre-Díaz, G., and Carrasco-Núñez, G. (1999). Space-time patterns of Cenozoic arc volcanism in central Mexico: from the Sierra Madre Occidental to the Mexican Volcanic Belt. *Geology* 27, 303–306.

Flórez-Rodríguez, A. G., Schellart, W. P., and Strak, V. (2019). Impact of aseismic ridges on subduction systems: insights from analog modeling. *J. Geophys. Res. Solid Earth* 124, 5951–5969. doi: 10.1029/2019JB017488

Ganguly, J., Freed, A. M., and Saxena, S. K. (2009). Density profiles of oceanic slabs and surrounding mantle: integrated thermodynamic and thermal modeling, and implications for the fate of slabs at the 660 km discontinuity. *Phys. Earth Planet. Inter.* 172, 257–267. doi: 10.1016/j.pepi.2008.10.005

Gordon, R. G., and Jurdy, D. M. (1986). Cenozoic global plate motions. *J. Geophys. Res.* 91, 12389–12406. doi: 10.1029/jb091ib12p12389

Gutscher, M. A., Spakman, W., Bijwaard, H., and Engdahl, E. R. (2000). Geodynamics of flat subduction: seismicity and tomographic constraints from the Andean margin. *Tectonics* 19, 814–833. doi: 10.1029/1999tc001152

Hall, R. (2002). Cenozoic geological and plate tectonic evolution of SE Asia and the SW Pacific; computer-based reconstructions, model and animations. *J. Asian Earth Sci.* 20, 353–431. doi: 10.1016/s1367-9120(01)00069-4

Hall, R. (2012). Late Jurassic–Cenozoic reconstructions of the Indonesian region and the Indian Ocean. *Tectonophysics*. 570-571, 1–41. doi: 10.1016/j.tecto.2012.04.021

Hastie, A. R., Mitchell, S. F., Treloar, P. J., Kerr, A. C., Neill, I., and Barfod, D. N. (2013). Geochemical components in a Cretaceous island arc: the Th/La–(Ce/Ce*)$_{Nd}$ diagram and implications for subduction initiation in the inter-American region. *Lithos* 162, 57–69. doi: 10.1016/j.lithos.2012.12.001

Hayes, G. P., Wald, D. J., and Johnson, R. L. (2012). Slab1.0: a three-dimensional model of global subduction zone geometries. *J. Geophys. Res.* 117:B01302. doi: 10.1029/2011JB008524

Henderson, L. J., Gordon, R. G., and Engebretson, D. C. (1984). Mesozoic aseismic ridges on the Farallon plate and southward migration of shallow subduction during the Laramide orogeny. *Tectonics* 3, 121–132. doi: 10.1029/tc003i002p00121

Hu, J., and Liu, L. (2016). Abnormal seismological and magmatic processes controlled by the tearing South American flat slabs. *Earth Planet. Sci. Lett.* 450, 40–51. doi: 10.1016/j.epsl.2016.06.019

Hu, J., Liu, L., Hermosillo, A., and Zhou, Q. (2016). Simulation of Late Cenozoic South American flat-slab subduction using geodynamic models with data assimilation. *Earth Planet. Sci. Lett.* 438, 1–13. doi: 10.1016/j.epsl.2016.01.011

Ishizuka, O., Tani, K., Reagan, M. K., Kanayama, K., Umino, S., Harigane, Y., et al. (2011). The timescales of subduction initiation and subsequent evolution of an oceanic island arc. *Earth Planet. Sci. Lett.* 306, 229–240. doi: 10.1016/j.epsl.2011.04.006

Jarrard, R. D. (1986). Relations among subduction parameters. *Rev. Geophys.* 24, 217–284.

Jicha, B. R., Scholl, D. W., Singer, B. S., and Yogodzinski, G. M. (2006). Revised age of Aleutian Island Arc formation implies high rate of magma production. *Geology* 34, 661–664. doi: 10.1130/G22433.1

Kay, S. M., and Abbruzzi, J. M. (1996). Magmatic evidence for Neogene lithospheric evolution of the Central Andean "flat-slab" between 30°S and 32°S. *Tectonophysics* 259, 15–28. doi: 10.1016/0040-1951(96)00032-7

Kim, Y., Clayton, R. W., and Jackson, J. M. (2010). Geometry and seismic properties of the subducting cocos plate in Central Mexico. *J. Geophys. Res.* 115:B06310. doi: 10.1029/2009JB006942

Kincaid, C., and Olson, P. (1987). An experimental study of subduction and slab migration. *J. Geophys. Res.* 92, 812–813.

Kreemer, C., Holt, W. E., and Haines, A. J. (2003). An integrated global model of present-day plate motions and plate boundary deformation. *Geophys. J. Inter.* 154, 8–34. doi: 10.1046/j.1365-246x.2003.01917.x

Lallemand, S., Font, Y., Bijwaard, H., and Kao, H. (2001). New insights on 3-D plates interaction near Taiwan from tomography and tectonic implications. *Tectonophysics* 335, 229–253. doi: 10.1016/s0040-1951(01)00071-3

Lallemand, S., Heuret, A., and Boutelier, D. (2005). On the relationship between slab dip, back-arc stress, upper plate absolute motion, and crustal nature in subduction zones. *Geochem. Geophys. Geosyst.* 6:Q09006. doi: 10.1029/2005GC000917

Larter, R. D., Vanneste, L. E., Morris, P., and Smythe, D. K. (2003). "Structure and tectonic evolution of the South Sandwich arc," in *Intra-Oceanic Subduction Systems: Tectonic and Magmatic Processes*, eds R. D. Larter, and P. T. Leat (Bath: The Geological Society of London), 255–284. doi: 10.1144/gsl.sp.2003.219.01.13

LeBrun, J. F., Lamarche, G., and Collot, J. Y. (2003). Subduction initiation at a strike-slip plate boundary: the Cenozoic Pacific-Australian plate boundary, south of New Zealand. *J. Geophys. Res.* 108:2453. doi: 10.1029/2002JB002041

Li, C. F., Xu, X., Lin, J., Sun, Z., Zhu, J., Yao, Y., et al. (2014). Ages and magnetic structures of the South China Sea constrained by deep tow magnetic surveys and IODP Expedition 349. *Geochem. Geophys. Geosyst.* 15, 4958–4983. doi: 10.1002/2014GC005567

Li, Z. X., and Li, X. H. (2007). Formation of the 1300-km-wide intracontinental orogen and postorogenic magmatic province in Mesozoic South China: a flat-slab subduction model. *Geology* 35, 179–182. doi: 10.1130/G23193A.1

Liu, L., Gurnis, M., Seton, M., Saleeby, J., Muller, R. D., and Jackson, J. M. (2010). The role of oceanic plateau subduction in the Laramide orogeny. *Nat. Geosci.* 3, 353–357. doi: 10.1038/NGEO829

Liu, S., and Currie, C. A. (2016). Farallon plate dynamics prior to the Laramide orogeny: numerical models of flat subduction. *Tectonophysics* 666, 33–47. doi: 10.1016/j.tecto.2015.10.010

Lonergan, L., and White, N. (1997). Origin of the Betic-Rif mountain belt. *Tectonics* 16, 504–522. doi: 10.1029/96tc03937

Lonsdale, P. (2005). Creation of the Cocos and Nazca plates by fission of the Farallon plate. *Tectonophysics* 404, 237–264. doi: 10.1016/j.tecto.2005.05.011

Mackaman-Lofland, C., Horton, B. K., Fuentes, F., Constenius, K. N., and Stockli, D. F. (2019). Mesozoic to Cenozoic retroarc basin evolution during changes in tectonic regime, southern Central Andes (31–33°S): insights from zircon U-Pb geochronology. *J. South Am. Earth Sci.* 89, 299–318. doi: 10.1016/j.jsames.2018.10.004

Mackwell, S. J., Bai, Q., and Kohlstedt, D. L. (1990). Rheology of olivine and the strength of the lithosphere. *Geophys. Res. Lett.* 17, 9–12. doi: 10.1029/gl017i001p00009

Maloney, K. T., Clarke, G. L., Klepeis, K. A., and Quevedo, L. (2013). The Late Jurassic to present evolution of the Andean margin: drivers and the geological record. *Tectonics* 32, 1049–1065. doi: 10.1002/tect.20067

Manea, V. C., Manea, M., Ferrari, L., Orozco-Esquivel, T., Valenzuela, R. W., Husker, A., et al. (2017). A review of the geodynamic evolution of flat slab subduction in Mexico, Peru, and Chile. *Tectonophysics* 695, 27–52. doi: 10.1016/j.tecto.2016.11.037

Manea, V. C., Pérez-Gussinyé, M., and Manea, M. (2012). Chilean flat slab subduction controlled by overriding plate thickness and trench rollback. *Geology* 40, 35–38. doi: 10.1130/G32543.1

Meffre, S., Falloon, T. J., Crawford, T. J., Hoernle, K., Hauff, F., Duncan, R. A., et al. (2012). Basalts erupted along the Tongan fore arc during subduction initiation: evidence from geochronology of dredged rocks from the Tonga fore arc and trench. *Geochem. Geophys. Geosyst.* 13:Q12003. doi: 10.1029/2012GC004335

Mériaux, C. A., Mériaux, A. S., Schellart, W. P., Duarte, J. C., Duarte, S. S., and Chen, Z. (2016). Mantle plumes in the vicinity of subduction zones. *Earth Planet. Sci. Lett.* 454, 166–177. doi: 10.1016/j.epsl.2016.09.001

Morán-Zenteno, D. J., Tolson, G., Martínez-Serrano, R. G., Martiny, B., Schaaf, P., Silva-Romo, G., et al. (1999). Tertiary arc-magmatism of the Sierra Madre del Sur, Mexico, and its transition to the volcanic activity of the trans-Mexican Volcanic Belt. *J. South Am. Earth Sci.* 12, 513–535. doi: 10.1016/s0895-9811(99)00036-x

Moresi, L., Quenette, S., Lemiale, V., Mériaux, C., Appelbe, B., and Mühlhaus, H. B. (2007). Computational approaches to studying non-linear dynamics of the crust and mantle. *Phys. Earth Planet. Inter.* 163, 69–82. doi: 10.1016/j.pepi.2007.06.009

Müller, R. D., Seton, M., Zahirovic, S., Williams, S. E., Matthews, K. J., Wright, N. M., et al. (2016). Ocean basin evolution and global-scale plate reorganization events since Pangea breakup. *Ann. Rev. Earth Planet. Sci.* 44, 107–138. doi: 10.1146/annurev-earth-060115-12211

O'Driscoll, L. J., Richards, M. A., and Humphreys, E. D. (2012). Nazca–South America interactions and the late Eocene–late Oligocene flat-slab episode in the Central Andes. *Tectonics* 31:TC2013. doi: 10.1029/2011TC003036

Ohta, Y., Freymueller, J. T., Hreinsdóttir, S., and Suito, H. (2006). A large slow slip event and the depth of the seismogenic zone in the south central Alaska subduction zone. *Earth Planet. Sci. Lett.* 247, 108–116. doi: 10.1016/j.epsl.2006.05.013

Phillips, K., and Clayton, R. W. (2014). Structure of the subduction transition region from seismic array data in southern Peru. *Geophys. J. Inter.* 196, 1889–1905. doi: 10.1093/gji/ggt504

Pilger, R. H. (1981). Plate reconstructions, aseismic ridges, and low-angle subduction beneath the Andes. *Geol. Soc. Am. Bull.* 92, 448–456.

Pindell, J., Kennan, L., Stanek, K. P., Maresch, W. V., and Draper, G. (2006). Foundations of Gulf of Mexico and Caribbean evolution: eight controversies resolved. *Geol. Acta* 4, 303–341.

Ramos, V. A., and Folguera, A. (2009). "Andean flat-slab subduction through time," in *Ancient Orogens and Modern Analogues*, eds J. B. Murphy, J. D. Keppie, and A. J. Hynes (Bath: The Geological Society of London), 31–54. doi: 10.1144/SP327.3

Ranalli, G. (1995). *Rheology of the Earth*, 2nd Edn, London: Chapman and Hall.

Ribe, N. M. (2010). Bending mechanics and mode selection in free subduction: a thin-sheet analysis. *Geophys. J. Inter.* 180, 559–576. doi: 10.1111/j.1365-246X.2009.04460.x

Richards, S., Holm, R., and Barber, G. (2011). When slabs collide: a tectonic assessment of deep earthquakes in the Tonga-Vanuatu region. *Geology* 39, 787–790. doi: 10.1130/G31937.1

Rodríguez-González, J., Negredo, A. M., and Billen, M. I. (2012). The role of the overriding plate thermal state on slab dip variability and on the occurrence of flat subduction. *Geochem. Geophys. Geosyst.* 13:Q01002. doi: 10.1029/2011GC003859

Rosenbaum, G., Giles, D., Saxon, M., Betts, P. G., Weinberg, R. F., and Duboz, C. (2005). Subduction of the Nazca Ridge and the Inca Plateau: insights into the formation of ore deposits in Peru. *Earth Planet. Sci. Lett.* 239, 18–32. doi: 10.1016/j.epsl.2005.08.003

Rosenbaum, G., Lister, G. S., and Duboz, C. (2002). Reconstruction of the tectonic evolution of the Western Mediterranean since the Oligocene. *J. Virt. Explor.* 8, 107–130.

Sarma, D. S., Jafri, S. H., Fletcher, I. R., and McNaughton, N. J. (2010). Constraints on the tectonic setting of the Andaman ophiolites, Bay of Bengal, India, from SHRIMP U-Pb zircon geochronology of plagiogranite. *J. Geol.* 118, 691–697. doi: 10.1086/656354

Schellart, W. P. (2008). Kinematics and flow patterns in deep mantle and upper mantle subduction models: influence of the mantle depth and slab to mantle viscosity ratio. *Geochem. Geophys. Geosyst.* 9:Q03014. doi: 10.1029/2007GC001656

Schellart, W. P. (2017). Andean mountain building and magmatic arc migration driven by subduction-induced whole mantle flow. *Nat. Commun.* 8:2010. doi: 10.1038/s41467-017-01847-z

Schellart, W. P., Freeman, J., Stegman, D. R., Moresi, L., and May, D. (2007). Evolution and diversity of subduction zones controlled by slab width. *Nature* 446, 308–311. doi: 10.1038/nature05615

Schellart, W. P., Jessell, M. W., and Lister, G. S. (2003). Asymmetric deformation in the backarc region of the Kuril arc, northwest Pacific: new insights from analogue modeling. *Tectonics* 22:1047. doi: 10.1029/2002TC001473

Schellart, W. P., Lister, G. S., and Toy, V. G. (2006). A Late Cretaceous and Cenozoic reconstruction of the Southwest Pacific region: tectonics controlled by subduction and slab rollback processes. *Earth Sci. Rev.* 76, 191–233. doi: 10.1016/j.earscirev.2006.01.002

Schellart, W. P., and Spakman, W. (2012). Mantle constraints on the plate tectonic evolution of the Tonga-Kermadec-Hikurangi subduction zone and the South Fiji Basin. *Austr. J. Earth Sci.* 59, 933–952. doi: 10.1080/08120099.2012.679692

Schellart, W. P., Stegman, D. R., Farrington, R. J., Freeman, J., and Moresi, L. (2010). Cenozoic tectonics of western North America controlled by evolving width of Farallon slab. *Science* 329, 316–319. doi: 10.1126/science.1190366

Schepers, G., van Hinsbergen, D. J. J., Spakman, W., Kosters, M. E., Boschman, L. M., and McQuarrie, N. (2017). South-American plate advance and forced Andean trench retreat as drivers for transient flat subduction episodes. *Nat. Commun.* 8:15249. doi: 10.1038/ncomms15249

Scheuber, E., Bogdanic, T., Jensen, A., and Reutter, K. J. (1994). "Tectonic development of the North Chilean Andes in relation to plate convergence and magmatism since the Jurassic," in *Tectonics of the Southern Central Andes*, eds K.-J. Reutter, E. Scheuber, and P. J. Wigger (Berlin: Springer), 121–139. doi: 10.1007/978-3-642-77353-2_9

Scholl, D. W., Vallier, T. L., and Stevenson, A. J. (1986). Terrane accretion, production, and continental growth: a perspective based on the origin and tectonic fate of the Aleutian-Bering Sea region. *Geology* 14, 43–47.

Sdrolias, M., Roest, W. R., and Muller, R. D. (2004). An expression of Philippine Sea plate rotation: the Parece Vela and Shikoku Basins. *Tectonophysics* 394, 69–86. doi: 10.1016/j.tecto.2004.07.061

Séranne, M. (1999). "The gulf of Lion continental margin (NW Mediterranean) revisited by IBS: an overview," in *The Mediterranean Basins: Tertiary Extension Within the Alpine Orogen*, eds B. Durand, L. Jolivet, F. Horváth, and M. Séranne (London: Geological Society), 15–36. doi: 10.1144/gsl.sp.1999.156.01.03

Seton, M., Müller, R. D., Zahirovic, S., Gaina, C., Torsvik, T., Shephard, G., et al. (2012). Global continental and ocean basin reconstructions since 200 Ma. *Earth Sci. Rev.* 113, 212–270. doi: 10.1016/j.earscirev.2012.03.002

Skinner, S. M., and Clayton, R. W. (2011). An evaluation of proposed mechanisms of slab flattening in central Mexico. *Pure Appl. Geophys.* 168, 1461–1474. doi: 10.1007/s00024-010-0200-203

Skinner, S. M., and Clayton, R. W. (2013). The lack of correlation between flat slabs and bathymetric impactors in South America. *Earth Planet. Sci. Lett.* 37, 1–5. doi: 10.1016/j.epsl.2013.04.013

Spakman, W., and Hall, R. (2010). Surface deformation and slab–mantle interaction during Banda arc subduction rollback. *Nat. Geosci.* 3, 562–566. doi: 10.1038/NGEO917

Stadler, G., Gurnis, M., Burstedde, C., Wilcox, L. C., Alisic, L., and Ghattas, O. (2010). The dynamics of plate tectonics and mantle flow: from local to global scales. *Science* 329, 1033–1038. doi: 10.1126/science.1191223

Stegman, D. R., Freeman, J., Schellart, W. P., Moresi, L., and May, D. (2006). Influence of trench width on subduction hinge retreat rates in 3-D models of slab rollback. *Geochem. Geophys. Geosyst.* 7:Q03012. doi: 10.1029/2005GC001056

Taramón, J. M., Rodríguez-González, J., Negredo, A. M., and Billen, M. I. (2015). Influence of cratonic lithosphere on the formation and evolution of flat slabs: insights from 3-D time-dependent modeling. *Geochem. Geophys. Geosyst.* 16, 2933–2948. doi: 10.1002/2015GC005940

Torii, Y., and Yoshioka, S. (2007). Physical conditions producing slab stagnation: constraints of the Clapeyron slope, mantle viscosity, trench retreat, and dip angles. *Tectonophysics* 445, 200–209. doi: 10.1016/j.tecto.2007.08.003

Tovish, A., Schubert, G., and Luyendyk, B. P. (1978). Mantle flow pressure and the angle of subduction: non-Newtonian corner flows. *J. Geophys. Res.* 83, 5892–5898. doi: 10.1029/jb083ib12p05892

van de Lagemaat, S. H. A., van Hinsbergen, D. J. J., Boschman, L. M., Kamp, P. J. J., and Spakman, W. (2018). Southwest Pacific absolute plate kinematic reconstruction reveals major Cenozoic Tonga-Kermadec slab dragging. *Tectonics* 37, 2647–2674. doi: 10.1029/2017TC004901

van der Meer, D. G., van Hinsbergen, D. J. J., and Spakman, W. (2018). Atlas of the underworld: slab remnants in the mantle, their sinking history, and a new outlook on lower mantle viscosity. *Tectonophysics* 723, 309–448. doi: 10.1016/j.tecto.2017.10.004

van Hinsbergen, D. J. J., Hafkenscheid, E., Spakman, W., Meulenkamp, J. E., and Wortel, R. (2005). Nappe stacking resulting from subduction of oceanic and continental lithosphere below Greece. *Geology* 33, 325–328.

van Hinsbergen, D. J. J., Vissers, R. L. M., and Spakman, W. (2014). Origin and consequences of Western Mediterranean subduction, rollback, and slab segmentation. *Tectonics* 33, 393–419. doi: 10.1002/tect.20125

van Hunen, J., Van Den Berg, A. P., and Vlaar, N. J. (2002). On the role of subducting oceanic plateaus in the development of shallow flat subduction. *Tectonophysics* 352, 317–333. doi: 10.1016/s0040-1951(02)00263-9

van Hunen, J., van den Berg, A. P., and Vlaar, N. J. (2004). Various mechanisms to induce present-day shallow flat subduction and implications for the younger earth: a numerical parameter study. *Phys. Earth Planet. Inter.* 146, 179–194. doi: 10.1016/j.pepi.2003.07.027

Vásquez, P., Glodny, J., Franz, G., Frei, D., and Romer, R. L. (2011). Early Mesozoic plutonism of the Cordillera de la Costa (34°–37°S), Chile: constraints on the onset of the Andean orogeny. *J. Geol.* 119, 159–184. doi: 10.1086/658296

Vérard, C., Flores, K., and Stampfli, G. (2012). Geodynamic reconstructions of the South America–Antarctica plate system. *J. Geodyn.* 53, 43–60. doi: 10.1016/j.jog.2011.07.007

Wortel, M. J. R., and Spakman, W. (2000). Subduction and slab detachment in the Mediterranean-Carpathian region. *Science* 290, 1910–1917. doi: 10.1126/science.290.5498.1910

Conflict of Interest: The author declares that the research was conducted in the absence of any commercial or financial relationships that could be construed as a potential conflict of interest.

APPENDIX

Justification for Data Selection and Uncertainties Associated With the Data

There are uncertainties associated with the data presented in **Tables 1**, **2** that are used as a basis for **Figure 2**. For the present-day slab width values listed in **Table 2**, the uncertainties are relatively small, in general less than 5–10%, which will therefore have no discernable impact on the data distribution as shown in **Figure 2A**. Uncertainties with estimated slab width values for the geological past will be larger and are generally hard to quantify, as they mostly result from differences in plate tectonic configurations in the published literature. For the relatively narrow subduction zones listed in **Table 2** (numbers 6–14) the uncertainties can be up to several hundred kilometers, but this will have no discernable impact on the general distribution of data points in **Figure 2A**. For the slab width data of the other subduction zones, which have a moderate to very large width (numbers 1–5 and 15–22) there are larger uncertainties. These subduction zones generally also have a larger associated uncertainty in subduction zone age, or a subduction zone age that is more controversial. Below, each of these subduction zones will be briefly discussed and a justification for the choice of subduction zone age and width is provided.

South American Subduction Zone (Points 1a-f and 3 in Figure 2 and Tables 1, 2)

The age of the South American subduction zone has long been interpreted as very old, around 200 Ma, and thus dating from the Late Triassic/Early Jurassic (e.g., Coira et al., 1982; Vásquez et al., 2011; Maloney et al., 2013). This old age has very recently been contested by Chen et al. (2019), who argue for an 80 Ma subduction zone in the north, becoming progressively younger southward. The young age for the South American subduction zone proposed by Chen et al. (2019) is in contradiction with geological data showing a continuous arc magmatic record from the Jurassic to the present (~200–0 Ma), such as reported for northern Chile (Scheuber et al., 1994). It is also in contradiction with seismic tomographic data presented in van der Meer et al. (2018), which show a continuous slab from the trench down to 2400 ± 200 km depth in the Peru segment of the South American subduction zone, which they interpreted as subduction being active from 200–173 Ma (Jurassic) to the present. Recent work on sedimentary systems in the retroarc and arc region in the southern Central Andes also imply continuous subduction activity since the Late Triassic/Early Jurassic (e.g., Mackaman-Lofland et al., 2019). Based on these different lines of evidence, I adopt an old age (~200 Ma) for the South American subduction zone.

Tectonic reconstructions show that at ~200 Ma the entire western margin of the South American continent was an east-dipping subduction zone and generally also show it to be continuous with the Mexico-Central America segment (e.g., Seton et al., 2012). This gives a subduction zone width of the order 11,000 ± 1000 km.

For data points 1a, 1b and 1c, the flat slab formed at ~4, ~8, and ~20 Ma and so formed when the Nazca plate had already separated from the Cocos plate, which occurred at ~23 Ma (Lonsdale, 2005). Thus the width of the subduction zone was roughly the north-south length of the western margin of South America, which is of the order 7000 km. The flat slab for data point 3 formed at ~35 Ma, so before Nazca-Cocos separation, and so the slab width at that time was roughly the sum of the South American subduction zone width and the width of the Baja California-Mexico-Central America segment.

Mexico-Central America Subduction Zone (Points 2a and 2b in Figure 2 and Tables 1, 2)

The Mexican flat slab formed at ~30–25 Ma (Ferrari et al., 1999; Morán-Zenteno et al., 1999; Kim et al., 2010), and the Cocos spreading ridge separating the Cocos plate from the Nazca plate formed only at ~23 Ma (Lonsdale, 2005). Thus, the Nazca + Cocos single plate subducted eastward as one very large slab, most likely along one continuous subduction zone at 30–25 Ma that would be ~10,500–12,000 km wide (some 7000 km for the South American subduction segment and some 3000–5000 km for the Mexico-Central America segment). This is consistent with tectonic reconstructions (e.g., Gordon and Jurdy, 1986; Seton et al., 2012; Müller et al., 2016).

Recent work indicates that at least the Mexico-Central America subduction segment has been active for a very long time. Indeed, according to Boschman et al. (2018) there is a continuous record of subduction since 220 Ma along the Mexico-Central America subduction zone, as indicated by a continuous slab geometry from the surface down to 2500–2800 km depth in seismic tomography models. According to van der Meer et al. (2018) this old subduction zone had a large lateral extent, stretching from the Cocos ridge in the south to the Mendocino triple junction in the north (their page 351), which would imply a subduction zone extent of ~5800 km. This width is used as a lower limit of the slab width of the subduction zone during its formation. As an upper limit the reconstruction of Seton et al. (2012) is used, which shows a continuous subduction zone from Mexico in the north to Patagonia in the south at 200 Ma, which would thus imply an ~11,000 km wide subduction zone at a time close to its inception.

Another reconstruction, that of Müller et al. (2016), shows a different tectonic setting in the Mexico-Central America-Caribbean region with a subduction flip and ~west-dipping subduction at ~130–90 Ma, which would not be consistent with the current work and that of Seton et al. (2012). The recent work of Boschman et al. (2018), however, can be used to refute the proposed tectonic scenario from Müller et al. (2016), as it shows a long and continuous subducted slab, from the surface down to ~2500–2800 km depth, which implies long-lived continuous east-dipping subduction along the Central America-Mexico subduction zone.

South China Subduction Zone (Point 4 in Figure 2 and Table 1)

The age of inception and the width of the South China subduction zone have been derived from the reconstruction papers of

Collins (2003) and Domeier and Torsvik (2014). It is clear that there are large uncertainties associated with the estimated age and width, because we are concerned with subduction that was active in the Paleozoic and Triassic, and flat slab subduction that started in the Triassic (Li and Li, 2007). Despite these large uncertainties, the results are consistent with the conceptual model proposed in the paper (**Figure 2A**).

Farallon Subduction Zone (Points 5 and 15 in Figure 2 and Tables 1, 2)

The Farallon subduction zone is generally thought to have been a very large, east-dipping subduction zone along the west coast of the Americas that subducted the Farallon oceanic plate during part of the Mesozoic and the Early Cenozoic (Burchfiel and Davis, 1975; Gordon and Jurdy, 1986; DeCelles, 2004). Earlier work indicates that the subduction zone is very old and formed in the Triassic or Jurassic (160–210 Ma) (Burchfiel and Davis, 1975; DeCelles, 2004), and relatively recent reconstructions imply a comparably old age (e.g., Seton et al., 2012). Such reconstructions also imply a very large subduction zone extent during subduction zone infancy exceeding 10,000 km (Seton et al., 2012). Only at ∼45–30 Ma, significantly after the inception of Farallon flat slab formation at ∼85–65 Ma (Henderson et al., 1984; Liu et al., 2010; Copeland et al., 2017), do reconstructions show that the Farallon plate, slab and subduction zone segment due to the formation of slab windows (Gordon and Jurdy, 1986; Schellart et al., 2010), resulting in the formation of a relatively small Farallon/Juan de Fuca plate subducting along the Cascadia subduction zone and a much larger Nazca-Cocos plate.

Nankai-Ryukyu Subduction Zone (Point 16 in Figure 2 and Table 2)

The Nankai-Ryukyu subduction zone likely formed in the earliest Miocene (∼18 Ma) through subduction of the Philippine Sea plate below Eurasia (Lallemand et al., 2001). When the subduction zone formed, it was initially narrower (∼1600 km) and from ∼8 Ma it grew southwestward to include the southern Ryukyu subduction segment (Lallemand et al., 2001).

Lesser Antilles-Puerto Rico Subduction Zone (Point 17 in Figure 2 and Table 2)

The age and the subduction zone width at the time of subduction zone formation of the Lesser Antilles subduction zone are somewhat controversial. The minimum age of 45 Ma is based on the oldest ages of Lesser Antilles arc magmatism (Burke, 1988). There is a ∼50 Ma age based on a reconstruction of Boschman et al. (2014), a 71–94 Ma age based on reported ages of arc magmatism from Hispaniola (Hastie et al., 2013), and a ∼120 Ma age as argued and shown in a reconstruction in Pindell et al. (2006). van der Meer et al. (2018) estimate the age using tomography and geological data and propose subduction initiation at 45–55 Ma for the lesser Antilles. Estimates of subduction zone width at subduction initiation vary significantly, as shown in tectonic reconstructions, including ∼1400 km (Boschman et al., 2014) and ∼3300 km (Pindell et al., 2006). Considering the controversy, the average is taken for both the subduction zone age and width.

Tonga-Kermadec-Hikurangi Subduction Zone (Point 18 in Figure 2 and Table 2)

The subduction zone age and the width at the time of the Tonga-Kermadec-Hikurangi subduction zone formation are somewhat controversial as well. The minimum age is generally based on the oldest ages of fore-arc magmatism in the Tonga arc (49–51 Ma) (Meffre et al., 2012) and reconstructions that adhere to this relatively young formation age imply that the subduction zone width during initiation was relatively small (1800 ± 800 km) (Meffre et al., 2012). More recently, an even younger minimum age has been suggested for the formation of the subduction zone (∼30 Ma) based on the termination of the New Caledonia subduction zone around that time (van de Lagemaat et al., 2018). This very young age is not likely, though, as backarc spreading in the North Loyalty Basin and South Fiji Basin was already active before 30 Ma. Reconstructions from Schellart et al. (2006) show a subduction zone that was already active at 90 Ma, as implied by convergence between the Australian plate and the Pacific plate, with a large width (∼5000 km) that incorporates the Tonga-Kermadec-Hikurangi segment and the Vitiaz-Solomon segment. Due to the uncertainty and controversy regarding the slab width at subduction initiation and time of subduction initiation, an average between that of Meffre et al. (2012) and Schellart et al. (2006) has been taken.

Aleutians-Alaska Subduction Zone (Point 19 in Figure 2 and Table 2)

It is generally agreed upon that the Aleutians-Alaska subduction zone formed sometime in the Early Cenozoic as based on ages of the oldest arc magmatic rocks in the Aleutian Islands, with an older age of ∼55 Ma suggested earlier (Scholl et al., 1986) and a younger age (∼46 Ma) suggested more recently (Jicha et al., 2006). The younger age is here taken as the best estimate of the true age. The Aleutians segment is thought to have formed in an intra-oceanic setting and was limited in the west by the Shirshov Ridge, after which the subduction zone grew westward to form a cusp with the Kuril-Kamchatka arc (Schellart et al., 2003). Hence, the subduction zone had a smaller width (by ∼500 km) at subduction initiation than its present width.

Melanesia Subduction Zone (Point 20 in Figure 2 and Table 2)

It is generally agreed upon that the Melanesia subduction zone is very young and formed in the Late Cenozoic, around 10–15 Ma (Hall, 2002; Schellart et al., 2006; Richards et al., 2011). In the short time since 15 Ma it has grown to a relatively wide subduction zone with a width of ∼4400 km (Schellart et al., 2007).

Northwest Pacific Subduction Zone (Points 21, 21a, and 21b in Figure 2 and Table 2)

The width of the Northwest Pacific subduction zone, or Kamchatka-Kuril-Japan-Izu-Bonin-Mariana subduction zone, is very large, ∼6550 km, but it formed rather recently due to the conjoining of the Izu-Bonin-Mariana segment and the Kamchatka-Kuril-Japan segment. The former segment formed around 52 Ma, as implied by dated forearc magmatic rocks

(Ishizuka et al., 2011), while the latter segment formed at ∼60 Ma, after accretion of the Okhotsk terrane to Eurasia (Schellart et al., 2003). A maximum age of subduction zone formation is thus 52 Ma (assuming that the two segments conjoined immediately, which is not very likely due to the difference in strike of the two segments at that time), while a minimum age of subduction zone formation is based on a reconstruction of Sdrolias et al. (2004), who show that the two segments connected at ∼25 Ma.

Sunda Subduction Zone (Points 22, 22a, and 22b in Figure 2 and Table 2)

The width of the slab subducting at the Sunda subduction zone is very large, ∼7850 km, as it includes the Burma-Andaman segment, the Sumatra-Java-Bali-Nusa segment and the Timor-Banda segment (Schellart et al., 2007). These individual segments, however, formed at different times. The Andaman subduction segment likely started around 94 Ma based on supra-subduction-zone ophiolites of this age, as dated by Sarma et al. (2010) and interpreted as such by Advokaat et al. (2018), but this subduction segment is only ∼1400 km wide (∼3150 km if one includes the Burma segment). The central segment of the Sunda subduction zone (Sumatra-Java-Bali-Nusa), which is ∼3300 km wide, formed at ∼50–45 Ma (Hall, 2012), while the easternmost segment (Banda segment), which is ∼1400 km wide, formed only at ∼15 Ma (Spakman and Hall, 2010). So from ∼94–50 Ma the slab was ∼3150 km wide, from ∼50–15 Ma it was ∼6450 km wide, and from ∼15–0 Ma it was ∼7850 km wide. As such, it acquired its large width only very recently.

frontiers
in Earth Science

ORIGINAL RESEARCH
published: 07 May 2020
doi: 10.3389/feart.2020.00117

2-D Numerical Simulations on Formation and Descent of Stagnant Slabs: Important Roles of Trench Migration and Its Temporal Change

Mana Tsuchida and Masanori Kameyama*

Geodynamics Research Center, Ehime University, Matsuyama, Japan

We conducted numerical simulations of thermal convection of highly viscous fluids in a 2-D spherical annulus in order to study what mechanisms control the dynamic behaviors of subducting slabs such as the formation of “stagnant slabs” in the mantle transition zone (MTZ) and their descent into the lower mantle. Two series of experiments are carried out, by applying the different histories of migrating motion of “trench” where the slab of cold fluids descends from the top surface, together with systematically varying the velocities of subducting slabs and trench migration, the Clapeyron slope at around 660 km depth, and the viscosity jump between the upper and lower mantle. In the first series of experiments where the migration rate of trench is kept constant with time, our model successfully reproduces the diverse morphology of subducting slabs depending on the delicate combinations of control parameters, including five fundamental types named penetration, accumulation, entrainment, long-term stagnation and short-term stagnation (SS). In addition to the above fundamental types, we found two distinctive types of slab behaviors (named pS and cS) where the slabs are stagnated at the base of MTZ after they experience the penetration or collapse into the lower mantle and yield the snapshot behaviors very close to those of SS at some time instances. In the second series of experiments where we imposed a step-like change in the trench retreat velocity with time, we found that a deceleration of trench retreat enhances the collapse of the horizontally-lying or stagnant slabs into the lower mantle by, for example, inducing the avalanche of stagnant slabs from its hinge. In particular, we obtained in some cases the flattening of slabs well below the 660 km discontinuity without any discontinuous changes in mantle properties at the depth. Our results suggest that the formation and descent of stagnant slabs are strongly related to the trench retreat, particularly through its temporal changes. In other words, the variations in the shapes of subducting slabs in nature are most likely to reflect the difference in the history of trench migration.

Keywords: numerical simulation, mantle convection, stagnant slab, trench retreat, subduction zone

Edited by:
Jeroen Van Hunen,
Durham University, United Kingdom

Reviewed by:
Hana Cizkova,
Charles University, Czechia
Ikuro Sumita,
Kanazawa University, Japan

****Correspondence:***
Mana Tsuchida
tsuchida@sci.ehime-u.ac.jp

Specialty section:
This article was submitted to
Solid Earth Geophysics,
a section of the journal
Frontiers in Earth Science

Received: *31 January 2020*
Accepted: *27 March 2020*
Published: *07 May 2020*

Citation:
Tsuchida M and Kameyama M (2020)
2-D Numerical Simulations on
Formation and Descent of Stagnant
Slabs: Important Roles of Trench
Migration and Its Temporal Change.
Front. Earth Sci. 8:117.
doi: 10.3389/feart.2020.00117

1. INTRODUCTION

Seismic tomography studies (e.g., Fukao and Obayashi, 2013) have revealed that the slabs of subducted plates show diverse behaviors in the mantle beneath various subduction zones. In several regions such as Japan and Izu-Bonin arc, for example, so-called “stagnant slabs” are observed at the base of the mantle transition zone (MTZ), without penetrating into the lower mantle owing to the horizontal flattening at around the 660 km discontinuity. In other subduction zones where (parts of) the slabs have entered into the lower mantle, not all slabs can reach the deep lower mantle readily and smoothly as observed in, for example, beneath Central America arc: It is now recognized that in some regions subducted slabs seem to be stagnated at about 1,000 km depths (e.g., Java arc), experiencing a stagnation at the MTZ and penetration into the lower mantle simultaneously (e.g., Tonga arc), or stagnating at the MTZ before collapsing from its hinge (e.g., Mariana arc).

Since the numerical studies of mantle convection first arose (e.g., McKenzie et al., 1973), the dynamic behaviors of subducted plates in the mantle have been intensively studied, particularly focusing on the mechanisms of the formation of stagnant slabs in the MTZ. Christensen (1996) developed a 2-D numerical model in Cartesian geometry which incorporates the effects of an endothermic phase boundary and viscosity jump at the 660 km discontinuity together with imposed motions of subducting plate and trench at the surface, and reported that the trench retreat plays an important role in flattening of subducting slabs at the base of MTZ. Torii and Yoshioka (2007) systematically studied the influence of these physical parameters on the formation of stagnant slabs, and showed that stagnant slabs can be generated in realistic parameter ranges. These numerical models are further improved by many workers through incorporating other complicated factors such as the effects of the age of the subducting and overriding plate (Garel et al., 2014), the viscosity reduction in slabs due to the grain-size reduction (Čížková et al., 2002; Nakakuki et al., 2010), the presence of metastable phase transitions in the cold slabs (Tetzlaff and Schmeling, 2000; Agrusta et al., 2014).

In addition to the dynamics of the slabs at the base of MTZ, a growing number of numerical studies have been conducted on the avalanche of the subducting slabs into the lower mantle. Yoshioka and Naganoda (2010) carried out numerical experiments in a 2-D box model with imposed surface velocity, and pointed out that the trench advance and trench jumps cause the eventual fall of stagnant slabs into the lower mantle as proposed by van der Hilst and Seno (1993). Agrusta et al. (2017) used a 2-D self-consistent subduction models to investigate the transition between the stagnation and penetration of slabs, and have revealed that these transitions are strongly influenced by many agents such as the temporal changes in trench retreat velocity, the Clapeyron slope at the 660 km discontinuity, the subducting plate age, and so on. On the other hand, recent numerical models of the subduction in the Mariana arc (e.g., Čížková and Bina, 2015; Faccenna et al., 2018) suggested the double subduction system as a possible mechanism that triggers the change from trench retreat to trench advance in this region.

In this study, we will further develop numerical model of subducted slabs in the convecting mantle using 2-D model in spherical annulus, in order to study what mechanisms control the behaviors of subducted slabs in the mantle at various depths, such as the formation of stagnant slabs in the MTZ and the course of its avalanche into the lower mantle. Compared with earlier works, we will perform numerical calculations by varying the values of control parameters systematically over broad ranges. As our initial attempt to study the effects of various parameters, we will follow the strategy by Torii and Yoshioka (2007) and focus on the effects of trench migration rate and its temporal change. By carefully comparing the shapes of slabs obtained in our simulation models with those estimated from seismic tomography, we aim at deepening the understanding on the dynamics and temporal evolutions of subducting slabs in the mantle.

2. MODEL DESCRIPTION

2.1. Model Setup

Our numerical model is schematically shown in **Figure 1A**. We consider thermal convection of mantle materials which is driven

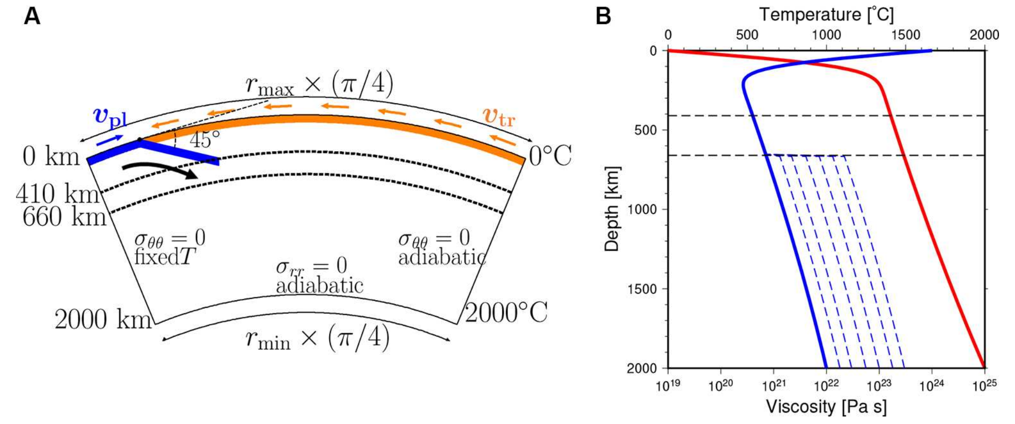

FIGURE 1 | (A) A schematic figure of our 2-D numerical model in a spherical annulus. The blue segment indicates the channel of cold fluid as a model of subducting plate. The maximum depth of its upper plane is 400 km. The orange segment shows the overriding plate. The dashed lines are the phase boundaries around 410 and 660 km. **(B)** The initial depth distribution of temperature T (red line) and viscosity η (blue lines). The horizontal axes show the viscosity (bottom) and the temperature (top), and the vertical axis shows the depth. The blue solid line indicates the viscosity calculated by Equation (1) with $r_\eta = 1$, and blue dashed lines indicate those with $r_\eta = 1.8$, 3, 5.6, 10, 18, and 30, respectively.

by a subducting and retreating motion of a cold slab in one eighth (azimuth $\theta_{\min} \leq \theta \leq \theta_{\max}$ where $\theta_{\max} - \theta_{\min} = 45^\circ$) of a two-dimensional spherical annulus whose outer and inner radii are $r_{\max} = 6,400$ km and $r_{\min} = 4,400$ km, respectively. We take into account the effects of the phase transition from olivine to wadsleyite at around 410 km depth and that from ringwoodite to bridgmanite and ferro-periclase at around 660 km depth. The density contrasts associated with these phase transitions are taken to be 8.3 and 7.8%, respectively (Dziewonski and Anderson, 1981). The Clapeyron slope of the phase transition at 410 km depth is taken to be $\gamma^{410} = +3$ MPa/K, while that of 660 km depth γ^{660} is varied from -3 MPa/K or -1 MPa/K, based on the result of laboratory experiments (e.g., Ito and Takahashi, 1989; Katsura et al., 2003; Fei et al., 2004). The meanings and values of parameters used in this study are given in **Table 1**.

The viscosity η of mantle material is assumed to depend exponentially on the temperature T and pressure p (or the depth from the top surface), and given by

$$\eta = \eta_{\text{surf}} \exp\left[-E_T \frac{T - T_{\text{surf}}}{\Delta T} + E_p \frac{r_{\max} - r}{r_{\max} - r_{\min}}\right] f(\Gamma_{660}) \quad (1)$$

where $T_{\text{surf}} = 0^\circ$C is the temperature at the top surface, r ($r_{\min} \leq r \leq r_{\max}$) is the distance from the center of the Earth, η_{surf} is the viscosity at the top surface ($r = r_{\max}$ and $T = T_{\text{surf}}$), ΔT is the temperature scale which is arbitrarily chosen to be $2,000^\circ$C, and $E_T = \ln(10^6)$ and $E_p = \ln(10^4)$ express temperature and depth dependence of the viscosity. In addition, the effect of the viscosity jump between the upper and lower mantle is introduced by $f(\Gamma^{660})$ through the "phase function" Γ^{660} of the endothermic phase transition at around 660 km depth (Christensen and Yuen, 1985); $f(\Gamma^{660})$ is taken to be 1 and r_η in the upper and lower mantle, respectively. Here, we assume the value of r_η to be $1 \leq r_\eta \leq 30$ (see **Figure 1B**) as had been employed in earlier studies (e.g., Torii and Yoshioka, 2007; Yoshioka and Naganoda, 2010; Kameyama and Nishioka, 2012).

In this study, the kinematic motions of subducting and overriding plates are imposed near the top surface, as in our earlier work (Kameyama and Nishioka, 2012). First, as in the works by Yoshioka and coworkers (Yoshioka and Sanshadokoro, 2002; Torii and Yoshioka, 2007; Yoshioka and Naganoda, 2010), the subducting plate is modeled by a downward flow of cold and viscous fluid at a uniform velocity v_{pl} along with a channel of 80 km thick which guides the cold fluid from the top surface into the MTZ. The channel is bent downward with the dip angle 45° at the trench which is located $\theta_{tr} = 5.625^\circ$ away from the left-side of the top surface ($\theta = \theta_{\max}$). In addition, the length of the channel is assumed to increase with time, in order to model the descent of cold slab. The maximum depth of the upper plane of the 80 km thick channel is taken to be 400 km. Second, we take into account the effect of trench retreat by the similar method as van Hunen et al. (2000). Here the overriding plate is assumed to migrate together with the trench and channel at a rate of v_{tr} in the horizontal direction with respect to the deep mantle. That is, the effect of trench migration is numerically implemented through the coordinate transformation between the two "reference frames" which laterally moves with respect to each other at the angular velocity $\omega_{tr} \equiv \dfrac{v_{tr}}{r_{\max}}$.

TABLE 1 | Meanings and values of symbols in this study.

Symbols	Meaning	Values
ρ	Reference density	3.3×10^3 kg/m^3
ΔT	Temperature scale	$2,000$ K
d	Model thickness	$2,000$ km
α	Thermal expansivity	2×10^{-5} K^{-1}
C_p	Specific heat	1.029×10^3 J/kgK
κ	Thermal diffusivity	1×10^{-6} m^2/s
η_{surf}	Reference viscosity	1×10^{24} Pa s
g	Gravitational acceleration	9.8 m/s^2

In the present numerical model, the rate of plate convergence v_c at the trench is given by the sum of the subducting plate velocity (v_{pl}) and the overriding plate velocity (v_{tr}).

$$v_c \equiv v_{pl} + v_{tr} \quad (2)$$

When non-dimensionalized using a velocity scale of $v_{\text{scale}} \equiv \kappa/(r_{\max} - r_{\min})$ (where $\kappa = 10^{-6}$ m^2/s is thermal diffusivity), the dimensionless rate of plate convergence $v_c' = v_c/v_{\text{scale}}$ is kept to be $5,000$ throughout this study, while that of trench migration $v_{tr}' = v_{tr}/v_{\text{scale}}$ are changed from 0 to $3,000$. That is, $v_c = 7.88$ cm/yr and $v_{tr} \leq 4.73$ cm/yr are employed.

The initial distribution of temperature T is given by

$$T(\theta, r) = (T_{\text{surf}} - T_{\text{pot}}) \operatorname{erfc}\left[\frac{r_{\max} - r}{2\sqrt{\kappa \tau(\theta)}}\right] + T_{\text{pot}} \exp\left[\frac{\alpha g (r_{\max} - r)}{C_p}\right] \quad (3)$$

where $T_{\text{pot}} = 1280^\circ$C is the potential temperature of the mantle, α is thermal expansivity, and C_p is specific heat. In the right-hand side, the first and second terms represent the effects of half-space cooling (Turcotte and Schubert, 2002) and adiabatic compression (**Figure 1B**), respectively. In this equation, $\tau(\theta)$ is the age of plate as a function of the horizontal position θ. At the trench ($\theta = \theta_{\max} - \theta_{tr}$), $\tau(\theta)$ is taken to be τ_{pl} (=101Ma). On the other hand, $\tau(\theta)$ decreases with θ in the oceanic region ($\theta \geq \theta_{\max} - \theta_{tr}$), while $\tau(\theta) = \tau_{pl}$ is fixed in the continental region ($\theta \leq \theta_{\max} - \theta_{tr}$).

The boundary conditions for temperature T are (i) fixed temperature $T = T_{\text{surf}} = 0^\circ$C at the top surface ($r = r_{\max}$), (ii) fixed temperature at the left boundary ($\theta = \theta_{\max}$) in order to maintain the initial thermal structure of subducting oceanic plate given by Equation (3), and (iii) adiabatic conditions at the bottom ($r = r_{\min}$) and right ($\theta = \theta_{\min}$) boundaries. On the other hand, the boundary conditions for velocity $\boldsymbol{v}$ are given by (i) $v_r = 0$ and fixed v_θ at the top surface, (ii) $v_r = 0$ and $\dfrac{\partial v_\theta}{\partial \theta} = 0$ at the both side boundaries ($\theta = \theta_{\min}, \theta_{\max}$) and (iii) $v_\theta = 0$ and $\dfrac{\partial v_r}{\partial r} = 0$ at the bottom boundary, where v_θ and v_r are θ- and r-components of the velocity, respectively. That is, no slip condition is assumed at the top surface, while at the other boundaries the flow is taken to be perpendicular to the boundaries and zero normal stress. In addition, the condition

$$\int_{r=r_{\min}}^{r=r_{\max}} v_\theta \, dr = 0 \tag{4}$$

is imposed at the right-hand side wall so as to keep the net mass flux zero across the boundary.

2.2. Numerical Techniques

We calculate the flow field, the distributions of temperature T and their temporal variations by solving the governing equations for conservations of mass, momentum and the thermal energy under the extended Boussinesq approximation (Christensen and Yuen, 1985). The conservation of the thermal energy includes the effects of adiabatic heating and latent heat due to the phase transitions. However, the effect of viscous dissipation (or frictional heating) is ignored in this study, in order to avoid a spuriously high dissipation near the trench where the channel is sharply bent in an artificial manner. The equations for conservation of mass and momentum are written in terms of the stream function ψ defined by

$$v_r \equiv \frac{1}{r}\frac{\partial \psi}{\partial \theta}, \quad v_\theta \equiv -\frac{\partial \psi}{\partial r} \tag{5}$$

instead of directly solving for the velocity $\boldsymbol{v}$ and pressure p. On the other hand, the time integration of energy equation is carried out by the Crank-Nicolson scheme.

The discretization of the basic equations are carried out based on the finite volume method. The region is uniformly divided into 256 and 640 meshes in r- and θ-directions, respectively. This pattern of mesh division yields almost square numerical meshes near the top surface. The discretized equations for temperature T and flow fields (velocity $\boldsymbol{v}$ and pressure p) are solved by our thermal convection simulation code for 2-D spherical annulus (Kameyama and Harada, 2017). The numerical validity of our code has been already verified by comparing with previous study (Zhong and Gurnis, 1993). The time increment δt is taken to be the half of the value determined from the numerical stability of energy equation, yielding $\delta t \sim 1.6 \times 10^4$ years. We confirmed that δt defined thus is small enough, by comparing the numerical results for several cases with the ones done using smaller time increments by factors of 0.5 and 0.25. The time integrations are carried out for more than 100 million years (My) for all the cases presented here, and for up to 150 My in some cases where the slab stagnation is observed (see below for details).

3. RESULTS

Two series of experiments are presented in this study, using different histories of the migrating motion of trench. In the first series of experiments, we carried out calculations where the rate v_{tr} of trench retreat is assumed to be constant with time. In the second series of experiments, on the other hand, we take into account the temporal changes in v_{tr}, by imposing its step-like change with time.

TABLE 2 | Cases and results of numerical simulations without time change in v_{tr}.

Case	Type	Case	Type	Case	Type
TR0H1G−3	P	TR0H1G−2	P	TR0H1G−1	P
TR1.58H1G−3	cS	TR1.58H1G−2	pS	TR1.58H1G−1	pS
TR3.15H1G−3	LS	TR3.15H1G−2	SS	TR3.15H1G−1	pS
TR4.73H1G−3	LS	TR4.73H1G−2	LS	TR4.73H1G−1	pS
TR0H1.8G−3	P	TR0H1.8G−2	P	TR0H1.8G−1	P
TR1.58H1.8G−3	cS	TR1.58H1.8G−2	pS	TR1.58H1.8G−1	pS
TR3.15H1.8G−3	LS	TR3.15H1.8G−2	SS	TR3.15H1.8G−1	pS
TR4.73H1.8G−3	LS	TR4.73H1.8G−2	LS	TR4.73H1.8G−1	SS
TR0H3G−3	P	TR0H3G−2	P	TR0H3G−1	P
TR1.58H3G−3	cS	TR1.58H3G−2	pS	TR1.58H3G−1	pS
TR3.15H3G−3	LS	TR3.15H3G−2	LS	TR3.15H3G−1	pS
TR4.73H3G−3	LS	TR4.73H3G−2	LS	TR4.73H3G−1	SS
TR0H5.6G−3	P	TR0H5.6G−2	P	TR0H5.6G−1	P
TR1.58H5.6G−3	cS	TR1.58H5.6G−2	pS	TR1.58H5.6G−1	pS
TR3.15H5.6G−3	LS	TR3.15H5.6G−2	LS	TR3.15H5.6G−1	SS
TR4.73H5.6G−3	F	TR4.73H5.6G−2	F	TR4.73H5.6G−1	F
TR0H10G−3	P	TR0H10G−2	P	TR0H10G−1	P
TR1.58H10G−3	SS	TR1.58H10G−2	pS	TR1.58H10G−1	pS
TR3.15H10G−3	LS	TR3.15H10G−2	LS	TR3.15H10G−1	LS
TR4.73H10G−3	F	TR4.73H10G−2	F	TR4.73H10G−1	F
TR0H18G−3	A	TR0H18G−2	A	TR0H18G−1	A
TR1.58H18G−3	LS	TR1.58H18G−2	LS	TR1.58H18G−1	pS
TR3.15H18G−3	F	TR3.15H18G−2	F	TR3.15H18G−1	F
TR4.73H18G−3	F	TR4.73H18G−2	F	TR4.73H18G−1	F
TR0H30G−3	A	TR0H30G−2	A	TR0H30G−1	A
TR1.58H30G−3	LS	TR1.58H30G−2	LS	TR1.58H30G−1	LS
TR3.15H30G−3	F	TR3.15H30G−2	F	TR3.15H30G−1	F
TR4.73H30G−3	F	TR4.73H30G−2	F	TR4.73H30G−1	F

The cases are denoted by TRv_{tr}Hr_ηGγ^{660} in this table, where v_{tr} is the rate of trench retreat in cm/yr, r_η is the viscosity jump between the upper and lower mantle, and γ^{660} is the Clapeyron slope at the 660 km discontinuity in MPa/K.

3.1. Slab Behaviors Under Constant Rate of Trench Retreat

In the first series of experiments, we investigate the subduction dynamics obtained from a series of 84 numerical experiments where we systematically varied the values of viscosity jump r_η between the upper and lower mantle, Clapeyron slope γ^{660} at 660 km discontinuity, and the rate v_{tr} of trench retreat (see **Table 2**). The velocity v_{pl} of subducting plate is accordingly varied in order to fix the rate of plate convergence v_c at the trench. We here note that, rather than v_{pl}, v_c controls the amount of the slab of cold fluid which is "injected" into the mantle during the period of calculation. In other words, for all the cases with fixed v_c presented here, the effects of negative buoyancy of cold slabs are equal at the same elapsed times from the onset of subduction.

3.1.1. The Effects of Control Parameters on Slab Dynamics

We first discuss the effects of the control parameters in this study (r_η, γ^{660}, and v_{tr}) on the behaviors and shapes of subducting slab around the MTZ and in the lower mantle. In **Figure 2**

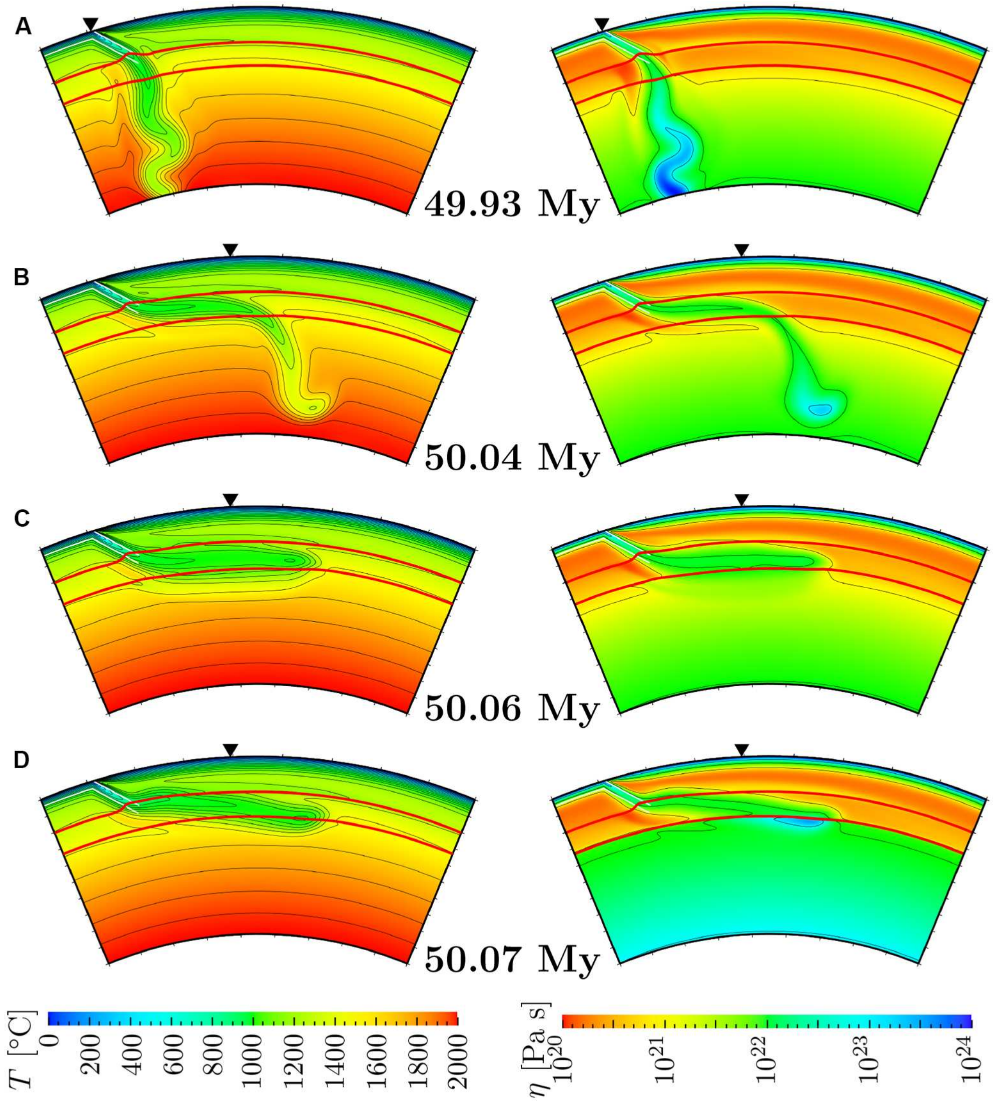

FIGURE 2 | Snapshots of the distribution of temperature T (left) and viscosity η (right) at around 50 My after the initiation of subduction for **(A)** reference case ($v_{tr} = 0$ cm/yr, $r_\eta = 1$, γ^{660} =-1 MPa/K), **(B)** case with lager trench retreat velocity ($v_{tr} = 3.15$ cm/yr, $r_\eta = 1$, γ^{660} =-1 MPa/K), **(C)** case with steeper negative Clapeyron slope ($v_{tr} = 3.15$ cm/yr, $r_\eta = 1$, γ^{660} =-3 MPa/K), and **(D)** case with larger viscosity jump ($v_{tr} = 3.15$ cm/yr, $r_\eta = 10$, γ^{660} =-1 MPa/K). The values of temperature T are shown in colors with the contour lines at 1,000, 1,100, 1,200, 1,300, 1,400, 1,500, 1,600, 1,700, 1,800, and 1,900 [°C], and the values of viscosity η are shown in colors with contour lines at 10^{20}, 10^{21}, 10^{22}, 10^{23}, and 10^{24} [Pa s]. The color scales are shown at the bottom of figure. The red lines indicate the phase boundaries around 410 km and 660 km, while the thin white lines indicate the channel of the cold descending fluid. In each figure, the initial positions of trench are indicated by the black triangles.

we show the snapshots of the distributions of temperature T and viscosity η at the elapsed time of about 50 million years (My) after the onset of subduction, obtained for four selected cases from the first series of calculations. Shown in **Figure 2A** are the snapshots of the case where we employed $r_\eta = 1$, $\gamma^{660} = -1$ MPa/K, and $v_{tr} = 0$ cm/yr. As can be clearly seen from the figure, a slab of cold and viscous fluid is subducting through the channel down to the top of MTZ (see the phase transition at around 410 km depth indicated by the upper red lines). The slab further sinks across the phase transition at around 660 km depth (indicated by the lower red lines), and finally penetrates into the lower mantle directly and smoothly.

In order to see the influence of the trench retreat, we show in **Figure 2B** the snapshot of the case where a non-zero rate of trench retreat is given ($v_{tr} = 3.15$ cm/yr) while the values of other parameters are the same as those in **Figure 2A**. By comparing **Figure 2B** and **Figure 2A** we can clearly see that the trench retreat enhances the flattening and stagnation of subducted slabs. Indeed, a horizontally-lying portion of cold slab can be observed in the MTZ in **Figure 2B**, which is in a stark contrast to the case in **Figure 2A**. However, as can be seen from **Figure 2B**, the entire portion of subducted slab is not stagnated around the 660 km depth; the tip of cold slab penetrates and sinks in the lower mantle. This indicates that the combined effect of v_{tr} = 3.15 cm/yr and γ^{660} = −1 MPa/K (and r_η =1) employed in this case is not strong enough for the entire cold slab to be stagnated.

We next present the snapshots of **Figures 2C,D** in order to see the influences of γ^{660} and r_η under a non-zero v_{tr}. Shown in **Figures 2C,D** are the cases where a steeper $\gamma^{660} = -3$ MPa/K and a larger jump $r_\eta = 10$ in viscosity is employed at the 660 km discontinuity than those in **Figure 2B**, respectively, while the values of other parameters are kept unchanged. We can clearly see that, from the comparison with **Figure 2B**, the entire portion of subducted slab stagnates at the 660 km discontinuity, either because of a positive buoyancy in the cold slab induced by the phase transition with strongly negative Clapeyron slope γ^{660} (in **Figure 2C**) or because of a strong viscous resistance coming from highly viscous lower mantle with large r_η (in **Figure 2D**). These results are consistent with the earlier findings by Torii and Yoshioka (2007) that classified the manner of slab stagnation into buoyancy-dominated and viscosity-dominated regimes.

Our results with 2-D spherical annulus showed that all of the control parameters in this study (the viscosity jump r_η and Clapeyron slope γ^{660} at the 660 km discontinuity, and the rate v_{tr} of trench retreat) enhances the slab stagnation at the base of MTZ. Among them, r_η and γ^{660} tend to prevent subducting slabs from penetrating into the lower mantle, whereas v_{tr} flattens the subducted slabs at around the MTZ. These results are consistent with those of earlier numerical studies in the 2-D box model (e.g, Torii and Yoshioka, 2007; Kameyama and Nishioka, 2012). The close similarity between the results of our experiments and earlier ones also suggests that the effect of the Earth's curvature is minor on the dynamic behavior of slabs in the shallow mantle.

3.1.2. Five Fundamental Types of Slab Behaviors

Our systematic calculations of 84 cases showed that there are five fundamental types for the behaviors of subducted slabs at around the MTZ, depending on the combinations of three control parameters (r_η, γ^{660}, and v_{tr}). **Figure 3** shows the temporal development of the five types of subducting slab behaviors. In **Table 2** and **Figure 4**, on the other hand, we summarize the classification of subducting slab behaviors for all 84 cases.

Among the five types of slab behaviors, first three are the ones where subducted slabs are not stagnated at the base of MTZ owing to extreme choices of control parameters other than γ^{660}. **Figure 3A** shows the "penetration" (P)-type behavior of slabs. The P-type is characterized by the penetration of cold slabs into the lower mantle immediately and vertically. This type of behavior is observed for 15 cases out of 84 calculations, and occurs for v_{tr} = 0 and small r_η ($r_\eta \leq 10$). On the other hand, **Figure 3B** shows the "accumulation" (A)-type behavior of slabs. In the A-type, subducted slabs do not penetrate into the lower mantle but accumulate at around the 660 km discontinuity,

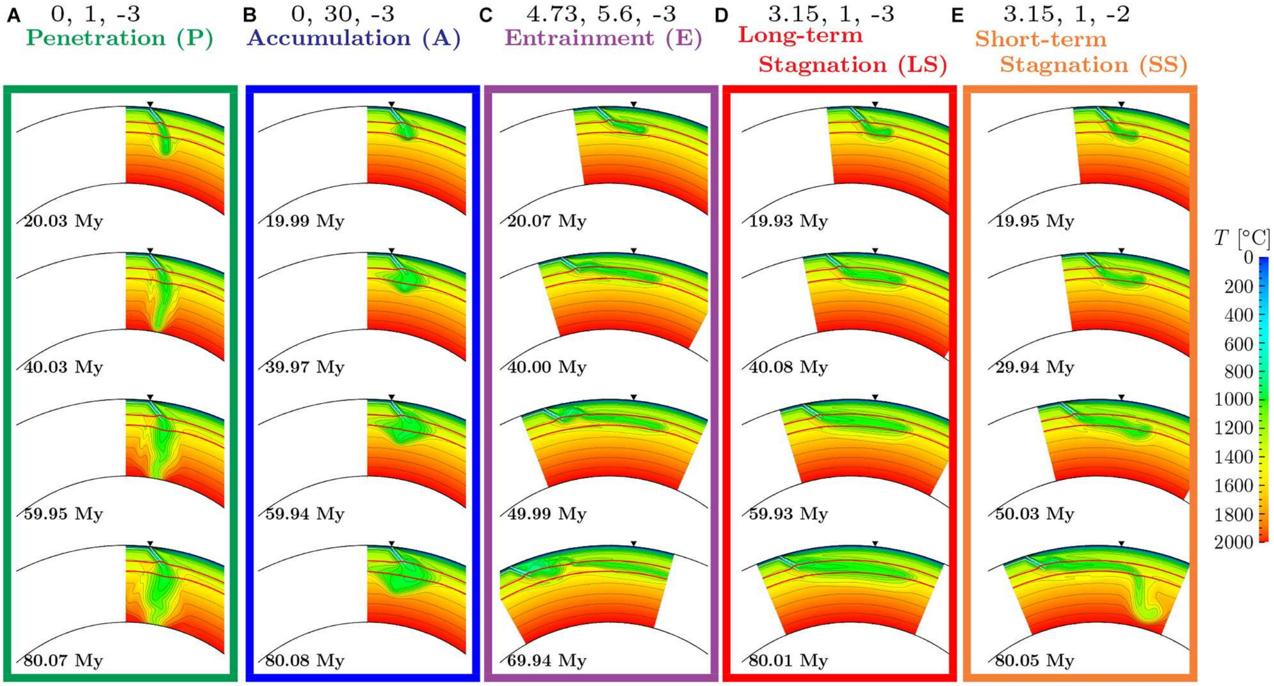

FIGURE 3 | Comparison between the evolution of five types of subducting slab morphologies: **(A)** Penetration (green), **(B)** Accumulation (blue), **(C)** Entrainment (purple), **(D)** Long-term Stagnation (red), and **(E)** Short-term Stagnation (orange). Indicated at the top of respective frames are the trench retreat velocity v_{tr} [cm/yr], the viscosity jump between the upper and lower mantle r_η, and the Clapeyron slope at the 660 km discontinuity γ^{660} [MPa/K] for each case, respectively. The meaning of the colors, contour lines, red and white lines, and black triangles are same as in **Figure 2**.

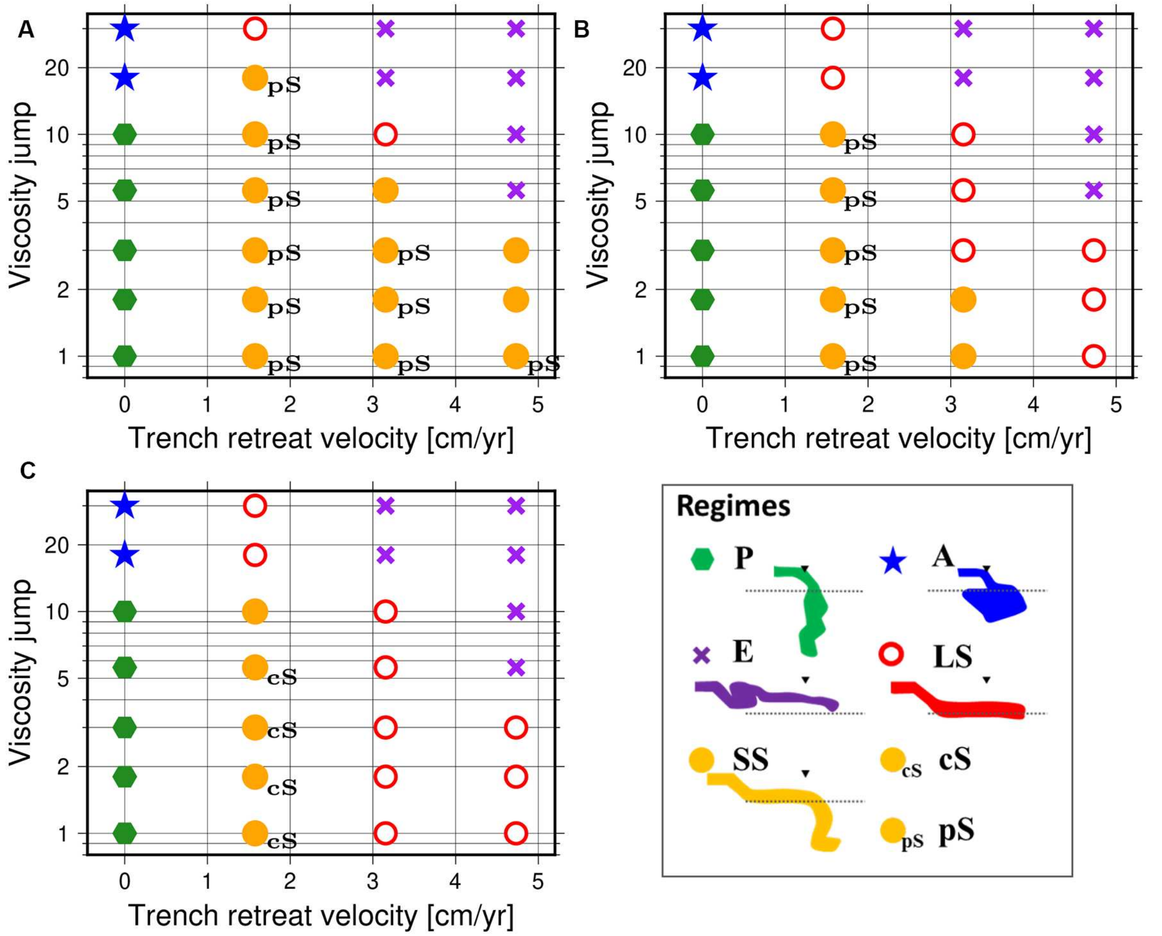

FIGURE 4 | Regime diagrams of the slab morphologies as a function of trench retreat velocity v_{tr} and viscosity jump r_η for the cases of **(A)** $\gamma^{660} = -1$ MPa/K, **(B)** $\gamma^{660} = -2$ MPa/K, and **(C)** γ^{660} =-3 MPa/K. The types of Penetration (P), Accumulation (A), Entrainment (E), Long-term Stagnation (LS), and Short-term Stagnation (SS) are represented by green hexagons, blue stars, purple crosses, red open circles, and orange filled circles, respectively. In addition, the types of stagnation after penetration (pS) and stagnation after collapse (cS) are represented by small letters of "pS" and "cS" in the right side of filled orange circles, respectively. In the schematic illustration of the regimes, the black triangles indicate the initial trench location, and the dashed lines indicate the 660 km discontinuity.

owing to the large viscosity jump between the upper and lower mantle. This type of behavior is observed for 6 cases out of 84 calculations, and occurs for $v_{tr} = 0$ and large r_η ($r_\eta \geq 18$). In **Figure 3C** we show the third type of slab behaviors, called "entrainment" (E)-type, observed for the cases when both v_{tr} and r_η are large. In the E-type, subducting slabs are entrained and pulled up by a local circulations in the shallow mantle driven by a trench retreat and is broken into pieces, since the effects of the imposed v_{tr} and r_η are too strong. This type is observed in 18 cases of our calculations.

The fourth and fifth types of slab behaviors are the ones where the stagnant slabs are observed in the presence of trench retreat ($v_{tr} \neq 0$) in addition to the effects of γ^{660} and r_η. Shown in **Figure 3D** is an example of "long-term stagnation" (LS)-type, while in **Figure 3E** is that of "short-term stagnation" (SS)-type. For both types, the subducting slab is bent and flattened at the 660 km discontinuity, forming a horizontally-lying stagnant slab at the base of MTZ in the earliest stage of subduction. In the LS-type, subducted slabs are stagnated around the 660 km discontinuity for a long time interval (at least more than 80 My) without penetrating into the lower mantle. The horizontally-lying portion of cold slab becomes longer with time along with the trench retreat. In the SS-type, in contrast, the stagnant slab starts to collapse into the lower mantle at its tip after the first several ten million years, because the negative buoyancy caused by the mass of the stagnant slab dominates the positive buoyancy owing to the negative Clapeyron slope γ^{660} and the resistance due to the viscosity jump between the upper and lower mantle. The LS- and SS-type of behaviors are observed for 20 and 6 cases out of 84 calculations, respectively.

We however note that not all the patterns of slab behaviors obtained here fall in any of five fundamental types: In several cases we observed distinctive temporal evolutions whose snapshots are very similar to those of SS-type at some time instances. In the next subsubsection, we will study the slab behaviors of such cases in more detail.

3.1.3. Distinctive Slab Behaviors: Stagnation After Penetration or Collapse

In the cases of short-term stagnation (SS) described in section 3.1.2, the cold slabs sink into the lower mantle after they lie horizontally at the base of MTZ. In some other cases, in contrast, we observed that a horizontally-lying (or "stagnated") portion of cold slab develops after a part of slab sinks into the lower mantle. By the letters "pS" or "cS" attached with the filled orange circles in **Figure 4**, we indicate the values of parameters which yield a "stagnation" of slab after its penetration (hereafter called "pS") or collapse ("cS") into the lower mantle. In **Figure 5**, on the other hand, we show the temporal evolution of the distributions of temperature T and horizontal stress $\sigma_{\theta\theta}$ around the subducting slabs for the cases with pS and cS, together with that of SS for comparison. As can be seen from the snapshots at around $t = 10$ My, the behaviors of subducting slabs are very similar for all the three types before the tips of subducting slabs impinge the 660 km discontinuity. In addition, the behaviors of slabs are quite similar for sufficiently large t (e.g., $t > 60$ My) between the types. However, during the period of temporal evolution except for very early and very late stages, the behaviors of slabs significantly differ between the types.

Figure 5A shows the temporal evolution of the slabs for the case with stagnation after penetration (pS) where we assumed $\gamma^{660} = -1$ MPa/K, $r_\eta = 1$ and $v_{tr} = 3.15$ cm/yr. From the snapshot at $t \simeq 15$ My, we can see the region with $\sigma_{\theta\theta} > 0$ (i.e., vertical compression) in the lower part of the slab just above the 660 km discontinuity both for the cases with pS and SS. However, the degree of vertical compression in this region is weaker than that for the case with SS (see **Figure 5C**), because of the weaker resistance coming from the gentler Clapeyron slope γ^{660} for given v_{pl} and v_{tr}. This results in a slab penetration to a greater depth by about 20 My than that for SS. At $t = 19.98$ My, the stress state near the tip of the subducting slab in the lower mantle is strong horizontal compression (vertical extension) in the upper part, indicating that the cold slab tends to sink owing to its negative buoyancy. During the subsequent period of $t < 39.95$ My, however, the horizontal compression becomes significantly weakened in the tip of slab in the lower mantle because the temperature difference becomes smaller between the slab and the surrounding mantle, leading to a slowing down of the descent of slab in the lower mantle. The deceleration of slab can be also seen from the stress state at the position of slab penetration at 660 km discontinuity; the horizontal compression gradually decreases with time there. On the other hand, the position of slab is almost unchanged at the base of the MTZ for $t > 29.96$ My, because the slab penetration also acts as a strong anchor of cold slab in the uppermost part of the lower mantle. Taken together with the effect of trench retreat, a subducting slab is flattened to form a horizontally-lying portion in the MTZ whose horizontal dimension increases with time. As can be seen from the snapshot of $t > 40$ My, the slab subduction for the pS-type finally yields a structure quite similar with those of SS for $t > 40$ My.

On the other hand, **Figure 5B** shows the temporal evolution of the slabs for the case with stagnation after collapse (cS) where we assumed $\gamma^{660} = -3$ MPa/K, $r_\eta = 1$ and $v_{tr} = 1.58$ cm/yr. Comparing the snapshots for t less than about 20 My in **Figures 5B,C**, the behavior of slab for the case with cS is quite similar with that for SS. Indeed, for both cases, horizontally-lying portions of cold slabs are about to be formed at the base of MTZ. In addition, there are regions with vertical compression ($\sigma_{\theta\theta} > 0$) in the lower part of the slab just above the 660 km discontinuity. However, the degree of vertical compression in this region is stronger for cS than that for SS (see **Figure 5C**), because of the slower trench retreat and faster imposed subduction together with the steeper Clapeyron slope γ^{660}. During the subsequent period of $t \leq 30.01$ My, the cold slab sinks into the lower mantle to a greater depth than for the case in **Figure 5C**. On the other hand, the imposed subduction also induces a horizontal compression near the tip of cold slab, which leads a buckling of slab and forms a concave structure of collapsed slab in the uppermost lower mantle at $t = 30.01$ My. During the subsequent period of $t \geq 39.93$ My, the collapsed slab further sinks in the lower mantle owing to its negative buoyancy. In addition, as in the cases of pS, the descent of slab in the lower mantle strongly anchors the cold slab in the uppermost part of the lower mantle, and a horizontally-lying portion develops at the base of MTZ along with the trench retreat. As can be seen from the snapshot of $t = 60.01$ My, the slab subduction for the cS-type finally yields a structure quite similar with those of SS.

3.2. Stagnant Slab Behaviors With Temporal Changes in Trench Retreat Velocity

In the first series of experiments where the rate of trench retreat v_{tr} is kept unchanged with time, we found that the trench retreat greatly helps to form and sustain the horizontally-lying or stagnant slabs (see section 3.1). In this section, we carry out the second series of experiments where the effect of trench retreat weakens with time, and study how the behaviors of subducting slabs are affected by the temporal changes in v_{tr} particularly for the cases where horizontally-lying or stagnant slabs are formed under the continuous retreating motion of trench. In this study, for simplicity, we assumed that the trench retreat occurs at a constant non-zero rate for the elapsed time $0 \leq t \leq t_{\text{stop}}$ while it does not for $t > t_{\text{stop}}$. Here we choose t_{stop} to be around 40 My, since the horizontally-lying slabs are well-developed or ready to be developed by $t = t_{\text{stop}}$ for all the cases with LS, SS, cS, and pS.

We conducted 45 numerical simulations by imposing sudden stop of the trench retreat at around 40 My after the onset of slab subduction, using the values of control parameters (r_η, γ^{660}, and non-zero v_{tr} for $t \leq t_{\text{stop}}$) which yield horizontally-lying slabs (LS, SS, cS, and pS in section 3.1). Among them, we observed the collapse of the stagnant slabs into the lower mantle only for the cases with $r_\eta \leq 10$. In particular, the avalanche styles of stagnant slabs observed in our simulations can be classified into four styles, depending not only on the types of slab behaviors described in section 3.1 but also on the slab shapes at the time instance of the sudden stop of the trench retreat ($t = t_{\text{stop}}$). In **Table 3** and **Figure 6**, we summarize the classification of slab behaviors for all

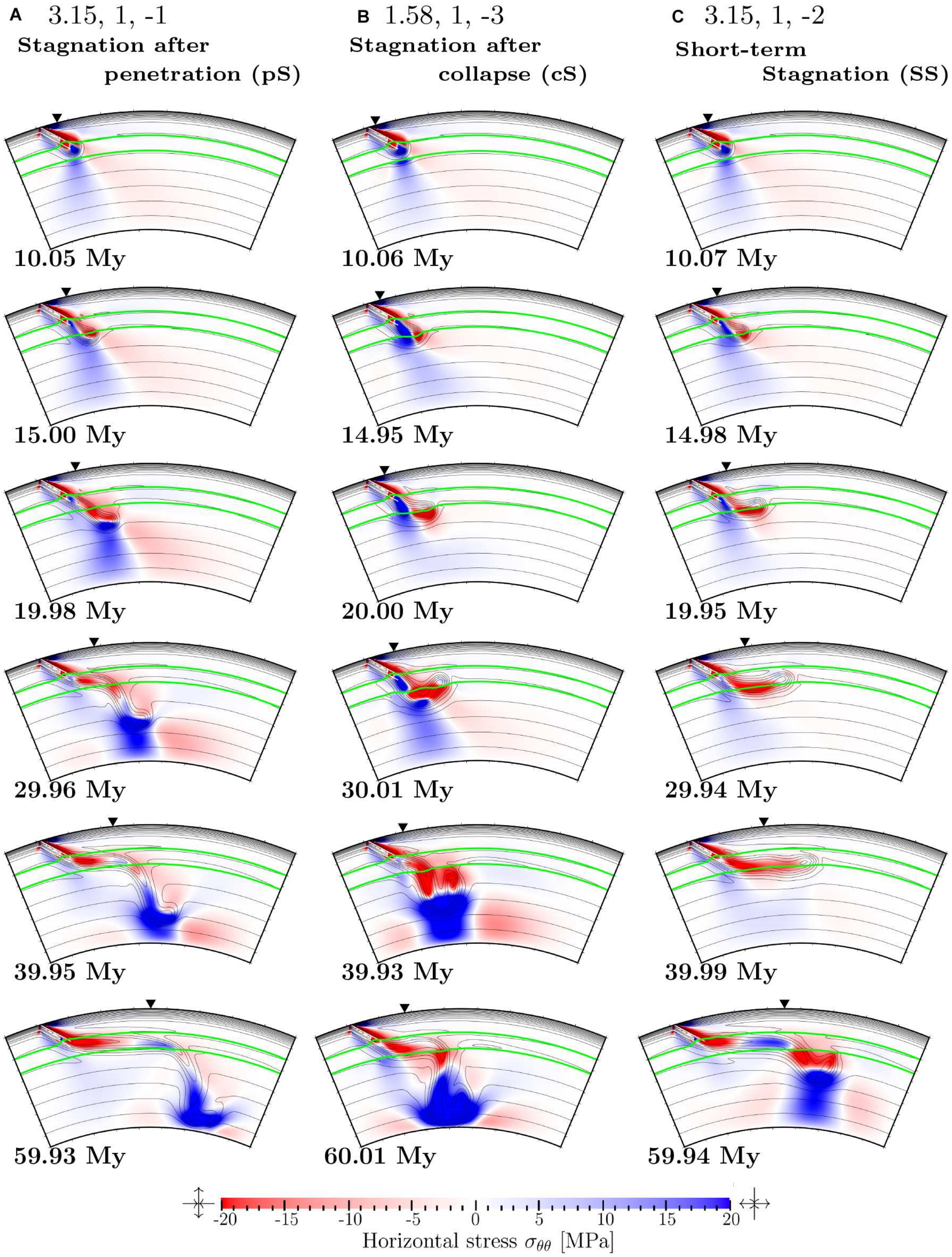

FIGURE 5 | Snapshots of the distributions of temperature T (contours) and horizontal stress $\sigma_{\theta\theta}$ (colors) for the time instances indicated in the figure, obtained for the cases with **(A)** stagnation after penetration, **(B)** stagnation after collapse, and **(C)** short-term stagnation. Indicated at the top of respective frames are the trench retreat velocity v_{tr} [cm/yr], the viscosity jump between the upper and lower mantle r_η, and the Clapeyron slope at the 660 km discontinuity γ^{660} [MPa/K] for each case, respectively. The contour interval for T is 100°C. The colorscale for $\sigma_{\theta\theta}$ is indicated at the bottom of figure. The regions with $\sigma_{\theta\theta} < 0$ is under horizontal compression (vertical extension), while those with $\sigma_{\theta\theta} > 0$ is under horizontal extension (vertical compression). We also show by the green lines in each figure the phase boundaries at around 410 km and 660 km depths.

TABLE 3 | Cases and results of numerical simulations with time change in v_{tr}.

Case	Type(40)	Type(∞)
TR1.58($0_{40\mathrm{My}}$)H1G−3	III	cS
TR3.15($0_{40\mathrm{My}}$)H1G−3	I	LS
TR4.73($0_{40\mathrm{My}}$)H1G−3	I	LS
TR1.58($0_{40\mathrm{My}}$)H1.8G−3	III	cS
TR3.15($0_{40\mathrm{My}}$)H1.8G−3	I	LS
TR4.73($0_{40\mathrm{My}}$)H1.8G−3	I	LS
TR1.58($0_{40\mathrm{My}}$)H3G−3	III	cS
TR3.15($0_{40\mathrm{My}}$)H3G−3	I	LS
TR4.73($0_{40\mathrm{My}}$)H3G−3	I	LS
TR1.58($0_{40\mathrm{My}}$)H5.6G−3	III	cS
TR3.15($0_{40\mathrm{My}}$)H5.6G−3	I	LS
TR1.58($0_{40\mathrm{My}}$)H10G−3	I	SS
TR3.15($0_{40\mathrm{My}}$)H10G−3	I	LS
TR1.58($0_{40\mathrm{My}}$)H18G−3	Did not fall	LS
TR1.58($0_{40\mathrm{My}}$)H30G−3	Did not fall	LS
TR1.58($0_{40\mathrm{My}}$)H1G−2	III	pS
TR3.15($0_{40\mathrm{My}}$)H1G−2	I	SS
TR4.73($0_{40\mathrm{My}}$)H1G−2	I	LS
TR1.58($0_{40\mathrm{My}}$)H1.8G−2	II	pS
TR3.15($0_{40\mathrm{My}}$)H1.8G−2	I	SS
TR4.73($0_{40\mathrm{My}}$)H1.8G−2	I	LS
TR1.58($0_{40\mathrm{My}}$)H3G−2	II	pS
TR3.15($0_{40\mathrm{My}}$)H3G−2	I	LS
TR4.73($0_{40\mathrm{My}}$)H3G−2	I	LS
TR1.58($0_{40\mathrm{My}}$)H5.6G−2	II	pS
TR3.15($0_{40\mathrm{My}}$)H5.6G−2	I	LS
TR1.58($0_{40\mathrm{My}}$)H10G−2	II	pS
TR3.15($0_{40\mathrm{My}}$)H10G−2	I	LS
TR1.58($0_{40\mathrm{My}}$)H18G−2	Did not fall	LS
TR1.58($0_{40\mathrm{My}}$)H30G−2	Did not fall	LS
TR1.58($0_{40\mathrm{My}}$)H1G−1	III	pS
TR3.15($0_{40\mathrm{My}}$)H1G−1	III	pS
TR4.73($0_{40\mathrm{My}}$)H1G−1	IV	pS
TR1.58($0_{40\mathrm{My}}$)H1.8G−1	II	pS
TR3.15($0_{40\mathrm{My}}$)H1.8G−1	III	pS
TR4.73($0_{40\mathrm{My}}$)H1.8G−1	IV	SS
TR1.58($0_{40\mathrm{My}}$)H3G−1	II	pS
TR3.15($0_{40\mathrm{My}}$)H3G−1	III	pS
TR4.73($0_{40\mathrm{My}}$)H3G−1	I	SS
TR1.58($0_{40\mathrm{My}}$)H5.6G−1	II	pS
TR3.15($0_{40\mathrm{My}}$)H5.6G−1	I	SS
TR1.58($0_{40\mathrm{My}}$)H10G−1	II	pS
TR3.15($0_{40\mathrm{My}}$)H10G−1	I	LS
TR1.58($0_{40\mathrm{My}}$)H18G−1	Did not fall	pS
TR1.58($0_{40\mathrm{My}}$)H30G−1	Did not fall	LS

In this table the cases are denoted TRv_{tr0}($0_{40\mathrm{My}}$)Hr_ηGγ^{660} as in ***Table 2****, where v_{tr0} is the rate of trench retreat for $t < 40$ My in cm/yr.*

45 cases. (In **Figure 6**, we also plot 6 cases indicated by "did not fall" in **Table 3**, where the slabs did not fall into the lower mantle.) In **Table 3**, the symbol "type(40)" is meant for the type of the slab behavior for the cases with $t_{\text{stop}} = 40$ My, while "type(∞)" stands for the type presented in section 3.1 with the continuous trench retreat (i.e., $t_{\text{stop}} = \infty$).

3.2.1. Type I: Avalanche From the Hinge of Stagnant Slabs

Figure 7A shows the slab behavior obtained for the case where we employed $r_\eta = 3$, $\gamma^{660} = -2$ MPa/K and $v_{tr} = 3.15$ cm/yr is applied only for $t \leq 40$ My after the onset of subduction (For comparison, we also show in small panels attached with large ones the snapshots for the same time instances of $t > 40$ My for the corresponding case without a sudden stop of trench retreat). The choice of control parameters yields the LS-type without the sudden stop of trench retreat; the stagnant slab is formed at the base of MTZ by $t = 39.96$ My after the onset of subduction, and it hardly falls into the lower mantle for more than 80 My. In the case where we impose a sudden stop of trench retreat at 40 My after the onset of subduction, in contrast, we observe an avalanche of stagnant slab. As can be seen from the snapshot at $t = 60.08$ My, a cold plate is bent downward at the hinge (the left-hand end) of the stagnant slab along with the imposed downward motion of subducting plate, and starts to penetrate into the lower mantle. At $t = 80.00$ My, a large portion of subducted slab collapses into the lower mantle, owing to its negative buoyancy.

The type I of slab behavior is observed for 15 cases where type(∞) is LS. We also obtained the same type for 5 cases where type(∞) is SS. This reflects the fact that the shapes of slabs for SS are quite similar with those for LS at $t = t_{\text{stop}}$ before the collapse of slabs for SS. This result is also consistent with those of Yoshioka and Naganoda (2010) and Agrusta et al. (2017) where the collapse of stagnant slab enhanced by the change from trench retreat to trench advance.

3.2.2. Type II: Stagnation Below 660 km

Figure 7B shows the slab behavior for the case where the type(∞) is pS with $r_\eta = 3$, $\gamma^{660} = -2$ MPa/K and $v_{tr} = 1.58$ cm/yr. At $t = 39.93$ My just before the sudden stop of trench retreat, the subducting slab penetrates into the lower mantle almost smoothly, in spite of a small kink at the 660 km discontinuity. The descent of cold slab continues after the sudden stop of trench retreat along with the imposed downward motion of subducting plate. During the subsequent period of $t \leq 79.98$ My, the kink of subducting slabs gradually sinks down to about 1,500 km depth. The tip of subducting slab, on the other hand, reaches down to about 1,500 km depth by $t = 60.03$ My, and is almost anchored at this depth during $t \leq 79.98$ My. The difference in the rate of descent in the slab results in a horizontally-lying portion of cold slab in the lower mantle at around 1,500 km depth at this time instance, as if it is stagnated at this depth.

This type of slab behaviors can be seen in total of 8 cases where type(∞) is pS while a horizontally-lying portion of cold slab is not well-developed yet by $t = t_{\text{stop}}$. We also note that in two cases with $r_\eta = 10$ a thickening of cold slabs, similar to the accumulation in section 3.1.2, is observed at the 660 km discontinuity in addition to the trapping of slabs in the lower mantle.

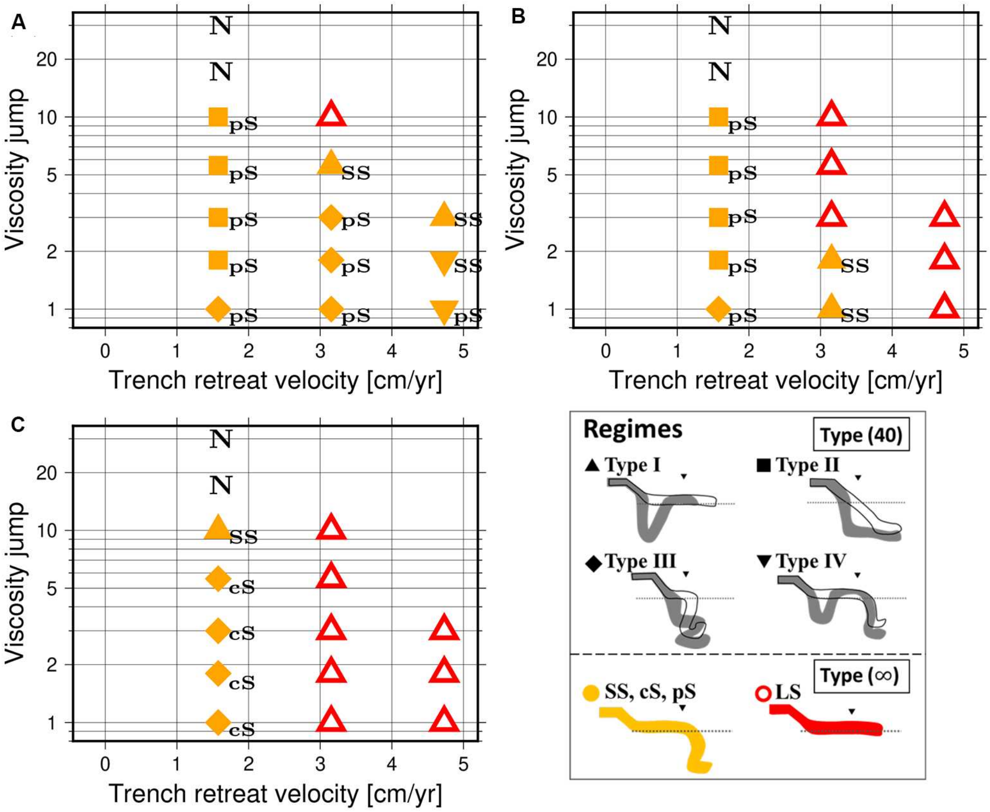

FIGURE 6 | Regime diagrams of the slab morphologies with sudden stop of trench retreat at around 40 My after the initiation of subduction as a function of trench retreat velocity v_{tr} and viscosity jump r_η for the cases of **(A)** $\gamma^{660} = -1$ MPa/K, **(B)** γ^{660} =-2 MPa/K, and **(C)** $\gamma^{660} = -3$ MPa/K. The symbols stand for the slab morphologies of Type(40); triangles, squares, diamonds, and inverted triangles indicate Types I, II, III, and IV, respectively. The cases with "did not fall" are also indicated by the letter "N" in the figure. On the other hand, the colors of symbols stand for the slab morphologies of Type(∞); red open symbols indicate LS, while yellow filled ones are other types whose Type(∞) are indicated by small letters ("SS", "pS," and "cS") attached to the symbols. In the schematic illustration of the regimes, slab morphologies before (black contour) and after (gray fill) changing v_{tr} for Type I, II, III, and IV are shown. The black triangles and the dashed lines indicate the initial trench location and the 660 km discontinuity, respectively.

3.2.3. Type III: Buckling After Penetration in the Lower Mantle

In **Figure 7C** we show the slab behaviors for the case where the type(∞) is cS with $r_\eta = 1$, $\gamma^{660} = -3$ MPa/K and $v_{tr} = 1.58$ cm/yr (see also **Figure 5B** in section 3.1). During the period of $t \leq 39.93$ My where the trench retreat continuously occurs, the subducting slab collapses into the lower mantle at its hinge owing to its negative buoyancy. In addition, during the subsequent period of $t < 59.98$ My where the trench retreat is turned off, the behavior of subducting slab is quite similar with those for the case with cS where the trench retreat continuously occurs (see also **Figure 5B**). However, because of the absence of trench retreat and enhanced rate of imposed subduction, the subducted slab is intensively buckled in the uppermost part of the lower mantle.

This type of slab behavior is observed in a total of 9 cases where type(∞) is pS or cS. This is because in these cases the horizontally-lying portion of cold slab is not significantly developed by the time of the sudden stop of trench retreat ($t = t_{\text{stop}}$). On the other hand, for the cases with $3 \leq r_\eta \leq 5.6$ and $\gamma^{660} = -3$ MPa/K, we observed that the slabs accumulate at around the MTZ, owing to the resistance force from large r_η and steep γ^{660}.

3.2.4. Type IV: Avalanche From the Hinge After Penetration From the Head of a Slab

Figure 7D shows the slab behaviors in the case with type(∞) is pS where we employed $r_\eta = 1$, $\gamma^{660} = -1$ MPa/K and $v_{tr} = 4.73$ cm/yr. At $t = 40.01$ My just after the sudden stop of trench retreat, a well-developed SS-type slab takes place, which is characterized by a very long horizontally-lying portion and its tip sunk in the lower mantle. However, as can be seen from the snapshot of $t = 59.92$ My after the sudden stop of trench retreat, the enhanced motion of imposed subduction newly induces a penetration of cold slab at the hinge of stagnant slab in addition to that at its tip. During the subsequent period, the cold subducting plate is preferentially supplied to the newly penetrating portion, while in the old penetrating portion the temperature difference becomes smaller between the slab and the surrounding mantle.

This type can be observed in 2 cases out of 45 calculations for the cases where type(∞) is pS or SS, particularly when a

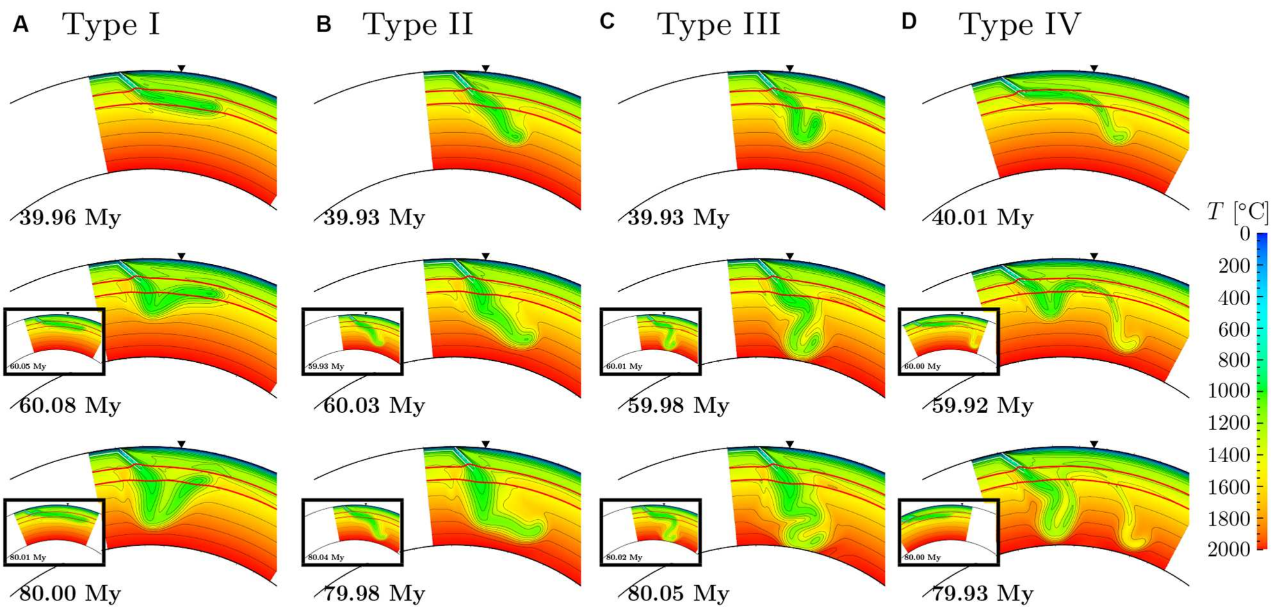

FIGURE 7 | Evolutions of slab behaviors with the sudden stop of trench retreat at around 40 My after the initiation of subduction. Snapshots of temperature distribution at 40 My (top), 60 My (middle), and 80 My (bottom) for the cases of **(A)** $v_{tr} = 3.15$ cm/yr, $r_\eta = 3$, γ^{660} =-2 MPa/K, **(B)** $v_{tr} = 1.58$ cm/yr, $r_\eta = 3$, $\gamma^{660} = -2$ MPa/K, **(C)** $v_{tr} = 1.58$ cm/yr, $r_\eta = 1$, γ^{660} =-3 MPa/K, and **(D)** $v_{tr} = 4.73$ cm/yr, $r_\eta = 1$, γ^{660} =-1 MPa/K. The small panels within the black frames show the slab behaviors with constant v_{tr}. The meaning of the colors, contour lines, red and white lines, and black triangles are same as in **Figure 2**.

horizontally-lying stagnant portion of cold slab is sufficiently long at around the 660 km discontinuity by the time of the sudden stop of trench retreat.

4. DISCUSSION AND CONCLUDING REMARKS

In this paper we conducted numerical experiments of mantle convection with imposed kinematic motion of cold slabs and trench migration, aiming to understand the cause of the diverse morphology of subducting slabs observed by the seismic tomography. In particular, we studied the effects of control parameters (the viscosity jump r_η and the Clapeyron slope γ^{660} at the 660 km discontinuity, and the rate v_{tr} of trench retreat) on the formation of "stagnant slabs" in the MTZ and their avalanche into the lower mantle. In the first series of our experiments where v_{tr} is kept constant with time, we confirmed that the trench retreat greatly helps to form horizontally-lying or stagnant slabs at the 660 km discontinuity. In particular, we found distinctive temporal evolutions of slabs in some ranges of control parameters, in addition to the fundamental five types named penetration (P), accumulation (A), entrainment (E), long-term stagnation (LS), and short-term stagnation (SS). In these distinctive types (named pS and cS), the subducted slabs tend to stagnate at the 660 km discontinuity after they experience the penetration or the collapse into the lower mantle, yielding the shapes of slabs quite similar to those of SS at some time instances. In the second series of our experiments, we investigated the effects of the sudden stop of trench retreat on the horizontally-lying slabs (LS, SS, cS, and pS types in the first series of experiments). We found that the styles of avalanche of stagnant slabs vary depending not only on the types of slab behaviors described in section 3.1 but also on the slab shapes at the time instance of the sudden stop of the trench retreat. In these experiments, we also observed wider variations of slab behaviors than in the cases with continuous trench retreat, such as the slabs which look as if they are stagnated below the 660 km discontinuity. The results of our experiments suggest that the history of trench migration (the retreat velocity and its temporal change) plays the greatest role in the formation and avalanche of stagnant slabs, among the control parameters which may affect the dynamics of subducting slabs.

The fundamental five types of slab behaviors, particularly the LS and SS, obtained in the first series of our experiments can be well-compared with those of natural ones observed by the seismic tomography. For example, the "stagnant slab" behaviors observed beneath the Northeast Japan or Izu-Bonin arcs (e.g., Zhao, 2009; Fukao and Obayashi, 2013) can be well-explained either by the LS or SS types in this study: These slabs seem to be LS, if the western tip of the flat slab in the MTZ observed beneath the East Asia arc is the tip of the Pacific slab whose subduction started about 60 Ma (e.g., Seton et al., 2012, 2015) and the Pacific slab has not yet penetrated into the lower mantle (Honda, 2016). On the other hand, these slabs seem to be SS, if the western tip of the stagnant Pacific slab represents the subduction which occurred about 20–30 My as suggested in Liu et al. (2017). Similarly, the slab morphology observed in the Tonga subduction zone, characterized by a horizontally-flattening portion of the slab in MTZ and the remnant slabs in the lower mantle (van der Hilst, 1995; Richards et al., 2011), is also comparable with that of SS type in this study, although the seismological interpretation is still controversial for Tonga slab (Fukao and Obayashi, 2013).

On the other hand, the occurrence of pS and cS types (stagnation after penetration or collapse) in addition to the fundamental five types in the first series of our experiments strongly indicate that the morphology of slabs similar to SS can also come out from the slabs which start to stagnate horizontally in the MTZ after their penetration or collapse into the lower mantle. In other words, it is difficult to distinguish the SS type from the pS or cS type solely from the comparison of slab shapes at some time instances given by the snapshot of slab behavior observed by seismic tomography. We can certainly speculate that, if simply based on the comparison of control parameters relevant for each type with those of the subduction zones listed above, the pS and/or cS types are more likely to occur than SS in natural subduction zones. However, more careful inspection should be necessary to accurately determine the types of slab behaviors for particular subduction zones by, for example, taking into account the detailed history of trench migration.

In addition, the occurrence of four types of slab behaviors in the second series of our experiments suggests that the temporal variations in the rate of trench retreat can significantly induce the complexities in the collapse of stagnant slabs into the lower mantle which can be hardly observed for the cases with constant rate of trench retreat. For example, the collapse of the stagnant slabs at their hinges obtained for the types I and IV can be well-compared with that observed in the Mariana arc (Fukao and Obayashi, 2013). In particular, the occurrence of horizontally-lying portion of slabs significantly below the 660 km discontinuity for the type II is very similar to that observed in the Western Java arc which looks to be "trapped"at about 1,000 km depth (Fukao and Obayashi, 2013). The occurrence of type II simply due to the sudden stop of trench retreat may therefore suggests that a "trapped" slab at some depths in the lower mantle does not necessarily imply the existence of discontinuous changes in physical properties such as viscosity (Marquardt and Miyagi, 2015; Rudolph et al., 2015) at that depth.

Although we do believe that our model successfully reproduces the slab behaviors such as the stagnant slabs at the MTZ and their avalanches into the lower mantle, we need further numerical calculations without several simplifications which we made in the present study. For example, the slab behaviors in the lower mantle, such as the flattened slab well below the 660 km discontinuity, are probably affected by the limited model thickness of 2,000 km as well as the imposed boundary condition at the bottom boundary, which may therefore need more careful validation using improved model with a full mantle thickness. In addition, the assumption of the imposed motions of subducting and overriding plates in this study are most likely to modulate the flow in the mantle wedge and, in turn, the behaviors of subducting slabs. Implicit in this assumption is a further presumption that the trench migration occurs independently of the deformation of slabs or other model parameters such as the Clapeyron slope and the viscosity jump at around 660 km depth, which may not necessarily hold in natural subduction zones. Besides, we employed the prescribed kinematic motions of subducting plate and trench (v_{pl} and v_{tr}) using a highly simplified history of trench migration (constant through time or sudden stop at 40 My after the initiation of the subduction), which may not necessarily occur in natural subduction zone. In particular, the assumption of the constant rate of plate convergence at the trench ($v_{pl} + v_{tr}$) throughout the calculations may not be fully consistent with the dynamics in the underlying mantle. Hence, it is quite important to conduct further numerical simulations by using models with the self-consistent motions of subducting and overriding plate, including the complexities in geometry of the subduction zones such as the presence of back-arc opening (e.g., Nakakuki and Mura, 2013) and the double subduction system (e.g., Čížková and Bina, 2015; Faccenna et al., 2018), in order to fully understand the diversity of slab behaviors in the natural subduction zones.

DATA AVAILABILITY STATEMENT

The datasets generated for this study are available on request to the corresponding author.

AUTHOR CONTRIBUTIONS

MT and MK conceived and designed the experiments and wrote the paper. MT performed the experiments and analyzed the data.

FUNDING

This work was supported by JSPS KAKENHI Grant numbers 26400457 and 18K03724 and Joint Usage/Research Center PRIUS, Ehime University, Japan. MT received travel support from the Ehime University.

ACKNOWLEDGMENTS

We would like to thank two reviewers for their constructive comments and suggestions which greatly improved the paper.

REFERENCES

Agrusta, R., Goes, S., and van Hunen, J. (2017). Subducting-slab transition-zone interaction: stagnation, penetration and mode switches. *Earth Planet. Sci. Lett.* 464, 10–23. doi: 10.1016/j.epsl.2017.02.005

Agrusta, R., van Hunen, J., and Goes, S. (2014). The effect of metastable pyroxene on the slab dynamics. *Geophys. Res. Letters* 41, 8800–8808. doi: 10.1002/2014GL062159

Christensen, U. R. (1996). The influence of trench migration on slab penetration into the lower mantle. *Earth Planet. Sci. Lett.* 140, 27–39. doi: 10.1016/0012-821X(96)00023-4

Christensen, U. R., and Yuen, D. A. (1985). Layered convection induced by phase transitions. *J. Geophys. Res. Solid Earth* 90, 10291–10300. doi: 10.1029/JB090iB12p10291

Čížková, H., and Bina, C. R. (2015). Geodynamics of trench advance: insights from a philippine-sea-style geometry. *Earth*

Planet. Sci. Lett. 430, 408–415. doi: 10.1016/j.epsl.2015.07.004

Čížková, H., van Hunen, J., van den Berg, A. P., and Vlaar, N. J. (2002). The influence of rheological weakening and yield stress on the interaction of slabs with the 670 km discontinuity. *Earth Planet. Sci. Lett.* 199, 447–457. doi: 10.1016/S0012-821X(02)00586-1

Dziewonski, A. M., and Anderson, D. L. (1981). Preliminary reference Earth model. *Phys. Earth Planet. Interiors* 25, 297–356. doi: 10.1016/0031-9201(81)90046-7

Faccenna, C., Holt, A. F., Becker, T. W., Lallemand, S., and Royden, L. H. (2018). Dynamics of the Ryukyu/Izu-Bonin-Marianas double subduction system. *Tectonophysics* 746, 229–238. doi: 10.1016/j.tecto.2017.08.011

Fei, Y., Van Orman, J., Li, J., Van Westrenen, W., Sanloup, C., Minarik, W., et al. (2004). Experimentally determined postspinel transformation boundary in Mg_2SiO_4 using MgO as an internal pressure standard and its geophysical implications. *J. Geophys. Res. Solid Earth* 109:B02305. doi: 10.1029/2003JB002562

Fukao, Y., and Obayashi, M. (2013). Subducted slabs stagnant above, penetrating through, and trapped below the 660 km discontinuity. *J. Geophys. Res. Solid Earth* 118, 5920–5938. doi: 10.1002/2013JB010466

Garel, F., Goes, S., Davies, D., Davies, J. H., Kramer, S. C., and Wilson, C. R. (2014). Interaction of subducted slabs with the mantle transition-zone: a regime diagram from 2-d thermo-mechanical models with a mobile trench and an overriding plate. *Geochem. Geophys. Geosyst.* 15, 1739–1765. doi: 10.1002/2014GC005257

Honda, S. (2016). Slab stagnation and detachment under northeast china. *Tectonophysics* 671, 127–138. doi: 10.1016/j.tecto.2016.01.025

Ito, E., and Takahashi, E. (1989). Postspinel transformations in the system Mg_2SiO_4-Fe_2SiO_4 and some geophysical implications. *J. Geophys. Res. Solid Earth* 94, 10637–10646. doi: 10.1029/JB094iB08p10637

Kameyama, M., and Harada, A. (2017). Supercontinent cycle and thermochemical structure in the mantle: Inference from two-dimensional numerical simulations of mantle convection. *Geosciences* 7:126. doi: 10.3390/geosciences7040126

Kameyama, M., and Nishioka, R. (2012). Generation of ascending flows in the Big Mantle Wedge (BMW) beneath northeast Asia induced by retreat and stagnation of subducted slab. *Geophys. Res. Lett.* 39. doi: 10.1029/2012GL051678

Katsura, T., Yamada, H., Shinmei, T., Kubo, A., Ono, S., Kanzaki, M., et al. (2003). Post-spinel transition in Mg_2SiO_4 determined by high P-T *in situ* X-ray diffractometry. *Phys. Earth Planet. Interiors* 136, 11–24. doi: 10.1016/S0031-9201(03)00019-0

Liu, X., Zhao, D., Li, S., and Wei, W. (2017). Age of the subducting pacific slab beneath east Asia and its geodynamic implications. *Earth Planet. Sci. Lett.* 464, 166–174. doi: 10.1016/j.epsl.2017.02.024

Marquardt, H., and Miyagi, L. (2015). Slab stagnation in the shallow lower mantle linked to an increase in mantle viscosity. *Nat. Geosci.* 8:311. doi: 10.1038/ngeo2393

McKenzie, D. P., Roberts, J., and Weiss, N. O. (1973). Convection in the Earth's mantle. *Tectonophysics* 19, 89–103. doi: 10.1016/0040-1951(73)90034-6

Nakakuki, T., and Mura, E. (2013). Dynamics of slab rollback and induced back-arc basin formation. *Earth Planet. Sci. Lett.* 361, 287–297. doi: 10.1016/j.epsl.2012.10.031

Nakakuki, T., Tagawa, M., and Iwase, Y. (2010). Dynamical mechanisms controlling formation and avalanche of a stagnant slab. *Phys. Earth Planet. Interiors* 183, 309–320. doi: 10.1016/j.pepi.2010.02.003

Richards, S., Holm, R., and Barber, G. (2011). When slabs collide: a tectonic assessment of deep earthquakes in the Tonga-Vanuatu region. *Geology* 39, 787–790. doi: 10.1130/G31937.1

Rudolph, M. L., Lekić, V., and Lithgow-Bertelloni, C. (2015). Viscosity jump in Earth's mid-mantle. *Science* 350, 1349–1352. doi: 10.1126/science.aad1929

Seton, M., Flament, N., Whittaker, J., Müller, R. D., Gurnis, M., and Bower, D. J. (2015). Ridge subduction sparked reorganization of the pacific plate-mantle system 60-50 million years ago. *Geophys. Res. Lett.* 42, 1732–1740. doi: 10.1002/2015GL063057

Seton, M., Müller, R., Zahirovic, S., Gaina, C., Torsvik, T., Shephard, G., et al. (2012). Global continental and ocean basin reconstructions since 200ma. *Earth Sci. Rev.* 113, 212–270. doi: 10.1016/j.earscirev.2012.03.002

Tetzlaff, M., and Schmeling, H. (2000). The influence of olivine metastability on deep subduction of oceanic lithosphere. *Phys. Earth Planet. Interiors* 120, 29–38. doi: 10.1016/S0031-9201(00)00139-4

Torii, Y., and Yoshioka, S. (2007). Physical conditions producing slab stagnation: constraints of the Clapeyron slope, mantle viscosity, trench retreat, and dip angles. *Tectonophysics* 445, 200–209. doi: 10.1016/j.tecto.2007.08.003

Turcotte, D. L., and Schubert, G. (2002). *Geodynamics*. Cambridge: Cambridge University Press. doi: 10.1017/CBO9780511807442

van der Hilst, R. (1995). Complex morphology of subducted lithosphere in the mantle beneath the tonga trench. *Nature* 374, 154–157. doi: 10.1038/374154a0

van der Hilst, R., and Seno, T. (1993). Effects of relative plate motion on the deep structure and penetration depth of slabs below the izu-bonin and mariana island arcs. *Earth Planet. Sci. Lett.* 120, 395–407. doi: 10.1016/0012-821X(93)90253-6

van Hunen, J., van den Berg, A. P., and Vlaar, N. J. (2000). A thermo-mechanical model of horizontal subduction below an overriding plate. *Earth Planet. Sci. Lett.* 182, 157–169. doi: 10.1016/S0012-821X(00)00240-5

Yoshioka, S., and Naganoda, A. (2010). Effects of trench migration on fall of stagnant slabs into the lower mantle. *Phys. Earth Planet. Interiors* 183, 321–329. doi: 10.1016/j.pepi.2010.09.002

Yoshioka, S., and Sanshadokoro, H. (2002). Numerical simulations of deformation and dynamics of horizontally lying slabs. *Geophys. J. Int.* 151, 69–82. doi: 10.1046/j.1365-246X.2002.01735.x

Zhao, D. (2009). Multiscale seismic tomography and mantle dynamics. *Gondwana Res.* 15, 297–323. doi: 10.1016/j.gr.2008.07.003

Zhong, S., and Gurnis, M. (1993). Dynamic feedback between a continent like raft and thermal convection. *J. Geophys. Res. B* 98, 12219–12232. doi: 10.1029/93JB00193

Conflict of Interest: The authors declare that the research was conducted in the absence of any commercial or financial relationships that could be construed as a potential conflict of interest.

frontiers
in Earth Science

ORIGINAL RESEARCH
published: 08 May 2020
doi: 10.3389/feart.2020.00121

Southward-Directed Subduction of the Farallon–Aluk Spreading Ridge and Its Impact on Subduction Mechanics and Andean Arc Magmatism: Insights From Geochemical and Seismic Tomographic Data

Sofía B. Iannelli[1,2]*, Lucía Fernández Paz[1,2], Vanesa D. Litvak[1,2], Guido Gianni[1,2], Lucas M. Fennell[1,2], Javiera González[3], Friedrich Lucassen[4], Simone Kasemann[4], Verónica Oliveros[3] and Andrés Folguera[1,2]

[1] Departamento de Ciencias Geológicas, Universidad de Buenos Aires, Buenos Aires, Argentina, [2] Instituto de Estudios Andinos 'Don Pablo Groeber', CONICET- Universidad de Buenos Aires, Buenos Aires, Argentina, [3] Departamento de Ciencias de la Tierra, Universidad de Concepción, Concepción, Chile, [4] MARUM - Center for Marine Environmental Sciences and Faculty of Geosciences, University of Bremen, Bremen, Germany

Edited by:
Marina Manea,
National Autonomous University of Mexico, Mexico

Reviewed by:
Luca Ferrari,
Geosciences Center, National Autonomous University of Mexico, Mexico
Jiashun Hu,
California Institute of Technology, United States

****Correspondence:***
Sofía B. Iannelli
sofia.iannelli@hotmail.com.ar

Specialty section:
This article was submitted to Structural Geology and Tectonics, a section of the journal Frontiers in Earth Science

Received: *14 December 2019*
Accepted: *30 March 2020*
Published: *08 May 2020*

Citation:
Iannelli SB, Fernández Paz L, Litvak VD, Gianni G, Fennell LM, González J, Lucassen F, Kasemann S, Oliveros V and Folguera A (2020) Southward-Directed Subduction of the Farallon–Aluk Spreading Ridge and Its Impact on Subduction Mechanics and Andean Arc Magmatism: Insights From Geochemical and Seismic Tomographic Data. Front. Earth Sci. 8:121. doi: 10.3389/feart.2020.00121

Since the initial proposal of the past existence of a southward-directed mid-ocean ridge–subduction interaction in the Andes during Late Cretaceous–Paleogene times, several studies have been devoted to uncover the tectonomagmatic evidence of this process. The collision of a spreading ridge against a subduction margin provokes important tectonomagmatic changes, including, between them, variations in arc-related magmatic activity and in the plate-margin stress regime. However, the cryptic nature of the geological record often hampers assessing the influence and along-strike evolution of this process. In this study, we integrate new isotopic data with previous field and geochemical data on Andean arc-related magmatism, together with seismic tomography to track the main tectonic changes that affected the Andes between 35° and 42°S from Latest Cretaceous to early Miocene times. In particular, we carry out a new tomotectonic analysis combining the regional bedrock record of the Late Cretaceous–early Miocene arc with upper–lower mantle seismic tomography. This analysis allowed us to unravel the main geodynamic changes that affected the Andean active-margin when the Farallon–Aluk spreading ridge was subducting. Besides, new isotopic analyses reveal the variable nature of the mantle source that fed the Late Cretaceous–early Miocene arc. Hence, the integration of geological, geochemical, and geophysical data, together with new isotopic data studying the geochemical composition of the main Andean arc-related magmatic units in three main periods – (1) Latest Cretaceous–early Paleocene, (2) Early Paleocene–late Eocene, and (3) Late Eocene–early Miocene – allow us to understand with an unprecedented detail the geochemical and spatiotemporal evolution of the passage of this spreading ridge along the Andean margin.

Keywords: Southern Central Andes, spreading ridge subduction, Farallon–Aluk spreading ridge, Andean magmatism, Late Cretaceous–Cenozoic period

INTRODUCTION

The subduction of oceanic spreading ridges causes a significant impact on active margins producing multiple thermal, deformational, and magmatic effects and leaving a unique geological signature on overriding plates (e.g., DeLong et al., 1979; Thorkelson, 1996). During ridge subduction, sublithospheric divergence of oceanic plates provokes the unzipping of the mid-ocean ridge leading to the formation of slab windows (e.g., Dickinson and Snyder, 1979; Groome and Thorkelson, 2009). This phenomenon produces a slab gap that allows the sub-oceanic asthenosphere to well up in a complex 3-D mantle flow (e.g., Guillaume et al., 2010). The localized mantle upwelling causes a high heat flow area, often interrupting subduction-related magmatic activity, and produces dynamic uplift of the overriding plate driving major relief and drainage reorganizations in the upper-plate surface (Guillaume et al., 2009; Ávila and Dávila, 2018). The geological signature of this process can be tracked from the forearc to the back-arc regions of active margins and its distinctive character has allowed researchers to identify this process back to Precambrian times (e.g., Santosh and Kusky, 2010). In particular, in the back-arc area, variable degrees of mantle melting in the upwelling asthenosphere generate alkaline or tholeiitic magmas with OIB signatures (e.g., Gorring et al., 1997; D'Orazio et al., 2000; Gorring and Kay, 2001). In certain cases, partial fusion of young oceanic crust in the slab window edges forms magmas of adakitic composition (e.g., Kay et al., 1993; Johnston and Thorkelson, 1997). Intraplate magmatic activity in this area is often accompanied by extensional to transtensional tectonic activity (e.g., Thorkelson, 1996; Windley and Xiao, 2018). Identifying the precise location of past slab window event is a challenging task as these effects are time transgressive and are controlled by triple-junction kinematics (Thorkelson, 1996). This is further complicated in settings where mid-ocean ridge subduction took place obliquely to the subduction zone producing a time–space migration of the slab window process along the active margin. The latter tectonic configuration has been suggested in plate kinematic reconstructions in the southeast Pacific Ocean indicating that the Farallon–Aluk mid-ocean ridge should have subducted obliquely beneath the Andes sometime during Late Cretaceous to Paleogene times (Cande and Leslie, 1986; Ramos and Kay, 1992; Aragón et al., 2011; Somoza and Ghidella, 2012; Eagles and Scott, 2014; Iannelli et al., 2018; Fennell et al., 2019).

Recent plate kinematic reconstructions suggest that the Farallon–Aluk mid-ocean ridge collided against the Andean margin at ∼30°S during the Late Cretaceous (∼80 Ma) and started migrating southwards reaching Patagonian latitudes (∼42°S) by Eocene times (Cande and Leslie, 1986; Somoza and Ghidella, 2005; Aragón et al., 2011; Somoza et al., 2012; Eagles and Scott, 2014; Müller et al., 2016; Wright et al., 2016). Along these latitudes, the emplacement of scattered magmatic sequences with contrasting geochemical signatures and the development of magmatic lulls between Late Cretaceous to Eocene times have been associated with the development of slab windows directly linked to the progressive southward sweeping of this oceanic ridge (Ramos and Kay, 1992; Muñoz et al., 2000; Aragón et al., 2011; De La Fuente, 2014; Jalowitzki et al., 2017; Gianni et al., 2018a; Iannelli et al., 2017, 2018). Contrastingly, late Eocene–Oligocene magmatism show arc-related signature with no influence from the slab window (Iannelli et al., 2017; Fernández Paz et al., 2019). Furthermore, although there is much evidence in favor of the Aluk–Farallon ridge subduction, other authors question the existence of a slab window and link this important extensional stage and the voluminous magmatism to a diminished plate coupling (Ladino et al., 2000; Muñoz et al., 2018). Moreover, several aspects associated with this complex tectonic stage in the Andean evolution remain under debate. For instance, the precise location of the triple junction during the oldest stage in the Late Cretaceous remains partially uncertain (Somoza et al., 2012; Wright et al., 2016). Thus, a regional comparison of the geochemical signature of the arc-related products, from the Late Cretaceous to the Oligocene, would allow tracking the influence of this spreading ridge over the Andean margin.

In this study, we provide new isotopic data from three arc-related magmatic units located in key segments along the Andes between 35° and 42°S and integrate it with its previous field and geochemical data to test the potential influence of the southward migration of the Farallon–Aluk ridge over Andean magmatism between the Late Cretaceous to early Miocene times. These arc-related units include Los Ángeles Unit magmatism (67 Ma) at the Southern Central Andes (35°30′S); the Eocene Huitrera Formation (44 Ma) at the North Patagonian Andes (40°S) and the Auca Pan Formation (29 Ma) located in the transitional area between Southern Central and North Patagonian Andes (39°S) (Iannelli et al., 2017, 2018). To better evaluate the regional influence of the spreading ridge on Andean magmatism, we integrate geochemical evolution of these arc-related units with available geochemical data from coeval magmatic sequences from the whole arc region between the studied latitudes (35–42°S) (e.g., Kay et al., 2006; Zamora Valcarce et al., 2006). Thus, we focus the regional integrated study on three Andean magmatic stages: (1) the Latest Cretaceous–early Paleocene (80–59 Ma), (2) the Paleocene–Eocene (59–37 Ma), and (3) the late Eocene–early Miocene (37–20 Ma).

Also, to locate the ancient positions of potential slab windows, we use a novel approach that combines plate kinematic reconstructions with the mantle structure illuminated by global seismic tomography (Gianni et al., 2019), which is suggested to retain previous subduction configurations back to Mesozoic times (van der Meer et al., 2010, 2012). These analysis aims to test the existence of preserved slab gaps that could match the geological record of slab window position and triple junction location derived from the recent plate kinematic model of Müller et al. (2016).

Hence, by integrating seismic tomography of the uppermost lower mantle with plate kinematic reconstructions and new and existing geochemical data from Andean arc magmatism, we can track the main geodynamic and tectonic changes that affected the Andes from Latest Cretaceous to early Miocene times. Finally, a new model based on this multidisciplinary approach is presented, which supports the collision and subsequent migration of the Farallon–Aluk spreading ridge since at least the Late Cretaceous times.

REGIONAL SETTING

In the following subsections, we describe the geology of the main morphostructural units of the Southern Central Andes between 35°S and 42°S. These subsections are divided according to the main studied areas: the first in the Southern Central Andes where Late Cretaceous Los Ángeles Unit (67 Ma; 35°30'S) is emplaced, and the second one in the North Patagonian Andes where Eocene Huitrera Formation (44 Ma; 40°S) and Oligocene Auca Pan Formation (29 Ma; 39°S) crop out.

Geology of the Southern Central Andes (35–36°S)

The first studied area is located in the Southern Central Andes (35–36°S) along the Malargüe fold and thrust belt (**Figures 1**, **2**). The oldest outcrops in this Andean orogenic segment correspond to the Upper Permian–Lower Triassic Choiyoi Group (**Figure 2**; Kleiman and Japas, 2009; Sato et al., 2015), which comprise mesosilicic to silicic ignimbrites, granite intrusions, and subvolcanic domes (Llambías et al., 2003). By Late Triassic–early Cretaceous times, back-arc extension triggered the development of the Neuquén Basin, which initially started in the Late Triassic as unconnected depocenters that were filled by an alternation of non-marine to volcanic deposits (Precuyo Group). Subsequently, during the Early Jurassic back-arc extension, the depocenters were connected and filled by interbedded continental and marine deposits (Cuyo Group) (Legarreta and Uliana, 1991; Nullo et al., 2005).

The westward motion of the South American plate in the Late Cretaceous along with a shallowing of the subduction angle provoked a shift toward a compressional regime that turned the extensional retroarc Neuquén Basin into a foreland basin (Ramos and Folguera, 2005; Somoza and Zaffarana, 2008; Gianni et al., 2018a). This period was dominated by the deposition of fluvial, aeolian, and shallow lacustrine continental sequences (Neuquén Group). In the latest Cretaceous, an extensional regimen developed represented by the Malargüe Group, together with the development of a magmatic arc east of the main Andean range (**Figure 2**; Aguirre Urreta et al., 2011; Llambías and Aragón, 2011; Spagnuolo et al., 2012). Latest Cretaceous–early Paleocene volcanism is scattered along the Andean margin (**Figure 1**), including at least three units: Plan de los Yeuques Formation (34°30′S), Los Ángeles Unit (35°30′S), and the Naunauco Group (36–38°S). In the studied area, Late Cretaceous Los Ángeles Unit crop out (67 Ma; 35°30′S), characterized by basaltic to andesitic lava flows interbedded with volcanic breccias and fine- to coarse-grained sandstones, intruded by subvertical basaltic dykes (**Figures 1**, **2**). West of the studied area, the Plan de los Yeuques Formation developed between ∼80 and 63 Ma composed of andesitic lavas, volcanic breccias, and tuffs with interbedded continental deposits (Mosolf, 2013; Muñoz et al., 2018). Southwards (36–38°S), Late Cretaceous–early Paleocene arc-related magmatism (Naunauco Group; e.g., Zamora Valcarce et al., 2006; Llambías and Aragón, 2011; Mateo-Fernández Caso et al., 2011; Salvioli et al., 2017) took place in an eastern retroarc position interbedded with the synorogenic deposits of the Malargüe Group, while intrusive bodies dominate the main Andean magmatism (**Figure 1**; e.g., Franchini et al., 2003; Lucassen et al., 2004; Ramos and Folguera, 2005; Kay et al., 2006; Spagnuolo et al., 2012).

Between the Paleocene and the early Eocene, a magmatic hiatus is described in the study area (Mosolf et al., 2019), while southwards (37–38°S), volcanism remains with a calc-alkaline composition and a strong arc signature (PVNM; *Provincia Volcánica Neuquino Mendocina*) (Llambías and Rapela, 1989).

The break-up of the Farallon plate and the beginning of the Nazca plate orthogonal subduction changed drastically the tectonic conditions by late Oligocene–early Miocene times (Cande and Leslie, 1986; Somoza and Ghidella, 2005). As a consequence, an extensional regime spread along the Andean margin, developing intra-arc volcanic basins. This volcanism is included in the Abanico Formation (∼36–20 Ma), settled along the study area as a tholeiitic arc-like magmatism (**Figures 1**, **2**; Charrier et al., 1996; Muñoz et al., 2006).

During the late Miocene, a compressional regime triggered by a slab shallowing event caused the inversion of the extensional basins, the expansion of arc magmatism, and consequently the uplift of the frontal sector of the Principal Cordillera and the San Rafael Block (Folguera et al., 2009; Silvestro and Atencio, 2009; Rojas Vera et al., 2010; Turienzo, 2010; Giambiagi et al., 2012; Turienzo et al., 2012; Litvak et al., 2015). This slab shallowing event has been recently connected to the potential subduction of the ancient Payenia plume (Gianni et al., 2017). This stage finished by 4 Ma when a re-steeping of the subducting plate led to the impact of the Payenia plume with the Andean back-arc leading to the emplacement of the Payenia Volcanic

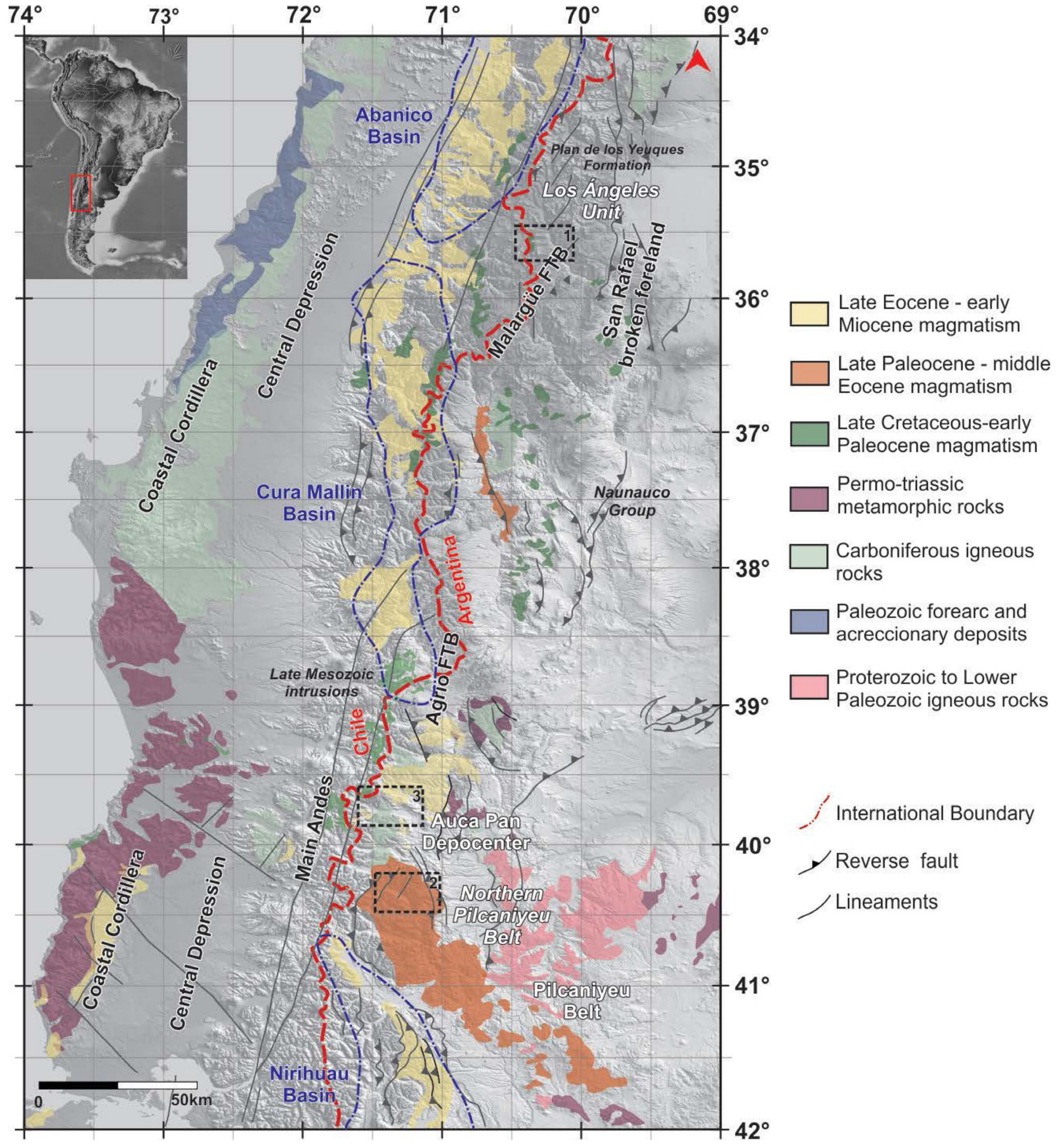

FIGURE 1 | Regional map of the Southern Central Andes between 35° to 42°S. The black squares show the locations of the studied areas. Based on Ramos et al. (2014), Sagripanti et al. (2015); Tapia et al. (2015), Charrier et al. (2002, 2007), Giambiagi et al. (2012); Jordan et al. (2001), Kay et al. (2005, 2006), Litvak et al. (2015, 2019), Lucassen et al. (2004); Rapela et al. (1983), and Zamora Valcarce et al. (2006).

Province (**Figure 2**; Llambías et al., 2010; Søager et al., 2013; Ramos et al., 2014).

Geology of North Patagonian Andes (39–41°S)

The second study area is located between 39° and 41°S and comprises the northernmost extreme of the North Patagonian Andes.

The oldest rocks of the Paleozoic basement correspond to Late Paleozoic metamorphic complex with U/Pb zircon ages between ∼420 and 380 Ma and biotite K/Ar ages between ∼375 and 310 Ma (**Figures 1**, **3**; Basei et al., 1999; Lucassen et al., 2004; Varela et al., 2005; Serra-Varela et al., 2019), whose evolution is related to the Patagonian Famatinian orogeny (Serra-Varela et al., 2019). Granites with ages between ∼350 and 270 Ma intruded the metamorphic basement (**Figure 3**;

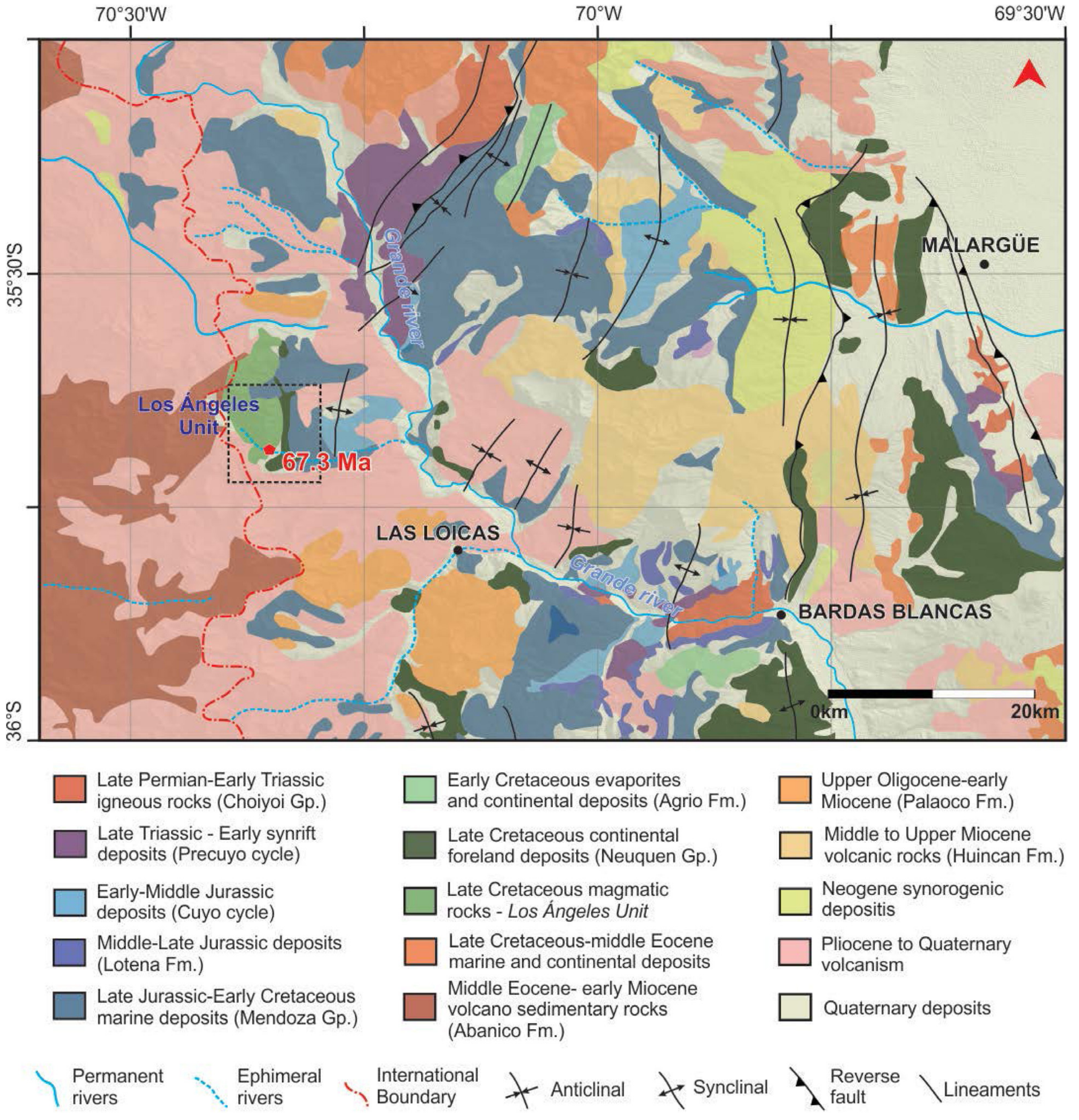

FIGURE 2 | Detailed map showing the main geological units recognized in the Southern Central Andes between 35 and 36°S. The black box shows the studied area where the Los Ángeles Unit crops out. Based on Fennell et al. (2019) and Nullo et al. (2005).

Varela et al., 1994; Basei et al., 1999; Lucassen et al., 2004) during the onset of subduction linked to the initiation of the Gondwanian orogenic cycle (Serra-Varela et al., 2019).

The Triassic to Early Jurassic period is characterized by an extensional regime that provokes the intrusion of magmatic rocks which mainly crop out in the western sector of the studied area. This magmatism is linked to the development of halfgrabens associated with the Pre-Cuyo basin filled by continental deposits (**Figure 3**; Giacosa and Heredia, 2001). Late Cretaceous magmatic rocks are emplaced to the west, mainly in the highest part of the Andes intruding the Paleozoic basement (North Patagonian Batholith; Pankhurst et al., 1999; Lucassen et al., 2004; Folguera and Ramos, 2011).

By Paleogene times (∼57–43 Ma), a decrease in arc-related magmatism is registered, and intraplate-like bimodal volcanism occurred in the broken foreland area grouped in the Pilcaniyeu Magmatic Belt, also referred to as the Huitrera Formation (**Figure 1**) (∼40–42°S; Rapela et al., 1988, 1984;

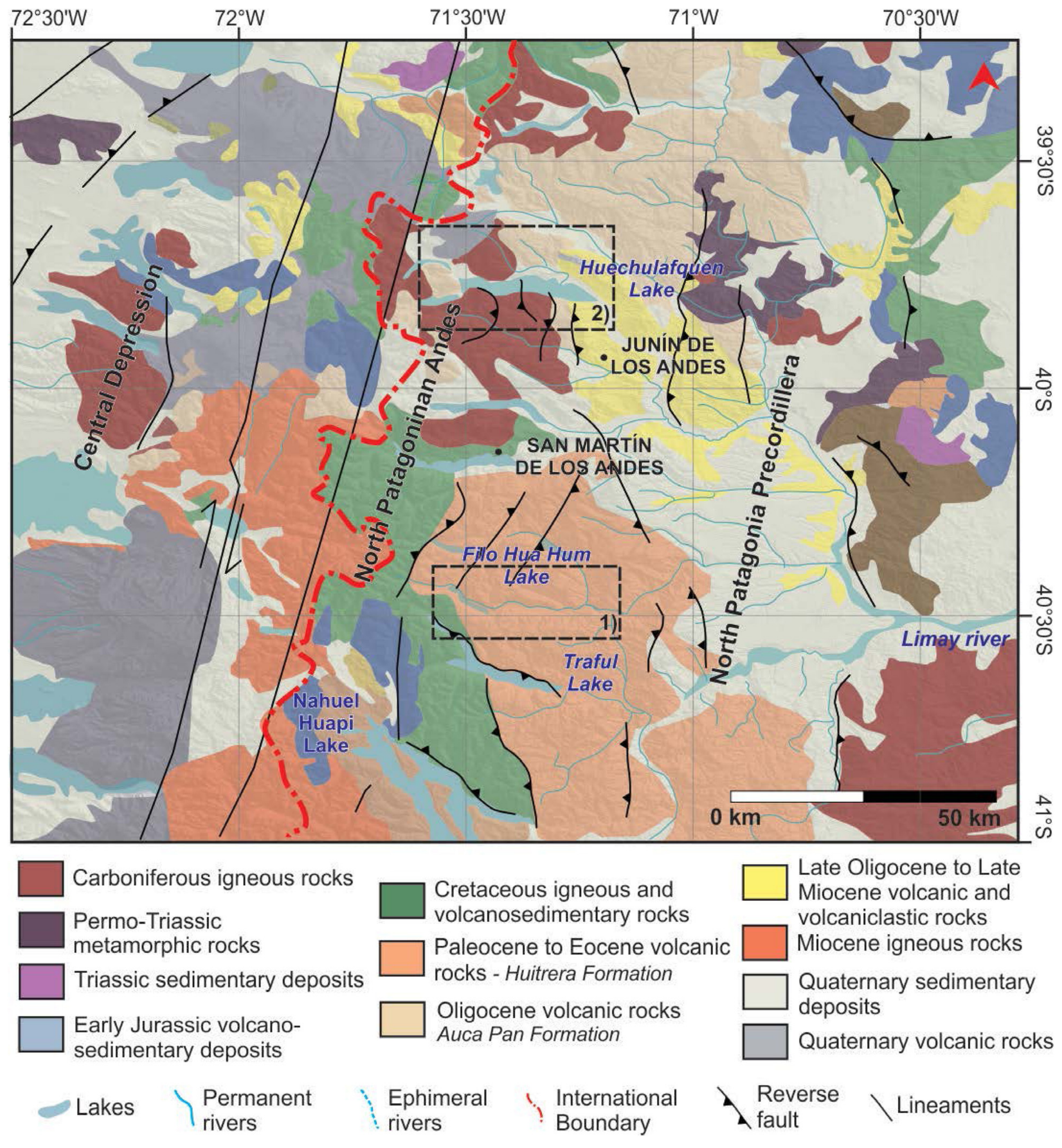

FIGURE 3 | Detailed map of the studied areas. The boxes outline the main studied areas, where (1) Paleocene to Eocene volcanic rocks crop out associated with the studied Huitrera Formation (44 Ma) and (2) Oligocene volcanic rocks appear related to the studied Auca Pan Formation (29 Ma). Modified from Ramos et al. (2014); Lucassen et al. (2004), Scasso (2012), Cazau et al. (1989), Rapela et al. (1983), and Iannelli et al. (2017).

Aragón et al., 2011; Iannelli et al., 2017). The Eocene volcanic rocks, which are one of the main focus of this paper, are located at 40°S and have been correlated with the Huitrera Formation, the northernmost and westernmost sections of the Pilcaniyeu Magmatic Belt (**Figure 3**; Iannelli et al., 2017). This magmatic stage was linked to a slab window event produced during the subduction of the Farallon–Aluk spreading ridge (Aragón et al., 2011). Afterward, the magmatic front returned to the main Andean margin by the late Eocene, represented by an arc-related volcanic belt referred to as the El Maitén Belt (González Bonorino, 1979; González Bonorino and González Bonorino, 1978; Rapela et al., 1988; Litvak et al., 2014; Fernández Paz et al., 2018, 2019). This younger volcanism (∼37–19 Ma) extended from 40° to 42°S and was mostly controlled by an extensional regime (Rapela et al., 1983; Bechis et al., 2014; Litvak et al., 2014; Fernández Paz et al., 2018, 2019). North of 40°S, the studied

Oligocene volcanic sequence is named Auca Pan Formation and is considered as the northernmost expression of this belt (Turner, 1973; Dalla Salla et al., 1981; Iannelli et al., 2017).

The latest Oligocene–early Miocene volcanic sequences were associated with the broad extensional basins induced by the rapid and orthogonal subduction of the Nazca plate and the steepening of the subducted slab (Muñoz et al., 2000; Jordan et al., 2001; Kay et al., 2006; Fennell et al., 2018). In particular, the initial infill lower section of the volcano-sedimentary Cura Mallín basin (27–20 Ma; 36–38°S) developed during this period under control of extensional structures (**Figures 1**, **3**), composed of pyroclastic deposits, lava flows, and interbedded lacustrine and delta facies (Suárez and Emparán, 1995; Jordan et al., 2001; Radic et al., 2002; Burns et al., 2006; Kay et al., 2006; Melnick et al., 2006; Folguera et al., 2010; Rojas Vera et al., 2010). To the west, the coeval Coastal Magmatic Belt developed with a predominant tholeiitic composition and variable geochemical signatures similar to the SVZ (Southern Volcanic Zone) (López-Escobar and Vergara, 1997; Muñoz et al., 2000). These volcanic rocks are interbedded with continental and marine sedimentary deposits.

During the late Miocene, a compressional regime caused the inversion of previous extensional structures with the intrusion of gabbros and leucogranites in the North Patagonian Andes, while the magmatic arc activity resurged and endures till today (Aragón et al., 2011). The intrusions emplaced mainly along dextral strike-slip system of the Liquiñe-Ofqui fault zone (LOFZ) between 19.7 and 7 Ma (Rapela et al., 1983; González Díaz and Lizuaín, 1984; Aragón et al., 2011). Furthermore, isolated within-plate magmatic bodies are also found in the Precordillera region, which have been attributed to a period of slab steepening in the late Pliocene after a restricted shallow subduction setting in the middle to late Miocene (Orts et al., 2015).

LATE CRETACEOUS TO OLIGOCENE ARC-LIKE MAGMATIC SEQUENCES FROM THE SOUTHERN CENTRAL ANDES TO THE NORTH PATAGONIAN ANDES (35–42°S)

Age and Distribution

The first and older studied sequence corresponds to the Late Cretaceous Los Ángeles Unit (∼67 Ma) emplaced at 35°30′S during the first magmatic period (80–59 Ma) (**Figure 2**). This sequence comprises basaltic to andesitic lava flows with interbedded volcanic breccias and lithic sandstones, intruded by basaltic dikes with typical columnar jointing (for a detailed description and stratigraphic columns, see Iannelli et al., 2018). Los Ángeles Unit appears in discordance over Cretaceous marine and non-marine deposits and show changes in dip and thickness along strike, indicating that its deposition was controlled by E-W syn-sedimentary normal faults (**Figure 3**; Fennell et al., 2019). The maximum depositional age of a lithic sandstone interbedded between the lava flows of the Los Ángeles Unit yielded 67.1 + 2.4/-0.9 Ma from U-Pb ages of detrital zircon and agrees with crystallization ages in other volcaniclastic rocks of the region (Fennell et al., 2019 and references therein).

The second studied sequence corresponds to the Eocene Huitrera Formation (Pilcaniyeu Belt) emplaced in the North Patagonian Andes (∼40°S; **Figure 3**) during the second magmatic period (∼59–37 Ma). It comprises bimodal sequences composed of porphyritic lava flows with rhyolitic and basaltic compositions interbedded with pyroclastic facies, such as lithic to vitreous tuffs and conglomerate deposits (Iannelli et al., 2017). The age of the sequence is constrained by a whole-rock Ar–Ar age obtained for a basaltic rock from the basal levels that yielded an age of 44.3 ± 0.13 Ma (Iannelli et al., 2017).

Finally, the last studied sequence corresponds to the Oligocene Auca Pan Formation located at 39°S (**Figure 3**) and associated with the northernmost expression of the El Maitén belt (Rapela et al., 1983). A whole-rock Ar–Ar age from a basaltic rock located in the basal levels of this Formation is 29.6 ± 1.2 Ma (Ramos et al., 2014). This magmatic sequence is composed of basaltic to andesitic lava flows with porphyritic texture with plagioclase, olivine, and clinopyroxene phenocrysts. Locally, lava flows with a thickness of ∼50–100 km grade toward more vesiculated lava facies. Pyroclastic deposits represented mostly by vitreous tuffs are also locally interbedded between lava flows (for details, see Iannelli et al., 2017). The deposition of Auca Pan Formation is controlled by normal faulting causing important variations in strata thickness along the area (Ramos et al., 2014). Locally, the northernmost studied section is controlled by a homoclinal structure with a 35° dip to the east.

Geochemical Features for Studied Late Cretaceous to Oligocene Magmatic Sequences Through Major and Trace Elements Composition

The following chapters summarize the results of the geochemical characterization using published major and trace element data from Los Ángeles Unit (67 Ma; 35°30′S) (Iannelli et al., 2018), Huitrera (44 Ma; 40°30′S), and Auca Pan Formations (29 Ma; 39°40′S) (Iannelli et al., 2017).

Late Cretaceous to Early Paleocene Stage: Los Ángeles Unit

The Late Cretaceous volcanic rocks (Los Ángeles Unit, ∼67 Ma) are composed of basaltic to andesitic lavas with a SiO_2 range between 44.4 and 53.8 wt.%. They are characterized by a subalkaline tholeiitic to alkaline trend (**Figure 4A**) (FeO_t/MgO:1.1–2.9). Fractional crystallization of olivine, clinopyroxene, and Fe-Ti oxides have been recognized as a minor process in the evolution of this sequence (Iannelli et al., 2018). Trace elements classification diagram shows that the Los Ángeles Unit presents a trend between the andesitic/basalt and andesite fields toward the trachy-andesitic one, consistent with major elements classification (**Figure 4B**). When considering the stratigraphic distribution, there is an increase in alkaline composition toward the upper levels of the sequence as can be seen in **Figure 4D**, where the samples display a trend of increasing Ta/Yb ratio at relatively constant Th/Yb. Moreover,

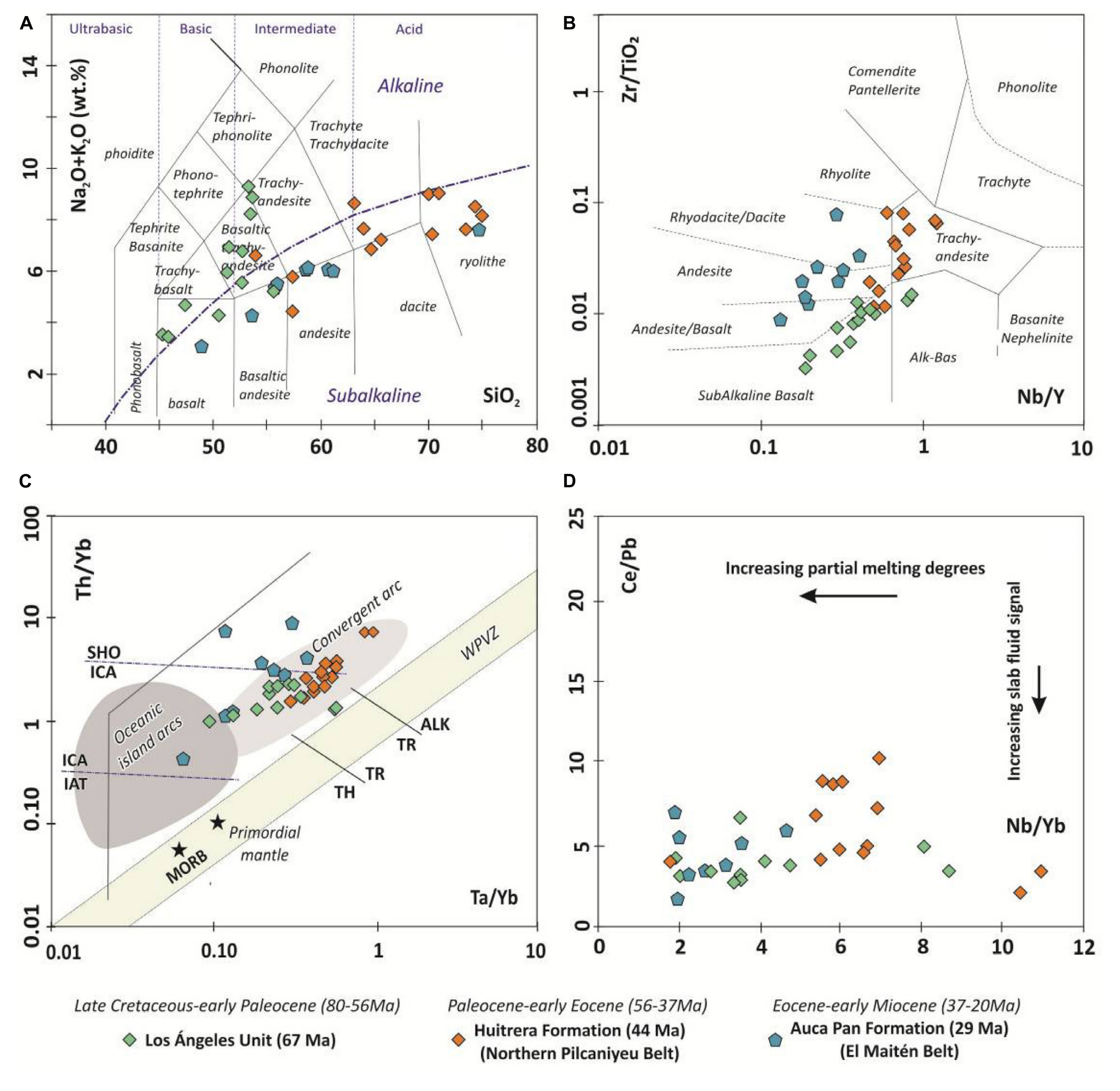

FIGURE 4 | (A) TAS classification diagram for studied Late Cretaceous, Eocene, and Oligocene sequences (Irvine and Baragar, 1971; Le Maitre et al., 1989). **(B)** Trace elements classification plot showing important differences between the three studied sequences. **(C)** Th/Yb vs. Ta/Yb diagram proposed by Pearce (1983) and modified from Xia and Li (2019), which allows constraining a tectonic setting for each studied sequence (SHO, Island arc Shoshonites; ICA, Island arcs Calc-alkaline basalts; IAT, Island arc Tholeiites; TH, Tholeiitic series; TR, Transitional series; ALK, Alkaline series; MORB, Mid-ocean ridge basalts; WPB, Within-plate basalts). **(D)** Ce/Pb vs. Nb/Yb as indicators of partial melting degrees and slab-fluid influence. Geochemical data are from Iannelli et al. (2017, 2018).

the decreasing Ce/Pb and increasing Nb/Yb trends indicate that the slab-fluid signal and partial melting degrees decrease during the magma evolution (**Figure 4D**).

Normalized N-MORB multi-element diagram shows a pronounced enrichment in LILE elements toward the upper magmatic pulses, also partially seen among all the REE elements (**Figure 5A**). This enrichment shows a subduction imprint evidenced by positive anomalies in Rb, Ba, and Th and the depletion in Nb and Ta. However, this sequence is more enriched in Nb, Ta, and REE incompatible elements than the average TSVZ (Transitional Southern Volcanic Zone) and shows, gradually, a similar multi-element pattern to the ocean island basalts (OIB) (**Figure 5A**).

Early Paleocene–Late Eocene Stage: Huitrera Formation

The studied Eocene Huitrera Formation (44 Ma) emplaced at ∼40°S is characterized by a bimodal volcanic sequence

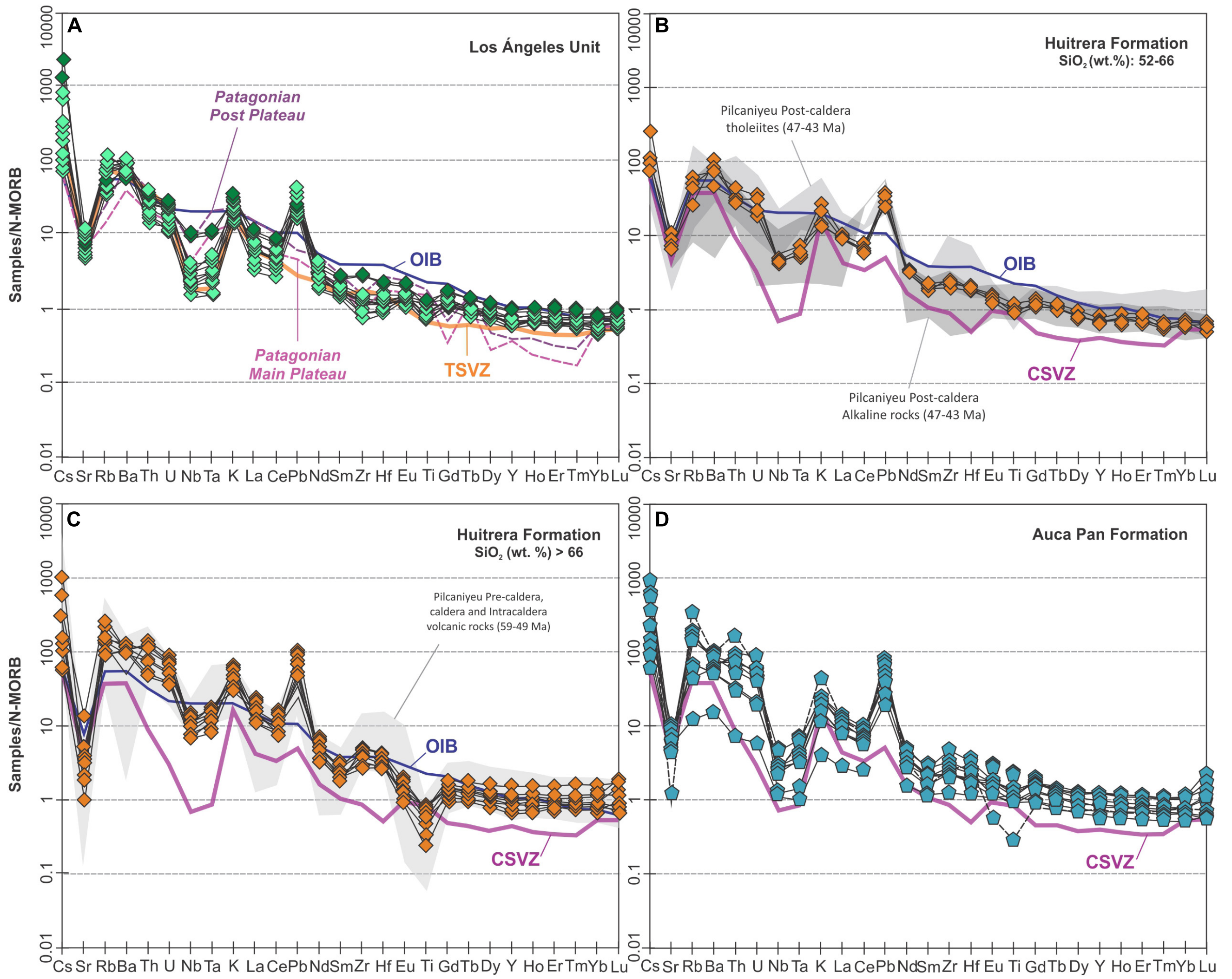

FIGURE 5 | (A) Multi-element diagram for the Late Cretaceous Los Ángeles Unit. **(B,C)** Multi-element diagrams for intermidiate and acid volcanic rocks of Huitrera Formation, respectively. **(D)** Multi-element diagram for the Auca Pan Formation. Geochemical data of the studied sequences are taken from Iannelli et al. (2017, 2018). Average of TSVZ (34.5–38°S) corresponds to Futa and Stern (1988); Hickey-Vargas et al. (1986), Ferguson et al. (1992); Wehrmann et al. (2014), and Jacques et al. (2013). The average of the CSVZ (38–43°S) corresponds to Mella et al. (2005); López-Escobar et al. (1992)López-Escobar et al. (1995); Deruelle (1982), and Wehrmann et al. (2014). The average of the OIB composition is from Sun and McDonough (1989), while the geochemical data for Pilcaniyeu pre-, intra-, and post-caldera stages are from Aragón et al. (2011). Patagonia Main and Post plateau data correspond to the Neogene back-arc magmatism presented by Gorring and Kay (2001).

with basaltic-andesites (SiO_2: 51.6–61.7 wt.%) and rhyolitic compositions (SiO_2:63.8–73.3 wt.%) (**Figure 4A**; Iannelli et al., 2017). When considering major and trace elements classification, a trend toward a transitional signature between subalkaline and alkaline compositions is seen (Nb/Y: 0.5–1.2) (**Figures 4A,B**). The relatively high Ta/Yb, Ce/Pb, and Nb/Yb ratios show a partially lower slab contributions influence and lower melting degrees than the CSVZ (Central Southern Volcanic Zone) composition (**Figures 4B,D**).

N-MORB normalized multi-element diagrams for intermediate (52–66 wt.%) and acid rocks (>66 wt.%) present typical arc-like patterns (e.g., relative depletion in Nb and Ta and enrichment in Rb, Ba, Th, and K). Huitrera Formation at 40°S shows a higher general enrichment in LILE and HFSE when compared to the average CSVZ (38–42°S), close to the OIB composition (**Figures 5B,C**; Sun and McDonough, 1989).

Late Eocene–Early Miocene Stage: Auca Pan Formation

The studied early Oligocene Auca Pan Formation (~29 Ma; 39°S), associated with the El Maitén Belt (~40–43°S), is composed of basaltic to andesitic lava flows interbedded with vitreous tuffs. Lava flows show a SiO_2 range between 47.2 and 60.5 wt.%, classifying mostly as subalkaline andesitic to basaltic rocks (**Figures 4A,B**). FeO/MgO ratios are indicative of a calc-alkaline composition, while trace elements ratios also show a basaltic to andesitic composition (**Figure 4B**). These rocks show a marked arc-like signature, characterized by the high Th/Yb and low Ta/Yb ratios, with significative slab-fluid contributions and high partial melting degrees, as indicated by the low Ce/Pb (1.7–6.9) and Nb/Yb (1.3–4.7) ratios, showing a similar range than CSVZ (38–43°S) (**Figures 4C,D**).

Auca Pan Formation presents a typical arc-like pattern in the multi-element diagram, with similar LILE contents than the CSVZ (38–43°S), although the most evolved samples present more enriched trace element compositions comparable to the UCC average composition (**Figure 5D**; Rudnick and Gao, 2003). Fractional crystallization process has been considered as one of the main mechanisms for controlling the evolution of the Auca Pan Formation sequence, while crustal contamination would have had a minor influence, according to trace elements composition (Iannelli et al., 2017).

METHODOLOGY

Compiled Arc-Like Andean Dataset

To make a regional comparison of the studied arc-related magmatic units along the Andean margin from Late Cretaceous to early Miocene times (∼80–20 Ma), we compiled geochemical data from previous works, based on three main temporal stages. **Figure 6** shows a schematic stratigraphic diagram that represents the coeval arc-related sequences included for the regional comparison in each magmatic stage: (1) For the first one, between Late Cretaceous and early Paleocene times (80–59 Ma), we included magmatism located between 34° and 35°S (Plan de Los Yeuques Formation; 80–63 Ma; Muñoz et al., 2018), arc-related magmatism between 36° and 38°S (Naunauco Group; 74–59 Ma; Zamora Valcarce et al., 2006; Llambías and Aragón, 2011; Mateo-Fernández Caso et al., 2011; Salvioli et al., 2017), and the Late Cretaceous intrusions located along the North Patagonian Cordillera (35–41°S, 94–65 Ma) together with the fore-arc intrusions at the same latitudes mainly emplaced in the Chilean Central Depression (91–80.5 Ma) (Lucassen et al., 2004; De La Fuente, 2014; **Figure 1**). (2) For the second magmatic period, between the Paleocene and the Eocene (59–37 Ma), we included arc-related sequences emplaced between 36° and 38°S (PVNM) (*Provincia Magmática Neuquino Mendocina*; 56-38 Ma; Rapela and Llambías, 1985; Llambías and Rapela, 1989) and magmatism located along the Patagonian Precordillera between 40° and 43°S (Pilcaniyeu magmatic belt; 57–43 Ma) (Rapela et al., 1988; Aragón et al., 2011; Iannelli et al., 2017). (3) For the last magmatic period defined between the latest Eocene to the early Miocene (37–20 Ma) we considered from north to south, the volcanic sequences developed along intra-arc basins mainly located between 33° and 36°S (Abanico Formation; 36–20 Ma; 33–36°S; Kay et al., 2005; Muñoz et al., 2006; Montecinos et al., 2008; Piquer et al., 2017), magmatic units between 36° and 38°S (lower Cura Mallín Formation; 27-20 Ma; 36-39°S; Burns et al., 2006; Kay et al., 2006; Utgé et al., 2009), and the arc-related sequences developed along the Central Depression between 37° and 43.5°S (Coastal Magmatic Belt, CMB; 28–20 Ma; López-Escobar and Vergara, 1997; Muñoz et al., 2000).

We also include for comparison the Southern Volcanic Zone recent magmatism according to the division criteria presented by Jacques et al. (2013, 2014). Thus, for comparing with the studied Los Ángeles Unit (67 Ma; 35°30′S), we considered the quaternary volcanoes between 34.5° and 38°S, grouped as the Transitional Southern Volcanic Zone (TSVZ) (Hickey-Vargas et al., 1986; Ferguson et al., 1992; Futa and Stern, 1988; Wehrmann et al., 2014), whereas for comparisons with the Huitrera (44 Ma; 40°S) and Auca Pan Formations (29 Ma; 39°S), we compare with the magmatic units from the Central Southern Volcanic Zone (CSVZ, 38–43°S) (Deruelle, 1982; López-Escobar et al., 1995, 1992; Mella et al., 2005; Wehrmann et al., 2014).

Isotopic Analysis

New Sr-Nd-Pb isotopic analysis has been made on six basaltic to andesitic lavas from the Los Ángeles Unit (67 Ma, 35°30′S), one basalt and three rhyolites from the Huitrera Formation (44 Ma, Northern Pilcaniyeu Belt, 40°S), and six basaltic to andesitic lavas from the Auca Pan Formation (29 Ma, El Maitén Belt, 39°S). Moreover, three basement rocks from the different areas and temporal stages were also analyzed, which comprises the Choiyoi Group (CHOI1, 35°S) and the metamorphic (PAT3J) and igneous (PAT2J) basement of North Patagonia (39–40°S). Whole-rock Sr, Nd and Pb isotope ratios were obtained through thermal ionization mass spectrometry (TIMS) on a Triton plus instrument (Thermo Scientific) at the Isotope Geochemistry Laboratory of MARUM, University of Bremen (Germany). Sample preparation, mass spectrometric analyses, and external reproducibility of the methods in the Bremen laboratory are documented in Höppner et al. (2018).

Calculation of Tomography Sections

To test the potential existence of slab windows since the Late Cretaceous with an independent methodology, we studied the mantle structure below South America. Recent studies revealed that due to the prolonged times involved in whole mantle convection (>100 Ma), the lower mantle still preserves positions of former subduction configurations back to latest Paleozoic times (van der Meer et al., 2010, 2012). In other words, the current distribution of the lower mantle can be linked to the paleo-subduction zone configuration, which yields coherent correlations of plate reconstructions with mantle structure for the last 300 Ma (van der Meer et al., 2010, 2012, 2018. Here, we combine plate kinematic reconstructions with the mantle structure to locate the ancient positions of potential slab windows (Gianni et al., 2019). A similar approach has been followed in previous studies to map ancient slab windows in North America (Gaina and Jakob, 2019) and Sumatra (Fabian et al., 2010). In South America, a recent study has shown that the oceanic slab at a depth of 1300 km

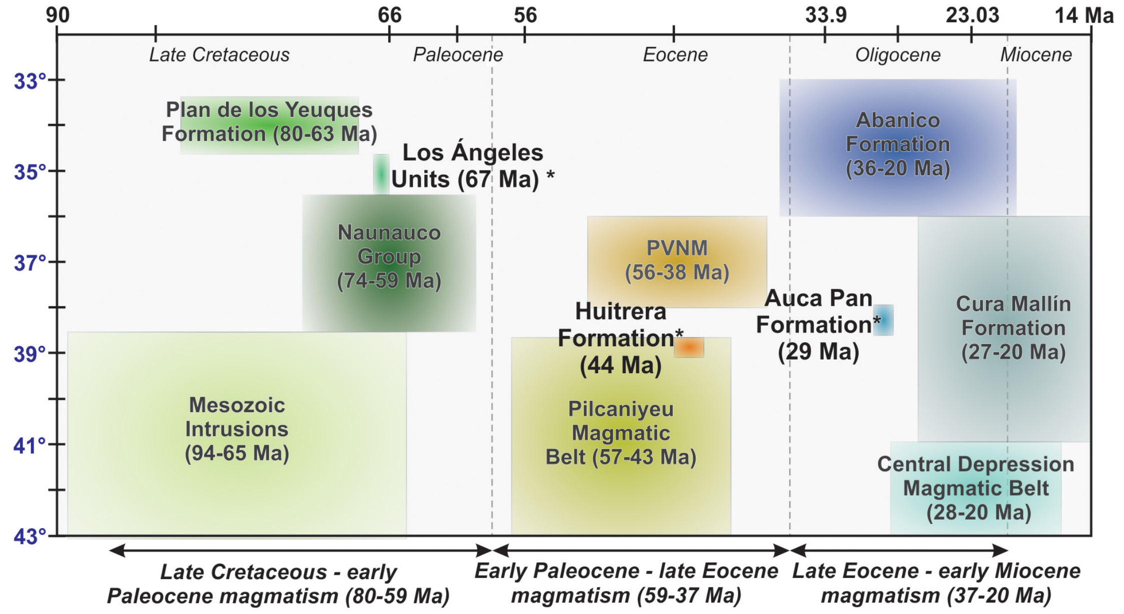

FIGURE 6 | Schematic diagram showing the main arc-related units used in the regional comparison. Geochemical data area from the following: for the first magmatic period (80–59 Ma): Casé et al. (2008); De La Fuente (2014), Franchini et al. (2003); Iannelli et al. (2018), Llambías and Aragón (2011); Lucassen et al. (2004), Mateo-Fernández Caso et al. (2011); Muñoz et al. (2018), and Zamora Valcarce et al. (2006); for the second magmatic period (59–37 Ma): Aragón et al. (2011); Iannelli et al. (2017), Kay et al. (2006), and Llambías and Rapela (1989); and for the last period (37–20 Ma): Iannelli et al. (2017); Kay et al. (2005)Kay et al. (2006); López-Escobar and Vergara (1997), Piquer et al. (2017), and Utgé et al. (2009).

below the Andean margin represents subduction since Late Cretaceous times (Chen et al., 2019). Hence, any relict of the past development of a slab window should be still being visible as a slab gap in the deeper slab (Fabian et al., 2010; Gianni et al., 2018a).

We analyze global P-wave and S-wave seismic tomography models in combination with a recent plate kinematic reconstruction model (Müller et al., 2016) using the Gplates 2.0 software[1]. For our analysis, we used a 1.5 cm/year slab sinking rate that has been previously calculated for the bottom of the subducted Aluk plate (van der Meer et al., 2018). This value is reasonable as it is between average values of 20 cm/year determined from geodynamic modeling (Steinberger et al., 2012) and 1.2 cm/year derived from global slab reconstructions (van der Meer et al., 2010; Shephard et al., 2017). This slab sinking rate was obtained for the study area by correlating the depths of the San Matías slab (i.e., Aluk plate previous to subduction) with the subduction magmatic history beneath Patagonia (van der Meer et al., 2018). This correlation strategy is based on linking slabs to their geological record assuming that slabs tend to sink vertically in the lower mantle, as was recently corroborated by Domeier et al. (2016). We carried out an additional reconstruction considering a slower slab sinking rate of 1.3 cm/year determined for subducted slabs beneath South America (Chen et al., 2019; **Supplementary Figure S1**).

We are aware that although used in many studies, assuming slab sinking vertically and at a constant rate is a simplification as slabs subduct at different rates in upper and lower mantle and can have different geometries, depending on ambient mantle viscosity, slab viscosity, and subduction history (see discussion in Billen, 2008). However, as shown in previous works and the analyses in the following sections, this assumption leads to a good correlation of the mantle structure with the bedrock record. Future studies could focus in reproducing the mantle structure through numerical modeling (e.g., Braz et al., 2018).

To test the existence of a slab window event by Late Cretaceous times, we analyzed the subducted slab with tomography slices from three seismic tomography models (PRI-05; Montelli et al., 2006; GAP-P4, Obayashi et al., 2013; SPani-P, Tesoniero et al., 2015) at a depth of 1200 km (∼80 Ma). Then, we searched for a slab gap or along-strike slab discontinuity and compared its position with the hypothetical location of the Farallon–Aluk mid-ocean ridge location derived from Müller et al.'s (2016) reconstruction, which incorporates the ridge kinematics determined by Eagles and Scott (2014). Then, we carried out a finer analysis using the high-resolution UU-P07 global P-wave seismic tomography model (Amaru, 2007). This model has been previously used to build plate reconstructions in the Mesozoic and is generally chosen for analyses like ours (van der Meer et al., 2010; Gianni et al., 2019). We present additional reconstructions for the PRI-05, GAP-P4, and Spani-P models in **Supplementary Figure S2**. In this analysis, we examine the time–space evolution of identified slab gaps to test the correlation with mid-ocean ridge positions from plate kinematic reconstructions and the location of anomalous magmatism attributed to slab window events. For this, we analyzed the subducted slab with tomography

---

[1] http://www.gplates.org/

slices at a depth of 1250, 850, and 450 km corresponding to the fossil record of subduction in Late Cretaceous (~80–65 Ma), Paleocene–Eocene (60–50 Ma), and late Eocene–Oligocene times (40–30 Ma).

RESULTS

Isotopic Signature of the Studied Late Cretaceous to Oligocene Magmatic Sequences

Late Cretaceous–Early Paleocene Los Ángeles Unit (67 Ma)

New isotopic data from the Los Ángeles Unit (67 Ma; 35°30′S) comprises basaltic to andesitic lavas from the basal, middle, and upper levels of the sequence and from the basaltic dikes, which are considered the last magmatic pulses of this volcanism (**Table 1**). Los Ángeles Unit volcanic rocks have $(^{87}Sr/^{86}Sr)_i$ ratios ranging from 0.70371 to 0.70496 and $(^{143}Nd/^{144}Nd)_i$ ratios between 0.51260 and 0.51279 (εNd = + 1.02 to + 4.63), plotting alongside the mantle array (**Figure 7A** and **Table 1**). The isotopic variation can be partially correlated with the stratigraphic position of the studied samples, which shows a trend toward a more depleted source in the youngest lavas (**Table 1**). However, the two samples from the basaltic dikes (SVA09-SVA26) present $(^{87}Sr/^{86}Sr)_i$ ratios of 0.70472 and 0.70496 and a $(^{143}Nd/^{144}Nd)_i$ range of 0.512789–0.512757, plotting away from the mantle array toward higher $(^{87}Sr/^{86}Sr)_i$ ratios (**Figure 7A**). High Sr isotopic ratios with positive εNd can be explained by hydrothermal alteration with seawater (e.g., Hofmann and White, 1982), but marine deposits and strong alteration are both absent through the sequence (Iannelli et al., 2018). An overprint of the real isotopic data due to meteoric alteration is the most adequate explanation, which have reduced the Rb/Sr ratios by producing Rb loss and Sr gain causing an under-correction of the initial ratios. $(^{87}Sr/^{86}Sr)_i$ ratios would be overestimated as the Sr and Rb (ppm) values used for recalculating the initial isotopic ratios might have been altered (e.g., Plimer and Elliott, 1979).

The general isotopic signature seen in the Late Cretaceous–early Paleocene Los Ángeles Unit contrasts with the isotopic values for the local basement corresponding to the Choiyoi Group (CHOI1), which presents higher $(^{87}Sr/^{86}Sr)_i$ and lower $(^{143}Nd/^{144}Nd)_i$ ratios consistent with the Paleozoic basement rocks (**Figure 7A** and **Table 1**; Lucassen et al., 2004).

Los Ángeles Unit rocks show $^{206}Pb/^{204}Pb$ = 18.40–18.57, $^{207}Pb/^{204}Pb$ = 15.51–15.57, and $^{208}Pb/^{204}Pb$ = 38.04–38.33 (**Table 1**). Most of the samples show Pb isotopic signatures similar to the isotopic compositional field for the depleted MORB (**Figures 8A,B**). No correlation between Pb isotopic composition and the stratigraphic position of the samples is seen (**Table 1**). Los Ángeles Unit presents a partially higher $^{206}Pb/^{204}Pb$ and $^{208}Pb/^{204}Pb$ ratios than the local basement represented by the Choiyoi Group sample (CHOI1) (**Figures 8A,B** and **Table 1**). Considering the plumbotectonic model from Zartman and Doe (1981), Pb isotopic composition varies between the mantle growth curve and the orogen growth curve, for both the uranogenic and the thorogenic Pb (**Figures 8A,B**).

Eocene Huitrera Formation (44 Ma)

The Eocene Huitrera Formation volcanism (~44 Ma; 40°S) presents $(^{86}Sr/^{87}Sr)_i$ ratios between 0.70399 and 0.70411, with $(^{143}Nd/^{144}Nd)_i$ ratios between 0.51267 and 0.51274 (εNd: + 1.76– + 3.10) (**Table 1**). Therefore, Eocene rocks are distributed along the mantle array, showing higher $(^{86}Sr/^{87}Sr)i$ and lower εNd values than the average depleted mantle composition (**Figure 7B**). However, one sample (DP49) shows a remarkably higher $(^{87}Sr/^{86}Sr)_i$ ratio of 0.70692 but with a similar εNd value, plotting outside the mantle array that could be associated with seawater alteration (**Figure 7B**). As a marine environment has not been described for the emplacement of this sequence, we considered that the high $(^{87}Sr/^{86}Sr)_i$ ratio is caused by meteoric alteration, which would have disturbed Rb/Sr ratios and so the under-correction of the initial isotopic ratios [see discussion in section Late Cretaceous- Early Paleocene Los Ángeles Unit (67 Ma)]. Thus, a reliable $(^{87}Sr/^{86}Sr)_i$ ratio cannot be calculated for this sample as it shows plagioclase altered to epidote and sericite, and so Sr content might have been affected by meteoric fluids (e.g., Plimer and Elliott, 1979). We dismiss its $(^{87}Sr/^{86}Sr)_i$ values from the final interpretation, although Nd and Pb isotopic ratios can still be reliable.

Sr and Nd isotopic composition of Huitrera Formation samples clearly differentiate from the two samples of the metamorphic and intrusive Paleozoic basement at the North Patagonian Andes (samples PAT2J and PAT3J) that plot outside the limits of **Figure 7C** at considerably high Sr ratios and low ε Nd.

Huitrera Formation Pb isotopic composition is presented in **Table 1**. This volcanic sequence shows $^{206}Pb/^{204}Pb$ = 18.49–18.61, $^{207}Pb/^{204}Pb$ = 15.53–15.59, and $^{208}Pb/^{204}Pb$ = 38.22–38.47 values, plotting along the orogenic growth curve (Zartman and Doe, 1981). The isotopic signature of studied Eocene volcanism is partially similar to the local basement samples (PAT2J and PAT3J) (**Figures 8C,D**).

Oligocene Auca Pan Formation (29 Ma)

The Oligocene Auca Pan Formation (~29 Ma; 39°S) is characterized by initial $^{86}Sr/^{87}Sr$ ratios between 0.70397 and 0.70486 and $(^{143}Nd/^{144}Nd)$ and between 0.51267 and 0.51275 (εNd: + 1.37– + 2.99) (**Table 1**). According to **Figure 7C**, Oligocene rocks show increasing initial $^{87}Sr/^{86}Sr$ ratios for a limited initial $^{143}Nd/^{144}Nd$ and ε Nd range.

The two samples that represent the metamorphic and intrusive Paleozoic basement at the North Patagonian Andes were included for comparison (samples PAT2J and PAT3J), showing considerably higher Sr ratios and lower εNd than Auca Pan Formation (**Figure 7C**).

Auca Pan Formation lavas show the following isotopic lead ratios: $^{206}Pb/^{204}Pb$ = 18.53–18.72, $^{207}Pb/^{204}Pb$ = 15.53–15.65, $^{208}Pb/^{204}Pb$ = 38.27–38.72 (**Table 1**). Pb isotope ratios in Oligocene volcanism are similar to those of the underlying basement represented by the samples PAT2J and PAT3J, although

TABLE 1 | Initial Sr, Nd, Pb isotope ratioscalculated from the measurements of the current isotope ratios (TIMS), and Rb, Sr, Sm, Nd, U, Th, Pb element concentration of whole rock samples.

Sample	Rb (ppm)	Sr (ppm)	^{87}Sr/^{86}Sr ± 2σ	(^{87}Sr/^{86}Sr)$_i$	Sm (ppm)	Nd (ppm)	^{143}Nd/^{144}Nd ± 2σ	(^{143}Nd/^{144}Nd)$_i$	eNd	U (ppm)	Th (ppm)	Pb (ppm)	^{206}Pb/^{204}Pb	^{207}Pb/^{204}Pb	^{208}Pb/^{204}Pb
LATE CRETACEOUS LOS ÁNGELES UNIT (67 Ma)															
SVA09	55	260	0.7053 ± 5	0.704716	6.9	31.2	0.512847 ± 7	0.512789	4.6	1.2	3.5	12	18.43	15.56	38.19
SVA26	37	574	0.705136 ± 7	0.704958	6.3	28.6	0.512815 ± 8	0.512756	3.9	1	3	16	18.5	15.61	38.48
SVA13	42	493	0.703993 ± 6	0.703757	3.8	16.2	0.512767 ± 5	0.512704	2.9	0.6	1.7	6	18.54	15.58	38.35
SVA17	45	555	0.704094 ± 4	0.703871	5.2	23	0.512663 ± 18	0.512603	1.1	1.2	4.3	11	18.58	15.58	38.42
SVA10	28	592	0.703837 ± 5	0.703707	4.5	19.3	0.512739 ± 7	0.512677	2.4	1.1	3.5	12	18.56	15.58	38.38
SVA28	19	470	0.703818 ± 4	0.703707	3.9	13.8	0.512717 ± 7	0.512642	1.8	0.6	2.1	< 5	18.53	15.58	38.36
SVA30	21	574	0.704306 ± 7	0.704205	3.5	12.6	0.512724 ± 6	0.512651	1.9	1.2	3.9	8	18.6	15.61	38.48
EOCENE HUITRERA FORMATION (44 Ma)															
DP41	77	241	0.704691 ± 8	0.704109	6.7	33.2	0.512744 ± 6	0.512708	2.5	2.63	10.4	16	0	0	0
DP49	91	144	0.708067 ± 10	0.706916	5.6	30.1	0.512708 ± 7	0.512675	1.8	2.61	10.5	8	18.56	15.61	38.49
DP51	113	126	0.70574 ± 5	0.7041068	5.6	29.3	0.512704 ± 5	0.512671	1.7	2.64	11	7	18.57	15.63	38.6
SA10	127	157	0.705801 ± 6	0.703988	4.8	28.2	0.512758 ± 6	0.512721	2.9	3.29	15.3	18	18.64	15.62	38.62
DP58	33	884	0.704223 ± 6	0.704155	5.5	27.5	0.512775 ± 6	0.512739	3.1	1.6	5.15	8	18.52	15.57	38.37
OLIGOCENE AUCA PAN FORMATION (29 Ma)															
AU01	25	854	0.704901 ± 8	0.704865	3.9	19.4	0.512711 ± 6	0.512687	1.7	4.06	11.3	24	18.76	15.69	38.87
AU06	91	408	0.704865 ± 5	0.704598	6.8	34.9	0.512693 ± 8	0.512671	1.4	2.27	9.49	12	18.67	15.65	38.7
AU09	89	401	0.704927 ± 6	0.704662	6.9	33.9	0.512726 ± 4	0.512702	1.9	2.01	8.51	13	18.63	15.59	38.5
AU12	39	463	0.704071 ± 5	0.703968	5.8	23.2	0.512724 ± 6	0.512694	1.8	0.95	3.82	6	18.57	15.61	38.53
AU15	82	486	0.704273 ± 6	0.704067	5.4	27.3	0.512777 ± 8	0.512754	2.9	1.82	6.67	14	18.58	15.59	38.47
AU21	100	481	0.704626 ± 7	0.704373	5.3	26.1	0.512719 ± 6	0.512695	1.8	2.64	8.64	17	18.59	15.57	38.42

Element concentrations by ICP-MS, corresponds to Iannelli et al. (2017, 2018).

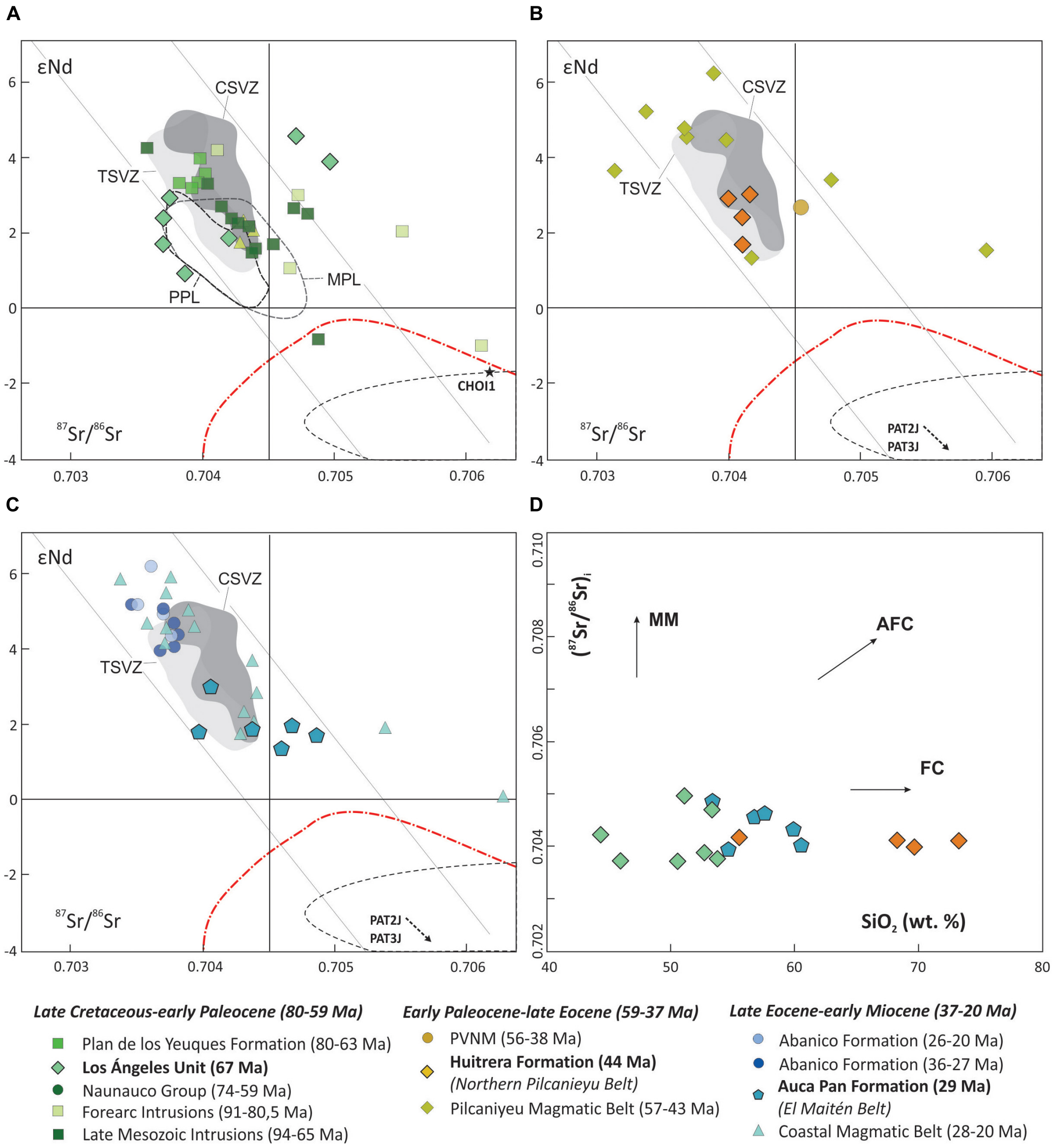

FIGURE 7 | Initial isotopic compositions for Los Ángeles Unit **(A)**, Huitrera Formation **(B)**, and Auca Pan Formation **(C)**. Recalculated initial isotopic ratios from coeval magmatic units are also included. CHOI1 corresponds to the Choiyoi Group considered as the local basement of the Los Angeles Unit area (35°30′S), while PAT2J and PAT3J correspond to the Late Paleozoic metamorphic and igneous local basement of the Huitrera and Auca Pan Formation in the North Patagoniana Andes (39–41°S). The black dashed line corresponds to the Southern Coastal Batholith 30–38°S (Parada et al., 1988; Lucassen et al., 2004), while the red dashed line corresponds to the Metamorphic basement and Late Paleozoic intrusions that represent the Pz basement of the region (Lucassen et al., 2004; Pankhurst et al., 2006). The Transitional Southern Volcanic Zone (TSVZ) isotopic data are from Mella et al. (2005) while Central Southern Volcanic Zone (CSVZ) data are taken from López-Escobar et al. (1992, 1995). The acronyms PPL and MPL correspond to post-plateau lavas and main-plateau lavas that represent the Neogene Patagonian slab window lavas studied by Gorring and Kay (2001). **(D)** $^{87}Sr/^{86}Sr$ vs. SiO_2 (wt.%) showing the AFC (assimilation and fractional crystallization), FC (fractional crystallization), and MM (mantle metasomatism) trends.

the local basement presents higher Pb isotopic compositions (**Figures 8E,F**; Lucassen et al., 2004).

Tomographic and Plate Kinematic Analyses

We begin with an analysis of the mantle structure at depths corresponding to the Late Cretaceous with the specific aim to test the existence of a potential slab window event at this time north of 35°30′–36°S (Iannelli et al., 2018). For this end, we analyzed tomography slices at a depth of 1200 km from global P-wave (PRI-05; Montelli et al., 2006; GAP-P04, Obayashi et al., 2013) and S-wave (SPani-P, Tesoniero et al., 2015) seismic tomography models showing the mantle structure corresponding to subduction at 80 Ma and representing the general subduction evolution in Late Cretaceous between ∼80 and 70 Ma. As seen in **Figure 9** in striking coincidence with

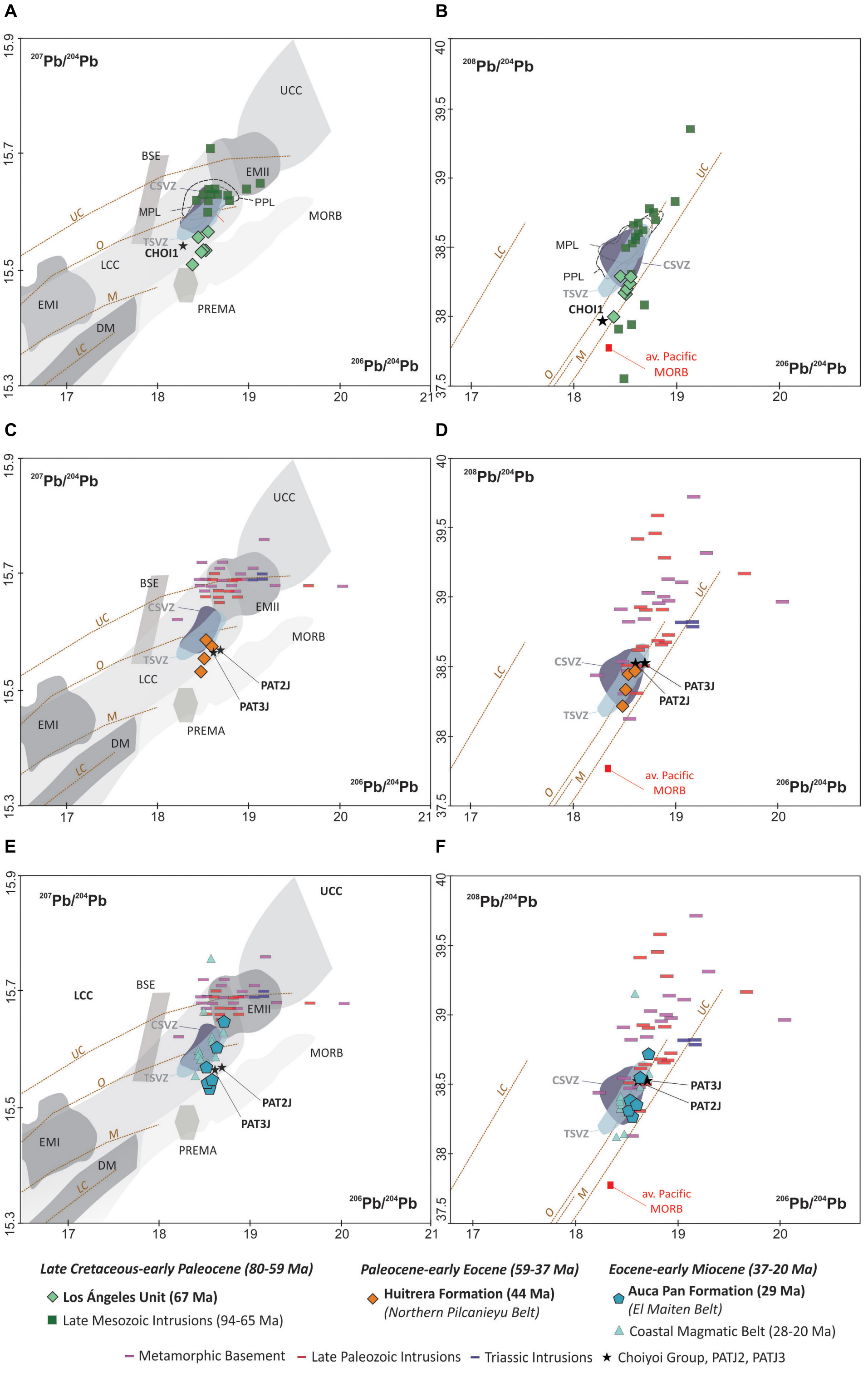

FIGURE 8 | Pb isotopic composition for the Late Cretaceous–early Paleocene Los Ángeles Unit **(A,B)**, the Eocene Huitrera Formation **(C,D)** and the Oligocene Auca Pan Formation **(E,F)**. The fields of the isotopic composition of the different mantle reservoirs are as in Zindler and Hart (1986): upper and lower continental crust (UCC and LCC), depleted mantle (DM), bulk silicate earth (BSE), mantle with high U/Pb ratio (HIMU), enriched mantle I (EMI), enriched mantle II (EMII), and observed prevalent mantle composition (PREMA). Moreover, we also included the isotopic composition of mid-ocean ridge basalt (MORB) and the average Pacific MORB from Lucassen et al. (2001), Neogene Patagonian main and post-plateau lavas from Gorring and Kay (2001), and the compositional fields for the TSVZ and CSVZ from López-Escobar et al. (1992, 1995) and Mella et al. (2005). Figures also include the lead-isotope evolution curves from the plumbotectonic model presented by Zartman and Doe (1981) for the mantle (M), the orogen (O), the upper crust contributed to the orogen (UC), and the lower crust contributions to the orogen (LC).

the area of anomalous magmatism, attributed to a slab window (Iannelli et al., 2018), and the position of the Farallon–Aluk mid-ocean ridge, reconstructed in the plate kinematic model (Müller et al., 2016), a slab gap is clearly observed between 35°S and 30°S in the seismic tomography model. The position of this slab gap in Late Cretaceous is roughly coincident with the analysis of Chen et al. (2019) that locates the southern tip of the Farallon slab at the same latitudes coinciding with the subducted mid-ocean ridge. Also, the inexistence of a slab gap in the inferred triple junction location in the study of Somoza et al. (2012) at 22°S in the Late Cretaceous allows discarding a slab window origin for deformation and magmatism interpreted by those authors (**Figure 10A**). These reconstructions also show that a subducting slab is present beneath Patagonia, south of the Farallon–Aluk ridge (**Figure 9**). The latter is consistent with the presence of significant Late Cretaceous subduction-related magmatism at those latitudes (e.g., Gianni et al., 2018a), and contrasts with the results of Chen et al. (2019).

Furthermore, this slab gap migrated southward along the active Andean margin between Late Cretaceous to Oligocene times following the reconstructed position inferred from plate kinematic reconstructions (Cande and Leslie, 1986; Eagles and Scott, 2014) and slab window-related magmatism (Ramos and Kay, 1992; Aragón et al., 2011; Iannelli et al., 2018; **Figure 10**). This is also illustrated by the southward propagation of subduction initiation between 80–70 and 30 Myr (**Figures 10B,C**). We note that this evolution is not as clear in the Spani-P as this model does not show an evident slab gap at 60 Ma (900 km at Central Patagonian latitudes) (**Supplementary Figure S2**). However, as the slab gap in this model is present at 80 Ma (1200 km, **Figure 9**) and reappears at 30 Ma (450 km, **Supplementary Figure S2**) at the southern extreme of South America, it likely just indicates a lack of resolution of the model at 900 km. With this analysis, we complement the previous study of Chen et al. (2019), which identified a southward propagation of subduction only up to 38–40°S. An additional reconstruction in **Supplementary Figure S1** considering a slower slab sinking rate of 1.3 cm/year (Chen et al., 2019) still indicate the presence of a slab gap at this time, but slightly shifted southward with respect to previous reconstruction in **Figure 10**. However, this reconstruction presents a faster propagation of subduction onset to the south that is fully completed at ∼50 Ma. The latter is not consistent with geological constraints indicating a full active margin magmatism after 40 Ma (Iannelli et al., 2017; Fernández Paz et al., 2018, 2019; Gianni et al., 2018b).

DISCUSSION

Geochemical Evolution of the Studied Arc-Related Magmatic Units From Late Cretaceous to Late Oligocene

Late Cretaceous Los Ángeles Unit Magmatism (35°30′S)

The Latest Cretaceous magmatism of the Los Ángeles Unit (67 Ma; 35°30′S), emplaced during the first studied magmatic period (80–59 Ma), is represented by basaltic to andesitic lava flows intruded by basaltic dikes and controlled by extensional faulting. Lava flows show a transitional subalkaline–tholeiitic to alkaline composition and a decreasing arc-like signature and partial melting degrees toward the younger lavas (**Figures 4**, **11A,B**; Iannelli et al., 2018). Enrichment in incompatible elements is also seen upward in the sequence, associated with possible crustal contamination and/or the input from a more LILE-enriched portion of the mantle (Iannelli et al., 2018).

New isotopic data suggest the contribution of a more pristine and depleted source toward the upper levels of the sequence considering the increasing εNd values from + 1.02 to + 4.63 (**Figure 7A**), also consistent with trace elements behavior (**Figures 4A,B**, **5A**). Los Ángeles Unit isotopic composition is concentrated between the fields of the OIB and the TSVZ, although the last one is even more isotopically depleted (Sun and McDonough, 1989; Gorring and Kay, 2001). Although the Sr isotopic values of the basaltic dikes, considered as the youngest magmatic pulses (SVA09 and SVA26) cannot be used for interpretation (see discussion in section Isotopic Signature of the Studied Late Cretaceous to Oligocene Magmatic Sequences), the Sr isotopic range for the rest of the sequence indicates no evidence in favor of crustal contamination when comparing with the local basement isotopic composition (CHOI1).

Pb isotopes have always been used as indicators of crustal components as this element is highly concentrated in the crust. In particular, Los Ángeles Unit magmatism shows a Pb isotopic range consistent with the depleted MORB isotopic composition (**Figures 8A,B**; Zindler and Hart, 1986). Higher mantle influence is also reflected since these lavas plot nearer the mantle growth curve (Zindler and Hart, 1986). The local basement sample (CHO1) presents lower $^{206}Pb/^{204}Pb$ and $^{208}Pb/^{204}Pb$ ratios and a partially lower $^{207}Pb/^{204}Pb$ ratio, which indicates that this local basement had no influence on the composition of Los Ángeles Unit magmatism (**Figures 8A,B**).

Overall, the new results presented in this work dismissed the incorporation of crustal contributions as the main cause for the enrichment in LILE seen in Los Ángeles Unit, and allow to consider the participation of a more enriched magmatic source as a plausible explanation for its evolution.

Eocene Huitrera Formation Magmatism (40°S)

The second magmatic period (59–34 Ma) is represented by the Huitrera Formation (∼44 Ma) (Northern Pilcaniyeu Belt) composed of rhyolitic and basaltic andesitic lavas interbedded with vitreous and lapillitic tuffs (Iannelli et al., 2017). A transitional alkaline signature associated with a retroarc setting is seen together with minor slab-fluid influence and also minor partial melting degrees (**Figures 4**, **11C,D**; Iannelli et al., 2017).

The new isotopic data for Huitrera Formation shows positive εNd values (1.76–3.10) for a limited $(^{87}Sr/^{86}Sr)_i$, which plot range along the mantle array, with a partially similar enriched composition as the OIB field. When considering Huitrera Formation isotopic behavior relative to the local basement, the latter shows considerably higher $(^{87}Sr/^{86}Sr)_i$ ratios and negative εNd (**Figure 7B** and **Table 1**). Thus, assimilation of the local basement continental crust should have been negligible.

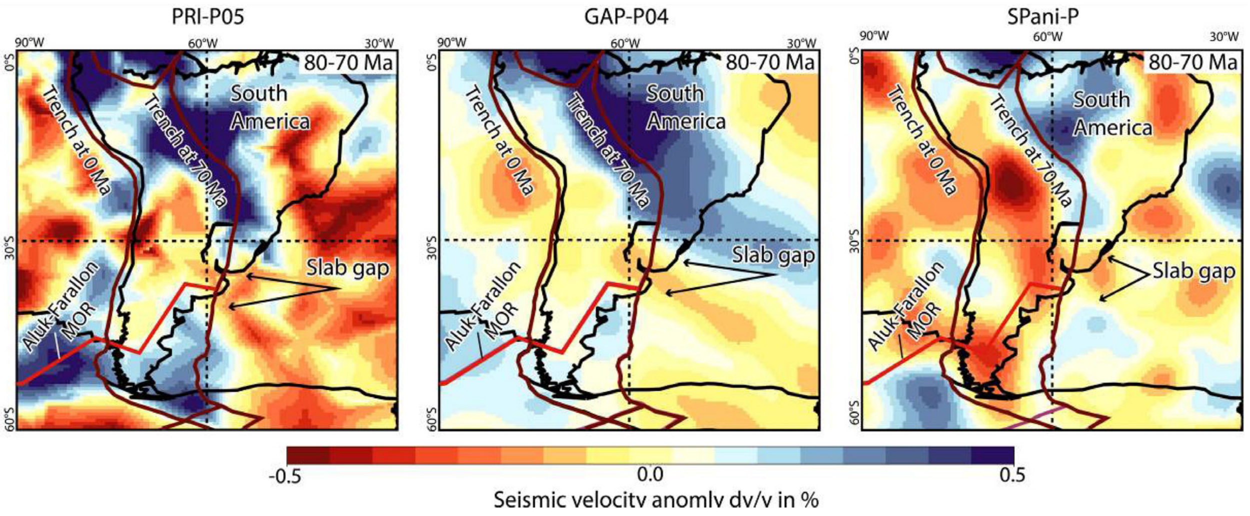

FIGURE 9 | Tomography slices at a depth of 1200 km from global P-wave (PRI-05; Montelli et al., 2006; GAP-P04, Obayashi et al., 2013) and S-wave (SPani-P, Tesoniero et al., 2015) seismic tomography models showing the mantle structure corresponding to subduction in Late Cretaceous (~80–70 Ma).

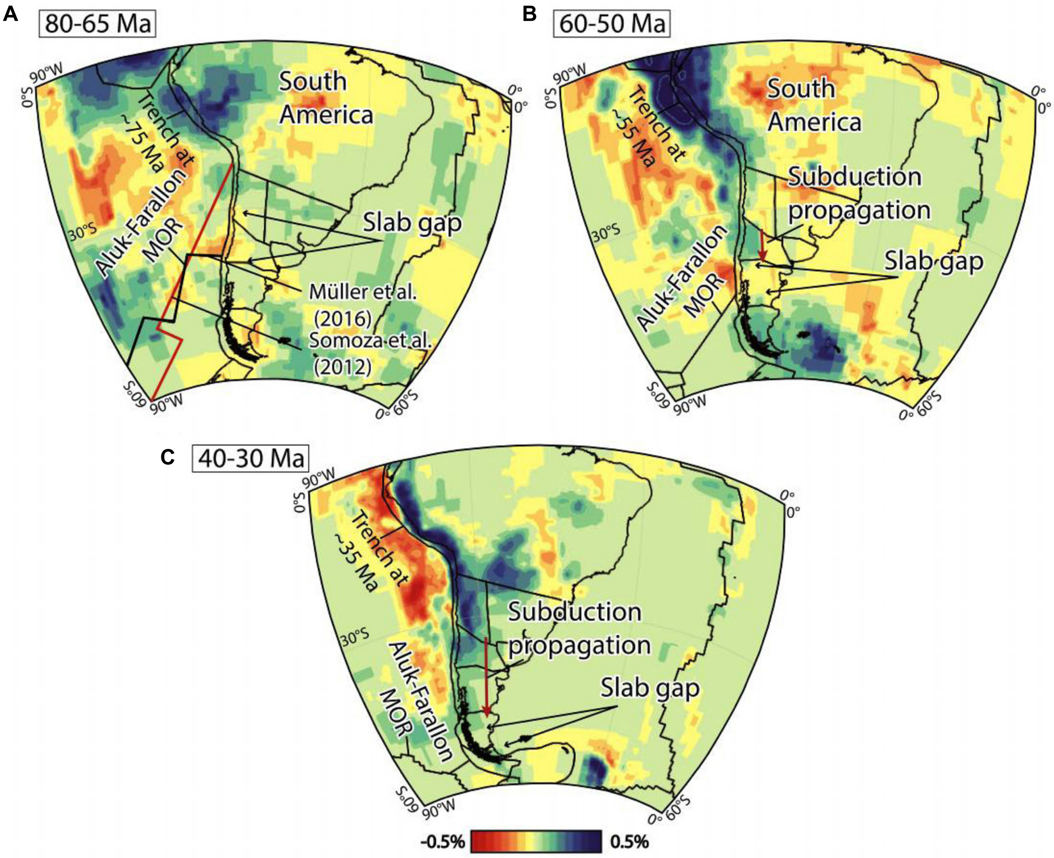

FIGURE 10 | Tomography slices at a depth of **(A)** 1200 km, **(B)** 850 km, and **(C)** 450 km from the UU-P07 global P-wave seismic tomography model (Amaru, 2007). These depths represent three stages of Andean subduction where the preserved mantle structure would correspond to the fossil record of subduction in Late Cretaceous (~80–65 Ma), Paleocene–Eocene (60–50 Ma), and late Eocene–Oligocene times (40–30 Ma), respectively. This image shows a striking coincidence between the southward migrations of a slab gap inferred from a discontinuity in fast anomalies below the Andean margin and the inferred position of the Farallon–Aluk mid-ocean ridge (MOR) from plate kinematic reconstructions (Cande and Leslie, 1986; Eagles and Scott, 2014; Müller et al., 2016).

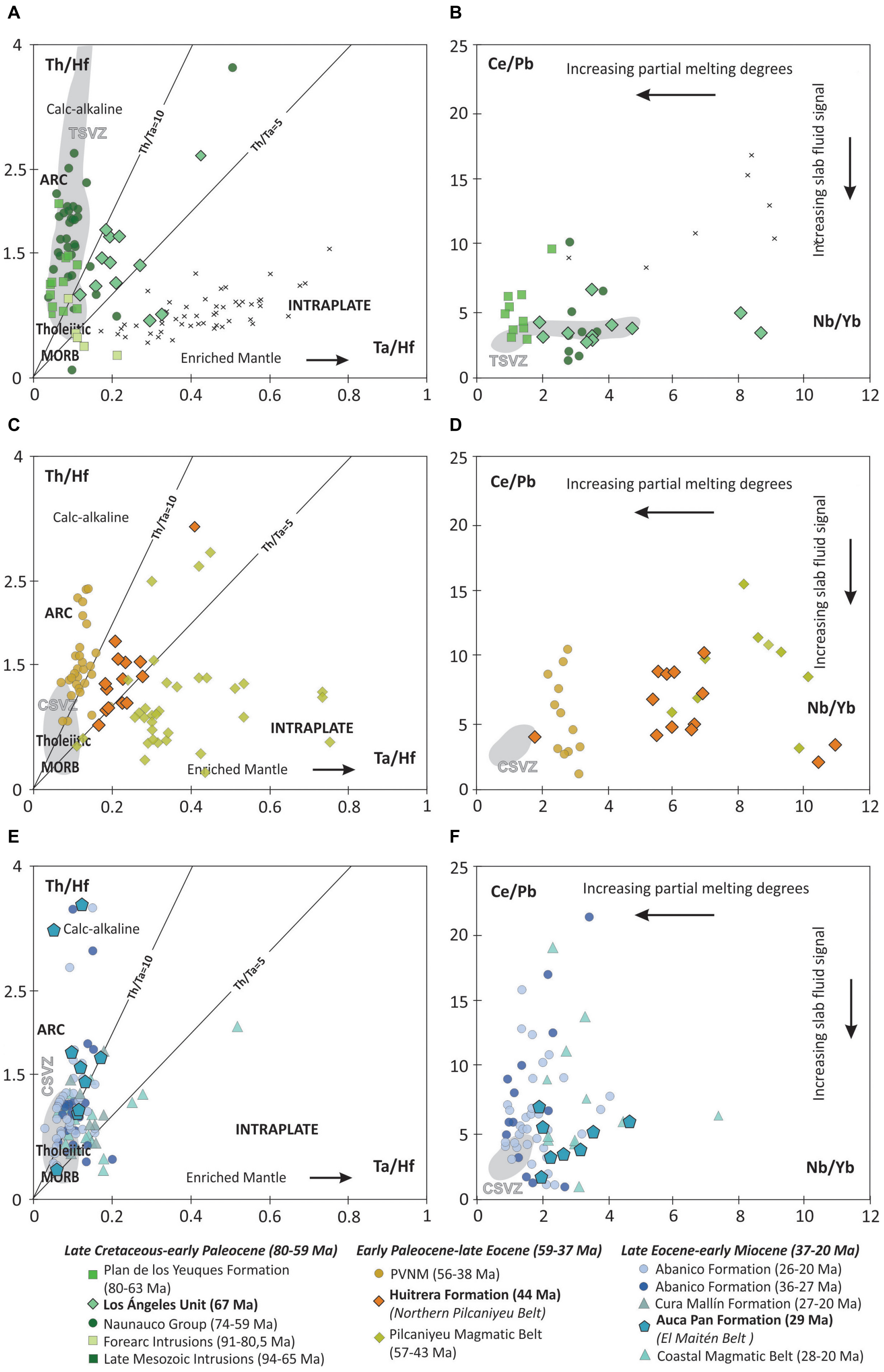

FIGURE 11 | (A,B) Th/Hf vs. Ta/Hf and Ce/Pb vs. Nb/Yb for Late Cretaceous-early Paleocene magmatic units along the Southern Central Andes. **(C,D)** Th/Hf vs. Ta/Hf and Ce/Pb vs. Nb/Yb for early Paleoceno-late Eocene magmatic units along the Southern Central Andes. **(E,F)** Th/Hf vs. Ta/Hf and Ce/Pb vs. Nb/Yb for late Eocene-early Miocene magmatic units along the Southern Central Andes. Gray crosses correspond to the Neogene Main and Post-Plateau lavas from Patagonia retroarc (Gorring and Kay, 2001; Guivel et al., 2006). For references to the data sources, see details in the text (references in section Compiled Arc-Like Andean Dataset). TSVZ corresponds to the Transitional Southern Volcanic Zone (34.5–38°S) while CSVZ corresponds to the Central Southern Volcanic Zone (38–43°S) (references in section Compiled Arc-Like Andean Dataset).

Pb isotopic signature for the Huitrera Formation samples indicates almost similar values for all the samples with almost similar $^{207}Pb/^{204}Pb$ ratios than the basement samples (PAT2J and PAT3J) and a tendency toward the Paleozoic metamorphic and intrusive basement of the North Patagonian Andes (**Figures 8C,D**; Lucassen et al., 2004). This tendency is in favor with the minor amounts of crustal contamination considered for $(^{87}Sr/^{86}Sr)_i$ vs. εNd values. The new isotopic dataset together with previously published major and trace elements composition indicate a partially enriched mantle source for this bimodal magmatic sequence, while crustal contamination could only have a minor influence in its evolution.

Oligocene Auca Pan Formation Magmatism (39°S)

The basaltic to andesitic lavas and pyroclastic rocks of the Auca Pan Formation (29 Ma; Ramos et al., 2014; Iannelli et al., 2017) present a calc-alkaline composition with a typical arc-like behavior and significant slab-fluid contributions associated with high partial melting degrees (**Figures 4**, **11E,F**; Iannelli et al., 2017).

Auca Pan Formation shows variable $(^{87}Sr/^{86}Sr)_i$ with little variation in most εNd (**Figure 7C**). The Sr isotopic signature of studied lava flows is lower than the analyzed basement samples (PAT2J and PAT3J), which might indicate a minor involvement of the local continental crust during magma evolution (**Figure 7C**).

Variable $^{207}Pb/^{204}Pb$ and $^{208}Pb/^{204}Pb$ isotopic ratios are seen for the Oligocene Auca Pan Formation lavas, with an almost constant $^{206}Pb/^{204}Pb$. The most radiogenic samples present similar Pb isotopic values as the local basement (PAT2J and PAT3J), reaching the Paleozoic metamorphic and intrusive basement field (**Figures 8E,F**; Lucassen et al., 2004). Sr, Nd, and Pb isotopic composition of the Auca Pan Formation is in agreement with the clear arc-like signature seen through its major and trace elements composition also revealing minor crustal assimilation.

Regional Comparison of Arc-Related Magmas From the Southern Central to North Patagonian Andean (35–42°S)

Late Cretaceous–Early Paleocene Magmatic Evolution

Late Cretaceous–early Paleocene arc-related magmatism (80–59 Ma) presents a scattered distribution with contrasting geochemical signatures and important magmatic gaps (∼35–42°S, **Figure 1**). Different magmatic units have been recognized along the Southern Central Andes (**Figures 1**, **6**), which are now compared with the studied Los Ángeles Unit magmatism in order to track main geochemical variations along space (**Figures 1**, **6**). From north to south, Late Cretaceous–early Paleocene magmatism is described at 34°30′S named as Plan de Los Yeuques Formation (∼80–63 Ma; Tapia, 2015; Muñoz et al., 2018; Mosolf et al., 2019). Southwards, arc-related sequences have been recognized at 36–38°S, gathered into the Naunauco Group (74–59 Ma; Franchini et al., 2003; Zamora Valcarce et al., 2006; Casé et al., 2008; Llambías and Aragón, 2011; Mateo-Fernández Caso et al., 2011; Salvioli et al., 2017; Iannelli et al., 2018), together with a series of Late Mesozoic intrusions emplaced between 36° and 41°S between the fore-arc and arc zone along the North Patagonian Andes and the Chilean Central Depression (94–65 Ma; Munizaga et al., 1988; Lucassen et al., 2004; De La Fuente et al., 2012, De La Fuente, 2014; **Figures 1**, **6**).

In particular, the geochemical signature of the studied Late Cretaceous Los Ángeles Unit (67 Ma; 35°30′S) shows an increasing alkaline tendency with decreasing arc-like signatures and decreasing partial melting degrees (Iannelli et al., 2018). The enrichment in incompatible elements, together with a change toward a more isotopically depleted signature in the youngest lava flows, suggest a possible change in the magmatic source of the Los Ángeles volcanism.

Northwards (∼34°30′S), Latest Cretaceous magmatic rocks (Plan de Los Yeuques Formation; ∼80–63 Ma) have been recognized in a westward position with respect to the studied Los Ángeles Unit (35°30′S), which present a higher arc-like signature, as seen by their higher Th/Hf, Th/Yb and La/Ta ratios (**Figures 11A**, **12A**). The lower Nb/Yb and Nb/Y ratios of this northern sequence also indicate higher partial melting degrees when compared to the Los Ángeles Unit (**Figures 7B**, **14B**). Isotopic composition shows higher εNd and partially higher $^{87}Sr/^{86}Sr$ ratios for the northern magmatism (34°30′S) relative to the studied Los Ángeles Unit (67 Ma, 35°30′S) (**Figure 7A**).

Southwards (36–41°S), Late Cretaceous–early Paleocene magmatism is characterized by granitic intrusions located in a forearc to arc position with ages between 94 and 65 Ma (**Figure 1**). Geochemical variations are seen between these partially coeval magmatic sequences (36–41°S) and the Los Ángeles Unit (35°30′S). First of all, fore-arc intrusions (∼91–80.5 Ma; 39–40°S) present a calc-alkaline composition with a peraluminous signature seen in their partially high La/Ta ratios, although they present similar Ta/Hf ratios to the Los Ángeles Unit. They show a similar $(^{143}Nd/^{144}Nd)_i$ range to the Los Ángeles Unit but with increasing $(^{87}Sr/^{86}Sr)_i$ ratios that have been associated with possible contamination with the basement rocks (**Figures 11A**, **B**). Some of these rocks show an adakitic imprint, which has been related to a possible slab window during the Late Cretaceous (De La Fuente, 2014). On the other hand, partially eastern coeval Late Mesozoic magmatic intrusions (94–65 Ma; 36–40°S), consist of subalkaline gabbroic to granitic mantle-derived rocks. They present a similar range of εNd than the Los Ángeles Unit but higher $(^{87}Sr/^{86}Sr)_i$ values, suggesting small crustal contributions (**Figure 7A**) and a typical arc-like geochemical imprint (**Figures 11A,B**, 12).

In an eastward position relative to the Late Mesozoic magmatic intrusions, between 36° and 38°S, coeval magmatism (Naunauco Group) is represented by arc-like andesitic rocks with a calc-alkaline composition emplaced during an extensional phase in Andean evolution (Zamora Valcarce et al., 2006; Casé et al., 2008; Llambías and Aragón, 2011). They present higher slab-fluid signal and partial melting degrees than the Los Ángeles Unit (35°30′S), although both of them share a similar retroarc position (**Figures 11A,B**, 12A,B).

Overall, variable geochemical features have been identified in these coeval magmatic units. A predominance of arc-like compositions is seen along the Southern Central Andes, mainly

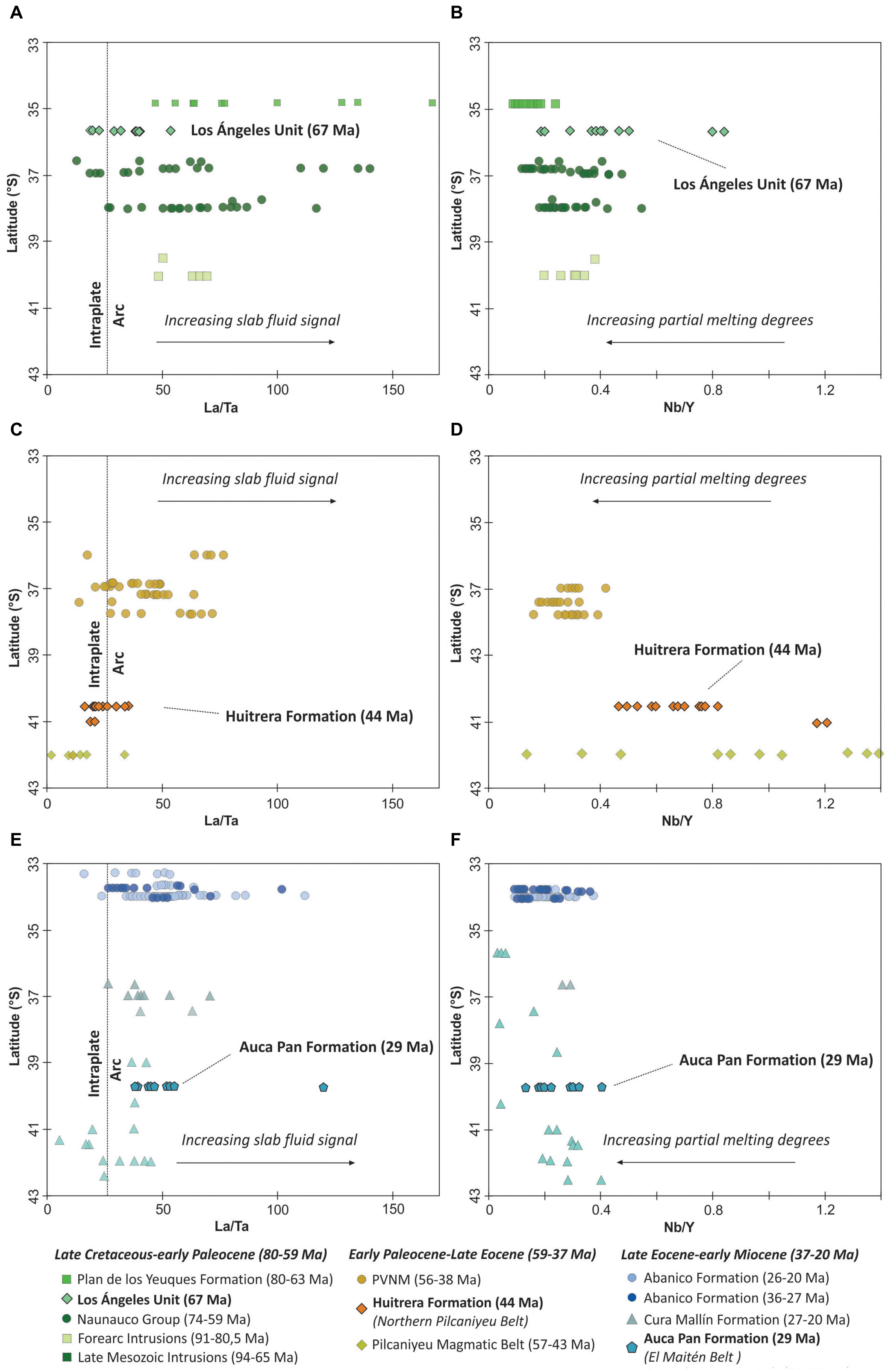

FIGURE 12 | (A,B) Latitude °(S) vs. La/Ta and Latitude (°S) vs. Nb/Y for Late Cretaceous-early Paleocene magmatic units along the Southern Central Andes. **(C,D)** Latitud (°S) vs. La/Ta and Latitude (°S) vs. Nb/Y for early Paleoceno-late Eocene magmatic units along the Southern Central Andes. **(E,F)** Latitud (°S) vs. La/Ta and Latitude (°S) vs. Nb/Y for late Eocene-early Miocene magmatic units along the Southern Central Andes. These diagrams show the variations in slab-fluid influence and partial melting degrees regarding the time and location of emplacement for each magmatic sequence.

between 36° and 41°S. However, a tholeiitic to slightly alkaline and more enriched magmatism is registered at 35°30′S (Los Ángeles Unit), which, together with the presence of adakite-like intrusions at 39°S (De La Fuente, 2014), may indicate variable magmatic sources and/or geochemical process, affecting Andean magmatism during this stage.

Late Paleocene–Middle Eocene Magmatic Evolution

The late Paleocene–middle Eocene magmatic stage (59–37 Ma) is characterized by the development of arc-related sequences with contrasting geochemical signatures and a limited and disperse distribution (**Figures 1**, **6**). Along the Andean margin, between the studied latitudes (35–42°S), a magmatic lull is registered at 34–36°S (**Figure 1**). Southwards (36–38°S), late Paleocene–middle Eocene arc-related magmatism is recognized as the *Provincia Volcánica Neuquino Mendocina* (PVNM) developed from 56 to 38 Ma (Llambías and Rapela, 1989; Kay et al., 2006). Coevally, but in a eastern retroarc position, at 40–43°S, the magmatic products of the Pilcaniyeu Belt (Huitrera Formation) are exposed with a NW–SE direction (57–43 Ma; Rapela et al., 1983, 1988; Aragón et al., 2011, 2018), whose northern outcrops (40°S) correspond to the studied area (44 Ma; Iannelli et al., 2017).

From north to south, arc-like magmatism between 36° and 38°S (PVNM) presents a strong arc-like imprint (**Figures 11C,D**, **12**). In contrast, immediately to the south at 40°S, studied Huitrera Formation (44 Ma; Northern Pilcaniyeu Belt) shows minor arc-like signature given the lower Th/Hf, La/Ta, and the higher Ce/Pb, and a tendency toward an alkaline composition, as shown by higher Ta/Hf, Nb/Yb, and Nb/Y ratios (**Figures 11C,D**, **12**). Furthermore, Eocene Huitrera Formation at 40°S, presents lower Sr isotopic signature for a similar εNd range relative to the northern coeval magmatism (PVNM, 36–38°S) (**Figure 7B**).

When considering the late Paleocene–early Eocene magmatism (Pilcaniyeu Belt; ∼57–43.1 Ma) emplaced at 40–43°S in the Patagonian Precordillera, a decrease in arc-like influence with an increase in alkaline composition are recognized from the northern (40°S) to the southern (42–43°S) outcrops of this belt. This is shown by the higher Ta/Hf and lower Th/Hf, Ce/Pb, and La/Ta ratios seen in the southern outcrops (42–43°S) relative to the northern ones (**Figures 11C,D**, **12A**). The higher Nb/Yb and Nb/Y ratios in the southern sections (42–43°S) also indicate lower melting degrees relative to the northern studied sequence (40°S) (**Figures 11D**, **12B**). This magmatism has been described as the products of extensional collapsed calderas associated with an intraplate setting and the development of a slab window (Aragón et al., 2011, 2013, 2018). The isotopic signature of these southern outcrops (42–43°S) is variable, but showing partially higher εNd and lower $(^{87}Sr/^{86}Sr)_i$ that the studied northern sequences of Huitrera Formation at 40°S (**Figure 7B**; Aragón et al., 2011, 2018).

Late Eocene–Early Miocene Magmatic Evolution

By the last magmatic period (37–20 Ma) Andean arc-like sequences show a more widespread and continuous distribution in comparison with the previous magmatic stages, as well as less pronounced geochemical differences. A regional comparison is made between studied Auca Pan Formation (29 Ma, 39°S; Iannelli et al., 2017), the volcanic units of the Abanico Formation emplaced at 33–36°S (36–20 Ma; Charrier et al., 2002; Kay et al., 2005; Muñoz et al., 2006; Piquer et al., 2017), the lower sections of the Cura Mallín Formation at 36–38°S (27–20 Ma; Suárez and Emparán, 1995; Burns et al., 2006; Kay et al., 2006; Utgé et al., 2009), and the southern Coastal Magmatic Belt developed between 37° and 43.5°S (28–20 Ma; López-Escobar and Vergara, 1997; Muñoz et al., 2000; **Figure 1**).

Between 37 Ma and 25 Ma, arc sequences were recognized at the Southern Central Andes mainly between 33° and 36°S (Abanico Formation), whereas in the North Patagonian Andes, the late Eocene–early Oligocene period comprises studied volcanism from the Auca Pan Formation (29 Ma; 39°S) (**Figure 1**). Both units share a slab-fluid signal and a partially calc-alkaline source as shown by the high Th/Hf and low Ce/Pb, Ta/Hf, and Nb/Yb (**Figures 11E,F**). Changes in geochemical signature are seen after ∼26–23 Ma, when this magmatism developed strongly controlled by the widespread extensional conditions. This younger magmatism developed along the Southern Central Andes between 33° and 38°S (Abanico Formation, ∼26–20 Ma; Cura Mallín Formation, ∼27–20 Ma) and southwards, mainly located in the fore-arc area, between 37° and 43.5°S (Coastal Magmatic Belt; 28–20 Ma) (**Figures 1**, **6**). Overall, magmatism within 26–23 Ma presents a strong tholeiitic signature with partially higher slab-fluid influence and higher melting degrees than 37–25 Ma magmatic sequences (**Figures 7C**, **11E,F**). Decreasing Sr and increasing Nd isotope ratios are seen toward these younger magmatic units, indicating also an increasing influence of a depleted mantle source (**Figure 7C**). A decrease in $^{206}Pb/^{204}Pb$ and similar values of $^{207}Pb/^{204}Pb$ and $^{208}Pb/^{204}Pb$ are seen when comparing the younger magmatism of the Coastal Magmatic Belt (28–20 Ma; 37–43.5°S) with the partially older Auca Pan Formation (29 Ma) (**Figures 7C**, **8E,F**; López-Escobar and Vergara, 1997; Muñoz et al., 2000).

Integrated Tectonic Evolution

During the Late Cretaceous, the Farallon–Aluk spreading ridge began to interact with the Andean margin at ∼30°S (Seton et al., 2012; Müller et al., 2016; Wright et al., 2016). This segmented spreading ridge moved southwards, and by 70 Ma, it was subducting at ∼35°S with an NW- to NNW-directed motion, reducing dramatically the convergence velocity and so leading to plate divergence despite the continued westward motion of the South American plate (Somoza and Ghidella, 2005; Müller et al., 2016; Wright et al., 2016). At this time, the South American upper plate kinematics had no significant role in the upper plate tectonic regime as a reduction in trench normal upper plate motion from ∼2 to ∼1 cm/year is only observed at ∼65 Ma (see **Figure 4**, Maloney et al., 2013) after the onset of extension in several areas (Cornejo et al., 1994; Emparán and Pineda, 1997, 2000; Ladino et al., 2000; Aragón et al., 2011; Muñoz et al., 2018; Fennell et al., 2019). Also, the fact that current values of trench normal absolute motion of the South American plate, lower than those between 65 and 45 Ma (see **Figure 4**; Maloney et al., 2013), cause significant neotectonic contractional activity in Central Andes (see Costa et al., 2006 for a synthesis) precludes linking extension to upper-plate motion at this time. The negative to closely neutral convergence velocity between 20°S and 36°S (i.e., plate divergence) (Maloney et al., 2013; **Figure 4**), responsible for the widespread deformation, would have been caused by the demise of the obliquely subducting Farallon–Chasca and Chasca–Catequil mid-ocean ridges that were producing a fast and roughly orthogonal subduction of the Chasca plate and onset of subduction of the Farallon–Aluk mid-ocean ridge plate at studied latitudes, causing the Farallon plate and so the Farallon–Aluk spreading ridge to subduct with a NW to NNW direction (Müller et al., 2016; Wright et al., 2016). This process reduced dramatically the convergence velocity leading to plate divergence despite the continued westward motion of South America to the west (Müller et al., 2016; Wright et al., 2016).

Meanwhile, Late Cretaceous–early Paleocene arc-related magmatism shows a scattered occurrence with significant magmatic gaps along the Southern Central Andes (**Figures 1**, **13A**). Contrasting geochemical signatures from typical arc-like to more enriched geochemical compositions are seen between the magmatic units considered in this work. Los Ángeles Unit magmatism (35°30′S; 67 Ma) presents a transitional alkaline-like signature and an OIB-like isotopic composition emplaced in an extensional setting, however, immediately to the north (Plan de los Yeuques Formation; 34°30′S) and to the south (Naunauco Group, 36–38°S; Late Cretaceous intrusives, 36°–41°S), magmatic activity shows a typical arc-like geochemical behavior and variable depleted isotopic compositions (**Figures 7A**, **11**) (see discussion in section Late Cretaceous-Early Paleocene Magmatic Evolution). Furthermore, by the same time, adakite-like intrusions also appeared in the fore-arc zone at ∼39°S (De La Fuente et al., 2012, De La Fuente, 2014).

In addition, coeval synextensional magmatism emplaced in arc to back-arc settings with alkaline and enriched signatures is also described northwards of the studied region (**Figure 13A**), as the alkaline lavas and dikes from the Cerro Totola Formation (66 Ma, 22–24°S, Mpodozis et al., 2005), the back-arc enriched basalts of the Río Frío Formation (∼56 Ma, 29°50′S) (Litvak et al., 2007; Jones et al., 2016), and the rift sequences depicted at 32°S by Lucassen et al. (2002). Coeval extensional settings are also described between the Coquimbo (30°S), El Salvador (26°S), and Calama (23°S) areas, where Late Cretaceous–early Paleocene (∼85–65 Ma) collapse magmatic calderas have been described, associated with extensional settings and indicating a change between arc-like to intraplate magmatic products (**Figure 13A**; Rivera and Mpodozis, 1991, 1994; Arévalo et al., 1994; Cornejo et al., 1994; Emparán and Pineda, 1997, 2000; Cornejo and Mathews, 2000; Ladino et al., 2000). Most of these latest Cretaceous–early Paleocene sequences have been associated with the highly oblique subduction of the Farallon plate during this studied period (Cornejo et al., 1994; Emparán and Pineda, 1997, 2000; Cornejo and Mathews, 2000).

On the other hand, the joint analysis of P- and S-seismic tomography and plate kinematic reconstructions supports the existence of a slab gap below the study area during the Late Cretaceous times (**Figures 9**, **10A**), which is interpreted as a relict of the Late Cretaceous slab window that is still preserved in the uppermost lower mantle. This behavior can be comparable with an analog model documented in western North America and eastern Sumatra (Fabian et al., 2010; Gaina and Jakob, 2019). The location of the enriched sequences emplaced in extensional settings is consistent with the areas affected by the collision of the Farallon–Aluk spreading ridge according to the tomography results (**Figure 13A**). Thus, the contrasting geochemical signature between neighboring coeval units, the presence of adakite-like intrusions in the fore-arc, and the extensional regimen recognized in the overriding plate, could be related to the initial passage of the segmented Farallon–Aluk spreading ridge and the beginning of its influence in the Andean magmatism at the studied latitudes (35–42°S) (**Figure 15A**; Iannelli et al., 2018). The oblique collision of a segmented spreading ridge as the Farallon–Aluk would have probably favored the development of diachronic slab windows or at least the participation of more enriched mantle sources that affected discrete portions of the Andes since Late Cretaceous times (Thorkelson, 1996; Somoza and Ghidella, 2005). The contrasting angle and direction of subduction between both plates during their southward migration controlled the full development of the slab windows with time (Thorkelson, 1996; Somoza and Ghidella, 2005, 2012). In consequence, the subduction and simultaneous migration of this segmented spreading ridge could explain the emplacement of the contrasting but coeval magmatic units along the Andean margin, and the participation of an enriched and isotopically depleted mantle source for studied Los Ángeles magmatism during this period (**Figures 13A**, **14A**).

Modern analogs have also been used to finally interpret the Los Ángeles Unit volcanism and justify this premise, as for example the Neogene Plateau lavas in Patagonia (46.5–49.5°S) (Gorring and Kay, 2001; Guivel et al., 2006) associated with the collision of the Chilean Ridge. The similar isotopic signature, partially similar geochemical composition (**Figures 5**, **7A**, **11**), and the tectonic context between the Neogene plateau lavas and the Los Ángeles Unit could be in favor of a similar magmatic origin for the evolution of both sequences. In particular, Los Ángeles Unit shows an arc-like signature partially higher than the plateau lavas (**Figures 11A,B**), which can be explained due to their position closer to the Andean arc. The origin of the Neogene Plateau lavas has been attributed to the melting of limited OIB-like heterogeneities in a depleted MORB-like subslab asthenosphere (Gorring and Kay, 2001; Gorring et al., 2003). In this case, the mixing with "stored" arc components at the base of the continental lithosphere was also considered (Gorring and Kay, 2001; Espinoza et al., 2005). Furthermore, the tholeiitic composition register in the initial levels of Los Ángeles Unit magmatism is consistent with the ascent and decompression melting of hot asthenospheric mantle associated to the opening of a slab window, as proposed for the Eocene magmatism during the Caribbean–North America–Farallon triple boundary evolution in Mexico (e.g., Ferrari et al., 2014).

For the early Paleocene–late Eocene period (∼59–37 Ma), the combined analysis of seismic tomography and plate kinematic reconstruction indicates that the previous slab gap migrated southwards following the kinematics of the Farallon–Aluk–South American triple junction (**Figures 10B**, **13B**). During this period,

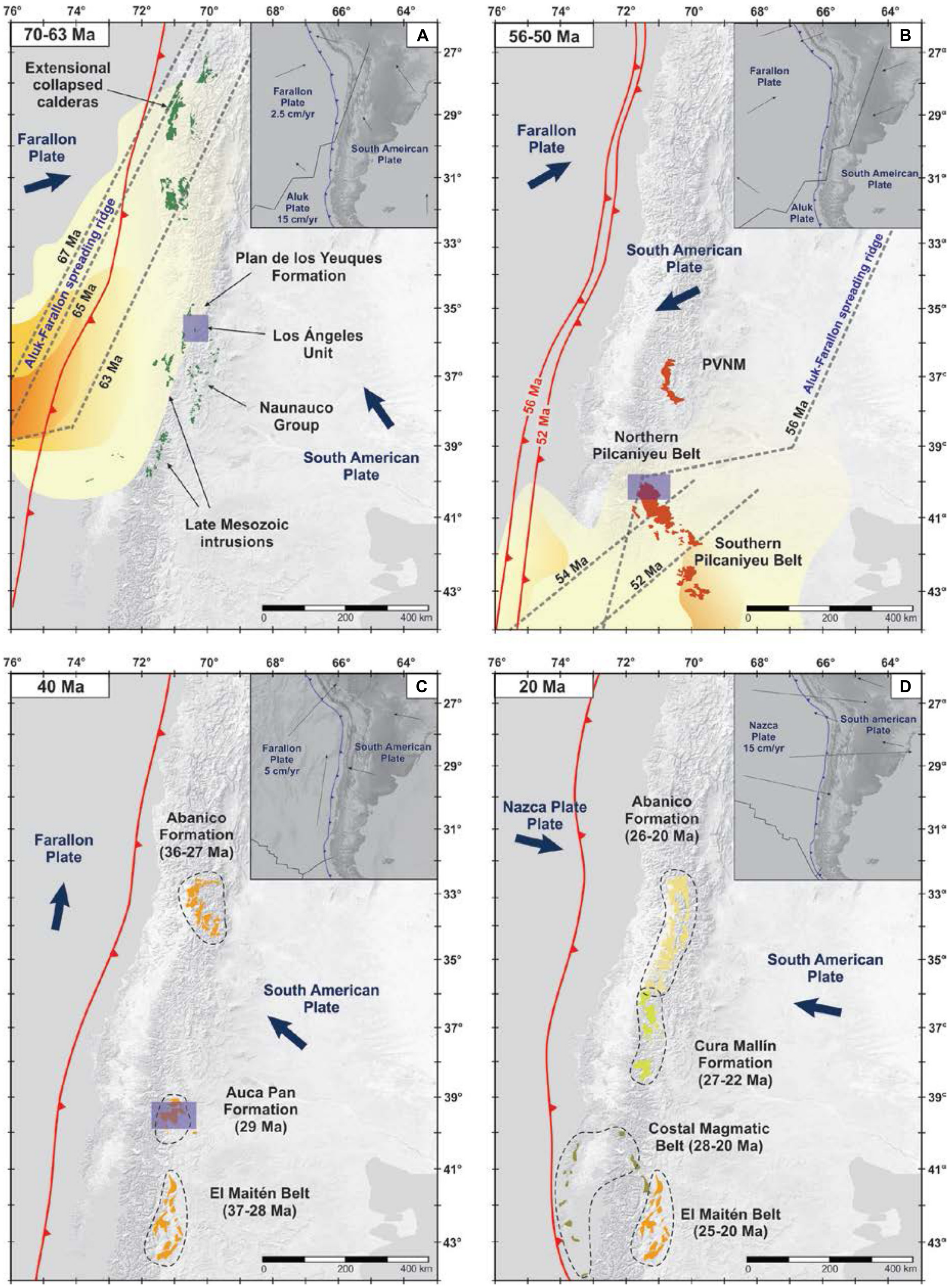

FIGURE 13 | (A,B) Schematic maps that represent the southward movement of the Farallon–Aluk spreading ridge for the Late Cretaceous–early Paleocene (70–63 Ma) and the early Eocene (56–50 Ma) period. The orange to yellow field represents the location of the Farallon–Aluk spreading ridge according to the tomography results. The blue shaded squares show the studied areas in each figure. The green outcrops represented in **(A)** corresponds to the Late Cretaceous–early Paleocene magmatism (80–59 Ma) while the orange outcrops in **(B)** are the early Paleocene–late Eocene magmatism (59–37 Ma). **(C)** Late Eocene–early Oligocene magmatic units emplaced along the Southern Central Andes (35–42°S). Blue arrows represent the convergence direction for both the Farallon and South American plates. **(D)** Early Oligocene–early Miocene magmatic units emplaced along the Southern Central Andes after Farallon plate break-up. In this case, blue arrows represent the convergence direction for both Nazca and South American plates.

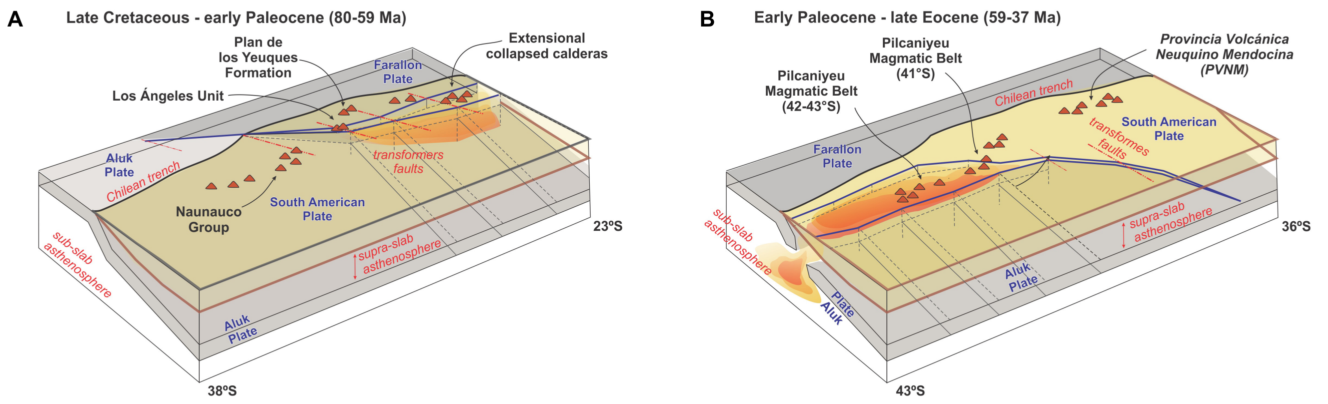

FIGURE 14 | Schematic model representing the passage of the Farallon–Aluk spreading ridge since **(A)** Late Cretaceous–early Paleocene time (80–59 Ma) to **(B)** Early Paleocene–late Eocene (59–37 Ma), and the main magmatic units from each period.

the Farallon–Aluk spreading ridge reached Patagonian latitudes (Espinoza et al., 2005; Breitsprecher and Thorkelson, 2009), while northwards the Farallon plate was subducting with a NE direction beneath the South American plate (Somoza and Ghidella, 2012). The high degrees of obliquity partially decrease by 49 Ma, but remained during most of this stage, triggering an extensional regime in the upper plate (Pardo-Casas and Molnar, 1987; Somoza and Ghidella, 2005; Müller et al., 2016).

Magmatism during this period (59–37 Ma) is also characterized by the emplacement of coeval magmatic units with contrasting geochemical signatures as in the former magmatic period (80–59 Ma) (**Figure 13B**). In this sense, Eocene magmatism at 36–38°S (PVNM) presents a geochemical and isotopic composition typical of an arc-like magmatism with a calc-alkaline source that differs from the transitional to intraplate-like character seen along the Paleocene–early Eocene magmatism between 40° and 43°S (Pilcaniyeu Belt–Huitrera Formation) (**Figures 11B,C, 12A,B, 13B**). This southern magmatic unit (57–43 Ma) developed in a retroarc position with a NW–SE direction between 40° and 43°S (**Figure 13B**). Geochemical differences have been distinguished along this magmatic belt. Toward the north (40°S), the studied magmatic sequences (northern Pilcaniyeu Belt, Huitrera Formation; 44 Ma) (**Figure 15B**) show a transitional subalkaline to alkaline signature with minor slab-fluid influence (**Figures 4A, 11B,C, 12A,B**). In contrast, southern magmatic collapse calderas at 42–43°S (∼57–43 Ma) show a pronounced intraplate character, which have been associated with the development of a slab window based on their geochemical signatures and a 2-D seismic tomography cross-section showing a detached slab in the mantle transition zone (**Figures 13B, 14B**; Aragón et al., 2011, 2013). The increment of an arc-like signature in the northern and also younger outcrops of this magmatic belt (Huitrera Formation; 44 Ma; 40°S) is consistent with its position closer to the arc-zone and its development during the last influences of the subducting spreading ridge (Iannelli et al., 2017; **Figures 13B, 14B**).

Hence, the new isotopic data from Eocene magmatism at 40°S, and its regional comparison with coeval units, together with horizontal seismic tomography slice data presented in this study, allow confirming the existence of this slab gap and unraveling the regional extent of this tectonic feature (**Figures 10B, 13B, 14B**). The segmented magmatic and tectonic nature of Patagonia during this period have already been associated with the development of a slab-window event (e.g., Ramos and Kay, 1992; Espinoza et al., 2005) and more recently with diachronic slab windows (Gianni et al., 2018b). Thus, the presence of the active spreading ridge in Patagonian latitudes can explain the geochemically contrasting magmatic sequences and the gaps between them (**Figures 10B, 13B, 14B**).

Previous plate kinematic reconstructions suggested that after the final subduction of the Aluk plate at ∼40–35 Ma, Farallon plate was subducting with a highly oblique direction and low convergence rate beneath the South American plate (Cande and Leslie, 1986; Somoza and Ghidella, 2005). By late Oligocene times, Farallon plate finally broke up into Nazca and Cocos plates, and consequently, Nazca plate started to subduct with an orthogonal direction and high-velocity rates (∼15 cm/year) (Pardo-Casas and Molnar, 1987; Somoza and Ghidella, 2012). The combined analysis of seismic tomography and plate kinematic reconstruction indicates that, at that time, the slab gap positioned below the southern sector of South America and the fast anomaly linked to the presence of the subducted slab propagated southward, forming a continued subduction zone (**Figures 10C, 13C,D**).

As recently suggested by the numerical modeling presented in Fennell et al. (2018), this new subduction zone triggered extensional conditions along the Southern Central and Patagonian Andean margin as the tip of the slab subducted rapidly before approaching the mantle transition zone (e.g., Jordan et al., 2001; Fennell et al., 2018). The new tectonic conditions affected directly the development of the late Eocene–early Miocene magmatism, which presents variable geochemical signatures with time along the North Patagonian Andes (**Figure 13C**).

Late Eocene–early Oligocene volcanism is recognized with an N–S distribution all along the Southern Central and North

Patagonian Andes between 33° and 43°S (Abanico Formation, Auca Pan Formation and the El Maitén Belt). In the studied area (39 Ma), Auca Pan Formation (29 Ma) shows an arc-like calc-alkaline composition with an isotopic signature that resembles an arc-like source. Coeval magmatism in the Andean margin is also recognized northwards between 33° and 36°S, in the oldest magmatic pulses of the Abanico Formation (∼36–27 Ma), which present a partially similar geochemical character to the Auca Pan Formation (29 Ma). To the south, arc resumption was characterized by an initially arc-like tholeiitic composition that progressively shows a more calc-alkaline signature (Fernández Paz et al., 2018, 2019).

After the major tectonic changes by latest Oligocene (∼25–23 Ma), extensional conditions fully installed in the Andean margin, leading to the expansion of a widespread magmatism and the southern thinning of the continental crust. The new tectonic parameters of the newly Nazca plate provoked a period of roll-back that affected the Oligocene–early Miocene sequences (**Figure 13C**; Muñoz et al., 2000; Jordan et al., 2001). These tectonic changes are consistent with the involvement of a more depleted mantle source and the rapid emplacement of this tholeiitic magmatism without interaction with the continental crust (e.g., Muñoz et al., 2000). In consequence, the lower Cura Mallín Formation (27–20 Ma; 36–38°S) (Suárez and Emparán, 1995; Jordan et al., 2001) and the upper magmatic levels of the Abanico Formation (∼26–20 Ma; 33–36°S) (Charrier et al., 2002; Kay et al., 2005; Muñoz et al., 2006) show a tholeiitic imprint and an isotopic composition typical of a depleted mantle source (**Figures 7C**, **11E,F**, **13C**). North Patagonian volcanism at 40–43°S shows again a tholeiitic and depleted imprint (Litvak et al., 2014; Fernández Paz et al., 2018, 2019), partially similar to the arc-like tholeiitic and isotopically depleted coeval magmatism emplaced in the Central Depression between 37° and 43.5°S (**Figure 13C**) (Coastal Magmatic Belt; 28–20 Ma) (López-Escobar and Vergara, 1997; Muñoz et al., 2000).

CONCLUSION

Early Cenozoic magmatic arc had experienced compositional and geodynamic changes in response to the interaction of a spreading ridge with the South American margin between 35 and 42°. Based on the three independent methodologies—(i) Sr, Nd, and Pb isotopic analysis; (ii) seismic tomography; and (iii) kinematic reconstructions – we provided evidence of the extent and the consequences in arc magmatism of the migration of the Farallon–Aluk ridge from the Late Cretaceous to middle Eocene. Thus, along the Andean magmatic arc, some areas show isotopic compositions that reflect partially enriched mantle sources: the Los Ángeles Unit (69 Ma; 35°30′S) and the Huitrera Formation (44 Ma; 40°S). On the other hand, the tomotectonic analysis, together with the kinematic reconstructions, revealed a slab gap that correlates with the occurrence of these enriched portions of the asthenospheric wedge. Our model shows the interaction of the Farallon–Aluk spreading ridge with the South American margin, whereas, integrated in a regional magmatic context, it provides robust evidence about the existence of a slab window event by latest Cretaceous–early Paleocene times and its southward migration along the Southern Central Andes till Eocene times.

In the Southern Central Andes (∼35°S), the interaction of the Farallon–Aluk mid-ocean ridge with the Andean margin would have promoted extensional deformation during Latest Cretaceous–early Paleocene times (80–59 Ma), the development of the collapse calderas magmatism in the north (23–28°S), the transitional intraplate-like magmatic character recognized in specific arc-related magmas (35°30′S), and the presence of adakite-like intrusions in the fore-arc area (39°S). Despite the fact that the influence of this spreading ridge would have better developed in the north (∼23–28°S), the Los Ángeles Unit (35°30′S) reflects a trend from tholeiitic to a more alkaline enriched composition with isotopically depleted mantle sources. Meanwhile, to the south of the Los Ángeles Unit, a typical arc developed without influence of this spreading ridge (∼36–38°S). The contrasting geochemical composition between coeval magmatism during the Late Cretaceous–early Paleocene is consistent with the segmented configuration of the Farallon–Aluk spreading ridge. In the North Patagonian Andes (39–43°S), the segmented distribution and composition seen in early Paleocene–late Eocene magmatism (59–37 Ma) similar to the previous period (80–59 Ma) is also consistent with the tomography sections that tracked the location of the triple junction point toward the south. By this period, the Farallon–Aluk spreading ridge moved toward Patagonian latitudes where an asthenospheric window developed (42–43°S) and caused the emplacement of intraplate-like magmatism. In contrast, northern coeval sequences (36–38°S) showed a typical arc-like signature. The geochemical composition of coeval magmatism fully coincides with tomography sections that show an anomaly at 42°S, while northwards, a normal subduction setting was developing.

Finally, by the late Eocene–early Miocene period, a typical arc-like magmatism developed, consistent with the establishment of a continuous subduction zone as seen in the tomography sections. New isotopic data show the participation of arc-like sources with minor crustal contribution, consistent with the development of the calc-alkaline arc magmatism of the Auca Pan Formation (29 Ma). A more depleted mantle source is seen for the late Oligocene–early Miocene related to the major tectonic reconfiguration at 25–23 Ma.

DATA AVAILABILITY STATEMENT

All datasets generated for this study are included in the article/**Supplementary Material**.

AUTHOR CONTRIBUTIONS

SI, LF, and VL are specialists in the interpretation and use of geochemical data and experts in petrogeneis of magmatic suites. GG contributed to tomography reconstructions and modeling while LF and AF contributed to structural field data and tectonic interpretation. JG and VO helped with the lab work and isotopic data. FL and SK made it possible to obtain the complete amount of isotopic data in the Geochemical Lab of the MARUM Institute at the University of Bremen (Germany) and helped to improve the isotopes interpretation.

ACKNOWLEDGMENTS

We specially acknowledge the two reviewers and the editor Dr. Marina Manea for their fruitful suggestions that improved this manuscript. We also acknowledge the financial support from CONICET (grant 11220150100426CO), University of Buenos Aires (grant UBACYT 20020150100166BA), and ANPCyT (PICT-2012-1490 and PICT-2014-2240).

SUPPLEMENTARY MATERIAL

The Supplementary Material for this article can be found online at: https://www.frontiersin.org/articles/10.3389/feart.2020.00121/full#supplementary-material

REFERENCES

Aguirre Urreta, B., Tunik, M., Naipauer, M., Pazos, P., Ottone, E., Fanning, M., et al. (2011). Malargüe Group (Maastrichtian-Danian) deposits in the neuquén andes, argentina: implications for the onset of the first atlantic transgression related to western gondwana break-up. *Gond. Res.* 19, 482–494. doi: 10.1016/j.gr.2010.06.008

Amaru, M. (2007). *Global Travel Time Tomography with 3-D Reference Models, Geology Traiectina*. Ph. D. thesis, University of Utrecht, Utrecht.

Aragón, E., Castro, A., Díaz-Alvarado, J., Pinotti, L., Fernando, D., Demartis, M., et al. (2018). Mantle derived crystal-poor rhyolitic ignimbrites: eruptive mechanism from geochemical and geochronological data of the Piedra Parada caldera, Southern Argentina. *Geosci. Front.* 9, 1529–1553. doi: 10.1016/j.gsf.2017.09.004

Aragón, E., D'Eramo, F., Castro, A., Pinotti, L., Brunelli, D., Rabbia, O., et al. (2011). Tectono-magmatic response to major convergence changes in the North Patagonian suprasubduction system; the Paleogene subduction–transcurrent plate margin transition. *Tectonophysics* 509, 218–237. doi: 10.1016/j.tecto.2011.06.012

Aragón, E., Pinotti, L., D'Eramo, F., Castro, A., Rabbia, O., Coniglio, J., et al. (2013). The farallon-aluk ridge collision with south america: implications for the geochemical changes of slab window magmas from fore- to back-arc. *Geosci. Front.* 4, 377–388. doi: 10.1016/j.gsf.2012.12.004

Arévalo, C., Rivera, O., Iriarte, S., and Mpodoszis, C. (1994). Cuencas extensional y campos de calderas del Cretácico Superior-Terciario inferior en la precordillera de Copiapó (27°-28°S), Chile in VII Congreso Geológico Chileno Concepción. *J. Geophys. Res.* 2, 1288–1292.

Ávila, P., and Dávila, F. M. (2018). Heat flow and lithospheric thickness analysis in the Patagonian asthenospheric windows, southern South America. *Tectonophysics* 747, 99–107.

Basei, M., Ramos, V. A., Vujovich, G. I., and Poma, S. (1999). El basamento metamórfico de la Precordillera Frontal de Mendoza: nuevos datos geocronlógicos e isotópicos" in X Congreso Latinoamericano de Geología y VI congreso nacional de geología económica actas. *J. Geophys. Res.* 2, 412–417.

Bechis, F., Encinas, A., Concheyro, A., Litvak, V. D., Aguirre-Urreta, B., and Ramos, V. A. (2014). New age constraints for the Cenozoic marine transgressions of northwestern Patagonia, Argentina (41–43°S): paleogeographic and tectonic implications. *J. S. Am. Earth Sci.* 52, 72–93.

Billen, M. I. (2008). Modeling the dynamics of subducting slabs. *Annu. Rev. Earth Planet. Sci.* 36, 325–356.

Braz, C., Seton, M., Flament, N., and Müller, R. D. (2018). Geodynamic reconstruction of an accreted Cretaceous back-arc basin in the Northern Andes. *J. Geodyn.* 121, 115–132.

Breitsprecher, K., and Thorkelson, D. J. (2009). Neogene kinematic history of Nazca–Antarctic–Phoenix slab windows beneath Patagonia and the Antarctic Peninsula. *Tectonophysics* 464, 10–20.

Burns, W. M., Jordan, T. E., Copeland, P., and Kelley, S. A. (2006). "The case for extensional tectonics in the Oligocene-Miocene Southern Andes as recorded in the Cura Mallín basin (36°–38°S)," in *Evolution of an Andean Margin: A Tectonic And Magmatic View From The Andes To The Neuquén Basin (35°–39°S lat)*, Vol. 407, eds S. M. Kay and V. A. Ramos (Boulder: Geological Society of America), 163–184. doi: 10.1130/2006.2407(08)

Cande, S. C., and Leslie, R. B. (1986). Late cenozoic tectonic of the Southern Chile Trench. *J. Geophys. Res.* 91, 471–496.

Casé, A. M., López-Escobar, L., Danieli, J. C., and Schalamuk, A. (2008). Butalón igneous rocks, Neuquén, Argentina: age, stratigraphic relationships and geochemical features. *J. S. Am. Earth Sci.* 26, 188–203.

Cazau, L., Mancini, D., Cangini, J., and Spalletti, L. (1989). "Cuenca de Nirihuau," in *Cuencas Sedimentarias Argentinas*, Vol. 6, eds G. Chebli and L. Sapalletti (London: Serie Correlación Geológica), 299–318.

Charrier, R., Baeza, O., Elgueta, S., Flynn, J., Gans, P., Kay, S. M., et al. (2002). Evidence for Cenozoic extensional basin development and tectonic inversion south of the flat-slab segment, southern Central Andes Chile, (33°–36°S). *J. S. Am. Earth Sci.* 15, 117–139.

Charrier, R., Pinto, L., and Rodríguez, M. P. (2007). "Tectonostratigraphic evolution of the Andean Orogen in Chile," in *The Geology of Chile*, eds T. Morenoand and W. Gibbons (London: Geology Society), 21–114.

Charrier, R., Wyss, A., Flynn, J. J., Swisher, C. C., Norell, M. A., Zapatta, F., et al. (1996). New evidence for late Mesozoic-early Cenozoic evolution of the Chilean andes in the upper tinguiririca valley (35°S), central Chile. *J. South Am. Earth Sci.* 9, 393–422. doi: 10.1016/S0895-9811(96)00035-1

Chen, Y. W., Wu, J., and Suppe, J. (2019). Southward propagation of Nazca subduction along the Andes. *Nature* 565, 441–447. doi: 10.1038/s41586-018-0860-1

Cornejo, P., and Mathews, S. (2000). "Relación entre magmatismo-tectónica y su implicancia en la formación de sistemas de pórfiros cupríferos: yacimiento El Salvador, 3 Región, Chile," in *Proceedings of the IX Congreso Geológico Chileno*, Puerto Varas.

Cornejo, P. C., Mpodozis, C., Kay, S. M., and Tomlianson, A. J. (1994). "Volcanismo Bimodal Potásico en Regimen Extensional del Cretácico Superior-Eoceno en la región de El Salvador (26-27°),"in *Proceedings of the VII Congreso Geológico Chileno Concepción, Actas*, Chile.

Dalla Salla, L., Leguizawjn, M., Mazzoni, M., Merodlo, J., Rapela, C., and Spalletti, L. (1981). *Características del vulcanismo paleógeno en la Cordillera Nordpatagónica entre las latitudes 39°30' y 41°20' S", in VIII Congreso Geológico Argentino*. Chile: University of Concepcion.

De La Fuente, D., Figueroa, O., Duhart, P., Quiroz, D., Demaiffe, D., Oliveros, V., et al. (2012). *Los* intrusivos de Antearco del Cretácico Superior de Chile Centro Sur (39°S-40°S): Petrografía y geoquímica," in *XIII Congreso Geológico Chileno Actas*. 336–338.

De La Fuente, D. A. (2014). *Los Intrusivos de Ante-Arco Del Cretácico Su'Perior Del Centro-Sur De Chile (39-40°S): Petrografía y Geoquímica*. Master thesis, University of Concepción, Chile.

DeLong, S. E., Schwarz, W. M., and Anderson, R. N. (1979). Thermal effects of ridge subduction. *Earth Planet. Sci. Lett.* 44, 239–246.

Deruelle, B. (1982). Petrology of the Plio-Quaternary volcanism of the south-central and meridional Andes. *J. Volcanol. Geotherm. Res.* 14, 77–124.

Dickinson, W. R., and Snyder, W. S. (1979). Geometry of triple junctions related to San Andreas transform. *J. Geophys. Res.* 84, 561–572.

Domeier, M., Doubrovine, P. V., Torsvik, T. H., Spakman, W., and Bull, A. L. (2016). Global correlation of lower mantle structure and past subduction. *Geophys. Res. Lett.* 43, 4945–4953. doi: 10.1002/2016GL068827

D'Orazio, M., Agostini, S., Mazzarini, F., Innocenti, F., Manetti, P., Haller, M. J., et al. (2000). The Pali Aike Volcanic Field, Patagonia: slab-window magmatism near the tip of South America. *Tectonophysics* 321, 407–427.

Eagles, G., and Scott, B. G. (2014). Plate convergence west of Patagonia and the Antarctic Peninsula since 61 Ma. *Glob. Planet. Chang.* 123, 189–198.

Emparán, C., and Pineda, G. (2000). Estratigrafía y geocronología U-Pb y K-Ar de los sistemas volcánicos del Cretácico superior- Paleógeno en la zona de Condoriaco-Rivadavia, región de Coquimbo" in IX Congreso Geológico Chileno. *Puerto Varas* 1, 782–786.

Emparán, C. C., and Pineda, G. F. (1997). "El sistema de calderas anidadas Condoriaco (Cretácico superior-Eoceno inferior), IV región de Coquimbo," in *Proceedings of the VIII Congreso Geológico Chileno*, Antofagasta.

Espinoza, F., Morata, D., Pelleter, E., Maury, R. C., Suárez, M., Lagabrielle, Y., et al. (2005). Petrogenesis of the Eocene and Mio–Pliocene alkaline basaltic magmatism in Meseta Chile Chico, southern Patagonia, Chile: Evidence for the participation of two slab windows. *Lithos* 82, 315–343.

Fabian, T., Whittaker, J., and Müller, D. (2010). Mapping Tertiary mid-ocean ridge subduction and slab window formation beneath Sundaland using seismic tomography. *ASEG Extended Abstr.* 1, 1–4.

Fennell, L. M., Iannelli, S. B., Encinas, A., Naipauer, M., Valencia, V., and Folguera, A. (2019). Alternating contraction and extension in the Southern Central Andes (35°–37° S). *Am. J. Sci.* 5, 381–429. doi: 10.2475/05.2019.02

Fennell, L. M., Quinteros, J., Iannelli, S. B., Litvak, V. D., and Folguera, A. (2018). The role of the slab pull force in the late Oligocene to early Miocene extension in the Southern Central Andes (27°-46° S): Insights from numerical modeling. *J. South Am. Earth Sci.* 87, 174–187. doi: 10.1016/j.jsames.2017.12.012

Ferguson, K. M., Dungan, M. A., Davidson, J. P., and Colucci, M. T. (1992). The tatara–san pedro volcano, 36°s, chile: a chemically variable, dominantly mafic magmatic system. *J. Petrol.* 33, 1–43. doi: 10.1093/petrology/33.1.1

Fernández Paz, L., Bechis, F., Litvak, V. D., Echaurren, A., Encinas, A., et al. (2019). Constraints on trenchward arc migration and back-arc magmatism in the North Patagonian Andes in the context of Nazca plate rollback. *Tectonics* 38, 3794–3817. doi: 10.1029/2019TC005580

Fernández Paz, L., Litvak, V. D., Echaurren, A., Iannelli, S. B., Encinas, A., Folguera, A., et al. (2018). Late Eocene volcanism in North Patagonia (42° 30'–43° S): Arc resumption after a stage of within-plate magmatism. *J. Geod.* 113, 13–31. doi: 10.1016/j.jog.2017.11.005

Ferrari, L., Bergomi, M., Martini, M., Tunesi, A., Orozco-Esquivel, T., and López-Martínez, M. (2014). Late Cretaceous-Oligocene magmatic record in southern Mexico: the case for a temporal slab window along the evolving Caribbean-North America-Farallon triple boundary. *Tectonics* 33, 1738–1765.

Folguera, A., Naranjo, J. A., Orihashi, Y., Sumino, H., Nagao, K., Polanco, E., et al. (2009). Retroarc volcanism in the northern San Rafael Block (34°–35°30'S), southern Central Andes: occurrence, age, and tectonic setting. *J. Volcanol. Geotherm. Res.* 186, 169–185.

Folguera, A., and Ramos, V. A. (2011). Repeated eastward shifts of arc magmatism in the Southern Andes: a revision to the long-term pattern of Andean uplift and magmatism. *J. S. Am. Earth Sci.* 32, 531–546.

Folguera, A., Vera, E. R., Bottesi, G., Valcarce, G. Z., and Ramos, V. A. (2010). The Loncopué Trough: a Cenozoic basin produced by extension in the southern Central Andes. *J. Geodyn.* 49, 287–295. doi: 10.1016/j.jog.2010.01.009

Franchini, M. B., Lopez Escobar, L., Shalamuk, I. B. A., and Melnert, L. D. (2003). Paleocene, calc-alkaline subvolcanic rocks from Nevazón Hill area (NW Chos Malal Fold Belt), Neuquén, Argentina, and comparison with granitoids of the Neuqu6n-Mendoza volcanic province. *J. S. Am. Earth Sci.* 16, 399–422.

Futa, K., and Stern, C. R. (1988). Sr and Nd isotopic and trace element compositions of Quaternary volcanic centers of the Southern Andes. *Earth Planet Sci. Lett.* 88, 253–262.

Gaina, C., and Jakob, J. (2019). Global Eocene tectonic unrest: possible causes and effects around the North American plate. *Tectonophysics* 760, 136–151.

Giacosa, R., and Heredia, N. (2001). *Hoja geológica 4172-IV San Carlos de Bariloche*. Buenos Aires: Instituto de Geología y Recursos Minerales.

Giambiagi, L., Mescua, J., Bechis, F., Tassara, A., and Hoke, G. (2012). Thrust belts of the southern Central Andes: along-strike variations in shortening, topography, crustal geometry, and denudation. *Bulletin* 124, 1339–1351. doi: 10.1130/B30609.1

Gianni, G. M., García, H. P., Lupari, M., Pesce, A., and Folguera, A. (2017). Plume overriding triggers shallow subduction and orogeny in the southern Central Andes. *Gondwana Res.* 49, 387–395.

Gianni, G. M., Navarrete, C., and Spagnotto, S. (2019). Surface and mantle records reveal an ancient slab tear beneath Gondwana. *Sci. Rep.* 9:19774. doi: 10.1038/s41598-019-56335-9

Gianni, G. M., Dávila, F. M., Echaurren, A., Fennell, L., Tobal, J., Navarrete, C., et al. (2018a). A geodynamic model linking Cretaceous orogeny, arc migration, foreland dynamic subsidence and marine ingression in southern South America. *Earth Sci. Rev.* 185, 437–462.

Gianni, G. M., Pesce, A., and Soler, S. R. (2018b). Transient plate contraction between two simultaneous slab windows: insights from Paleogene tectonics of the Patagonian Andes. *J. Geody.* 121, 64–75. doi: 10.1016/j.jog.2018.07.008

González Bonorino, F. (1979). Esquema de la evolución geológica de la Cordillera Norpatagónica. *Rev. Asoc. Geol. Argent.* 34, 184–202.

González Bonorino, F., and González Bonorino, G. (1978). Geología de la región de San Carlos de Bariloche. *Rev. Asoc. Geol. Argent.* 33, 175–210.

González Díaz, E. F., and Lizuaín, A. (1984). El Complejo volcano-clástico y plutónico del sector cordillerano. *Geol. Recur. Natur. Río Negro.* 1, 119–129.

Gorring, M., Singer, B., Gowers, J., and Kay, S. M. (2003). Plio–Pleistocene basalts from the meseta del lago buenos aires, argentina: evidence for asthenosphere–lithosphere interactions during slab window magmatism. *Chem. Geol.* 193, 215–235. doi: 10.1016/S0009-2541(02)00249-8

Gorring, M. L., and Kay, S. M. (2001). Mantle processes and sources of Neogene slab window magmas from southern Patagonia, Argentina. *J. Petrol.* 42, 1067–1094. doi: 10.1093/petrology/42.6.1067

Gorring, M. L., Kay, S. M., Zeitler, P. K., Ramos, V. A., Rubiolo, D., Fernandez, M. I., et al. (1997). Neogene Patagonian plateau lavas: continental magmas associated with ridge collision at the Chile triple junction. *Tectonics* 16, 1–17. doi: 10.1029/96TC03368

Groome, W. G., and Thorkelson, D. J. (2009). The three-dimensional thermo-mechanical signature of ridge subduction and slab window migration. *Tectonophysics* 464, 70–83. doi: 10.1016/j.tecto.2008.07.003

Guillaume, B., Martinod, J., Husson, L., Roddaz, M., and Riquelme, R. (2009). Neogene uplift of central eastern Patagonia: dynamic response to active spreading ridge subduction? *Tectonics* 28:TC2009.

Guillaume, B., Moroni, M., Funiciello, F., Martinod, J., and Faccenna, C. (2010). Mantle flow and dynamic topography associated with slab window opening: insights from laboratory models. *Tectonophysics* 496, 83–98.

Guivel, C., Morata, D., Pelleter, E., Espinoza, F., Maury, R. C., Lagabrielle, Y., et al. (2006). Miocene to Late Quaternary Patagonian basalts (46–47°S): geochronometric and geochemical evidence for slab tearing due to active spreading ridge subduction. *J. Volcanol. Geotherm. Res.* 149, 346–370. doi: 10.1016/j.jvolgeores.2005.09.002

Hickey-Vargas, R. L., Frey, F. A., Gerlach, D. C., and López- Escobar, L. (1986). Multiple sources for basaltic arc rocks from the southern volcanic zone of the Andes (34°41'S): trace element and isotopic evidence for contributions from subducted oceanic crust, mantle and continental crust. *J. Geoph. Res.* 91, 5963–5983.

Hildreth, W., and Morbath, S. (1988). Crustal contributions to arc magmatism in the Andes of central Chile. *Contribut. Mineral. Petrol.* 98, 455–489.

Hofmann, A. W., and White, W. M. (1982). Mantle plumes from ancient oceanic crust. *Earth Planet. Sci. Lett.* 57, 421–436.

Höppner, N., Lucassen, F., Chiessi, C. M., Sawakuchi, A. O., and Kasemann, S. A. (2018). Holocene provenance shift of suspended particulate matter in the Amazon River basin. *Quat. Sci. Rev.* 190, 66–80.

Iannelli, S. B., Fennell, L. M., Litvak, V. D., Lucía, F. P., Alfonso, E., and Andrés, F. (2018). Geochemical and tectonic evolution of Late Cretaceous to early Paleocene magmatism along the Southern Central Andes (35-36°S). *J.South Am. Earth Sci.* 87, 139–156. doi: 10.1016/j.jsames.2017.12.008

Iannelli, S. B., Litvak, V. D., Fernández Paz, L., Folguera, A., Ramos, M. E., and Ramos, V. A. (2017). Evolution of Eocene to Oligocene arc-related volcanism in the North Patagonian Andes (39°-41°S), prior to the break-up of the Farallon plate. *Tectonophysics* 69, 70–87. doi: 10.1016/j.tecto.2016.12.024

Irvine, T. N., and Baragar, W. R. A. (1971). A guide to chemical classification of the common volcanic rocks. *Can. J. Earth Sci.* 8, 523–548.

Jacques, G., Hoernle, K., Gill, J., Wehrmann, H., Bindeman, I., and Lara, L. E. (2014). Geochemical variations in the central southern volcanic zone, chile (38–43 S): the role of fluids in generating arc magmas. *Chem. Geol.* 371, 27–45. doi: 10.1016/j.chemgeo.2014.01.015

Jacques, G., Hoernle, K., Gill, J. B., Hauff, F., Wehrmann, D., Garbe-Schönber, P., et al. (2013). Across-arc geochemical variations in the Southern Volcanic Zone, Chile (34.5–38°S): constraints on mantle wedge and source input compositions. *Geochim. Cosmochim.* 123, 218–243. doi: 10.1016/j.gca.2013.05.016

Jalowitzki, T., Gervasoni, F., Conceição, R. V., Orihashi, Y., Bertotto, G. W., Sumino, H., et al. (2017). Slab-derived components in the subcontinental lithospheric mantle beneath Chilean Patagonia: geochemistry and Sr–Nd–Pb isotopes of mantle xenoliths and host basalt. *Lithos* 292, 179–197.

Johnston, S. T., and Thorkelson, D. J. (1997). Cocos-Nazca slab window beneath central America. *Earth Planet. Sci. Lett.* 146, 465–474.

Jones, R. E., Kirstein, L. A., Kasemann, S. A., Litvak, V. D., Poma, S., Alonso, R. N., et al. (2016). The role of changing geodynamics in the progressive contamination of Late Cretaceous to Late Miocene arc magmas in the southern Central Andes. *Lithos* 262, 169–191. doi: 10.1016/j.lithos.2016.07.002

Jordan, T., Burns, W., Veiga, R., Pángaro, F., Copeland, P., Kelley, S., et al. (2001). Extension and basin formation in the Southern Andes caused by increased convergence rate: amid-Cenozoic trigger for the Andes. *Tectonics* 20, 308–324.

Kay, S. M., Burns, M., and Copeland, P. (2006). "Upper Cretaceous to Holocene magmatism and evidence for transient Miocene shallowing of the Andean subduction zone under the northern Neuquén Basin," in *Evolution of an Andean margin: A Tectonic And Magmatic View From The Andes To the Neuquén Basin (35–39°S)*, eds S. M. Kay and V. A. Ramos (London: The Geological Society),

Kay, S. M., Godoy, E., and Kurtz, A. (2005). Episodic arc migration, crustal thickening, subduction erosion, and magmatism in the south-central Andes. *Geol. Soc. Am. Bull.* 117, 67–88.

Kay, S. M., Ramos, V. A., and Marquez, M. (1993). Evidence in Cerro Pampa volcanic rocks for slab-melting prior to ridge-trench collision in southern South America. *J. Geol.* 101, 703–714.

Kleiman, L. E., and Japas, M. S. (2009). The Choiyoi volcanic province at 34 S–36 S (San Rafael, Mendoza, Argentina): implications for the Late Palaeozoic evolution of the southwestern margin of Gondwana. *Tectonophysics* 473, 283–299.

Ladino, M., Blanco, N., Matthews, S., and Tomlinson, A. J. (2000). "Cambios geoquímicos en el magmatismo del límite Cretácico- Terciario en la precordillera de Calama, II región de Antofagasta, norte de Chile" in IX Congreso Geológico Chileno. *Puerto Varas* 1, 630–634.

Le Maitre, R. W., Bateman, P., Dudek, A., Keller, J., Lameyre, J., and Le Bas, M. J. (1989). *A Classification of Igneous Rocks and Glossary of Terms: Recommendations of the International Union of Geological Sciences Subcommission on the Systematics of Igneous Rocks*. Oxford: Blackwell Scientific Publications.

Legarreta, L., and Uliana, M. A. (1991). Jurassic-Cretaceous marine oscillations and geometry of back-arc basin fill, central argentine andes, in sedimentation, tectonics and eustasy: sea-level changes at active margins. *IAS Spec. Publ.* 12, 429–450.

Litvak, V. D., Encinas, A., Oliveros, V., Bechis, F., Folguera, A., and Ramos, V. A. (2014). "El volcanismo mioceno inferior vinculado a las ingresiones marinas en los Andes Nordpatagónicos," in *Proceedings of the 19° Congreso Geológico Argentino*, Córdoba.

Litvak, V. D., Fernández Paz, L., Iannelli, S., Poma, S., and Folguera, A. (2019). "Cenozoic arc-related magmatism in the southern Central and North Patagonian Andes," in *Andean Tectonics*, eds B. Horton and A. Folguera (Amsterdam: Elsevier), 573–607. doi: 10.1016/B978-0-12-816009-1.00021-6

Litvak, V. D., Poma, S., and Kay, S. M. (2007). Paleogene and Neogene magmatism in the Valle del Cura region: new perspective on the evolution of the Pampean flat slab, San Juan province, Argentina. *J. South American Ear. Sci.* 24, 117–137. doi: 10.1016/j.jsames.2007.04.002

Litvak, V. D., Spagnuolo, M. G., Folguera, A., Poma, S., Jones, R. E., and Ramos, V. A. (2015). Late Cenozoic calc-alkaline volcanism over the Payenia shallow subduction zone, South-Central Andean back-arc (34° 30'–37° S), Argentina. *J. South Am. Earth Sci.* 64, 365–380.

Llambías, E. J., and Aragón, E. (2011). "Volcanismo Paleógeno", in *Proceedings of the Geología y Recursos Naturales de la Provincia del Neuquén in XVIII Congreso Geológico Argentino*, Neuquén.

Llambías, E. J., Bertotto, G. W., Risso, C., and Hernando, I. (2010). El volcanismo cuaternario en el retroarco de Payenia: una revisión. *Rev. Asoc. Geol. Argent.* 67, 278–300.

Llambías, E. J., Quenardelle, S. Y., and Montenegro, T. (2003). The Choiyoi group from central Argentina: a subalkaline transitional to alkaline association in the craton adjacent to the active margin of the Gondwana continent. *J. S. Am. Earth Sci.* 16, 243–257.

Llambías, E. J., and Rapela, C. W. (1989). Las vulcanitas de collipilli, neuquén, y su relación con otras unidades paleógenas de la cordillera. *Rev. Asoc. Geol. Argent.* 44, 224–236.

López-Escobar, L., Cembrano, J., and Moreno, H. (1995). Geochemistry and tectonics of the Chilean Southern andes basaltic quaternary volcanism (37-46°S). *Andean Geol.* 22, 219–234.

López-Escobar, L., Parada, M. A., Moreno, H., Frey, F. A., and Hickey-Vargas, R. L. (1992). A contribution to the petrogenesis of osorno and Calbuco volcanoes, southern Andes (41° 00'-41° 30'S): comparative study. *Andean Geol.* 19, 211–226.

López-Escobar, L., and Vergara, M. (1997). Eocene-Miocene longitudinal depression and quaternary volcanism in the Southern Andes, Chile (33-42.5 S): a geochemical comparison. *Andean Geol.* 24, 227–244.

Lucassen, F., Becchio, R., Harmon, R., Kasemann, S., Franz, G., Trumbull, R., et al. (2001). Composition and density model of the continental crust at an active continental margin in the Central Andes between 21° and 27°S. *Tectonophysics* 341, 195–223.

Lucassen, F., Escayola, M., Romer, R. L., Viramonte, J., Koch, K., and Franz, G. (2002). Isotopic composition of late mesozoic basic and ultrabasic rocks from the Andes (23–32°S): implications for the Andean mantle. *Cont. Mineral. Petrol.* 143, 336–349.

Lucassen, F., Trumbull, R., Franz, G., Creixell, C., Vásquez, P., Romer, R. L., et al. (2004). Distinguishing crustal recycling and juvenile additions at active continental margins: the paleozoic to recent compositional evolution of the Chilean Pacific margin (36–41 S). *J. South Am. Earth Sci.* 17, 103–119.

Maloney, K. T., Clarke, G. L., Klepeis, K. A., and Quevedo, L. (2013). The Late Jurassic to present evolution of the Andean margin: drivers and the geological record. *Tectonics* 32:67. doi: 10.1002/tect.20067

Mateo-Fernández Caso, M. P., Montero, D. G., Leal, P. R., and Ramos, V. A. (2011). Petrografía y geoquímica del magmatismo cretácico superior-eoceno en el área de pichaihue. *Provincia Neuquén. Rev. Asoc. Geol. Argent.* 68, 173–184.

Mella, M., Muñoz, J., Vergara, M., Klohn, E., Farmer, L., and Stern, C. R. (2005). Petrogenesis of the pleistocene tronador volcanic Group, Andean Southern Volcanic Zone. *Andean Geol.* 32, 131–154.

Melnick, D., Folguera, A., and Ramos, V. A. (2006). Structural control on arc volcanism: the Caviahue-Copahue complex (38°S). *J. S. Am. Earth Sci.* 22, 66–88.

Montecinos, P., Schärer, U., Vergara, M., and Aguirre, L. (2008). Lithospheric origin of Oligocene–Miocene magmatism in Central chile: U–Pb ages and Sr–Pb–Hf isotope composition of minerals. *J. Petrol.* 49, 555–580.

Montelli, R., Nolet, G., Dahlen, F. A., and Masters, G. (2006). A catalogue of deep mantle plumes: new results from finite-frequency tomography. *Geoch. Geophy. Geosyst.* 7:1248.

Mosolf, J. G. (2013). *Stratigraphy, Structure, And Geochronology Of The Abanico Formation In The Principal Cordillera, Central Chile: Evidence Of Protracted Volcanism And Implications For Andean Tectonics*. Ph. D. thesis, University of Santa Barbara, California, MA.

Mosolf, J. G., Gans, P. B., Wyss, A. R., Cottle, J. M., and Flynn, J. J. (2019). Late cretaceous to miocene volcanism, sedimentation, and upper-crustal faulting and folding in the principal cordillera, central Chile: field and geochronological evidence for protracted arc volcanism and transpressive deformation. *GSA Bulletin* 131, 252–273. doi: 10.1130/B31998.1

Mpodozis, C., Arriagada, C., Basso, M., Roperch, P., Cobbold, P., and Reich, M. (2005). Late mesozoic to paleogene stratigraphy of the salar de atacama basin, antofagasta, northern chile: implications for the tectonic evolution of the central andes. *Tectonophysics* 399, 125–154.

Müller, R. D., Seton, M., Zahirovic, S., Williams, S. E., Matthews, K. J., Wright, N. M., et al. (2016). Ocean basin evolution and global-scale plate reorganization events since Pangea breakup. *Annu. Rev. Earth Plant Sc.* 44, 107–138.

Munizaga, F., Hervé, F., Drake, R., Pankhurst, R. J., Brook, M., and Snelling, N. (1988). Geochronology of the Lake Region of south-central Chile (39–42 S): preliminary results. *J. S. Am. Earth Sci.* 1, 309–316.

Muñoz, J., Troncoso, R., Duhart, P., Crignola, P., Farmer, L., and Stern, C. R. (2000). The relation of the mid-Tertiary coastal magmatic belt in south-central Chile to the late oligocene increase in plate convergence rate. *Rev. Geol. Chile.* 27, 177–203.

Muñoz, M., Fuentes, F., Vergara, M., Aguirr, L., Olov Nyström, J., Féraud, G., et al. (2006). Abanico East Formation: petrology and geochemistry of volcanic rocks behind the Cenozoic arc front in the Andean Cordillera, central Chile (33° 50'S). *Rev. Geol. Chile.* 331, 109–140.

Muñoz, M., Tapia, F., Persico, M., Benoit, M., Charrier, R., Farías, M., et al. (2018). Extensional tectonics during Late Cretaceous evolution of the Southern central andes: evidence from the chilean main range at˜ 35° S. *Tectonophysics* 744, 93–117. doi: 10.1016/j.tecto.2018.06.009

Nullo, F. E., Stephens, G., Combina, A., Dimieri, L., Baldauf, P., Bouza, P., et al. (2005). *Hoja Geológica 3569-III Malargüe, Programa Nacional de Cartas Geológicas de la República Argentina a escala 1:250.000, Boletín 346*. Buenos Aires: SEGEMAR.

Obayashi, M., Yoshimitsu, J., Nolet, G., Fukao, Y., Shiobara, H., Sugioka, H., et al. (2013). Finite frequency whole mantle P wave tomography: improvement of subducted slab images. *Geophy. Res. Lett.* 40, 5652–5657.

Orts, D. L., Folguera, A., Giménez, M., Ruiz, F., Vera, E. A. R., and Klinger, F. L. (2015). Cenozoic building and deformational processes in the North patagonian andes. *J. Geodyn.* 86, 26–41.

Pankhurst, R. J., Rapela, C. W., Fanning, C. M., and Marquez, M. (2006). Gondwanide continental collision and the origin of Patagonia. *Earth Sci. Rev.* 76, 235–257.

Pankhurst, R. J., Weaver, S. D., Hervé, F., and Larrondo, P. (1999). Mesozoic–cenozoic evolution of the north patagonian batholith in aysén, Southern Chile. *Geol. Soc. Lond.* 156, 673–694.

Parada, M. A., Rivano, S., Sepúlveda, P., Hervé, M., Hervé, F., Puig, A., et al. (1988). Mesozoic and Cenozoic plutonic development in the andes of central Chile (30°30'-32°30S). *J. S. Am. Earth Sci.* 1, 249–260.

Pardo-Casas, F., and Molnar, P. (1987). Relative motion of the Nazca (Farallon) and South American plates since late Cretaceous time. *Tectonics* 6, 233–248.

Pearce, J. A. (1983). "Role of the sub-continental lithosphere in magma genesis at active continental margins," in *Continental Basalts and Mantle Xenoliths* eds C.J. Hawkesworth, and M.J. Norry (Nantwich, UK: Shiva Press), 230–249.

Piquer, J., Hollings, P., Rivera, O., Cooke, D. R., Baker, M., and Testa, F. (2017). Along-strike segmentation of the abanico basin, central chile: new chronological, geochemical and structural constraints. *Lithos* 268, 174–197.

Plimer, I. R., and Elliott, S. M. (1979). The use of Rb/Sr ratios as a guide to mineralization. *J. Geochem. Expl.* 12, 21–34.

Radic, J. P., Rojas, L., Carpinelli, A., and Zurita, E. (2002). "Evolución tectónica de la cuenca terciaria de Cura-Mallín, región cordillerana chileno argentina (36°30°-39°00°S)," in *Proceedings of the 15° Congreso Geológico Argentino*, Calafate.

Ramos, M. E., Folguera, A., Fennell, L., Giménez, M., Litvak, V. D., Dzierma, Y., et al. (2014). Tectonic evolution of the North patagonian andes from field and gravity data (39–40 S). *J. S. Am. Earth Sci.* 51, 59–75.

Ramos, V., and Kay, S. M. (1992). Southern Patagonian plateau basalts and deformation; back-arc testimony of ridge collisions. *Tectonophysics* 205, 261–282.

Ramos, V. A., and Folguera, A. (2005). "Tectonic evolution of the andes of neuquén: constraints derived from the magmatic arc and foreland deformation," in *The Neuquén Basin, Argentina: A case Study in Sequence Stratigraphy and Basin Dynamics*, Vol. 252, eds G. D. Veiga, A. Spalletti, J. A. Howell, and E. Schwarz (London: Geology Society), 15–35.

Rapela, C., Spalletti, L., Merodio, J., and And Aragón, E. (1984). "El vulcanismo paleoceno-eoceno de la provincia andino-patagónica," in *Geología y Recursos Naturales de la Provincia de Río Negro*, ed. V. Ramos (Buenos Aires: Geology Society), 189–214.

Rapela, C., Spalletti, L., Merodio, J., and Aragón, E. (1988). Temporal evolution and spatial variation of early Terciary volcanism in the Patagonian Andes (40°S-42°30'S). *J. S. Am. Earth Sci.* 1, 75–88.

Rapela, C. W., and Llambías, E. J. (1985). "La secuencia andesítica terciaria de Andacollo, Neuquén, Argentina," in *Actas 4° Congreso Geológico Chileno*, 458–488.

Rapela, C. W., Spalletti, L. A., and Merodio, C. J. (1983). Evolución magmática y geotectónica de la "Serie Andesítica" andina (paleoceno-eoceno) en la cordillera nordpatagónica. *Rev. Asoc. Geol. Argent.* 38, 469–484.

Rivera, O., and Mpodozis, C. (1991). "Volcanismo explosivo del Terciario inferior en la Precordillera de Copiapo Región de Atacama, Chile. Las calderas Lomas Bayas y Durazno" in *Proceedings of the VI Congreso Geológico Chileno*, Viña del Mar.

Rivera, O., and Mpodozis, C. (1994). *La Megacaldera Carrizalillo y sus Calderas Anidadas: Volcanismo Sinextensional Cretácico Superior-Terciario Inferior en la Precordillera de Copiapó" in VII° Congreso Geológico Chileno*. Concepción: University of Concepcion.

Rojas Vera, E. A., Folguera, A., Valcarce, G. Z., Giménez, M., Ruiz, F., Martínez, P., et al. (2010). Neogene to Quaternary extensional reactivation of a fold and thrust belt: the agrio belt in the southern central andes and its relation to the loncopué trough (38°–39°S). *Tectonophysics* 492, 279–294.

Rudnick, R. L., and Gao, S. (2003). Composition of the continental crust. *The crust* 3, 1–64.

Sagripanti, L., Vera, E. A. R., Gianni, G. M., Folguera, A., Harvey, J. E., Farías, M., et al. (2015). Neotectonic reactivation of the western section of the malargüe fold and thrust belt (tromen volcanic plateau, Southern Central Andes). *Geomorphology* 232, 164–181.

Salvioli, M., Lanfranchini, M. E., Recio, C., and de Barrio, R. E. (2017). El magmatismo cretácico-terciario y su relación con sistemas hidrotermales polimetálicos en la región de colipilli-naunauco, provincia del Neuquén. *Rev. Asoc. Geol. Arg.* 75, 46–63.

Santosh, M., and Kusky, T. (2010). Origin of paired high pressure–ultrahigh-temperature orogens: a ridge subduction and slab window model. *Terra Nova.* 22, 35–42.

Sato, A. M., Llambías, E. J., Basei, M. A., and Castro, C. E. (2015). Three stages in the Late Paleozoic to Triassic magmatism of southwestern Gondwana, and the relationships with the volcanogenic events in coeval basins. *J. S. Am. Earth Sci.* 63, 48–69.

Scasso, J. A. (2012). *Geología del Sector Oriental Del Lago Huechulafquen Y Nacientes Del Río Chimehuín, Comarca Junín De Los Andes, Provincia del Neuquén*. Master thesis, University of Buenos Aires, Buenos Aires.

Serra-Varela, S., González, P. D., Giacosa, R. E., Heredia, N., Pedreira Rodríguez, D., Martín González, F., et al. (2019). Evolution of the Palaeozoic basement of the North Patagonian Andes in the San Martín de los Andes area (Neuquén, Argentina): petrology, age and correlations. *Andean Geol.* 46, 102–130.

Seton, M., Müller, R. D., Zahirovic, S., Gaina, C., Torsvik, T., Shepard, G., et al. (2012). Global continental and ocean basin reconstructions since 200 Ma. *Earth Sci. Rev.* 113, 212–270.

Shephard, G. E., Matthews, K. J., Hosseini, K., and Domeier, M. (2017). On the consistency of seismically imaged lower mantle slabs. *Sci. Rep.* 7:10976. doi: 10.1038/s41598-017-11039-w

Silvestro, J., and Atencio, M. (2009). La cuenca cenozoica del río grande y palauco: edad, evolución y control estructural, faja plegada de malargüe. *Rev. Asoc. Geol. Arg.* 65, 154–169.

Søager, N., Holm, P. M., and Llambías, E. J. (2013). Payenia volcanic province, southern mendoza, Argentina: OIB mantle upwelling in a backarc environment. *Chem. Geol.* 349, 36–53.

Somoza, R., and Ghidella, M. E. (2005). Convergencia en el margen occidental de América del Sur durante el Cenozoico: subducción de las placas de Nazca, Farallón y Aluk. *Rev. Asoc. Geol. Argent.* 60, 797–809.

Somoza, R., and Ghidella, M. E. (2012). Late Cretaceous to recent plate motions in western South America revisited. *Earth Planet. Sci. Lett.* 33, 152–163. doi: 10.1016/j.epsl.2012.03.003

Somoza, R., Tomlinson, A. J., Caffe, P. J., and Vilas, J. F. (2012). Paleomagnetic evidence of earliest Paleocene deformation in Calama (22° S), northern Chile: andean-type or ridge-collision tectonics? *J. S. Am. Earth Sci.* 37, 208–213.

Somoza, R., and Zaffarana, C. B. (2008). Mid-Cretaceous polar standstill of South America, motion of the Atlantic hotspots and the birth of the Andean cordillera. *Earth Planet. Sci. Lett.* 271, 267–277.

Spagnuolo, M. G., Folguera, A., Litvak, V. D., Rojas Vera, E. A., and Ramos, V. A. (2012). Late Cretaceous arc rocks in the Andean retroarc region at 36.5°S: evidence supporting a Late Cretaceous slab shallowing. *J. S. Am. Earth Sci.* 38, 44–56.

Steinberger, B., Trond, H. T., and Thorsten, W. B. (2012). Subduction to the lower mantle-a comparison between geodynamic and tomographic models. *Solid Earth* 3, 415–432.

Suárez, M., and Emparán, C. (1995). The stratigraphy, geochronology and paleophysiography of a Miocene fresh water interarc basin. *S. Chile. J. S. Am. Earth Sci.* 8, 17–31.

Sun, S. S., and McDonough, W. F. (1989). "Chemical and isotopic systematics of oceanic basalts: implications for mantle composition and processes," in *Magmatism in Ocean Basins*, eds A. D. Saunders and M. J. Norry (London: Geological Society), 313–345.

Tapia, F. (2015). *Evolución Tectónica Y Configuración Actual De Los Andes Centrales Del Sur (34° 45'-35° 30'S)*. Ph. D. thesis, Universidad de Chile, Santiago.

Tapia, F., Farías, M., Naipauer, M., and Puratich, J. (2015). Late Cenozoic contractional evolution of the current arc-volcanic region along the southern Central Andes (35° 20' S). *J. Geod.* 88, 36–51.

Tesoniero, A., Auer, L., Boschi, L., and Cammarano, F. (2015). Hydration of marginal basins and compositional variations within the continental lithospheric mantle inferred from a new global model of shear and compressional velocity. *J. Geophy. Res. Solid Earth* 120, 7789–7813.

Thorkelson, D. J. (1996). Subduction of diverging plates and the principles of slab window formation. *Tectonophysics* 255, 47–63.

Turienzo, M., Dimieri, L., Frisicale, C., Araujo, V., and Sánchez, N. (2012). Cenozoic structural evolution of the Argentinean Andes at 34 40'S: a close relationship between thick and thin-skinned deformation. *Andean Geol.* 39, 317–357.

Turienzo, M. M. (2010). Structural style of the Malargüe fold-and-thrust belt at the Diamante River area (34° 30'–34° 50' S) and its linkage with the cordillera frontal, andes of central Argentina. *J. S. Am. Earth Sci.* 29, 537–556.

Turner, J. C. M. (1973). Descripción geológica de la Hoja 37 a-b, Junín de los Andes, provincia del Neuquén. *Serv. Nacional Minero Geol. Boletín* 138, 1–86.

Utgé, S., Folguera, A., Litvak, V., and Ramos, V. A. (2009). Geología del sector norte de la cuenca de Cura Mallín en las lagunas de Epulaufquen. *Neuquén. Rev. Asoc. Geol. Argent.* 64, 231–248.

van der Meer, D. G., Spakman, W., van Hinsbergen, D. J. J., Amaru, M. L., and Torsvik, T. H. (2010). Towards absolute plate motions constrained by lower-mantle slab remnants. *Nat. Geosci.* 3, 36–40.

van der Meer, D. G., Torsvik, T. H., Spakman, W., van Hinsbergen, D. J. J., and Amaru, M. L. (2012). Intra-Panthalassa Ocean subduction zones revealed by fossil arcs and mantle structure. *Nat. Geosci.* 5, 215–219.

van der Meer, D. G., van Hinsbergen, D. J., and Spakman, W. (2018). Atlas of the underworld: slab remnants in the mantle, their sinking history, and a new outlook on lower mantle viscosity. *Tectonophysics* 723, 309–448.

Varela, R., Basei, M. A. S., Cingolani, C. A., and Passarelli, C. R. (2005). El basamento cristalino de los Andes norpatagónicos en Argentina: geocronología e interpretación tectónica. *Rev. Geol. Chile.* 32, 167–187.

Varela, R., Teixeira, W., Cingolani, C., and Dalla Salda, L. (1994). "Edad Rubidio-Estroncio de granitoides de Aluminé-rahue, cordillera norpatagónica, Neuquén, Argentina," in *Proceedings of the VII°Congreso Geológico Chileno*, Concepción.

Wehrmann, H., Hoernle, K., Garbe-Schönberg, D., Jacques, G., Mahlke, J., and Schumann, K. (2014). Insights from trace element geochemistry as to the roles of subduction zone geometry and subduction input on the chemistry of arc magmas. *Int. J. Ear. Sci.* 103, 1929–1944. doi: 10.1007/s00531-013-0917-1

Windley, B. F., and Xiao, W. (2018). Ridge subduction and slab windows in the Central Asian orogenic belt: tectonic implications for the evolution of an accretionary orogen. *Gondwana Res.* 61, 73–87.

Wright, N. M., Seton, M., Williams, S. E., and Müeller, R. D. (2016). The late cretaceous to recent tectonic history of the pacific ocean basin. *Earth Sci. Rev.* 154, 138–173.

Xia, L., and Li, X. (2019). Basalt geochemistry as a diagnostic indicator of tectonic setting. *Gondwana Res.* 65, 43–67.

Zamora Valcarce, G., Zapata, T., del Pinto, A., and Ansa, A. (2006). "Structural evolution and magmatic characteristics of the Agrio fold-and-thrust belt," in *Evolution of an Andean Margin: A Tectonic And Magmatic View From The Andes To The Neuquén Basin (35–39°S)*, Vol. 407, eds S. M. Kay and V. A. Ramos (London: Geological Society), 125–146.

Zartman, R. E., and Doe, B. R. (1981). Plumbotectonics—the model. *Tectonophysics* 75, 135–162.

Zindler, A., and Hart, S. (1986). Chemical geodynamics. *Ann. Rev. Earth Planet. Sci.* 14, 493–571.

Conflict of Interest: The authors declare that the research was conducted in the absence of any commercial or financial relationships that could be construed as a potential conflict of interest.

frontiers
in Earth Science

ORIGINAL RESEARCH
published: 16 June 2020
doi: 10.3389/feart.2020.00155

Active 650-km Long Fault System and Xolapa Sliver in Southern Mexico

***Ekaterina Kazachkina*[1]*, *Vladimir Kostoglodov*[1], *Nathalie Cotte*[2], *Andrea Walpersdorf*[2], *Maria Teresa Ramirez-Herrera*[3], *Krzysztof Gaidzik*[3,4], *Allen Husker*[1] and *Jose Antonio Santiago*[1]**

[1] Instituto de Geofísica, Departmento de Sismología, Universidad Nacional Autónoma de México, Ciudad Universitaria, Mexico City, Mexico, [2] Université Grenoble Alpes, Université Savoie Mont Blanc, Centre National de Recherche Scientifique, Institut de Recherche pour le Développement, Institut Français des Sciences et Technologies des Transports, de l'Aménagement et des Réseaux, Institut de Sciences de la Terre, Grenoble, France, [3] Laboratorio de Tsunami y Paleosismología, Instituto de Geografía, Universidad Nacional Autónoma de México, Ciudad Universitaria, Mexico City, Mexico, [4] Institute of Earth Sciences, University of Silesia, Sosnowiec, Poland

New estimates of long-term velocities of permanent GPS stations in Southern Mexico reveal that the geologically discernible ∼650-km long shear zone, which strikes parallel to the Middle America trench, is active. This left-lateral strike-slip, La Venta–Chacalapa (LVC) fault system, is apparently associated with a motion of the Xolapa terrain and at the present time is the northern boundary of a ∼110–160-km wide forearc sliver with a sinistral motion of 3–6 mm/year with respect to the North America plate. This sliver is the major tectonic feature in the Guerrero and Oaxaca regions, which accommodates most of the oblique component of the convergence between the Cocos and North America plates. Previous studies based purely on the moment tensor coseismic slips exceedingly overestimated the sliver inland extent and allocated its northern margin on or to the north of the Trans-Mexican Volcanic Belt. While the LVC fault system probably slips slowly over geologic scale time and there is not any historic evidence of large earthquakes on the fault so far, its seismic potential could be very high, assuming a feasible order of $\sim 10^3$ years recurrence cycle. A detailed analysis of long-term position time series of permanent GPS stations in the Guerrero and Oaxaca states, Southern Mexico discards previous models and provides clear evidence of an active LVC fault zone bounding the Xolapa forearc sliver. The southeastward motion of this sliver may have persisted for the last ∼8–10 Million year and played an important role in the tectonic evolution of the region.

Keywords: fault system, oblique subduction, sliver motion, tectonics, GPS, earthquake slip

Edited by:
Jeroen Van Hunen,
Durham University, United Kingdom

Reviewed by:
Bernard Mercier De Lépinay,
Centre National de la Recherche Scientifique (CNRS), France
Luis E. Lara,
Servicio Nacional de Geología y Minería de Chile (SERNAGEOMIN), Chile

****Correspondence:***
Ekaterina Kazachkina
kazachkina@igeofisica.unam.mx

Specialty section:
This article was submitted to Structural Geology and Tectonics, a section of the journal Frontiers in Earth Science

Received: *01 February 2020*
Accepted: *27 April 2020*
Published: *16 June 2020*

Citation:
Kazachkina E, Kostoglodov V, Cotte N, Walpersdorf A, Ramirez-Herrera MT, Gaidzik K, Husker A and Santiago JA (2020) Active 650-km Long Fault System and Xolapa Sliver in Southern Mexico. Front. Earth Sci. 8:155. doi: 10.3389/feart.2020.00155

INTRODUCTION

The existence of a forearc sliver with contemporary sinistral motion with respect to the stable North America plate (wrt NA) should be expected as a result of the strain partitioning produced by oblique subduction of the Cocos plate (CO). Geological studies indicate the sinistral transpression during Late Cretaceous to Early Tertiary in the coastal area of the present-day southern Mexico (Cerca et al., 2007). Significant left-lateral strike-slip motion characterized by the mylonitization of the Xolapa metamorphic complex (Campa and Coney, 1983) was dated as Early Eocene in the La Venta

(Solari et al., 2007) and as Oligocene in the Chacalapa shear zones (Tolson, 2005). Nonetheless, there was not any evidence of the ongoing tectonic activity on the La Venta–Chacalapa (LVC) fault system (Ramírez-Herrera et al., 2018) or on other trench-parallel faults in the central Mexico, except the Central Trans-Mexican Volcanic Belt (TNVB; Suter et al., 1992).

Sliver models (e.g., McCaffrey, 1992) provide simple methods to appraise the forearc deformation and relative sliver velocity using slip vectors of shallow subduction thrust earthquakes. Nevertheless, these models are unable to restrict the geometry and location of strike-slip fault zones bordering slivers. One attempt to use this technique for the subduction zone in central Mexico was the study of Ego and Ansan (2002). Using focal mechanisms of thrust earthquakes corresponding to the seismogenic segment of the plate interface they considered the left-lateral slip rate of the forearc to be less than 8 mm/year. As the only known active E–W fault zone with left-lateral transtensive deformation was in the Central TNVB, the northern limit of the forearc sliver has been assigned to this fault zone, which is located as far as ∼350–380 km from the Middle America trench (MAT). A further study by Andreani et al. (2008), proposed that this sliver, the so-called "Southern Mexico Block," undergoes a counterclockwise rotation wrt NA and may be not related to oblique subduction.

To ascertain that the LVC fault system is tectonically active and represents the northern boundary of the forearc Xolapa sliver in Southern Mexico we analyzed continuous GPS data collected since 1997 at permanent GNSS networks in the Guerrero and Oaxaca areas. Long-term GPS velocities definitely indicate a left-lateral strike-slip motion across the fault zone with the rate of 3–6 mm/year. This result agrees with revised estimates of the sliver speed obtained from slip vectors of the subduction thrust earthquakes. An overall stretching of the forearc of ∼40 km between the Michoacan and Guerrero regions may be produced by a relative to the Michoacan sinistral retreat of the Xolapa sliver. Supposing that the Cocos–North America convergence conditions have not radically changed since the Late Miocene time, the reactivation of the LVC fault system could have occurred some ∼8–10 Ma ago.

DATA AND ANALYSIS

GPS Observations

The data used in this study (**Figure 1**) are 5–16 years of continuous measurements on the permanent GPS stations operated by the Instituto de Geofísica, UNAM, and one station, TOL2, of the Instituto Nacional de Estadística y Geografía, INEGI. To establish the reference frame ITRF2008 (Altamimi et al., 2011) we added also the data from several global IGS (International GNSS Service) GPS stations. The total GPS dataset was processed with the GAMIT-GLOBK software (version 10.60, Herring et al., 2015). Modeling of environmental effects on the GPS measurements (see Vergnolle et al., 2010) decreased notably the noise in the position time series. Years-lasting GPS observations are essential in the presence of periodic signals (e.g., Blewitt and Lavallée, 2002) to estimate secular tectonic deformations and velocities. This is of particular importance in the Guerrero and Oaxaca areas, where large subduction slow slip events (SSE) are happening regularly, about every 4 and 1 year, respectively (e.g., Cotte et al., 2009; Graham et al., 2016).

For several GPS stations in the Michoacan state we used already processed position time series from the Tlalocnet network, downloaded from the UNAVCO[1].

Secular GPS velocities, V_S, were calculated by weighted least-square linear fit to the time series at each station. To avoid the effect of recent large subduction thrust earthquakes, we subtracted beforehand corresponding coseismic displacements of the 2014 Papanoa, Mw 7.3 event (Unam_Seismology_Group, 2015) from the time series in Guerrero and truncated the Oaxaca time series by the date of the 2012 Ometepec, Mw 7.5 earthquake (Unam_Seismology_Group, 2013). **Figure 2** demonstrates an example of linear fits to the CAYA northern time series affected by several large quasiperiodic SSEs. Of course, in this extreme case the SSEs produce very large displacements and resulting V_{SN} value varies within some ∼10% depending on the end bound of the fitting window. For the Oaxaca time series, an effect of the SSE on the V_S is relatively smaller because of slow events smaller displacement and their shorter recurrence period.

The trench-parallel component of secular velocity, V_{SS}, rests on an assessment of the trench normal azimuth, Tn, at each location of GPS station. The shape of the MAT is arc-curved and may be approximated by a few segments of small circles on a spherical Earth (Guzman-Speziale, 1995). Using this approach, we selected four successive sections of the MAT with approximately consistent curvatures and fitted each of those to a small circle (**Supplementary Figure A1**). Thus, the pole of best fitting small circle is the center of curvature of the trench section (**Supplementary Table A1**). The azimuth of big circle passing through this pole and a location point of GPS station corresponds to the Tn. The trench normal at each station is calculated according its location in a sector of corresponding small circle (see **Table 1** and **Supplementary Figure A1**). By applying the same method, it is possible to define the obliquity angle variation along the MAT as the angle between plate convergence direction (we used PVEL Cocos-North America plates model, DeMets et al., 2010) and trench normal (**Figure 3**). The obliquity in Guerrero and Oaxaca segment of the MAT is relatively higher (10°–15°) than in Michoacan and Chiapas, where it is close to ∼0° in average.

All V_S and V_{SS} vectors are plotted in **Figure 1**, where an abrupt reduction of secular trench-parallel velocity, V_{SS}, is obvious from south-west to north-east, across the LVC fault zone, especially in Guerrero, with a broader coverage of the GPS network. To reveal a tectonic significance of the LVC fault zone, we projected V_{SS} amplitudes onto a general profile perpendicular to the MAT (**Figure 4**). As it is seen in **Figure 4**,

---

[1] https://www.unavco.org/instrumentation/networks/status/tlalocnet

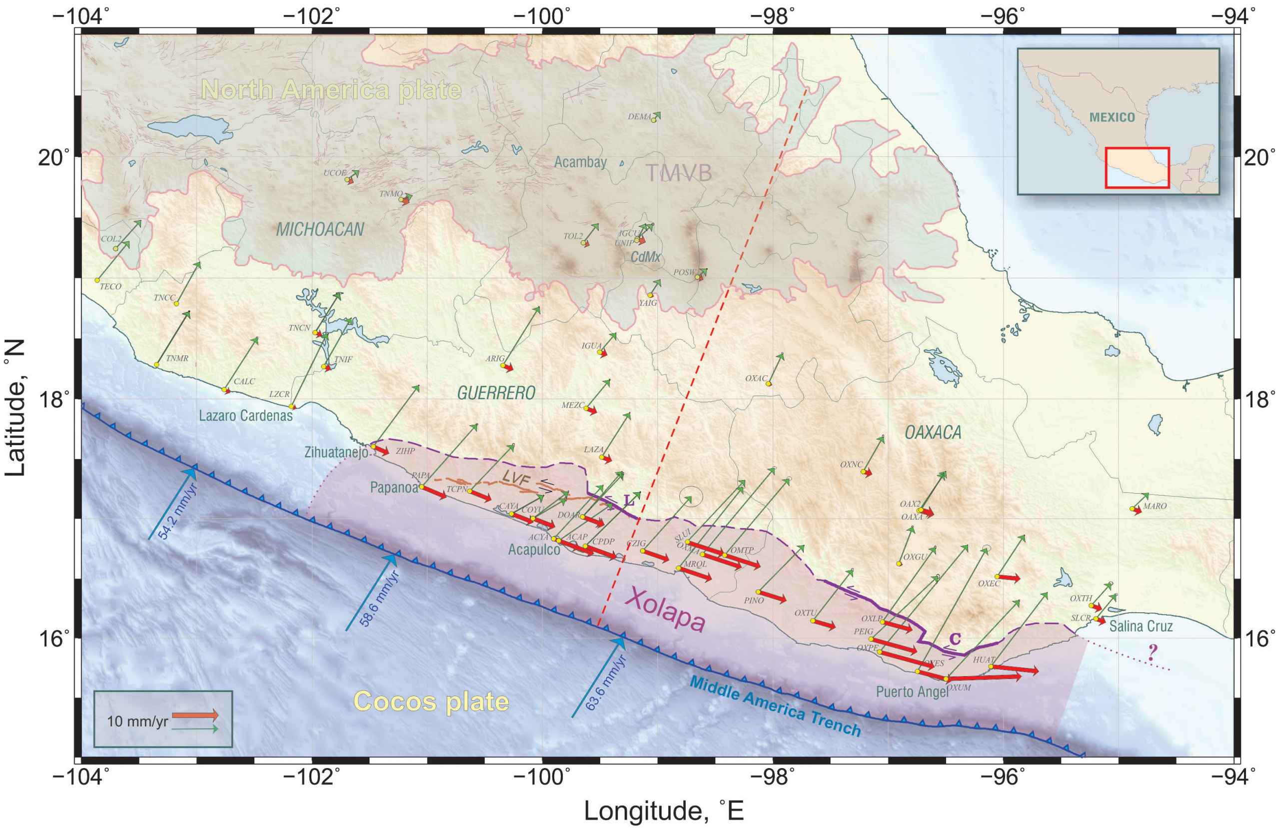

FIGURE 1 | The study area (Inset) and location of permanent GPS stations (small yellow circles). Secular GPS velocities (wrt North America plate, mm/year) are shown as green vectors, and red vectors are their oblique components (parallel to the MAT). The solid-dashed purple line delineates the La Venta–Chacalapa (LVC) fault zone according to Tolson (2005). *L*, La Venta segment (Solari et al., 2007). *C*, Chacalapa segment (Tolson, 2005). The segmented dark brown line is a trace of the LVF according to Gaidzik et al. (2016). An abrupt decrease of the secular oblique velocity is noticeable across the LVC fault zone (Ramírez-Herrera et al., 2018), which is roughly the northern border of the Xolapa allochthonous terraine (XOLAPA, shaded area located between the MAT and the LVC). Blue vectors are the Cocos–North America PVEL convergence velocities (DeMets et al., 2010) at the MAT. The red dashed line normal to the MAT specifies the horizontal axis of a cross-section shown in **Figures 2**, **3**. The gray shaded region to the north of 19°N shows the Trans Mexican Volcanic Belt (TMVB) with a dense E–W extended fault cluster [adapted from Ferrari et al. (2012)]. The fault sequence mapped close to the Acambay area is the northern margin of the sliver proposed by Ego and Ansan (2002).

the strain rate in Guerrero suddenly changes roughly from −93 to −4 nrad/year at approximately 100–120 km inland from the MAT, which is an average location of the LVC shear zone. At the same distance, the Vss diminishes by 2–5 mm/year in Guerrero and by more than 6 mm/year in Oaxaca. These velocity slumps may represent a partitioning of the oblique convergence between the Cocos and North America plates with a sinistral motion (wrt NA) of the forearc Xolapa sliver. Abrupt fault-parallel velocity change as a function of fault-perpendicular distance is a usual attribute of major active strike-slip faults (e.g., Smith and Sandwell, 2006; Alchalbi et al., 2010; Smith-Konter et al., 2011; Jolivet et al., 2015); thus, our observations suggest that the LVC fault area is tectonically active, at least during the GPS epoch.

There are not enough GPS stations to reliably model the LVC fault properties along all of its extent (**Figure 1**). The only fairly acceptable GPS covered area is in Guerrero, where the ∼450-km-long cross-section could be roughly appraised using a simple screw dislocation model (Savage and Burford, 1973; Cohen, 1999) for the infinite vertical strike-slip fault (**Figure 5**). The modeled fits to the observed Vss data show strike-slip displacement on the surface produced by the creeping fault at the depth more than 10 km while its shallower section is locked. Of course, these models cannot constrain the fault coupling depth, but they highlight the slower strike-slip motion (∼3 mm/year) on the LVC fault zone within the Guerrero seismic gap compared to the adjacent areas (∼5 mm/year). This inconsistency may be related to the influence of periodic SSEs, which effectively reduce the long-term subduction plate interface coupling in the gap area (e.g., Radiguet et al., 2012).

Based on the variation of GPS sinistral secular velocities along the coast (**Figure 1**), the active LVC fault zone strikes off the Zihuatanejo city area, some ∼650 km eastward along the Pacific coast, and gets somewhere close to the Salina Cruz city on the land. A continuation of the LVC into the Guatemala basin

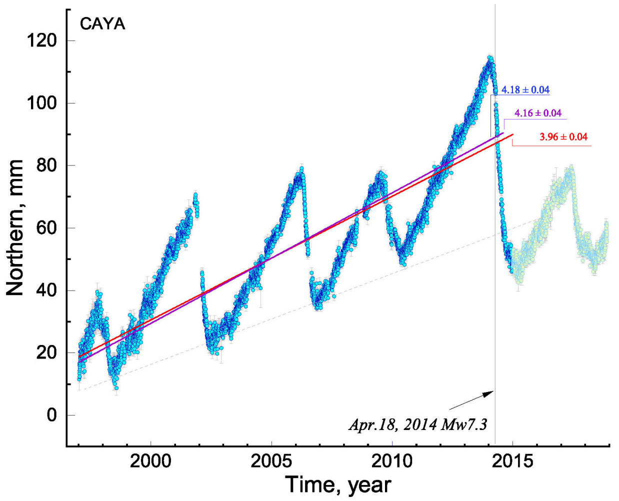

FIGURE 2 | Example of few linear fits to the CAYA northern time series. The resulting estimate of V_{SN} value depends on the selected time interval. To eliminate the impact of the Papanoa Mw 7.3 earthquake the fitting window closes just before the earthquakes starts.

remains problematic to trace as yet without detailed bathymetry and marine geophysics data.

Seismicity

Large historic strike-slip earthquakes are unknown in the continental crust along the entire length of the fault system. Only a few shallow and small magnitude earthquakes have probably occurred on it, according to the catalog of the National Seismological Service of Mexico (SSN). Just one well-documented normal type with a small strike-slip component, Mw 5.8, Coyuca earthquake, followed by numerous aftershocks, has been recorded on October 8, 2001 (Pacheco et al., 2002; Pacheco and Singh, 2010), on the reactivated sub-fault, south of the La Venta fault (LVF; **Figure 6**). This rare event occurred right after the large 2001 SSE that created a temporal extension of the forearc (Kostoglodov et al., 2003).

Seismic events hypocenters in the SSN catalog (1962–2015) do not have sufficient precision to make a definite conclusion on the LVC seismicity. **Supplementary Figure A2** shows only that the fault zone approximately coincides with the location where density of seismic events drops significantly to the north of the fault trace. The higher-precision catalog obtained from the local seismic network in the seismic gap of Guerrero [1.0 < Mc < 4.0, (Suárez et al., 1990)] may be used to examine the seismic activity of the LVC. Seismicity cross-sections perpendicular to the MAT show that this fault zone is mainly aseismic for the time span of the catalog (1987–1995; **Figure 6**). Very low seismicity on active faults needs to be explained. One of the plausible insights may be a the model of Lamb and Smith (2013), where the strike-slip fault is totally locked in the surface elastic layer during a long-lasting interseismic period and is thus behaving almost aseismically. This locked shallow patch of the fault produces a background secular linear surface strain trend of ∼4 nrad/year (see **Figure 4**). In the deeper part of the crust, beneath the locked fault zone, the fault is creeping on a narrow shear zone that produces an apparent near-fault geodetic signal, which depends on the maximum depth of the locked segment of the fault. This model may explain the total observed GPS surface displacements and a lack of seismicity on the LVC. Strain accumulation on the upper locked zone of the fault is relatively slow, ΔVss = 3–5 mm/year (**Figure 5**), which should lead to a long-lasting seismic cycle of the order of thousand years.

Recently reported local seismic swarms in the Oaxaca section of the LVC (Fasola et al., 2019) are apparently related to someway relocated fault. Still insufficient accuracy and precision of the local seismic catalog (Fasola et al., 2016) does not permit us to make a definitive conclusion on the seismic activity of the LVC.

LA VENTA–CHACALAPA FAULT TRACE MAPPING

The fault shape and its location are essential to analyze the stress pattern and appraise the elastic strain accumulation, which may finally be released seismically. The precise position of the LVC shear zone is unknown for most of its length. There are only two explored segments of this zone detected by geological studies, Chacalapa (Tolson, 2005) and La Venta (Solari et al., 2007)—C and L annotations accordingly in **Figure 1**. All published LVC fault configurations render a geologically depicted borderline of the Xolapa terrane (e.g., Cerca et al., 2007). Gaidzik et al. (2016), acquired and analyzed abundant structural field data in the western part of the Xolapa terrane (∼99°–101.3°W), and after a morphotectonic interpretation of 15-m resolution digital elevation model (DEM) and satellite images of the area, they could trace the superficial left-lateral strike-slip continuation of the La Venta fault zone (LVF in **Figure 1**). According to this study, the LVF is segmented with 4- to 8-km-wide compressional or extensional step-overs and its nearly E–W average trace crosses the coastline close to the town of Papanoa.

The westernmost segment of the fault is less well constrained. As the Zihuatanejo GPS (ZIHP in **Figure 1**) has a clear secular trench-parallel motion comparable to other GPS sites on the Xolapa sliver, we can assume that the active LVF extends up to that longitude of approximately −101.5°. An absence of GPS stations between LVF and LVC does not permit us to determine the northern limit of the Xolapa sliver, while the LVF trace is more reliable based on detailed study of Gaidzik et al. (2016). It is important to note that the Xolapa sliver is not identical to the geologically determined Xolapa complex (Ducea et al., 2004) or the same name terrain. The LVF location may be considered as a trace of active LVC fault system (Ramírez-Herrera et al., 2018) in western Guerrero mainly because the northern boundary of

TABLE 1 | Secular velocities of the GPS stations (V_{SE}, V_{SN}, east and north components accordingly, referenced to the fixed North America plate), and corresponding standard errors (σVs_E, σVs_N); trench parallel velocities (Vss) with standard errors (σVss) and azimuth of trench normal (ϑTn, clockwise from North); T1 and T2 are the start and end limits of the fitting time span, respectively.

Station (site)	Lon °E	Lat °N	V_{SE} mm/year	V_{SN} mm/year	σ V_{SE} mm/year	σ V_{SN} mm/year	V_{SS} mm/year	σ V_{SS} mm/year	ϑTn °cw from N	T1 Year	T2 Year
ACAP	−99.857	16.822	11.64	7.99	0.02	0.05	8.10	0.04	−20.51	1999.92	2013.08
ACYA	−99.903	16.838	10.72	11.58	0.03	0.06	5.96	0.04	−20.59	2004.12	2014.28
ANIG	−104.521	21.054	0.94	1.67	0.03	0.02	−0.79	0.03	−53.97	2006.84	2014.93
ARIG	−100.344	18.281	7.86	12.63	0.05	0.06	2.43	0.05	−22.49	2009.88	2014.21
AYUT	−99.145	16.988	0.37	12.54	0.13	0.12	−3.91	0.13	−19.45	2010.34	2013.68
CALC	−102.762	18.079	7.19	11.20	0.08	0.11	1.40	0.09	−26.66	2007.94	2013.65
CAYA	−100.267	17.049	6.98	3.91	0.02	0.04	5.08	0.03	−21.35	1997.09	2014.28
CHAM	−105.045	19.498	5.11	10.07	0.03	0.03	−3.75	0.03	−46.26	2006.83	2014.72
COL2	−103.702	19.244	5.50	6.14	0.02	0.02	0.61	0.02	−37.66	2006.87	2014.97
COMI	−92.137	16.282	3.04	3.53	0.01	0.02	0.87	0.02	−30.01	2002.12	2014.91
COYB	−100.081	17.008	7.11	4.17	0.09	0.20	5.14	0.16	−21.01	2008.18	2012.62
COYU	−100.081	17.008	7.67	5.78	0.03	0.10	5.09	0.07	−21.01	2003.29	2014.23
CPDP	−99.628	16.776	11.92	11.71	0.03	0.05	7.17	0.04	−20.10	2003.42	2014.25
CZIG	−99.131	16.736	10.53	11.78	1.05	0.92	6.06	0.99	−19.25	2009.87	2010.30
DEMA	−99.035	20.300	1.41	1.76	0.01	0.01	0.65	0.01	−22.02	2003.87	2014.95
DOAP	−99.651	17.021	8.84	9.35	0.06	0.11	5.04	0.09	−20.32	2004.41	2011.92
DOAR	−99.651	17.021	8.56	9.78	0.03	0.06	4.64	0.05	−20.32	2003.23	2013.43
HUAT	−96.108	15.769	12.23	16.03	0.01	0.01	10.53	0.01	−5.88	2000.57	2014.32
IGCU	−99.176	19.327	3.36	3.13	0.11	0.08	1.99	0.09	−21.38	2011.40	2014.31
IGUA	−99.502	18.392	3.52	4.11	0.02	0.03	1.80	0.03	−21.15	2000.43	2014.28
INEG	−102.284	21.856	1.30	2.33	0.01	0.02	−0.79	0.01	−46.45	2006.83	2014.94
LAZA	−99.487	17.519	6.11	9.60	0.04	0.04	2.38	0.04	−20.42	2006.71	2014.26
LZCR	−102.178	17.939	7.76	15.83	0.12	0.11	1.17	0.12	−22.32	2008.94	2011.37
MARO	−94.884	17.091	3.58	3.41	0.01	0.02	2.22	0.02	−19.74	2005.03	2014.97
MEZC	−99.620	17.925	5.09	6.14	0.04	0.07	2.55	0.06	−20.97	2005.04	2014.28
MRQL	−98.817	16.594	13.97	17.58	0.17	0.14	7.63	0.15	−18.62	2010.23	2012.19
OAX2	−96.717	17.078	4.96	7.89	0.04	0.05	2.70	0.04	−15.29	2006.85	2012.20
OAXA	−96.733	17.073	5.82	8.53	0.02	0.02	3.36	0.02	−15.32	2001.20	2012.18
OMTP	−98.419	16.700	14.01	16.59	0.20	0.18	8.19	0.19	−18.02	2009.83	2012.18
OXAC	−98.041	18.130	3.08	6.52	0.08	0.09	0.86	0.09	−18.37	2009.23	2012.19
OXEC	−96.055	16.520	5.93	9.02	0.04	0.04	5.05	0.04	−5.48	2009.01	2013.85
OXES	−96.746	15.727	15.03	26.74	0.37	0.29	7.82	0.35	−14.58	2009.12	2010.86
OXGU	−96.910	16.630	3.06	8.02	0.08	0.08	0.83	0.08	−15.37	2009.00	2013.85
OXLP	−97.051	16.142	11.49	16.19	0.09	0.12	6.80	0.10	−15.33	2009.13	2013.99
OXMA	−98.611	16.709	15.65	18.74	0.13	0.13	8.96	0.13	−18.35	2009.16	2011.75
OXNC	−97.218	17.400	4.34	7.60	0.08	0.13	2.02	0.09	−16.39	2009.11	2012.18
OXPE	−97.075	15.889	19.11	23.17	0.03	0.05	12.36	0.04	−15.23	2008.02	2014.25
OXTH	−95.239	16.281	4.27	4.77	0.18	0.15	2.50	0.16	−18.87	2009.00	2010.62
OXTU	−97.654	16.151	8.61	11.03	0.10	0.14	5.52	0.11	−16.37	2009.01	2013.86
OXUM	−96.499	15.662	15.90	17.02	0.06	0.08	16.45	0.07	1.90	2009.14	2013.99
PAPA	−101.047	17.273	11.98	13.53	0.08	0.06	5.81	0.07	−22.78	2010.14	2014.00
PEIG	−97.148	15.998	14.51	13.61	0.14	0.18	10.37	0.16	−15.42	2012.87	2015.00
PENA	−104.101	19.391	4.02	7.01	0.02	0.02	−1.54	0.02	−40.78	2007.12	2019.93
PINO	−98.127	16.393	9.94	10.10	0.02	0.03	6.48	0.03	−17.33	2000.53	2012.18
POPO	−98.628	19.067	−0.72	7.91	0.56	0.55	−0.72	0.56	−20.17	2013.51	2014.29
POSW	−98.657	19.010	2.07	1.79	0.05	0.05	1.32	0.05	−20.17	1997.01	2003.44
SABY	−91.187	18.967	1.43	1.63	0.02	0.02	0.31	0.02	−33.28	2004.54	2014.10
SLCR	−95.197	16.168	4.34	5.24	0.13	0.09	2.28	0.11	−20.13	2009.00	2012.91
SLUI	−98.741	16.811	13.55	14.41	0.21	0.12	8.39	0.18	−18.13	2009.84	2011.92

(Continued)

TABLE 1 | Continued

Station (site)	Lon °E	Lat °N	V_{SE} mm/year	V_{SN} mm/year	σV_{SE} mm/year	σV_{SN} mm/year	V_{SS} mm/year	σV_{SS} mm/year	ϑTn °cw from N	T1 Year	T2 Year
TAMP	−97.864	22.278	0.88	1.25	0.02	0.01	0.36	0.02	−21.70	2006.83	2014.27
TCPN	−100.631	17.234	9.53	10.01	0.10	0.16	5.07	0.13	−22.08	2009.32	2014.28
TECO	−103.861	18.985	6.94	8.47	0.01	0.01	0.39	0.01	−37.29	2007.17	2019.95
TNCC	−103.173	18.791	4.98	9.02	0.04	0.03	−0.59	0.04	−32.15	2015.82	2019.98
TNCN	−101.971	18.554	5.31	8.52	0.32	0.06	1.58	0.27	−22.87	2016.18	2019.95
TNIF	−101.896	18.272	5.91	10.46	0.04	0.03	1.68	0.04	−21.40	2015.80	2019.99
TNMO	−101.228	19.649	2.43	0.83	0.02	0.02	1.98	0.02	−25.26	2008.48	2019.96
TNMR	−103.346	18.289	7.06	11.51	0.05	0.05	0.10	0.05	−31.09	2014.71	2018.72
TNMZ	−104.402	19.124	7.94	10.56	0.07	0.07	−0.94	0.07	−41.00	2015.49	2018.24
TOL2	−99.644	19.293	3.20	4.14	0.02	0.02	1.40	0.02	−22.18	2006.86	2014.23
UCOE	−101.694	19.813	2.57	1.88	0.01	0.01	1.50	0.01	−26.21	2005.81	2019.94
UNIP	−99.181	19.313	1.90	3.57	0.02	0.02	0.47	0.02	−21.38	2005.95	2013.77
YAIG	−99.067	18.862	2.18	3.35	0.02	0.02	0.85	0.02	−20.78	1999.82	2014.19
ZIHP	−101.465	17.607	9.86	13.26	0.03	0.04	3.69	0.03	−23.73	2000.53	2014.22

Position time series for the sites in italic are from the TLALOCNET network (https://www.unavco.org/instrumentation/networks/status/tlalocnet).

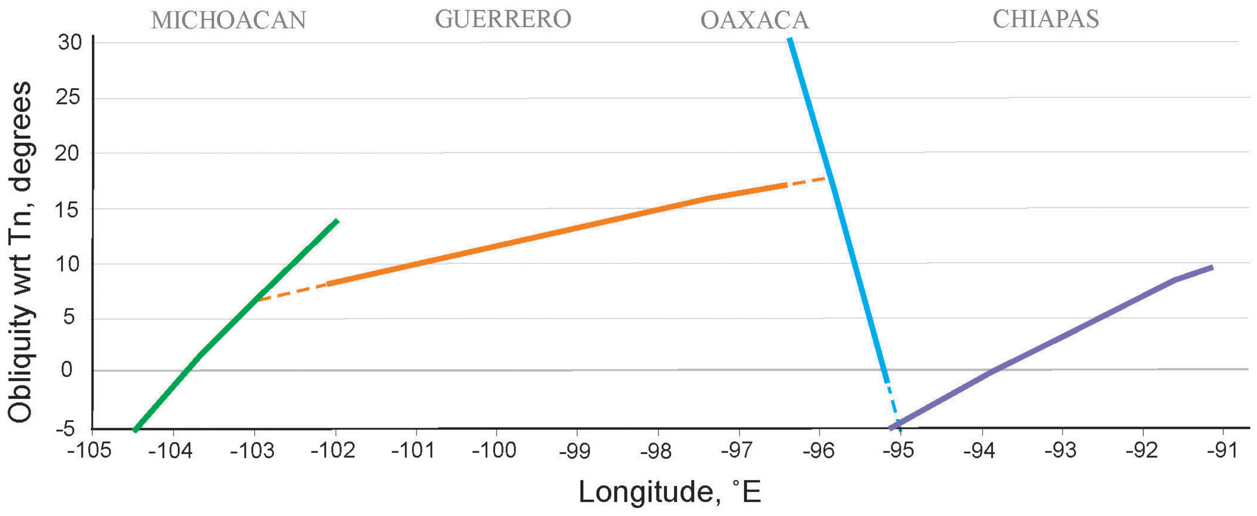

FIGURE 3 | Variation of obliquity angle along the Mexican fragment of the Middle America Trench. The obliquity is relatively higher in the Guerrero–Oaxaca segment of the MAT and low or negative in Michoacan and Chiapas.

the Xolapa complex has no clear expression on the landscape (Gaidzik et al., 2016). Part of the LVF (Gaidzik et al., 2016) appears to coincide with the geologically defined Eocene–Oligocene LVC shear zone (Riller et al., 1992; Tolson, 2005; Solari et al., 2007).

Nevertheless, GPS estimates show that the westernmost section of the LVC should extend up to the Zihuatanejo city area where the Xolapa sliver is stretching from the NA plate. Thus, some of the LVF segments possibly are subfaults of the LVC fault system (Ramírez-Herrera et al., 2018). Therefore, the principal conclusions of Gaidzik et al. (2016) study concerning the age of the LVF, its seismic activity, stress regime, and reactivation would be valid similarly for the LVC (Ramírez-Herrera et al., 2018).

The trace of the tectonically active eastern part of the LVC fault zone needs to be investigated using the same methodology as in Gaidzik et al. (2016) together with high resolution GPS and local seismological studies. Until now there is only geologically defined trace of the LVC shear zone (Ramírez-Herrera et al., 2018), which is poorly confirmed by any reliable observations, particularly in Oaxaca region (between −99.0 and −97°E; dashed line in **Figure 1**). Just a few GPS stations landward from and close to the LVC zone are not enough to estimate the active fault zone location. For that reason, the geological LVC trace is the only one that can tentatively be used as a reference for the active LVC in Oaxaca. Analyzing secular trench-parallel velocities, V_{SS}, of the easternmost GPS stations (OXUM, HUAT, SLCR, OZTH, and MARO; **Figure 1**) we conclude that the

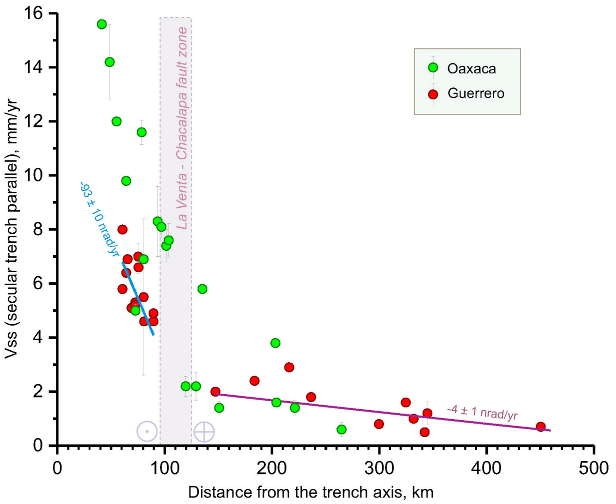

FIGURE 4 | Distribution of trench-parallel component of GPS secular velocity (V_{SS}) along the profile perpendicular to the MAT (**Figure 1**, red vectors amplitudes projected on the profile shown by the red dashed line). Red circles correspond to the GPS stations in the Guerrero state and green circles to those in the Oaxaca state. Blue line annotated with the strain rate estimate is a best fit to the V_{SS} measurements for the Xolapa sliver (south of the LVC fault zone) in Guerrero, while the magenta line is the best fit to the V_{SS} data north of the LVC. Sharp change in the strain rate across the LVC is evident as well as an abrupt drop of V_{SS} by 3–5 mm/year in Guerrero and by more than 6 mm/year in Oaxaca. Thus, the LVC fault zone is active at least during the epoch of GPS observations. Light gray band shows roughly the LVF zone.

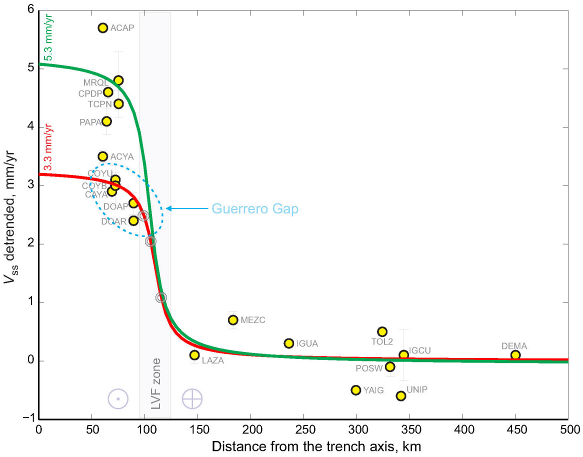

FIGURE 5 | Screw dislocation models in elastic half space for a vertical strike slip fault (Savage and Burford, 1973) in the LVC zone. The models show strike-slip displacement on the surface produced by the creeping fault at the depth more than 10 km. The fault is locked from 0 to 10 km. Yellow circles are detrended trench parallel rates (*V*ss, wrt NA fixed plate) at the permanent GPS stations (see **Figure 1**), Δ*V*ss, (after the secular linear strain trend is subtracted from the *V*ss). The trend north from the LVF fault zone is produced by the simple shear in the upper 10 km of the locked fault segment. Red line is a feasible fit for the *V*ss in the area of the Guerrero seismic gap (G-GAP, ∼100–101°W) for the Xolapa sliver velocity, Δ*V*ss, of 3.3 mm/year. Green line is the fit for *V*ss values for the Guerrero GPS stations located off the G-GAP, and Δ*V*ss = 5.3 mm/year. Light gray band indicates the LVF zone. Error bars are 3σ. Gray open circles show only locations of three GPS stations recently installed in the LVF zone to constrain better the fault model.

active LVC fault zone (Ramírez-Herrera et al., 2018) should cross the shoreline somewhere between Huatulco (HUAT) and Salina Cruz cities. Tectonic implication of this observation is considered later.

XOLAPA SLIVER

Azimuthal angle differences (slip partitioning) between slip vectors of subduction thrust earthquakes and the direction normal to the trench allow assessing the partial decoupling of the seismogenic plate interface and the rigid forearc sliver rate in oblique convergence margins (McCaffrey, 1992; Haq and Davis, 2010). Ego and Ansan (2002) thoroughly selected shallow thrust earthquakes on the subduction interface of Southern Mexico from the Harvard centroid moment tensor (CMT, 1977–2001, Mw ≥ 5.3) catalog. They analyzed 31 slip vector angles for the area between 96°W and 105°W, the subduction zone segment, which includes both partially the LVC fault zone (Ramírez-Herrera et al., 2018) and the area outside of it. For the Guerrero area, between 102°W and 96°W along the MAT, they observed a significant slip partitioning up to 10° and estimated an average sliver rate of $V_{sl} = 8 \pm 3$ mm/year. This inference is slightly higher but roughly consistent with our direct GPS observations of V_{SS}.

Using similar selection criteria for the CMT events as of Ego and Ansan (2002), we have compiled a more ample catalog of the CMTs from 1976 up to 2018, which contains 89 shallow thrust events that corresponded only to the LVC longitudinal extent (-95.5 and −101.5°E, see **Supplementary Table A2** for other criteria). Analyzing this CMT data subset, the average estimate of $V_{sl} \approx 5.4$–6.3 mm/year (see **Supplementary Figure A3**), which is closer to the V_{SS} values obtained with the GPS. The large dispersion of CMT slip vector angles is apparently related to uncertainties in the CMT catalog, complicated structures of the LVC fault system (Ramírez-Herrera et al., 2018) and the Xolapa sliver, inhomogeneous Co-NA plate interface, variation of the plate coupling (e.g., Kostoglodov and Ponce, 1994), and more complicated than just a simple friction rheology of the fault (Kazachkina et al., 2019). Furthermore, observed dispersion is partially related to the increase of the Co-NA convergence velocity southeastward along the MAT. Obviously, McCaffrey's model is too simple to allow for all these factors. Nevertheless, it provides some useful appraisals of sliver motion rate and average static friction coefficient on the fault (Haq and Davis, 2010), which in case of the LVC should be $\mu \leq 0.15$ (**Supplementary Figure A4**). For many crustal faults $\mu < 0.3$ (e.g., Behr and Platt, 2014; Middleton and Copley, 2014).

TECTONIC IMPLICATIONS

As the Xolapa sliver, in reality, is not a rigid block, it should undergo some internal deformation that depends on

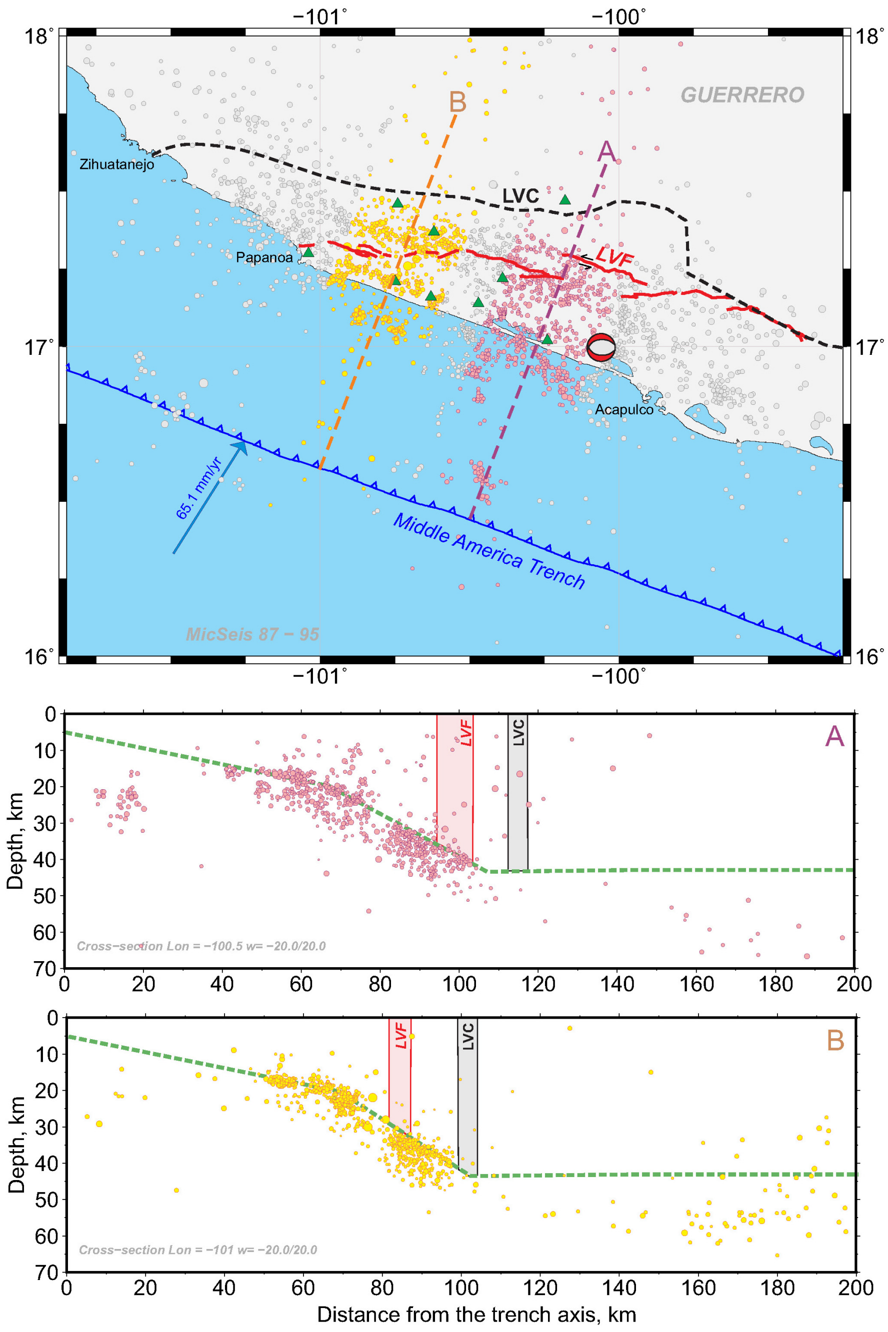

FIGURE 6 | Top map: seismicity in the Guerrero seismic gap area from the local network catalog [1987–1995, 1.0 < Mc < 4.0, (Suárez et al., 1990)]. Green triangles are locations of short period seismometers of the network. LVC, black dashed line shows location of the La Venta–Chacalapa fault zone from geological studies (Tolson, 2005; Solari et al., 2007). Red lines denote a trace of the La Venta fault, LVF, according to Gaidzik et al. (2016). Dashed lines A and B perpendicular to the trench mark two profiles on which the seismic events from the catalog were projected. The events in each cross-section, yellow and magenta on the map, are from the bands of 40-km-wide, centered along the profiles. Red-white focal mechanism shows a location of the October 8, 2001 Coyuca, Mw 5.8, Earthquake (Pacheco and Singh, 2010). A: seismicity cross-section along the profile A (magenta line and events on the map). Pink trapezoid shows roughly a projection of the LVF zone assuming that the fault is vertical. Gray rectangle is a projection of the LVC fault zone assuming that the fault is vertical. Green dashed line is an approximation of the plate interface. B: seismicity cross-section along the profile B (yellow line and seismic events on the map). Other notations are the same as for the cross-section A.

the convergence rate and the interplate coupling, which are changing along its extent. The systematic increase of the subduction velocity in the southeastern direction should result in general extension of the sliver. However, the plate coupling modulates the strain, and this results in some variation of the secular trench-parallel velocity, V_{SS}, for example in the

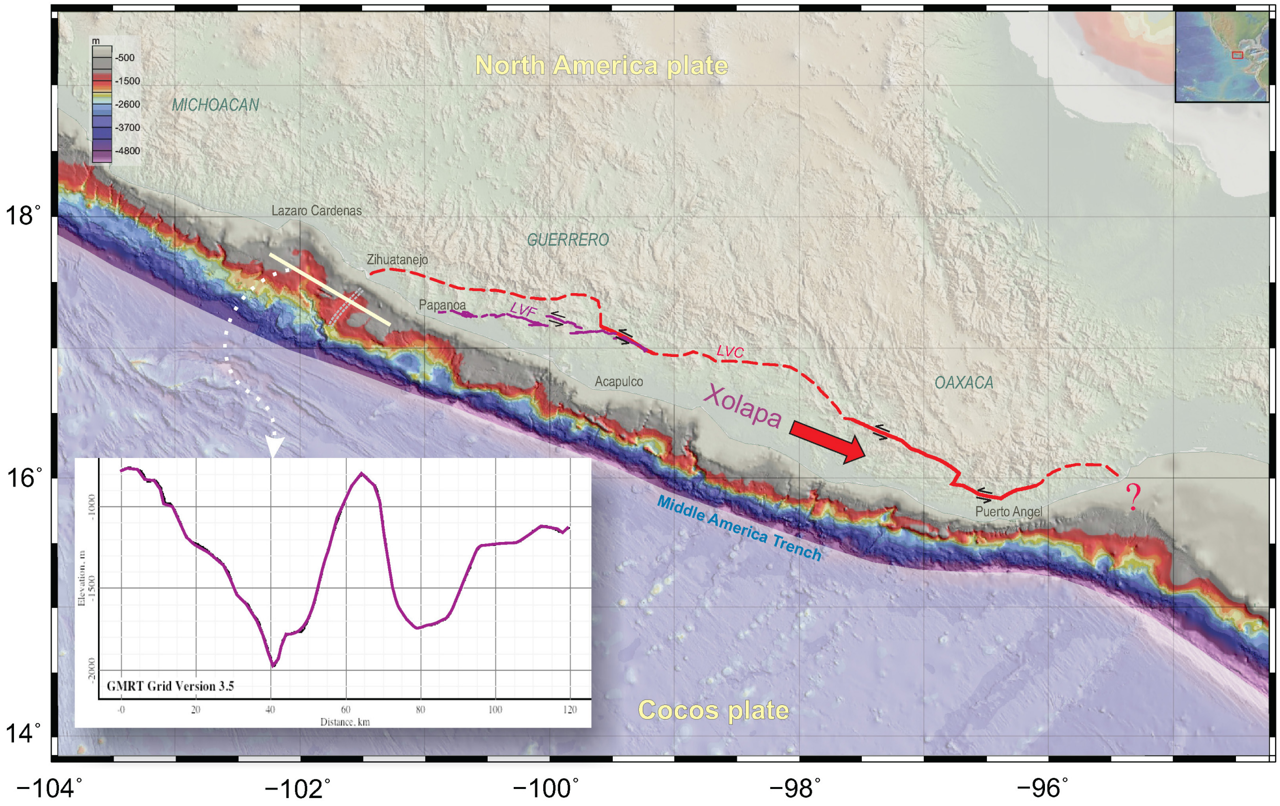

FIGURE 7 | Topographic and bathymetry map [The Global Multi-Resolution Topography synthesis, GMRT (Ryan et al., 2009)], exposing a continental margin in Southern Mexico. The 750–1,600 m depth range is in red. A bathymetric profile at ~1,500 m from Lazaro Cardenas city to Papanoa is shown in the bottom inlet. Two prominent depressions have a total average width of ~40 km (at 1,500 km depth). The red arrow indicates the Xolapa sliver southeast motion. Local concave shape of the continental margin is seen in the area of the Tehuantepec ridge. The red line is a trace of the LVC fault system (Tolson, 2005). Magenta lines in the coastal area show the LVF fault discovered by Gaidzik et al. (2016).

area of Guerrero seismic gap, between −101° and −100° of longitude (**Figure 1**).

Northwestern End of the Xolapa Sliver

In western Guerrero, an expected transtensional offshore continuation of the LVF on the continental slope is not so clear because of a lack of detailed bathymetric data. Low-resolution bathymetry offshore of Papanoa and Zihuatanejo [The Global Multi-Resolution Topography synthesis, GMRT (Ryan et al., 2009)] shows only two wide depressions on the continental slope that can be interpreted as an extension produced by the trailing edge of the Xolapa sliver moving southeastward (**Figure 7**). The total stretching of the continental margin estimated from the trench parallel bathymetric profile presented in **Figure 7** is of the order of 40 km (referenced to the depth of 1,500 m). Southeastern displacement of the Xolapa sliver leading edge is expected to be of a similar distance, assuming that the sliver was rigid. The Cocos–North America spreading rate was almost invariable since at least the Late Miocene (Cande and Kent, 1992; Conrad and Lithgow-Bertelloni, 2007) and if the average mobility of the sliver was unchanging (~5 mm/year), the reactivation of the LVC fault system (Ramírez-Herrera et al., 2018) could have occurred some ~8–10 million year ago after the reorganization of spreading from the failing Mathematician ridge to the new propagating East Pacific Rise (Klitgord and Mammerickx, 1982; Mammerickx et al., 1988).

Mexico–Guatemala Triple Junction and Eastern Extent of the Xolapa Sliver

While the geologic and tectonic history of the Xolapa terrain is still under discussion (e.g., Cerca et al., 2007; Moran-Zenteno et al., 2009; Talavera-Mendoza et al., 2013; Peña-Alonso et al., 2018), the earlier sinistral motion on the LVC fault system is recognized to occur in Early Eocene–Oligocene (50–25 Ma) (Tolson, 2005; Solari et al., 2007). Since then, it is unknown how long has been the LVC active and what the tectonic consequences are of the Xolapa sliver motion. The models of the Xolapa tectonic evolution are usually related to the translation of the Chortis block from its initial position, possibly bordering the Xolapa from the south (Schaaf et al., 1995), to its present location along the Polochic-Motagua fault system in Guatemala and Honduras (e.g., Ortega-Gutiérrez et al., 2007; Rogers et al., 2007). Regardless of the tectonic and geologic

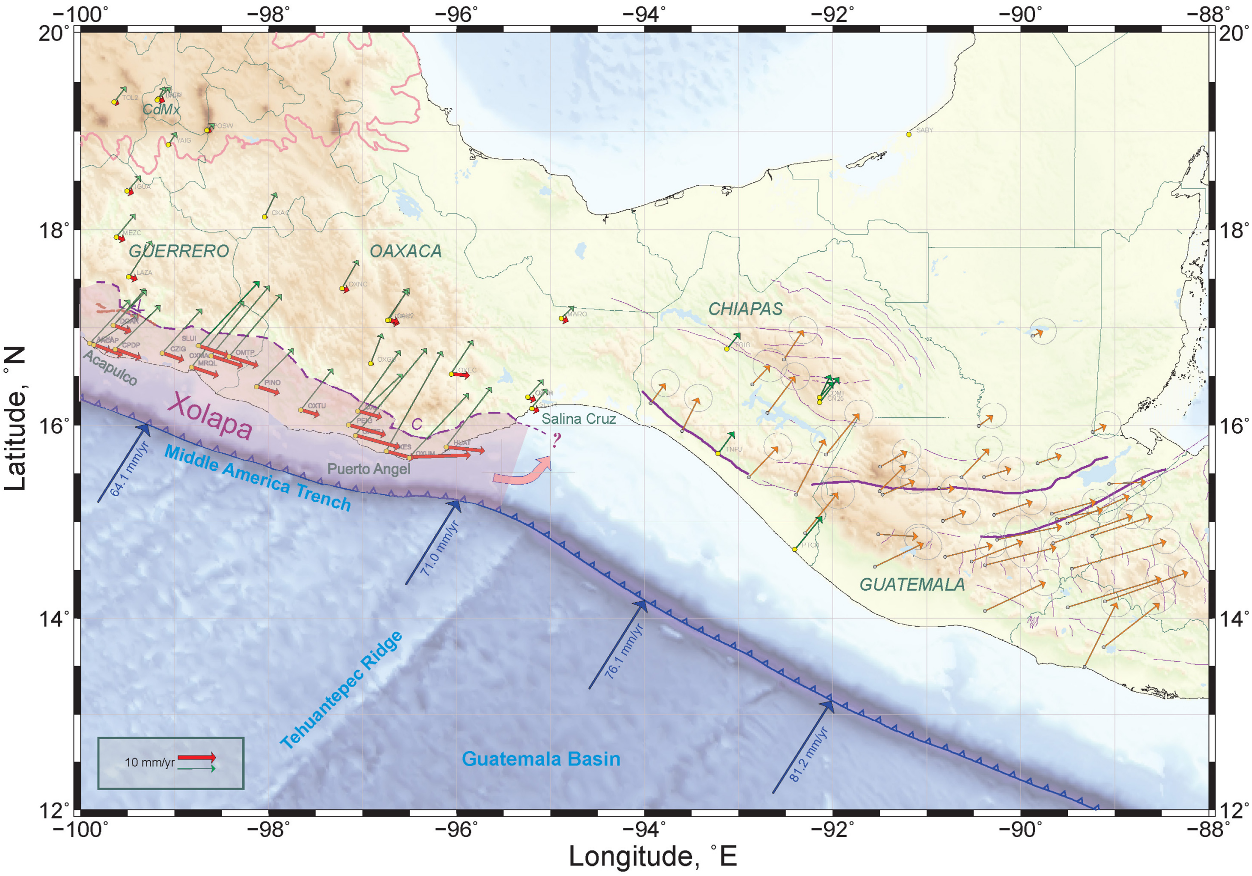

FIGURE 8 | A map of southern Mexico that illustrates models of LVC sliver progression in the Guatemala basin. There is no obliquity in the Cocos–North America convergence offshore of the Chiapas segment of the MAT (-95.0 to −92.0°E). That causes an absence of a driving force for the sliver at a distance of more than 300 km along the MAT. Pink curved arrow indicates probable northward bending of the Xolapa sliver. Orange GPS vectors in Chiapas and Guatemala are from Ellis et al. (2018). Other captions are the same as in **Figure 1**.

history of the Xolapa terrain, the present-day activity of the LVC fault system (Ramírez-Herrera et al., 2018) and the Xolapa sliver motion should be relevant to the seismotectonic situation in southern Mexico.

The next question, related to the challenging problem of the North America–Cocos–Caribbean tectonic plates triple junction, is how do the LVC (Ramírez-Herrera et al., 2018) and the Xolapa sliver continue to the continental margin of Chiapas. Lack of detailed bathymetry and marine geophysics data in this area leaves any hypothesis on the matter to be tentative. Thick accumulated sediments (e.g., Straume et al., 2019) entirely hide the tectonic structure on a wide continental margin. The Xolapa sliver movement into this area cannot stop abruptly. Still, it may lead to a deformation of the sliver body, or the sliver continues its trajectory along the trench. In the latter case, a left-lateral continuation of the LVC sub-parallel to the trench fault would exist on the continental margin of Chiapas (**Figure 8**). Further speculating, this fault may be lined up with the Polochic-Motagua fault system. Obviously, there are two main observations that would contradict this hypothesis: First, there is no obliquity in the Cocos-North America convergence offshore of the Chiapas segment of the MAT (-95.0 to −92.0°E). That causes an absence of a driving force for the sliver at a distance of more than 300 km along the trench. Second, the Central America forearc sliver (DeMets, 2001) southeastward motion in the NA reference frame starts only at −92°E, as it is seen at GPS stations (**Figure 8**; Franco et al., 2012; Ellis et al., 2018).

Bearing in mind the inconsistencies of the previous hypothesis, another model of the Xolapa sliver leading-edge progression may be that it is bending northeastward in the area of Tehuantepec ridge subduction. This bending may be accompanied by fracturing, which depends on the force moment loading rate (the function of coupling, etc.) and the mechanical properties of the sliver. This scenario is probably more reliable, but it requires the existence of a system of faults limiting the sliver on the continental margin of Chiapas. Scarce seismologic data (Roman-Reinoso, 2004) in this region indicate only that this concept may be valid. In **Figure 9**, we demonstrate several faults (the area location is on **Figure 9**) and just a few rare CMT solutions of the strike-slip type in the crust forearc of Chiapas, which may be interpreted as consequences of the Xolapa sliver northeastern bending and fracturing. Unfortunately, the last

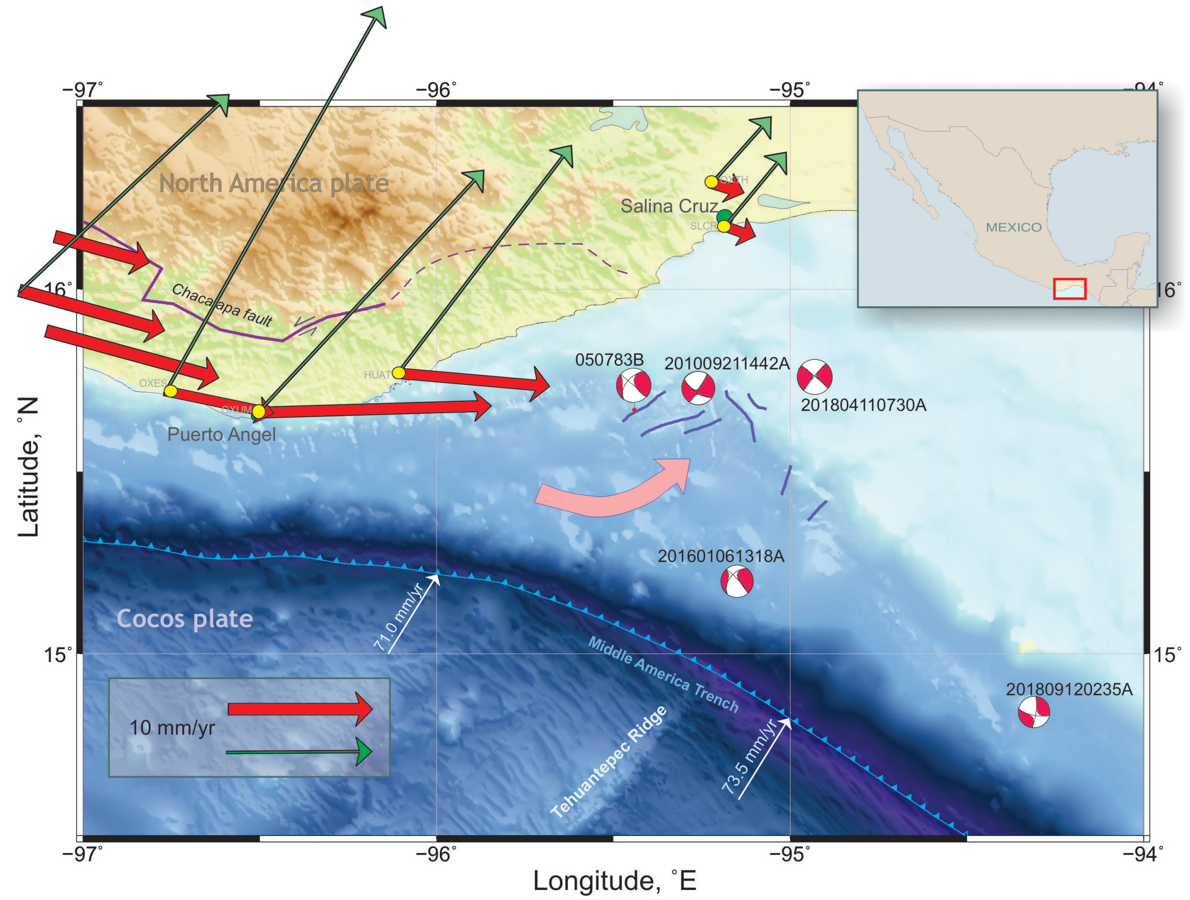

FIGURE 9 | Detailed map of the subduction zone in the region of the Tehuantepec ridge. The inset shows a location of this area. Red vectors are secular sinistral GPS velocities (the same as in **Figure 8**). The only crustal strike-slip events in the Global CMT catalog are shown as red beach balls with their catalog codes. Blue lines offshore, south of Salina Cruz city are conceivably active faults (Roman-Reinoso, 2004).

hypothesis leaves the triple junction problem still unresolved until more marine geophysics data would be available.

CONCLUSION

Long-lasting GPS observations and geomorphology studies in the Guerrero–Oaxaca area of the Mexican subduction zone show that, despite the almost complete absence of historic and instrumentally recorded seismicity in the western LVC fault zone, this mainly left-lateral shear zone is a complex and active system of numerous distributed strike-slip faults that accommodates strain partitioning produced by oblique subduction of the CO. The average velocity of the sinistral motion of the Xolapa sliver predicted from the slip vectors of subduction thrust earthquakes (∼5.4–6.3 mm/year) is consistent with the direct GPS observed trench parallel velocity component across the LVC fault (5–6 mm/year in Guerrero). As the result of the present study, we should admit that the LVC fault system is the principal active tectonic feature in Southern Mexico, which must be considered as a source of potential seismic hazard.

It is not known so far for how long time was the LVC fault zone active and what is a cumulative offset across the LVC fault zone in time. Existing GPS records only are not enough to constitute a previously unrecognized hazard in Southern Mexico related to the active LVC fault system. We need to obtain quantitative constraints on the age of the LVC faulting at least for the last few thousand years. Accurate trace and structure of the LVC was not yet explored except perhaps its western Guerrero segment (Gaidzik et al., 2016). The motion of the Xolapa sliver in Oaxaca remains rather hypothetic until more data would be available on new GPS stations installed inland from the LVC zone. Apart of the more precise location of the LVC fault and its coupling structure modeling, future investigations will also focus on a possible relationship between large subduction thrust SSE and displacements on the LVC fault zone.

The Xolapa sliver is not a rigid block and should undergo different internal deformations, which depend on subduction rate, coupling, and changes in the friction along the 650-km length of the LVC. The leading edge of the LVC in the Guatemala basin is still undefined. It is apparently not related to the triple junction, but a contortion of the Xolapa sliver in the area of the Tehuantepec ridge is probably a key to make this problem clearer.

DATA AVAILABILITY STATEMENT

All datasets generated for this study are included in the article/**Supplementary Material**.

AUTHOR CONTRIBUTIONS

EK carried out the main part of the study and wrote the manuscript. VK developed the main idea and wrote the manuscript. NC and AW participated in GPS data processing and analysis. MR-H and KG contributed to geomorphological interpretations. AH participated in project discussion and manuscript writing. JS managed the GPS network and provided the most of raw data used in this study.

FUNDING

This research was supported by the UNAM PAPIIT IN109117, IN110514, and IN110519, CONACYT 178058, 284212, and 284365 grants.

ACKNOWLEDGMENTS

Some of the GPS and seismological data are from the National Seismological Service of Mexico (SSN, http://www.ssn.unam.mx/). The GPS data for the Oaxaca region were partly provided by Enrique Cabral Cano. Several GPS position time series for the Michoacan and Colima states of Mexico are in free access from the UNAVCO web site (https://www.unavco.org/instrumentation/networks/status/tlalocnet). We thank Victor Cruz Atienza and Michel Campillo for helpful discussions. Several figures were generated with the Generic Mapping Tools (GMT) software (Wessel and Smith, 1998). We thank Jorge Real Perez and Juan Payero for their efforts in collecting the data and maintenance of the Guerrero GPS network in very complicated field conditions of Southern Mexico.

SUPPLEMENTARY MATERIAL

The Supplementary Material for this article can be found online at: https://www.frontiersin.org/articles/10.3389/feart.2020.00155/full#supplementary-material

REFERENCES

Alchalbi, A., Daoud, M., Gomez, F., Mcclusky, S., Reilinger, R., Romeyeh, M. A., et al. (2010). Crustal deformation in northwestern Arabia from GPS measurements in Syria: slow slip rate along the northern Dead Sea Fault. *Geophys. J. Int.* 180, 125–135. doi: 10.1111/j.1365-246X.2009.04431.x

Altamimi, Z., Collilieux, X., and Métivier, L. (2011). ITRF2008: an improved solution of the international terrestrial reference frame. *J. Geodesy* 85, 457–473. doi: 10.1007/s00190-011-0444-4

Andreani, L., Le Pichon, X., Rangin, C., and Martinez-Reyes, J. (2008). The southern Mexico block: main boundaries and new estimation for its Quaternary motion. *Bull. Soc. Geol. France* 179, 209–223. doi: 10.2113/gssgfbull.179.2.209

Behr, W. M., and Platt, J. P. (2014). Brittle faults are weak, yet the ductile middle crust is strong: implications for lithospheric mechanics. *Geophys. Res. Lett.* 41, 8067–8075. doi: 10.1002/2014GL061349

Blewitt, G., and Lavallée, D. (2002). Effect of annual signals on geodetic velocity. *J. Geophys. Res. Solid Earth* 107, 9–11. doi: 10.1029/2001JB000570

Campa, M. F., and Coney, P. J. (1983). Tectono-stratigraphic terranes and mineral resource distributions in Mexico. *Can. J. Earth Sci.* 20, 1040–1051. doi: 10.1139/e83-094

Cande, S. C., and Kent, D. V. (1992). A new geomagnetic polarity time scale for the Late Cretaceous and Cenozoic. *J. Geophys. Res. Solid Earth* 97, 13917–13951. doi: 10.1029/92JB01202

Cerca, M., Ferrari, L., Lopez-Martinez, M., Martiny, B., and Iriondo, A. (2007). Late Cretaceous shortening and early Tertiary shearing in the central Sierra Madre del Sur, southern Mexico: insights into the evolution of the Caribbean-North American plate interaction. *Tectonics* 26:TC3007. doi: 10.1029/2006tc001981

Cohen, S. C. (1999). "Numerical models of crustal deformation in seismic zones," in *Advances in Geophysics*, eds D. Renata and S. Barry (Elsevier), 133–231. doi: 10.1016/s0065-2687(08)60027-8

Conrad, C. P., and Lithgow-Bertelloni, C. (2007). Faster seafloor spreading and lithosphere production during the mid-Cenozoic. *Geology* 35, 29–32. doi: 10.1130/g22759a.1

Cotte, N., Walpersdorf, A., Kostoglodov, V., Vergnolle, M., Santiago, J.-A., Manighetti, I., et al. (2009). Anticipating the next large silent earthquake in Mexico. *Eos Trans. AGU* 90, 181–182. doi: 10.1029/2009EO210002

DeMets, C. (2001). A new estimate for present-day cocos-caribbean plate motion: implications for slip along the Central American Volcanic Arc. *Geophys. Res. Lett.* 28, 4043–4046. doi: 10.1029/2001gl013518

DeMets, C., Gordon, R. G., and Argus, D. F. (2010). Geologically current plate motions. *Geophys. J. Int.* 181, 1–80. doi: 10.1111/j.1365-246X.2009.04491.x

Ducea, M. N., Gehrels, G. E., Shoemaker, S., Ruiz, J., and Valencia, V. A. (2004). Geologic evolution of the Xolapa complex, southern Mexico: evidence from U-Pb zircon geochronology. *GSA Bull.* 116, 1016–1025. doi: 10.1130/B25467.1

Ego, F., and Ansan, V. (2002). Why is the central trans-mexican volcanic belt (102o-ì99oW) in transtensive deformation? *Tectonophysics* 359, 189–208. doi: 10.1016/s0040-1951(02)00511-5

Ellis, A., Demets, C., Briole, P., Cosenza, B., Flores, O., Graham, S. E., et al. (2018). GPS constraints on deformation in northern Central America from 1999 to 2017, Part 1 – Time-dependent modelling of large regional earthquakes and their post-seismic effects. *Geophys. J. Int.* 214, 2177–2194. doi: 10.1093/gji/ggy249

Fasola, S., Brudzinski, M. R., Ghouse, N., Solada, K., Sit, S., Cabral-Cano, E., et al. (2016). New perspective on the transition from flat to steeper subduction in Oaxaca, Mexico, based on seismicity, nonvolcanic tremor, and slow slip. *J. Geophys. Res. Solid Earth* 121, 1835–1848. doi: 10.1002/2015JB012709

Fasola, S. L., Brudzinski, M. R., Holtkamp, S. G., Graham, S. E., and Cabral-Cano, E. (2019). Earthquake swarms and slow slip on a sliver fault in the Mexican subduction zone. *Proc. Natl. Acad. Sci.* 116, 7198–7206. doi: 10.1073/pnas.1814205116

Ferrari, L., Orozco-Esquivel, T., Manea, V., and Manea, M. (2012). The dynamic history of the Trans-Mexican Volcanic Belt and the Mexico subduction zone. *Tectonophysics* 522-523, 122–149. doi: 10.1016/j.tecto.2011.09.018

Franco, A., Lasserre, C., Lyon-Caen, H., Kostoglodov, V., Molina, E., Guzman-Speziale, M., et al. (2012). Fault kinematics in northern Central America and coupling along the subduction interface of the Cocos Plate, from GPS data in Chiapas (Mexico), Guatemala and El salvador. *Geophys. J. Int.* 189, 1223–1236. doi: 10.1111/j.1365-246X.2012.05390.x

Gaidzik, K., Ramírez-Herrera, M. T., and Kostoglodov, V. (2016). Active crustal faults in the forearc region, Guerrero Sector of the Mexican Subduction Zone. *Pure Appl. Geophys.* 173, 3419–3443. doi: 10.1007/s00024-015-1213-8

Graham, S., Demets, C., Cabral-Cano, E., Kostoglodov, V., Rousset, B., Walpersdorf, A., et al. (2016). Slow Slip History for the MEXICO Subduction Zone: 2005 Through 2011. *Pure Appl. Geophys.* 173, 3445–3465. doi: 10.1007/s00024-015-1211-x

Guzman-Speziale, M. (1995). Hypocentral cross-sections and arc-trench curvature. *Geofisica Int.* 34, 131–141.

Haq, S. S. B., and Davis, D. M. (2010). Mechanics of fore-arc slivers: insights from simple analog models. *Tectonics* 29:TC5015. doi: 10.1029/2009tc002583

Herring, T. A., King, R. W., and Mcclusky, S. C. (2015). *Introduction to GAMIT/GLOBK*. Cambridge, MA: Mass. Inst. of Technol.

Jolivet, R., Simons, M., Agram, P. S., Duputel, Z., and Shen, Z. K. (2015). Aseismic slip and seismogenic coupling along the central San Andreas Fault. *Geophys. Res. Lett.* 42, 297–306. doi: 10.1002/2014GL062222

Kazachkina, E., Kostoglodov, V., Husker, A., and Cotte, N. (2019). Activity of crustal faults and the Xolapa sliver motion in Guerrero–Oaxaca forearc of Mexico, from seismic data. *Earth Planet. Space* 71:104. doi: 10.1186/s40623-019-1084-9

Klitgord, K. D., and Mammerickx, J. (1982). Northern East Pacific Rise: magnetic anomaly and bathymetric framework. *J. Geophys. Res. Solid Earth* 87, 6725–6750. doi: 10.1029/JB087iB08p06725

Kostoglodov, V., and Ponce, L. (1994). Relationship between subduction and seismicity in the Mexican Part of the Middle America Trench. *J. Geophys. Res. Solid Earth* 99, 729–742. doi: 10.1029/93jb01556

Kostoglodov, V., Singh, S. K., Santiago, J. A., Franco, S. I., Larson, K. M., Lowry, A. R., et al. (2003). A large silent earthquake in the Guerrero seismic gap, Mexico. *Geophys. Res. Lett.* 30:GL017219. doi: 10.1029/2003gl017219

Lamb, S., and Smith, E. (2013). The nature of the plate interface and driving force of interseismic deformation in the New Zealand plate-boundary zone, revealed by the continuous GPS velocity field. *J. Geophys. Res. Solid Earth* 118, 3160–3189. doi: 10.1002/jgrb.50221

Mammerickx, J., Naar, D. F., and Tyce, R. L. (1988). The mathematician paleoplate. *J. Geophys. Res. Solid Earth* 93, 3025–3040. doi: 10.1029/JB093iB04p03025

McCaffrey, R. (1992). Oblique plate convergence, slip vectors, and forearc deformation. *J. Geophys. Res. Solid Earth* 97, 8905–8915. doi: 10.1029/92jb00483

Middleton, T. A., and Copley, A. (2014). Constraining fault friction by re-examining earthquake nodal plane dips. *Geophys. J. Int.* 196, 671–680. doi: 10.1093/gji/ggt427

Moran-Zenteno, D. J. K., Duncan, J., Martiny, B., and Gonzales-Torres, E. (2009). Reassessment of the Paleogene position of the Chortis block relative to southern Mexico: hierarchical ranking of data and features. *Rev. Mexicana Ciencias Geol.* 26, 177–188.

Ortega-Gutiérrez, F., Solari, L. A., Ortega-Obregón, C., Elías-Herrera, M., Martens, U., Morán-Icál, S., et al. (2007). The maya-chortís boundary: a tectonostratigraphic approach. *Int. Geol. Rev.* 49, 996–1024. doi: 10.2747/0020-6814.49.11.996

Pacheco, J. F., Iglesias, A., Singh, S. K., Gutierrez, C., Espitia, G., and Alcantara, L. (2002). The 8 October 2001 Coyuca, Guerrero, Mexico earthquake (Mw 5.9): a normal fault in an expected compressional environment. *Seismol. Res. Lett.* 73, 263–264.

Pacheco, J. F., and Singh, S. K. (2010). Seismicity and state of stress in Guerrero segment of the Mexican subduction zone. *J. Geophys. Res.* 115:B01303. doi: 10.1029/2009jb006453

Peña-Alonso, T. A., Molina-Garza, R. S., Villalobos-Escobar, G., Estrada-Carmona, J., Levresse, G., and Solari, L. (2018). The opening and closure of the Jurassic-Cretaceous Xolapa basin, southern Mexico. *J. South Am. Earth Sci.* 88, 599–620. doi: 10.1016/j.jsames.2018.10.003

Radiguet, M., Cotton, F., Vergnolle, M., Campillo, M., Walpersdorf, A., Cotte, N., et al. (2012). Slow slip events and strain accumulation in the Guerrero gap, Mexico. *J. Geophys. Res.* 117:B04305. doi: 10.1029/2011jb008801

Ramírez-Herrera, M. T., Gaidzik, K., Forman, S., Bürgmann, R., and Johnson, C. W. (2018). Relating long-term and short-term vertical deformation across of the foreac in the Central mexican subduction zone. *Geosphere* 14, 419–439. doi: 10.1130/GES01446.1

Riller, U., Ratschbacher, L., and Frisch, W. (1992). Left-lateral transtension along the Tierra Colorada deformation zone, northern margin of the Xolapa magmatic arc of southern Mexico. *J. S. Am. Earth Sci.* 5, 237–249. doi: 10.1016/0895-9811(92)90023-R

Rogers, R. D., Mann, P., and Emmet, P. A. (2007). "Tectonic terranes of the Chortis block based on integration of regional aeromagnetic and geologic data," in *Geologic and Tectonic Development of the Caribbean Plate Boundary in Northern Central America*, ed. P. Mann (Boulder: Geological Society of America).

Roman-Reinoso, S. J. (2004). *Procesamiento y Análisis Estratigrátigrafico de Perfiles de Reflexión Sísmica en el Talud Continental del Golfo de Tehuantepec*. BSc thesis, Universidad Nacional Atónoma de México, México.

Ryan, W. B. F., Carbotte, S. M., Coplan, J. O., O'hara, S., Melkonian, A., Arko, R., et al. (2009). Global Multi-Resolution Topography synthesis. *Geochem. Geophys. Geosyst.* 10:GC002332. doi: 10.1029/2008gc002332

Savage, J. C., and Burford, R. O. (1973). Geodetic determination of relative plate motion in central California. *J. Geophys. Res.* 78, 832–845. doi: 10.1029/JB078i005p00832

Schaaf, P., Morán-Zenteno, D., Hernández-Bernal, M. D. S., Solís-Pichardo, G., Tolson, G., and Köhler, H. (1995). Paleogene continental margin truncation in southwestern Mexico: Geochronological evidence. *Tectonics* 14, 1339–1350. doi: 10.1029/95TC01928

Smith, B. R., and Sandwell, D. T. (2006). A model of the earthquake cycle along the San Andreas Fault System for the past 1000 years. *J. Geophys. Res. Solid Earth* 111:B01405. doi: 10.1029/2005JB003703

Smith-Konter, B. R., Sandwell, D. T., and Shearer, P. (2011). Locking depths estimated from geodesy and seismology along the San Andreas Fault System: implications for seismic moment release. *J. Geophys. Res. Solid Earth* 116:B06401. doi: 10.1029/2010JB008117

Solari, L. A., De León, R. T., Hernández Pineda, G., Solé, J., Solís-Pichardo, G., and Hernández-Treviño, T. (2007). Tectonic significance of Cretaceous, Tertiary magmatic and structural evolution of the northern margin of the Xolapa Complex, Tierra Colorada area, southern Mexico. *Geol. Soc. Am. Bull.* 119, 1265–1279. doi: 10.1130/b26023.1

Straume, E. O., Gaina, C., Medvedev, S., Hochmuth, K., Gohl, K., Whittaker, J. M., et al. (2019). GlobSed: updated total sediment thickness in the World's Oceans. *Geochem. Geophys. Geosyst.* 20, 1756–1772. doi: 10.1029/2018gc008115

Suárez, G., Monfret, T., Wittlinger, G., and David, C. (1990). Geometry of subduction and depth of the seismogenic zone in the Guerrero gap, Mexico. *Nature* 345:336. doi: 10.1038/345336a0

Suter, M., Quintero, O., and Johnson, C. A. (1992). Active faults and state of stress in the central part of the Trans-Mexican Volcanic Belt, Mexico 1. The Venta de Bravo Fault. *J. Geophys. Res. Solid Earth* 97, 11983–11993. doi: 10.1029/91JB00428

Talavera-Mendoza, O., Ruiz, J., Corona-Chavez, P., Gehrels, G. E., Sarmiento-Villagrana, A., García-Díaz, J. L., et al. (2013). Origin and provenance of basement metasedimentary rocks from the Xolapa Complex: new constraints on the Chortis–southern Mexico connection. *Earth Planet. Sci. Lett.* 36, 188–199. doi: 10.1016/j.epsl.2013.03.021

Tolson, G. (2005). La falla Chacalapa en el sur de Oaxaca. *Boletín Soc. Geol. Mexic.* 57, 111–122. doi: 10.18268/bsgm2005v57n1a6

Unam_Seismology_Group (2013). Ometepec-Pinotepa Nacional, Mexico Earthquake of 20 March 2012 (Mw 7.5): a preliminary report. *Geofísica Int.* 52, 173–196. doi: 10.1016/S0016-7169(13)71471-5

Unam_Seismology_Group (2015). Papanoa, Mexico earthquake of 18 April 2014 (M w 7.3). *Geofísica Int.* 54, 363–386.

Vergnolle, M., Walpersdorf, A., Kostoglodov, V., Tregoning, P., Santiago, J. A., Cotte, N., et al. (2010). Slow slip events in Mexico revised from the processing of 11 year GPS observations. *J. Geophys. Res.* 115:B08403. doi: 10.1029/2009jb006852

Wessel, P., and Smith, W. H. F. (1998). New, improved version of generic mapping tools released. *EOS Trans. Am. Geophys. Union* 79, 579–579. doi: 10.1029/98EO00426 doi: 10.1029/98eo00426

Conflict of Interest: The authors declare that the research was conducted in the absence of any commercial or financial relationships that could be construed as a potential conflict of interest.

frontiers in Earth Science

HYPOTHESIS AND THEORY
published: 10 July 2020
doi: 10.3389/feart.2020.00244

Effects of Oceanic Crustal Thickness on Intermediate Depth Seismicity

Lara S. Wagner[1]*, Mark J. Caddick[2], Abhash Kumar[3], Susan L. Beck[4] and Maureen D. Long[5]

[1] Department of Terrestrial Magnetism, Carnegie Institution for Science, Washington, DC, United States, [2] Department of Geosciences, Virginia Polytechnic Institute and State University, Blacksburg, VA, United States, [3] Department of Geology and Environmental Science, University of Pittsburgh, Pittsburgh, PA, United States, [4] Department of Geosciences, University of Arizona, Tucson, AZ, United States, [5] Department of Geology and Geophysics, Yale University, New Haven, CT, United States

The occurrence of intermediate depth seismicity (70–300 km) is commonly attributed to the dehydration of hydrous phases within the downgoing oceanic plate. While some water is incorporated into the oceanic crust at formation, a significant amount of water is introduced into the plate immediately before subduction along outer-rise faults. These faults have been shown to extend to depths of over 30 km and can channel water to depths of 20 km or more beneath the seafloor. However, the amount of water introduced into the oceanic mantle lithosphere, and the role of that water in the formation of intermediate depth seismicity, has been the topic of ongoing research. Here we compile evidence from areas where the subducted oceanic crust is likely thicker than the penetration depth of water into the downgoing plate. These regions comprise aseismic plateaus and ridges (hot spot tracks) that can be compared directly to adjacent segments of the oceanic plate where oceanic crust of normal thickness is subducted. Regions with thick oceanic crust show little to no seismicity at intermediate depths, whereas adjacent regions with normal oceanic crust (∼6–8 km thick) have significant seismicity at similar depths and distances from the trench. We hypothesize that intermediate depth earthquakes observed in regions with thinner oceanic crust are caused by mantle dehydration reactions that are not possible in regions where the oceanic mantle was never hydrated because the thickness of the oceanic crust exceeded the penetration depth of water into the plate. We compare our observations to phase diagrams of hydrous basalt and hydrated depleted peridotite to determine pressures and temperatures that would be consistent with our observations. These can provide valuable constraints, not only on the degree of hydration and dehydration in the downgoing plate, but also as ground-truth for thermal models of these regions, all of which have complex, three-dimensional, time-variant subduction geometries and thermal histories.

Keywords: flat-slab, seismicity, hydration, intermediate-depth, aseismic-ridges, oceanic crust, oceanic ridges

Edited by:
Vlad Constantin Manea,
National Autonomous University of Mexico, Mexico

Reviewed by:
Fenglin Niu,
Rice University, United States
Wasja Bloch,
German Research Centre for Geosciences, Helmholtz Centre Potsdam, Germany

****Correspondence:***
Lara S. Wagner
lwagner@carnegiescience.edu

Specialty section:
This article was submitted to Structural Geology and Tectonics, a section of the journal Frontiers in Earth Science

Received: *28 December 2019*
Accepted: *04 June 2020*
Published: *10 July 2020*

Citation:
Wagner LS, Caddick MJ, Kumar A, Beck SL and Long MD (2020) Effects of Oceanic Crustal Thickness on Intermediate Depth Seismicity. Front. Earth Sci. 8:244. doi: 10.3389/feart.2020.00244

INTRODUCTION

Intermediate depth earthquakes (70–300 km depth) occur at pressures and temperatures (*P*/*T*) that should produce ductile deformation rather than brittle failure (e.g., Green and Houston, 1995). There has long been significant debate about the role of dehydration reactions in the formation of intermediate depth seismicity. The *P*/*T* conditions at which intermediate depth earthquakes occur have repeatedly been shown to be consistent with dehydration phase boundaries for both crustal and mantle lithospheric hydrous compositions (e.g., Kirby, 1995; Kirby et al., 1996; Peacock, 2001; Hacker et al., 2003; Yamasaki and Seno, 2003; Abers et al., 2013). The most commonly cited link between dehydration and intermediate depth seismicity is dehydration embrittlement. As originally conceived, the term "dehydration embrittlement" means the hydraulic fracturing of rock caused by the production of free fluids and resultant overpressure in pore spaces that in turn could overcome the ambient pressure (e.g., Raleigh and Paterson, 1965; Meade and Jeanloz, 1991). However, more recent experimentation has shown that (a) above some pressure, volume change associated with dehydration reactions is likely negative, complicating the overpressure argument (e.g., Dobson et al., 2002; Jung et al., 2004; Gasc et al., 2011), and (b) some experiments on antigorite and other hydrous phases have produced no acoustic emissions (AEs) upon dehydration and/or show evidence solely of stable sliding or distributed deformation, bringing the concept of "dehydration embrittlement" into question (e.g., Chernak and Hirth, 2010; Chernak and Hirth, 2011; Gasc et al., 2011; Proctor and Hirth, 2015; Gasc et al., 2017). One possible contribution from dehydration reactions unrelated to pore pressure is the formation of nanocrystalline reaction products whose small grain size might contribute to vein growth, channel flow, and/or localized weakening (e.g., Incel et al., 2017; Plümper et al., 2017). Other theories have focused more directly on localized weakening due to slip, i.e., thermal run-away/shear heating mechanisms that also incorporate reduced grain size along discrete planes of weakness (e.g., Kelemen and Hirth, 2007; John et al., 2009; Prieto et al., 2013; Poli et al., 2016; Proctor and Hirth, 2016; Ohuchi et al., 2017). Thermal run-away mechanisms may be self-initiating or may serve as a propagation mechanism for events triggered by another mechanism (e.g., Zhan, 2017). A recent theory that matches many of these observations is the "dehydration destabilization stress transfer" mechanism (DDST; Ferrand et al., 2017; Ferrand, 2019). In this model, hydrated peridotite produces AEs at specific conditions that depend on the amount of hydrated material present within the peridotite matrix and the pressure at which the dehydration reaction occurs. Rather than increasing pore pressure to hydraulically fracture the surrounding rock matrix, the dehydration of antigorite (or other hydrous phases) results in an extreme weakening and volume decrease of the dehydrating phase, which in turn transfers ambient stresses onto the enclosing dry peridotite rock matrix. The amount of hydrous phase in the rock has to be sufficient that its dehydration-related weakening will sufficiently load the surrounding matrix to the point of failure, but not so great that the surrounding matrix does not possess sufficient strength to accumulate strain. According to the calculations of Ferrand et al. (2017) at 3.5 GPa, relatively little antigorite (∼5%) is needed to induce seismicity, consistent with small amounts of hydrated material that might be present deep within the mantle lithosphere of subducted slabs.

There has also been increased interest in the relationship between observations of heterogeneities within the oceanic plate as it enters the trench, and seismicity patterns in the subducting slab at intermediate depths (e.g., Shillington et al., 2015). Recent studies looking at the seismic velocity structure of oceanic plates as they approach the trench show that outer-rise faulting consistently results in extensive hydration of the oceanic plate (see Grevemeyer et al., 2018 and references therein). In studies with sufficiently deep resolution, hydration is observed to extend ∼10–12 km below the oceanic Moho (e.g., Ranero et al., 2003). Fromm et al. (2006) used aftershock locations from a M_w 6.7 outer-rise earthquake to show faulting to depths of ∼ 25 km. In rare cases (e.g., Bloch et al., 2018; Cai et al., 2018), evidence exists for even deeper hydration. Recent work by Boneh et al. (2019) shows a correlation between the observed fault offsets on outer-rise faults from bathymetry data and the rate of intermediate depth seismicity observed down-dip, which suggests the extent of hydration in the oceanic plate due to outer rise faulting may control the amount of seismicity that is possible at intermediate depths.

While links between hydration and seismicity are consistent with dehydration embrittlement or related mechanisms, they do not address whether it is the dehydration of the oceanic crust or mantle that is responsible for the generation of intermediate depth earthquakes. Our hypothesis is that regions with thinner oceanic crust produce intermediate depth seismicity due to mantle dehydration reactions, and that slabs with very thick oceanic crust do not produce intermediate depth events because the previously hydrated overthickened crust has already experienced its most important dehydration reactions by this point, and because the mantle below was never hydrated to begin with and therefore cannot produce the dehydration reactions needed to generate seismicity.

Our hypothesis is based on the clearest and simplest observation of this pattern: along the Nazca Ridge in Peru (∼18 km thick oceanic crust) (Hampel et al., 2004; Kumar et al., 2016). We present our hypothesis in the context of this location, and investigate other possible factors such as plate age, evidence for outer rise faulting, oceanic crustal structure, and any available direct evidence for oceanic mantle hydration. We also investigate the plausibility of our hypothesis in terms of the metamorphic reactions and pressure-temperature conditions required for this to be true. We then assess the hypothesis at a number of other locations where overthickened oceanic crust is being subducted, including the Juan Fernandez Ridge in Chile which produces an overabundance of seismicity rather than an absence thereof, the Carnegie Ridge subducting beneath Ecuador, and the Cocos Ridge subducting beneath Costa Rica. We show that while these other situations are often more complicated and less clear, they are each consistent with our hypothesis given existing data. Finally, we suggest a number of regions where additional research could be used for further testing of this hypothesis, and could help to constrain the relationship between water penetration depth, crustal thickness, and intermediate depth seismicity.

NAZCA RIDGE SEISMICITY PATTERNS WITHIN THE PERUVIAN FLAT SLAB

The Nazca Ridge comprises a 1200 km long, ∼200 km wide seamount chain that extends southwest from the southern Peruvian margin. The crustal structures of the Nazca Ridge and adjacent regions of "typical" Nazca plate are constrained by analyses of a suite of trench perpendicular and trench parallel active source surveys and gravity studies (e.g., Hampel et al., 2004; Krabbenhoeft et al., 2004; Grevemeyer et al., 2018; Contreras-Reyes et al., 2019). These show a ∼100 km wide (trench parallel), 17 km thick crustal root beneath the Nazca Ridge, thinning to ∼6.4 km on either side (**Figure 1**). These crustal thickness results are consistent with earlier surface wave dispersion estimates of ∼18 km (Woods and Okal, 1994). The Nazca Ridge's conjugate on the Pacific Plate, the Tuamotu Ridge, has been used to determine the initial timing of collision of this ridge with the South American continent at ∼15–12 Ma, and to project its current location onto the subducted slab (i.e., Pilger, 1981; Woods and Okal, 1994; Gutscher et al., 1999b; Hampel, 2002; Rosenbaum et al., 2005). The difference in the strike of the Nazca Ridge and the relative convergence direction between the Nazca and South American plates (see **Figure 1**) has resulted in a progressive southward migration of the ridge relative to the overriding continental margin since that time (i.e., Gutscher et al., 1999b; Rosenbaum et al., 2005). This, together with the inferred subduction of the conjugate to the Marquesas Plateau, named the Inca Plateau, are often cited as contributing to the formation of the unusually long (along strike) extent of the Peruvian flat slab (i.e., Gutscher et al., 1999b; Antonijevic et al., 2015). The current location of the Nazca Ridge beneath the South American continent has been assessed using adjacent oceanic magnetic anomalies that allow for an alignment of the projection of the conjugate Tuamotu Plateau both along the Nazca Ridge and to regions of the slab already subducted (Hampel, 2002). Note that this location depends only on observations of magnetic anomalies and does not make assumptions about current or past relative plate motions.

Over the past decade, three broadband seismic deployments (PULSE: Wagner et al., 2010; CAUGHT: Beck et al., 2010; PeruSE, 2013) have collected data in central and southern Peru, providing dense seismic coverage across the projected location of the Nazca Ridge. Tomographic and scattered wave imaging based on these data indicate that, as with many regions with subducted overthickened oceanic crust, the projected location of the subducted Nazca Ridge coincides closely with the shallowest portion of the southern Peruvian flat slab (Antonijevic et al., 2015, 2016; Bishop et al., 2017; Wagner and Okal, 2019).

The hypothesis that thicker oceanic crust could lead to an absence of intermediate depth seismicity was first proposed by Kumar et al. (2016) in their study of intermediate depth seismicity using the PULSE, CAUGHT, and PeruSE networks in Peru. The earthquake locations from recent studies using local data (Kumar et al., 2016; Lim et al., 2018) are roughly consistent with catalog data available from the International Seismological Center for events occurring 1990–2017 (International Seismological Centre, 2019 Reviewed Event Catalog, retrieved October 1, 2019). Notably, there is a distinct gap in seismicity located in the middle of the PULSE array where event locations using these data should be most complete (Hampel, 2002; Kumar et al., 2016). This gap corresponds closely to the projected location of the subducted Nazca Ridge based on the projected location of the Tuamotu Plateau (**Figure 1**). The Tuamotu Plateau, however, is much broader than the unsubducted portions of the Nazca Ridge, highlighting the uncertainties about the geometry of the Nazca Ridge location and crustal thickness at depth. However, we note that the region of the observed seismic gap is well within the contours of the projected Tuamotu Plateau, consistent with our hypothesis, and consistent with previous observations of the correlation between the modern projection of the Tuamotu Plateau and the observed gap in seismicity (e.g., Hampel, 2002).We note, however, that at depths shallower than 60 km (i.e., closer to the trench), there is no gap in seismicity along the projected Nazca Ridge track. The right-hand panel of **Figure 1** (A,A′) shows the locations of intermediate depth earthquakes within 75 km of the roughly ridge-perpendicular cross section extending from (−11.3°S; −76.9°W) to (−16.8°S; −71.1°W). Also shown is the oceanic Moho topography and bathymetry from Contreras-Reyes et al. (2019), showing the wavelength of the overthickened crust associated with the Nazca Ridge, which is similar to the size of the gap in seismicity. The red line plotted beneath the seismicity profile indicates the top of the subducted slab as determined by Antonijevic et al. (2015) and Wagner and Okal (2019). Unfortunately, while receiver function studies such as Bishop et al. (2017) are able to identify seismic conversions from the oceanic Moho in some places, the errors in absolute depth for both the receiver functions and the earthquake locations make a determination of whether these events are occurring in the slab crust or mantle impossible.

While it is not currently possible to know the detailed structure of the already subducted Nazca plate collocated with these observed seismicity patterns, it is instructive to look directly offshore at the structure of the Nazca Ridge and adjacent areas that are about to be subducted to infer some constraints on possible structures that could be influencing intermediate depth seismicity. The age of the Nazca plate at the Peruvian margin along and adjacent to the Nazca Ridge varies only slightly from 43 to 46 Ma, except south of the Nazca Fracture Zone (south of our study area) where ages increase to ∼52 Ma (Mueller et al., 2008). This is significant because the age of the plate strongly affects the temperature, and therefore the potential locations of dehydration reactions. In this case, not only is the overall range in ages small, intermediate depth seismicity is located on either side of the gap at the Nazca Ridge, while plate age increases monotonically from north to south. It is therefore unlikely that plate age or slab temperature are responsible for the observed seismicity patterns.

Another possible explanation for this pattern is that the thick crust of the subducting Nazca Ridge does not form as many outer-rise faults as the adjacent thinner oceanic crust, and is therefore

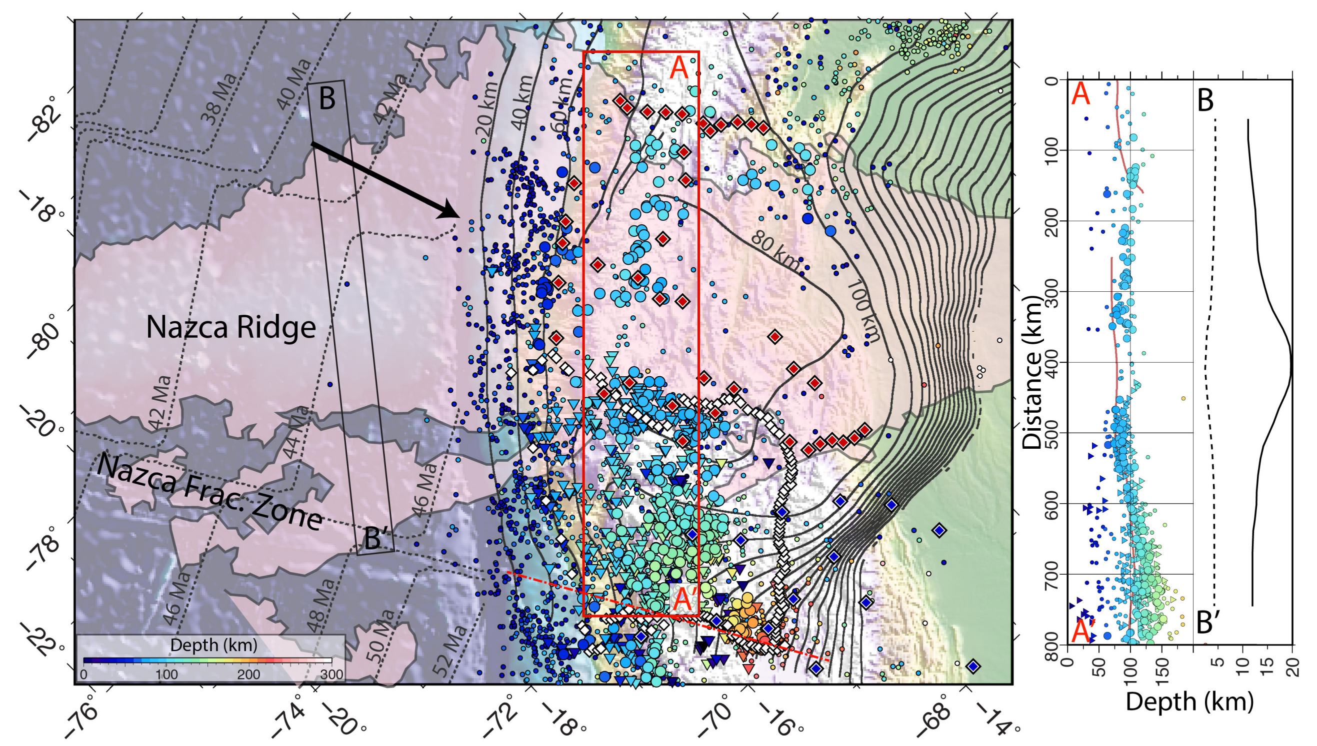

FIGURE 1 | Nazca Ridge subduction and earthquake distribution. **Left:** Map showing seismicity from the Reviewed International Seismological Center's earthquake catalog (1990–2017) – small circles. Large circles are hypocenters from Kumar et al. (2016), and inverted triangles are hypocenters from Lim et al. (2018). Offshore dashed lines show oceanic plate age contours from Mueller et al. (2008). Bold arrow shows convergence direction from DeMets et al. (2010). Pink shaded region shows the outline of the projected conjugate Tuamotu Ridge from Hampel (2002). Red diamonds, blue diamonds, and white diamonds show seismic station locations for the PULSE, CAUGHT, and PERUSE experiments, respectively. Dash-dot red line shows inland projected location of Nazca Fracture Zone. Solid black lines show slab contours from Wagner and Okal (2019). Red rectangular box shows area over which events were projected onto cross section to the right. Black rectangular box shows region over which oceanic Moho topography was compiled by Contreras-Reyes et al., 2019. **Right:** Cross-section across the projected location of the subducted Nazca Ridge. Symbols same as to the left. Panel A,A′ cross section showing event depths (in km) for events projected from area in red box on map. Red line indicates the slab surface from Antonijevic et al. (2015) and Wagner and Okal (2019). Right panel (B,B′) shows depth below sea level in km for the oceanic Moho (solid black line) and bathymetry (dotted line) across the Nazca Ridge from Contreras-Reyes et al. (2019).

less hydrated overall. However, side swath bathymetry surveys show evidence of trench parallel normal faults across both the Nazca Ridge and the adjacent normal oceanic plate with similar vertical offsets on the order of ~200 m across our study area irrespective of crustal thickness (Hussong et al., 1988; Hagan and Moberly, 1994; Hampel et al., 2004; Kukowski et al., 2008). A more direct way to determine the hydration state of the oceanic plate is through tomographic modeling of seismic velocities. Wide-angle seismic studies north of the Nazca Ridge indicate average uppermost mantle velocities of ~7.8 km/s, consistent with moderate hydration (Krabbenhoeft et al., 2004). However, along the ridge, somewhat higher uppermost mantle velocities are observed (~8.0 km/s) consistent with an absence of mantle hydration (Contreras-Reyes et al., 2019), though the resolution of these studies at upper mantle depths is limited. Finally, Hu and Liu (2016) propose a slab tear as a possible cause for the observed absence in seismicity along the projected Nazca Ridge track based on geodynamic modeling and patterns of volcanism. However, given the clear evidence from seismic imaging for a continuous slab in this region from receiver functions (i.e., Bishop et al., 2017, 2018), teleseismic tomography (Scire et al., 2015), and surface wave tomography (Antonijevic et al., 2015, 2016), this explanation for the observed seismic gap is inconsistent with existing detailed imaging of the region.

METAMORPHIC IMPLICATIONS

Figure 2A shows a simplified schematic version of the cross section shown in **Figure 1** (A,A′) that we use to model our hypothesis. We assume the top of the oceanic crust is at the same depth along the transect, placing it at 70 km depth based on the depths of observed seismicity and the thickness of the overriding continental crust (Bishop et al., 2017). The base of the "normal" oceanic crust to either side of the ridge is assumed to be 77 km depth (assuming a 7 km thick crust) and the base of the Nazca Ridge crust is at 88 km depth (based on the 18 km crustal thickness imaged offshore). Here we show the penetration depth of water into the Nazca plate to also be 18 km beneath the surface of the oceanic crust (i.e., at 88 km depth), consistent with a number of previous studies investigating the depth of mantle hydration (e.g., Ranero et al., 2003; Contreras-Reyes et al., 2011;

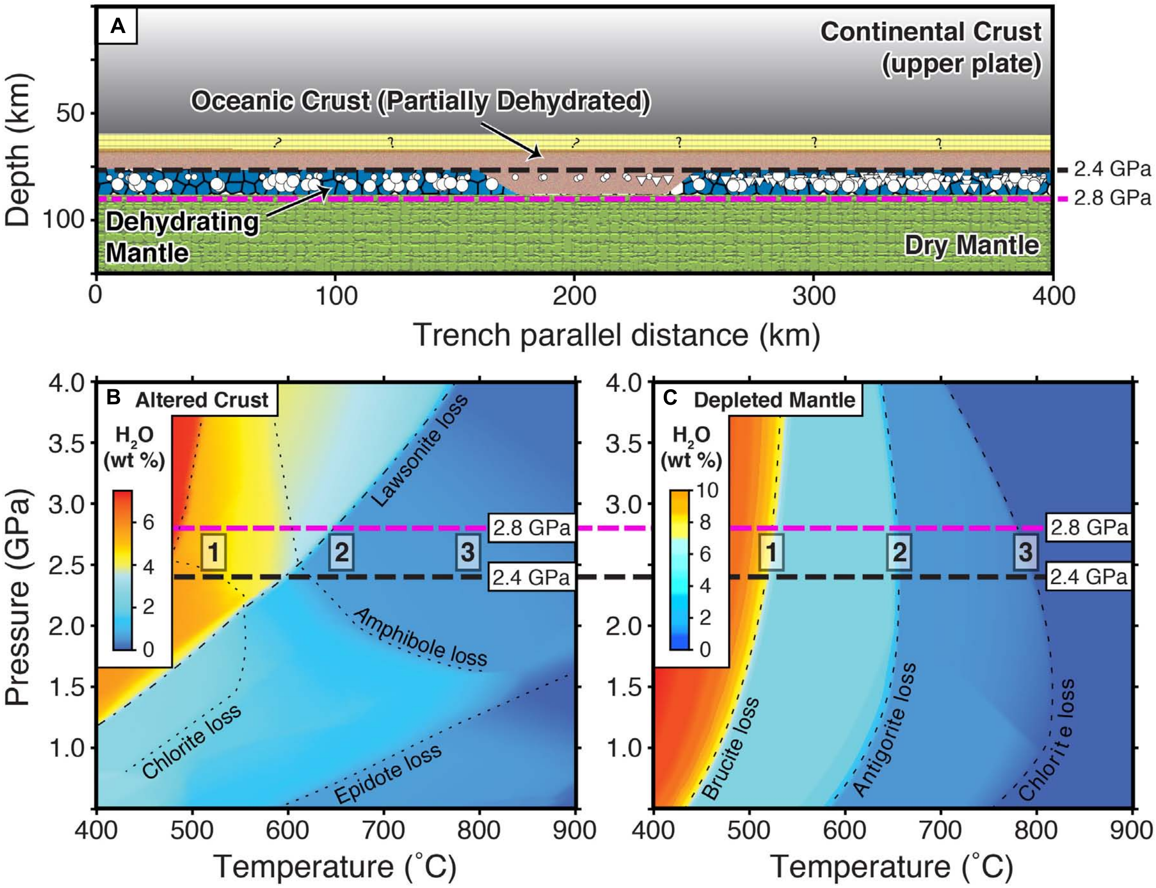

FIGURE 2 | Schematic diagram of our hypothesis: **(A)** Simplified trench-parallel cross section based on geometry shown in **Figure 1**. Section has been simplified so that the plate is perfectly flat across the interior 400 km (∼150 km on either side of the ridge) and so that all seismicity is projected to the depth range of our proposed hydrated mantle lithosphere (lateral distribution still the same as in the cross section in **Figure 1**). Green region indicates dry oceanic mantle lithosphere. Blue indicates hydrated oceanic mantle lithosphere. White circles/triangles are seismic events (same symbols as in **Figure 1**). Light brown region is oceanic crust (MORB). Yellow region indicates possible mantle material trapped between the oceanic crust and the overlying continental crust (grayscale). Black dashed line is depth to the base of "normal" oceanic crust (i.e., top of hydrated mantle lithosphere). Magenta line is proposed maximum depth of hydration into the oceanic plate. **Bottom:** Mineralogically bound H_2O contents of hydrated MORB **(B)** and peridotite **(C)**, based on phase equilibria calculations. Dashed lines show pressures corresponding to lines of the same color in the cross section above. Boxes 1, 2, and 3 indicate regions where oceanic mantle undergoes significant dehydration at pressures experienced by hydrated mantle lithosphere. Versions of these diagrams labeled with the mineral assemblages associated with the H_2O contents are available in **Supplementary Information**.

Lefeldt et al., 2012). We note that in order for our model to hold, the penetration depth of water simply needs to be greater than normal oceanic crustal thickness, and less than or equal to the ridge crustal thickness. For clarity, we have projected seismicity from cross-section A,A′ (**Figure 1**) vertically to depths between the normal oceanic Moho and the maximum penetration depth of water into the slab. This allows us to demonstrate along-strike variability in intermediate depth seismicity, and is reasonable given that (a) the slab is unlikely to be perfectly horizontal along the cross section and (b) depth errors in hypocentral locations typically significantly exceed errors in latitude and longitude.

According to our hypothesis, the blue region in **Figure 2A** (hydrated mantle lithosphere) generates seismicity at these depths because it is undergoing dehydration reactions and the brown region (oceanic crust) is not dehydrating, and is therefore not generating seismicity. Because there is no hydrated mantle below the thick crust of the Nazca Ridge, there is a seismic gap. The discriminating region, then, lies between the 77 km depth of normal oceanic Moho (black dashed line in **Figure 2C**) and the assumed 88 km depth that marks the lowermost penetration depth of water into outer rise faults (magenta dashed line in **Figure 2C**). If our hypothesis is correct, the temperature of this region should correspond to a P/T condition at which hydrated peridotite would dehydrate but hydrated MORB would not, based on the assumption that temperature would be the same at these depths, regardless of whether the material is MORB or hydrated oceanic mantle lithosphere.

Figures 2B,C show the amount of structurally bound H_2O that can be incorporated into altered crust and depleted mantle, respectively. These diagrams are based on phase equilibria that were calculated for a composite crustal composition from DSDP sites 417 and 418 (Staudigel et al., 1989, 1996) and for harzburgitic mantle (Ringwood, 1982). Sufficient H_2O was added to each bulk composition to saturate mineral assemblages at every P/T condition with fluid, and the amount of water contained in the coexisting mineral assemblage is contoured in **Figure 2** (see also Hacker, 2008, for water contents of a larger range of possible rock composition). Calculations utilized Perple_X (Connolly, 2005) and a 2004 update to the Holland and Powell (1998) thermodynamic dataset for mineral end-members. We used the suite of mineral solution models employed by Baxter and Caddick (2013), with the exception of updated models for antigorite (Padrón-Navarta et al., 2013) and amphibole and omphacite (Diener and Powell, 2012). Silicate melt was not considered. Calculated mineral assemblages are labeled in more detail in the **Supplementary Information**, where calculated densities of both rocks are also shown.

The dashed lines in **Figures 2B,C** correspond to the dashed lines of the same colors in **Figure 2A** – indicating the pressures at the base of the normal oceanic crust (∼2.4 GPa) and at the maximum penetration depth of water into the oceanic plate (∼2.8 GPa) as determined by converting the associated depths to pressures based on the Preliminary Reference Earth Model (PREM; Dziewonski and Anderson, 1981). We identify three temperature ranges within this pressure range at which hydrated peridotite releases a significant amount of water: ∼500°C upon the loss of brucite (box 1, **Figure 2C**), ∼640°C upon the loss of antigorite (box 2, **Figure 2C**) and ∼800°C upon chlorite breakdown (box 3, **Figure 2C**). We note that ∼640°C is similar to the temperature modeled for a flat slab at similar depth by van Hunen et al. (2002). If we then plot these same temperature boxes on the MORB phase diagram, we note that indeed, boxes 2 and 3 lie in regions at which MORB has already undergone extensive dehydration and is not dehydrating further, consistent with our hypothesis. Colder subduction that intersects box 1 would, however, be associated with crust that retains water in both lawsonite and amphibole.

According to our hypothesis, the oceanic crust along and adjacent to the subducted Nazca Ridge will be undergoing little dehydration by the time it reaches the P/T conditions of our seismic gap, implying that it has already fully dehydrated or that its H_2O content is sequestered in stable phases at these conditions. Subducting oceanic crust undergoes a sequence of dehydration reactions, but one of the most commonly attributed to the formation of intermediate depth seismicity is the breakdown of lawsonite (e.g., Kim et al., 2015; Okazaki and Hirth, 2016; Incel et al., 2017). In the Nazca Ridge case, this suggests that the oceanic crust must have exceeded the maximum temperatures of lawsonite (and amphibole) stability by the time the top of the slab reaches 70 km depth and the bottom of the hydrated layer of the slab reaches 88 km depth. Our hypothesis requires that off-ridge regions of thinner crust are still undergoing peridotite dehydration reactions at these same P/T conditions, which is true in **Figures 2B,C** for box 2 (dehydration of antigorite in the slab mantle) and box 3 (dehydration of chlorite in the slab mantle), but not box 1 (dehydration of brucite in the slab mantle that would be accompanied by dehydration of crust in the on-ridge section). Choosing whether peridotite dehydration at 640 or 800°C is most appropriate is more equivocal, given that the temperatures within regions of flat slab subduction are highly dependent on the three-dimensional geometry of the slab and the duration of time the overriding plate has been insulated from asthenospheric temperatures by the slab. Detailed time-dependent thermal modeling is required to better assess the implications of these predicted temperatures. However, either option demonstrates that our hypothesis is viable from a simplified petrologic perspective.

SEISMICITY PATTERNS ASSOCIATED WITH OTHER REGIONS OF SUBDUCTED THICK OCEANIC CRUST

Pampean Flat Slab

The most obvious and contrasting comparison to the lack of seismicity along the subducting Nazca Ridge along the Peruvian flat slab is the notable abundance of seismicity present along the subducting Juan Fernandez ridge along the Pampean flat slab in Chile and Argentina (**Figure 3**). Unlike the Nazca Ridge which is formed by a hot spot located along the Nazca-Pacific spreading center, the Juan Fernandez Ridge results from an intraplate hot-spot located 900 km from the South American margin (von Huene et al., 1997; Yañez et al., 2001, 2002). This means that, unlike the Nazca Ridge, there is no conjugate ridge to provide constraints on its projected location beyond the trench. It also means that unlike the Nazca Ridge, the Juan Fernandez ridge is not the same age as the surrounding plate – the oldest observed seamount close to the trench is ∼ 8.5 Ma, whereas the oceanic plate it sits on is ∼38 Ma (von Huene et al., 1997; Yañez et al., 2001; Mueller et al., 2008).

Reconstructions based on past plate motions indicate a major inflection point in the ridge track at 25 Ma coincident with the fracturing of the Farallon plate and the formation of the Nazca plate. This inflection point is believed to have subducted ∼11 Ma (Yañez et al., 2001) (white circles, **Figure 3**). Prior to that time, the Juan Fernandez Ridge would have been migrating southward along the Chilean margin much as the Nazca Ridge is migrating southward today. However, since 11 Ma, the ridge track and plate convergence directions have been nearly parallel, resulting in only a minor southward migration since the mid-Miocene (Yañez et al., 2001).

Over the past twenty years, a number of broadband seismic deployments (i.e., OVA99 and CHARSME (e.g., Marot et al., 2013), CHARGE (Beck et al., 2000); SIEMBRA (Beck and Zandt, 2007); ESP (Gilbert, 2008) have collected data above the projected location of the Juan Fernandez Ridge that have been used to constrain the geometry of the downgoing plate, and to relocate intermediate slab seismicity (e.g., Anderson et al., 2007; Marot et al., 2013; **Figure 3**). As was the case in Peru, the projected location of the subducted Juan Fernandez ridge coincides closely with the shallowest portion of the Pampean flat slab (Anderson et al., 2007). Unlike Peru, however, both global catalogs and local catalogs based on regional networks (i.e., Anderson et al., 2007; Marot et al., 2013) show the highest concentration of seismicity and moment release concentrated directly along the projected

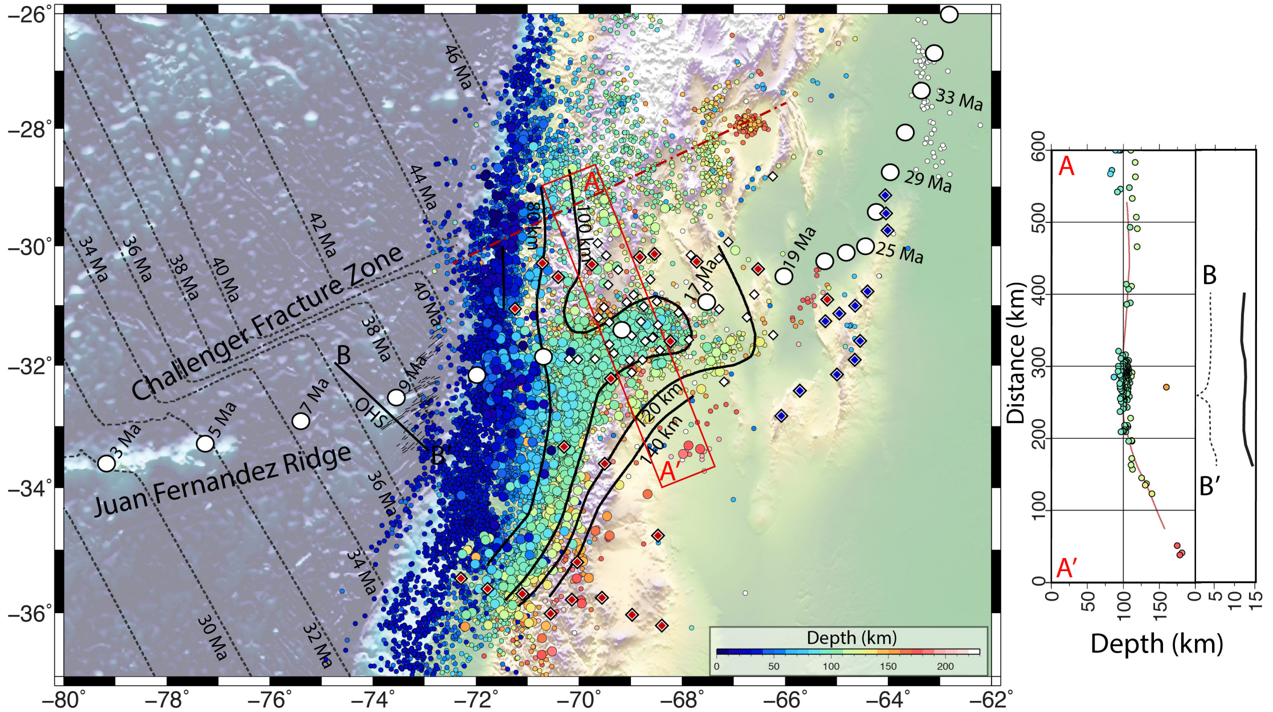

FIGURE 3 | Juan Fernandez Ridge subduction and earthquake distribution. **Left:** Map showing seismicity from the Reviewed International Seismological Center's earthquake catalog (1990–2017), with events shallower than 50 km removed east of –70°W for clarity. Large circles are hypocenters from Anderson et al. (2007) also with hypocenters shallower than 50 km removed east of –70°W. Offshore dashed lines show age contours from Mueller et al. (2008). Offshore solid black line shows the location panel B,B′ of the cross section from Kopp et al. (2004). Label "OHS" indicates the location of the O'Higgins seamount. Thin black lines offshore near the OHS indicate the locations of ridge-parallel normal faults from Ranero et al. (2005). White circles show projected track of the Juan Fernandez Ridge, along with ages of the seamount at those locations, from Yañez et al. (2001). Red diamonds, blue diamonds, and white diamonds show seismic station locations for the CHARGE, ESP, and SIEMBRA experiments, respectively. Dash-dot red line shows projected location of Challenger Fracture Zone. Solid black lines show slab contours from Anderson et al. (2007). Red rectangular box panel A,A′ shows area over which events were projected onto cross section to the right. **Right:** Cross-section panel A,A′ across the projected location of the subducted Juan Fernandez Ridge. Circles show event locations (depth in km) from Anderson et al. (2007), and red line shows top of slab from Anderson et al. (2007). Right panel (B,B′) shows depth below sea level in km for the oceanic Moho (solid black line) and bathymetry (dotted line) across the O'Higgins seamount from Kopp et al. (2004).

location of the Juan Fernandez Ridge. The right-hand panel of **Figure 3** (A,A′) shows the locations of intermediate depth earthquakes within 50 km of the roughly ridge-perpendicular cross section extending from (−28.8°S; −70.2°W) to (−33.8°S; −67.85°W). The red line plotted beneath the seismicity profile indicates the top of the subducted slab as determined by Anderson et al. (2007). As is the case in Peru, while some receiver function studies such as Gans et al. (2011) show evidence of the oceanic Moho in this region, the errors in the absolute depths locations of the receiver function are too great to allow an assessment of whether the observed seismicity is due to slab mantle or slab crustal processes.

To understand the cause of this seismicity, especially in contrast to the absence of seismicity along the Nazca Ridge, we again look at the structure of the downgoing oceanic plate, comparing the ridge track to normally subducted crust on either side. The age of the Nazca plate along the Chilean margin near the Juan Fernandez Ridge ranges from ∼34 to ∼40 Ma, becoming progressively older to the north (Mueller et al., 2008). Side swath bathymetry shows trench parallel normal faults close to the trench similar to the plate near the Nazca Ridge. These trench parallel normal faults associated with the downward bending of the oceanic plate are limited to an area within 30 km of the trench (Kopp et al., 2004; Ranero et al., 2005). However, these bathymetry studies also show extensive normal faults parallel to the Juan Fernandez ridge track that have no analog in Peru (**Figure 3**; von Huene et al., 1997; Kopp et al., 2004; Ranero et al., 2005). These ridge-parallel faults are particularly pronounced, with some such as the O'Higgins Fracture extending over 100 km across the oceanic plate (Kopp et al., 2004). A M_w = 6.7 normal fault earthquake occurred on April 9, 2001 that likely ruptured along the O'Higgins Fracture zone with northeast-southwest striking nodal planes (Fromm et al., 2006). This earthquake and aftershock sequence was relocated with data from seismic stations on-shore and the aftershocks extended to a depth of ∼25–30 km suggesting that outer-rise normal faults can rupture through the oceanic crust and into the mantle lithosphere (Fromm et al., 2006).

Wide angle seismic refraction profiles provide excellent constraints on the structure of the oceanic crust and mantle in the vicinity of the Juan Fernandez Ridge. Orthogonal survey lines across the O'Higgins Seamount at the eastern end of the ridge indicate only modest crustal thickening (8–10 km thick crust) beneath the highest elevations of the seamount (Kopp et al., 2004), though the receiver function study of Gans et al. (2011) argues that the oceanic crust currently located within the horizontal portion of the subducted slab is at least 13 km thick locally. Velocity modeling of the oceanic crust and mantle across the region shows evidence for reduced crustal and upper mantle velocities (Kopp et al., 2004; Contreras-Reyes et al., 2014, 2015; Moscoso and Grevemeyer, 2015). Kopp et al. (2004) indicate that hydration beneath the O'Higgins Seamount Group likely extends at least 6 km below the Moho, indicating a total hydration thickness of 16–18 km. This hydration is likely enhanced by the presence of extensive ridge-parallel normal faulting, whose spatial extent is similar to the area of low upper mantle velocities (Kopp et al., 2004; Contreras-Reyes et al., 2015).

Taken together, these data suggest that the Juan Fernandez Ridge has a much less extensive crustal root than the Nazca Ridge, and that trench parallel and perpendicular faulting has produced extensive hydration of the mantle lithosphere beneath the ridge that can explain intermediate depth seismicity on the projected location of the Juan Fernandez Ridge. This leaves outstanding the question of why intermediate depth seismicity is more pronounced along the projected Juan Fernandez Ridge track than in adjacent areas with more normal oceanic crust. One possible explanation could be the ridge-parallel faulting that is largely confined to the region close to the ridge itself (e.g., Ranero et al., 2005). Another possible explanation could be related to enhanced bending related stresses due to the contortion necessary to accommodate the abrupt along-strike transition (from north to south) from flat slab to normally dipping slab. Recent work by Sandiford et al. (2019) attributed bending related stresses to increases in seismicity at the hinge zones of the northern Peruvian flat slab and the Mexican flat slab. A similar, but trench perpendicular, bending geometry might be able to explain the high concentration of seismicity along the subducted Juan Fernandez Ridge. Finally, we note that because the Juan Fernandez Ridge has been subducting beneath the same part of the South American continent for ~11 Ma, it is likely to be colder than the corresponding portion of the southward progressing Nazca Ridge due to the greater amount of time the overriding continent has been isolated from asthenospheric corner flow (van Hunen et al., 2002). Based on the phase diagrams in **Figure 2**, MORB compositions at temperatures below 640°C would still contain a significant amount of water, particularly in the form of lawsonite, and are therefore still capable of dehydration reactions that might produce the observed seismicity.

Cocos and Carnegie Ridges

The Cocos and Carnegie Ridges are structurally much more similar to the Nazca Ridge than the Juan Fernandez Ridge. Both ridges formed at the Galapagos hot spot near the plate boundary no earlier than at the time of the fracturing of the Farallon plate and the formation of the Cocos and Nazca plates (~23 Ma) (Lonsdale, 2005). The Cocos ridge crust is ~18.5–20 km thick (Sallares et al., 2003; Walther, 2003), thinning at the flanks to ~8–10 km thick (Walther, 2003). Sallares et al. (2003) do not indicate any resolution below the oceanic Moho. Walther (2003) argues that Pn velocities indicate low uppermost mantle velocities at the flanks (7.8 km/s) that appear to decrease below the thickest portions of the crust. However, because of a lack of apparent density decrease, Walther (2003) suggests the decrease in velocity is not likely due to hydration but rather to an imperfect separation of basaltic melt and residual mantle peridotite during ridge formation. Adjacent regions north of the Cocos ridge indicate mantle hydration up to 10 km below the oceanic Moho (Ranero et al., 2003; Lefeldt et al., 2012). Unlike the Nazca Ridge, however, while adjacent regions show evidence of significant outer rise faulting (Ranero et al., 2003), there is limited – to – no evidence of outer rise faulting along the Cocos Ridge (e.g., von Huene et al., 2000).

The Carnegie Ridge crustal structure is similar to that of the Cocos Ridge. Its crustal thickness ranges from 14 to 19 km (e.g., Graindorge et al., 2004; Sallares et al., 2005; Gailler et al., 2007; Collot et al., 2017), but no robust estimates of sub-ridge Moho velocities are available at this time. The Carnegie Ridge, however, does show some evidence from bathymetry and seismic surveys for trench-parallel normal faulting in the oceanic plate, at least along the northern flanks of the ridge (Marcaillou et al., 2016).

Seismic gaps have been noted along both the Cocos (e.g., Husen et al., 2003; Peacock et al., 2005) and Carnegie (e.g., Gutscher et al., 1999a; Font et al., 2013; Yepes et al., 2016; Rosenbaum et al., 2018) ridges (**Figure 4**). Intermediate depth seismicity in the downgoing Cocos plate decreases in volume and maximum depth from northwest to southeast (cross-section C,C′ showing seismicity within 75 km of 11°N, −85.9°W to 8.3°N, −81°W, **Figure 4**) leading up to the projected location of the Cocos ridge. The Cocos Ridge is just west of the seismically active Panama Fracture Zone (PFZ) whose north-south band of seismicity appears to continue past the trench up to its projected intersection point with the Cocos ridge, though little of this seismicity extends below 50 km depth. The absence of seismicity east of the east-west trending Carnegie Ridge is complicated by its projected intersection with the Grijalva Fracture Zone (Lonsdale, 2005; Yepes et al., 2016) which comprises the southern flank of the Nazca-Cocos rift zone. Seismicity is ample and extends to over 200 km depth for locations south of the Grijalva Fracture zone (cross-section A,A′ showing seismicity within 75 km of 1.9°N, −77.7°W to −3.8°S, −78.7°W), but is notably absent at depths below 50 km to the north along the projected location of the Carnegie Ridge. While the geometry of the slab between the Grijalva Fracture zone and central Colombia is not well defined by Wadati-Benioff zone seismicity, it has been postulated that slab tears may help accommodate rapid changes in slab geometry and the subduction of the Carnegie ridge (Gutscher et al., 1999a; Yepes et al., 2016; Rosenbaum et al., 2018).

Broadly speaking, the combination of a subducting thick oceanic crust that is coincident with a gap in intermediate depth seismicity for both the Cocos and Carnegie ridges is consistent and supportive of our hypothesis. However, there are several possible potentially confounding tectonic factors. First, for both ridges, the age of the oceanic plate increases rapidly away from the ridge in the direction of increased seismicity. Given the comparatively young age of the oceanic plate along these ridges (14–18 Ma (Mueller et al., 2008), and the even

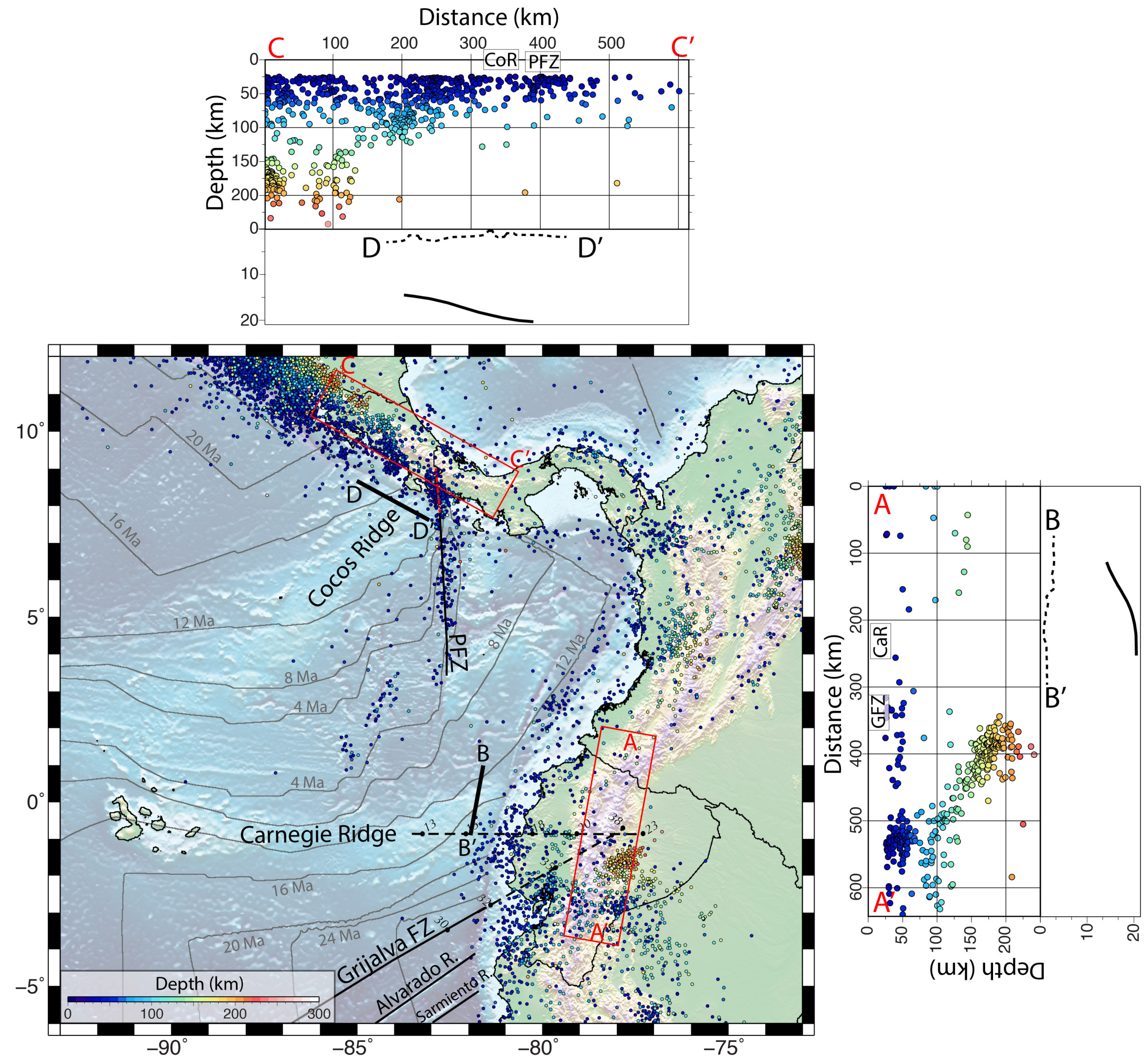

FIGURE 4 | Carnegie and Cocos Ridge subduction and earthquake distribution. **Left:** Map showing seismicity from the Reviewed International Seismological Center's earthquake catalog (1990–2017) as small circles. Offshore gray lines show age contours from Mueller et al. (2008). Offshore solid black line across the Carnegie Ridge shows the location panel B,B′ of the cross section from Sallares et al. (2005). Offshore solid black line across the Cocos Ridge shows the location panel D,D′ of the cross section from Sallares et al. (2003). Black dashed lines and italic numbers show the projected Carnegie Ridge and Grijalva Fracture Zone locations and ages from Lonsdale (2005). Dash-dot red line shows projected location of the Panama Fracture Zone. Red rectangular box panel A,A′ shows area over which events were projected onto cross section to the right. **Right:** Cross-section panel A,A′ across the projected location of the subducted Carnegie Ridge. Circles show projected event locations (depth in km) from the Reviewed ISC catalog (1990–2017). Left panel (B,B′) shows depth below sea level in km for the oceanic Moho (solid black line) and bathymetry (dotted line) across the Carnegie ridge from Sallares et al. (2005). **Top:** Cross-section panel C,C′ across the projected location of the subducted Cocos Ridge. Circles show projected event locations (depth in km) from the Reviewed ISC catalog (1990–2017). Lower panel (D,D′) shows depth below sea level in km for the oceanic Moho (solid black line) and bathymetry (dotted line) across the Carnegie ridge from Sallares et al. (2003).

younger ages on the sides of the ridges with less seismicity (<12 Ma), it is possible that a significant portion of the observed patterns are due to the younger plates being too warm to stay hydrated much deeper than 50 km. Secondly, because there is no conjugate to these ridges that is not currently being subducted, it is difficult to know how much of the ridge has actually been subducted, and whether either ridge extends far enough landward from the trench to be responsible for the observed gaps. Estimates from the timing of first subduction for the Cocos Ridge range from 8 to 1 Ma, though many prefer ages of <3 Ma (e.g., Protti et al., 1994; Kolarsky et al., 1995; von Huene et al., 2000; MacMillan et al., 2004; Dzierma et al., 2011; Morell et al., 2012) which would extend the Cocos Ridge as far landward as the former arc, but not much farther ENE. For the Carnegie Ridge, if ridge formation began at 23 Ma with the breakup of the Farallon plate, onset of ridge subduction would have started 6–8 Ma (Lonsdale, 2005). However, this is far from certain, and other estimates suggest that there is little evidence for subduction of the Carnegie Ridge prior to 5 Ma (e.g., Bourdon et al., 2003; Michaud et al., 2009). The abundance of volcanic arc activity suggests that flat slab subduction that might be associated with the downgoing Carnegie Ridge must be relatively recent. A number of studies point to petrological changes along the arc to suggest that a shallowly subducting Carnegie Ridge may affect arc magmatism at the surface, either by affecting the depth of melting (e.g., Chiaradia et al., 2020) or through the melting of overthickened oceanic crust due to adjacent tears in the downgoing plate (e.g., Gutscher et al., 1999a; Bourdon et al., 2003; Rosenbaum et al., 2018). One way or the other, 5 Ma of subduction would still imply a substantial amount of subducted ridge, certainly sufficient to be responsible for the observed seismic gap within uncertainties. Finally, because both the Cocos and Carnegie ridges are intercepted by fracture zones, associated tears or slab windows could result in changes in the thermal structures of the adjacent subduction zone that could affect not only arc volcanism, but also the dehydration reactions responsible for observed seismicity patterns (e.g., Gutscher et al., 1999a; Bourdon et al., 2003; Dzierma et al., 2011; Rosenbaum et al., 2018). For these reasons, without further data, we must consider these ridges consistent with, but not necessarily supportive of, our hypothesis.

DISCUSSION

The nature of the relationship (if any) between oceanic crustal structures and intermediate/deep seismicity has long been discussed. For example, Kirby et al. (1996) consider the relationship between the "mechanically flawed and heterogeneous lithosphere" and intermediate depth seismicity. In particular, they note the effects of fractures, both from outer-rise faults and fracture zones on the hydration of the oceanic lithosphere and associated potential for increased intermediate depth seismicity. We note that similar patterns are visible in all of our study areas along the projected locations of the Nazca Fracture Zone, Challenger Fracture Zone, Grijalva Fracture Zone, and Panama Fracture Zone for the study areas near the Nazca, Juan Fernandez, Carnegie, and Cocos ridges, respectively. However, to our knowledge, we are the first to suggest that the presence of overthickened oceanic crust can result in an absence of intermediate depth seismicity if crustal thickness exceeds the maximum penetration depth of water into the subducted plate. Kirby et al. (1996) do mention the role of ridges in the formation of seismicity, and while they note the apparent absence or dearth of seismicity associated with the Nazca, Cocos, Carnegie and D'Entrecasteaux ridges, they focus instead on the overabundance of seismicity present along the Juan Fernandez Ridge.

We would argue that the Juan Fernandez Ridge is fundamentally different from the type of ridge we would expect to produce a gap in intermediate depth seismicity, both because of its limited crustal root and because of its extensive ridge-parallel faulting. Interestingly, these structures may be related to the location and timing of ridge emplacement – the Juan Fernandez Ridge is the only one considered here that did not form at or near a spreading center. This may affect the architecture of the crust in important ways. The Juan Fernandez Ridge crustal thickness is primarily due to increases in upper crustal layers, but a relatively constant thickness lower crust (e.g., Kopp et al., 2004). In contrast, the Nazca, Carnegie, and Cocos ridges all attained their increased Moho depths through thickening of the lower crust, with little to no increase in the thicknesses of layers in the upper crust (e.g., Sallares et al., 2003; Krabbenhoeft et al., 2004; Sallares et al., 2005; Contreras-Reyes et al., 2019). An intriguing analog to the Juan Fernandez Ridge might be the Louisville Ridge on the Pacific plate that also formed at an intraplate hotspot (the Louisville hotspot, Watts et al., 1988). Here, as with the Juan Fernandez Ridge, most of the additional crustal volume is added intrusively into the upper crust with only modest variations in lower crustal thickness (Contreras-Reyes et al., 2010; Robinson et al., 2018). However, unlike the Juan Fernandez Ridge, there is no evidence of ridge-parallel fracturing or hydration of the mantle beneath the ridge itself (Contreras-Reyes et al., 2010). While the Louisville Ridge has been associated with a reduction in seismicity at shallow to intermediate depths (Giardini and Woodhouse, 1984; Habermann et al., 1986; Scholtz and Small, 1997), the seismicity pattern is less clear in part due to the oblique subduction of the ridge, and uncertainty about its projected location. More work is needed to understand how crustal thickening mechanisms, Moho depth, and seismicity patterns are related in this region.

At this stage, we know of no example that contradicts our hypothesis that if the oceanic crust is thicker than the maximum penetration depth of water into the slab, intermediate depth seismicity will be reduced or absent. The precise mechanism by which dehydration results in intermediate depth seismicity, whether it be by traditional "dehydration embrittlement" via an increase in pore pressure, by the formation of nanocrystalline/fine grained dehydration products or fault plane weakening, by DDST, or some combination of the above, may depend on the precise P/T conditions of the subducting slab, and is certainly a field of ongoing scientific research. Our hypothesis does, however, strongly suggest that dehydration plays a dominant role in the generation of intermediate depth seismicity, even if the precise mechanism remains uncertain.

For future work, more information is needed on the crust and mantle structures of subducting bathymetric features. Better constraints on the depth of hydration at trench outer-rise settings, both in regions with and without overthickened crust will dramatically improve our understanding of the role of slab mantle hydration on the genesis of intermediate depth seismicity. If our hypothesis is true, then intermediate depth seismicity adjacent to seismic gaps like the one in Peru can be used as a virtual thermometer to provide direct evidence of the temperature at a specific range of depths within a subducting plate at significant distance from the trench. These types of constraints could prove very valuable as ground truth for geodynamic models of subduction zone thermal structures.

DATA AVAILABILITY STATEMENT

Publicly available datasets were analyzed in this study. This data can be found here: https://doi.org/10.31905/D808B830, http://www.isc.ac.uk/iscbulletin/search/catalogue/.

AUTHOR CONTRIBUTIONS

LW is responsible for the original content and initial manuscript of this work. MC provided the Perplex modeling and contributions to the metamorphic petrology portions of this manuscript. LW, ML, and SB led the collection of the PULSE dataset. SB and LW were leaders in the collection of the CAUGHT dataset. SB, AK, and ML contributed to discussions and revisions of the manuscript. All authors read and approved the submitted version.

FUNDING

SB's contribution to this work was supported by NSF grant EAR 1723065.

ACKNOWLEDGMENTS

Thanks are due to Geoff Abers, Greg Hirth, and many others for insightful discussions and support for this manuscript. Many thanks to George Zandt for his leadership on the CAUGHT deployment and for all of his support and helpful suggestions over the years. We thank our reviewers for their constructive comments and the editor, VM, for his support of this manuscript.

SUPPLEMENTARY MATERIAL

The Supplementary Material for this article can be found online at: https://www.frontiersin.org/articles/10.3389/feart.2020.00244/full#supplementary-material

REFERENCES

Abers, G. A., Nakajima, J., van Keken, P. E., Kita, S., and Hacker, B. R. (2013). Thermal–petrological controls on the location of earthquakes within subducting plates. *Earth Planet. Sci. Lett.* 369, 178–187. doi: 10.1016/j.epsl.2013.03.022

Anderson, M., Alvarado, P., Zandt, G., and Beck, S. (2007). Geometry and brittle deformation of the subducting Nazca Plate, central Chile and Argentina. *Geophys. J. Int.* 171, 419–434. doi: 10.1111/j.1365-246x.2007.03483.x

Antonijevic, S. K., Wagner, L. S., Beck, S. L., Long, M. D., Zandt, G., and Tavera, H. (2016). Effects of change in slab geometry on the mantle flow and slab fabric in Southern Peru. *J. Geophys. Res.* 121, 7252–7270. doi: 10.1002/2016jb013064

Antonijevic, S. K., Wagner, L. S., Kumar, A., Beck, S. L., Long, M. D., Zandt, G., et al. (2015). The role of ridges in the formation and longevity of flat slabs. *Nature* 524, 212–215. doi: 10.1038/nature14648

Baxter, E. F., and Caddick, M. J. (2013). Garnet growth as a proxy for progressive subduction zone dehydration. *Geology* 41, 643–646. doi: 10.1130/g34004.1

Beck, S. L., Wallace, T., and Zandt, G. (2000). *Slab Geometry in the Southern Andes. International Federation of Digital Seismograph Networks. Dataset/Seismic Network*. doi: 10.7914/SN/YC_2000

Beck, S. L., and Zandt, G. (2007). *Lithospheric Structure and Deformation of the Flat Slab Region of Argentina. International Federation of Digital Seismograph Networks. Dataset/Seismic Network*. doi: 10.7914/SN/ZL_2007

Beck, S. L., Zandt, G., and Wagner, L. S. (2010). *Central Andean Uplift and the Geodynamics of the High Topography. International Federation of Digital Seismograph Networks. Dataset/Seismic Network*. doi: 10.7914/SN/ZG_2010

Bishop, B., Beck, S. L., Zandt, G., Wagner, L. S., Long, M. D., Antonijevic, S. K., et al. (2017). Causes and consequences of flat-slab subduction in southern Peru. *Geosphere* 13, 1392–1407. doi: 10.1130/GES01330.1

Bishop, B., Beck, S. L., Zandt, G., Wagner, L. S., Long, M. D., and Tavera, H. (2018). Foreland uplift during flat subduction: insights from the Peruvian Andes and Fitzcarrald Arch. *Tectonophysics* 73, 73–84. doi: 10.1016/j.tecto.2018.03.005

Bloch, W., John, T., Kummerow, J., Salazar, P., Krüger, O. S., and Shapiro, S. A. (2018). Watching dehydration: seismic indication for transient fluid pathways in the oceanic mantle of the subducting Nazca slab. *Geochem. Geophys. Geosyst.* 19, 3189–3207. doi: 10.1029/2018gc007703

Boneh, Y., Schottenfels, E., Kwong, K., van Zelst, I., Tong, X., Eimer, M., et al. (2019). Intermediate-depth earthquakes controlled by incoming plate hydration along bending-related faults. *Geophys. Res. Lett.* 46, 3688–3697. doi: 10.1029/2018gl081585

Bourdon, E., Eissen, J.-P., Gutscher, M.-A., Monzier, M., Hall, M. L., and Cotton, J. (2003). Magmatic response to early aseismic ridge subduction: the Ecuadorian margin case (South America). *Earth Planet Sci. Lett.* 205, 123–138. doi: 10.1016/s0012-821x(02)01024-5

Cai, C., Wiens, D. A., Shen, W., and Eimer, M. (2018). Water input into the Mariana subduction zone estimated from ocean-bottom seismic data. *Nature* 563, 389–394. doi: 10.1038/s41586-018-0655-4

Chernak, L. J., and Hirth, G. (2010). Deformation of antigorite serpentinite at high temperature and pressure. *Earth Planet. Sci. Lett.* 296, 23–33. doi: 10.1016/j.epsl.2010.04.035

Chernak, L. J., and Hirth, G. (2011). Syndeformational antigorite dehydration produces stable fault slip. *Geology* 39, 847–850. doi: 10.1130/g31919.1

Chiaradia, M., Müntener, O., and Beate, B. (2020). Effects of aseismic ridge subduction on the geochemistry of frontal arc magmas. *Earth Planet. Sci. Lett.* 531:115984. doi: 10.1016/j.epsl.2019.115984

Collot, J.-Y., Sanclemente, E., Nocquet, J.-M., Leprêtre, A., Ribodetti, A., Jarrin, P., et al. (2017). Subducted oceanic relief locks the shallow megathrust in central Ecuador. *J. Geophys. Res.* 122, 3286–3305. doi: 10.1002/2016JB013849

Connolly, J. A. D. (2005). Computation of phase equilibria by linear programming: a tool for geodynamic modeling and its application to subduction zone decarbonation. *Earth Planet. Sci. Lett.* 236, 524–541. doi: 10.1016/j.epsl.2005.04.033

Contreras-Reyes, E., Becerra, J., Kopp, H., Reichert, C., and Diaz-Naveas, J. (2014). Seismic structure of the north-central Chilean convergent margin: subduction erosion of a paleomagnetic arc. *Geophys. Res. Lett.* 41, 1523–1529. doi: 10.1002/2013gl058729

Contreras-Reyes, E., Grevemeyer, I., Watts, A. B., Flueh, E. R., Peirce, C., Moeller, S., et al. (2011). Deep seismic structure of the Tonga subduction zone: implications for mantle hydration, tectonic erosion, and arc magmatism. *J. Geophys. Res.* 116:2011JB008434. doi: 10.1029/2011JB008434

Contreras-Reyes, E., Grevemeyer, I., Watts, A. B., Planert, L., Flueh, E. R., and Peirce, C. (2010). Crustal intrusion beneath the Louisville hotspot track. *Earth Planet. Sci. Lett.* 289, 323–333. doi: 10.1016/j.epsl.2009.11.020

Contreras-Reyes, E., Muñoz-Linford, P., Cortes-Rivas, V., Bello-Gonzales, J. P., Ruiz, J. A., and Krabbenhoeft, A. (2019). Structure of the collision zone between the Nazca Ridge and the Peruvian convergent margin: geodynamic and seismotectonic implications. *Tectonics* 38, 3416–3435. doi: 10.1029/2019TC005637

Contreras-Reyes, E., Ruiz, J. A., Becerra, J., Kopp, H., Reichert, C., Maksymowicz, A., et al. (2015). Structure and tectonics of the central Chilean margin (31 – 33 S): implications for subduction erosion and shallow crustal seismicity. *Geophys. J. Int.* 203, 776–791. doi: 10.1093/gji/ggv309

DeMets, C., Gordon, R. G., and Argus, D. F. (2010). Geologically current plate motions. *Geophys. J. Int.* 181, 1–80. doi: 10.1111/j.1365-246x.2009.04491.x

Diener, J. F. A., and Powell, R. (2012). Revised activity–composition models for clinopyroxene and amphibole. *J. Metamorph. Geol.* 30, 131–142. doi: 10.1111/j.1525-1314.2011.00959.x

Dobson, D. P., Meredith, P. G., and Boon, S. A. (2002). Simulation of subduction zone seismicity by dehydration of serpentine. *Science* 298, 1407–1410. doi: 10.1126/science.1075390

Dzierma, Y., Rabbel, W., Thorwart, M. M., Flueh, E. R., Mora, M. M., and Alvarado, G. E. (2011). The steeply subducting edge of the Cocos Ridge: evidence from receiver functions beneath the northern talamanca range, south-central Costa Rica. *Geochem. Geophy. Geosys.* 12:3477. doi: 10.1029/2010GC003477

Dziewonski, A. M., and Anderson, D. L. (1981). Preliminary reference Earth model. *Phys. Earth Planet. Int.* 25, 297–356. doi: 10.1016/0031-9201(81)90046-7

Ferrand, T. P. (2019). Seismicity and mineral destabilizations in the subducting mantle up to 6 GPa, 200 km depth. *Lithos* 334, 205–230. doi: 10.1016/j.lithos.2019.03.014

Ferrand, T. P., Hilairet, N., Incel, S., Deldicque, D., Labrousse, L., Gasc, J., et al. (2017). Dehydration-driven stress transfer triggers intermediate-depth earthquakes. *Nat. Commun.* 8:15247.

Font, Y., Segovia, M., Vaca, S., and Theunissen, T. (2013). Seismicity patterns along the Ecuadorian subduction zone: new constraints from earthquake location in a 3-D a priori velocity model. *Geophys. J. Int.* 193, 263–286. doi: 10.1093/gji/ggs083

Fromm, R., Alvarado, P., Beck, S. L., and Zandt, G. (2006). The April 9, 2001 Juan Fernández Ridge (Mw 6.7) tensional outer-rise earthquake and its aftershock sequence. *J. Seismol.* 10, 163–170. doi: 10.1007/s10950-006-9013-3

Gailler, A., Charvis, P., and Flueh, E. R. (2007). Segmentation of the Nazca and South American plates along the Ecuador subduction zone from wide angle seismic profiles. *Earth Planet. Sci. Lett.* 260, 444–464. doi: 10.1016/j.epsl.2007.05.045

Gans, C. R., Beck, S. L., Zandt, G., Gilbert, H., Alvarado, P., Anderson, M., et al. (2011). Continental and oceanic crustal structure of the Pampean flat slab region, western Argentina, using receiver function analysis: new high-resolution results. *Geophys. J. Int.* 186, 45–58. doi: 10.1111/j.1365-246x.2011.05023.x

Gasc, J., Hilairet, N., Yu, T., Ferrand, T., Schubnel, A., and Wang, Y. (2017). Faulting of natural serpentinite: Implications for intermediate-depth seismicity. *Earth Plant. Sci. Lett.* 474, 138–147. doi: 10.1016/j.epsl.2017.06.016

Gasc, J., Schubnel, A., Brunet, F., Guillon, S., Mueller, H. J., and Lathe, C. (2011). Simultaneous acoustic emissions monitoring and synchrotron X-ray diffraction at high pressure and temperature: Calibration and application to serpentinite dehydration. *Phys. Earth Planet Int.* 189, 121–133. doi: 10.1016/j.pepi.2011.08.003

Giardini, D., and Woodhouse, J. H. (1984). Deep seismicity and modes of deformation in Tonga subduction zone. *Nature* 307, 505–509. doi: 10.1038/307505a0

Gilbert, H. (2008). *Eastern Sierras Pampeanas, Lithospheric Structure Above the Variably Dipping Nazca Slab. International Federation of Digital Seismograph Networks. Dataset/Seismic Network*. doi: 10.7914/SN/XH_2008

Graindorge, D., Calahorrano, A., Charvis, P., Collot, J.-Y., and Bethoux, N. (2004). Deep structures of the Ecuador convergent margin and the Carnegie Ridge, possible consequence on great earthquakes recurrence interval. *Geophys. Res. Lett.* 31:e018803. doi: 10.1029/2003GL018803

Green, H. W., and Houston, H. (1995). The mechanics of deep earthquakes. *Annu. Rev. Earth Planet. Sci.* 23, 169–213.

Grevemeyer, I., Ranero, C. R., and Ivandic, M. (2018). Structure of oceanic crust and serpentinization at subduction trenches. *Geosphere* 14, 395–410. doi: 10.1130/GES01537.1

Gutscher, M. A., Malavielle, J., Lallemand, S., and Collot, J.-Y. (1999a). Tectonic segmentation of the North Andean margin: impact of the Carnegie Ridge collision. *Earth Planet Sci. Lett.* 168, 255–270. doi: 10.1016/s0012-821x(99)00060-6

Gutscher, M. A., Olivet, J.-L., Aslanian, D., Eissen, J.-P., and Maury, R. (1999b). The "lost Inca Plateau": cause of flat subduction beneath Peru. *Earth Planet. Sci. Lett.* 171, 335–341. doi: 10.1016/s0012-821x(99)00153-3

Habermann, R. E., McCann, W. R., and Perin, B. (1986). Spatial seismicity variations along convergent plate boundaries. *Geophys. J. R. Astr. Soc.* 85, 43–68. doi: 10.1111/j.1365-246x.1986.tb05171.x

Hacker, B. R. (2008). H_2O subduction beyond arcs. *Geochem. Geophys. Geosyst.* 9:Q03001. doi: 10.1029/2007GC001707

Hacker, B. R., Peacock, S. M., Abers, G. A., and Holloway, S. D. (2003). Subduction factory -2. Are intermediate-depth earthquakes in subducting slabs linked to metamorphic dehydration reactions? *J. Geophys. Res.* 108:1129. doi: 10.1029/2001JB001129

Hagan, R. A., and Moberly, R. (1994). Tectonic effects of a subducting aseismic ridge: the subduction of the Nazca Ridge at the Peru trench. *Mar. Geophys. Res.* 16, 145–161. doi: 10.1007/bf01224757

Hampel, A. (2002). The migration history of the Nazca Ridge along the Peruvian active margin: a re-evaluation. *Earth Planet. Sci Lett.* 203, 665–679. doi: 10.1016/s0012-821x(02)00859-2

Hampel, A., Kukowski, N., Bialas, J., Huebscher, C., and Heinbockel, R. (2004). Ridge subduction at an erosive margin: the collision zone of the Nazca Ridge in southern Peru. *J. Geophys. Res.* 109:B02101. doi: 10.1029/2003JB002593

Holland, T. J. B., and Powell, R. (1998). An internally consistent thermodynamic data set for phases of petrological interest. *J. Metamorph. Geol.* 16, 309–343. doi: 10.1111/j.1525-1314.1998.00140.x

Hu, J., and Liu, L. (2016). Abnormal seismological and magmatic processes controlled by the tearing South American flat slabs. *Earth Planet Sci. Lett.* 450, 40–51. doi: 10.1016/j.epsl.2016.06.019

Husen, S., Quintero, R., Kissling, E., and Hacker, B. (2003). Subduction-zone structure and magmatic processes beneath Costa Rica constrained by local earthquake tomography and petrological modelling. *Geophys. J. Int.* 155, 11–32. doi: 10.1046/j.1365-246x.2003.01984.x

Hussong, D. M., Reed, T. B., and Bartlett, W. A. (1988). "SeaMarc II sonar imagery and bathymetry of the Nazca Plate and Peru forearc, ODP Leg 112," in *Proceedings of the ODP, Init. Repts., 112*, College Station, TX.

Incel, S., Hilairet, N., Labrousse, L., John, T., Deldicque, D., Ferrand, T., et al. (2017). Laboratory earthquakes triggered during eclogitization of lawsonite-bearing blueschist. *Earth Planet. Sci. Lett.* 459, 320–331. doi: 10.1016/j.epsl.2016.11.047

International Seismological Centre (2019). *On-Line Bulletin*. Thatcham: International Seismological Centre. doi: 10.31905/D808B830

John, T., Medvedev, S., Rüpke, L. H., Andersen, T. B., Podladchikov, Y. Y., and Austrheim, H. (2009). Generation of intermediate-depth earthquakes by self-localizing thermal runaway. *Nat. Geosci.* 2, 137–140. doi: 10.1038/ngeo419

Jung, H., Green, H., and Dobrzhinetskaya, L. (2004). Intermediate-depth earthquake faulting by dehydration embrittlement with negative volume change. *Nature* 428, 545–549. doi: 10.1038/nature02412

Kelemen, P. B., and Hirth, G. (2007). A periodic shear-heating mechanism for intermediate-depth earthquakes in the mantle. *Nature* 446, 787–790. doi: 10.1038/nature05717

Kim, D., Katayama, I., Wallis, S., Michibayashi, K., Miyake, A., Seto, Y., et al. (2015). Deformation microstructures of glaucophane and lawsonite in experimentally deformed blueschists: implications for intermediate-depth intraplate earthquakes. *J. Geophys. Res. Solid Earth* 120, 1229–1242. doi: 10.1002/2014jb011528

Kirby, S. (1995). Interslab earthquakes and phase changes in subducting lithosphere. *Rev. Geophys.* 33, 287–297.

Kirby, S. H., Engdahl, E. R., and Dehlinger, R. (1996). Intermediate depth intraslab earthquakes amd arc volcanism as physical expressions of crustal and uppermost mantle in subducting slabs. *Subduct. Top Bottom Geophys. Monogr. Ser.* 96, 347–355.

Kolarsky, R. A., Mann, P., and Monetero, P. W. (1995). "Island arc response to shallow subduction of the Cocos Ridge, Costa Rica," in *Geologic and Tectonic Development of the Caribbean Plate Boundary in Southern Central America*, , Vol. 295, ed. P. Mann (Boulder, CO: Geological Society of America), 235–262.

Kopp, H., Flueh, E. R., Papenberg, C., and Klaeschen, D. (2004). Seismic investigations of the O'Higgins seamount group and Juan Fernandez Ridge: aseismic ridge emplacement and lithosphere hydration. *Tectonics* 23:TC2009. doi: 10.1029/2003TC001590

Krabbenhoeft, A., Bialas, J., Kopp, H., Kukowski, N., and Hübscher, C. (2004). Crustal structure of the Peruvian continental margin from wide-angle seismic studies. *Geophys. J. Intern.* 159, 749–764. doi: 10.1111/j.1365-246x.2004.02425.x

Kukowski, N., Hampel, A., Hoth, S., and Bialas, J. (2008). Morphotectonic and morphometric analysis of the Nazca plate and the adjacent offshore Peruvian continental slope – Implications for submarine landscape evolution. *Mar. Geol.* 254, 107–120. doi: 10.1016/j.margeo.2008.05.017

Kumar, A., Wagner, L. S., Beck, S. L., Long, M. D., Zandt, G., Young, B., et al. (2016). Seismicity and state of stress in the central and southern Peruvian flat slab. *Earth Planet. Sci. Lett.* 441, 71–80. doi: 10.1016/j.epsl.2016.02.023

Lefeldt, M., Ranero, C. R., and Grevemeyer, I. (2012). Seismic evidence of tectonic control on the depth of water influx into incoming oceanic plates at subduction trenches. *Geochem. Geophys. Geosys.* 13:Q05013. doi: 10.1029/2012GC004043

Lim, H., Kim, Y., Clayton, R. W., and Thurber, C. H. (2018). Seismicity and structure of Nazca Plate subduction zone in southern Peru. *Earth Planet. Sci. Lett.* 498, 334–347. doi: 10.1016/j.epsl.2018.07.014

Lonsdale, P. (2005). Creation of the cocos and nazca plates by fission of the farallon plate. *Tectonophysics* 404, 237–264. doi: 10.1016/j.tecto.2005.05.011

MacMillan, I., Gans, P. B., and Alvarado, G. (2004). Middle Miocene to present plate tectonic history of the southern central american volcanic arc. *Tectonophysics* 404, 237–264.

Marcaillou, B., Collot, J.-Y., Ribodetti, A., d'Acremont, E., Mahamat, A.-A., and Alvarado, A. (2016). Seamount subduction at the North-Ecuadorian convergent margin: effects on structures, inter-seismic coupling and seismogenesis. *Earth Planet. Sci. Lett.* 433, 146–158. doi: 10.1016/j.epsl.2015.10.043

Marot, M., Monfret, T., Pardo, M., Ranalli, G., and Nolet, G. (2013). A double seismic zone in the subducting Juan Fernandez Ridge of the Nazca Plate (32° S), central Chile. *J. Geophys Res.* 118, 3462–3475. doi: 10.1002/jgrb.50240

Meade, C., and Jeanloz, R. (1991). Deep-focus earthquakes and recycling of water into the Earth's mantle. *Science* 252, 68–72. doi: 10.1126/science.252.5002.68

Michaud, F., Witt, C., and Royer, J.-Y. (2009). "Influence of the subduction of the Carnegie volcanic ridge on Ecuadorian geology: reality and fiction," in *Backbone of the Americas: Shallow Subduction, Plateau Uplift, and Ridge and Terrane Collision*, Vol. 204, eds S. M. Kay, V. A. Ramos, and W. R. Dickinson (Washington, DC: Geological Society of America Memoir). doi: 10.1130/2009.1204

Morell, K. D., Kirby, E., Fischer, D. M., and van Soest, M. (2012). Geomorphic and exhumational response of the Central American Volcanic arc to Cocos Ridge subduction. *J. Geophys. Res.* 117:4409. doi: 10.1029/2011JB008969

Moscoso, E., and Grevemeyer, I. (2015). Bending-related faulting of the incoming oceanic plate and its effect on lithospheric hydration and seismicity: a passive an active seismological study offshore Maule, Chile. *J. Geodyn.* 90, 58–70. doi: 10.1016/j.jog.2015.06.007

Mueller, R. D., Sdrolias, M., Gaina, C., and Roest, W. R. (2008). Age, spreading rates, and spreading asymmetry of the world's ocean crust. *Geochem. Geophys. Geosys.* 9:Q04006. doi: 10.1029/2007GC001743

Ohuchi, T., Lei, X., Ohfuji, H., Higo, Y., Tange, Y., Sakai, T., et al. (2017). Intermediate-depth earthquakes linked to localized heating in dunite and harzburgite. *Nat. Geosci.* 10, 771–776. doi: 10.1038/ngeo3011

Okazaki, K., and Hirth, G. (2016). Dehydration of lawsonite could directly trigger earthquakes in subducting oceanic crust. *Nature* 530, 81–84. doi: 10.1038/nature16501

Padrón-Navarta, J. A., Sánchez-Vizcaíno, V. L., Hermann, J., Connolly, J. A. D., Garrido, C. J., Gómez-Pugnaire, M. T., et al. (2013). Tschermak's substitution in antigorite and consequences for phase relations and water liberation in high-grade serpentinites. *Lithos* 178, 186–196. doi: 10.1016/j.lithos.2013.02.001

Peacock, S. M. (2001). Are the lower planes of double seismic zones caused by serpentine dehydration in subducting oceanic mantle? *Geology* 29, 299–302.

Peacock, S. M., van Keken, P. E., Holloway, S. D., Hacker, B. R., Abers, G. A., and Fergason, R. L. (2005). Thermal structure of the Costa Rica–Nicaragua subduction zone. *Phys. Earth Planet. Inter.* 149, 187–200. doi: 10.1016/j.pepi.2004.08.030

PeruSE (2013). *Peru Subduction Experiment*. Pasadena: Caltech.

Pilger, R. H. (1981). Plate reconstructions, aseismic ridges, and low-angle subduction beneath the Andes. *Geol. Soc. Am. Bull.* 29, 448–456.

Plümper, O., Botan, A., Los, C., Liu, Y., Malthe-Sørenssen, A., and Jamtveit, B. (2017). Fluid-driven metamorphism of the continental crust governed by nanoscale fluid flow. *Nat. Geosci.* 10, 685–690. doi: 10.1038/ngeo3009

Poli, P., Prieto, G., Rivera, E., and Ruiz, S. (2016). Earthquakes initiation and thermal shear instability in the Hindu Kush intermediate depth nest. *Geophys. Res. Lett.* 43, 1537–1542. doi: 10.1002/2015gl067529

Prieto, G. A., Florez, M., Barrett, S. A., Beroza, G. C., Pedraza, P., Blanco, J. F., et al. (2013). Seismic evidence for thermal runaway during intermediate-depth earthquake rupture. *Geophys. Res. Lett.* 40, 6064–6068. doi: 10.1002/2013gl058109

Proctor, B., and Hirth, G. (2015). Role of pore fluid pressure on transient strength changes and fabric development during serpentine dehydration at mantle conditions: implications for subduction-zone seismicity. *Earth Planet. Sci. Lett.* 421, 1–12. doi: 10.1016/j.epsl.2015.03.040

Proctor, B., and Hirth, G. (2016). Ductile to brittle" transition in thermally stable antigorite gouge at mantle pressures. *J. Geophys. Res. Solid Earth* 121, 1652–1663. doi: 10.1002/2015jb012710

Protti, M., Guendel, F., and McNally, K. (1994). The geometry of the Wadati-Benioff zone under southern Central America and its tectonic significance: results from a high-resolution local seismographic network. *Phys. Earth Planet. Int.* 84, 271–287. doi: 10.1016/0031-9201(94)90046-9

Raleigh, C. B., and Paterson, M. S. (1965). Experimental deformation of serpentinite and its tectonic implications. *J. Geophys. Res.* 70, 3965–3985. doi: 10.1029/jz070i016p03965

Ranero, C. R., Phipps Morgan, J., McIntosh, K., and Reichert, C. (2003). Bending-related faulting and mantle serpentinization at the Middle America trench. *Nature* 425, 367–373. doi: 10.1038/nature01961

Ranero, C. R., Villaseñor, A., Morgan, J. P., and Weinrebe, W. (2005). Relationship between bend-faulting at trenches and intermediate-depth seismicity. *Geochem. Geophys. Geosys.* 6:Q12002. doi: 10.1029/2005GC000997

Ringwood, A. E. (1982). Phase transformations and differentiation in subducted lithosphere: implications for mantle dynamics, basalt petrogenesis, and crustal evolution. *J. Geol.* 90, 611–643. doi: 10.1086/628721

Robinson, A. H., Peirce, C., and Funnell, M. J. (2018). Construction and subduction of the Louisville Ridge, SW Pacific – insights from wide-angle seismic data modelling. *Geophys. J. Int.* 214, 2222–2245. doi: 10.1093/gji/ggy397

Rosenbaum, G., Giles, D., Saxon, M., Betts, P. G., Weinberg, R. F., and Duboz, C. (2005). Subduction of the Nazca Ridge and the Inca Plateau: insights into the formation of ore deposits in Peru. *Earth Planet. Sci. Lett.* 239, 18–32. doi: 10.1016/j.epsl.2005.08.003

Rosenbaum, G., Sandiford, M., Caulfield, J., and Garrison, J. M. (2018). A trapdoor mechanism for slab tearing and melt generation in the northern Andes. *Geology* 47, 23–26. doi: 10.1130/g45429.1

Sallares, V., Charvis, P., Flueh, E., and Bialas, J. (2003). Seismic structure of Cocos and Mapelo volcanic ridges and implications for hot spot – ridge interaction. *J. Geophys. Res.* 108:2431. doi: 10.1029/2003JB002431

Sallares, V., Charvis, P., Flueh, E., and Bialas, J. (2005). Seismic structure of the Carnegie ridge and the nature of the Galapagos hotspot. *Geophys. J. Int.* 161, 763–788. doi: 10.1111/j.1365-246x.2005.02592.x

Sandiford, D., Moresi, L., Sandiford, M., and Yang, T. (2019). Geometric controls on flat slab seismicity. *Earth Planet. Sci. Lett.* 527:115787. doi: 10.1016/j.epsl.2019.115787

Scholtz, C. H., and Small, C. (1997). The effect of seamount subduction on seismic coupling. *Geology* 25, 487–490.

Scire, A., Zandt, G., Beck, S., Long, M., Wagner, L., Minaya, E., et al. (2015). Imaging the transition from flat to normal subduction: variations in the structure of the Nazca slab and upper mantle under southern Peru and northwestern Bolivia. *Geophys. J. Int.* 204, 457–479. doi: 10.1093/gji/ggv452

Shillington, D. J., Bécel, A., Nedimoviæ, M. R., Kuehn, H., Webb, S. C., Abers, G. A., et al. (2015). Link between plate fabric, hydration and subduction zone seismicity in Alaska. *Nat. Geosci.* 8, 961–964. doi: 10.1038/ngeo2586

Staudigel, H., Hart, S. R., Schmincke, H.-U., and Smith, B. M. (1989). Cretaceous ocean crust at DSDP Sites 417 and 418: carbon uptake from weathering versus loss by magmatic outgassing. *Geochim. Cosmochim. Acta* 53, 3091–3094. doi: 10.1016/0016-7037(89)90189-0

Staudigel, H., Plank, T., White, B., and Schmincke, H.-U. (1996). "Geochemical fluxes during seafloor alteration of the basaltic upper oceanic crust: DSDP Sites 417 and 418," in *Subduction: Top to Bottom*, ed. E. Bebout (Washington, DC: American Geophyiscal Union), 19–38. doi: 10.1029/gm096p0019

van Hunen, J., van den Berg, A. P., and Vlaar, N. J. (2002). On the role of subducting oceanic plateaus in the development of shallow flat subduction. *Tectonophysics* 352, 317–333. doi: 10.1016/s0040-1951(02)00263-9

von Huene, R., Corvalan, J., Flueh, E. R., Hinz, K., Korstgard, J., Ranero, C. R., et al. (1997). Tectonic control of the subducting juan fernandez ridge on the andean margin near Valparaiso. *Chile. Tecton.* 16, 474–488. doi: 10.1029/96tc03703

von Huene, R., Ranero, C. R., Weinrebe, W., and Hinz, K. (2000). Quaternary convergent margin tectonics of Costa Rica, segmentation of the Cocos Plate, and Central American volcanism. *Tectonics* 19, 314–334. doi: 10.1029/1999tc001143

Wagner, L. S., Beck, S. L., and Long, M. D. (2010). *PerU Lithosphere and Slab Experiment. International Federation of Digital Seismograph Networks. Dataset/Seismic Network*. doi: 10.7914/SN/ZD_2010

Wagner, L. S., and Okal, E. A. (2019). The Pucallpa nest and its constraints on the geometry of the Peruvian Flat Slab. *Tectonophysics* 762, 97–108. doi: 10.1016/j.tecto.2019.04.021

Walther, C. H. E. (2003). The crustal structure of the Cocos Ridge off Costa Rica. *J. Geophys. Res.* 108:888. doi: 10.1029/2001JB000888

Watts, A. B., Weissel, J. K., Duncan, R. A., and Larson, R. L. (1988). Origin of the Louisville Ridge and its relationship to the Eltanin fracture zone system. *J. Geophys. Res.* 93, 3051–3077.

Woods, M. T., and Okal, E. A. (1994). The structure of the Nazca ridge and Sala y Gomez seamount chain from the dispersion of Rayleigh waves. *Geophys. J. Int.* 117, 205–222. doi: 10.1111/j.1365-246x.1994.tb03313.x

Yamasaki, T., and Seno, T. (2003). Double seismic zone and dehydration embrittlement of the subducting slab. *J. Geophys. Res.* 108:2212. doi: 10.1029/2002JB001918

Yañez, G. A., Cembrano, J., Pardo, M., Ranero, C. R., and Selles, D. (2002). The challenger – Juan Fernandez – Maipo major tectonic transition of the Nazca – Andean subduction system at 33 – 34 S: geodynamic evidence and implications. *J. South Am. Earth Sci.* 15, 23–38. doi: 10.1016/s0895-9811(02)00004-4

Yañez, G. A., Ranero, C. R., von Huene, R., and Diaz, J. (2001). Magnetic anomaly interpretation across the southern central Andes (32 – 34 S): the role of the Juan Fernandez Ridge in the late Tertiary evolution of the margin. *J. Geophys Res.* 106, 6325–6345. doi: 10.1029/2000jb900337

Yepes, H., Audin, L., Alvarado, A., Beauval, C., Aguilar, J., Font, Y., et al. (2016). A new view for the geodynamics of Ecuador: implication in seismogenic source definition and seismic hazard assessment. *Tectonics* 35, 1249–1279. doi: 10.1002/2015tc003941

Zhan, Z. (2017). Gutenberg–Richter law for deep earthquakes revisited: a dual-mechanism hypothesis. *Earth Planet. Sci. Lett.* 461:30. doi: 10.1016/j.epsl.2016.12.030

Conflict of Interest: The authors declare that the research was conducted in the absence of any commercial or financial relationships that could be construed as a potential conflict of interest.

frontiers in Earth Science

ORIGINAL RESEARCH
published: 16 July 2020
doi: 10.3389/feart.2020.00254

Contributions of Grain Damage, Thermal Weakening, and Necking to Slab Detachment

Marcel Thielmann[1]* *and Stefan M. Schmalholz*[2]

[1] Bayerisches Geoinstitut, Universität Bayreuth, Bayreuth, Germany, [2] Institut des Sciences de la Terre (ISTE), Université de Lausanne, Lausanne, Switzerland

We investigate the impact of three coupled weakening mechanisms on the viscous detachment of a stalled lithospheric slab: structural weakening due to necking, material weakening due to grain size reduction, using a two-phase grain damage model, and thermal weakening due to shear heating (thermal damage). We consider a combined flow law of dislocation and diffusion creep. To understand and quantify the coupling of these three nonlinear weakening processes, we derive a mathematical model, which consists of three coupled nonlinear ordinary differential equations describing the evolution of slab thickness, grain size, and temperature. With dimensional analysis, we determine the dimensionless parameters which control the relative importance of the three weakening processes and the two creep mechanisms. We derive several analytical solutions for end-member scenarios that predict the detachment time, that is the duration of slab detachment until slab thickness becomes zero. These analytical solutions are then tested against numerical solutions for intermediate cases. The analytical solutions are accurate for end-member scenarios where one of the weakening mechanisms and one of the creep mechanisms is dominant. Furthermore, we use numerical solutions of the system of equations to systematically explore the parameter space with a Monte Carlo approach. The numerical approach shows that the analytical solutions typically never deviate by more than 50% from the numerical ones, even for scenarios where all three weakening and both creep mechanisms are important. When both grain and thermal damage are important, the two damage processes generate a positive feedback loop resulting in the fastest detachment times. For Earth conditions, we find that the onset of slab detachment is controlled by grain damage and that during later stages of slab detachment thermal weakening becomes increasingly important and can become the dominating weakening process. We argue that both grain and thermal damage are important for slab detachment and that both damage processes could also be important for lithosphere necking during continental rifting leading to break-up and ocean formation.

Keywords: slab detachment, grain size evolution, shear heating, model, deep earthquakes

Edited by:
Jeroen Van Hunen,
Durham University, United Kingdom

Reviewed by:
Sébastien Merkel,
Lille University of Science and Technology, France
Mark Behn,
Boston College, United States

***Correspondence:**
Marcel Thielmann
marcel.thielmann@uni-bayreuth.de

Specialty section:
This article was submitted to Solid Earth Geophysics, a section of the journal Frontiers in Earth Science

Received: *31 January 2020*
Accepted: *09 June 2020*
Published: *16 July 2020*

Citation:
Thielmann M and Schmalholz SM (2020) Contributions of Grain Damage, Thermal Weakening, and Necking to Slab Detachment. Front. Earth Sci. 8:254. doi: 10.3389/feart.2020.00254

1. INTRODUCTION

Since the establishment of plate tectonic theory and early seismicity observations at subduction systems (Isacks and Molnar, 1969), *slab detachment*, also often called *slab break-off*, is considered as a prominent process associated with subduction systems. During slab detachment, the lower part of a subducting lithospheric plate detaches from its upper portion and sinks into the mantle. There is overall agreement that buoyancy forces within subducting slabs induce extensional stresses which can result in slab detachment. This process has been suggested to cause seismicity patterns in subduction zones (Isacks and Molnar, 1969), magmatism during orogeny (Davies and von Blanckenburg, 1995), rapid surface uplift (e.g., Fox et al., 2015; Sternai et al., 2019), the transition from Flysch to Molasse sedimentation in the European Alps (Schlunegger and Kissling, 2015), and abrupt changes in plate motions (McKenzie, 1969; Bercovici et al., 2015). The abruptness of these events suggests that slab detachment has to occur in equally short timescales. The occurrence of slab detachment has been suggested for various regions, among them the Mediterranean (Wortel and Spakman, 2000), the Pamir-Hindu Kush region (Kufner et al., 2016), and the European Alps (Lippitsch et al., 2003). However, geodynamic interpretations that consider slab detachment as controlling process are frequently contentious (see Garzanti et al., 2018, for a review). Also, indirect observations of slab detachment based on seismic tomography are sometimes contradictory, such as in the Central and Western Alps (Kästle et al., 2020), where seismic tomography is interpreted as showing a detached slab (Lippitsch et al., 2003) but also a continuous slab (Zhao et al., 2016). Some of the controversies concerning slab detachment are also due to the fact that the thermo-mechanical process of slab detachment is still incompletely understood.

Using simplified models, Wong A Ton and Wortel (1997) found that the rheology of the subducting lithosphere is the most important parameter affecting slab detachment, while buoyancy and resistive forces are less significant. To investigate the impact of additional processes, such as brittle failure, mineral phase transitions, partial melting, grain size reduction, or shear heating, and to study the inherent three-dimensionality of slab detachment, complex numerical models have been conducted in both 2D (e.g., Gerya et al., 2004; Andrews and Billen, 2009; Duretz et al., 2011) and 3D (e.g., Burkett and Billen, 2010; van Hunen and Allen, 2011; Capitanio and Replumaz, 2013; Duretz et al., 2014; von Tscharner et al., 2014; Chen and Gerya, 2016; Magni et al., 2017; Pusok et al., 2018). In general, these models confirm the finding of Wong A Ton and Wortel (1997) that slab rheology is the most important parameter controlling slab detachment. However, when standard olivine rheologies are employed, slab detachment is usually slow and occurs on time scales of tens of millions of years, thus resulting in large detachment depths (e.g., Schott and Schmeling, 1998; van Hunen and Allen, 2011), contrary to what is suggested from tomographic images and seismicity patterns. However, additional mechanisms have been suggested to significantly accelerate slab detachment, such as weakening due to grain size reduction (Bercovici et al., 2015, 2019; Bellas et al., 2018), elaborated viscoelastoplastic rheology models (Duretz et al., 2011, 2012), preexisting weak zones (Burkett and Billen, 2010) or thermal weakening due to shear heating (Gerya et al., 2004; Duretz et al., 2012). Shear heating can efficiently localize deformation and form large-scale shear zones under lithospheric deformation conditions (Thielmann and Kaus, 2012; Duretz et al., 2015, 2019; Kiss et al., 2019). In particular, the combined action of shear heating and grain size reduction may result in significant weakening of the slab and associated strain localization (Thielmann et al., 2015; Foley, 2018), which may even trigger earthquakes in slab detachment settings (Thielmann, 2018). Therefore, it seems important to include different ductile weakening effects in models of slab detachment. Shear heating and grain size reduction have been shown to result in comparable weakening (Duretz et al., 2012; Bercovici et al., 2015), but it is not yet clear which of these mechanisms ultimately control slab detachment under what conditions and whether these processes are competitive or collaborative processes (Kameyama et al., 1997; Thielmann et al., 2015; Foley, 2018; Thielmann, 2018).

While 2D and 3D numerical models capture the complex geometrical interactions during slab detachment, their computational expense makes it difficult to systematically investigate the impact of different weakening mechanisms and their mutual feedbacks. Furthermore, due to the many equations and parameters involved, such 2D and 3D models are often little transparent. In contrast, simple 0D and 1D models are usually more transparent and have proven to provide fundamental physical insight into the slab detachment process and to efficiently test the impact of different model parameters (Schmalholz, 2011; Duretz et al., 2012; Bercovici et al., 2015, 2019; Ribe and Xu, 2020).

While slab detachment is likely dominated by viscous necking, it has also been invoked to explain deep seismicity in various regions on Earth, such as e.g., the Hindu-Kush (Kufner et al., 2017), the Vrancea region (Mitrofan et al., 2016), or the Alboran slab in the Mediterranean (Sun and Bezada, 2020). The mechanisms resulting in the observed seismicity are still contentious, as brittle failure at this depth seems to be unlikely due to the high pressures and temperatures. However, since rocks are intrinsically viscoelastic, a significant local increase of strain rates during slab detachment could shift the rock deformation mechanism from effectively viscous to effectively elastic, and hence potentially cause brittle failure. Currently, it is still unclear which mechanism(s) result in seismicity generation, but two mechanisms are frequently favored, namely dehydration embrittlement and thermal runaway (see Zhan, 2019, and citations therein). Some intermediate-depth earthquakes pose, despite their depth, a significant seismic hazard (Frohlich, 2006) and it is hence important to identify their rupture mechanisms and the conditions favoring their occurrence.

Here, we investigate viscous slab detachment for a combination of dislocation creep and diffusion creep flow laws. We quantify the coupling of three nonlinear weakening mechanisms during slab detachment: (1) structural weakening due to a necking instability (see Schmalholz and Mancktelow, 2016, and citations therein) causing localized thinning of the slab, (2) weakening due to grain size reduction and grain size sensitive diffusion creep, referred to here as grain damage, and (3) weakening due to shear heating and temperature sensitive effective rock viscosities, referred to here as thermal damage. We consider a simple slab detachment setting and use a simple 0D mathematical model that allows us to comprehensively examine the parameter space. We derive a system of three coupled nonlinear differential equations that describe the evolution of grain size, temperature and slab thickness. We apply dimensional analysis to determine the controlling non-dimensional parameters. We further derive several analytical solutions for the duration of slab detachment, that is when the slab thickness is zero, for end-member scenarios where one of the weakening mechanisms or one of the two flow laws is dominant. Using a Monte Carlo simulation with 2×10^5 simulations, we are able to determine the most important parameters controlling slab detachment. Based on the results from these simulations, we derive empirical relationships that can be used to predict detachment times for a given set of parameters. Finally, we determine which mechanism is most likely to govern slab detachment.

2. METHODS

In this section, we introduce our detachment model (section 2.1), together with the equations governing the evolution of slab thickness. In sections 2.2–2.4, we introduce the governing equations for rheology, for the evolution of grain interface curvature (as a proxy of grain size) and for the temperature evolution. In section 2.5, we non-dimensionalize the governing equations to derive a set of non-dimensional equations and parameters that will be used to investigate the impact of different parameters on the detachment process. The meaning of the derived non-dimensional parameters is discussed in section 2.6.

2.1. Detachment Model

We consider a vertical slab with initially zero velocity attached to a rigid surface; a so-called stalled slab. The slab has a length H, width D_0 and density ρ_1, which is larger than the density ρ_2 of the surrounding mantle (see also **Figure 1**). Due to this density difference $\Delta\rho = \rho_1 - \rho_2$, a negative buoyancy force per unit length, $F_B = \Delta\rho g D_0 H$, is induced, which causes the slab to sink and to stretch. For this configuration, localized thinning and necking will develop in the upper region of the slab where the buoyancy-driven stresses are highest. The extensional strain rate $\dot{\varepsilon}$ is related to the temporal evolution of the slab thickness D at the necking region by equation (Schmalholz, 2011):

$$\dot{\varepsilon} = -\frac{1}{D}\frac{dD}{dt} \tag{1}$$

where t is time. As the buoyancy force remains constant and the slab is considered much stronger than the surrounding, the deviatoric stress in the necking region is half the total stress, F_B/D, and is given by (Turcotte and Schubert, 2014)

$$\tau = \frac{1}{2}\frac{F_B}{D} \tag{2}$$

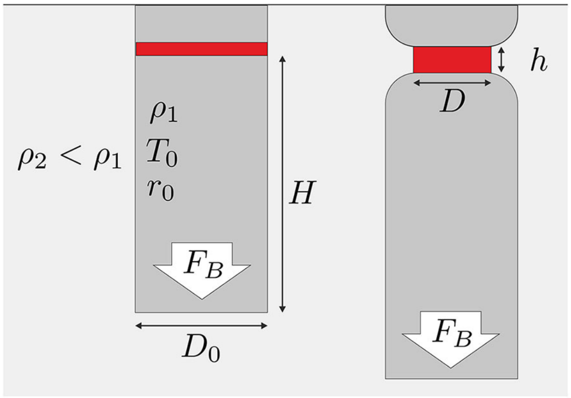

FIGURE 1 | Model setup. **(Left)** Initial configuration of a slab with length H and thickness D_0. The red region is the necking region with height h_0 and thickness D_0. **(Right)** Later stage, at which the thickness D of the necking region is significantly reduced and its height h increased.

The initial state of the system is thus given by the initial stress $\tau_0 = \frac{1}{2}\frac{\rho g H D_0}{D_0}$ and the mean temperature T_0 of the slab. We will link the above two equations by rheological flow laws, which are mathematical relations between $\dot{\varepsilon}$ and τ and are described in the next section.

2.2. Rheology

The buoyancy force F_B induces deformation in the stalled slab. We assume that deformation is governed by a viscous composite rheology consisting of grain size insensitive dislocation and grain size sensitive diffusion creep (e.g., Hirth and Kohlstedt, 2003; Billen and Hirth, 2007; Kohlstedt and Hansen, 2015):

$$\dot{\varepsilon} = A_{dis} e^{-\frac{Q_{dis}}{T}} \tau^{n} + A_{dif} e^{-\frac{Q_{dif}}{T}} \mathcal{R}^{-m} \tau \tag{3}$$

where the strain rate $\dot{\varepsilon}$ is a function of stress τ, temperature T, and grain size $\mathcal{R}$. A_{dis} and A_{dif} are rheological prefactors, n is the stress exponent of dislocation creep and m the grain size exponent (see also **Table 1** for the definition of the different rheological parameters). Q_{dis} and Q_{dif} are the respective activation enthalpies divided by the gas constant R given by:

$$Q_i = \frac{E_i + PV_i}{R} \tag{4}$$

where P is pressure and E_i, V_i are activation energy and volume, respectively. The index i denotes either diffusion or dislocation creep. It is useful to define a transition grain size $\mathcal{R}_t$ at which the contributions from dislocation and diffusion creep equally contribute to deformation:

$$\mathcal{R}_t = \left(\frac{A_{dis} e^{-\frac{Q_{dis}}{T}} \tau^{n}}{A_{dif} e^{-\frac{Q_{dif}}{T}} \tau} \right)^{-\frac{1}{m}} \tag{5}$$

TABLE 1 | Material properties used in this study.

	Variable	Symbol	Value	Unit
Dislocation creep	Prefactor	A_{dis}	1.1×10^5	$\mathrm{MPa}^{-n}\ \mathrm{s}^{-1}$
	Activation energy	E_{dis}	530	$\mathrm{kJ\ mol}^{-1}$
	Activation volume	V_{dis}	14×10^{-6}	$\mathrm{m}^3\ \mathrm{mol}^{-1}$
	thermal parameter	Q_{dis}	$\frac{E_{dis}+V_{dis}P}{R}$	K
	Stress exponent	n	3.5	
Diffusion creep	Prefactor	A_{dif}	1.5×10^9	$\mu\mathrm{m}^m\ \mathrm{MPa}^{-1}\mathrm{s}^{-1}$
	Activation energy	E_{dif}	300	$\mathrm{kJ\ mol}^{-1}$
	Activation volume	V_{dif}	6×10^{-6}	$\mathrm{m}^3\ \mathrm{mol}^{-1}$
	thermal parameter	Q_{dif}	$\frac{E_{dif}+V_{dif}P}{R}$	K
	Grain size exponent	m	3	
Interface coarsening	Prefactor	$\mathcal{G}_{I,0}$		$\mu\mathrm{m}^q\ \mathrm{MPa}^{-1}\mathrm{s}^{-1}$
	Activation energy	E_g	300	$\mathrm{kJ\ mol}^{-1}$
	Activation volume	V_g	6×10^{-6}	$\mathrm{m}^3\ \mathrm{mol}^{-1}$
	thermal parameter	Q_g	$\frac{E_g+V_gP}{R}$	K
	Coarsening exponent	q	4	
Other	Reference density	ρ	3300	$\mathrm{kg/m}^3$
	Heat capacity	c	1050	$\mathrm{J\ kg}^{-1}\mathrm{K}^{-1}$
	Thermal expansion coefficient	α	3×10^{-5}	

Creep parameters are taken from Hirth and Kohlstedt (2003), while interface coarsening parameters are taken from Bercovici and Ricard (2012).

Using this transition grain size, Equation (3) can be rewritten as:

$$\dot{\varepsilon} = A_{dis} e^{-\frac{Q_{dis}}{T}} \tau^n \left[1 + \left(\frac{\mathcal{R}_t}{\mathcal{R}}\right)^m\right] \tag{6}$$

where the ratio $\frac{\mathcal{R}_t}{\mathcal{R}}$ indicates whether dislocation creep ($\frac{\mathcal{R}_t}{\mathcal{R}} < 1$) or diffusion creep ($\frac{\mathcal{R}_t}{\mathcal{R}} > 1$) is the dominant deformation mechanism.

2.3. Grain Size Evolution

Grain size can significantly affect rock rheology if it is sufficiently small and if it changes with progressive deformation. The evolution of grain size is therefore crucial to determine the transient response of the rock to an applied stress. The reduction of the effective viscosity, quantifying viscous strength, due to a reduction in grain size is frequently termed grain damage. As mantle rocks are polymineralic, consisting of mostly olivine and pyroxene, we here treat grain size evolution using the two-phase grain size evolution law of Bercovici and Ricard (2012). This evolution law takes into account that a rock does not consist of a single mineral phase, but of at least two phases, which in the case of the mantle lithosphere corresponds to an olivine-pyroxene mixture. Due to the presence of pyroxene, the grain boundary mobility of olivine is strongly reduced due to Zener pinning. Due to this effect, the curvature of the grain boundaries is also significantly distorted, as illustrated in **Figure 2**. If we consider a single grain with radius $\mathcal{R}_1$, its interface curvature without the effect of secondary particles would equal $\mathcal{R}_1$. However, due to the presence of secondary particles with radius $\mathcal{R}_2$, this interface is significantly distorted and its mean interface curvature, or roughness, is quantified by r. In the "pinned state" limit, the system is assumed to be in a state where grain size evolution is controlled by the evolution of interface roughness r. Grain damage is therefore solely controlled by grain interface damage in the pinned state limit. Although we focus here on grain interface damage, we will use the more general term grain damage throughout the manuscript. If the secondary phase is dispersed (which we assume here), this effect results in interface roughness depending on the grain size $\mathcal{R}_i$ of each phase as (see Bercovici and Ricard, 2012, Appendix G):

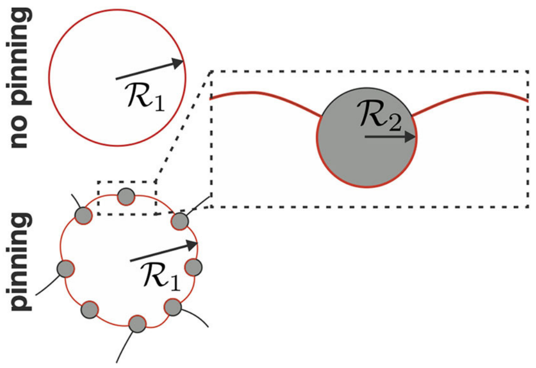

FIGURE 2 | Sketch of the impact of Zener pinnning on grain interface roughness (after Bercovici and Ricard, 2012; Mulyukova and Bercovici, 2019). Shown is a sketch of a grain surrounded by secondary particles, with a zoom on the interface around one of the secondary particles.

$$r = \sqrt{\mathfrak{c} \sum_i (1-\phi_i)^2 \mathcal{R}_i^2} \tag{7}$$

where $\mathfrak{c} = \frac{3\lambda_4}{160\lambda_2} = \frac{3}{160}e^{6\sigma^2}$ is a factor which depends on the half width σ of the lognormal grain size distributions, which are assumed to have the same shape (see Bercovici and Ricard, 2012, Appendix F.4). Consequently, the grain sizes of both phases depend on r as (e.g., Bercovici and Ricard, 2012; Bercovici et al., 2015; Mulyukova and Bercovici, 2018):

$$\mathcal{R}_i = \frac{r}{\sqrt{\mathfrak{c}\,(1-\phi_i)}}, \tag{8}$$

where ϕ_i are the respective volume fractions of the two phases. With this definition, the mean grain size $\overline{\mathcal{R}}$ can be computed as:

$$\overline{\mathcal{R}} = \sum_i \frac{r\phi_i}{\sqrt{\mathfrak{c}\,(1-\phi_i)}} \tag{9}$$

Assuming a pyroxene content of 40 % and a half width of the lognormal grain size distributions of 0.8 (e.g., Bercovici and Ricard, 2013), the mean grain size is given by $\overline{\mathcal{R}} \approx \frac{\pi}{2}r$. Additionally assuming that both mineral phases have approximately the same rheological properties, we can—in analogy to the transition grain size $\mathcal{R}_t$ (Equation 5)—define a transition interface roughness r_t, which only differs by a constant prefactor $\left(\frac{\pi}{2}\right)^m$ from the transition grain size $\mathcal{R}_t$:

$$r_t = \left(\frac{A_{dis}e^{-\frac{Q_{dis}}{T}}\tau^n}{\left(\frac{\pi}{2}\right)^{-m} A_{dif}e^{-\frac{Q_{dif}}{T}}\tau}\right)^{-\frac{1}{m}} \tag{10}$$

Therefore, the composite rheology can be re-written in the same manner as Equation (6), only replacing $\frac{\mathcal{R}}{\mathcal{R}_t}$ with $\frac{r}{r_t}$:

$$\dot{\varepsilon} = A_{dis}e^{-\frac{Q_{dis}}{T}}\tau^n\left[1+\left(\frac{r_t}{r}\right)^m\right] \tag{11}$$

In the "pinned state", the grain size of either mineral phase is assumed to be solely determined by the interface curvature r. The interface curvature r evolves with time according to (Bercovici and Ricard, 2012):

$$\frac{dr}{dt} = \frac{\eta\mathcal{G}_I}{qr^{q-1}} - \frac{\lambda_I r^2}{\gamma\eta}\Psi \tag{12}$$

where q is an effective grain growth exponent, γ the interfacial energy, $\eta = 3\phi_1\phi_2$ is a parameter that depends on the volume fraction ϕ_i of both phases, $\mathcal{G}_{\mathcal{I}}$ is the temperature-dependent interface coarsening rate given by (e.g., Mulyukova and Bercovici, 2017):

$$\mathcal{G}_I = \mathcal{G}_{I,0}e^{-\frac{Q_g}{T}} \tag{13}$$

The deformational work rate Ψ, given by the product of $\dot{\varepsilon}$ and τ, is:

$$\Psi = 2A_{dis}\tau^{n+1}e^{-\frac{Q_{dis}}{T}}\left[1+\left(\frac{r_t}{r}\right)^m\right] \tag{14}$$

Both the work done in dislocation and diffusion creep contribute to grain damage and hence interface roughness. Last, the partitioning factor λ_I determines the relative amount of deformational work that is used for grain damage. This factor is relatively unconstrained and is most likely dependent on temperature (Rozel et al., 2011; Mulyukova and Bercovici, 2017), phase dispersion (Bercovici and Ricard, 2016; Bercovici and Skemer, 2017) as well as dislocation density (Chrysochoos and Belmahjoub, 1992; Holtzman et al., 2018). Given the missing constraints on most of these dependencies, we neglect these effects for simplicity.

In steady state, when grain damage and recovery balance each other such that $dr/dt = 0$, we can define a steady state roughness r_s that has to fulfill the following equation:

$$r_s^{q+1}\left[1+\left(\frac{r_t}{r_s}\right)^m\right] = \frac{\gamma\eta^2\mathcal{G}_{I,0}}{2q\lambda_I A_{dis}\tau^{n+1}}e^{-\frac{Q_{dis}}{T}\left(\frac{Q_g}{Q_{dis}}-1\right)} \tag{15}$$

This equation is not analytically solvable for r_s for the general case. However, we can consider two particular cases, one where deformation is dominated by dislocation creep and another where diffusion creep is dominant. In the dislocation-dominated case ($r_s \gg r_t$), the steady state interface roughness is given by:

$$r_{s,dis} = \left(\frac{\gamma\eta^2\mathcal{G}_{I,0}}{2q\lambda_I A_{dis}\tau^{n+1}}e^{-\frac{Q_{dis}}{T}\left(\frac{Q_g}{Q_{dis}}-1\right)}\right)^{\frac{1}{q+1}} \tag{16}$$

whereas in the diffusion-dominated case ($r_s \ll r_t$), it is:

$$\begin{aligned} r_{s,dif} &= \left(\frac{\gamma\eta^2\mathcal{G}_{I,0}}{2q\lambda_I A_{dis}\tau^{n+1}}e^{-\frac{Q_{dis}}{T}\left(\frac{Q_g}{Q_{dis}}-1\right)}r_t^{-m}\right)^{\frac{1}{q+1-m}} \\ &= \left(\frac{\gamma\eta^2\mathcal{G}_{I,0}}{2q\lambda_I A_{dif}\tau^2}e^{-\frac{Q_{dis}}{T}\left(\frac{Q_g}{Q_{dis}}-\frac{Q_{dif}}{Q_{dis}}\right)}\right)^{\frac{1}{q+1-m}} \end{aligned} \tag{17}$$

Using Equations (16) and (17), we find that $r_{s,dis}$ and $r_{s,dif}$ are related by:

$$r_{s,dif} = \left(r_{s,dis}^{q+1}r_t^{-m}\right)^{\frac{1}{q+1-m}} \tag{18}$$

2.4. Thermal Evolution

Assuming adiabatic conditions, the temperature evolution in the necking region is given by:

$$\frac{\partial T}{\partial t} = \frac{(1-\lambda_I)\,\Psi}{\rho c} = \frac{2\,(1-\lambda_I)\,A_{dis}\tau^{n+1}e^{-\frac{Q_{dis}}{T}}}{\rho c}\left[1+\left(\frac{r_t}{r}\right)^m\right] \tag{19}$$

Only the deformational work Ψ that is not used for grain damage results in heating, which is controlled by the coefficient $1-\lambda_I$ (this coefficient is also frequently called the Taylor-Quinney coefficient). We neglect the surface energy that is released during interface coarsening as its contribution is likely negligible at typical interface roughnesses (Thielmann et al., 2015; Thielmann, 2018).

2.5. Reference State and Non-dimensionalization

The equations derived above contain a large number of material parameters. To identify potential trade-offs between different material parameters and to reduce their number it is useful to (i) define them in terms of a reference state and (ii) non-dimensionalize them using appropriate scales.

We use the initial state as the reference state with initial stress τ_0, initial temperature T_0 and initial grain interface transition roughness $r_{t,0}$. First, we express the temperature T as the sum of the initial temperature T_0 and a temperature perturbation $\tilde{T}$:

$$T = T_0 + \tilde{T} \tag{20}$$

Using this, an Arrhenius term of the form $e^{-Q_i\left(\frac{1}{T}-\frac{1}{T_0}\right)}$ can be rewritten as:

$$e^{-Q_i\left(\frac{1}{T}-\frac{1}{T_0}\right)} = e^{-Q_i\left(\frac{1}{T_0+\tilde{T}}-\frac{1}{T_0}\right)} = e^{Q_i\left(\frac{\tilde{T}}{T_0^2+T_0\tilde{T}}\right)} \tag{21}$$

Second, with the above form of the Arrhenius term the flow law given in Equation (11) can be rewritten in terms of the reference state:

$$\begin{aligned}\dot{\varepsilon} = {} & A_{dis} e^{-\frac{Q_{dis}}{T_0}} \tau_0^n \left[e^{Q_{dis}\left(\frac{\tilde{T}}{T_0^2+T_0\tilde{T}}\right)} \left(\frac{\tau}{\tau_0}\right)^n \right. \\ & \left. + \; e^{Q_{dif}\left(\frac{\tilde{T}}{T_0^2+T_0\tilde{T}}\right)} \left(\frac{\tau}{\tau_0}\right) \left(\frac{r_{t,0}}{r}\right)^m \right]\end{aligned} \tag{22}$$

where we used Equation (10). Rewriting the rheology also allows to rewrite the grain size evolution Equation (12) in terms of the reference state:

$$\frac{dr}{dt} = \frac{\eta \mathcal{G}_I}{q r^{q-1}} - \frac{2\lambda_I r^2}{\gamma \eta} \tau \left(A_{dis} \tau^n e^{-\frac{Q_{dis}}{T}} + A_{dif} \tau e^{-\frac{Q_{dif}}{T}} r^{-m} \right) \tag{23}$$

$$\begin{aligned} = {} & \frac{2\lambda_I r_{t,0}^2}{\gamma \eta} \dot{\varepsilon}_{dis,0} \tau_0 \left[\left(\frac{r_{s,dis,0}}{r_{t,0}}\right)^{q+1} \frac{r_{t,0}{}^{q-1} e^{Q_g\left(\frac{\tilde{T}}{T_0^2+T_0\tilde{T}}\right)}}{r^{q-1}} \right. \\ & - e^{Q_{dis}\left(\frac{\tilde{T}}{T_0^2+T_0\tilde{T}}\right)} \left(\frac{\tau}{\tau_0}\right)^{n+1} \left(\frac{r}{r_{t,0}}\right)^2 \\ & \left. - e^{Q_{dif}\left(\frac{\tilde{T}}{T_0^2+T_0\tilde{T}}\right)} \left(\frac{\tau}{\tau_0}\right)^2 \left(\frac{r}{r_{t,0}}\right)^{2-m} \right]\end{aligned} \tag{24}$$

where, using Equation (16), we can identify:

$$\left(\frac{r_{s,dis,0}}{r_{t,0}}\right)^{q+1} = \frac{\gamma \eta^2 \mathcal{G}_{I,0} e^{-\frac{Q_g}{T_0}}}{2\lambda_I q \dot{\varepsilon}_{dis,0} \tau_0 r_{t,0}^{q+1}} \tag{25}$$

It is useful to define a normalized grain interface roughness $\hat{r} = \frac{r}{r_{t,0}}$ and introduce $\frac{dr}{dt} = r_{t,0} \frac{d\hat{r}}{dt}$, to obtain an equation for the evolution of the normalized interface roughness (which does not have any units):

$$\begin{aligned}\frac{d\hat{r}}{dt} = {} & \frac{2\lambda_I r_{t,0}}{\gamma \eta} \dot{\varepsilon}_{dis,0} \tau_0 \left[\hat{r}_{s,dis,0}^{q+1} \frac{e^{Q_g\left(\frac{\tilde{T}}{T_0^2+T_0\tilde{T}}\right)}}{\hat{r}^{q-1}} \right. \\ & \left. - e^{Q_{dis}\left(\frac{\tilde{T}}{T_0^2+T_0\tilde{T}}\right)} \left(\frac{\tau}{\tau_0}\right)^{n+1} \hat{r}^2 - e^{Q_{dif}\left(\frac{\tilde{T}}{T_0^2+T_0\tilde{T}}\right)} \left(\frac{\tau}{\tau_0}\right)^2 \hat{r}^{2-m} \right]\end{aligned} \tag{26}$$

Additionally, we can rewrite the relation between the steady state dislocation creep grain size and the steady state diffusion creep grain size given by Equation (18) in terms of normalized interface curvatures:

$$\hat{r}_{s,dif}^{q+1-m} = \hat{r}_{s,dis}^{q+1} \tag{27}$$

Using Equation (20) and the definition of the normalized grain interface roughness, the temperature Equation (19) can be written as:

$$\begin{aligned}\frac{d\tilde{T}}{dt} = {} & \frac{2(1-\lambda_I) \dot{\varepsilon}_{dis,0} \tau_0}{\rho c} \left[e^{Q_{dis}\left(\frac{\tilde{T}}{T_0^2+T_0\tilde{T}}\right)} \left(\frac{\tau}{\tau_0}\right)^{n+1} \right. \\ & \left. + \; e^{Q_{dif}\left(\frac{\tilde{T}}{T_0^2+T_0\tilde{T}}\right)} \left(\frac{\tau}{\tau_0}\right)^2 \hat{r}^{-m} \right]\end{aligned} \tag{28}$$

Equating (1) and (22) yields:

$$\begin{aligned}\frac{dD}{dt} = {} & -D A_{dis} e^{-\frac{Q_{dis}}{T_0}} \tau_0^n \left[e^{Q_{dis}\left(\frac{\tilde{T}}{T_0^2+T_0\tilde{T}}\right)} \left(\frac{\tau}{\tau_0}\right)^n \right. \\ & \left. + \; e^{Q_{dif}\left(\frac{\tilde{T}}{T_0^2+T_0\tilde{T}}\right)} \left(\frac{\tau}{\tau_0}\right) \left(\frac{r_{t,0}}{r}\right)^{-m} \right]\end{aligned} \tag{29}$$

This leaves us with three coupled ordinary differential equations for the three unknowns r, T, and D. While this notation may seem more complicated, it is significantly simplified when non-dimensionalizing Equations (26)–(29) with a set of characteristic scales for length, temperature, stress, and time, respectively, which are given by the initial slab thickness, initial slab temperature, initial slab stress, and the initial strain rate at the transition between diffusion and dislocation creep:

$$\begin{aligned} & L_c = D_0 && T_c = \frac{T_0^2}{Q_{dis}} \\ & \tau_c = \tau_0 = \frac{\Delta\rho g H}{2} && t_c = \dot{\varepsilon}_{t,0}^{-1} = 2A_{dis} e^{-\frac{Q_{dis}}{T_0}} \left(\frac{\Delta\rho g H}{2}\right)^n \end{aligned} \tag{30}$$

With the chosen characteristic temperature scale, the Arrhenius term can be rewritten as:

$$e^{-Q_i\left(\frac{1}{T}-\frac{1}{T_0}\right)} = e^{-Q_i\left(\frac{1}{T_0+\tilde{T}}-\frac{1}{T_0}\right)} = e^{Q_i\left(\frac{\tilde{T}}{T_0^2+T_0\tilde{T}}\right)}$$
$$= e^{Q_i\left(\frac{T_0^2\tilde{T}'}{Q_{dis}\left(T_0^2+T_0\frac{T_0^2}{Q_{dis}}\tilde{T}'\right)}\right)} = e^{\frac{Q_i}{Q_{dis}}\left(\frac{\tilde{T}'}{1+\frac{\tilde{T}'}{T_0'}}\right)} \tag{31}$$

where $T_0' = Q_{dis}/T_0$. Replacing $\frac{\tau}{\tau_0} = \frac{D_0}{D}$ and non-dimensionalizing the respective quantities in Equations (24), (28), and (29) with the respective scales then yields

$$\frac{d\hat{r}}{dt'} = \mathcal{I}\left[\hat{r}_{s,dis,0}^{q+1}\frac{e^{\delta Q_g \mathbb{T}}}{\hat{r}^{q-1}} - e^{\mathbb{T}}\left(\frac{1}{D'}\right)^{n+1}\hat{r}^2 - e^{\delta Q_{dif}\mathbb{T}}\left(\frac{1}{D'}\right)^2\hat{r}^{2-m}\right] \tag{32}$$

$$\frac{d\tilde{T}'}{dt'} = \mathcal{S}\left[e^{\mathbb{T}}\left(\frac{1}{D'}\right)^{n+1} + e^{\delta Q_{dif}\mathbb{T}}\left(\frac{1}{D'}\right)^2\hat{r}^{-m}\right] \tag{33}$$

$$\frac{dD'}{dt'} = -\left[e^{\mathbb{T}}\left(\frac{1}{D'}\right)^{n-1} + e^{\delta Q_{dif}\mathbb{T}}\hat{r}^{-m}\right] \tag{34}$$

where we introduced $\mathbb{T} = \frac{\tilde{T}'}{1+\frac{\tilde{T}'}{T_0'}}$ for better readability. As $\hat{r}$ is already a non-dimensional quantity, it does not have to be additionally non-dimensionalized. The superscript $'$ indicates a non-dimensionalization with the characteristic scales in Equation (30), whereas$\hat{}$ indicates a normalization with the initial transition roughness $r_{t,0}$. We use two characteristic length scales because our model involves both the scale of the lithosphere thickness and the scale of a mineral grain, which can be more than ten orders of magnitude different. The two length scales are useful because they provide a more intuitive meaning of both the $\hat{r}$ and D'. Additionally, the numerical treatment of this system of equations is made much easier, as values of $\hat{r}$ and D' do not attain extreme values prone to roundoff errors. The following non-dimensional numbers can be identified:

$$\begin{aligned}
\hat{r}_{s,dis,0} &= \frac{r_{s,dis,0}}{r_{t,0}} & \mathcal{I} &= \frac{2\lambda_I r_{t,0}\tau_0}{\gamma\eta} \\
\delta Q_g &= \frac{Q_g}{Q_{dis}} & \delta Q_{dif} &= \frac{Q_{dif}}{Q_{dis}} \\
\mathcal{S} &= \frac{2Q_{dis}\left(1-\lambda_I\right)\tau_0}{\rho c T_0^2} & T_0' &= Q_{dis}/T_0 \\
\hat{r}_0 &= \frac{r_0}{r_{t,0}}
\end{aligned} \tag{35}$$

as well as the three non-dimensional exponents n, m, and q.

2.6. Nondimensional Parameters

It is worthwhile to discuss the meaning of the different non-dimensional parameters introduced in Equation (35) as well as the values they may take for Earth-like conditions. Due to their definition, the initial values for temperature $\tilde{T}_0'$ and slab thickness D_0' are 0 and 1, respectively. The meaning of the non-dimensional initial temperature and interface curvature T_0' and $\hat{r}_0$ are straightforward, with values of $\hat{r}_0 > 1$ indicating that the initial deformation is mostly accommodated by dislocation creep and for $\hat{r}_0 < 1$ mostly accommodated by diffusion creep. The values of δQ_g and δQ_{dif} indicate the respective temperature sensitivity of grain growth and diffusion creep with respect to dislocation creep. Values larger than 1 denote that dislocation creep is more sensitive to a temperature change than either grain growth or diffusion creep. This may, for example, be important during the necking process, as an increase in temperature due to shear heating may result in a switch from diffusion to dislocation creep.

The value for $\hat{r}_{s,dis,0}$ is the normalized steady state interface curvature in dislocation creep at the initial conditions, which is closely linked to the normalized steady state interface curvature in dislocation creep (see Equation 27). Depending on the initial grain size $\hat{r}_0$, the interface curvature will either increase ($\hat{r}_0 < \hat{r}_{s,dis,0}$) or decrease ($\hat{r}_0 > \hat{r}_{s,dis,0}$) to attain this steady state value. As for the initial interface curvature $\hat{r}_0$, values of $\hat{r}_{s,dis,0} > 1$ indicate that the steady state interface curvature will favor dislocation creep. However, this is only true at the initial conditions. During the necking process, stress (being inversely proportional to the slab thickness D), temperature and interface curvature will change and thus also the transition curvature and steady state curvature. Whether deformation in these cases will be governed by dislocation or diffusion creep then depends on the values of n, m, and δQ_{dif}.

Finally, the damage numbers $\mathcal{I}$ and $\mathcal{S}$ determine the importance and speed of grain damage and temperature induced damage, respectively. Large values of the respective parameter denote fast and efficient weakening. Both the grain damage number $\mathcal{I}$ and the thermal damage number $\mathcal{S}$ can be considered as expressions of the available energies in the system. The grain damage number $\mathcal{I}$ can be considered as the ratio between the specific deformation energy available for grain damage, given by the term $\lambda_I\tau_0$ and the energy stored in the grain interfaces, which is given by the term $\frac{\gamma\eta}{r_{t,0}}$ (Bercovici and Ricard, 2012). Hence, when the available specific deformation energy is also much larger than the energy stored in the interface (resulting in a large value of $\mathcal{I}$), grain damage is more efficient. The same applies to the thermal damage number $\mathcal{S}$, which can be considered as the ratio between the specific deformation energy available for thermal damage, $(1-\lambda_I)\tau_0$, and the specific thermal energy, $\rho c T_0$. Due to our choice of non-dimensionalization, this ratio is then additionally scaled by the factor Q_{dis}/T_0, also known as the Arrhenius number (e.g., Peters et al., 2016), which is in itself a measure of the ratio between activation energy and thermal energy. A large value of $\mathcal{S}$ thus requires that (1) the system is highly temperature dependent (represented by large values of the Arrhenius number) and (2) the available deformation energy is much larger than the thermal energy.

To determine Earth-like ranges of $\mathcal{S}$, $\mathcal{I}$, $\hat{r}_{s,dis,0}$, and T_0', we assume slab lengths H of 100–500 km, mean slab temperatures T_0 of 900–1,200 K and an interface partitioning factor λ_I within the range of $10^{-6} - 10^{-3}$ (e.g., Bercovici and Ricard, 2016; Mulyukova and Bercovici, 2017). There are at present no experimental constraints on the value of λ_I, thus its value is usually assumed based on indirect evidence. With the material parameters given in **Table 1**, we then compute the respective non-dimensional numbers for 10^5 random combinations of the input parameters to estimate their range. The resulting histograms for $\mathcal{I}$ and $\mathcal{S}$, $\hat{r}_{s,dis,0}$, and T_0' are shown in **Figure 3**. For the chosen parameters, $\mathcal{I}$ ranges between 1 and 1,000, $\mathcal{S}$ shows much less variation and varies between 1 and 10. $\hat{r}_{s,dis,0}$ and T_0' vary in the range of 10^{-3}–10^{-2} and 50–70, respectively (see also **Table 2**).

2.7. Comparison to Previous Studies

Before applying these models to Earth, we will first have a general look at the system of equations given by (32)–(34). Unless otherwise noted specifically, the primes indicating non-dimensional values are dropped for the remainder of the paper for better readability. We can identify several particular cases that have been studied in the literature, the first being the analytical necking model by Schmalholz (2011). In this model, only dislocation (powerlaw) creep was considered, without taking into account either shear heating or grain size evolution. In this case, only (34) has to be considered, where the grain size dependent diffusion creep term is dropped. This is equivalent to setting $\mathcal{I} = \mathcal{S} = 0$ and $\hat{r}_0 = \infty$. As $\tilde{T} = 0$, the remaining Arrhenius term equals one (34), which results in:

$$\frac{dD}{dt} = -\frac{1}{D^{n-1}} \tag{36}$$

The above equation corresponds to the equation derived in Schmalholz (2011). For $n = 1$, the detachment time t_d, that is the duration until the slab thickness becomes zero, is given by the characteristic time scale t_c. For $n > 1$, the detachment time then depends on the powerlaw exponent as $t_d = \frac{1}{n}$. Additionally considering shear heating (by setting $\mathcal{S} > 0$) then yields the following system of equations:

$$\frac{d\tilde{T}}{dt} = \mathcal{S} e^{\mathbb{T}} \left(\frac{1}{D}\right)^{n+1} \tag{37}$$

$$\frac{dD}{dt} = -e^{\mathbb{T}} \left(\frac{1}{D}\right)^{n-1} \tag{38}$$

which corresponds to the system investigated by Duretz et al. (2012) (the thermal damage number $\mathcal{S}$ is equal to A in their Equation 6). Finally, Bercovici et al. (2015) investigated the effect of grain damage and a composite dislocation/diffusion creep rheology on slab detachment, but not shear heating ($\mathcal{S} = 0$, $\mathcal{I} > 0$, $0 < \hat{r}_0 < \infty$). In that case, (32)–(34) reduce to (due to the constant temperature, the respective Arrhenius terms equal 1):

$$\frac{d\hat{r}}{dt} = \mathcal{I} \left[\frac{\hat{r}_{s,dis,0}^{q+1}}{\hat{r}^{q-1}} - \left(\frac{1}{D}\right)^{n+1} \hat{r}^2 - \left(\frac{1}{D}\right)^2 \hat{r}^{2-m} \right] \tag{39}$$

$$\frac{dD}{dt} = -\left[\left(\frac{1}{D}\right)^{n-1} + \hat{r}^{-m} \right] \tag{40}$$

This system of equations is equal to the one used in Bercovici et al. (2015), except that they additionally included the effect of the viscous resistance of the mantle to the sinking slab. The damage number $\mathcal{D}$ used in their paper is equal to $\mathcal{I}$ used here, whereas the $\hat{r}_{s,dis,0}$ used here equals their $\frac{\mathcal{C}}{q\mathcal{I}}$. Both the studies of Duretz et al. (2012) and Bercovici et al. (2015) concluded that the respective weakening mechanism resulted in a significant reduction of the detachment time.

3. RESULTS

To determine the impact of different parameters on the necking process, we assessed their effect on the detachment time of the slab, t_d. We follow a two-fold approach which consists of (1) analytical considerations of several simplified cases and (2) a numerical Monte-Carlo approach to test the prediction potential of the analytical approximations. We solved the set of ordinary differential Equations (32)–(34) numerically using a stiff ordinary differential equation solver of the software Matlab. The numerical code can be found in the online repository on figshare (Thielmann and Schmalholz, 2020a).

3.1. Representative Slab Detachment Simulations

In **Figure 4**, we show a comparison of eight cases, where we chose different extreme parameters to illustrate their impact on the necking process. For all cases we assumed $n = m = 3$, $q = 4$, $\delta Q_{dis} = \delta Q_g = 0.5$ and an initial temperature $T_0 = 60$. The different cases are: (1) a case without grain and thermal damage where deformation is dominated by dislocation creep ($\hat{r}_0 = 10^1$, $\hat{r}_{s,dis,0} = 10^1$, $\mathcal{S} = \mathcal{I} = 0$), (2) a case without grain and thermal damage where deformation is dominated by diffusion creep ($\hat{r}_0 = 10^{-0.5}$, $\hat{r}_{s,dis,0} = 10^1$, $\mathcal{S} = \mathcal{I} = 0$), (3) a thermal damage case with dislocation creep governed deformation ($\hat{r}_0 = 10^1$, $\hat{r}_{s,dis,0} = 10^1$, $\mathcal{S} = 10^2$, $\mathcal{I} = 0$), (4) a thermal damage case with diffusion creep governed deformation ($\hat{r}_0 = 10^{-0.5}$, $\hat{r}_{s,dis,0} = 10^{-1}$, $\mathcal{S} = 10^2$, $\mathcal{I} = 0$), (5) an grain damage case initially in dislocation creep, but switching to diffusion creep ($\hat{r}_0 = 10^{0.5}$, $\hat{r}_{s,dis,0} = 10^{-1}$, $\mathcal{S} = 0$, $\mathcal{I} = 10^2$), (6) a case where weakening occurs via grain damage dominated by diffusion creep ($\hat{r}_0 = 10^{-0.5}$, $\hat{r}_{s,dis,0} = 10^{-1}$, $\mathcal{S} = 0$, $\mathcal{I} = 10^2$), (7) a case where weakening equally occurs due to both damage mechanisms, with deformation starting initially in dislocation creep but likely to switch to diffusion creep due to a reduction in interface curvature ($\hat{r}_0 = 10^{0.5}$, $\hat{r}_{s,dis,0} = 10^{-1}$, $\mathcal{S} = 10^2$, $\mathcal{I} = 10^2$), and finally (8) a case where weakening equally occurs due to both damage mechanisms, with deformation starting initially in diffusion creep ($\hat{r}_0 = 10^{-0.5}$, $\hat{r}_{s,dis,0} = 10^{-1}$, $\mathcal{S} = 10^2$, $\mathcal{I} = 10^2$).

For the two non-damage cases, detachment times are longest. However, once a single or both damage mechanisms are activated, detachment times are significantly reduced. The reduction is largest when both interface and thermal damage are active. For all cases where damage is activated, we observe a very rapid, almost instantaneous detachment phase. As can be seen in **Figure 4C**, the interface curvature is significantly reduced if grain damage is active and rapidly approaches very small values. On the contrary, if thermal damage is active, temperatures significantly rise during the detachment

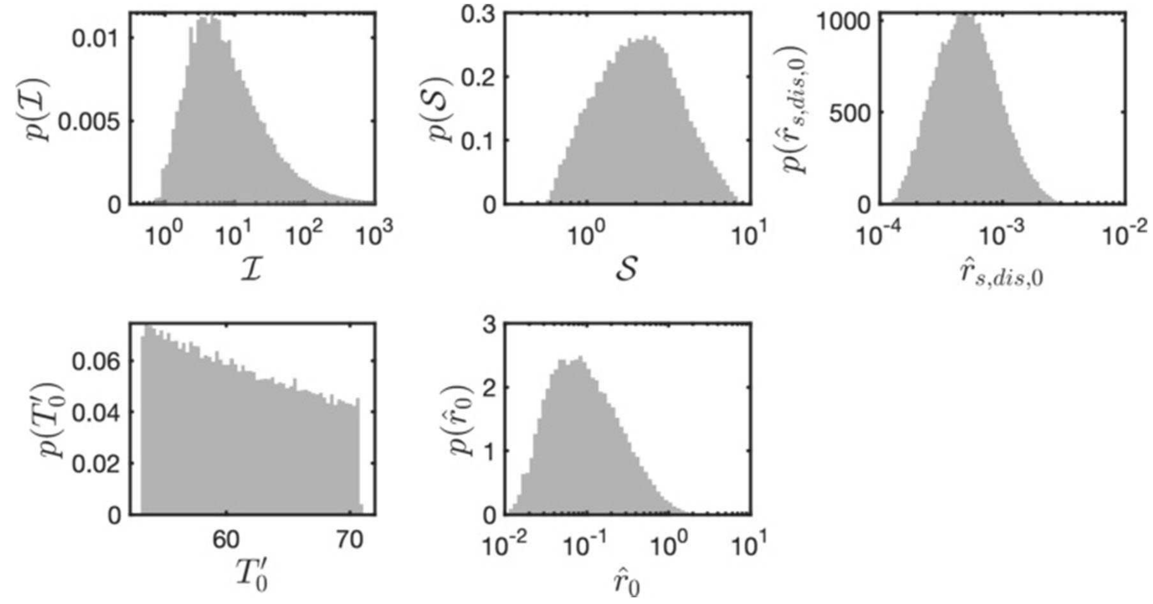

FIGURE 3 | Probability density functions of the parameter ranges of the nondimensional numbers $\mathcal{S}$, $\mathcal{I}$, $\hat{r}_{s,dis,0}$, and T_0' and $\hat{r}_0$ for Earth-like parameters.

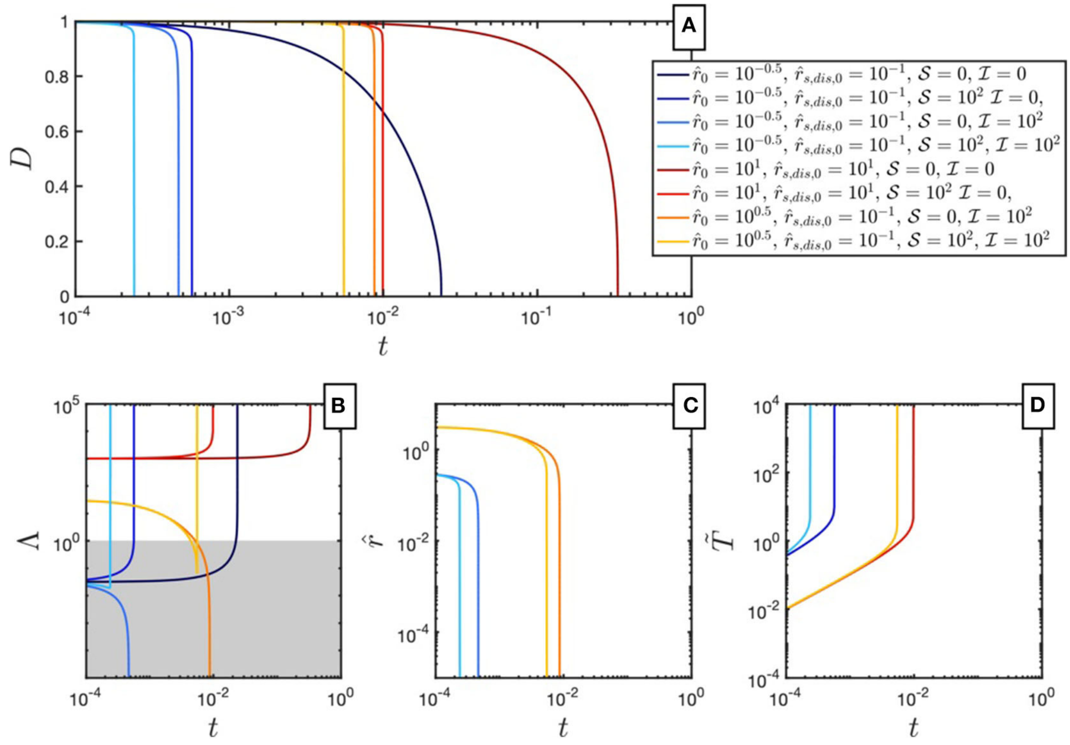

FIGURE 4 | Comparison of eight simulations with different parameters for $\hat{r}_0$, $\hat{r}_{s,dis,0}$, $\mathcal{S}$ and $\mathcal{I}$. **(A)** Evolution of neck thickness D. **(B)** Evolution of $\Lambda = \dot{\varepsilon}_{dis}/\dot{\varepsilon}_{dif}$, which denotes the importance of dislocation creep vs. diffusion creep during necking. **(C)** Evolution of interface curvature $\hat{r}$. **(D)** Evolution of the temperature perturbation $\tilde{T}$. In **(C,D)**, only the cases are shown where either interface roughness or temperature experience a change.

phase (**Figure 4D**), which in some cases results in a switch from diffusion to dislocation creep at late detachment stages (**Figure 4B**).

While these examples qualitatively show the impact of both damage mechanisms on detachment times, we aim at quantifying these effects. We will first develop analytical approximations for t_d for several extreme cases before turning to numerical modeling. Even though Earth-like values for different nondimensional parameters are restricted (see **Figure 3**), we will also investigate regimes that go beyond these parameter ranges.

3.2. Analytical Considerations

3.2.1. Low Damage Numbers ($\mathcal{I} \ll 1$, $\mathcal{S} \ll 1$)

At low damage numbers, both Equations (32) and (33) can be neglected and the evolution of slab thickness is solely governed by Equation (34). Due to the low damage numbers, the interface curvature $\hat{r}$ as well as the temperature perturbation $\tilde{T}$ remain at their initial values $\hat{r}_0$ and 0. Depending on $\hat{r}_0$, deformation will either be dominated by diffusion or dislocation creep and the evolution of the slab thickness D is governed by:

$$\frac{dD}{dt} = \begin{cases} -\hat{r}_0^{-m} & \text{if } \hat{r}_0 \ll 1 \\ -\left(\frac{1}{D}\right)^{n-1} & \text{if } \hat{r}_0 \gg 1 \end{cases} \tag{41}$$

which can be integrated to yield:

$$D(t) = \begin{cases} 1 - \hat{r}_0^{-m} t & \text{if } \hat{r}_0 \ll 1 \\ (1 - nt)^{\frac{1}{n}} & \text{if } \hat{r}_0 \gg 1 \end{cases} \tag{42}$$

from which we can compute the detachment time t_d at which $D = 0$:

$$t_d = \begin{cases} \hat{r}_0^m & \text{if } \hat{r}_0 \ll 1 \\ \frac{1}{n} & \text{if } \hat{r}_0 \gg 1 \end{cases} \tag{43}$$

3.2.2. Shear Heating Dominated Weakening ($\mathcal{I} \ll 1$)

In the case of shear heating dominated weakening, only Equation (32) can be neglected. The system of equations is then given by Equations (33) and (34). As in section 3.2.1, we will also distinguish between a diffusion and a dislocation dominated case. To understand the necking evolution in this case, we now examine it at the initial stages where temperature changes can be assumed to be small. The evolution of slab thickness in each case is then given by Equation (42). The evolution of temperature (Equation 33) reads as:

$$\frac{d\tilde{T}}{dt} = \begin{cases} \mathcal{S} e^{\delta Q_{dif} \mathbb{T}} \left(\frac{1}{D}\right)^2 \hat{r}_0^{-m} & \text{if } \hat{r}_0 \ll 1 \\ \mathcal{S} e^{\mathbb{T}} \left(\frac{1}{D}\right)^{n+1} & \text{if } \hat{r}_0 \gg 1 \end{cases} \tag{44}$$

As we are only considering initial stages, we can additionally approximate the term $e^{\mathbb{T}}$ using a Taylor series expansion around $\tilde{T} = 0$:

$$e^{\mathbb{T}} = e^{\frac{\tilde{T}}{1 + \frac{\tilde{T}}{T_0}}} \approx e^{\tilde{T}} \tag{45}$$

where we neglect higher order terms. Rewriting Equation (44) and inserting Equation (42) then results in:

$$\frac{d\tilde{T}}{dt} = \begin{cases} \mathcal{S} e^{\delta Q_{dif} \tilde{T}} \left(1 - \hat{r}_0^{-m} t\right)^{-2} \hat{r}_0^{-m} & \text{if } \hat{r}_0 \ll 1 \\ \mathcal{S} e^{\tilde{T}} (1 - nt)^{-\frac{n+1}{n}} & \text{if } \hat{r}_0 \gg 1 \end{cases} \tag{46}$$

which can be integrated using separation of variables to yield:

$$\tilde{T}(t) = \begin{cases} -\frac{1}{\delta Q_{dif}} \ln \left[\frac{\hat{r}_0^m - t\left(\delta Q_{dif} \mathcal{S} + 1\right)}{\hat{r}_0^m - t} \right] & \text{if } \hat{r}_0 \ll 1 \\ -\ln\left[\mathcal{S}\left(1 - (1 - nt)^{-1/n}\right) + 1\right] & \text{if } \hat{r}_0 \gg 1 \end{cases} \tag{47}$$

As can be seen in **Figure 4**, $\tilde{T}(t)$ goes to infinity as D approaches zero when thermal damage is important. For the expressions of $T(t)$ given above, the critical time t_{crit} at which $T \rightarrow \infty$ is therefore an indicator of the detachment time t_d. This occurs when:

$$\frac{\hat{r}_0^m - t\left(\delta Q_{dif} \mathcal{S} + 1\right)}{\hat{r}_0^m - t} = 0 \qquad \text{if } \hat{r}_0 \ll 1 \tag{48}$$

$$\mathcal{S}\left(1 - (1 - nt)^{-1/n}\right) + 1 = 0 \qquad \text{if } \hat{r}_0 \gg 1 \tag{49}$$

which yields the following expressions for t_{crit}:

$$t_{crit} = \begin{cases} \frac{\hat{r}_0^m}{\delta Q_{dif} \mathcal{S} + 1} & \text{if } \hat{r}_0 \ll 1 \\ \frac{1}{n} - \frac{1}{n\left(\frac{1}{\mathcal{S}} + 1\right)^n} & \text{if } \hat{r}_0 \gg 1 \end{cases} \tag{50}$$

For small values of $\mathcal{S}$, these expressions are equal to the low-damage case derived in section 3.2.1, thus reproducing the prediction of Schmalholz (2011) in the case of dislocation creep dominated deformation. For large values of $\mathcal{S}$, t_{crit} approaches values of $t_{crit} = \frac{\hat{r}_0^{-m}}{\delta Q_{dif} \mathcal{S}}$, whereas in the case of dislocation creep dominated deformation, t_{crit} becomes independent of n and approaches values of $t_{crit} = \frac{1}{\mathcal{S}}$.

3.2.3. Grain Damage Dominated Weakening ($\mathcal{S} \ll 1$)

If grain damage dominates weakening during the detachment process, the necking process can be described by Equations (32) and (34). When deformation is governed by dislocation creep, grain damage does not affect the necking process. Necking within this regime can thus be described using Equation (42). In this case (and assuming that grain growth is negligible), grain size evolution is described by

$$\frac{d\hat{r}}{dt} = -\mathcal{I} (1 - nt)^{-\frac{n+1}{n}} \hat{r}^2 \tag{51}$$

which can be integrated to yield:

$$\hat{r}(t) = \frac{\hat{r}_0 (1 - nt)^{\frac{1}{n}}}{(1 - nt)^{\frac{1}{n}} - \mathcal{I} \hat{r}_0 \left[(1 - nt)^{\frac{1}{n}} - 1\right]} \tag{52}$$

Using this equation, we can now determine the time t_t at which the rheological transition between diffusion and dislocation creep is reached, which is the case when the dislocation and diffusion creep yield equal strain rates. If grain size evolution is sufficiently fast, this will be the case when $\hat{r} \approx 1$. Inserting this value for $\hat{r}(t)$ in the above equation and solving for t results in:

$$t_t = \frac{1}{n} \left[1 - \left(\frac{I \hat{r}_0}{I \hat{r}_0 + \hat{r}_0 - 1}\right)^n\right] \tag{53}$$

TABLE 2 | Nondimensional model parameters and parameter ranges computed with the material parameters given in **Table 1** and for slab lengths *H* of 100–500 km, average slab temperatures *T* of 900–1,200 K, pressures of 3–9 GPa, and partitioning factors λ_I ranging from 10^{-6} to 10^{-3}.

Variable	Meaning	Investigated range	Earth-like range
$\hat{r}_{s,dis,0}$	Steady state dislocation creep grain size	10^{-3}–10^{3}	10^{-3}–10^{-2}
$\mathcal{I}$	Grain grain damage parameter	10^{-3}–10^{3}	0–2000
$\mathcal{S}$	Shear heating parameter	10^{-3}–10^{3}	1–10
δQ_{dif}	Diffusion creep activation enthalpy ratio (fixed)	0.566	0.566
δQ_{g}	Growth activation enthalpy ratio (fixed)	0.566	0.566
T'_0	Initial temperature (fixed)	60	55–70
$\hat{r}_0$ (fixed)	Initial grain size	2	10^{-2} to 10^{1}

TABLE 3 | Summary of analytical detachment time predictions for different regimes.

	Dislocation creep Dominated $\hat{r}_0 \gg 1$	Diffusion creep Dominated $\hat{r}_0 \ll 1$
Low damage, $\mathcal{I} \ll 1$, $\mathcal{S} \ll 1$	$t_d = \frac{1}{n}$	$t_d = \hat{r}_0^m$
Low grain damage, $\mathcal{I} \ll 1$	$t_d = \frac{1}{n} - \frac{1}{n\left(\frac{1}{\mathcal{S}}+1\right)^n}$	$t_d = \frac{\hat{r}_0^m}{\delta Q_{dif}\mathcal{S}+1}$
Low thermal damage[a], $\mathcal{S} \ll 1$	$t_d = \frac{1}{n}\left[1-\left(\frac{I\hat{r}_0}{I\hat{r}_0+\hat{r}_0-1}\right)^n\right]+\frac{1}{2\mathcal{I}(m-1)}$	$t_d = \frac{r_0^{m-1}}{\mathcal{I}(m-1)}$

[a] *In the dislocation dominated case deformation is initially controlled by dislocation creep, but eventually switches to diffusion creep.*

Once this time is reached, the importance of diffusion creep will increase. To assess the necking behavior in this necking phase, we again consider its initial stage, where we assume that slab thickness *D* does not change significantly. In this case, only Equation (32) has to be considered. At $\hat{r}_0 = 1$, dislocation and diffusion creep yield the same strain rate so that Equation (32) can be rewritten as (additionally neglecting grain growth):

$$\frac{d\hat{r}}{dt} = -2\mathcal{I}\hat{r}^{2-m} \tag{54}$$

which, upon integration, results in the following expression for the evolution of $\hat{r}$:

$$\hat{r}(t) = \left[1 - 2\mathcal{I}\,(m-1)\,t\right]^{m-1} \tag{55}$$

For this equation, we can now define a critical time t_{crit} at which $\hat{r}$ approaches zero:

$$t_{crit} = \frac{1}{2\mathcal{I}\,(m-1)} \tag{56}$$

The total detachment time for the case of grain damage dominated weakening with the initial deformation dominated by dislocation creep is therefore the sum of t_t and t_{crit}:

$$t_d = t_t + t_{crit} = \frac{1}{n}\left[1 - \left(\frac{I\hat{r}_0}{I\hat{r}_0 + \hat{r}_0 - 1}\right)^n\right] + \frac{1}{2\mathcal{I}\,(m-1)} \tag{57}$$

If, on the other hand, the initial interface curvature $\hat{r}_0 < 1$, deformation at the initial stages will directly be governed by diffusion creep. In this case, Equation (32) can be written as (again neglecting grain growth):

$$\frac{d\hat{r}}{dt} = -\mathcal{I}\hat{r}^{2-m} \tag{58}$$

which, can again be integrated and used to compute a critical time t_t, which only slightly differs from the one derived above:

$$\begin{aligned} \hat{r} &= \left[r_0^{m-1} - \mathcal{I}\,(m-1)\,t\right]^{m-1} \\ t_{crit} &= \frac{r_0^{m-1}}{\mathcal{I}\,(m-1)} \end{aligned} \tag{59}$$

This critical time then represents the detachment time of the slab in the case of grain damage dominated weakening with the initial deformation dominated by diffusion creep.

In sections 3.2.1–3.2.3, we have derived a set of analytical predictions for the detachment time t_d for different deformation regimes using simple approximations. These predictions are summarized in **Table 3**.

3.3. Numerical Monte Carlo Study

As the analytical approximations derived above are based on several simplification, it is important to determine to which extent they are capable of predicting the detachment time t_d. To further quantify the impact of different material parameters on the detachment time t_d, we now turn to numerical modeling. Here we define t_d as the time it takes for the neck to reach a thickness of 1% of its original value. We determined the detachment time of 2×10^5 different simulations where we randomly varied $\mathcal{S}$, $\mathcal{I}$, $\hat{r}_{s,dis,0}$ and T_0 within the ranges given in **Table 2**. Random numbers were drawn from uniform distributions using the Mersenne Twister pseudorandom number generator. As the number of non-dimensional parameters is still large, we used some simplifying assumptions: (1) Based on existing flow laws and two-phase growth laws for olivine (Hirth and Kohlstedt, 2003; Hiraga et al., 2010; Bercovici and Ricard, 2012), we assume fixed values for *n*, *m*, and *q* of 3.5, 3, and 4, respectively, (2) we assume that the activation energies for diffusion creep and interface coarsening are equal ($\delta Q_{dif} = \delta Q_g = 0.566$, e.g., Bercovici et al., 2019), and (3) at the initial conditions, grain size is large enough so that necking is dominated by dislocation creep ($\hat{r}_0 = 2$).

The results of this Monte Carlo simulation are shown in **Figure 5**, where we plot the detachment time of each simulation with respect to the grain and thermal damage numbers $\mathcal{I}$ and $\mathcal{S}$ as well as the initial dislocation dominated steady state interface roughness $\hat{r}_{s,dis,0}$. Although the results are quite scattered, some potential underlying trends can be observed: (1) for small values of $\mathcal{I} < 1$ and $\mathcal{S} < 1$, necking times seem to be insensitive to both values, (2) for values of $\mathcal{I} < 1$ and $\mathcal{S} > 1$, necking times seem to primarily depend on $\mathcal{S}$ (**Figure 5A**), (3) $\mathcal{I} > 1$, and $\hat{r}_{s,dis,0} < 1$ significantly reduce detachment times (**Figure 5B**), albeit not in all simulations and (4) if $\hat{r}_{s,dis,0} > 1$, necking times seem to be primarily affected by $\mathcal{S}$. To further explore these dependencies and to verify the previously derived analytical solutions, we will now consider three separate regimes: (1) a low grain damage regime, (2) a high grain damage, low thermal damage regime, and (3) a regime where both damage mechanisms play a role. As the initial grain size $\hat{r}_0$ is fixed at a value of 2, thus favoring dislocation creep, our analysis will be concerned with the analytical solutions derived for cases where initial deformation is governed by dislocation creep.

3.3.1. Low Grain Damage ($\mathcal{I}$ < 1)

As derived in section 3.2.2, detachment times in this regime are independent of $\mathcal{I}$. In **Figure 6A**, we show the computed detachment times for all simulations with $\mathcal{I} < 1$ as a function of $\mathcal{S}$. In addition, the theoretical prediction of t_d using Equation (50) with $\hat{r}_0 > 1$ is shown in gray. We see that, despite the simplifying assumptions made in deriving Equation (50), the analytical solution predicts the numerical result well and provides an accurate upper bound for t_d. Only at the transition from small to large values of $\mathcal{S}$, numerical results deviate from the analytical prediction by up to 35% (**Figure 6B**). Deviations are largest for simulations where a large value of $\mathcal{I}$ is employed, indicating that in those cases grain damage already has an impact on the necking process. The larger deviations at values of $\mathcal{S}$ around 1 reflect the approximation errors introduced while deriving the respective approximations. In general, at values of $\mathcal{S} < 10^{-1}$, detachment times are not influenced by thermal damage and thus are only dependent on the value of the stress exponent n, while at large values of $\mathcal{S} > 10^{1.5}$, detachment times scale with $1/\mathcal{S}$.

3.3.2. Large Grain Damage and Low Thermal Damage ($\mathcal{I}$ > 1, $\mathcal{S}$ < 1)

In this regime, detachment times should be largely independent of $\mathcal{S}$, but rather depend on $\mathcal{I}$. Due to the chosen value of $\hat{r}_0 = 2$, deformation in this regime is always dominated by dislocation creep at the initial stages, but may switch to diffusion creep depending on the value of $\hat{r}_{s,dis,0}$. In **Figure 7A**, the detachment times for all simulations are shown, with their color denoting the employed value of $\hat{r}_{s,dis,0}$. The two solid black lines show the predictions for t_d given by Equations (43) and (57). The first equation predicts the detachment time in the case of dislocation creep dominated deformation (which is grain size insensitive and thus independent of $\mathcal{I}$), while the second equation predicts the detachment time in the case of deformation governed by dislocation creep at the initial stages, but switching to diffusion creep at later stages, thus essentially being governed by diffusion creep.

The numerical results are quite scattered, but exhibit two main characteristics: at values of $\sim \hat{r}_{s,dis,0} > 10^{0.5}$ detachment times are independent of $\mathcal{I}$ and are well predicted by Equation (50) for dislocation creep dominated deformation. This is illustrated in **Figure 7B**, where we plotted the ratio $t_{d,num}/t_{d,ana}$ between the numerically computed and the predicted detachment time as a function of $\mathcal{S}$. Here, colors denote the value of $\hat{r}_{s,dis,0}$ for each simulation. As expected, the analytical prediction for t_d in this dislocation creep dominated regime fits best for small values of $\mathcal{S}$, while detachment times deviate from the prediction when $\mathcal{S}$ approaches 1. For values of $\sim r_{s,dis,0} < 10^{-0.5}$ (diffusion dominated deformation), detachment times are well predicted by Equation (57) at values of $\mathcal{I} > 10^1$ and deviate from the analytical prediction as $\mathcal{I}$ approaches 1 (**Figure 7C**). The analytical solutions thus predict detachment times well, except for the transition from grain damage dominated weakening to structural weakening (at $\mathcal{I} = 1$) or the transition between dislocation creep dominated deformation to diffusion creep dominated deformation (at $r_{s,dis,0} = 1$).

3.3.3. Large Interface and Thermal Damage ($\mathcal{I}$ > 1, $\mathcal{S}$ > 1)

This regime is the most interesting one, as both interface and thermal damage will influence the necking process. Additionally, as **Figure 3** indicates, detachment processes on Earth are most likely to lie within this regime. In **Figure 8A**, the detachment times of all simulations within this subset are shown, with colors denoting the value of $\hat{r}_{s,dis,0}$. Although detachment times are very scattered, a clear pattern can be seen, with diffusion creep dominated simulations ($\hat{r}_{s,dis,0} < 10^{-0.5}$) representing a lower bound to detachment times. From this subset, we therefore extracted two additional subsets, one of which contained dislocation creep dominated simulations ($\hat{r}_{s,dis,0} > 10^{0.5}$), the other one containing diffusion creep dominated simulations ($\hat{r}_{s,dis,0} < 10^{-0.5}$). In the case of dislocation creep dominated simulations, Equation (50) should predict the detachment time, since grain damage does not affect the rheology. In **Figure 8B**, the ratio $t_{d,num}/t_{d,ana}$ between the numerically computed detachment times and the analytical prediction is plotted vs. thermal damage parameter $\mathcal{S}$. It can be seen that the analytical prediction predicts the detachment time very well, with deviations becoming larger as $\mathcal{S}$ approaches 1. Similarly, for diffusion creep dominated simulations, Equation (57) provides a good prediction for t_d. The comparison between this prediction and the numerically computed results is shown in **Figure 8C**, where we plot the ratio $t_{d,num}/t_{d,ana}$ between the numerically computed detachment times and the analytical prediction vs. the thermal damage parameter $\mathcal{I}$. Colors denote the ratio between the grain damage parameter $\mathcal{I}$ and the thermal damage parameter $\mathcal{S}$. We can see that if $\mathcal{I}$ is much larger than $\mathcal{S}$, detachment times are best predicted, with numerically computed detachment times becoming significantly decreased for (1) similar values of $\mathcal{I}$ and $\mathcal{S}$

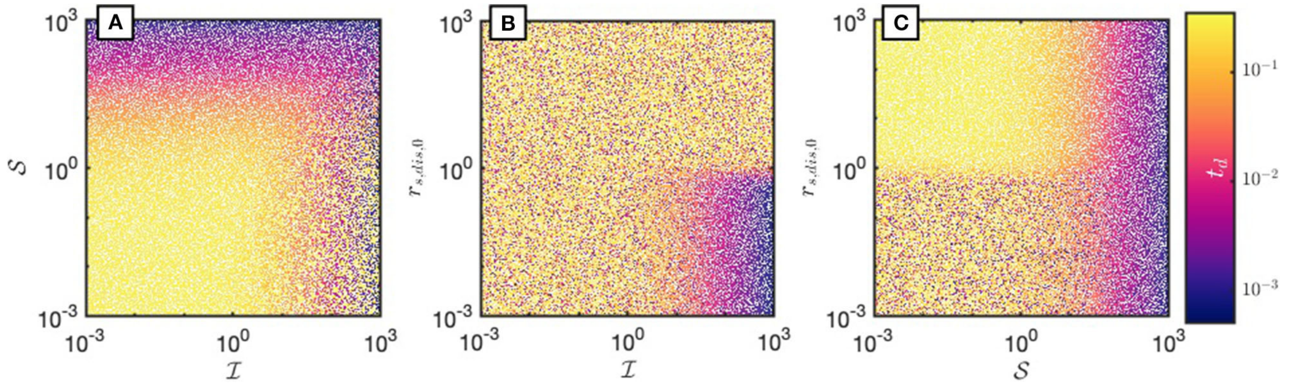

FIGURE 5 | Detachment times t_d for a set of 2×10^5 simulations with different input parameters (see text for details). **(A)** t_d as a function of the grain damage parameter $\mathcal{I}$ and thermal damage parameter $\mathcal{S}$. **(B)** t_d as a function of $\mathcal{I}$ and $\hat{r}_{s,dis,0}$. **(C)** t_d as a function of $\mathcal{S}$ and $\hat{r}_{s,dis,0}$.

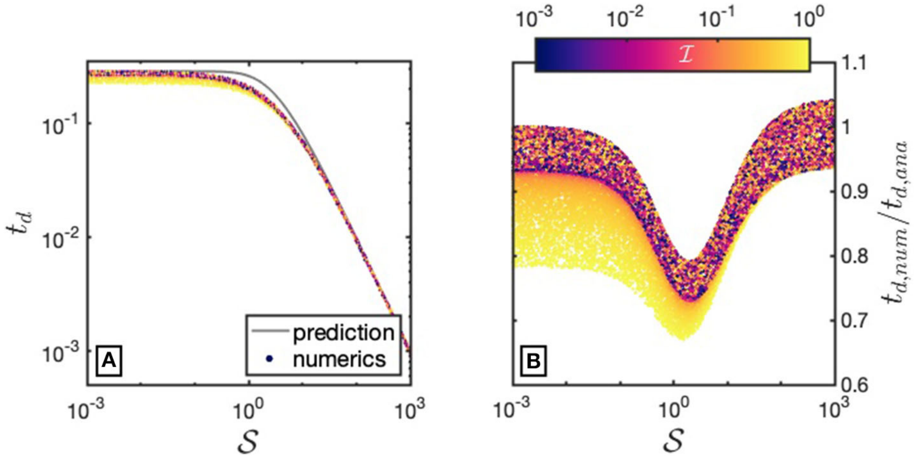

FIGURE 6 | Detachment times t_d for a simulation subset with $\mathcal{I} < 1$ (low grain damage). **(A)** t_d as a function of the thermal damage parameter $\mathcal{S}$. Colors denote the value of $\mathcal{I}$ for each simulation. The gray line denotes the analytical prediction for shear heating dominated weakening (Equation 50). **(B)** Ratio $t_{d,num}/t_{d,ana}$ between the numerically computed detachment time and the analytically predicted one. As in **(A)**, colors denote the value of $\mathcal{I}$ for each simulation.

and (2) for $\mathcal{I}$ approaching 1. As could be already seen in **Figure 4**, this highlights the cumulative effect of grain and thermal damage.

In summary, the comparison between numerical model results and analytically derived detachment time predictions shows that the analytical predictions are capable to reasonably predict numerical model behavior for either dislocation creep dominated cases ($\hat{r}_{s,dis,0} > 10^{0.5}$) or diffusion creep dominated cases ($\hat{r}_{s,dis,0} < 10^{-0.5}$), when thermal and grain damage parameters attain extreme values. At the transition between dislocation creep and diffusion creep dominated regimes as well as when thermal and grain damage parameters take values around 1, numerically computed detachment times deviate strongest from the analytical predictions. However, these largest deviations typically never exceed 50%.

3.4. Impact of Thermal Diffusion

In the analysis presented above we have so far neglected thermal diffusion for simplicity, thus omitting the diffusion term in Equation (19) and its non-dimensional counterpart in Equation (34). During slab detachment, the cold slab will be heated due to thermal diffusion by the surrounding hotter mantle. This heating will weaken the slab and, hence, thermal diffusion may have a significant effect on the necking process (e.g., Gerya et al., 2004). However, thermal diffusion is only important, if the time scale of diffusive heating is not significantly longer than the time scale of slab detachment. To assess the time scale and importance of thermal diffusion during slab detachment and how it may affect detachment times, we here employ a simple analysis. First, we approximate the diffusion term $\kappa\frac{\partial^2 T}{\partial x^2}$ using a simple finite difference approximation:

$$\kappa\frac{\partial^2 T}{\partial x^2} \approx \kappa\frac{T_m - T}{D^2} = \kappa\frac{T_m - \left(T_0 + \tilde{T}\right)}{D^2} \qquad (60)$$

where T_m is the ambient mantle temperature and κ the thermal diffusivity. This term has units of K/s, which implies that it

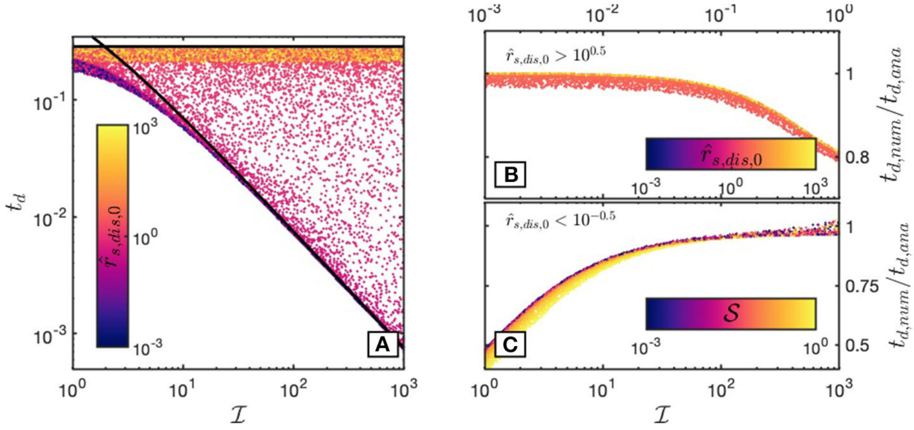

FIGURE 7 | Detachment times t_d for a simulation subset with $\mathcal{I} > 1$ and $\mathcal{S} < 1$ (large grain damage, low thermal damage). **(A)** t_d as a function of the grain damage parameter $\mathcal{I}$. Colors denote the value of $\hat{r}_{s,dis,0}$ for each simulation (large values indicating that dislocation creep is more dominant during necking). The solid black lines denote the analytical predictions for grain damage dominated weakening (given by Equation 57) and damage insensitive necking (Equation 43). **(B)** Validity of the analytical detachment time prediction for a subset of the simulations shown in **(A)** with $\hat{r}_{s,dis,0} > 10^1$ (dislocation creep controlled necking). Shown is the ratio $t_{d,num}/t_{d,ana}$ between the respective numerically computed detachment time [given by Equation (50)] and the analytical prediction vs. the thermal damage parameter $\mathcal{S}$. Colors denote the value of the thermal damage parameter $\mathcal{S}$ for each simulation. **(C)** Ratio $t_{d,num}/t_{d,ana}$ but for a subset of the simulations shown in **(A)** with $\hat{r}_{s,dis,0} < 10^{-1}$ (diffusion creep controlled necking) vs. the grain damage parameter $\mathcal{I}$. Here, Equation (57) is appropriate to predict the detachment time.

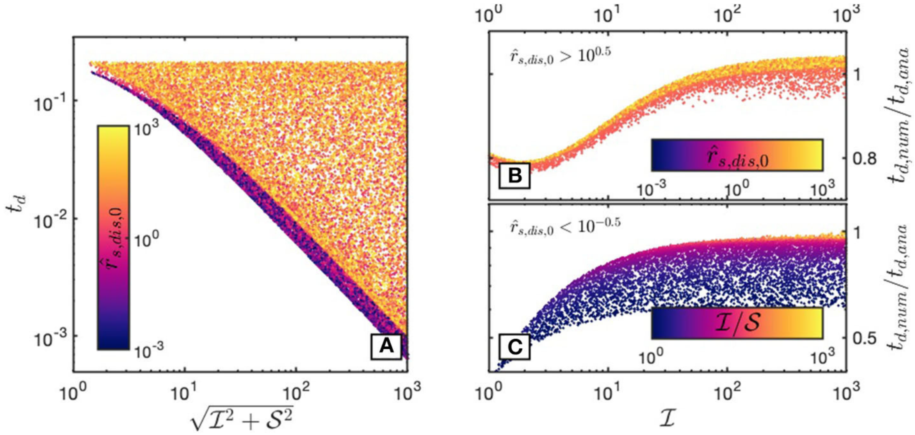

FIGURE 8 | Detachment times t_d for a simulation subset with $\mathcal{I} > 1$ and $\mathcal{S} > 1$ (large interface and thermal damage). **(A)** t_d as a function of the combination of the grain damage parameter $\mathcal{I}$ and the thermal damage parameter $\mathcal{S}$. Colors denote the value of $\hat{r}_{s,dis,0}$ for each simulation (large values indicating that dislocation creep is more dominant during necking). **(B)** Validity of the analytical detachment time prediction for a subset of the simulations shown in **(A)** with $\hat{r}_{s,dis,0} > 10^{0.5}$ (dislocation creep controlled necking). Shown is the ratio $t_{d,num}/t_{d,ana}$ between the respective numerically computed detachment time and the analytical prediction (given by Equation 50). **(C)** Same as **(B)**, but for a subset of the simulations shown in **(A)** with $\hat{r}_{s,dis,0} < 10^{-0.5}$ (diffusion creep controlled necking). Here, Equation (57) is appropriate to predict the detachment time. Colors denote the ratio between the grain damage parameter and the thermal damage parameter.

has to be multiplied with t_c/T_c for non-dimensionalization. In non-dimensional form, this approximated diffusion term can be written as:

$$\frac{t_c}{T_c}\frac{\kappa T_c\left(T_m'-T_0'-\tilde{T}'\right)}{D_0^2 D'^2} = \frac{t_c}{t_{diff}}\frac{\left(T_m'-T_0'-\tilde{T}'\right)}{D'^2} = \frac{t_c}{t_{diff}}\frac{T_0'\left(\delta T_m-1\right)-\tilde{T}'}{D'^2} \quad (61)$$

where $t_{diff} = D_0^2/\kappa$ is the diffusion time scale and t_c is the characteristic time scale chosen for non-dimensionalization, here the dislocation creep strain rate at the initial conditions (see Equation 30). $\delta T_m = T_m/T_0$ is the ratio between the ambient mantle temperature and the slab temperature. Considering temperature diffusion thus introduces the two additional non-dimensional numbers t_c/t_{diff} and δT_m.

For Earth-like parameters, the range of δT_m is relatively small and lies between ∼ 1.3–1.8, while the range of t_c/t_{diff} is significantly larger and may range between $\sim\ 10^{-4} and 10^1$. Values for t_{diff} are limited by the range of Earth-like values for thermal diffusivity and slab thickness. Both these properties cannot vary orders of magnitude, thus the variations in t_d are a result of variations in t_c. This characteristic time scale is determined by the nonlinear rheology (see Equation 30) and yields large values for cold and short slabs and small values for long and warm slabs.

A large value of t_c/t_{diff} implies that the slab may be significantly heated due to thermal diffusion. Due to this heating, the slab will be weakened and detachment times will be reduced. On Earth, thermal diffusion therefore may become important for cold and short slabs with long detachment times. This is also reflected in a value of 200 Ma for t_{diff} (assuming a slab with thickness 80 km and a thermal diffusivity of 10^{-6} m^2s^{-1}).

4. DISCUSSION

4.1. Application to Earth

To determine the impact of grain size reduction and shear heating on slab detachment on Earth, we now compute detachment times for Earth-like parameter ranges. As shown in **Figure 3**, parameter ranges for $\mathcal{I}$ and $\mathcal{S}$ include values that span from $\sim 10^{-1}$ *to* 10^2 and $\sim 10^{-1}$ *to* 10^1, respectively, thus putting Earth-like detachment processes right within the transitional regime, where both grain and thermal damage are important. Employing the Earth-like parameters (**Table 1**) and assuming a range of slab lengths H and temperatures T_{slab}, we computed the resulting detachment times numerically for these transitional regimes. Additionally, as the value of the partitioning factor λ_I is highly unconstrained, we varied its value from 10^{-6} to 10^{-4}. The results show that for the chosen parameters, the detachment times range between 10,000 and more than 10 billion years (**Figures 9A–C**), with the extremely long detachment times being a result of cold slab temperatures in short slabs. When thermal diffusion is considered, these extremely long detachment times are reduced to values less than ~100 million years for cold and short slabs (**Figures 9A–C**). As the value of λ_I is increased, detachment times decrease, but the effect is limited to very cold slab temperatures and short stalled slab lengths.

To better illustrate the effect of thermal diffusion and variations in the partitioning factor λ_I, we show a comparison of six different cases in **Figure 10**, where we assumed a slab temperature of 1,100 K, a slab thickness of 80 km and an initial interface curvature of 1 cm. Increasing λ_I from 10^{-6} to 10^{-4} results in more than a 9-fold reduction of the detachment time (**Figure 10A**, thus highlighting the importance of this parameter. The effect of thermal diffusion can only be seen in simulations where λ_I is small and hence detachment times large. When looking at the evolution of the deformation mechanism ratio Λ (**Figure 10B**), which indicates dominant dislocation creep for $\Lambda > 1$, it becomes apparent that λ_I is crucial in determining the dominant deformation mechanism due to its strong impact on interface curvature (**Figure 10C**). The significant reduction in detachment time for the cases where $\lambda_I = 10^{-4}$ indicates that the initial stages of slab detachment may be governed by grain damage. Indeed, interface curvature experiences a rapid decrease from 10^{-2} m to about $5{\cdot}10^{-4}$ m at initial stages where slab thickness is reduced from 80 to 70 km (yellow line in **Figure 10C**). On the other hand, temperatures do not increase significantly at the initial necking stages. However, when a slab thickness of ~30 km is reached, temperatures start to increase significantly. This implies that while shear heating may not govern initial stages of slab detachment, it becomes important at later stages.

Seismic imaging has revealed several regions on Earth where high-velocity bodies have been identified in the upper mantle, among them the Northwestern US (Schmandt and Humphreys, 2011; Wang et al., 2013; Jiang et al., 2018), the Hindu-Kush (Lister et al., 2008; Kufner et al., 2017), the Mediterranean (Wortel and Spakman, 2000), the Carpathians (Sperner et al., 2001; Ismail-Zadeh et al., 2012), and the European Alps (Lippitsch et al., 2003; Kästle et al., 2020). These high velocity bodies are commonly interpreted as cold lithospheric material. However, their origin is often debated, as they could be interpreted as either subducted slabs or lithospheric drips (e.g., Sperner et al., 2001; Zandt et al., 2004; Lister et al., 2008; Lorinczi and Houseman, 2009; Kufner et al., 2017; Molnar and Bendick, 2019). Observations linked to slab detachment processes in these regions suggest slab detachment events occurring within a few million years after continental collision. Only in cases for which short slabs remain after a previous detachment event, longer "stalling times" in excess of tens of millions of years have been suggested (e.g., Jiang et al., 2018). This is in accordance with our results (see **Figure 9**), which also only predict detachment times in excess of 10 Ma for sufficiently short or cold slabs.

Despite the initial detachment process being mainly controlled by grain size, shear heating may have a strong impact on the "terminal stage of subduction" (Kufner et al., 2017), when elevated stresses result in increased viscous dissipation and thus heating. These elevated stresses together may not only trigger brittle failure and thus earthquakes, but may also trigger ductile instabilities at larger depths that have been proposed to be the cause for intermediate-depth earthquakes (Kelemen and Hirth, 2007; John et al., 2009; Deseta et al., 2014; Thielmann et al., 2015; Kufner et al., 2017; Ohuchi et al., 2017; Thielmann, 2018; Zhan, 2019). To further investigate this issue, it will be necessary to additionally take into account plastic failure, as the large stresses in the slab at final detachment stages may also result in brittle deformation.

4.2. Model Limitations

Owing to the simplicity of our model, computed detachment times should not be taken at face value, but rather as a first-order constraint. Due to the simplifying assumptions, our model most likely underestimates the time scales of the detachment process, as we do not account for additional forces such as (1) the viscous resistance of the mantle to the sinking slab (2) resistance of the asthenosphere to flow into the necking region of the slab and (3) the viscous resistance of the lower mantle when a slab tip reaches the bottom of the transition zone during detachment (e.g., Burkett and Gurnis, 2013). These effects could potentially slow down slab detachment (Bercovici et al., 2015). However, it is not clear to which extent these viscous forces would contribute to a delay in slab detachment. This is partly due to the nonlinear rheology of the mantle itself, which may be affected by dislocation

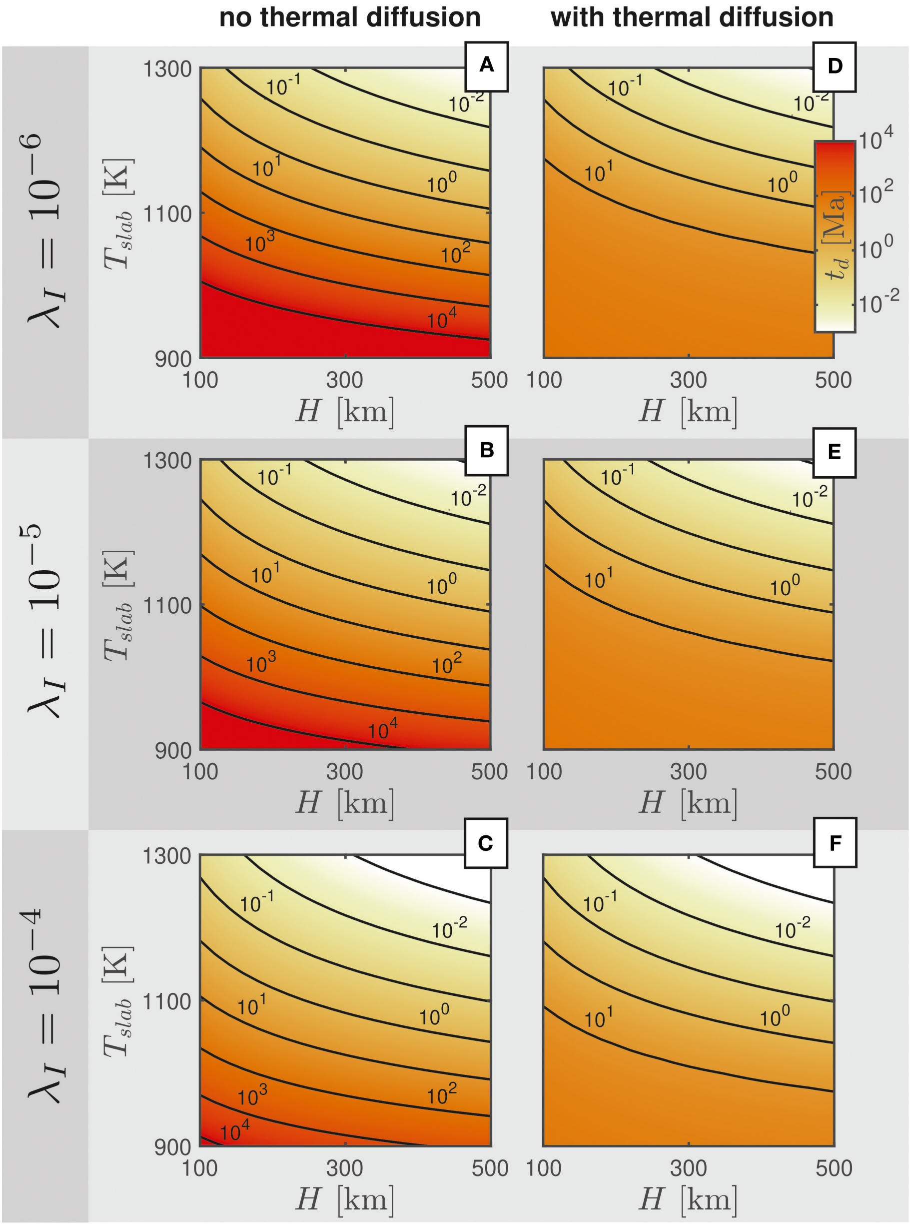

FIGURE 9 | Application to Earth. Detachment times t_d for a range of slab lengths H and mean slab temperatures T_{slab}. Detachment times were computed using the parameters listed in **Table 1**. **(A–C)** Detachment times computed with three different values for λ_I, neglecting thermal diffusion. **(D–F)** Same as **(A–C)**, but with thermal diffusion included.

creep and/or grain size reduction. In both cases, the viscosity of the mantle would be significantly reduced, thus reducing its resistance to the sinking slab (see also discussion in Bercovici et al., 2019).

The force balance assumed in our model may also be modified by other factors, such as the presence of positively buoyant crustal material at the top of the slab or negatively buoyant material due to the phase transition to eclogite at greater depths. Also, if the slab were not stalled, but rather subducting at a certain speed, the downward buoyancy force would be governed by their interplay with a number of other forces such as the viscous coupling of the plate at the surface to the asthenosphere and the coupling between subducting and overriding plate (e.g., Forsyth, 1975; Bercovici et al., 2019). Nevertheless, the fundamental interplay between the necking instability and the two damage processes will remain unchanged, whereas absolute time scales may change due to different stress levels in the slab. Combining the present model with the recent model by Ribe and Xu (2020) could potentially account for several of these effects.

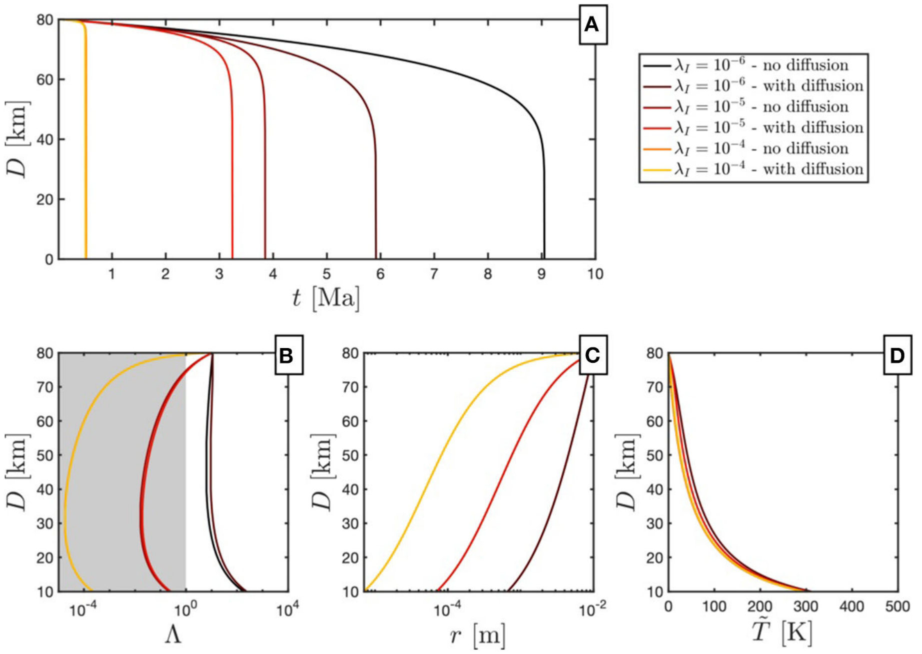

FIGURE 10 | Examples of six simulations with a slab temperature of 1,100 K, a slab thickness of 80 km and an initial interface curvature of 1 cm are shown to illustrate the impact of thermal diffusion and the interface partitioning factor λ_I. **(A)** Evolution of neck thickness D vs. time. **(B)** Relationship between neck thickness D and deformation mechanism ratio Λ (with values smaller than 1 indicating diffusion creep dominated deformation. **(C)** Relationship between interface curvature r and D. **(D)** Relationship between temperature increase $\tilde{T}$ and neck thickness D. Non-visible lines in the respective plots lie on top of each other.

One uncertainty for all mathematical models arises from the uncertainty of the different material parameters. Rheological parameters for dislocation and diffusion creep are to some extent constrained by laboratory experiments, but the extrapolation to tectonic time scales and the application to kilometer-scale heterogeneous rock units generates uncertainties. One of the largest parameter uncertainty of our model arises from the lack of constraints on the partitioning factor λ_I, which was assumed to be constant in this study. However, there is evidence that this factor depends on several other variables such as grain size, temperature, dislocation density, and phase mixing (see section 2.3). Some of these effects could potentially mitigate the effect of grain size reduction, as for example λ_I is thought to decrease at small grain sizes (Bercovici and Skemer, 2017) and larger temperatures (Mulyukova and Bercovici, 2018). Due to the strong effect of λ_I on model results, it is indispensable to obtain better constraints on this parameter, which could prove to be a challenge for experimental geoscientists. Additional constraints on the interplay between necking, grain damage and shear heating can also be obtained from structural geology (e.g., Linckens et al., 2015).

Despite the uncertainties of our model, it provides the means to analyze the fundamental physical relationship between necking, grain damage, and thermal weakening, all of which have a first-order impact on slab detachment. It also shows the importance of different material parameters (or combinations thereof), thus indicating which parameters are necessary to constrain accurately and which parameters are less important. This not only has implications for slab detachment, but also for other necking processes (e.g., Brune et al., 2016), where continental plate breakup, following lithosphere necking (e.g., Chenin et al., 2018), may be significantly accelerated due to the action of ductile weakening.

5. CONCLUSIONS

We have developed a fundamental mathematical model of slab detachment, considering structural weakening due to necking, thermal weakening due to shear heating (thermal damage) and microstructural weakening due to grain size reduction (grain damage; here represented by changes in interface curvature between two phases). Our model extends previously developed models (Schmalholz, 2011; Duretz et al., 2012; Bercovici et al., 2015) and is, to the best of our knowledge, the first model to link these three coupled weakening processes in a system of three nonlinear differential equations. The derived system of equations allows investigating the fundamental interplay of the three weakening mechanisms and to determine the conditions for which one, two or all three mechanisms are important. With dimensional analysis we determined the controlling dimensionless parameters of this system and we derived analytical solutions for the duration of slab detachment for several end-member regimes. We verified the controlling parameters and analytical solutions with a systematic numerical Monte-Carlo study. The analytical solutions for the detachment time are useful for understanding the fundamental control of the three weakening mechanisms and the involved parameters on slab detachment. Numerical solutions show that the analytical solutions are inaccurate for transitional regimes where more than one weakening mechanism is important. However, in these transitional regimes the analytical solutions typically do not deviate by more than 50% from the numerical solution, thus lying well within the range originating from uncertainties in the applied material parameters.

Both grain damage, due to grain size reduction, and thermal damage, due to shear heating, result in rapid detachment, showing that both damage mechanisms have a first order impact on the slab detachment process. Models where both damage mechanisms are equally active exhibit the shortest detachment times as a result of the positive feedback between necking, grain size reduction and shear heating. This positive feedback shows that both damage mechanisms should be considered in models of lithosphere necking.

For lithospheric-scale conditions on Earth, all three weakening mechanisms are presumably important during slab detachment. We find that for these conditions, grain damage and thermal weakening act in a collaborative manner, thus minimizing the detachment time. Grain damage is likely dominant during the initial stages of slab detachment, whereas thermal weakening becomes more important and presumably dominant during the later stages. Our results suggest that the typical duration of slab detachment is between 1 and 10 million years. Detachment times in excess of 10 Million years are only predicted for short ($<\approx 200$ km) and cold slabs, which is in broad agreement with results from other theoretical studies and indirect estimates based on geological and geophysical observations.

DATA AVAILABILITY STATEMENT

The datasets generated for this study are available on request to the corresponding author. The code to create the datasets and figures used in this study are available on figshare (Thielmann and Schmalholz, 2020a,b).

AUTHOR CONTRIBUTIONS

MT and SS designed the study, analyzed the data, and wrote the manuscript. MT derived the governing equations and performed simulations. All authors contributed to the article and approved the submitted version.

FUNDING

MT was funded by the Bayerisches Geoinstitut Visitor's program and SS by the University of Lausanne.

ACKNOWLEDGMENTS

Colormaps were designed using the *colorcet* function (Kovesi, 2015).

REFERENCES

Andrews, E., and Billen, M. I. (2009). Rheologic controls on the dynamics of slab detachment. *Tectonophysics* 464, 60–69. doi: 10.1016/j.tecto.2007.09.004

Bellas, A., Zhong, S., Bercovici, D., and Mulyukova, E. (2018). Dynamic weakening with grain-damage and implications for slab detachment. *Phys. Earth Planet. Inter*. 285, 76–90. doi: 10.1016/j.pepi.2018.09.001

Bercovici, D., Mulyukova, E., and Long, M. D. (2019). A simple toy model for coupled retreat and detachment of subducting slabs. *J. Geodyn*. 129, 275–289. doi: 10.1016/j.jog.2018.03.002

Bercovici, D., and Ricard, Y. (2012). Mechanisms for the generation of plate tectonics by two-phase grain-damage and pinning. *Phys. Earth Planet. Inter*. 202–203, 27–55. doi: 10.1016/j.pepi.2012.05.003

Bercovici, D., and Ricard, Y. (2013). Generation of plate tectonics with two-phase grain-damage and pinning: source–sink model and toroidal flow. *Earth Planet. Sci. Lett*. 365, 275–288. doi: 10.1016/j.epsl.2013.02.002

Bercovici, D., and Ricard, Y. (2016). Grain-damage hysteresis and plate tectonic states. *Phys. Earth Planet. Inter*. 253, 31–47. doi: 10.1016/j.pepi.2016.01.005

Bercovici, D., Schubert, G., and Ricard, Y. (2015). Abrupt tectonics and rapid slab detachment with grain damage. *Proc. Natl. Acad. Sci. U.S.A*. 112, 1287–1291. doi: 10.1073/pnas.1415473112

Bercovici, D., and Skemer, P. (2017). Grain damage, phase mixing and plate-boundary formation. *J. Geodyn*. 108, 40–55. doi: 10.1016/j.jog.2017.05.002

Billen, M. I., and Hirth, G. (2007). Rheologic controls on slab dynamics. *Geochem. Geophys. Geosyst.* 8:Q08012. doi: 10.1029/2007GC001597

Brune, S., Williams, S. E., Butterworth, N. P., and Müller, R. D. (2016). Abrupt plate accelerations shape rifted continental margins. *Nature* 536, 201–204. doi: 10.1038/nature18319

Burkett, E., and Gurnis, M. (2013). Stalled slab dynamics. *Lithosphere* 5, 92–97. doi: 10.1130/L249.1

Burkett, E. R., and Billen, M. I. (2010). Three-dimensionality of slab detachment due to ridge-trench collision: laterally simultaneous boudinage versus tear propagation. *Geochem. Geophys. Geosyst*. 11:Q11012. doi: 10.1029/2010GC003286

Capitanio, F. A., and Replumaz, A. (2013). Subduction and slab breakoff controls on Asian indentation tectonics and Himalayan western syntaxis formation. *Geochem. Geophys. Geosyst*. 14, 3515–3531. doi: 10.1002/ggge.20171

Chen, L., and Gerya, T. V. (2016). The role of lateral lithospheric strength heterogeneities in orogenic plateau growth: insights from 3-D thermo-mechanical modeling. *J. Geophys. Res*. 121, 3118–3138. doi: 10.1002/2016JB012872

Chenin, P., Schmalholz, S. M., Manatschal, G., and Karner, G. D. (2018). Necking of the lithosphere: a reappraisal of basic concepts with thermo-mechanical numerical modeling. *J. Geophys. Res*. 123, 5279–5299. doi: 10.1029/2017JB014155

Chrysochoos, A., and Belmahjoub, F. (1992). Thermographic analysis of thermomechanical couplings. *Arch. Mech*. 44, 55–68.

Davies, J. H., and von Blanckenburg, F. (1995). Slab breakoff: a model of lithosphere detachment and its test in the magmatism and deformation of collisional orogens. *Earth Planet. Sci. Lett*. 129, 85–102. doi: 10.1016/0012-821X(94)00237-S

Deseta, N., Andersen, T. B., and Ashwal, L. D. (2014). A weakening mechanism for intermediate-depth seismicity? Detailed petrographic and microtextural observations from blueschist facies pseudotachylytes, Cape Corse, Corsica. *Tectonophysics* 610, 138–149. doi: 10.1016/j.tecto.2013.11.007

Duretz, T., Gerya, T. V., and May, D. A. (2011). Numerical modelling of spontaneous slab breakoff and subsequent topographic response. *Tectonophysics* 502, 244–256. doi: 10.1016/j.tecto.2010.05.024

Duretz, T., Gerya, T. V., and Spakman, W. (2014). Slab detachment in laterally varying subduction zones: 3-D numerical modeling. *Geophys. Res. Lett*. 41, 1951–1956. doi: 10.1002/2014GL059472

Duretz, T., Räss, L., Podladchikov, Y. Y., and Schmalholz, S. M. (2019). Resolving thermomechanical coupling in two and three dimensions: spontaneous strain localization owing to shear heating. *Geophys. J. Int*. 216, 365–379. doi: 10.1093/gji/ggy434

Duretz, T., Schmalholz, S. M., and Gerya, T. V. (2012). Dynamics of slab detachment. *Geochem. Geophys. Geosyst*. 13:Q03020. doi: 10.1029/2011GC004024

Duretz, T., Schmalholz, S. M., and Podladchikov, Y. Y. (2015). Shear heating-induced strain localization across the scales. *Philos. Mag*. 1–16. doi: 10.1080/14786435.2015.1054327

Foley, B. J. (2018). On the dynamics of coupled grain size evolution and shear heating in lithospheric shear zones. *Phys. Earth Planet. Inter*. 283, 7–25. doi: 10.1016/j.pepi.2018.07.008

Forsyth, D., and Uyeda, S. (1975). On the relative importance of the driving forces of plate motion. *Geophys. J. R. Astr. Soci*. 43, 163–200. doi: 10.1111/j.1365-246X.1975.tb00631.x

Fox, M., Herman, F., Kissling, E., and Willett, S. D. (2015). Rapid exhumation in the Western Alps driven by slab detachment and glacial erosion. *Geology* 43, 379–382. doi: 10.1130/G36411.1

Frohlich, C. (2006). *Deep Earthquakes*. Cambridge: Cambridge University Press. doi: 10.1017/CBO9781107297562

Garzanti, E., Radeff, G., and Malusá, M. G. (2018). Slab breakoff: A critical appraisal of a geological theory as applied in space and time. *Earth Sci. Rev*. 177, 303–319. doi: 10.1016/j.earscirev.2017.11.012

Gerya, T. V., Yuen, D. A., and Maresch, W. V. (2004). Thermomechanical modelling of slab detachment. *Earth Planet. Sci. Lett*. 226, 101–116. doi: 10.1016/j.epsl.2004.07.022

Hiraga, T., Tachibana, C., Ohashi, N., and Sano, S. (2010). Grain growth systematics for forsterite-enstatite aggregates: effect of lithology on grain size in the upper mantle. *Earth Planet. Sci. Lett*. 291, 10–20. doi: 10.1016/j.epsl.2009.12.026

Hirth, G., and Kohlstedt, D. L. (2003). *Rheology of the Upper Mantle and the Mantle Wedge: A View From the Experimentalists*. Geophys. Monogr. Ser. Washington, DC: AGU. 83–105. doi: 10.1029/138GM06

Holtzman, B. K., Chrysochoos, A., and Daridon, L. (2018). A thermomechanical framework for analysis of microstructural evolution: application to olivine rocks at high temperature. *J. Geophys. Res*. 123, 8474–8507. doi: 10.1029/2018JB015613

Isacks, B. and Molnar, P. (1969). Mantle earthquake mechanisms and the sinking of the lithosphere. *Nature*. doi: 10.1038/2231121a0

Ismail-Zadeh, A., Matenco, L., Radulian, M., Cloetingh, S., and Panza, G. (2012). Geodynamics and intermediate-depth seismicity in Vrancea (the south-eastern Carpathians): current state-of-the art. *Tectonophysics* 530–531, 50–79. doi: 10.1016/j.tecto.2012.01.016

Jiang, C., Schmandt, B., Hansen, S. M., Dougherty, S. L., Clayton, R. W., Farrell, J., et al. (2018). Rayleigh and S wave tomography constraints on subduction termination and lithospheric foundering in central California. *Earth Planet. Sci. Lett*. 488, 14–26. doi: 10.1016/j.epsl.2018.02.009

John, T., Medvedev, S., Rüpke, L., and Andersen, T. B. (2009). Generation of intermediate-depth earthquakes by self-localizing thermal runaway. *Nat. Geosci*. 2, 137–140. doi: 10.1038/ngeo419

Kameyama, M., Yuen, D., and Fuijmoto, H. (1997). The interaction of viscous heating with grain-size dependent rheology in the formation of localized slip zones. *Geophys. Res. Lett*. 24, 2523–2526. doi: 10.1029/97GL02648

Kästle, E. D., Rosenberg, C., Boschi, L., Bellahsen, N., Meier, T., and El-Sharkawy, A. (2020). Slab break-offs in the Alpine subduction zone. *Int. J. Earth Sci*. 109, 587–603. doi: 10.1007/s00531-020-01821-z

Kelemen, P. B., and Hirth, G. (2007). A periodic shear-heating mechanism for intermediate-depth earthquakes in the mantle. *Nature* 446, 787–790. doi: 10.1038/nature05717

Kiss, D., Podladchikov, Y., Duretz, T., and Schmalholz, S. M. (2019). Spontaneous generation of ductile shear zones by thermal softening: Localization criterion, 1D to 3D modelling and application to the lithosphere. *Earth Planet. Sci. Lett*. 519, 284–296. doi: 10.1016/j.epsl.2019.05.026

Kohlstedt D. L., and Hansen, L. N. (2015). "Constitutive equations, rheological behavior, and viscosity of rocks," in *Treatise on Geophysics, 2nd Edn*, Vol. 2, ed G. Schubert (Oxford: Elsevier), 441–472.

Kovesi, P. (2015). Good colour maps: how to design them. *arxiv.org*. doi: 10.1071/ASEG2015ab107

Kufner, S.-K., Schurr, B., Haberland, C., Zhang, Y., Saul, J., Ischuk, A., et al. (2017). Zooming into the Hindu Kush slab break-off: A rare glimpse on the terminal stage of subduction. *Earth Planet. Sci. Lett*. 461, 127–140. doi: 10.1016/j.epsl.2016.12.043

Kufner, S.-K., Schurr, B., Sippl, C., Yuan, X., Ratschbacher, L., Akbar, A. M., et al. (2016). Deep India meets deep Asia: Lithospheric indentation, delamination and break-off under Pamir and Hindu Kush (Central Asia). *Earth Planet. Sci. Lett*. 435, 171–184. doi: 10.1016/j.epsl.2015.11.046

Linckens, J., Herwegh, M., and Müntener, O. (2015). Small quantity but large effect —How minor phases control strain localization in upper mantle shear zones. *Tectonophysics* 643, 26–43. doi: 10.1016/j.tecto.2014.12.008

Lippitsch, R., Kissling, E., and Ansorge, J. (2003). Upper mantle structure beneath the Alpine orogen from high-resolution teleseismic tomography. *J. Geophys. Res*. 108:277. doi: 10.1029/2002JB002016

Lister, G., Kennett, B., Richards, S., and Forster, M. (2008). Boudinage of a stretching slablet implicated in earthquakes beneath the Hindu Kush. *Nat. Geosci*. 1, 196–201. doi: 10.1038/ngeo132

Lorinczi, P., and Houseman, G. A. (2009). Lithospheric gravitational instability beneath the Southeast Carpathians. *Tectonophysics* 474, 322–336. doi: 10.1016/j.tecto.2008.05.024

Magni, V., Allen, M. B., van Hunen, J., and Bouilhol, P. (2017). Continental underplating after slab break-off. *Earth Planet. Sci. Lett*. 474, 59–67. doi: 10.1016/j.epsl.2017.06.017

McKenzie, D. P. (1969). Speculations on the consequences and causes of plate motions. *Geophys. J. Int*. 18, 1–32. doi: 10.1111/j.1365-246X.1969.tb00259.x

Mitrofan, H., Anghelache, M.-A., Chitea, F., Damian, A., Cadicheanu, N., and Visan, M. (2016). Lateral detachment in progress within the Vrancea slab (Romania): inferences from intermediate-depth seismicity patterns. *Geophys. J. Int*. 205, 864–875. doi: 10.1093/gji/ggv533

Molnar, P., and Bendick, R. (2019). Seismic moments of intermediate-depth earthquakes beneath the hindu kush: active stretching of a blob of sinking thickened mantle lithosphere? *Tectonics* 38, 1651–1665. doi: 10.1029/2018TC005336

Mulyukova, E. and Bercovici, D. (2017). Formation of lithospheric shear zones: Effect of temperature on two-phase grain damage. *Phys. Earth Planet. Inter*. 270, 195–212. doi: 10.1016/j.pepi.2017.07.011

Mulyukova, E., and Bercovici, D. (2018). Collapse of passive margins by lithospheric damage and plunging grain size. *Earth Planet. Sci. Lett*. 484, 341–352. doi: 10.1016/j.epsl.2017.12.022

Mulyukova, E., and Bercovici, D. (2019). The generation of plate tectonics from grains to global scales: a brief review. *Tectonics* 38, 4058–4076. doi: 10.1029/2018TC005447

Ohuchi, T., Lei, X., Ohfuji, H., Higo, Y., Tange, Y., Sakai, T., et al. (2017). Intermediate-depth earthquakes linked to localized heating in dunite and harzburgite. *Nat. Geosci*. 298:1407. doi: 10.1038/ngeo3011

Peters, M., Herwegh, M., Paesold, M. K., Poulet, T., Regenauer-Lieb, K., and Veveakis, M. (2016). Boudinage and folding as an energy instability in ductile deformation. *J. Geophys. Res*. 121, 3996–4013. doi: 10.1002/2016JB012801

Pusok, A. E., Kaus, B. J. P., and Popov, A. A. (2018). The effect of rheological approximations in 3-D numerical simulations of subduction and collision. *Tectonophysics* 746, 296–311. doi: 10.1016/j.tecto.2018.04.017

Ribe, N. M., and Xu, B. (2020). Subduction of non-Newtonian plates: thin-sheet dynamics of slab necking and break-off. *Geophys. J. Int*. 220, 910–927. doi: 10.1093/gji/ggz500

Rozel, A., Ricard, Y., and Bercovici, D. (2011). A thermodynamically self-consistent damage equation for grain size evolution during dynamic recrystallization. *Geophys. J. Int*. 184, 719–728. doi: 10.1111/j.1365-246X.2010.04875.x

Schlunegger, F., and Kissling, E. (2015). Slab rollback orogeny in the Alps and evolution of the Swiss Molasse basin. *Nat. Commun*. 6, 1–10. doi: 10.1038/ncomms9605

Schmalholz, S. M. (2011). A simple analytical solution for slab detachment. *Earth Planet. Sci. Lett*. 304, 45–54. doi: 10.1016/j.epsl.2011.01.011

Schmalholz, S. M., and Mancktelow, N. S. (2016). Folding and necking across the scales: a review of theoretical and experimental results and their applications. *Solid Earth* 7, 1417–1465. doi: 10.5194/se-7-1417-2016

Schmandt, B., and Humphreys, E. (2011). Seismically imaged relict slab from the 55 Ma Siletzia accretion to the northwest United States. *Geology* 39, 175–178. doi: 10.1130/G31558.1

Schott, B. and Schmeling, H. (1998). Delamination and detachment of a lithospheric root. *Tectonophysics* 296, 225–247. doi: 10.1016/S0040-1951(98)00154-1

Sperner, B., Lorenz, F., Bonjer, K., Hettel, S., Müller, B., and Wenzel, F. (2001). Slab break-off –abrupt cut or gradual detachment? New insights from the Vrancea Region (SE Carpathians, Romania). *Terra Nova* 13, 172–179. doi: 10.1046/j.1365-3121.2001.00335.x

Sternai, P., Sue, C., Husson, L., Serpelloni, E., Becker, T. W., Willett, S. D., et al. (2019). Present-day uplift of the European alps: evaluating mechanisms and models of their relative contributions. *Earth Sci. Rev*. 190, 589–604. doi: 10.1016/j.earscirev.2019.01.005

Sun, M., and Bezada, M. (2020). Seismogenic necking during slab detachment: evidence from relocation of intermediate-depth seismicity in the Alboran Slab. *JGR* 125:e2019JB017896. doi: 10.1029/2019JB01789

Thielmann, M. (2018). Grain size assisted thermal runaway as a nucleation mechanism for continental mantle earthquakes: impact of complex rheologies. *Tectonophysics* 746, 611–623. doi: 10.1016/j.tecto.2017.08.038

Thielmann, M., and Kaus, B. J. P. (2012). Shear heating induced lithospheric-scale localization: does it result in subduction? *Earth Planet. Sci. Lett*. 359–360, 1–13. doi: 10.1016/j.epsl.2012.10.002

Thielmann, M., Rozel, A., Kaus, B. J. P., and Ricard, Y. (2015). Intermediate-depth earthquake generation and shear zone formation caused by grain size reduction and shear heating. *Geology* 43, 791–794. doi: 10.1130/G36864.1

Thielmann, M., and Schmalholz, S. M. (2020a). Code for "Contributions of grain damage, thermal weakening and necking to slab detachment". figshare.

Thielmann, M., and Schmalholz, S. M. (2020b). Figures for "Contributions of grain damage, thermal weakening and necking to slab detachment". figshare.

Turcotte, D., and Schubert, G. (2014). "Stress and strain in solids," in *Geodynamics* (Cambridge: Cambridge University Press), 92–129. doi: 10.1017/CBO9780511843877.003

van Hunen, J., and Allen, M. B. (2011). Continental collision and slab break-off: A comparison of 3-D numerical models with observations. *Earth Planet. Sci. Lett*. 302, 27–37. doi: 10.1016/j.epsl.2010.11.035

von Tscharner, M., Schmalholz, S. M., and Duretz, T. (2014). Three-dimensional necking during viscous slab detachment. *Geophys. Res. Lett*. 41, 4194–4200. doi: 10.1002/2014GL060075

Wang, Y., Forsyth, D. W., Rau, C. J., Carriero, N., Schmandt, B., Gaherty, J. B., et al. (2013). Fossil slabs attached to unsubducted fragments of the Farallon plate. *Proc. Natl. Acad. Sci. U.S.A*. 110, 5342–5346. doi: 10.1073/pnas.1214880110

Wong A Ton, S. Y. M., and Wortel, M. J. R. (1997). Slab detachment in continental collision zones: an analysis of controlling parameters. *Geophys. Res. Lett*. 24, 2095–2098. doi: 10.1029/97GL01939

Wortel, M., and Spakman, W. (2000). Subduction and slab detachment in the Mediterranean-Carpathian region. *Science* 290, 1910–1916. doi: 10.1126/science.290.5498.1910

Zandt, G., Gilbert, H., Owens, T. J., Ducea, M., Saleeby, J., and Jones, C. H. (2004). Active foundering of a continental arc root beneath the southern Sierra Nevada in California. *Nature* 431, 41–46. doi: 10.1038/nature02847

Zhan, Z. (2019). Mechanisms and implications of deep earthquakes. *Annu. Rev. Earth Planet. Sci*. 48:060314. doi: 10.1146/annurev-earth-053018-060314

Zhao, L., Paul, A., Malusá, M. G., Xu, X., Zheng, T., Solarino, S., et al. (2016). Continuity of the Alpine slab unraveled by high-resolution P wave tomography. *J. Geophys. Res*. 121, 8720–8737. doi: 10.1002/2016JB013310

Conflict of Interest: The authors declare that the research was conducted in the absence of any commercial or financial relationships that could be construed as a potential conflict of interest.

ORIGINAL RESEARCH
published: 18 September 2020
doi: 10.3389/feart.2020.00374

Orphaning Regimes: The Missing Link Between Flattened and Penetrating Slab Morphologies

Antoniette Greta Grima[1], Carolina Lithgow-Bertelloni[2] and Fabio Crameri[3]*

[1] Earth Sciences Department, University College London, London, United Kingdom, [2] Department of Earth, Planetary, and Space Sciences, University of California, Los Angeles, Los Angeles, CA, United States, [3] Center for Earth Evolution and Dynamics, University of Oslo, Oslo, Norway

Slab orphaning is a newly discovered phenomenological behavior, where the slab tip breaks off at the top of the lower mantle (∼660 km depth) and is abandoned by its parent slab. Upon orphaning, subduction continues uninterrupted through the lateral motion of the parent slab above 660 km depth. In this work, we present a regime diagram for the range of conditions under which slabs can orphan at the top of the lower mantle. Our models show that a viscosity jump at 1,000 km depth not coincident with the endothermic phase change responsible for the 660 km seismic discontinuity, is necessary for orphaning as is the presence of a low viscosity channel between 660 and 1,000 km depth. We show that orphan slabs, similar to other deep slab morphologies, can be the end result for a wide range of physical parameters governing slab dynamics: slab orphaning persists across wide variations in slab dip, slab yield stress/strength, Clapeyron slope values, and overriding plate nature. The diversity in orphan slab sizes and orphaning periods is tied to the orphaning regime space, which describes a hitherto unexplored region between deflected and penetrating deep-subduction modes. Orphaning provides a simple dynamic link between the well-known deflection and penetration, and provides one possible way for slabs to switch from direct penetration to deflection, littering the mantle with abandoned fragments. Orphan slabs are therefore the intermediary between these two extensively studied slab morphologies.

Keywords: slab orphaning, slab dynamics, slab orphaning regimes, deep slab morphologies, deep slab breakoff, subduction dynamics, slab fragmentation, remnant slabs

Edited by:
Marina Manea,
National Autonomous University of Mexico, Mexico

Reviewed by:
Masanori Kameyama,
Ehime University, Japan
Luca Dal Zilio,
California Institute of Technology, United States
Bernhard Maximilian Steinberger,
Helmholtz Center Potsdam, Germany

****Correspondence:***
Antoniette Greta Grima
a.grima.11@ucl.ac.uk

Specialty section:
This article was submitted to Solid Earth Geophysics, a section of the journal Frontiers in Earth Science

Received: *01 April 2020*
Accepted: *10 August 2020*
Published: *18 September 2020*

Citation:
Grima AG, Lithgow-Bertelloni C and Crameri F (2020) Orphaning Regimes: The Missing Link Between Flattened and Penetrating Slab Morphologies. Front. Earth Sci. 8:374. doi: 10.3389/feart.2020.00374

1. INTRODUCTION

Upper-lower mantle slab morphology and dynamics are currently described in terms of slab deflection and flattening or direct penetration (e.g., Christensen and Yuen, 1984; Christensen, 1996; Fukao et al., 2001, 2009; Čížková et al., 2002; Yoshioka et al., 2010; Yoshida et al., 2012; Fukao and Obayashi, 2013; Garel et al., 2014; Goes et al., 2017; Yoshida, 2017; Čížková and Bina, 2019). Despite the well-entrenched presence of these key terms in the literature, the debate is still out on what leads a slab to adopt one behavior over the other at any point throughout its evolutionary history. Many previous studies have hypothesized that the age, and hence the strength of the slab is the determining factor that shapes its behavior (e.g., Garel et al., 2014; Goes et al., 2017). This would suggest that older, colder and therefore stronger slabs should always penetrate into the lower mantle while younger, warmer slabs should deflect and flatten at the top of the lower mantle. However, as attested by the slabs of the Pacific this does not always hold true (e.g., Yoshioka et al., 2010; Goes et al., 2017).

What ultimately controls the slab behavior is the relationship between the buoyancy and strength of the slab with respect to the surrounding ambient mantle. Understanding the nuances of this relationship depends on our knowledge of the mantle viscosity structure. Previous work based on inversions of post-glacial rebound and the gravity field has extensively explored the effects of a viscosity increase at 660 km depth (e.g., Hager and Richards, 1984, 1989; Hager et al., 1985; Čížková et al., 2002; Funiciello et al., 2003; Billen and Hirth, 2007; Billen, 2010; Garel et al., 2014). However, when the viscosity jump is not prescribed to occur at 660 km depth, the increase in viscosity occurs much closer to ∼ 900–1,200 km depth (King and Masters, 1992; Forte and Mitrovica, 2001; Mitrovica and Forte, 2004; Rudolph et al., 2015). New geophysical evidence from trans-dimensional, trans-hierarchical Bayesian inversions of the geoid, which do not prescribe the number or depth of viscosity jumps show both the deeper viscosity increase (∼ 1,000 km) and a low viscosity layer of moderate contrast above it (∼ 10 times less viscous than the upper mantle). It is not uncommon for a low viscosity layer (LVL) to emerge from geoid inversions for the radial viscosity structure of the mantle. In previous work this has often been prescribed to be in the transition zone (Hager and Richards, 1984, 1989; Hager et al., 1985). Our recent inversions suggest it is not (Rudolph et al., 2015). Recent mineral physics studies aimed at understanding the flattening of slabs at a 1,000 km in the absence of known phase transitions suggest mechanisms for a viscosity jump at 1,000 km rather than 660 km depth related to changes in strength in ferropericlase (Marquardt and Miyagi, 2015). Karato et al. (1995, 2001) have shown evidence for a superplastic layer below 660 km depth, though thinner and much less viscous that what is seen in the geoid inversion. This difference can be understood in terms of the Cathles parameter—a ratio of the thickness of the layer and the flow wavelength cubed multiplied by the viscosity contrast of the layer (Richards and Lenardic, 2018). At long wavelengths, such as those appropriate to infer the radial viscosity structure of the mantle, the Cathles parameter shows that a thick, moderately low viscosity layer is equivalent to a thin, very low viscosity layer. New evidence from Mohiuddin et al. (2020) also suggests that cold slabs undergo extensive weakening due to the grain size reduction in ringwoodite. A significant reduction in the slab strength at the top of the lower mantle would be seen as a moderate reduction in viscosity in the spherical average to which the geoid is sensitive. Both the new geophysical constraints and the mineral physics studies suggest it is worth revisiting the traditional viscosity structure used to understand the controls on slab morphology. In this study we add to the existing body of work on slab behavior by exploring the effects of this new viscosity structure. The results are significant, as we find a new morphological feature with implications for the interpretation of the slabs observed in seismic tomography.

We term this new morphological feature *slab orphaning* (Grima et al., submitted). Orphaning enables a penetrative slab to split in to separate *orphan* and *parent* slabs at upper-lower mantle depths. Upon the abandonment of its orphan the parent slab deflects at the top of the upper-lower mantle. The flattened parent slab travels laterally across the top of the lower mantle and its negative buoyancy sustains the ongoing, continuous, and uninterrupted, subduction and plate convergence at the trench. Meanwhile the abandoned orphan slowly sinks under its own weight toward the core-mantle boundary (CMB) (see **Videos S1**, **S2**).

Slab orphaning results from intrinsic buoyancy changes within the slab at the depth of the perovskite forming reaction at 660 km depth and is an expression of an opposing force balance within the slab at the top of the lower mantle (**Figure 1**, step 1). Key to orphaning is the temperature dependence of the phase boundary depth associated with the transition. At 660 km depth the anomalously buoyant, untransformed material within cold slab core resists subduction into the lower mantle (**Figures 2a,b**). Contrary to Yoshioka et al. (2010), we find that the presence of an LVL encourages faster slab sinking speeds in the *proto-orphan*, leading to a proto-orphan in tension down-dip and a *proto-parent* in compression up-dip (**Figure 1**, step 2a,b). Higher slab sinking velocities in the LVL translate to higher strain rates for the proto-orphan (**Figures 2d–f**), which as the slab is at its maximum stress, decrease the viscosity of proto-orphan, weakening it (**Figure 1**, step 3, **Figure 2g**). The presence of a viscosity increase at the bottom of the LVL mainly confines the induced slab-mantle coupled viscous flow to the mantle above 1,000 km depth (e.g., Dal Zilio et al., 2018), and forces flow that was predominantly vertically oriented in the upper mantle, to switch to predominantly horizontal between 660 and 1,000 km depth (**Figure 1**, step 4, **Figures 2g–i**). The change in flow direction contributes to the slab shearing that takes place around the lens of anomalously buoyant material within the slab (**Figure 1**, step 5). Contemporaneous to the shearing of the proto-orphan, the increase in the lateral extent of the low density lens (due to continued subduction and hence accumulation of cold slab material at this depth) encourages the deflection of the proto-parent slab until it flattens at the top of the lower mantle (**Figures 2a–c**, **f,i**). Contrary to shallow slab tearing which is typically caused by extrinsic changes in the slab buoyancy (e.g., Yoshioka et al., 1995; Buiter et al., 2002; Burkett and Billen, 2009, 2010; Duretz et al., 2011, 2012; van Hunen and Allen, 2011), slab orphaning occurs independently of any external forces and is entirely a slab intrinsic process. The slab weakening at depth is also independent of the bending and unbending of the slab at the trench (e.g., Čížková et al., 2007). As we do not implement damage rheology the slab heals "instantly" from the increase in strain rates at shallow depths due to the slab bending at the trench, which hence does not influence orphaning at depth. For further in-detail discussions and descriptions of orphaning we refer the reader to Grima et al. (submitted).

A key question that naturally follows on from the observed diversity in slab morphologies, is the link that connects penetrative, flattened and orphaned slabs. Can slabs switch from one mode to another (and possibly back again) over time. If so, how? Mode switching has been proposed as a viable interpretation for the observed morphology in tomographic models of slabs such as those in the *Tethys*, *Japan*, and *Tonga* subduction zones (e.g., Hafkenscheid et al., 2006; Agrusta

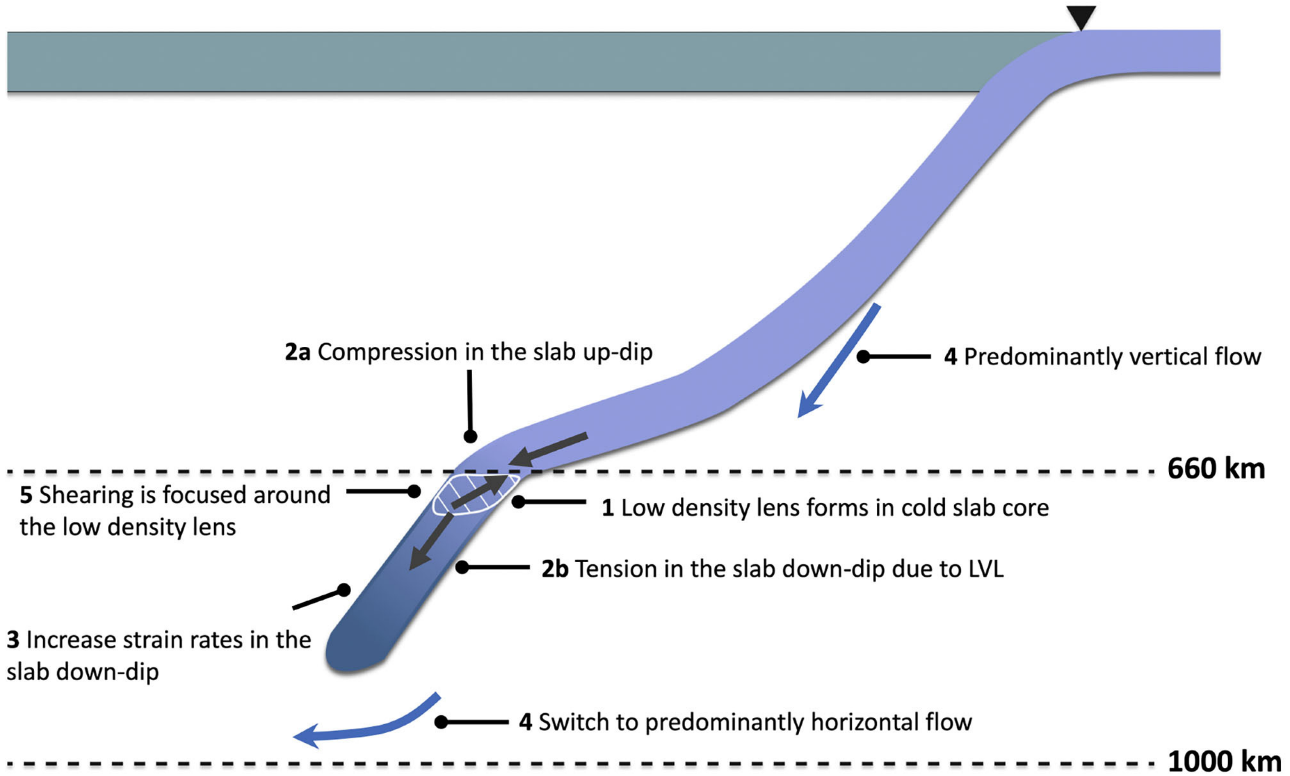

FIGURE 1 | Schematic showing the slab orphaning process. A lens of anomalously buoyant material forms within the cold slab core due to the temperature dependence of the phase boundary depth of the phase change (1). The anomalously buoyant material resists subduction and compresses the slab up-dip (2a). Faster sinking speeds in the LVL result in a proto-orphan in tension (2b) and give rise to an opposing force balance up and down-dip of the phase change. Faster slab sinking speeds in the LVL increase the strain rates in the proto-orphan and reduce its viscosity resulting in weakening (3). An increase in viscosity at 1,000 km mainly confines the induced slab-mantle viscous flow to the mantle above 1,000 km depth, forcing a switch in predominantly vertical flow above 660 km depth to predominantly horizontal flow in the LVL (4). Horizontal flow in the LVL increases the shearing and stretching of the slab around the low density lens (5) until the slab splits into separate flattened parent slab and a quasi-vertical orphan slab. The flattened parent slab travels laterally on top of the lower mantle sustaining subduction at the trench as the orphan slowly sinks toward the CMB.

et al., 2017; Yoshida, 2017). Plate reconstruction models often require slabs to switch from one behavior to the other to fit the geological observations at the surface (e.g., van der Hilst, 1995). Previous studies have suggested that one way slabs could mode switch, from flattening to penetrating, is through slab avalanching, where slab material piles up within the mantle transition zone until it avalanches, or flushes, downwards into the lower mantle (e.g., Machetel and Weber, 1991; Tackley et al., 1993; Zhong and Gurnis, 1995; Yoshioka et al., 2010; Yoshida, 2017). It has also been suggested that a flattened slab could switch to a penetrative mode if its viscosity is reduced through heating over time (Nakakuki et al., 2010). Agrusta et al. (2017) have proposed that mode switching is linked to factors such as the presence of phase transitions, slab age, changing upper plate forcing and changes in Clapeyron slope values due to slab dehydration. We propose that slabs can also mode switch from penetration to flattening, through slab orphaning (Grima et al., submitted). We suggest that slab break-off at the top of the lower mantle can split the previously penetrative slab into a separate flattened parent slab at the upper-mantle lower-mantle interface and an abandoned orphan that slowly sinks downwards toward the core mantle boundary. Similar to slab avalanching, slab orphaning is entirely independent of extrinsic surface plate dynamics and hence different from shallow slab break-off. Orphaning introduces the idea that slab fragmentation does not require major shifts in surface plate kinematics, nor the cessation of subduction, which are both often a staple in previous interpretations of slab break-off (e.g., Wortel, 2000; Sigloch et al., 2008; van der Meer et al., 2010, 2012, 2017; Richards et al., 2011; Sigloch, 2011; Schellart and Spakman, 2012; Sigloch and Mihalynuk, 2013; Honda, 2014, 2016).

We illustrate below with a regime diagram how slab orphaning links the two previously described archetypal slab morphologies observed in seismic tomography models, and how it is possible for a slab to dynamically transition from an initially penetrative mode dominated by vertical sinking to a flattened mode dominated by lateral motion above 660 km depth. The abundant abandoned orphans observed in the present-day Earth at upper-lower mantle depths and deeper (e.g., Hafkenscheid et al.,

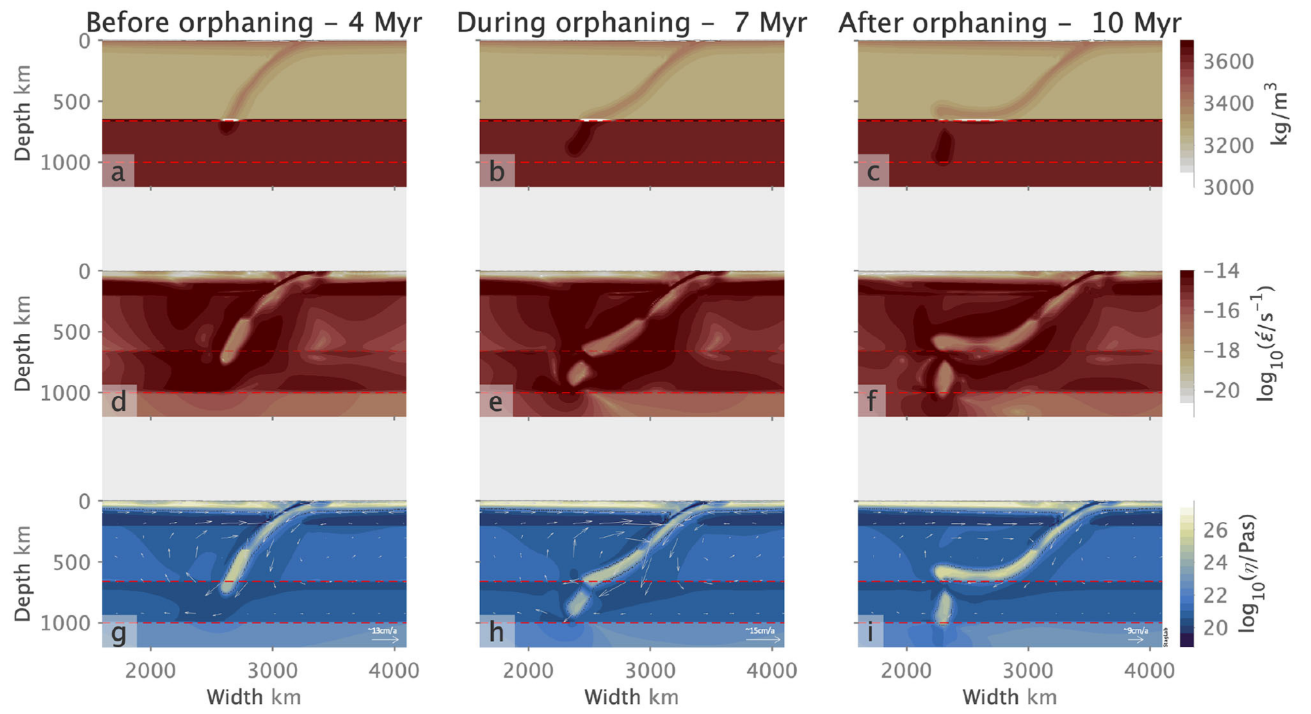

FIGURE 2 | Each panel represents a time slice in the evolution of our standard model $V3(600)_i$. **(a–c)** (Density) The temperature dependence of the phase boundary depth introduces a low density lens within the cold slab core at 660 km depth and resists the slab's penetration into the lower mantle. Continued subduction increases the lateral extent of the lens and encourages the flattening of the proto-parent **(d–f)** (Strain Rate) Higher slab sinking velocities in the LVL increase the strain rates within the proto-orphan. As the slab and proto-orphan have reached their maximum stress, the higher strain-rates are accommodated by a decrease in viscosity of the proto-orphan, weakening it. **(g–i)** (Viscosity) The change in flow direction from predominantly vertical in the upper mantle to horizontal in the LVL encourages the shearing of the proto-orphan from its parent.

2006; Sigloch et al., 2008; Sigloch, 2011; Honda, 2014; van der Meer et al., 2017) are therefore both a consequence and a testament to the penetrative-to-flattened mode switch itself (Grima et al., submitted).

Subduction dynamics within the traditional viscosity structure for the mantle have been explored extensively, but slab orphaning occurs within a hitherto overlooked region in the regime space between slab penetration and flattening. Similar to flattening and penetration, orphaning can occur for a wide variety of slab yield stresses, and therefore slab strengths and slab ages, initial subduction angles, overriding plate types, and Clapeyron slopes. We show that slab orphaning persists across various model setups, initial conditions and model resolutions, indicating that orphaning is a robust dynamical phenomenon. Slab orphaning also introduces an additional, intermediary mode to our previous binary understanding of slab dynamics. Not only can slabs flatten or penetrate but they can also adjust dynamically to changes in the relative strength of slab vs. mantle as a function of depth, giving rise to a new slab mode that is *slab orphaning* (Grima et al., submitted). Our results highlight the fundamental importance of the radial viscosity structure of the background mantle for slab morphology. For an extended discussion on the effects of different viscosity structures on deep slab morphology we refer the reader to the **Supplementary Section 1.4** and **Figures S15, S16**.

2. MATERIALS AND METHODS

2.1. Physical Model

Similar to previous work (e.g., Tackley, 2011; Crameri et al., 2012b; Garel et al., 2014; Crameri and Lithgow-Bertelloni, 2018; Čížková and Bina, 2019), we model an incompressible mantle by solving the non-dimensional equations for the conservation of mass (Equation 1), momentum (Equation 2), and energy (Equation 3) in the Boussinesq approximation, using the multi-grid finite difference/volume code StagYY (Tackley, 2008):

$$\vec{\nabla}\cdot\vec{v} = 0 \tag{1}$$

$$\vec{\nabla}\cdot\sigma_{ij} - \vec{\nabla}p = Ra(1 + P_B\cdot\frac{\partial\Gamma}{\partial\pi})\cdot T\hat{\vec{e}}_z \tag{2}$$

$$\frac{\partial T}{\partial t} = \nabla^2 T - \vec{v}\cdot\vec{\nabla}T + H \tag{3}$$

where v is the velocity, σ_{ij} is the deviatoric stress tensor, p the pressure, Ra the Rayleigh number, P_B, the phase buoyancy parameter, Γ the phase function, π the excess pressure, T the temperature, $\hat{\vec{e}}_z$ the vertical unit vector, t the time and H the non-dimensional internal heating rate.

The Rayleigh number (Ra) (see e.g., Turcotte and Schubert, 2014) can be expressed in terms of density (ρ), gravitational acceleration (g), the thermal expansivity (α), temperature scale

TABLE 1 | Model parameters.

Parameter	Symbol	Non-dimensional value	Dimensional value	Unit
Reference viscosity	η_0	1	7.74×10^{21}	Pa s
Mantle depth	D	1	2890	km
Upper-mantle depth	D_{UM}	0.23	660	km
Gravitational acceleration	g	–	9.81	ms^{-2}
Thermal conductivity	k	–	3	$Wm^{-1}K^{-1}$
Thermal diffusivity	κ	1	7.58×10^{-7}	m^2s^{-1}
Thermal expansivity	α	–	3×10^{-5}	K^{-1}
Temperature difference	ΔT	1	2,500	K
Reference density	ρ_0	1	3,300	$kg\ m^{-3}$
Heat capacity	C_{p0}	–	1,200	$Jkg^{-1}K^{-1}$
Internal heating rate	H	18.08	4.92×10^{-12}	Wkg^{-1}
Gas Constant	R	–	8.314	$Jmol^{-1}K^{-1}$
Ref. Clapeyron slope at 660 km	γ_{660}	–	−2.5	$MPaK^{-1}$
Density jump at 660 km	ρ_{660}	–	341	$kg\ m^{-3}$
Activation Stress	σ_{TS}	–	20	MPa
Plasticity				
Friction coefficient	μ	0.25	–	–
Cohesion	C	1,577	10×10^6	Pa
Max. yield stress	S	8.551×10^5	600×10^6	Pa
Diffusion creep				
Activation energy	$E*_{diff}$	14.43	300	$kJmol^{-1}$
Activation volume	$V*_{diff}$	9.0	2×10^{-6}	m^3mol^{-1}
Dislocation creep				
Activation energy	$E*_{disl}$	20.7	430	$kJmol^{-1}$
Activation volume	$V*_{disl}$	4.5	1×10^{-6}	m^3mol^{-1}
Powerlaw index	n	3.5	–	–
Sticky-air layer				
Thickness	d_{st}	0.05	150	km
Viscosity	η_{st}	$10^{-3}\eta_0$	7.74×10^{18}	Pa s
C-condition[a]	C_{Stokes}	0.013	–	–
Weak crustal layer				
Thickness	d_{crust}	0.005	15.2	km
Viscosity	η_{crust}	η_0	7.74×10^{21}	Pa s
Friction coefficient	μ_{crust}	0.001	–	–
Cohesion	C_{crust}	1577	10×10^6	Pa
Continent				
Thickness	d_c	0.071	200	km
Width	W_c	0.712	2000	km
Viscosity	η_c	$100\eta_0$	7.74×10^{24}	Pa s
Friction coefficient	μ_c	0.5	–	–
Density contrast	$\Delta\rho_c$	0.087	-25.0	$kg\ m^{-3}$

The reference Clapeyron slope refers to the Clapeyron slope value of our standard model $V3(600)_i$. *We vary this value in subsequent models as per* ***Table 2***.

[a] *Indicates suitable free-surface approximation with sticky-air approach if* $C_{Stokes} \ll 1$ *(Crameri et al., 2012a).*

(ΔT), mantle depth (D), thermal diffusivity (κ), and reference viscosity (η_0) as

$$Ra = \frac{\rho g \alpha \Delta T D^3}{\eta_0 \kappa} \tag{4}$$

The Rayleigh number is 10^7 and the internal heating rate has a value of 4.92×10^{-12} Wkg^{-1} which is equivalent to a non-dimensional value of 18.08, giving an internal heating-based Rayleigh number of 1.8×10^8 (see e.g., Turcotte and Schubert, 2014).

P_B (Christensen, 1995) is given by:

$$P_B = \frac{\gamma \delta\rho}{g\alpha\rho^2 D} \tag{5}$$

where γ is the Clapeyron slope, Γ is a phase function ($0 \leq \Gamma \leq 1$) indicating the relative portion of the dense phase and π is the excess pressure (Christensen and Yuen, 1985), defined as:

$$\pi = P - (p_0 + \gamma T) \tag{6}$$

where P is the hydrostatic pressure, p_0 is the transition pressure at 0 K.

We use a fixed depth discontinuous phase mode implemented as a sheet mass anomaly (Tackley, 1994, 1996) where the buoyancy deflection associated with the phase change is concentrated into one cell to represent an infinitely sharp transition rather than one with a finite width (Christensen and Yuen, 1984; Christensen, 1995). This method is equivalent to the effective thermal expansivity method of Christensen and Yuen (1984). The buoyancy associated with the deflection due to the phase transition is added to the momentum equation (Equation 2). A consequence of the sheet mass anomaly is that this is visually represented as a lens of anomalously low density material at 660 km depth. The density jump associated with the phase change is $\sim$ 10%, assuming an olivine mantle and a slab age at 660 km depth of 100 Myr with a density of $\sim$ 3,380 kgm^{-3}, this would be approximately equivalent to 340 kgm^{-3}. As required by the Boussinesq approximation, no effects due to the phase change are added to the energy equation (Christensen, 1995). We refer the reader to **Table 1** for values of the Clapeyron slope and other parameters.

The components of the viscosity have the form:

$$\eta_i(P,T) = \eta_0 \cdot \eta_b(P)(\frac{\sigma}{\sigma_{TS}}^{1-n_i} exp[\frac{E_i^* + PV_i^*}{RT}]) \tag{7}$$

where $\eta_b(P)$ contains the viscosity jumps at 660 and 1,000 km, $E*$ and $V*$ are the activation energy and volume, respectively, R is the gas constant, and n is the stress exponent. Subscripts i refer to the two different deformation mechanisms: diffusion or dislocation creep. σ_{TS} is the stress value above which dislocation creep is activated. For diffusion creep, the power law exponent is $n = 1$.

The viscosity at any pressure and temperature in the model is given by

$$\eta_{eff} = min[(\frac{1}{\eta_{diffusion}} + \frac{1}{\eta_{dislocation}})^{-1}, \eta_y] \tag{8}$$

where the limiting plastic viscosity η_y combines a Drucker-Pager yield criterion for brittle failure and a homogeneous ductile yield stress limit S which is applied everywhere throughout our model with the exception of the sticky-air layer;

$$\eta_y = (1/2\epsilon) min[C + P\mu, S] \tag{9}$$

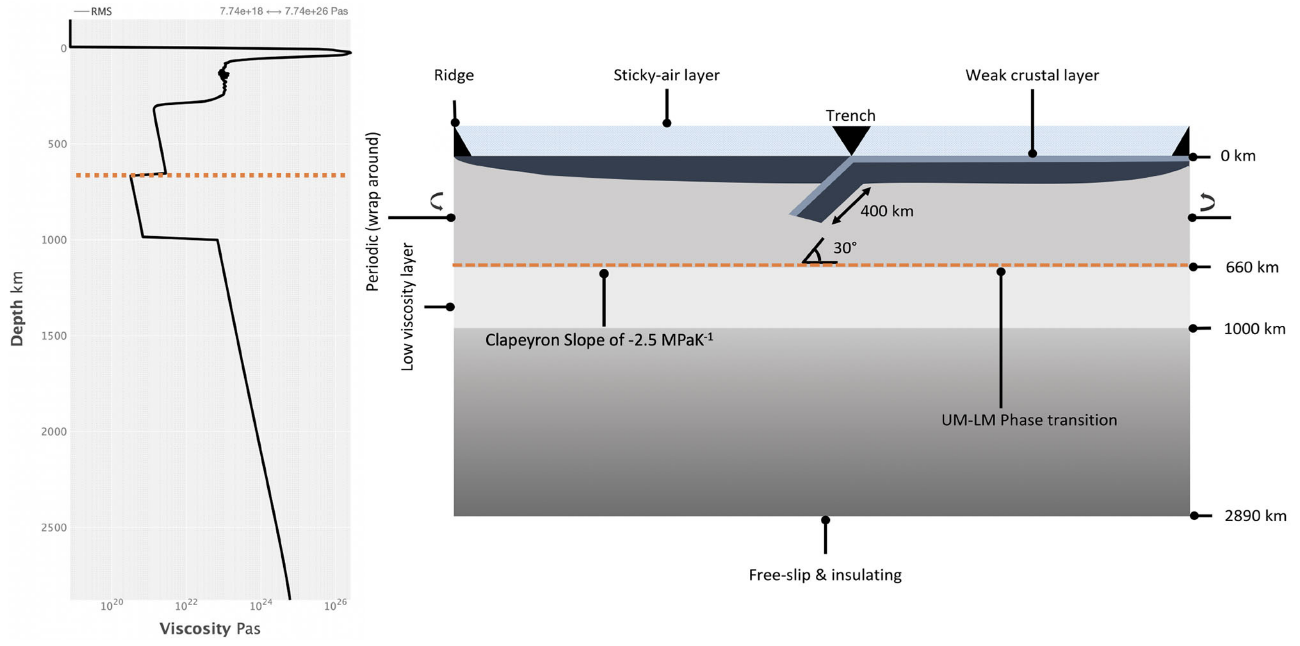

FIGURE 3 | Schematic showing a 1-D root-mean-square, horizontally averaged viscosity profile of our model on the left. The high viscosity at the top-most upper mantle is the result of the high viscosity of the initial slab, which adds to the average viscosity at this depth and overprints the viscosity of the asthenosphere that is present in all our models. The minimum and maximum values of the viscosity are included at the top right of the RMS profile. On the right we show our model setup where changes in the background viscosity follow from Equations (7)–(9). Viscosity increases are indicated by darker shades of gray.

with cohesion C, strain rate ϵ and friction coefficient μ. Finally, for numerical stability, the viscosity is bounded such that: $10^{-4}\eta_0 \leq \eta_{eff} \leq 10^5\eta_0$.

The models include a weak hydrated crustal layer on top of the subducting plate. This develops on the surface of ~10 Myr old portions of the lithospheric plate away from the ridge, and is allowed to form a freely evolving weak subduction channel once the plate subducts (Crameri and Tackley, 2015). The weak crustal layer differs from the mantle material by its lower yield stress, and has a thickness of 15 km. It is converted to regular mantle material once it is subducted below a depth $d >$ 400 km. To simulate a low-viscosity asthenosphere underneath the overriding and subducting plates, we implement a melting viscosity reduction (MVR). The MVR describes the decrease in viscosity by a factor of 10 in regions where the temperature exceeds a simple linear, depth-dependent solidus (Tackley, 2000). It has been shown that the MVR aids in maintaining plate like behavior (see e.g., Tackley, 2000; Crameri and Tackley, 2015, 2016). Finally, all our models include a low viscosity layer (LVL), between 660 and 1,000 km depth (see **Figure 3**) that is 10 times less viscous than the upper mantle, and an increase of an order of magnitude with respect to the upper mantle at 1,000 km (Rudolph et al., 2015). **Table 1** also provides further physical parameter details and **Figure 3** provides a visual representation of the physical model setup used in this study complete with an average 1D viscosity profile illustrating the root-mean-square, horizontally averaged viscosity of our models (see left hand side of **Figure 3**).

2.2. Numerical Model

Our numerical simulations are implemented in a two-dimensional Cartesian box with an aspect ratio of 2:1 (x:z). The model is discretized to 512 × 256 grid points. The horizontal grid spacing is constant and the resolution in the box is approximately 11 km. The vertical grid spacing is refined toward the rock-air interface, yielding a maximum vertical resolution of 4 km. On average, 100 Lagrangian tracers per grid cell are used to track the composition (i.e., mantle, weak crust, continent, and air) and physical interfaces (e.g., the free surface) in sub-grid resolution. The extensive tests carried out in previous studies such as Crameri and Tackley (2015) and Crameri and Lithgow-Bertelloni (2018) indicate that our simulations have the required resolution to capture the dynamics presented here. However, we have further verified that there are no under-resolved numerical issues, through resolution tests specifically performed for orphaning. The latter are described in detail in the **Supplementary Material**.

2.3. Boundary and Initial Conditions

The top boundary, including the sticky air layer after Crameri et al. (2012a), is set to a constant 300 K, while the bottom boundary is insulating with a zero heat flux condition. The bottom boundary is free slip and the top simulates a free surface. The side boundaries are periodic to prevent unnatural effects during the model's longer time evolution (Chertova et al., 2012).

The initial condition of our model is one of on-going subduction, with a down-going 400 km long, straight slab (see **Figure 3**). The slab initially has a constant thickness corresponding to the surface plate thickness at the trench. The slab dip angle is initially defined at the shallow depth range of around $150 - 250$ km and subsequently evolves freely. During model evolution, slab tip angles are measured at a depth of 175 km, to account for effects of mantle phase- and/or viscosity transitions.

The initial model setup features a spreading plate boundary at the edge of the box, which self-consistently evolves into a divergent plate boundary during subsequent model evolution. The initial temperature field consists of a standard $\sqrt{age}$-law to account for a thickening plate from the ridge toward the subduction trench. The initial plate thickness $w_{BL}(x) = w_{BL,0} \cdot \sqrt{\Delta x_{sc}}$, where $w_{BL,0}$ is a constant controlling the maximum thickness of the plate, x is the horizontal coordinate and Δx_{sc} is the distance from the spreading center at any given position x. The initial temperature is related to plate age as $T_z(x) = T_0 \cdot erf[(1 - z)/w_{BL}(x)]$, with $T_0 = 0.64$ the initial, non-dimensional mantle temperature and z the vertical coordinate ranging between 0 at the bottom to 1 at the top boundary. The plate's non-dimensional initial thickness at the trench is chosen to be $\sim 0.04D$ based on the observation that this is a typical boundary layer thickness with the chosen $Ra = 10^7$ and $H = 18.08$ (Crameri and Tackley, 2015). The resulting buoyancy contrast across the plate with variable thickness naturally supports the subsequent movement of the plate away from the ridge. The plate, as everything else in our model, is allowed to evolve freely out of this initial condition within the given boundary conditions and no artificial forcing is imposed (i.e., the model can evolve freely, and what goes out on one side of the domain, comes in on the other side of the domain). No weakening is imposed at the ridge and spreading occurs naturally due to the half space cooling law that we implement as an initial condition, and the subsequent internal dynamics.

While the model setup remains unchanged throughout our various implementations, we do vary key parameters to map out the slab orphaning regime space. We vary the slab yield stress (a measure of slab strength) via the ductile yield stress limit (see Equation 9), the Clapeyron slope, the initial subduction angles and the overriding plate type. When implemented, the continent is 2,000 km wide and 200 km deep, such that its roots extend to the bottom of the asthenosphere into the high viscosity upper mantle. The continental geometry is rectangular with an angled edge facing the trench similar to Crameri and Lithgow-Bertelloni (2018) and Grima et al. (submitted). The continental overriding plate also varies from its oceanic counterpart, due to its lighter density, higher viscosity, and friction coefficient, meaning that continental lithosphere is both lighter and stronger than oceanic lithosphere. Model parameters can be found in **Table 1**. Details of the model variants and the associated key parameter modifications are detailed in **Table 2** below.

Finally, all our data and results are post processed and analyzed using the geodynamic diagnostic, post-processing, and visualization software StagLab 3.0 (Crameri, 2018) (http://doi.org/10.5281/zenodo.1199037).

TABLE 2 | Model variations reflecting the different initial conditions.

Model	Slab yield stress (MPa)	Clapeyron slope (MPaK^{-1})	Slab dip angle (°)	Continental overriding plate
Group 1				
V3(600)$_i$	600	−2.5	30	X
V3(500)$_i$	500	−2.5	30	X
V3(400)$_i$	400	−2.5	30	X
V3(300)$_i$	300	−2.5	30	X
V3(200)$_i$	200	−2.5	30	X
Group 2				
V3(600)$_{ii}$	600	−2.0	30	X
V3(500)$_{ii}$	500	−2.0	30	X
V3(400)$_{ii}$	400	−2.0	30	X
V3(300)$_{ii}$	300	−2.0	30	X
V3(200)$_{ii}$	200	−2.0	30	X
Group 3				
V3(600)$_{iii}$	600	−1.5	30	X
V3(500)$_{iii}$	500	−1.5	30	X
V3(400)$_{iii}$	400	−1.5	30	X
V3(300)$_{iii}$	300	−1.5	30	X
V3(200)$_{iii}$	200	−1.5	30	X
Group 4				
V3(200)$_{iv}$	200	−1.0	30	X
V3(100)$_{iv}$	100	−1.0	30	X
Group 5				
V3(30°)	600	−2.5	30	X
V3(40°)	600	−2.5	40	X
V3(50°)	600	−2.5	50	X
V3(60°)	600	−2.5	60	X
Group 6				
V3$_c$(30°)	600	−2.5	30	✓
V3$_c$(40°)	600	−2.5	40	✓
V3$_c$(50°)	600	−2.5	50	✓
V3$_c$(60°)	600	−2.5	60	✓

Group 1 shows variations in slab yield stress with Clapeyron slope values of −2.5 MPaK $^{-1}$. Group 2 depicts variations in slab yield stress with Clapeyron slope values of −2.0 MPaK $^{-1}$. Group 3 represents variations in slab yield stress combined with Clapeyron slope values of −1.5 MPaK $^{-1}$. In group 4, low slab yield stresses are combined with Clapeyron slope values of −1.0 MPaK $^{-1}$. Groups 5 and 6 show variations in the subduction angle for intra-oceanic (group 5) and continental-ocean subduction (group 6) from 30° to 60° initial dip angles. Note that models V3(30°) and V3(600)$_i$ are identical.

3. RESULTS

3.1. Orphaning Regimes

We explore a range of subduction parameters (see **Table 2**) to delimit the conditions under which slabs can orphan. The orphaning regime space for our standard ocean-ocean convergence models is mapped out in **Figure 4**. **Figure 4** clearly highlights how orphaning is an intermediary, transitional stage occupying an optimal space between the two major slab end-member morphologies (i.e., flattened and penetrative slabs) as illustrated in **Figure 5**.

We find that slab orphaning is a pervasive slab behavior that is independent of the initial conditions or the model setup. Our

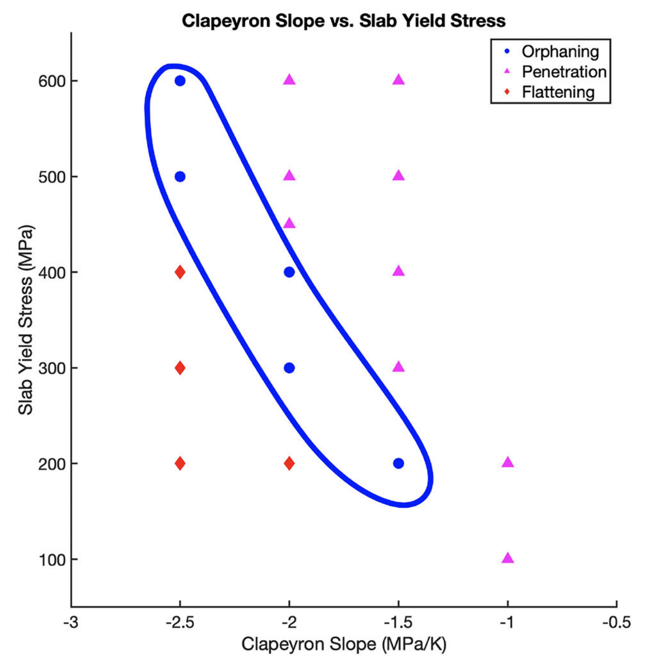

FIGURE 4 | Regime diagram for orphaning (blue circles), penetrating (magenta triangles), and deflected (red diamonds) slab morphologies in an ocean-ocean convergence setting. The orphaning regime space is highlighted in blue and shows that orphaning is prevalent for a range of slab yield stresses/slab strengths and Clapeyron slope values. Slab orphaning describes an intermediary space in the regime diagram between deflected and penetrating morphologies, indicating that orphaning as shown in **Figure 9**, **Videos S1**, **S2**, can be one way for slabs to switch from one mode to the other.

results highlight the prevalence of slab orphaning and show that orphaning can occur for a wide range of subduction parameters. We observe that slab orphaning behavior is common to all slabs regardless of their yield stress, indicating that orphaning can occur for both strong and weak slabs (see **Figure 6**). This is not to say the slab behavior and orphaning are entirely independent of the plate age. Provided that the slab's strength is offset by the appropriate resistance at the depth of the perovskite forming reaction, orphaning will persist. **Figure 4** highlights this point further and illustrates slab orphaning occurring for a variety of Clapeyron slope values ranging from −2.5 to −1.5 MPaK $^{-1}$. Slab orphaning is largely independent of the overriding plate type and occurs in simulations with both oceanic and continental overriding plate types (see **Table 4** and **Figures 7**, **8**). Finally, we test the effect of steepening the subduction angle of the slab at the trench and find that in our models, steeper subducting slabs will still orphan at the top of the lower mantle (see **Figures 7B–D**).

3.1.1. Slab Yield Stress and Orphaning

The subset of cases in **Figure 4** and **Table 3** illustrate that slab orphaning is a persistent phenomenon, common to both slabs with high yield stress (i.e., strong slabs) and low yield stress (i.e., weak slabs) observed for a range of Clapeyron slope values (see **Figure 6**). **Figure 4** also indicates that for strong slabs to orphan, a considerably negative Clapeyron slope value of −2.5 MPaK^{-1} is necessary. Introducing less negative Clapeyron slope values for strong slabs, with yield stress values of 600 and 500 MPa, pushes the slab behavior out of the orphaning regime into a penetrative one. On the other hand, maintaining the same Clapeyron slope value of −2.5 MPaK $^{-1}$ but reducing the slab yield stress to 400 MPa and below, firmly places the slab into a flattened regime.

Slab orphaning is possible across all slab yield stress values between 600 and 200 MPa under the condition that this is offset by the right amount of resistance, allowing for the relationship between strength of the slab and that of the mantle to remain in balance. Slabs only orphan when the anomalous buoyancy associated with the delayed endothermic phase reaction in the cold slab core is large enough to resist the subduction of the slab into the LVL but not large enough to prevent the slab's initial sinking into the LVL. Strong slabs (yield stress 500–600 MPa) therefore only orphan at a Clapeyron slope value of −2.5 MPaK $^{-1}$. Weaker slabs (yield stresses of 400 MPa or less) require less negative Clapeyron slopes values to orphan (−1.5 and −2.0 MPaK $^{-1}$). When the slab yield stress is <200 MPa, the slab behavior is drastically altered. Slabs with yield stress values of 100 MPa are too weak to reproduce any of the morphologies observed in seismic tomography models. Clapeyron slope values of −1.0 MPaK $^{-1}$ and lower do not offer enough resistance to either flatten or orphan slabs, even at a yield stress of 200 MPa.

For a Clapeyron slope of −2.0 MPaK $^{-1}$ slabs are equally inclined to flatten, deflect, or orphan depending on their strength. At this Clapeyron slope and using yield stress as a proxy for age, it seems the slab age determines whether the slab will penetrate into the lower mantle, orphan or deflect and flatten across the top of the lower mantle. While orphaning generally does not preferentially occur in older (stronger) or younger (weaker) slabs, we find that for this value of the Clapeyron slope the age of the subducting slab plays a role in determining which mode it will adopt at the upper to lower mantle interface, in agreement with previous studies (e.g., van der Hilst and Seno, 1993; Goes et al., 2011, 2017; Garel et al., 2014; Agrusta et al., 2017).

Variations in the slab yield stress produce variations in the length of the orphaning period. We define the orphaning period as the time it takes for the proto-orphan to be completely separated from the parent. It encompasses the period of time from the initial weakening of the proto-orphan at the top of the lower mantle to the time of complete abandonment by its parent. Longer orphaning periods, not surprisingly, produce bigger orphan sizes. The slab with the lowest yield stress from model $V3(200)_{iii}$ produces the largest orphan sizes, exhibits the longest orphaning period (**Table 3**) and the tip of its orphan undergoes the most folding and deformation (**Figure 6f**). Models with higher slab yield stresses [e.g., $V3(500)_{i}$ and $V3(300)_{ii}$] are associated with smaller orphan sizes and shorter orphaning periods.

We compare the amount of trench retreat that occurred during the individual orphaning periods for each model. The amount of trench retreat across all models from the initiation of orphaning at 660 km depth to complete separation of parent and orphan is similar across models. For three of the five models presented the trench retreat is on the order of 460 km for an

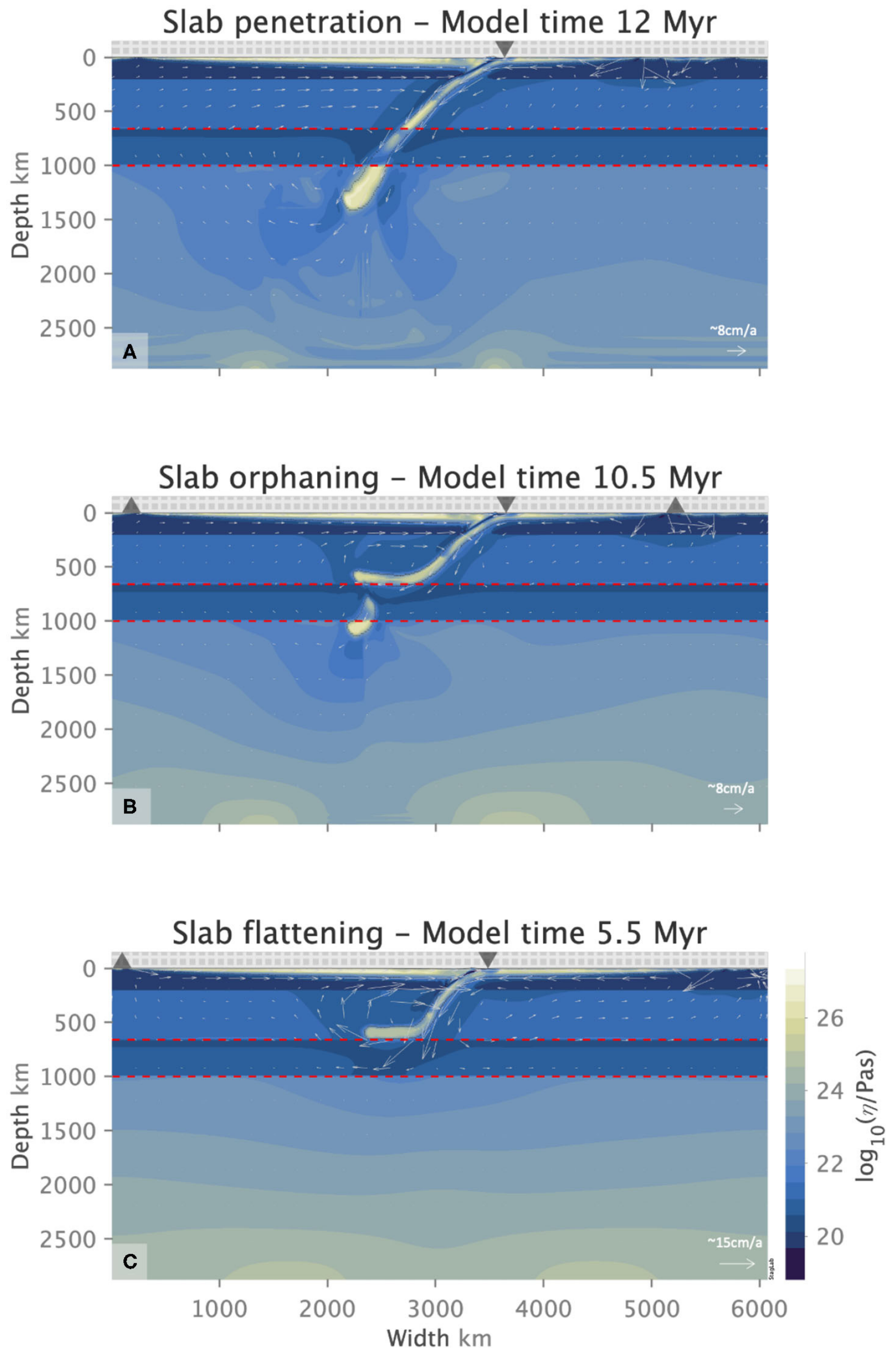

FIGURE 5 | Penetrative **(A)**, orphaning **(B)**, and flattening **(C)** behavior for a slab with a yield stress value of 400 MPa, the subduction of which is being offset by Clapeyron slope values of −1.5, −2.0 and −2.5 MPaK^{-1}, respectively. Sharp changes in the lower mantle viscosity underneath the slab tip are caused by sudden changes in the stress field. This is due to a heavy slab that is cold and therefore very viscous, subducting into the lower mantle where the viscosity is still stress-dependent due to dislocation creep. Orphaning occurs at the top of the lower mantle and is unaffected by the deeper lower mantle behavior. Flow arrows indicate the sense of flow direction and its relative magnitude for each figure.

average orphaning period of 1.9 Myr. Model $V3(600)_i$ exhibits significantly larger retreat of 689 km over orphaning periods of 3 Myr. The orphaning period is comparable to other cases and does not explain the larger retreat values. It seems in this case the resistance to subduction is accommodated through significant trench roll-back during the orphaning period. Why for this

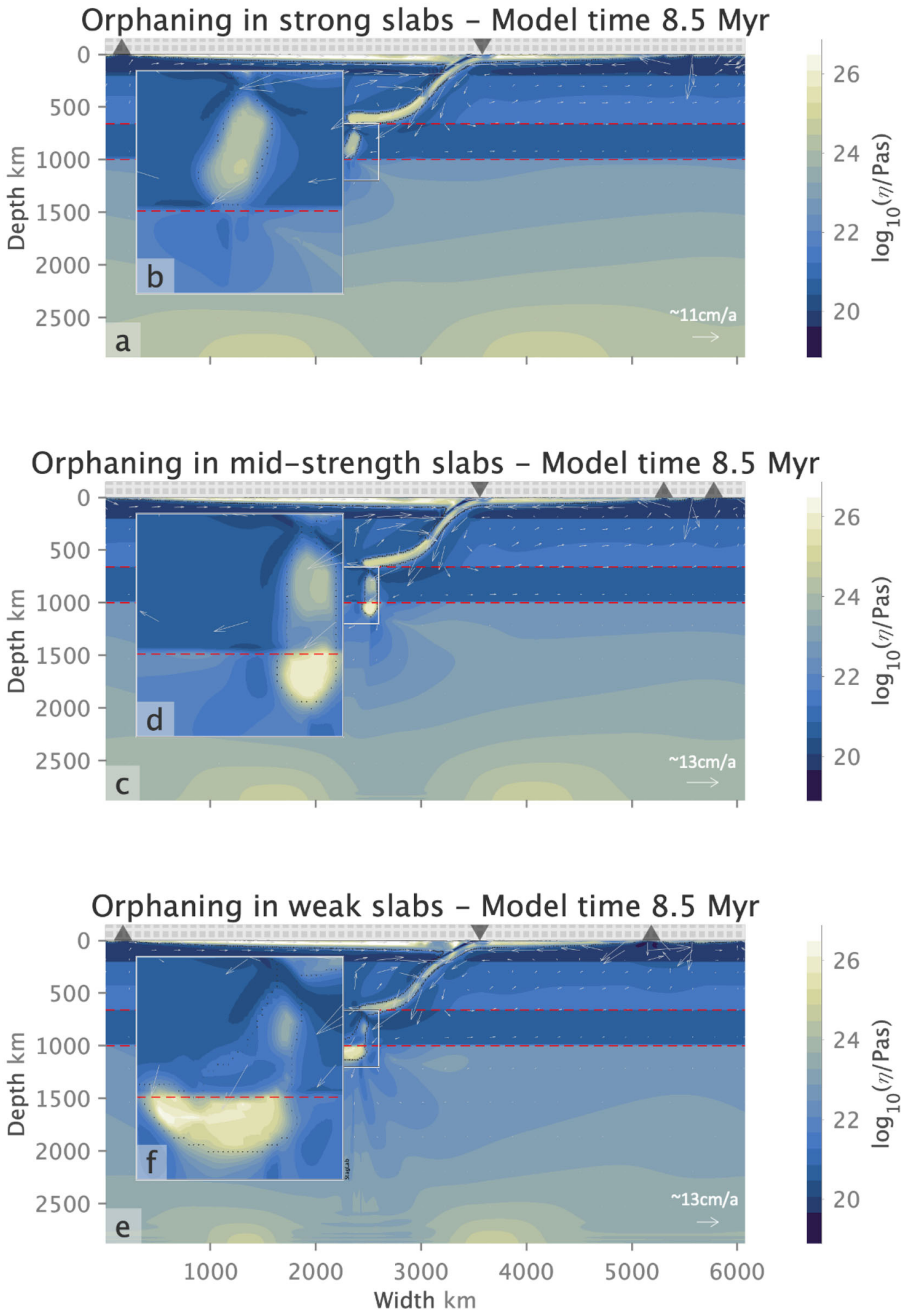

FIGURE 6 | Slab orphaning for slab yield stress values of 600 MPa **(a,b)**, 400 MPa **(c,d)**, and 200 MPa **(e,f)** with respective Clapeyron slope values of −1.5, −2.0, −2.5 MPaK^{-1}. Variations in orphan slab viscosity across **(a–e)** reflect the variations in the slab yield stress. Slabs with lower yield stresses produce weaker orphans that deform more [compare **(b,d)** with **(f)**]. **(c–f)** Show penetration of the orphan slab tip into the lower mantle due to the large size of the proto-orphan. In both cases the proto-orphan slab tip penetration occurs before orphaning and does not influence it. Flow arrows indicate the sense of flow direction and its relative magnitude for each figure.

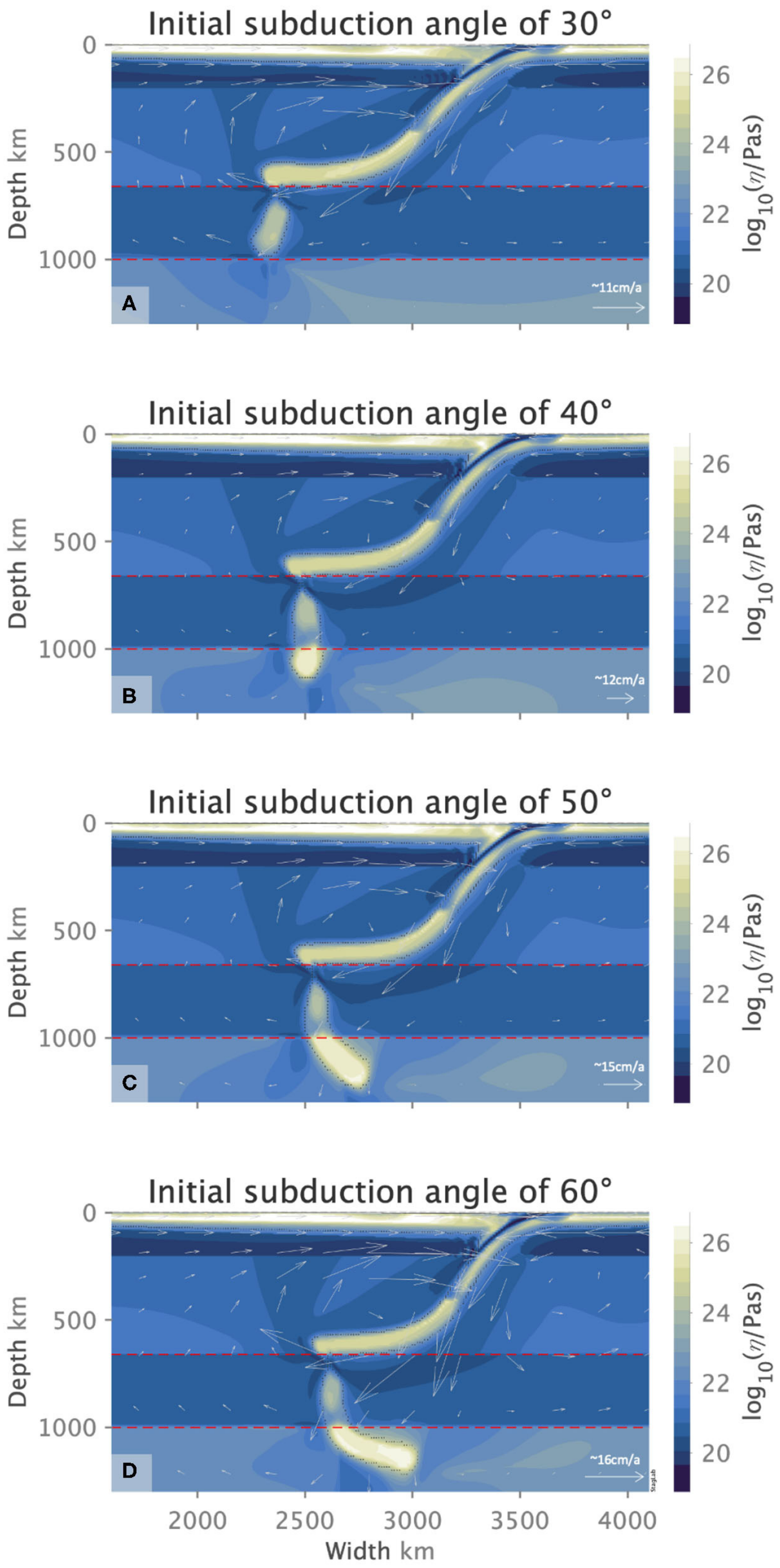

FIGURE 7 | Slab orphaning at 8.5 Myr for initial subduction angle of 30° **(A)**, at 9 Myr for 40° **(B)**, and 10 Myr for 50° and 60° **(C,D)**, respectively, in ocean-ocean settings. Flow arrows indicate the sense of flow direction and its relative magnitude for each figure.

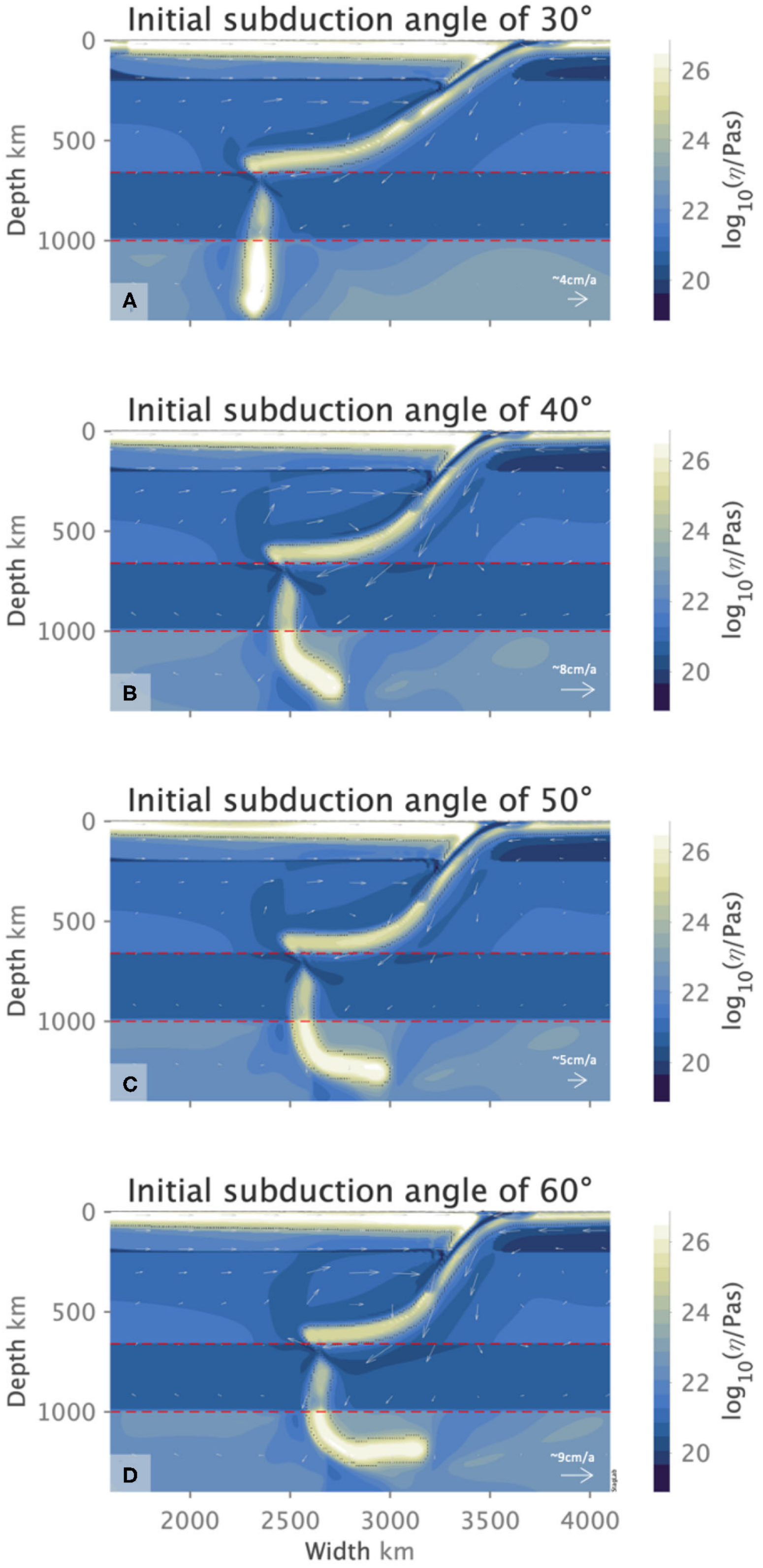

FIGURE 8 | Slab orphaning at 22.5 Myr **(A)**, 16.5 Myr **(B)**, 17 Myr **(C)**, and 18 Myr **(D)** for initial subduction angles of 30°, 40°, 50°, and 60°, respectively in the presence of a continental overriding plate, showing steep, curved, and overturned orphan slabs. The deep continental roots of the overriding plate reduces the overall subduction velocities due to increased coupling between the overriding plate and the uppermost-upper mantle. This encourages longer orphaning periods. Flow arrows indicate the sense of flow direction and its relative magnitude for each figure.

combination of parameters and not others? In the case of model $V3(600)_i$ the strong slab is able to both sink into the lower mantle to produce a considerably larger orphan (**Table 3**) and continue to act as a coherent stress guide (Conrad and Lithgow-Bertelloni, 2002) transmitting the stresses felt by the slab up to the surface pushing the trench back. In model $V3(300)_{ii}$ we see the most restricted trench retreat out of all the orphaning simulations. In this case the slab's yield stress is a factor of two lower and the slab is not able to transmit stresses up the plate as efficiently. The weaker slab has the second smallest orphan, the shortest orphaning period and the least trench retreat. Out of all our simulations, model $V3(200)_{iii}$ has the lowest possible slab yield stress that can still reproduce the slab morphologies observed in seismic tomography. In this case the slab's ability to transmit stresses to the surface is greatly reduced. The resistance to the slab's subduction is reflected in the deformation of the proto-orphan slab tip/toe and later on as the slab orphans, in the orphan slab tip, as it piles up at 1000 km depth before it sinks into the deeper lower mantle (see **Figure 6f**). Concurrently to orphaning the parent slab flattens at the depth of the endothermic phase change.

While a comprehensive correlation for all the orphaning behaviors described in **Table 3** is difficult, it is possible to tease out some important trends. The most obvious of these is the relationship between the orphan size and the amount of time it takes for the orphan to be separated from its parent (i.e., the orphaning period). The longer the orphaning period, the bigger the orphan. This is because extended orphaning periods allow for more slab material to sink into the lower mantle before the orphan slab is completely abandoned by its parent. The largest orphaning sizes and longest orphaning periods are associated with those slabs of medium and weakest strengths [models $V3(400)_{ii}$ and $V3(200)_{iii}$]. On the other hand, there seems to be no correlation between the amount of trench retreat and the length of the orphaning period, orphan sizes, the slab yield stress or any other variable. This seems to indicate that trench retreat during orphaning and in general is a complex process (Jarrard, 1986; Tagawa et al., 2007; Torii and Yoshioka, 2007), shaped by many interacting factors such as slab stiffness and strength, arc deformation and upper mantle flow, amongst others (e.g., Funiciello et al., 2003; Schellart, 2004; Faccenna et al., 2007; Di Giuseppe et al., 2008; Boutelier and Cruden, 2013; Čížková and Bina, 2013) most of which are not taken into account here.

3.1.2. Subduction Angles

Slab orphaning is also independent of the initial subduction angle of the slab at the trench. Our results show that varying the initial, shallow-depth angle of subduction from 30° to 60° does not in anyway act as a deterrent to orphaning. We note that the steeper the initial, shallow-depth slab angle, the bigger the orphans which also tend to be highly curved and overturned (see **Figure 7**).

3.1.3. Orphaning and the Overriding Plate Type

As an upper-lower mantle process, slab orphaning occurs regardless of the nature of the overriding plate. Orphaning occurs both in ocean-ocean and continent-ocean convergence. However, our results indicate that there are small, subtle differences between the two. A continental overriding plate encourages longer orphaning periods and bigger orphans than its oceanic counterpart (**Table 4**). Slab orphans in a continent-ocean setting also exhibit steeper angles and overturning, characteristics that are less pronounced in the orphan slabs of ocean-ocean settings (see **Figures 7**, **8**).

TABLE 3 | Orphan sizes, orphaning periods, and their associated trench retreats compared across orphan variants with different slab yield stresses and Clapeyron slopes for ocean-ocean convergence models.

Model	Slab yield stress (MPa)	Clapeyron slope (MPaK $^{-1}$)	Slab dip Angle (°)	Orphaning period (Myr)	Orphan size (km)	Trench retreat (km)
$V3(600)_i$	600	−2.5	30	3	271	689
$V3(500)_i$	500	−2.5	30	1.5	100	463
$V3(400)_{ii}$	400	−2.0	30	3.5	364	475
$V3(300)_{ii}$	300	−2.0	30	1.5	144	380
$V3(200)_{iii}$	200	−1.5	30	4.5	684	451

Table 4 details the orphaning statistics for both overriding-plate types and the associated subduction angles. The time it takes for a slab to orphan (i.e., the orphaning period) in our models ranges between 5.5 and 2.5 Myr. Models with a continental overriding plate exhibit longer orphaning periods with model $V3_c(30^\circ)$ exhibiting the longest orphaning period. For models with an oceanic overriding plate, the longest slab orphaning periods are those for $V3(50^\circ)$ where the slab orphans over 3.5 Myr. In this case the longest orphaning periods do not necessarily correspond to the largest orphan sizes. Comparing the results from **Table 4** with those in **Table 3**, we observe that the relationship between slab yield stress, orphan size, and orphaning periods is disrupted once we introduce variations in overriding plate type and initial subduction angles. This indicates that changes in these subduction parameters introduce additional forcing to the system with consequences to the relationship between the forces driving subduction and those resisting it.

The amount of trench retreat measured during the orphaning period varies across models, from 546 to 772 km over orphaning periods of 3–5.5 Myrs. The most conservative trench retreat is recorded for models with a continental overriding plate and an initial subduction angle of 60° for an orphaning period of 4 Myr. The largest trench retreats overall are measured for models with a continental overriding plate and an initial subduction angle of 30° and models with an oceanic overriding plate and an initial subduction angle of 40°, over orphaning periods of 5.5 and 3 Myr, respectively. Similar to our results presented in **Table 3** in section 3.1.1, we note that there is no obvious correlation between the amount of trench retreat during orphaning and any orphaning variable recorded in **Table 4**.

4. DISCUSSION

4.1. Variations in Orphaning

Slab orphaning is a new morphological feature that similar to slab flattening and penetration, prevails under a wide range of

TABLE 4 | Orphan sizes, orphaning periods, and their associated trench retreat compared across all orphan variants in intra-oceanic and continent-ocean subductions.

Model	Slab yield stress (MPa)	Clapeyron slope (MPaK $^{-1}$)	Overriding plate type	Slab dip Angle (°)	Orphaning period (Myr)	Orphan size (km)	Trench retreat (km)
V3(600)$_i$	600	−2.5	Oceanic	30	3	271	689
V3(40°)	600	−2.5	Oceanic	40	3	457	772
V3(50°)	600	−2.5	Oceanic	50	3.5	455	665
V3(60°)	600	−2.5	Oceanic	60	2.5	535	677
V3$_c$(30°)	600	−2.5	Continental	30	5.5	656	772
V3$_c$(40°)	600	−2.5	Continental	40	3.5	531	641
V3$_c$(50°)	600	−2.5	Continental	50	3	768	594
V3$_c$(60°)	600	−2.5	Continental	60	4	878	546

subduction parameters and initial model setups. We present examples of slab orphaning occurring for a wide variety of subduction angles, slab yield stresses, Clapeyron slope values and different overriding plate types. Key to orphaning is the presence of an LVL below 660 km and above 1,000 km depth (cf. **Supplementary Section 1.4** and **Figures S15**, **S16**). This choice of the mantle viscosity structure is motivated by geophysical data and mineral physics studies that suggest the presence of an LVL directly below the upper mantle (Karato et al., 1995, 2001; Mitrovica and Forte, 2004; Rudolph et al., 2015) and a viscosity increase at 1,000 km depth (King and Masters, 1992; Kido and Čadek, 1997; Forte and Mitrovica, 2001; Mitrovica and Forte, 2004; Marquardt and Miyagi, 2015; Rudolph et al., 2015). Our choice of viscosity structure does not exclude penetrative or flattened slab morphologies in favor of slab orphaning, all three slab morphologies can be observed, depending on the slab yield stress and the Clapeyron slope value. The different slab behaviors for the same viscosity structure highlights the role of the dynamic relationship between the strength and buoyancy of the slab and those of the surrounding ambient mantle. We thus, bring to focus a more expansive role for the ambient mantle beyond that of a semi-permeable barrier to one where the deeper mantle directly affects and shapes slab behavior (Yoshioka et al., 2010).

The variations in subduction parameters give rise to a diversity of orphan slab sizes and orphaning periods. Compared to their shallower counterparts, slabs with initial shallow-depth steep subduction angles of 50° and 60° encourage steeper slab angles at the top of the lower mantle. Steeper slab angles at 660 km depth restrict the amount of untransformed, anomalous buoyant material at this depth, which reduces the resistance to the slab's subduction into the LVL and allows for more material to sink into the lower mantle to produce bigger orphans (see **Figures 7C,D**, **8B–D**). We also observe that for steeper subduction angles particularly in the presence of a continental overriding plate, the subducted slab displays an acutely concave geometry (**Figure 8**) similar to that observed in previous work (e.g., Schellart, 2005; Arredondo and Billen, 2016, 2017; Billen and Arredondo, 2018) and produces overturned, upside-down slab orphans. The concave slab geometry attests to a strong slab that is forced into an acute bend before it is abandoned by its parent. The presence of a continental overriding plate slows down the subduction velocities and induces a strong shear drag in the topmost lower mantle. This introduces additional forcing to the system and encourages slab steepening, yielding larger orphan slabs over longer orphaning periods (see **Figure 8** vs. **Figure 7**).

Slab orphaning is inherently an upper-lower mantle interface process, intrinsically tied to the internal buoyancy changes in the slab. It is entirely independent of surface plate dynamics, or specific conditions at the trench. The diversity of orphan slabs is intimately linked to the orphaning regime space and represents the dynamic balance between the slab strength $vis - a - vis$ that of the ambient, surrounding mantle. As the relationship between the slab and mantle strength varies with depth, the subducting slab is forced to switch from a penetrative mode to a flattened one, leaving a fragmented orphan behind. Orphaning allows a slab to adjust to this evolving ratio of slab and mantle strength without causing any interruptions to the surface kinematics. In this way slab orphaning provides a transitional pathway for a slab mode switch and illustrates one example of how penetrative morphologies can be linked to flattened ones (**Figure 9**). **Figure 4** clearly illustrates how strong, mid-strength and weak slabs can all orphan as long as the negative buoyancy of the slab is offset by an appropriate amount of anomalous buoyancy that resists the slab's subduction into the lower mantle.

Our results suggests that the slab orphaning process is not dependent on one particular case of subduction dynamics and can theoretically occur at most subduction zones for most slabs. The persistence of orphaning at different Clapeyron slopes indicates that orphaning should still occur for slabs in the mantle, which are not entirely made of olivine, and will have effectively less negative Clapeyron slopes. The Clapeyron slope for the ringwoodite to bridgmanite and periclase transition given in the literature, has evolved over time from −6 to −1 MPaK $^{-1}$ (Anderson, 1987; Van Hunen et al., 2001; Katsura et al., 2003; Ye et al., 2017; Ishii et al., 2019). In the presence of other elements and other phases it is likely to be less negative than −3 MPaK $^{-1}$. To cover the range in values, geodynamic studies tend to test for slopes between 0 and −2.5 MPaK $^{-1}$ (e.g., Billen, 2008; Yoshioka et al., 2010; Honda, 2016; Mao and Zhong, 2018). We illustrate here that orphaning does happen at less negative Clapeyron slope values and is not tied to one pre-determined slab yield stress.

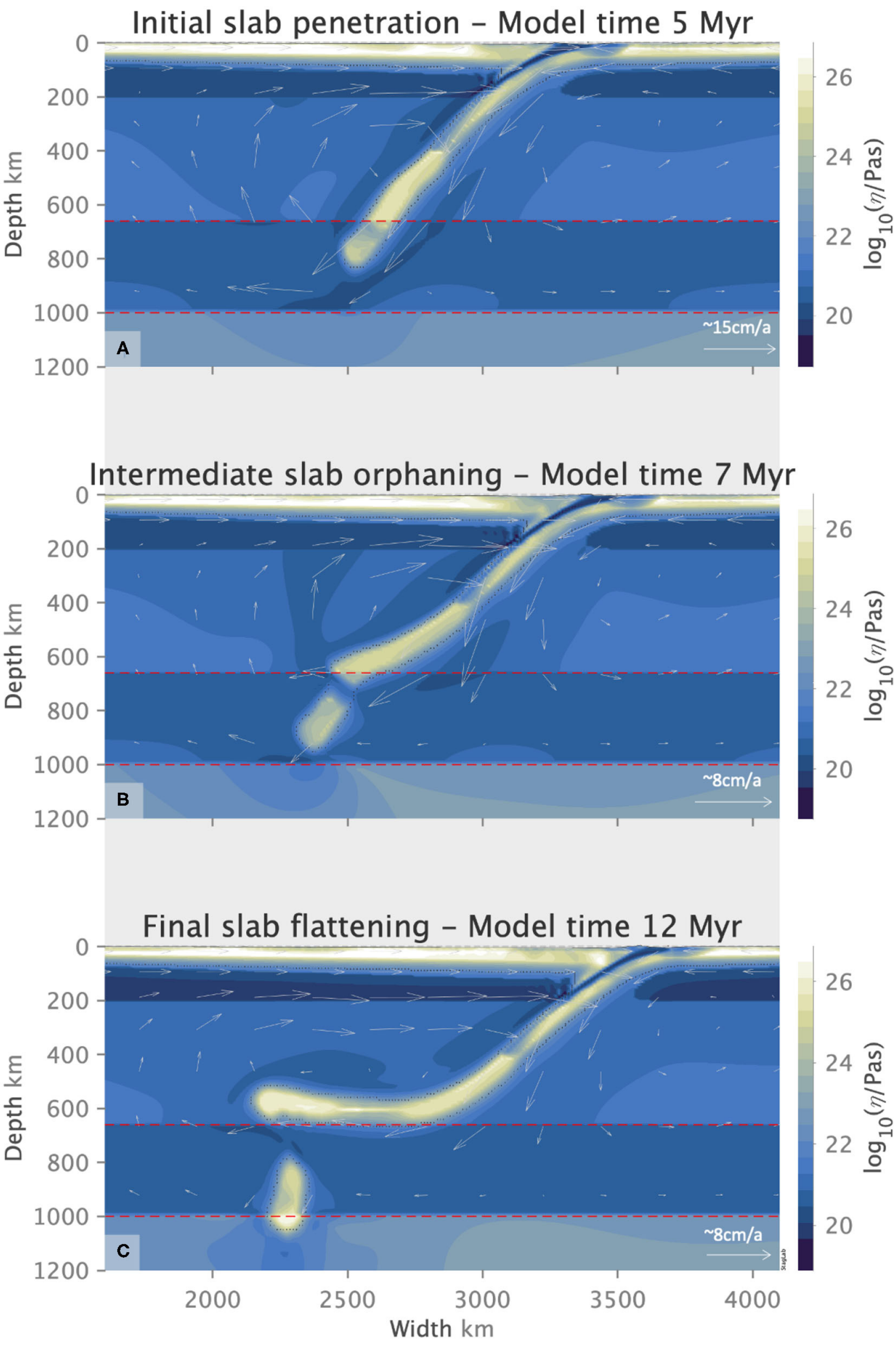

FIGURE 9 | A slab with yield stress of 600 MPa transitions from an initial penetrative behavior **(A)** to a flattened morphology **(C)** through orphaning **(B)**, showing how orphaning allows a slab to mode switch and transition from one morphology to the other. Flow arrows indicate the sense of flow direction and its relative magnitude for each figure.

4.2. Orphan Slabs as an Intermediate Slab Morphology

Our results show that there is no simple and direct correlation between subduction angles, slab strength/age, and slab orphaning periods, orphan sizes and the trench retreat throughout the orphaning period. This is in agreement with the work of Jarrard (1986), who has also argued that there is no direct correlation between flattened or penetrative slab morphologies and any one subduction parameter. However, we do note that for Clapeyron slopes values of -2.0 MPaK $^{-1}$ all three major slab behaviors are equally possible. This is the only case we observe where, provided all subduction parameters remain constant, slab age can determine whether the slab deflects, orphans or penetrates. At a Clapeyron slope value of -2.0 MPaK $^{-1}$, if the slab has high yield stress values, then it is strong enough to overcome the resistance to its sinking. If the slab has low yield stress values then the anomalous buoyancy due to the delayed endothermic phase transition in the cold slab core will force it to flatten and deflect. Intermediary slab strengths result in orphaning (c.f. **Figure 4**). However, a change in the Clapeyron slope, to reflect a change in the resistance to sinking, quickly upsets this balance and leads to slab penetration or deflection. This indicates that the slab behavior at deeper mantle depths is more complex than a simple reflection of the slab age and is interdependent on both variations in slab and mantle strength.

It is clear that orphaning morphologies are representative of an intermediary slab behavior between deflected, flattened slabs and deep, penetrative ones (**Figure 9**). Orphaning fills the gap in the subduction regime diagram between these two end member slab behaviors. Slab orphaning also provides a possible answer to two important questions in slab dynamics: "Can slabs switch from one behavior to the other?" and "How can this transition in slab dynamics be accomplished?" A slab that has split into a parent and orphan is one that has undergone intrinsic buoyancy changes and metamorphosed through all three slab morphologies (see **Figure 9**). Prior to orphaning the slab adopts a penetrative morphology. Changes in the force balance within the slab in the uppermost-lower mantle force the slab to undergo orphaning, which allows it to adjust from a steep, penetrative morphology to a flattened, deflected one. Orphaning, therefore, provides one pathway through which slabs can switch modes and is available to all slabs, irrespective of their strength, the nature of the overriding plate, or the subduction angle, provided that they reach the top of the lower mantle.

5. CONCLUSION

We have added a new and potentially transformative element to understanding the slab morphologies observed in seismic tomography by exploring the effects of a new background mantle viscosity structure, different from the traditional viscosity increase at 660 km depth. The new viscosity structure is motivated by new geophysical and mineral physics studies (Marquardt and Miyagi, 2015; Rudolph et al., 2015; Mohiuddin et al., 2020). Slab orphaning presents for the first time, a dynamic link between penetrating and deflecting slab behaviors, and fills a gap in the subduction regime space. We propose that slab orphaning is an important facet in deep slab dynamics, and one that allows slabs to evolve from one morphology to the other as a result of slab intrinsic buoyancy changes at depth. Similar to deflected and penetrating morphologies, slab orphaning ensues for a variety of slab strengths, slab dip angles, and overriding plate types. We note that slab strength is not the only major deciding factor in shaping orphan slabs. Slab morphologies in the lower mantle are an interplay between the slab yield stress and the Clapeyron slope value, where a less negative Clapeyron slope necessitates a lower slab yield stress for orphaning to take place. This signifies that it is the relationship between the forces driving subduction and those resisting it at any given depth, which is far more important than any one single slab/subduction parameter. The new orphaning morphology and its appearance in the presence of a low viscosity layer at the top of the lower mantle, brings to the forefront the importance of determining the viscosity structure of the mantle to understand slab dynamics and interpreting seismic tomography.

Orphan slabs clearly fill the gap in the subduction regime diagram between flattened and penetrating slabs and are the intermediary between these two extensively studied slab morphologies. Seismic tomography models confirm the presence of fragmented slabs at the upper mantle lower mantle interface (e.g., Sigloch et al., 2008; Yoshida et al., 2012; Honda, 2014, 2016; Yoshida, 2017). Our results suggest that the presence of orphan slabs beneath subduction systems such as the Farallon, Tonga, Japan, Tethys, and under NE China could indicate a slab behavior switch from penetrative to flattened morphology, leaving an abandoned orphan in its wake (Grima et al., submitted). For a detailed comparison with seismic tomography we refer the reader to Grima et al. (submitted).

DATA AVAILABILITY STATEMENT

The raw data supporting the conclusions of this article will be made available by the authors, without undue reservation. The post-processing diagnostic tool StagLab is available from https://zenodo.org/record/3783701#.X1DNSS2w2B0.

AUTHOR CONTRIBUTIONS

AG performed the research, analyzed the results, and wrote the manuscript. FC provided the numerical model and post processing tools as well as guidance and advice. CL-B supervised the project, provided guidance, and support. All authors contributed to the article and approved the submitted version.

FUNDING

AG was supported by the Commonwealth Scholarship Commission and the Slichter endowed chair to CL-B, and FC was supported by the Research Council of Norway Centers of Excellence (223272). Computational support was provided by ARCHER (NE/M00046X/1) and sigma2 (NN9283K).

ACKNOWLEDGMENTS

We thank the editor and reviewers for their constructive and helpful comments that greatly improved the manuscript. We also thank Lars Stixrude, Jeroen van Hunen, and John Brodholt for their fruitful discussions.

SUPPLEMENTARY MATERIAL

The Supplementary Material for this article can be found online at: https://www.frontiersin.org/articles/10.3389/feart.2020.00374/full#supplementary-material

Video S1 | Orphaning in ultra high resolution.

Video S2 | Orphaning in standard high resolution.

Data Sheet 1 | Tests and evaluations.

REFERENCES

Agrusta, R., Goes, S., and Hunen, J. V. (2017). Subducting-slab transition-zone interaction : stagnation, penetration and mode switches. *Earth Planet. Sci. Lett.* 464, 10–23. doi: 10.1016/j.epsl.2017.02.005

Anderson, D. L. (1987). Thermally induced phase changes, lateral heterogeneity of the mantle, continental roots, and deep slab anomalies. *J. Geophys. Res.* 92, 13968–13980. doi: 10.1029/JB092iB13p13968

Arredondo, K. M., and Billen, M. I. (2016). The effects of phase transitions and compositional layering in two-dimensional kinematic models of subduction. *J. Geodyn.* 100, 159–174. doi: 10.1016/j.jog.2016.05.009

Arredondo, K. M., and Billen, M. I. (2017). Coupled effects of phase transitions and rheology in 2D dynamical models of subduction. *J. Geophys. Res.* 122, 5813–5830. doi: 10.1002/2017JB014374

Billen, M. (2010). Slab dynamics in the transition zone. *Phys. Earth Planet. Inter.* 183, 296–308. doi: 10.1016/j.pepi.2010.05.005

Billen, M. I. (2008). Modeling the dynamics of subducting slabs. *Annu. Rev. Earth Planet. Sci.* 36, 325–356. doi: 10.1146/annurev.earth.36.031207.124129

Billen, M. I., and Arredondo, K. M. (2018). Decoupling of plate-asthenosphere motion caused by non-linear viscosity during slab folding in the transition zone. *Phys. Earth Planet. Inter.* 281, 17–30. doi: 10.1016/j.pepi.2018.04.011

Billen, M. I., and Hirth, G. (2007). Rheologic controls on slab dynamics. *Geochem. Geophys. Geosyst.* 8, 1–24. doi: 10.1029/2007GC001597

Boutelier, D., and Cruden, A. (2013). Slab rollback rate and trench curvature controlled by arc deformation. *Geology* 41, 911–914. doi: 10.1130/G34338.1

Buiter, S. J., Govers, R., and Wortel, M. J. (2002). Two-dimensional simulations of surface deformation caused by slab detachment. *Tectonophysics* 354, 195–210. doi: 10.1016/S0040-1951(02)00336-0

Burkett, E. R., and Billen, M. I. (2009). Dynamics and implications of slab detachment due to ridge-trench collision. *J. Geophys. Res.* 114, 1–16. doi: 10.1029/2009JB006402

Burkett, E. R., and Billen, M. I. (2010). Three-dimensionality of slab detachment due to ridge-trench collision: laterally simultaneous boudinage versus tear propagation. *Geochem. Geophys. Geosyst.* 11, 1–21. doi: 10.1029/2010GC003286

Chertova, M. V., Geenen, T., Van Den Berg, A., and Spakman, W. (2012). Using open sidewalls for modelling self-consistent lithosphere subduction dynamics. *Solid Earth* 3, 313–326. doi: 10.5194/se-3-313-2012

Christensen, U. R. (1995). Effects of phase transitions on mantle convection. *Annu. Rev. Earth Planet. Sci.* 23, 65–88. doi: 10.1146/annurev.ea.23.050195.000433

Christensen, U. R. (1996). The influence of trench migration on slab penetration into the lower mantle. *Earth Planet. Sci. Lett.* 140, 27–39. doi: 10.1016/0012-821X(96)00023-4

Christensen, U. R., and Yuen, D. (1984). The interaction of a subducting lithospheric slab with a chemical or phase boundary. *J. Geophys. Res.* 89, 4389–4402. doi: 10.1029/JB089iB06p04389

Christensen, U. R., and Yuen, D. (1985). Layered convection induced by phase transitions. *J. Geophys. Res.* 90, 10,291–10,300. doi: 10.1029/JB090iB12p10291

Čížková, H., and Bina, C. R. (2013). Effects of mantle and subduction-interface rheologies on slab stagnation and trench rollback. *Earth Planet. Sci. Lett.* 379, 95–103. doi: 10.1016/j.epsl.2013.08.011

Čížková, H., and Bina, C. R. (2019). Linked influences on slab stagnation: Interplay between lower mantle viscosity structure, phase transitions, and plate coupling. *Earth Planet. Sci. Lett.* 509, 88–99. doi: 10.1016/j.epsl.2018.12.027

Čížková, H., van Hunen, J., and van den Berg, A. (2007). Stress distribution within subducting slabs and their deformation in the transition zone. *Phys. Earth Planet. Inter.* 161, 202–214. doi: 10.1016/j.pepi.2007.02.002

Čížková, H., Van Hunen, J., Van den Berg, A. P., and Vlaar, N. J. (2002). The influence of rheological weakening and yield stress on the interaction of slabs with the 670 km discontinuity. *Earth Planet. Sci. Lett.* 199, 447–457. doi: 10.1016/S0012-821X(02)00586-1

Conrad, C. P., and Lithgow-Bertelloni, C. (2002). How mantle slabs drive plate tectonics. *Science* 298, 207–209. doi: 10.1126/science.1074161

Crameri, F. (2018). Geodynamic diagnostics, scientific visualisation and StagLab 3.0. *Geosci. Model Dev.* 11, 2541–2562. doi: 10.5194/gmd-11-2541-2018

Crameri, F., and Lithgow-Bertelloni, C. (2018). Abrupt upper-plate tilting during slab-transition-zone collision. *Tectonophysics* 746, 199–211 doi: 10.1016/j.tecto.2017.09.013

Crameri, F., Schmeling, H., Golabek, G. J., Duretz, T., Orendt, R., Buiter, S. J. H., et al. (2012a). A comparison of numerical surface topography calculations in geodynamic modelling: an evaluation of the sticky air method. *Geophys. J. Int.* 5, 38–54. doi: 10.1111/j.1365-246X.2012.05388.x

Crameri, F., and Tackley, P. J. (2015). Parameters controlling dynamically self-consistent plate tectonics and single-sided subduction in global models of mantle convection. *J. Geophys. Res.* 3, 1–27. doi: 10.1002/2014JB011664

Crameri, F., and Tackley, P. J. (2016). Subduction initiation from a stagnant lid and global overturn: new insights from numerical models with a free surface. *Prog. Earth Planet. Sci.* 3:30. doi: 10.1186/s40645-016-0103-8

Crameri, F., Tackley, P. J., Meilick, I., Gerya, T. V., and Kaus, B. J. P. (2012b). A free plate surface and weak oceanic crust produce single-sided subduction on Earth. *Geophys. Res. Lett.* 39, 1–7. doi: 10.1029/2011GL050046

Dal Zilio, L., Faccenda, M., and Capitanio, F. (2018). The role of deep subduction in supercontinent breakup. *Tectonophysics* 746, 312–324. doi: 10.1016/j.tecto.2017.03.006

Di Giuseppe, E., Van Hunen, J., Funiciello, F., Faccenna, C., and Giardini, D. (2008). Slab stiffness control of trench motion: insights from numerical models. *Geochem. Geophys. Geosyst.* 9, 1–19. doi: 10.1029/2007GC001776

Duretz, T., Gerya, T. V., and May, D. A. (2011). Numerical modelling of spontaneous slab breakoff and subsequent topographic response. *Tectonophysics* 502, 244–256. doi: 10.1016/j.tecto.2010.05.024

Duretz, T., Schmalholz, S. M., and Gerya, T. V. (2012). Dynamics of slab detachment. *Geochem. Geophys. Geosyst.* 13, 1–17. doi: 10.1029/2011GC004024

Faccenna, C., Heuret, A., Funiciello, F., Lallemand, S., and Becker, T. W. (2007). Predicting trench and plate motion from the dynamics of a strong slab. *Earth Planet. Sci. Lett.* 257, 29–36. doi: 10.1016/j.epsl.2007.02.016

Forte, A. M., and Mitrovica, J. X. (2001). Deep-mantle high-viscosity flow and thermochemical structure inferred from seismic and geodynamic data. *Nature* 410, 1049–1056. doi: 10.1038/35074000

Fukao, Y., and Obayashi, M. (2013). Subducted slabs stagnant above, penetrating through, and trapped below the 660 km discontinuity. *J. Geophys. Res.* 118, 5920–5938. doi: 10.1002/2013JB010466

Fukao, Y., Obayashi, M., and Nakakuki, T. (2009). Stagnant slab: a review. *Annu. Rev. Earth Planet. Sci.* 37, 19–46. doi: 10.1146/annurev.earth.36.031207.124224

Fukao, Y., Widiyantoro, S., and Obayashi, M. (2001). Stagnant slabs in the upper and lower mantle transition region. *Rev. Geophys.* 39, 291–323. doi: 10.1029/1999RG000068

Funiciello, F., Faccenna, C., Giardini, D., and Regenauer-Lieb, K. (2003). Dynamics of retreating slabs: 2. Insights from three-dimensional laboratory experiments. *J. Geophys. Res.* 108, 1–16. doi: 10.1029/2001JB000896

Garel, F., Goes, S., Davies, D. R., Davies, J. H., Kramer, S. C., and Wilson, C. R. (2014). Interaction of subducted slabs with the mantle transition-zone: a regime diagram from 2-D thermo-mechanical models with a mobile trench and an overriding plate. *Geochem. Geophys. Geosyst*. 15, 1739–1765. doi: 10.1002/2014GC005257

Goes, S., Agrusta, R., van Hunen, J., and Garel, F. (2017). Subduction-transition zone interaction: a review. *Geosphere* 13:GES01476.1. doi: 10.1130/GES01476.1

Goes, S., Capitanio, F. A., Morra, G., Seton, M., and Giardini, D. (2011). Signatures of downgoing plate-buoyancy driven subduction in Cenozoic plate motions. *Phys. Earth Planet. Inter*. 184, 1–13. doi: 10.1016/j.pepi.2010.10.007

Hafkenscheid, E., Wortel, M. J. R., and Spakman, W. (2006). Subduction history of the Tethyan region derived from seismic tomography and tectonic reconstructions. *J. Geophys. Res*. 111, 1–26. doi: 10.1029/2005JB003791

Hager, B. H., Clayton, R. W., Richards, M. A., Comer, R. P., and Dziewonski, A. M. (1985). Lower mantle heterogeneity, dynamic topography and the geoid. 313, 541–545. doi: 10.1038/314752a0

Hager, B. H., and Richards, M. A. (1984). Geoid anomalies in a dynamic Earth. *J. Geophys. Res*. 89, 5987–6002. doi: 10.1029/JB089iB07p05987

Hager, B. H., and Richards, M. A. (1989). Long-wavelength variations in Earth's geoid: physical models and dynamical implications. *Philos. Trans. R. Soc. Lond. Ser. A* 328, 309–327. doi: 10.1098/rsta.1989.0038

Honda, S. (2014). Strength of the slab inferred from the seismic tomography and geologic history around the Japanese Islands. *Geochem. Geophys. Geosyst*. 1333–1347. doi: 10.1002/2014GC005225

Honda, S. (2016). Slab stagnation and detachment under northeast China. *Tectonophysics* 671, 127–138. doi: 10.1016/j.tecto.2016.01.025

Ishii, T., Huang, R., Myhill, R., Fei, H., Koemets, I., Liu, Z., et al. (2019). Sharp 660-km discontinuity controlled by extremely narrow binary post-spinel transition. *Nat. Geosci*. 12, 869–872. doi: 10.1038/s41561-019-0452-1

Jarrard, R. D. (1986). Relations among subduction parameters. *Rev. Geophys*. 24, 217–284. doi: 10.1029/RG024i002p00217

Karato, S., Riedel, M. R., and Yuen, D. A. (2001). Rheological structure and deformation of subducted slabs in the mantle transition zone: implications for mantle circulation and deep earthquakes. *Phys. Earth Planet. Inter*. 127, 83–108. doi: 10.1016/S0031-9201(01)00223-0

Karato, S.-i., Shuqing, Z., and Hans-Rudolf, W. (1995). Superplasticity in Earth's lower mantle: evidence from seismic anisotropy and rock physics. *Science* 270:458. doi: 10.1126/science.270.5235.458

Katsura, T., Yamada, H., Shinmei, T., Kubo, A., Ono, S., Kanzaki, M., et al. (2003). Post-spinel transition in Mg2SiO4 determined by high P - T *in situ* X-ray diffractometry. *Phys. Earth Planet. Inter*. 136, 11–24. doi: 10.1016/S0031-9201(03)00019-0

Kido, M., and Čadek, O. (1997). Inferences of viscosity from the oceanic geoid: Indication of a low viscosity zone below the 660-km discontinuity. *Earth Planet. Sci. Lett*. 151, 125–137. doi: 10.1016/S0012-821X(97)81843-2

King, S. D., and Masters, G. (1992). Scott D. King x and guy masters. *Geophys. Res. Lett*. 19, 1551–1554. doi: 10.1029/92GL01700

Machetel, P., and Weber, P. (1991). Intermittent layered convection in a model mantle with an endothermic phase change at 670 km. *Nature* 350, 55–57. doi: 10.1038/350055a0

Mao, W., and Zhong, S. (2018). Slab stagnation due to a reduced viscosity layer beneath the mantle transition zone. *Nat. Geosci*. 11, 876–881. doi: 10.1038/s41561-018-0225-2

Marquardt, H., and Miyagi, L. (2015). Slab stagnation in the shallow lower mantle linked to an increase in mantle viscosity. *Nat. Geosci*. 8, 311–314. doi: 10.1038/ngeo2393

Mitrovica, J. X., and Forte, A. M. (2004). A new inference of mantle viscosity based upon joint inversion of convection and glacial isostatic adjustment data. *Earth Planet. Sci. Lett*. 225, 177–189. doi: 10.1016/j.epsl.2004.06.005

Mohiuddin, A., ichiro Karato, S., and Girard, J. (2020). Slab weakening during the olivine to ringwoodite transition in the mantle. *Nat. Geosci*. 13, 170–174. doi: 10.1038/s41561-019-0523-3

Nakakuki, T., Tagawa, M., Iwase, Y., Suetsugu, D., Bina, C., Inoue, T., et al. (2010). Dynamical mechanisms controlling formation and avalanche of a stagnant slab. *Phys. Earth Planet. Inter*. 183, 309–320. doi: 10.1016/j.pepi.2010.02.003

Richards, M. A., and Lenardic, A. (2018). The Cathles Parameter (Ct): a geodynamic definition of the asthenosphere and implications for the nature of plate tectonics. *Geochem. Geophys. Geosyst*. 19, 4858–4875. doi: 10.1029/2018GC007664

Richards, S., Holm, R., and Barber, G. (2011). When slabs collide: a tectonic assessment of deep earthquakes in the Tonga-Vanuatu region. *Geology* 39, 787–790. doi: 10.1130/G31937.1

Rudolph, M. L., Lekić, V., and Lithgow-Bertelloni, C. (2015). Viscosity jump in Earth's mid-mantle. *Science* 350, 1349–1352. doi: 10.1126/science.aad1929

Schellart, W. P. (2004). Kinematics of subduction and subduction-induced flow in the upper mantle. *J. Geophys. Res. B* 109, 1–19. doi: 10.1029/2004JB002970

Schellart, W. P. (2005). Influence of the subducting plate velocity on the geometry of the slab and migration of the subduction hinge. *Earth Planet. Sci. Lett*. 231, 197–219. doi: 10.1016/j.epsl.2004.12.019

Schellart, W. P., and Spakman, W. (2012). Mantle constraints on the plate tectonic evolution of the Tonga-Kermadec-Hikurangi subduction zone and the South Fiji Basin region. *Austr. J. Earth Sci*. 59, 933–952. doi: 10.1080/08120099.2012.679692

Sigloch, K. (2011). Mantle provinces under North America from multifrequency P wave tomography- Supplement. *Geochem. Geophys. Geosyst*. 12, 1–27. doi: 10.1029/2010GC003421

Sigloch, K., and Mihalynuk, M. G. (2013). Intra-oceanic subduction shaped the assembly of Cordilleran North America. *Nature* 496, 50–56. doi: 10.1038/nature12019

Sigloch, K., Mihalynuk, M. G., McQuarrie, N., and Nolet, G. (2008). Two-stage subduction history under North America inferred from multiple-frequency tomography. *Nature* 1, 458–462. doi: 10.1038/ngeo231

Tackley, P. J. (1994). *Three-dimensional models of mantle convection : influence of phase transitions and temperature-dependent viscosity* (Ph.D. thesis). Caltech, Pasadena, CA, United States.

Tackley, P. J. (1996). Effects of strongly variable viscosity on three-dimensional compressible convection in planetary mantles. *J. Geophys. Res*. 101, 3311–3331. doi: 10.1029/95JB03211

Tackley, P. J. (2000). Self-consistent generation of tectonic plates in time dependent, three-dimensional mantle convection simulations 1. Pseudoplastic yielding. *Geochem. Geophys. Geosyst*. 1, 2002–2006. doi: 10.1029/2000GC000036

Tackley, P. J. (2008). Modelling compressible mantle convection with large viscosity contrasts in a three-dimensional spherical shell using the yin-yang grid. *Phys. Earth Planet. Inter*. 171, 7–18. doi: 10.1016/j.pepi.2008.08.005

Tackley, P. J. (2011). Living dead slabs in 3-D: The dynamics of compositionally-stratified slabs entering a " slab graveyard" above the core-mantle boundary. *Phys. Earth Planet. Inter*. 188, 150–162. doi: 10.1016/j.pepi.2011.04.013

Tackley, P. J., Stevenson, D. J., Glatzmaier, G. A., and Schubert, G. (1993). Effects of an endothermic phase transition at 670 km depth on spherical mantle convection. *Nature* 361, 699–704. doi: 10.1038/361699a0

Tagawa, M., Nakakuki, T., and Tajima, F. (2007). Dynamical modeling of trench retreat driven by the slab interaction with the mantle transition zone. *Earth Planets Space* 59, 65–74. doi: 10.1186/BF03352678

Torii, Y., and Yoshioka, S. (2007). Physical conditions producing slab stagnation: constraints of the Clapeyron slope, mantle viscosity, trench retreat, and dip angles. *Tectonophysics* 445, 200–209. doi: 10.1016/j.tecto.2007.08.003

Turcotte, D., and Schubert, G. (2014). *Geodynamics*. Cambridge: Cambridge University Press. doi: 10.1017/CBO9780511843877

van der Hilst, R. (1995). 1995_Van der Hilst_ Complex morpholohy of subducted lithoshpere in the mantle beneath the Tonga Trench.pdf. *Lett. Nat*. 374, 154–157. doi: 10.1038/374154a0

van der Hilst, R., and Seno, T. (1993). Effects of relative plate motion on the deep structure and penetration depth of slabs below the Izu-Bonin and Mariana island arcs. *Earth Planet. Sci. Lett*. 120, 395–407. doi: 10.1016/0012-821X(93)90253-6

van der Meer, D. G., Spakman, W., van Hinsbergen, D. J. J., Amaru, M. L., and Torsvik, T. H. (2010). Towards absolute plate motions constrained by lower-mantle slab remnants. *Nat. Geosci*. 3, 36–40. doi: 10.1038/ngeo708

van der Meer, D. G., Torsvik, T. H., Spakman, W., van Hinsbergen, D. J. J., and Amaru, M. L. (2012). Intra-Panthalassa Ocean subduction zones revealed by fossil arcs and mantle structure. *Nat. Geosci*. 5, 215–219. doi: 10.1038/ngeo1401 van der Meer, D. G., van Hinsbergen, D. J., and Spakman, W. (2017). Atlas of the underworld: Slab remnants in the mantle, their sinking history, and a new outlook on lower mantle viscosity. *Tectonophysics*. 723, 309–484 doi: 10.1016/j.tecto.2017.10.004

van Hunen, J., and Allen, M. B. (2011). Continental collision and slab break-off: a comparison of 3-D numerical models with observations. *Earth Planet. Sci. Lett*. 302, 27–37. doi: 10.1016/j.epsl.2010.11.035

Van Hunen, J., Van den Berg, A. P., and Vlaar, N. J. (2001). Latent heat effects of the major mantle phase transitions on low-angle subduction. *Earth Planet. Sci. Lett*. 190, 125–135. doi: 10.1016/S0012-821X(01)00383-1

Wortel, M. J. R. (2000). Subduction and slab detachment in the Mediterranean-Carpathian region. *Science* 290, 1910–1917. doi: 10.1126/science.290.5498.1910

Ye, Y., Prakapenka, V., Meng, Y., and Shim, S. H. (2017). Intercomparison of the gold, platinum, and MgO pressure scales up to 140 GPa and 2500 K. *J. Geophys. Res*. 122, 3450–3464. doi: 10.1002/2016JB013811

Yoshida, M. (2017). Trench dynamics: Effects of dynamically migrating trench on subducting slab morphology and characteristics of subduction zones systems. *Phys. Earth Planet. Inter*. 268, 35–53. doi: 10.1016/j.pepi.2017.05.004

Yoshida, M., Tajima, F., Honda, S., and Morishige, M. (2012). The 3D numerical modeling of subduction dynamics: Plate stagnation and segmentation, and crustal advection in the wet mantle transition zone. *J. Geophys. Res*. 117, 1–24. doi: 10.1029/2012JB009391

Yoshioka, S., Naganoda, A., Suetsugu, D., Bina, C., Inoue, T., Wiens, D., et al. (2010). Effects of trench migration on fall of stagnant slabs into the lower mantle. *Phys. Earth Planet. Inter*. 183, 321–329. doi: 10.1016/j.pepi.2010.09.002

Yoshioka, S., Yuen, D. A., and Larsen, T. B. (1995). Slab weakening: mechanical and thermal-mechanical consequences for slab detachment. *Island Arc* 4, 89–103. doi: 10.1111/j.1440-1738.1995.tb00134.x

Zhong, S. and Gurnis, M. (1995). Mantle convection with plates and mobile, faulted plate margins. *Science* 267, 838–843. doi: 10.1126/science.267.5199.838

Conflict of Interest: The authors declare that the research was conducted in the absence of any commercial or financial relationships that could be construed as a potential conflict of interest.

frontiers in Earth Science

ORIGINAL RESEARCH
published: 24 September 2020
doi: 10.3389/feart.2020.548724

Calibrating the Yield Strength of Archean Lithosphere Based on the Volume of Tonalite-Trondhjemite-Granodiorite Crust

Prasanna M. Gunawardana[1], Gabriele Morra[2], Priyadarshi Chowdhury[1] and Peter A. Cawood[1]*

[1] *School of Earth, Atmosphere and Environment, Monash University, Clayton, Victoria, Australia,* [2] *Department of Physics, School of Geosciences, University of Louisiana at Lafayette, Lafayette, LA, United States*

OPEN ACCESS

Edited by:
Jeroen Van Hunen,
Durham University, United Kingdom

Reviewed by:
Kent Condie,
New Mexico Institute of Mining and Technology, United States
J. Elis Hoffmann,
Freie Universität Berlin, Germany

Correspondence:
Prasanna M. Gunawardana
prasanna.gunawardana@monash.edu

Specialty section:
This article was submitted to Solid Earth Geophysics, a section of the journal Frontiers in Earth Science

Received: *03 April 2020*
Accepted: *24 August 2020*
Published: *24 September 2020*

Citation:
Gunawardana PM, Morra G, Chowdhury P and Cawood PA (2020) Calibrating the Yield Strength of Archean Lithosphere Based on the Volume of Tonalite-Trondhjemite-Granodiorite Crust. Front. Earth Sci. 8:548724. doi: 10.3389/feart.2020.548724

Lithospheric yield stress is a key parameter in controlling tectonic processes. Using high resolution, 2D numerical modeling, we calculate the yield stress for a range of conditions appropriate to the early-to-mid Archean Earth, including hotter mantle potential temperatures and Moho temperatures. We then evaluate its effect on generating tonalite-trondhjemite-granodiorite (TTG) crust and benchmark the results against the preserved igneous rock record. Our results indicate that lithospheric yield stress values lower than the present-day values (i.e., ≤100 MPa) can generate TTG volumes similar to those preserved in the rock record. The models further highlight the dominance of lithospheric dripping in producing the Archean TTGs. Large volumes of TTG melts form within the thin, tail portions of the drips as these regions are more efficiently heated by the enclosing hotter mantle. In contrast, only limited melting occurs within the thickened parts of lithosphere as they are significantly weak and cannot sustain crustal thickening for long time periods, resulting in its removal via dripping. This study, therefore, reaffirms the dominance of non-plate tectonic mechanisms in producing TTGs under the conditions that operated on the hotter Archean Earth.

Keywords: Archean, TTG, geodynamics, yield stress, dripping

INTRODUCTION

Continental crust has played a key role in the evolution of the Earth system (e.g., Cawood et al., 2013). While its production is controlled by plate tectonics on the modern Earth (e.g., Rudnick and Gao, 2003), the tectonic processes that formed felsic crust and continents on the early Earth remain debated and range from plate tectonic to non-plate tectonic settings (e.g., Martin and Moyen, 2002; Bedard, 2003; Foley et al., 2003; Rapp et al., 2003; Harrison, 2009; Smithies et al., 2009; Chowdhury et al., 2017; Johnson et al., 2017; Moyen and Laurent, 2018; Rosas and Korenaga, 2018; Capitanio et al., 2019; Smithies et al., 2019; Chowdhury et al., 2020; O'Neill et al., 2020; Turner et al., 2020). This uncertainty partly stems from the significant gap in the preserved rock record and therefore, in our limited knowledge about the proportion and nature of the early continental and oceanic lithospheres (Cawood et al., 2013; Cawood et al., 2018; Lenardic, 2018; Stern, 2018). Numerical modeling of the early Earth processes and ground truthing its results with the limited rock record is, therefore, an important way to understand the early Earth processes (Rozel et al., 2017; Capitanio et al., 2019; Gerya, 2019; Chowdhury et al., 2020).

One approach to understand the Archean continental crust forming processes is by constraining the physical properties of the lithosphere(s) prevalent at that time. Previous research has shown that whether or not a terrestrial planet manifests some form of plate tectonics will depend on the lithospheric yield stress, i.e., the plastic strength of the crustal and the underlying lithospheric mantle rocks (Moresi and Solomatov, 1998; Trompert and Hansen, 1998; Tackley, 2000; O'Neill and Lenardic, 2007; van Heck and Tackley, 2008; Korenaga 2010a; Korenaga, 2010b; Van Heck and Tackley, 2011). Based on the magnitude of this parameter, a planet can exist in stagnant-lid, episodic-lid or mobile-lid tectonic mode (Moresi and Solomatov, 1998), since changing the yield stress value affects the mantle convection pattern via affecting the viscosity contrast between the lithosphere and convecting mantle. For example, present-day continental crust production mainly occurs at subduction and orogenic settings within a plate tectonic (mobile-lid) regime where average lithospheric yield stresses vary within >100–150 MPa (Kohlstead et al., 1995; Gurnis, 1988; Lowman and Jarvis, 1999; Tackley, 2000). However, this parameter remains poorly constrained for the Archean lithosphere.

Here, we perform high resolution 2D numerical modeling of the lithospheric dynamics under hotter mantle conditions appropriate for the early-to-mid Archean (>3 Ga) time-period, for a range of yield stress values varying between 50 and 250 MPa. We evaluate the models by calibrating the tempo of granitoid formation as obtained from them with the preserved geological record, and thereby, seek to constrain the yield stress values of Archean lithosphere and the consequent tectonic settings responsible for the formation of early felsic crust. Changes in the lithospheric processes due to different yield stress values are likely to affect the pressure-temperature (*P-T*) conditions of tectonic environments where metamorphism and partial melting processes operate. This implies that yield stress values are implicitly linked to the formation conditions and volumes of Archean felsic crust, which can be independently constrained from other approaches, thus, can be used to trace it back for the ancient lithosphere.

METHODOLOGY

Numerical Methods

We model 2D-mantle convection at high mantle potential temperatures (T_p; ~1,475–1,600°C) inferred for the Archean (Herzberg et al., 2007; Herzberg et al., 2010; Korenaga, 2013; Ganne and Feng, 2017; Aulbach and Arndt, 2019) using the numerical code Underworld 2 (Moresi et al., 2007). This code is based on the finite element method and is coupled with the particle-in-cell approach (Evans and Harlow, 1957). It involves a Eulerian grid with the moving Lagrangian particles embedded in a finite element (Moresi et al., 2007). Each particle represents a specific solid or molten rock-type (termed as *rock-particle* hereafter) and carries the information about its physical properties like, *P*, *T*, density, etc., which can be tracked over the entire model duration. The mass, momentum, and energy conservation equations are solved under incompressible conditions to find the pressure, velocity, and thermal evolution of the mantle convection model. Physical properties such as density and viscosity associated with the Earth's interior are mapped to these equations through particle indexing. The mass, momentum, and energy conservation equations are:

$$\vec{\nabla} \cdot \vec{u} = 0 \tag{1}$$

$$-\vec{\nabla} \cdot P + \vec{\nabla} \cdot \left[\eta\left(\partial_i u_j + \partial_j u_i\right)\right] = -\rho \vec{g} \tag{2}$$

$$\partial_t T + \vec{u}\,\vec{\nabla} T = \nabla^2 T + H \tag{3}$$

where *u*, *P*, η, *T*, *H*, ρ, *g*, and *t* represent velocity, pressure, viscosity, temperature, internal heat, density, gravitational acceleration, and time, respectively, (see **Table 1** for the parameter values).

The temperature dependent diffusion creep rheology is applied using the Arrhenius equation (Rozel et al., 2017):

$$\eta_T = \eta_o \exp\left[\frac{E + d \cdot V}{T + 1} - \frac{E}{2}\right] \tag{4}$$

where η_o is the reference viscosity at $T = 1$. Here, the parameters *E*, *V*, and *d* represent the non-dimensional activation energy, activation volume, and depth coordinate of the model, respectively. Following some recent studies (e.g., Sizova et al., 2015; Rozel et al., 2017), the activation energy is applied in such a way that temperature dependent rheology creates a stagnant lid mode of convection in the model (Moresi and Solomatov, 1998). A lithospheric weakening mechanism is implemented using the yield stress (σ_Y) parameter by assuming the ductile (plastic strength) behavior of the lithospheric rocks (Moresi and Solomatov, 1998; Sizova et al., 2015; Rozel et al., 2017). This is the only weakening mechanism that we imposed in the model. The yield stress equation is:

$$\sigma_Y = \sigma_Y^o + d\sigma_Y' \tag{5}$$

where σ_Y^o is Earth's surface yield stress and σ_Y' is the depth dependent yield stress gradient. When the convective stresses exceed the yield stress, we choose the yield stress value to calculate the viscosity. The yielding viscosity is $\eta_Y = \sigma_Y/2\dot{\epsilon}$, where $\dot{\epsilon}$ is the second invariant of the strain rate tensor. The effective viscosity is then calculated by $\eta_e = [\eta_T^{-1} + \eta_Y^{-1}]^{-1}$. We have systematically varied the surface yield stress among the values of 50, 100, 150, 200, and 250 MPa, covering a range of weaker to stronger lithospheric strength profiles. These values are proximal to the yield stress compatible with plate tectonics (Moresi and Solomatov, 1998; Tackley, 2000a; Van Heck and Tackley, 2011).

The dimensional values of the above non-dimensional parameters are retrieved using the relationships:

$$t = \frac{d^2}{k}t', \quad \sigma = \frac{\eta_o k}{d^2}\sigma', \quad x_i = dx_i', \quad u_i = \frac{k}{d}u_i',$$
$$\eta = \eta_o \eta', \quad \text{and} \quad T = \Delta T T'$$

following scaling methods of Moresi and Solomatov (1998), Korenaga (2010b), and Van Heck and Tackley (2011). The primes represent the non-dimensional form of the variable

TABLE 1 | Physical properties used in numerical modeling.

Symbol	Definition	Non-dimensional value	Dimensional value
α	Thermal expansivity	10^7	3×10^{-5} 1/K
g	Gravitational acceleration	1	9.81 m/s^2
d	Mantle thickness	1	660 km
T_o	Surface temperature	0	0°C
ΔT	Temperature drop across the model	Vary based on T_p (1 for present Earth)	1,680°C for present Earth
$\rho_{o\,(peri)}$	Reference density for peridotite	1	3,300 kg/m^3
$\rho_{o\,(basalt)}$	Reference density for basalt	—	3,000 kg/m^3
$\rho_{o\,(TTG)}$	Reference density for TTG	—	2,700 kg/m^3
κ	Thermal diffusivity	1	10^{-6} m^2/s
η_o	Reference viscosity	1	10^{21} Pa s
E	Activation energy	—	270 kJ/mol
R	Universal gas constant	—	8.314 J/mol/K
σ'_Y	Yield stress gradient	10^7	~35 MPa/km

and will be dropped here onwards, as we will only be dealing with non-dimensional symbols.

Partial Melting

To model felsic and mafic crust production, we implemented partial melting of the mantle peridotite and basaltic crust, including melt extraction, residue formation and eclogitization. For any rock-particle, melting initiates whenever its temperature exceeds its solidus. The adiabatic component of the temperature is added to the temperature solution (T) of **Eq. 3** for the melt calculation. The P-T dependent peridotite melting model of Sizova et al. (2015) is used for the mantle melting and melt extraction processes to account for the realistic scenario of mantle melting over a range of temperature between its wet and dry

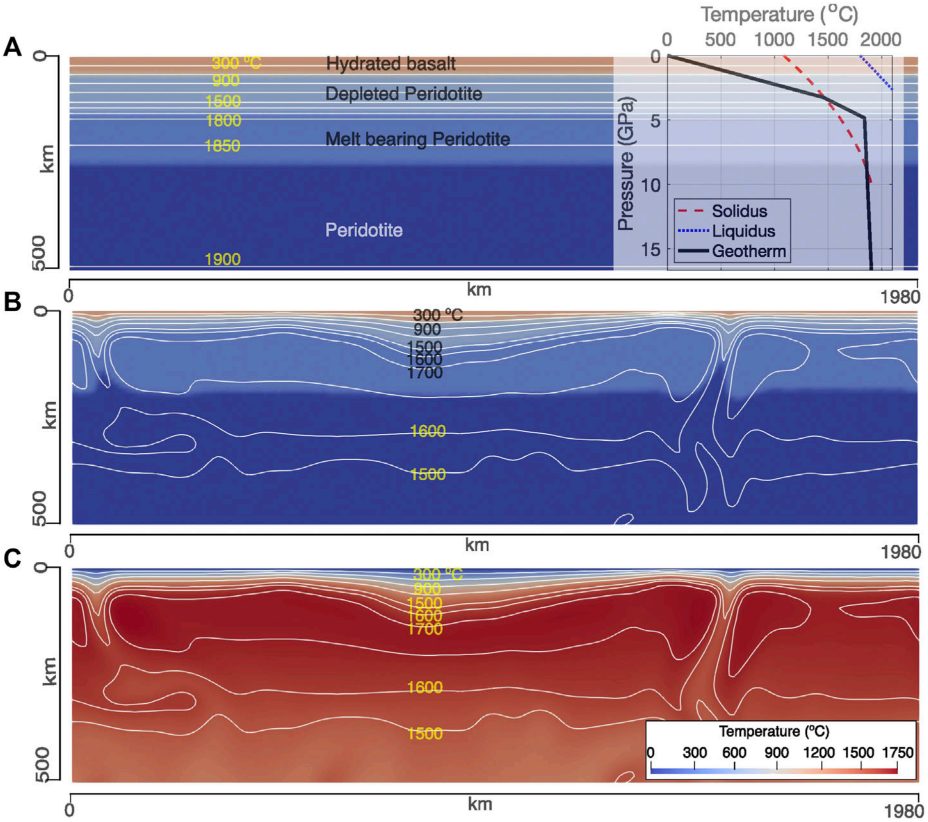

FIGURE 1 | (A) The initial compositional setup used to reach a state of stable mantle convection. The geotherm corresponds to a mantle T_p of 1,600°C and mantle adiabat of 0.5°C/km. The thickness of basaltic crust is defined by a Moho-T of 600°C. **(B,C)** The compositional and thermal profile derived after a stable mantle convection pattern is established. The lithological particles in **(B)** has been redefined using the thermal profile shown in **(C)**. This stage is considered as the start of model evolution for calculating the volume of tonalite-trondhjemite-granodiorite crust.

solidus depending on the extent of hydration. For the basaltic crust, the volumetric degree of melting, i.e., melt-fraction (M_o) is considered as a linear function of P-T and is calculated using the equation (Gerya, 2010; Sizova et al., 2015; Chowdhury et al., 2017; Chowdhury et al., 2020):

$$M_o = \begin{cases} 0, & T_1 < T_{\text{solidus}} \\ \dfrac{T_1 - T_{\text{solidus}}}{T_{\text{liquidus}} - T_{\text{solidus}}}, & T_{\text{solidus}} < T_1 < T_{\text{liquidus}} \\ 1, & T_1 > T_{\text{liquidus}} \end{cases} \tag{6}$$

where T_{solidus} and T_{liquidus} represent solidus and liquidus temperatures (**Figure 1**; also see **Appendix**) and are taken from the previous studies (e.g., Sizova et al., 2015; Rozel et al., 2017; Chowdhury et al., 2020). The melting of felsic crust has not been considered here.

To extract melt from partially-molten lithologies, we define four threshold parameters ($M1$, $M2$, $M3$, and $M4$) following the algorithm of Sizova et al. (2015) for each rock-particle. $M1$ represents the non-extractable melt volume that always remains in a partially molten rock-particle, while $M2$ represents the minimum melt volume required for the melt-extraction to take place. The extracted melt volume is assumed to instantaneously leave the melting region and move to the surface (Schmeling, 2006). $M3$ is the maximum amount of melt that can be sustained in a crystalizing melt particle without melt fractionation. $M4$ is the maximum amount of cumulative melt that can be extracted from a rock-particle. Once a rock-particle melts beyond $M4$, it is considered infertile for further melting. All the threshold parameters are assigned distinct values according to the rock-type (mantle peridotite or basalt; see **Appendix A1**). The melt volume borne by a rock-particle at any instant of time (M) during the model evolution is given by: $M = M_o - \sum_n M_{\text{ext}}$ where, M_o is given **Eq. 6**, M_{ext} is the amount of melt extracted in a single time-step and n is the number of times melt has been extracted from that rock-particle ($\sum_n M_{\text{ext}}$ gives the total melt-fraction extracted from that rock-particle). Whenever M exceeds $M2$ for a rock-particle, the extracted melt fraction (M_{ext}) is calculated as $M - M1$. This value is then added to the extracted cumulative volume of extracted melt for that rock-particle, which is then compared to $M4$ to check whether that rock-particle has reached its final limit for melt-extraction or not. The prefix *melt-bearing* is attached to the lithological name of a rock-particle (e.g., melt-bearing peridotite) whenever it carries some melt ($M > 0$). Once the cumulative melt-volume reaches $M4$, the melt-bearing rock-particle is converted to an equivalent depleted lithology like, from melt-bearing peridotite to depleted peridotite.

Density Calculations

The temperature dependent density (ρ) for different rock types is calculated using: $\rho_o[1 - \alpha\Delta T]$ where the ρ_o is the reference density at 1 MPa and 298 K, α is the thermal expansivity, and ΔT is the temperature drop across the model (**Table 1**). Partial melting and melt extraction also affect the density of the resultant rock types. The effective density of a melt-bearing rock type is calculated using (Gerya, 2010):

$$\rho_{\text{eff}} = \rho_{\text{solid}}(1 - M) + \rho_{\text{melt}} M \tag{7}$$

While ρ_{melt} represents the temperature dependent density of the melt volume (M), ρ_{solid} is the density of the solid part of the melt-bearing rock-types - called residue - that includes the effect of temperature, melt-extraction and eclogitization. It is calculated using:

$$\rho_{\text{solid}} = \rho_o[1 - \alpha\Delta T]\left(1 + \text{coef}_{\text{res}} + \text{coef}_{\text{phase}}\right) \tag{8}$$

where coef_{res} and $\text{coef}_{\text{phase}}$ represent the coefficients of density changes due to melting and eclogitization, respectively.

The density of solid peridotite decreases due to melt depletion (e.g., Poudjom Djomani et al., 2001), which we have implemented using the relation: $\text{coef}_{\text{res}} = -0.04\sum_n M_{\text{ext}}$ (Sizova et al., 2015). This corresponds to a decrease of ~1% in the density of solid residual peridotite for every 25% of extracted melt volume. For depleted peridotite (i.e., $M = M4$), ρ_{solid} is calculated at a fixed $\sum_n M_{\text{ext}}$ of 40%. No phase transitions are considered for the mantle peridotite ($\text{coef}_{\text{phase}} = 0$). During the melting of a metabasalt at amphibolite facies, the residue becomes rich in garnet, which makes it denser than the unmetamorphosed basalt (Rapp et al., 2003; Zhang et al., 2013). This effect is modeled using the following relation: $\text{coef}_{\text{res}} = 0.4\sum_n M_{\text{ext}}$ (Sizova et al., 2015). The effect of phase transitions, i.e., eclogitization on the basaltic density is implemented via the term coef_{ecl}. Following the experimental results (Ito and Kennedy, 1971), the values of this coefficient are varied from 0 to 16% within the P-T dependent garnet-in line [P (in kbar) = 0.014 T (in °C) − 5.4] and plagioclase-out line [P (in kbar) = 0.024 T (in °C) + 4] (Sizova et al., 2015), which approximates the conversion of basalt to eclogite through garnet-granulite. It must be noted that eclogitization is not necessarily dependent of melting and therefore, its effect on density is calculated for all the basaltic rock-particles (both solid and melt-bearing).

Initial Setup and Boundary Conditions

Our 2D model domain is created with a 64 × 192 resolution Eulerian mesh and with 20 Lagrangian particles per cell. The model dimension is 660 km × 1,980 km (**Figure 1A**). A lithosphere with thick, hydrous basaltic crust is used in the models (**Figure 1A**) in accordance to the recent geological findings (e.g., Herzberg et al., 2010; Herzberg and Rudnick, 2012; Kamber, 2015; Johnson et al., 2017). The crustal thickness is set by the Moho temperature (Moho-T). Whenever a rock-particle exists within the upper 60 km of the model domain and its temperature is less than Moho-T, it is defined as basaltic crust. We varied the crustal thickness using three different values of Moho-T (500, 600, and 700°C). The relevant average basaltic crustal thickness for the model with mantle T_p 1,600°C and yield stress of 50 MPa case is presented in **Appendix Figure A1**. These different Moho-T values also simulate the effect of relatively colder and hotter crustal geotherms. Following the studies of Rey et al. (2014) and Sizova et al. (2015), the lithospheric thickness is thermally defined by 0°C at the surface and a temperature at a fixed depth of 100 km depending on the mantle T_p values. We further increased the mantle T_p value by 125, 200, and 250°C above its present-day value of 1,350°C in successive steps, which are consistent with the thermal conditions of Archean mantle (Herzberg et al., 2010; Korenaga, 2013). The ambient mantle temperature linearly increases following an adiabatic geotherm of ~0.5°C/km below 150 km depth. Above 150 km, the mantle adiabat is linearly linked to the lithospheric geotherm over the depth interval of 100–150 km (**Figure 1A**). The top boundary is kept constant at 0°C while the bottom boundary is kept at constant temperature guided by the mantle T_p and the mantle adiabatic geothermal gradient (see **Table 1**). Free slip boundary conditions are imposed at the top and bottom of the model, while side walls are given periodic boundary condition. We have run all the models for a finite time at the beginning to reach a steady-state mantle convection (**Figure 1C**). Once this is achieved, the lithological layers are redefined according to the established steady-state thermal profile (**Figure 1B**). The stage is considered as the start of the model evolution.

Constraints From the Continental Rock Record

To evaluate our models, we predict the 1) relative abundances of various felsic igneous rocks and 2) the volume of continental crust that would have been formed during the early Archean (>3 Ga), and compare them against the volumes inferred from the rock record.

Comparison with the rock record of Tonalite-Trondhjemite-Granodiorites

To evaluate our models, we need information about the relative abundances of the different types of Tonalite-Trondhjemite-Granodiorite (TTG) - the dominant felsic lithologies that constitute Archean crust (reviewed in Moyen, 2011; Moyen and Laurent, 2018). Extant experimental and petrological studies show that the Archean TTGs mainly formed through the partial melting of hydrated metabasalts (Foley et al., 2003; Rapp et al., 2003; Moyen and Stevens, 2006; Qian and Hermann, 2013; Palin et al., 2016; Johnson et al., 2017). Our implemented algorithm of basalt melting is, thus, appropriate to model TTG formation. The trace element composition of TTGs further suggest that their formation occurred at three different pressure ranges: (Moyen, 2011): 1) at lower pressures (<1 GPa) where garnet-absent amphibolite residues are stable, called low-pressure (LP-) TTGs; 2) at intermediate pressures (~1–2 GPa) where both garnet and plagioclase are present in the residue, called medium-pressure (MP-) TTGs; and 3) at high pressures (>2 GPa) where garnet and rutile are stable in the residue but not plagioclase, called high-pressure (HP-) TTGs. The bracketing pressure ranges, however, may vary depending on the source rock composition; for example, MP-TTGs can form at P < 1 GPa (~0.7–0.8 GPa) from low-MgO enriched metabasalts (Johnson et al., 2017).

In this study, we focus on the formation of LP- and MP-TTGs as they dominate the >3 Ga rock record (cf. Moyen and Laurent, 2018), which is the time period of interest. We modeled partial melting of hydrous basaltic crust within a pressure range of 0.7–2.5 GPa, corresponding to a maximum depth of ~75 km (**Figure 2**). Notwithstanding the ambiguities of nomenclature, this pressure range overlaps with the overall physical conditions of LP- and MP-TTGs formation during the Archean (**Figure 2**) (Palin et al., 2016; Johnson et al., 2017; Moyen and Laurent, 2018). Regarding the relative abundances, MP-TTGs constitute nearly 60% of the total TTG volume whereas LP- and HP-TTGs contribute equally toward the remaining 40% (Moyen, 2011; Moyen and Laurent, 2018). Since we focus on the LP- and MP-TTGs, we renormalize their proportions and obtain a ratio of 1:3 (~25%:75%) between their abundances. Whenever a basaltic rock-particle melts, the resultant melt is classified as LP-/MP-/HP-TTG depending on in whose domain the melting took place (**Figure 2**). Melt is extracted once the melt-fraction reaches the threshold limit for extraction (*M*2) as mentioned above. The extracted melt volumes for each of the TTG-types are computed at each time step and added to the volumes of the previous time-steps. It must be noted that we did not consider water and basalt as separate entities and instead, assumed the basaltic crust to be sufficiently hydrated to produce the different TTG-types (e.g., Sizova et al., 2015; Chowdhury et al., 2020).

Comparison with the volume of ~3 Ga old continental crust

Comparing the total continental crustal volume between models and nature is not straightforward, particularly because of the large variations among different growth models and the difficulties in extrapolating the numerical model results at planetary scales. Estimates for the volume of continental crust at ~3 Ga vary from ca. 10 to 120% of its present-day volume between the different growth models (**Figure 3**) (cf. Cawood and Hawkesworth, 2019). This is because these models are based on different assumptions and datasets. While some growth models are based on the present-day distribution of the continental crust (e.g., Condie and Aster, 2010), some others are schematic (e.g., Armstrong, 1981). A third group of growth models also exist that are based on datasets such as the proportions of juvenile vs. reworked crust inferred from the zircon data, the evolution of atmospheric argon, and the trace element and isotopic composition of mafic-ultramafic rocks (Campbell, 2003; Belousova et al., 2010; Dhuime et al., 2012; Pujol et al., 2013; Roberts and Spencer, 2015; McCoy-West et al., 2019). Here, we consider the volume estimates of this group of growth models since: 1) they do not rely on the present-day crustal distribution; thus, accounting for the current paucity of the early rock record and 2) they all independently show that at least 65–70% of the present-day continental volume existed by ~3 Ga. It must be noted that besides granitoids, the Archean continental crust is also comprised of greenstone belt successions made up of mafic-ultramafic volcanic and volcaniclastic rock units (Moyen and Laurent, 2018; Smithies et al., 2018). The estimates of continental growth models are however, meant for the felsic component mainly (Dhuime et al., 2012; Pujol et al., 2013; cf.; Cawood et al., 2013).

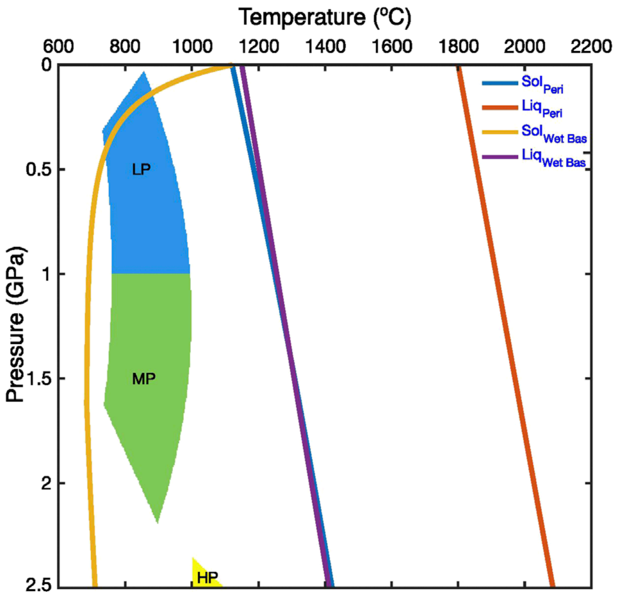

FIGURE 2 | Pressure and temperature conditions of Low-Pressure (LP), Medium-Pressure (MP) and High-Pressure (HP) tonalite-trondhjemite-granodiorite formation (Reproduced from Moyen (2011) and Jain et al. (2019) under the Creative Commons CCBY license). The solidii and liquidii for mantle peridotite and hydrous basaltic crust (Sizova et al., 2015) are also shown. See **Appendix** for details.

To measure crustal growth within our models, we introduce a parameter called the *Differentiation Index* (DI). Defined as the volume ratio of the continental crust to the upper mantle, this parameter quantifies how much continental crust has been extracted from the mantle and did not mix back (at least chemically); thus, accounting for the crustal recycling implicitly. Our approach follows the geochemical hypothesis that effectively continental crust has been extracted from the mantle (e.g., Rudnick and Gao, 2003). The DI value is estimated to be ~2.4% for the modern Earth. It is calculated using the continental volume of ~7.2 × 10^9 km (cf. Cawood et al., 2013) and an upper mantle volume of ~3.03 × 10^{11} km (based on a spherical Earth of radius 6,371 km and an upper-lower mantle boundary at the depth of 660 km). The DI value at ~3 Ga is ~1.7%, which is calculated assuming the continental crustal volume to be ~70% of the present-day volume and the same upper mantle volume. During the model evolution, we compute the total volume of TTG crust formed at each time-step (as mentioned above). We then use this accumulated TTG volume to compute DI at each time-step and trace over what duration its inferred value of ~1.7% is achieved.

MODEL RESULTS

Figure 4 illustrates the evolutionary stages of our reference numerical model, which has a surface yield stress of 50 MPa, a mantle T_P of 1,600°C (250°C higher than present-day), and a Moho-T of 600°C. The model evolution shows that two tectonic processes featuring local compression, called crustal thickening and dripping, occur under the influence of the convective flow of mantle. Thickening of the basaltic crust (**Figure 4A**) leads to phase transitions (i.e., eclogitization) within its deeper levels, which in turn increases the crustal density at those depths. Owing to a hotter geotherm set up by the hotter mantle and low yield stress, the crust could not support its gravitationally unstable eclogitized base and leads to the development of a Rayleigh-Taylor type instability within this region (**Figure 4B**).

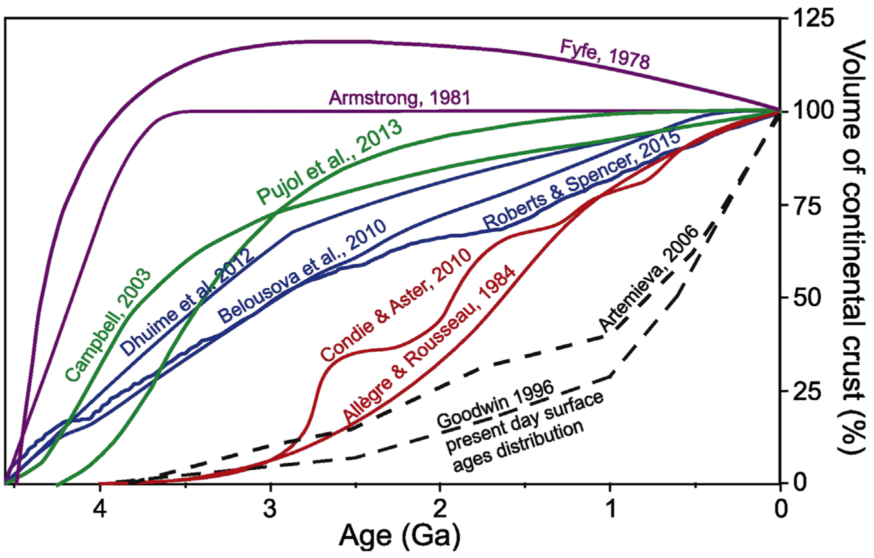

FIGURE 3 | The growth models of the continental crust relative to its present-day volume (Reproduced from Cawood and Hawkesworth (2019) under the Creative Commons CCBY license). Note that the curves of Belousova et al. (2010), Dhuime et al. (2012), Roberts and Spencer (2015), Campbell (2003), Pujol et al. (2013), all of which used different proxies, predict similar volumes of continental crust at ~3 Ga.

As this instability grows with time, a portion of the eclogitized crust drips back into the mantle (**Figures 4C,D**). Such a process has been suggested to occur during the early Archean by previous studies (Johnson et al., 2014; Sizova et al., 2015; Rozel et al., 2017). Our model however, shows that: 1) individual drips may grow in length, reaching up to few hundreds of km (**Figures 4A–D**) and 2) individual dripping phases, i.e., from the appearance of the Rayleigh-Taylor-instability to the detachment stage, may last for ~10 Myr. The cycle of crustal thickening evolving into dripping continue to occur over a periodicity of ~20–30 Myr.

Regarding the formation felsic crust, the model shows that drips are more efficient in producing TTGs as compared to the basal part of a thickened crustal segment (cf. **Figures 4A–D**). The narrow tail region of a basaltic drip easily reaches supra-solidus temperatures due to the conductive heating from the surrounding hot mantle, resulting in its melting and the formation of TTGs. It must be noted that in our models we have shown the residues (pink colored lithology) formed after the production of TTGs. Therefore, although residues get transported at great mantle depths with the drips (**Figures 4C,D**), they have necessarily formed at depths <75 km since we did not allow melting of the basaltic crust beyond this depth limit. **Figure 5** shows how the volumes of modeled LP-TTG and MP-TTG melts as well as their combined volume increase with time during the model evolution. The relative proportions of LP- to MP- TTG melts remain fairly constant (varying from ~22%:78% to ~30%:70%) around the ~1:3 ratio throughout the model evolution (**Figure 5B**), which agrees well with the rock record (Moyen, 2011; Moyen and Laurent, 2018). In terms of the absolute volume, prominent spikes implying significant growth in the TTG volume, can be seen at ~17.5, 56.8, and 100 Myr in the melt volume vs. time plot (**Figure 5A**). Notably, all these time-instants correspond to the active phases of dripping (**Figure 5C**). In contrast, melt volumes do not show any major increase when crustal thickening dominates the model

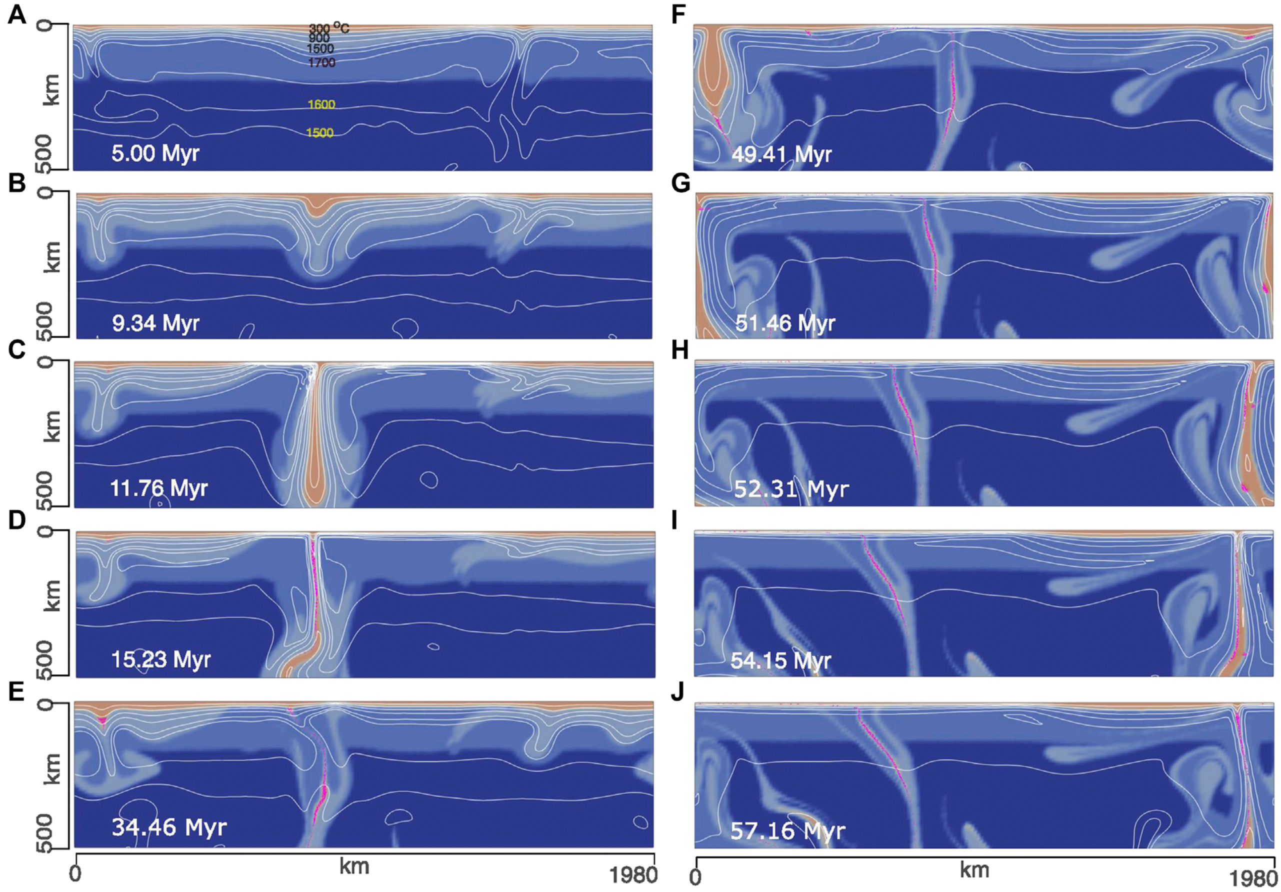

FIGURE 4 | Evolution of the reference model with a surface yield stress of 50 MPa, mantle T_p of 1,600°C and Moho-T of 600°C. Mantle convection drives thickening of the basaltic crust **(A)**, which eventually transform into a Rayleigh-Taylor type instability **(B)** and drips into the mantle **(C–E)**. This cycle of crustal thickening followed by dripping continues. The residue forms during the production of tonalite-trondhjemite-granodiorite melt is shown in pink color. Within a period of ~60 Myr, the model shows two major dripping phases: the first phase **(B–E)** between ~9 and 34 Myr and the second phase **(F–J)** between ~49 and 57 Myr. Note that this second phase is transferred across the (periodic) boundary from left to right in the model **(G–H)** around the ~51–52 Myr time-period. The TTG formation mostly occurs during the dripping phase as compared to the thickening phase.

evolution (**Figure 5A**), implying only limited mafic crustal melting in this setting.

To test the effects of higher yield stress and Moho-T, we have simulated a model with a surface yield stress of 200 MPa and a Moho-T of 700°C under the mantle T_p of 1,600°C. This model also feature dripping (**Figures 6A–C**) and crustal thickening phases (**Figures 6C–F**) similar to the reference model. But, in this model, crustal thickening phases exhibit melting of the basaltic crust and TTG production in noticeable volumes (**Figures 6E,F**). A higher Moho-T along with a higher yield stress value leading to sustaining of thickened crustal domains over ~20–30 Myr, facilitates melting at the base of the thickened basaltic crust. This substantiates our contention that Moho-T and yield stress values together influence the production of TTGs within thickened crustal domains. However, even within this setup, the overall volume of the TTGs is controlled by the melt produced during the dripping phase (**Figures 6A–G**). However, the relative proportion of modeled LP- to MP-TTG melt do not corroborate to the desired value of ~1:3, rather they show sub-equal abundances (**Figure 6H**). Models with other values of yield stress, Moho-T and mantle T_p do not show any major deviation in their evolution from that of the reference model.

Furthermore, the model results show that TTG production and the resulting DI values increase with the lowering of lithospheric yield strength for any given mantle and Moho temperature conditions (**Figure 7**). When the mantle T_p range is within 1,500–1,600°C, only the models having a lithospheric yield stress of ~50 to <100 MPa produces enough TTG volume such that their DI values approach or surpass the geological constrained DI value (~1.7%) of the Earth approximately at 3 Ga within few hundreds of Myr (**Figures 7A,B**). However, at low yield stresses, the DI reaches ~1.5–1.7% within ≤100 Myr when the Moho-T is 700°C irrespective of the mantle T_p (**Figures 7A–C**), implying an extremely rapid growth of felsic crust. In contrast, the DI values reach ~0.5–1.2 in 100 Myr when the Moho-T is ~600°C (**Figures 7A–C**); thereby, suggesting that the felsic crust grows steadily under these conditions and the DI values likely reach the ~1.7% value in a few hundreds of Myr. A colder Moho (~500°C) or mantle (<1,500°C T_p) seems to limit the TTG production such that the DI values remain <0.5 in 100 Myr (**Figures 7A–C**); thus, favoring a slow crustal growth. However, the estimated DI values likely reach the ~1.7% in less than 1.5 Gyr for colder Moho (~500°C) and/moderate T_p (~1,540°C) and/higher yield stress (250 MPa) suggesting that slow crustal growth rates require excessively high lithospheric yield stress values. Even when the relative proportion of LP- and MP-TTGs are considered (**Figures 7D–F**), models with a combination of hotter mantle (>1,550°C T_p), moderately high

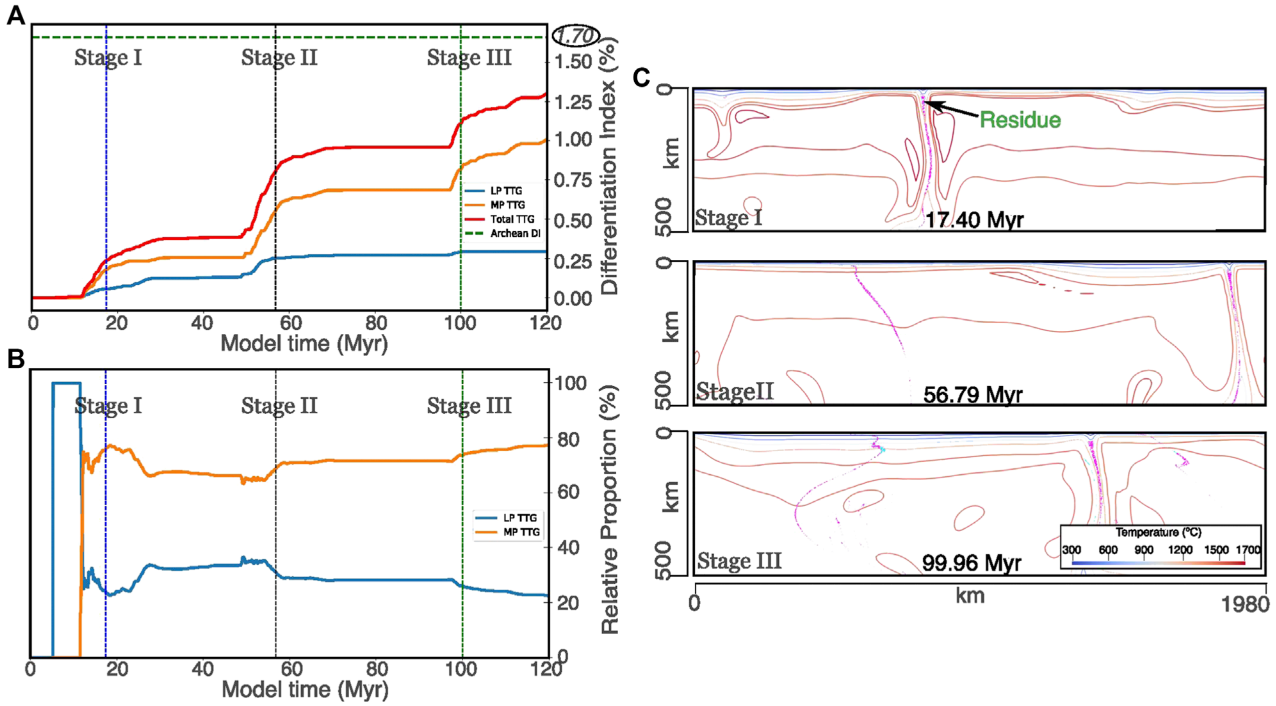

FIGURE 5 | Evolution of **(A)** the volume of low-P tonalite-trondhjemite-granodiorite (TTG), medium-P TTG and total TTG crust [represented *via* Differentiation Index (DI)], and **(B)** the relative proportion of low-Pressure (LP) to medium-Pressure (MP) TTGs through model-time. The dashed green line in **(A)** represents the geologically constrained DI value (≥1.7) at 3 Ga (termed as Archean DI), corresponding to a continental volume of 70% of its present-day present-value (see text for details). Note that Stage-I, II, and III represent the major changes in the volume of TTG melts and total TTG crust. These stages correspond to **(C)** the three major, successive dripping phases in the model. The pink-coloured material represents the residue of the TTG melts. It must be noted that the residues form at shallow depths ($P < 2$ GPa) where LP- and MP- TTGs are prescribed to form, and then they get transported to deep mantle owing to greater density. The relative proportions of LP-TTGs to MP-TTGs remain around the ~1:3 ratio throughout the model (except during the initial, few million years), which agrees with the preserved igneous rock record.

Moho-T (~500–600°C) and low lithospheric yield stresses (<150 MPa) provide the best agreement to the natural rock-record. A significantly hotter Moho (≥700°C; **Figures 7D–F**) or colder mantle (<1,500°C T_p; **Figure 7F**) would strongly favor or disfavour the production of LP-TTGs, respectively, (even for weak lithosphere), which in turn deviates the ratio of LP- to MP-TTGs from their geologically constrained value (~1:3).

DISCUSSION

Yield Stress of the Archean Lithosphere

Our modeling shows that Archean lithosphere has somewhat lower yield strength compared to the present-day lithosphere (>100 MPa). The presence of such weaker lithosphere (together with hotter mantle) is critical for producing the large volumes of the Archean continental crust. This is because lowering the lithospheric yield stress facilitate the dripping-off of basaltic crustal segments, where the most favourable melting conditions (~0.7–1.8 GPa; > 800°C) ascertained for the production of TTGs (e.g., Palin et al., 2016; Johnson et al., 2017; cf.; Moyen and Laurent, 2018), are easily attained. Furthermore, weaker lithosphere (with moderately high Moho-T) can aptly replicate the relative dominance of MP-TTGs over LP-TTGs similar to what is preserved in the rock-record. Higher values of yield stress (>100 MPa) would impede the formation of drips and therefore, would result in a lower abundance of MP-TTGs, particularly if the crust is not significantly thick and/or thermally pre-conditioned for melting. Consequently, we suggest that the yield strength of Archean lithosphere likely varied between ~50 and 100 MPa, provided the mantle was significantly hotter than today.

The yield stress of material is temperature dependent in most engineering applications (Liu et al., 2002; Senkova et al.,

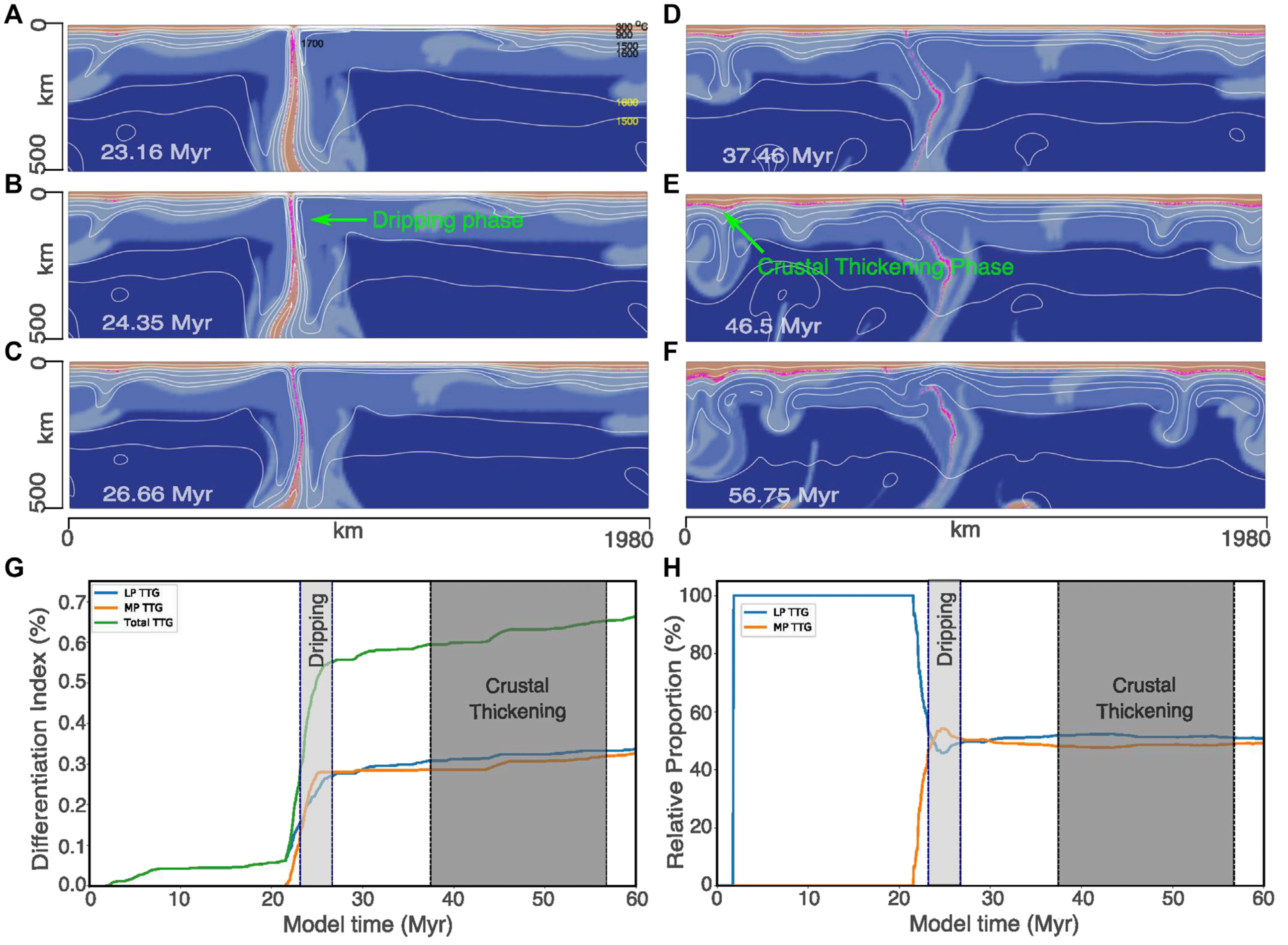

FIGURE 6 | Evolution of a model with yield stress of 200 MPa, mantle T_p of 1,600°C and Moho-T of 700°C. While the overall model evolution **(A–F)** resembles that of the reference model, an enhanced production of tonalite-trondhjemite-granodiorites (TTGs) at the sites of thickened crust **(E,F)** is observed in this model. Evolution of **(G)** the TTG melt- and total TTG crustal volumes, and **(H)** relative proportions of (low-pressure) LP- to (medium-pressure) MP-TTGs through time. Crustal growth during the thickening phases **(D–F)** can be seen but the major growth still occurs during the dripping phases **(A–C)**. Additionally, this model predicts an equal proportion of LP- and MP-TTGs during the Archean, which contrasts with the preserved rock record.

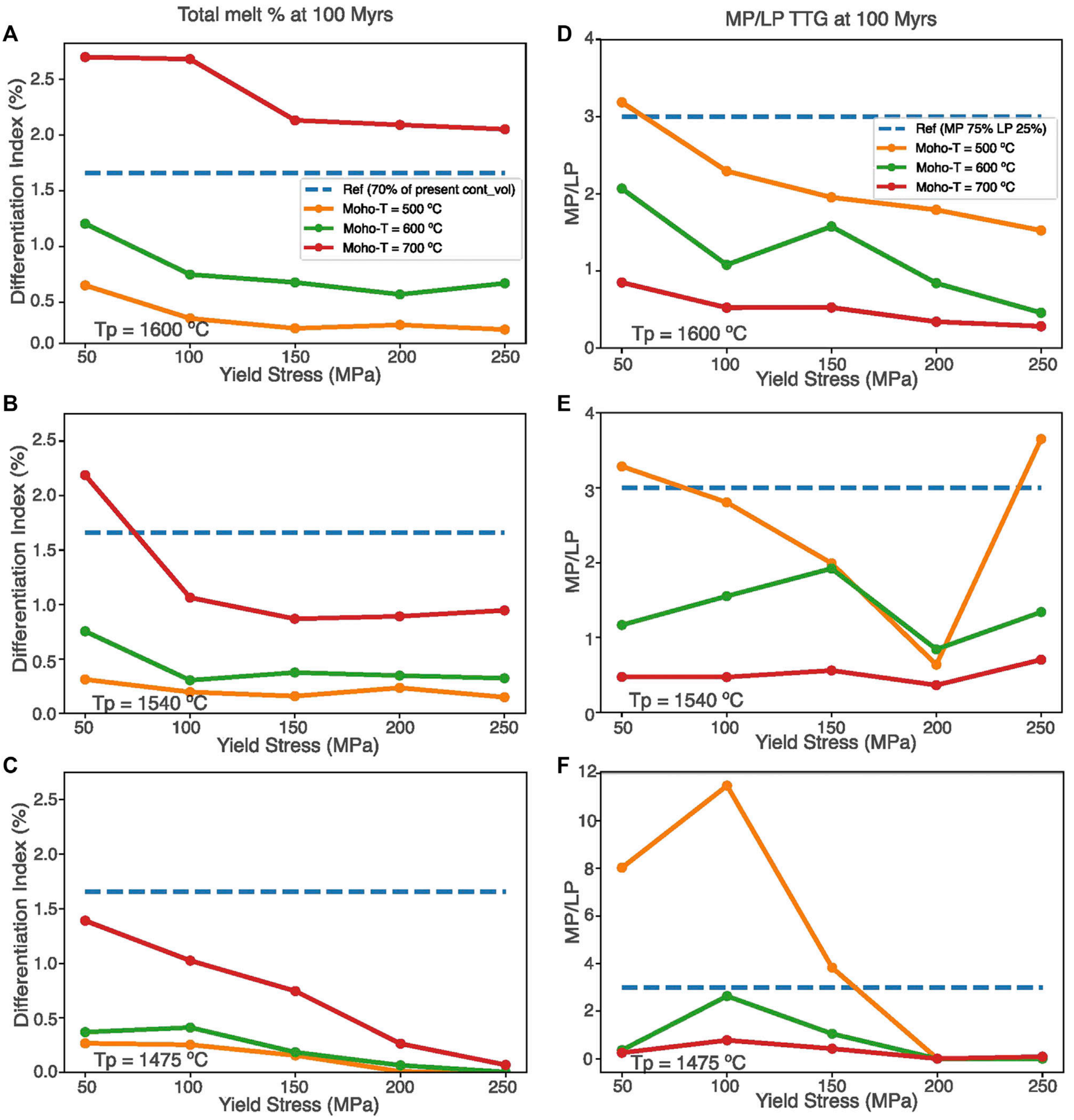

FIGURE 7 | Plots showing **(A–C)** the total tonalite-trondhjemite-granodiorite (TTG) crustal volume cast in terms of the Differentiation Index (DI) value and **(D–F)** the proportions of low-pressure (LP-) to medium-pressure (MP-)TTGs as a function of lithospheric yield stress, as obtained from our numerical models with different mantle T_p and Moho-T values. The DI values are computed at the end of the first 100 Myr of the model evolution in each case. The dashed blue lines in **(A–C)** represent the geologically constrained DI value (≥1.7) at 3 Ga, while in **(D–F)** they represent the relative proportion of the LP-to MP-TTGs as preserved in the rock record (see text for details). Note that the models with low lithospheric yield stresses (at hotter mantle and moderate hotter Moho conditions) produce the DI values that are likely to result a continental volume of 70% of its present-day value (DI = ~1.7) in few hundreds of Myr while matching the rock-record of the proportions of LP- and MP-TTGs.

2006; Heidarzadeh et al., 2014; Wu et al., 2014; Altenberger et al., 2015), as well as geological laboratory experiments related to different rock compositions (Evans and Goetze., 1979; Long et al., 2011; Sygała et al., 2013; Idrissi et al., 2016; Hansen et al., 2019). Therefore, owing to the hotter thermal structure and different crustal composition of Archean lithosphere relative to the present-day crust (Chardon et al., 2009; Dhuime et al., 2015; Tang et al., 2016; Brown et al., 2020), it is expected to have a lower yield strength. In fact, studies of how a lithosphere deforms have shown that it involves three main mechanisms: diffusion creep, dislocation creep and Peierls mechanism (Regenauer-Lieb et al., 2006), and ultimately results in a shear heating controlled rupture of the ductile harder lithospheric layer (Regenauer-Lieb et al., 2001; Thielmann and Kaus, 2012; Stern and Gerya, 2018). The yield stress that we apply is an average of a large number of processes, which are primarily thermally controlled and secondary pressure controlled, and determine the rupture of a lithosphere whose ultimate strength is thermally controlled (Braeck and Podladchikov, 2007). Consequently, the effect on the thermally driven tectonic style during the Archean, when the uppermost mantle boundary layer was hotter, is expected.

The results agree with laboratory experiments of rock deformation showing a lower yield stress with increasing temperature (Evans and Goetze., 1979; Long et al., 2011; Sygała et al., 2013; Idrissi et al., 2016; Hansen et al., 2019). Postulations of weaker lithosphere due to hotter mantle temperatures, higher radioactive heat generation and melt impregnation have been suggested by previous studies as well (e.g., van Hunen and van den Berg, 2008; Sizova et al., 2010; Magni et al., 2014; Rozel et al., 2017). Our results converge with these studies in finding a need for a weaker lithospheric strength. Overall, the lithospheric weakening could have occurred due to both viscous strength variations as well as yield strength variations with higher temperature conditions in the Archean Earth.

Tectonic Settings for the Early TTG Formation

Our modeling also bears implications for tectonic settings where the Archean felsic crust formation may have occurred. Previous studies have invoked both plate tectonic settings (mainly subduction) analogous to the present-day scenario (e.g., Foley et al., 2003; Harrison, 2009; Korenaga, 2018; Turner et al., 2020) or at various tectonic sites hosted within a stagnant-lid type tectonic regime (e.g., Smithies et al., 2009; Sizova et al., 2015; Johnson et al., 2017; Nebel et al., 2018; Smithies et al., 2019) for the formation of TTG-dominated crust during the Archean. Although the debate continues, recent studies are increasingly favoring the stagnant (squishy)-lid to transitional mobile-lid tectonic settings (not like *modern* plate tectonics) for the Archean crust formation (Johnson et al., 2014; Sizova et al., 2015; Chowdhury et al., 2017; Condie, 2017; Hawkesworth et al., 2017; Rozel et al., 2017; Johnson et al., 2017; Cawood et al., 2018; Moyen and Laurent, 2018; Capitanio et al., 2019; Smithies et al., 2019; Chowdhury et al., 2020). Tectonic processes like crustal thickening, dripping and local crustal overturns are suggested as settings for TTG production, particularly during the pre-3 Ga time-period (e.g., Smithies, 2000; Johnson et al., 2014; Sizova et al., 2015; Johnson et al., 2017). Our study highlights the relative dominance of these different non-plate tectonic mechanisms in producing TTGs. The reference model shows that production of TTG dominantly occurs during the dripping phase instead of during the crustal thickening phase. This partly contradicts the results of Sizova et al. (2015), which showed that crustal thickening promotes TTG production. However, they implemented an unusually high, initial Moho-T of ~1,200°C, which is markedly higher than 600°C value used in our model. Such lower Moho-T values together with the rapid transition of the thickened crustal domains into drips (within <10 Myr) at low yield stresses, impeded large-scale melting of the mafic crust during crustal thickening in the reference model. This becomes evident when we increase the Moho-T and yield stress compared to the reference model and observed a greater proportion of melting within the thickened crustal domains.

Nonetheless, in all our models, the dripping process dominates TTG formation. We infer that this is because dripping continuously brings newer basaltic material to the melting region, maintaining a steady melting of the source rock (**Figures 4** and **6**). Secondly, dripping leads to crustal thinning and the resultant, mantle upwelling around the locale of the drip. This heats up the surrounding crust, which facilitates its subsequent melting. In contrast, only a thin layer of the lower most crust reaches melting conditions within a thickened crustal segment (**Figures 6E,F**). Given that crustal thickening occurs at a local scale and is not laterally pervasive, the resultant melting and TTG production is also limited. We, however, do not suggest that crustal thickening did not contribute toward Archean crustal growth. Instead, we imply that this may have contributed significantly only when an unusually hot (Moho-T > 1,000–1,200°C) and thick (>35–40 km) mafic crust was available for melting conditions that may have existed in the Archean but perhaps not everywhere (cf. Cawood and Hawkesworth, 2019).

CONCLUSIONS

The preserved record of early Archean felsic crust is more consistent with the presence of weaker lithosphere during active tectonism at those times. Tectonic activity involving such weaker lithosphere atop hotter mantle would have led to the production of voluminous TTG melt prior to ~3 Ga, consistent with the inference of numerous crustal growth models. Our study further shows that TTG production may have dominantly occurred within mafic crustal drips, whereas crustal thickening made an only subordinate contribution unless the crust was significantly thicker. The low yield stress facilitated the drips to grow in length up to few hundreds of km and keeping them stable over tens of Myr. Furthermore, weaker lithosphere together with the dominance of dripping can also account for the large abundance of MP-TTGs relative to the LP-variant within the early Archean rock record.

DATA AVAILABILITY STATEMENT

The raw data supporting the conclusions of this manuscript will be made available by the authors, without undue reservation, to any qualified researcher.

AUTHOR CONTRIBUTIONS

PG—Overall research project is carried out from identifying the research problem, model development, and evaluation of results to drafting the manuscripts. GM—Provided support for the numerical model development, applying Geophysical significance, and Initial manuscript corrections. PC—Provided support in interpreting the model results, comparing them with the rock-record and manuscript development. PAC—The whole research project was guided by PAC from identifying the research problem to final manuscript development.

FUNDING

MIPRS and MGS PhD scholarship provided by Monash University, and Australian Research Council grant FL160100168.

ACKNOWLEDGMENTS

We acknowledge the computational resources provided by the Monash eResearch Center and eSolutions-Research Support Services (for the MonARCH HPC Cluster) and National Computational Infrastructure (NCI), Australia. We thank Jeroen van Hunen (Durham University) and two reviewers for their constructive comments that have immensely improved the manuscript. We also thank Christopher M. Gonzalez, Shayne McGregor, Fabio Capitanio, and John Mansour (Monash University) for insightful discussions.

REFERENCES

Allègre, C. J., and Rousseau, D. (1984). The growth of the continent through geological time studied by Nd isotope analysis of shales. *Earth Planet. Sci. Lett.* 67 (1), 19–34.

Altenberger, I., Kuhn, H.-A., Müller, H. R., Mhaede, M., Gholami-Kermanshah, M., and Wagner, L. (2015). Material properties of high-strength beryllium-free copper alloys. *Int. J. Mater. Prod. Technol.* 50 (2), 124–146. doi:10.1504/IJMPT.2015.067820

Armstrong, R. L. (1981). Radiogenic isotopes: the case for crustal recycling on a near-steady-state no-continental-growth earth. *Phil. Trans. A Math. Phys. Sci.* 301 (1461), 443–472. doi:10.1098/rsta.1981.0122

Artemieva, I. M. (2006). Global 1° × 1° thermal model TC1 for the continental lithosphere: implications for lithosphere secular evolution. *Tectonophysics* 416 (1–4), 245–277. doi:10.1016/j.tecto.2005.11.022

Aulbach, S., and Arndt, N. T. (2019). Eclogites as palaeodynamic archives: evidence for warm (not hot) and depleted (but heterogeneous) Archaean ambient mantle. *Earth Planet. Sci. Lett.* 505, 162–172. doi:10.1016/j.epsl.2018.10.025

Bédard, J. H. (2003). Evidence for regional-scale, pluton-driven, high-grade metamorphism in the archaean minto block, northern Superior province, Canada. *J. Geol.* 111, 183–205. doi:10.1086/345842

Belousova, E. A., Kostitsyn, Y. A., Griffin, W. L., Begg, G. C., O'Reilly, S. Y., and Pearson, N. J. (2010). The growth of the continental crust: constraints from zircon Hf-isotope data. *Lithos* 119 (3–4), 457–466. doi:10.1016/j.lithos.2010.07.024

Braeck, S., and Podladchikov, Y. Y. (2007). Spontaneous thermal runaway as an ultimate failure mechanism of materials. *Phys. Rev. Lett.* 98 (9), 095504. doi:10.1103/physrevlett.98.095504

Brown, M., Johnson, T., and Gardiner, N. J. (2020). Plate tectonics and the archean earth. *Annu. Rev. Earth Planet. Sci.* 48, 1–12. doi:10.1146/annurev-earth-081619–052705

Campbell, I. H. (2003). Constraints on continental growth models from Nb/U ratios in the 3.5 Ga Barberton and other Archaean basalt-komatiite suites. *Am. J. Sci.* 303 (4), 319–351. doi:10.2475/ajs.303.4.319

Capitanio, F. A., Nebel, O., Cawood, P. A., Weinberg, R. F., and Chowdhury, P. (2019). Reconciling thermal regimes and tectonics of the early Earth. *Geology* 47, 923–927. doi:10.1130/g46239.1

Cawood, P. A., and Hawkesworth, C. J. (2019). Continental crustal volume, thickness and area, and their geodynamic implications. *Gondwana Res.* 66, 116–125. doi:10.1016/j.gr.2018.11.001

Cawood, P. A., Hawkesworth, C. J., and Dhuime, B. (2013). The continental record and the generation of continental crust. *Geol. Soc. Am. Bull.* 125 (1–2), 14–32. doi:10.1130/b30722.1

Cawood, P. A., Hawkesworth, C. J., Pisarevsky, S. A., Dhuime, B., Capitanio, F. A., and Nebel, O. (2018). Geological archive of the onset of plate tectonics. *Philos. Trans. A Math. Phys. Eng. Sci.* 376 (2132), 20170405. doi:10.1098/rsta.2017.0405

Chardon, D., Gapais, D., and Cagnard, F. (2009). Flow of ultra-hot orogens: a view from the Precambrian, clues for the Phanerozoic. *Tectonophysics* 477, 105–118. doi:10.1016/j.tecto.2009.03.008

Chowdhury, P., Chakraborty, S., Gerya, T. V., Cawood, P. A., and Capitanio, F. A. (2020). Peel-back controlled lithospheric convergence explains the secular transitions in Archean metamorphism and magmatism. *Earth Planet. Sci. Lett.* 538, 116224. doi:10.1016/j.epsl.2020.116224

Chowdhury, P., Gerya, T., and Chakraborty, S. (2017). Emergence of silicic continents as the lower crust peels off on a hot plate-tectonic Earth. *Nat. Geosci.* 10, 698–703. doi:10.1038/ngeo3010

Condie, K. C. (2017). A planet in transition: the onset of plate tectonics on Earth between 3 and 2 Ga? *Geosci. Front.* 9, 51–60. doi:10.1016/j.gsf.2016.09.001

Condie, K. C., and Aster, R. C. (2010). Episodic zircon age spectra of orogenic granitoids: the supercontinent connection and continental growth. *Precambrian Res.* 180 (3–4), 227–236. doi:10.1016/j.precamres.2010.03.008

Dhuime, B., Hawkesworth, C. J., Cawood, P. A., and Storey, C. D. (2012). A change in the geodynamics of continental growth 3 billion years ago. *Science* 335, 1334–1336. doi:10.1126/science.1216066

Dhuime, B., Wuestefeld, A., and Hawkesworth, C. J. (2015). Emergence of modern continental crust about 3 billion years ago. *Nat. Geosci.* 8 (7), 552–555. doi:10.1038/ngeo2466

Evans, B., and Goetze, C. (1979). The temperature variation of hardness of olivine and its implication for polycrystaline yield stress. *J. Geophys. Res.* 84, 5505–5524. doi:10.1029/jb084ib10p05505

Evans, M. W., and Harlow, F. H. (1957). *The particle-in-cell method for hydrodynamic calculations*. Los Angels, CA: Los Almos National Laboratory Report, 2139.

Foley, S. F., Buhre, S., and Jacob, D. E. (2003). Evolution of the Archean crust by delamination and shallow subduction. *Nature* 421, 241–252. doi:10.1038/nature01319

Fyfe, W. S. (1978). The evolution of the earth's crust: modern plate tectonics to ancient hot spot tectonics? *Chem. Geol.* 23 (1–4), 89–114. doi:10.1016/0009-2541(78)90068-2

Ganne, J., and Feng, X. (2017). Primary magmas and mantle temperatures through time. *Geochem. Geophys. Geosyst.* 18, 872–888. doi:10.1002/2016gc006787

Gerya, T. V. (2010). *Introduction to numerical geodynamic modelling*. New York, NY: Cambridge University Press.

Gerya, T. V. (2019). Geodynamics of the early Earth: quest for the missing paradigm. *Geology* 47 (10), 1006–1007. doi:10.1130/focus-Oct2019

Goodwin, A. M. (1996). *Principles of precambrian geology*. London, UK: Academic Press, 327.

Gurnis, M. (1988). Large-scale mantle convection and the aggregation and dispersal of supercontinents. *Nature* 332 (6166), 695–699. doi:10.1038/332695a0

Harrison, T. M. (2009). The Hadean crust: evidence from >4 Ga zircons. *Annu. Rev. Earth Planet. Sci.* 37, 479–505. doi:10.1146/annurev.earth.031208.100151

Hansen, L. N., Kumamoto, K. M., Thom, C. A., Wallis, D., Durham, W. B., Goldsby, D. L., et al. (2019). Low-temperature plasticity in olivine: grain size, strain hardening, and the strength of the lithosphere. *J. Geophys. Res. Solid Earth* 124, 5427–5449. doi:10.1029/2018jb016736

Hawkesworth, C. J., Cawood, P. A., Dhuime, B., and Kemp, T. I. S. (2017). Earth's continental lithosphere through time. *Annu. Rev. Earth Planet. Sci*. 45, 169–198. doi:10.1146/annurev-earth-063016-020525

Heidarzadeh, A., Jabbari, M., and Esmaily, M. (2015). Prediction of grain size and mechanical properties in friction stir welded pure copper joints using a thermal model. *Int. J. Adv. Manuf. Technol* 77 (9–12), 1819–1829. doi:10.1007/s00170-014-6543-7

Herzberg, C., Asimow, P. D., Arndt, N., Niu, Y., Lesher, C. M., Fitton, J. G., et al. (2007). Temperatures in ambient mantle and plumes: constraints from basalts, picrites and komatiites. *Geochem. Geophys. Geosyst.* 8, Q02006. doi:10.1029/2006gc001390

Herzberg, C., Condie, K., and Korenaga, J. (2010). Thermal history of the Earth and its petrological expression. *Earth Planet. Sci. Lett*. 292, 79–88. doi:10.1016/j.epsl.2010.01.022

Herzberg, C., and Rudnick, R. (2012). Formation of cratonic lithosphere: an integrated thermal and petrological model. *Lithos* 149, 4–15. doi:10.1016/j.lithos.2012.01.010

Idrissi, H., Bollinger, C., Boioli, F., Schryvers, D., and Cordier, P. (2016). Low-temperature plasticity of olivine revisited with *in situ* tem nanomechanical testing. *Sci. Adv*. 2, e1501671. doi:10.1126/sciadv.1501671

Ito, K., and Kennedy, G. C. (1971). "An experimental study of the basalt-garnet granulite-eclogite transition." in *The structure and physical properties of the Earth's crust*. Editor J. G. Heacock (American Geophysical Union), Vol. 14, 303–314.

Jain, C., Rozel, A. B., Tackley, P. J., Sanan, P., and Gerya, T. V. (2019). Growing primordial continents self-consistently in global mantle convection models. *Gondwana Res*. 73, 96–122. doi:10.1016/j.gr.2019.03.015

Johnson, T. E., Brown, M., Gardiner, N. J., Kirkland, C. L., and Smithies, R. H. (2017). Earth's first stable continents did not form by subduction. *Nature* 543, 239–242. doi:10.1038/nature21383

Johnson, T. E., Brown, M., Kaus, B. J. P., and Van Tongeren, J. A. (2014). Delamination and recycling of Archaean crust caused by gravitational instabilities. *Nat. Geosci*. 7, 47–52. doi:10.1038/ngeo2019

Kamber, B. S. (2015). The evolving nature of terrestrial crust from the Hadean, through the Archaean, into the Proterozoic. *Precambrian Res*. 258, 48–82. doi:10.1016/j.precamres.2014.12.007

Kohlstedt, D. L., Evans, B., and Mackwell, S. J. (1995). Strength of the lithosphere: constraints imposed by laboratory experiments. *J. Geophys. Res*. 100, 17587–17602. doi:10.1029/95jb01460

Korenaga, J. (2010a). On the likelihood of plate tectonics on super-Earths: does size matter?*Astrophys. J. Lett*. 725, L43–L46. doi:10.1088/2041-8205/725/1/l43

Korenaga, J. (2010b). Scaling of plate-tectonic convection with pseudoplastic rheology. *J. Geophys. Res* 115, B11405. doi:10.1029/2010jb007670

Korenaga, J. (2013). Initiation and evolution of plate tectonics on Earth: theories and observations. *Annu. Rev. Earth Planet. Sci*. 41, 117–151. doi:10.1146/annurev-earth-050212-124208

Korenaga, J. (2018). Crustal evolution and mantle dynamics through Earth history. *Philos. Trans. A Math. Phys. Eng. Sci.* 376 (2132), 20170408. doi:10.1098/rsta.2017.0408

Lenardic, A. (2018). The diversity of volcanic-tectonic modes and thoughts about transitions between them. *Philos. Trans. A Math. Phys. Eng. Sci.* 376 (2132), 20170416. doi:10.1098/rsta.2017.0416

Liu, Z. C., Lin, J. P., Li, S. J., and Chen, G. L. (2002). Effects of Nb and Al on the microstructures and mechanical properties of high Nb containing TiAl base alloys. *Intermetallics* 10, 653–659. doi:10.1016/s0966-9795(02)00037-7

Long, H., Weidner, D. J., Li, L., Chen, J., and Wang, L. (2011). Deformation of olivine at subduction zone conditions determined from *in situ* measurements with synchrotron radiation. *Earth Planet. Sci. Lett.* 186, 23–35. doi:10.1016/j.pepi.2011.02.006

Lowman, J. P., and Jarvis, G. T. (1999). Effects of mantle heat source distribution on supercontinent sability. *J. Geophys. Res.* 104 (6), 12733–12747. doi:10.1029/1999jb900108

Magni, V., Bouilhol, P., and van Hunen, J. (2014). Deep water recycling through time Geochem. *Geochem. Geophys. Geosyst.* 15 (11), 4203–4216. doi:10.1002/2014GC005525

Martin, H., and Moyen, J.-F. (2002). Secular changes in TTG composition as markers of the progressive cooling of the Earth. *Geology* 30 (4), 319–322. doi:10.1130/0091-7613(2002)030<0319:scittg>2.0.co;2

McCoy-West, A. J., Chowdhury, P., Burton, K. W., Sossi, P., Nowell, G. M., Fitton, J. G., et al. (2019). Extensive crustal extraction in Earth's early history inferred from molybdenum isotopes. *Nat. Geosci*. 12, 946–951. doi:10.1038/s41561-019-0451-2

Moresi, L., Quenette, S., Lemiale, V., Mériaux, C., Appelbe, B., and Mülhaus, H. B. (2007). Computational approaches to studying non-linear dynamics of the crust and mantle. *Phys. Earth Planet. Inter.* 163 (1–4), 69–82. doi:10.1016/j.pepi.2007.06.009

Moresi, L., and Solomatov, V. (1998). Mantle convection with a brittle lithosphere: thoughts on the global tectonic styles of the Earth and Venus. *Geophys. J. Int*. 133, 669–682. doi:10.1046/j.1365-246x.1998.00521.x

Moyen, J.-F. (2011). The composite Archean grey gneisses: petrological significance, and evidence for a non-unique tectonic setting for Archean crustal growth. *Lithos* 123, 21–36. doi:10.1016/j.lithos.2010.09.015

Moyen, J.-F., and Laurent, O. (2018). Archaean tectonic systems: a view from igneous rocks. *Lithos* 302 (303), 99–125. doi:10.1016/j.lithos.2017.11.038

Moyen, J.-F., and Stevens, G. (2006). "Experimental constraints on TTG petrogenesis: implications for Archean geodynamics." in *Archean geodynamics and environments*. Editors K. Benn, J. -C. Mareschal, and K. C. Condie (AGU), 149–178.

Nebel, O., Capitanio, F. A., Moyen, J.-F., Weinberg, R. F., Clos, F., Nebel-Jacobsen, Y. J., et al. (2018). When crust comes of age: on the chemical evolution of Archaean, felsic continental crust by crustal drip tectonics. *Philos. Trans. A Math. Phys. Eng. Sci*. 376 (2132), 20180103. doi:10.1098/rsta.2018.0103

O'Neill, C., and Lenardic, A. (2007). Geological consequences of super-sized Earths. *Geophys. Res. Lett*. 34, L19204. doi:10.1029/2007gl030598

O'Neill, C., Marchi, S., Bottke, W., and Fu, R. (2020). The role of impacts on Archaean tectonics. *Geology* 48, 174–178. doi:10.1130/G46533.1

Palin, R. M., White, R. W., and Green, E. C. R. (2016). Partial melting of metabasic rocks and the generation of tonalitic–trondhjemitic–granodioritic (TTG) crust in the Archaean: constraints from phase equilibrium modelling. *Precambrian Res*. 287, 73–90. doi:10.1016/j.precamres.2016.11.001

Poudjom Djomani, Y. H., O'Reilly, S. Y., Griffin, W. L., and Morgan, P. (2001). The density structure of subcontinental lithosphere through time. *Earth Planet. Sci. Lett* 184, 605–621. doi:10.1016/s0012-821x(00)00362-9

Pujol, M., Marty, B., Burgess, R., Turner, G., and Philippot, P. (2013). Argon isotopic composition of Archaean atmosphere probes early Earth geodynamics. *Nature* 498, 87–90. doi:10.1038/nature12152

Qian, Q., and Hermann, J. (2013). Partial melting of lower crust at 10–15 kbar: constraints on adakite and TTG formation. *Contrib. Mineral. Petrol.* 165, 1195–1224, doi:10.1007/s00410-013-0854-9.

Rapp, R. P., Shimizu, N., and Norman, M. D. (2003). Growth of early continental crust by partial melting of eclogite. *Nature* 425, 605–609. doi:10.1038/nature02031

Regenauer-Lieb, K., Weinberg, R. F., and Rosenbaum, G. (2006). The effect of energy feedbacks on continental strength. *Nature* 442 (7098), 67–70. doi:10.1038/nature04868

Regenauer-Lieb, K., Yuen, D. A., and Branlund, J. (2001). The initiation of subduction: critically by addition of water? *Science* 294, 578–580. doi:10.1126/science.1063891

Rey, P. F., Coltice, N., and Flament, N. (2014). Spreading continents kick-started plate tectonics. *Nature* 513, 405–408. doi:10.1038/nature13728

Roberts, N. M. W., and Spencer, C. J. (2015). The zircon archive of continent formation through time. *Geol. Soc. Lond. Spec. Publ*. 389 (1), 197–225. doi:10.1144/sp389.14

Rosas, J. C., and Korenaga, J. (2018). Rapid crustal growth and efficient crustal recycling in the early Earth: implications for Hadean and Archean geodynamics. *Earth Planet. Sci. Lett.* 494, 42–49. doi:10.1016/j.epsl.2018.04.051

Rozel, A. B., Golabek, G. J., Jain, C., Tackley, P. J., and Gerya, T. V. (2017). Continental crust formation on early Earth controlled by intrusive magmatism. *Nature* 545, 332–335. doi:10.1038/nature22042

Rudnick, R. L., and Gao, S. (2003). "Composition of the continental crust," in *Treatise on geochemistry*. Editors H. D. Holland and K. K. Turekian (Amsterdam, Netherlands: Elsevier), Vol. 3, 1–64. doi:10.1016/B0-08-043751-6/03016-4

Schmeling, H. (2006). A model of episodic melt extraction for plumes. *J. Geophys. Res*. 111, B03202. doi:10.1029/2004jb003423

Senkova, S. V., Senkov, O. N., and Miracle, D. B. (2006). Cryogenic and elevated temperature strengths of an Al–Zn–Mg–Cu alloy modified with Sc and Zr. *Metall. Mater. Trans. A* 37, 3569–3575. doi:10.1007/s11661-006-1051-5

Sizova, E., Gerya, T., Brown, M., and Perchuk, L. L. (2010). Subduction styles in the Precambrian: insight from numerical experiments. *Lithos* 116, 209–229. doi:10.1016/j.lithos.2009.05.028

Sizova, E., Gerya, T., Stüwe, K., and Brown, M. (2015). Generation of felsic crust in the Archean: a geodynamic modeling perspective. *Precambrian Res*. 271, 198–224. doi:10.1016/j.precamres.2015.10.005

Smithies, R. H. (2000). The Archaean tonalite–trondhjemite–granodiorite (TTG) series is not an analogue of Cenozoic adakite. *Earth Planet. Sci. Lett*. 182, 115–125. doi:10.1016/s0012-821x(00)00236-3

Smithies, R. H., Champion, D. C., and Van Kranendonk, M. J. (2009). Formation of Paleoarchean continental crust through infracrustal melting of enriched basalt. *Earth Planet. Sci. Lett*. 281, 298–306. doi:10.1016/j.epsl.2009.03.003

Smithies, R. H., Ivanic, T. J., Lowrey, J. R., Morris, P. A., Barnes, S. J., Wyche, S., et al. (2018). Two distinct origins for Archean greenstone belts. *Earth Planet. Sci. Lett*. 487, 106–116. doi:10.1016/j.epsl.2018.01.034

Smithies, R. H., Lu, Y., Johnson, T. E., Kirkland, C. L., Cassidy, K. F., Champion, D. C., et al. (2019). No evidence for high-pressure melting of Earth's crust in the Archean. *Nat. Commun*. 10, 5559. doi:10.1038/s41467-019-13547-x

Stern, R. J. (2018). The evolution of plate tectonics. *Philos. Trans. A Math. Phys. Eng. Sci*. 376 (2132), 20170406. doi:10.1098/rsta.2017.0406

Stern, R. J., and Gerya, T. (2018). Subduction initiation in nature and models: a review. *Tectonophysics* 746, 173–198. doi:10.1016/j.tecto.2017.10.014

Sygała, A., Bukowska, M., and Janoszek, T. (2013). High temperature versus geomechanical parameters of selected rocks-the present state of research. *J. Sustain. Min*. 12 (4), 45–51. doi:10.7424/jsm130407

Tackley, P. J. (2000). Self-consistent generation of tectonic plates in time-dependent, three-dimensional mantle convection simulations, 1, Pseudoplastic yielding. *Geochem. Geophys. Geosyst*. 1 (8), 200GC000036. doi:10.1029/2000gc000036

Tackley, P. J. (2000a). "The quest for self-consistent incorporation of plate tectonics in mantle convection," in *History and dynamics of global plate Motions*. Editor M. A. Richards (AGU).

Tang, M., Chen, K., and Rudnick, R. L. (2016). Archean upper crust transition from mafic to felsic marks the onset of plate tectonics. *Science* 351, 372–375. doi:10.1126/science.aad5513

Thielmann, M., and Kaus, B. J. P. (2012). Shear heating induced lithospheric-scale localization: does it result in subduction? *Earth Planet. Sci. Lett*. 359 (360), 1–13. doi:10.1016/j.epsl.2012.10.002

Trompert, R., and Hansen, U. (1998). Mantle convection simulations with rheologies that generate plate-like behaviour. *Nature* 395, 686–689. doi:10.1038/27185

Turner, S., Wilde, S., Wörner, G., Schaefer, B., and Lai, Y.-J. (2020). An andesitic source for Jack Hills zircon supports onset of plate tectonics in the Hadean. *Nat. Commun*. 11, 1241. doi:10.1038/s41467-020-14857-1

van Heck, H. J., and Tackley, P. J. (2008). Planforms of self-consistently generated plates in 3-d spherical geometry. *Geophys. Res. Lett*. 35, L19312. doi:10.1029/2008gl035190

van Heck, H. J., and Tackley, P. J. (2011). Plate tectonics on super-earths: equally or more likely than on earth. *Earth Planet. Sci. Lett*. 310 (3–4), 252–261. doi:10.1016/j.epsl.2011.07.029

van Hunen, J., and van den Berg, A. P. (2008). Plate tectonics on the early Earth: limitations imposed by strength and buoyancy of subducted lithosphere. *Lithos* 103 (1–2), 217–235. doi:10.1016/j.lithos.2007.09.016

Wu, Z., Bei, H., Pharr, G. M., and George, E. P. (2014). Temperature dependence of the mechanical properties of equiatomic solid solution alloys with face-centered cubic crystal structures. *Acta Mater*. 81, 428e441. doi:10.1016/j.actamat.2014.08.026

Zhang, C., Holtz, F., Koepke, J., Wolff, P. E., Ma, C., and Bédard, J. H. (2013). Constraints from experimental melting of amphibolite on the depth of formation of garnet-rich restites, and implications for models of Early Archean crustal growth. *Precambrian Res*. 231, 206–217. doi:10.1016/j.precamres.2013.03.004

Conflict of Interest: The authors declare that the research was conducted in the absence of any commercial or financial relationships that could be construed as a potential conflict of interest.

APPENDIX

Appendix A1: Pressure-Temperature Conditions for Low-P, Medium-P and High-P TTG Formation

The pressure-temperature (*P*-*T*) conditions of LP- and MP-TTGs formation during the Archean (**Figure 2**) can be written as the following functions (Jain et al., 2019):

$$760 - 60\ (P-1)^2 < T < 1{,}000 - 150\left(\frac{P-1.2}{1.2}\right)^2 \tag{A1}$$

$$-0.5\left(\frac{T-870}{220}\right) < P < 1.5 + 0.7\left(\frac{T-700}{200}\right) \tag{A2}$$

where, T is in °C and P is in GPa. Low-*P* TTGs generally forms at $P <$ 0.8–1 GPa while the medium-P TTGs forms at $P >$ 0.7–1 GPa, depending upon the actual source rock composition (Moyen, 2011; Palin et al., 2016; Johnson et al., 2017). For simplicity, our employed functions put this pressure bracket between low-P and medium-P TTGs at 1 GPa, following the traditional definition scheme put forward by Moyen (2011). The *P*-*T* conditions for forming the High-P TTG via partial melting of basalts is given by (Jain et al., 2019):

$$1{,}000 < T < 1{,}100 + 50\left(\frac{P-3.5}{3.5}\right)^2 \tag{A3}$$

$$2.35 + 0.15\left(\frac{T-1{,}000}{100}\right) < P < 2.5 \tag{A4}$$

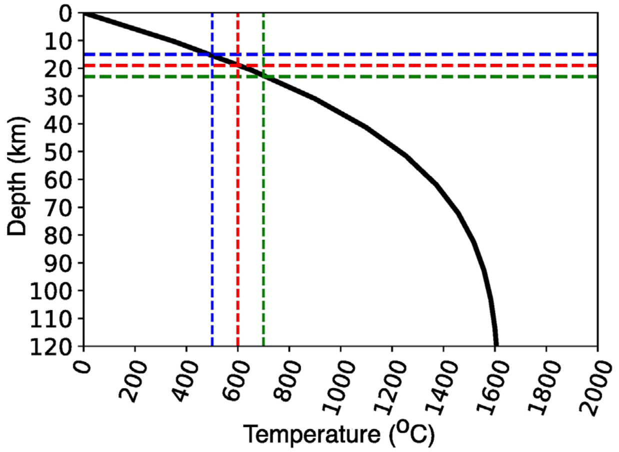

Figure A1 | The average basaltic crustal thickness relevant for different Moho-T values for a model with yield stress of 50 MPa and mantle T_p of 1,600°C.

TABLE A1 | Melt extraction threshold values.

Material	M1	M2	M3	M4
Peridotite	0.00	0.05	0.4	0.4
Hydrated basalt	0.02	0.04	0.4	0.4

Appendix A2: Solidii and Liquidii for Different Lithologies Used in the Modeling

For mantle melting, we used the *P*-*T* dependent peridotite melting model parametrized in Sizova et al. (2015).

$$T_{\text{sol}} = 1120.85 + 133P - 5.1P^2 \tag{A5}$$

$$T_{\text{liq}} = 1799.85 + 114P \tag{A6}$$

where P is in GPa and T is in °C. For the melting of hydrated basalt, we used the following parametrized solidus and liquidus functions (Sizova et al., 2015):
For, $P < 1.6$ GPa

$$T_{\text{sol}} = 699.85 - \frac{70{,}400}{1{,}000P + 354} + \frac{77{,}800{,}000}{(1{,}000P + 354)^2} \tag{A7}$$

$$T_{\text{liq}} = 1149.85 + 105P \tag{A8}$$

for, $1.6\ \text{GPa} < P < 10\ \text{GPa}$

$$T_{\text{sol}} = 661.85 + 3.5P + 6.2P^2 \tag{A9}$$

$$T_{\text{liq}} = 1149.85 + 105P \tag{A10}$$

frontiers
in Earth Science

ORIGINAL RESEARCH
published: 06 October 2020
doi: 10.3389/feart.2020.533392

Geodynamic Modeling of Edge-Delamination Driven by Subduction-Transform Edge Propagator Faults: The Westernmost Mediterranean Margin (Central Betic Orogen) Case Study

A. M. Negredo[1,2]*, **F. d. L. Mancilla**[3,4], **C. Clemente**[1], **J. Morales**[3,4] **and J. Fullea**[1]

[1] Departamento de Física de la Tierra y Astrofísica, Facultad de CC. Físicas, Universidad Complutense de Madrid, Madrid, Spain, [2] Instituto de Geociencias IGEO (CSIC, UCM), Madrid, Spain, [3] Instituto Andaluz de Geofisica, Universidad de Granada, Granada, Spain, [4] Departamento de Fisica Teorica y del Cosmos, Facultad de Ciencias, Universidad de Granada, Granada, Spain

OPEN ACCESS

Edited by:
Vlad Constantin Manea,
National Autonomous University of Mexico, Mexico

Reviewed by:
Oguz Gogus,
Istanbul Technical University, Turkey
Rob Govers,
Utrecht University, Netherlands

***Correspondence:**
A. M. Negredo
anegredo@fis.ucm.es

Specialty section:
This article was submitted to Solid Earth Geophysics, a section of the journal Frontiers in Earth Science

Received: 07 February 2020
Accepted: 08 September 2020
Published: 06 October 2020

Citation:
Negredo AM, Mancilla FdL, Clemente C, Morales J and Fullea J (2020) Geodynamic Modeling of Edge-Delamination Driven by Subduction-Transform Edge Propagator Faults: The Westernmost Mediterranean Margin (Central Betic Orogen) Case Study. Front. Earth Sci. 8:533392. doi: 10.3389/feart.2020.533392

Lithospheric tearing at slab edges is common in scenarios where retreating slabs face continental margins. Such tearing is often accommodated via subvertical STEP (Subduction-Transform Edge Propagator) faults that cut across the entire lithosphere and can result in sharp lateral thermal and rheological variations across the juxtaposed lithospheres. This setting favors the occurrence of continental delamination, i.e., the detachment between the crust and the lithospheric mantle. In order to evaluate this hypothesis, we have chosen a well-studied natural example recently imaged with unprecedented seismic resolution: the STEP fault under the central Betic orogen, at the northern edge of the Gibraltar Arc subduction system (westernmost Mediterranean Sea). The Gibraltar Arc subduction is the result of the fast westward roll-back of the Alboran slab and it is in its last evolutionary stage, where the oceanic lithosphere has been fully consumed and the continental lithosphere attached to it collides with the overriding plate. In this study we investigate by means of thermo-mechanical modeling the conditions for, and consequences of, delamination post-dating slab tearing in the central Betics. We consider a setup based on a STEP fault separating the orogenic Betic lithosphere and the adjacent thinned lithosphere of the overriding Alboran domain. Our model analysis indicates that delamination is very sensitive to the initial thermal and rheological conditions, transitioning from a stable to a very unstable and rapidly evolving regime. We find two clearly differentiated regimes according to the time at which the process becomes unstable: fast and slow delamination. Although the final state reached in both the fast and slow regimes is similar, the dynamic surface topography evolution is dramatically different. We suggest that given a weak enough Iberian lower crust the delaminating lithospheric mantle peels off the crust and adopts a geometry consistent with the imaged southward dipping Iberian lithosphere in the central Betics. The lack of spatial correspondence between the highest topography and the thickest crust, as well as the observed pattern of uplift/subsidence are properly reproduced by a model where relatively fast delamination (Reference Model) develops after slab tearing.

Keywords: subduction-transform edge propagator fault, slab tearing, continental delamination, topography evolution, Gibraltar Arc subduction system

INTRODUCTION

A Subduction-Transform Edge Propagator fault (STEP fault, as termed by Govers and Wortel, 2005) is a subvertical fault that tears a subducted slab at its edges facilitating subduction continuation in narrowed arcs. Tearing at slab edges is a consequence of lateral changes in the rate of subduction rollback, which in turn can be the result of lateral variation of slab buoyancy. Govers and Wortel (2005) identified about a dozen of STEP faults, being prominent examples the north end of the Tonga trench, the south end of New Hebrides trench, south Lesser Antilles trench and the north end of the South Sandwich trench. In addition to these reported examples in oceanic domains, a large number of STEP faults have been identified in the Mediterranean region: both ends of the Hellenic and Calabria trenches, the south edge of the Vrancea trench (Carpathians), and both edges of the western Mediterranean subduction system (Gibraltar Arc) (see Govers and Wortel, 2005; Özbakır et al., 2020; and references therein).

STEP faults cut across the entire lithosphere and eventually lead to sharp lateral contrasts in the thermal and rheological structure of juxtaposed lithospheres. This contrast is expected to be particularly important in the Mediterranean region, where "land-locked" basins surrounded by orogenic belts show significant thinning due to back-arc extension related to slab rollback. Vertical slab tearing would then put into direct contact thinned continental/oceanic lithosphere and normal or even thickened orogenic continental lithosphere of very different densities. The buoyancy forces associated with this density contrast generate mantle flow that can trigger continental delamination (edge-delamination), as proposed for the Betics STEP (Mancilla et al., 2013; Mancilla et al., 2015a; Heit et al., 2017) and for the Tell-Rif STEP in NW Algeria (Hidas et al., 2019). This scenario of delamination developing after slab tearing is completely different from other studies (e.g., Duggen et al., 2005; Faccenda et al., 2009; Gogus et al., 2011; Ueda et al., 2012; Levander et al., 2014; Baratin et al., 2016) where delamination operates in conjunction with slab sinking.

The 2D modeling presented here is inspired on the best imaged example of STEP fault, namely the fault associated with slab tearing along the eastern and central Betics, in the southern Iberian margin (**Figure 1**). To that aim we use recently obtained seismic images of the crustal and lithospheric structure of the area for comparison purposes with numerical simulations. The goal of this study is to consider this natural example to investigate by means of thermo-mechanical modeling the first order conditions for, and consequences of, lithospheric delamination after slab tearing via STEP faults. Here we focus on the central Betics area, where topography evolution and the crustal and lithospheric structure point to the occurrence of ongoing delamination (**Figure 1**).

GEODYNAMIC SETTING

The Betic-Rif orogenic belt, located in southern Iberian and northwestern African margins, represents the westernmost expression of the Alpine orogeny (**Figure 1**). It comprises the Gibraltar Arc and surrounds the extensional Alboran basin. This area is presently characterized by moderate seismicity and diffuse deformation, as a result of the slow convergence between Eurasia and Nubia (e.g., Negredo et al., 2002; Jiménez-Munt and Negredo, 2003; Cunha et al., 2012).

A number of tomographic studies have imaged a high-velocity body extending across the entire upper mantle beneath the Betics and Gibraltar Arc (e.g., Gutscher et al., 2002; Spakman and Wortel, 2004; Bezada et al., 2013; Palomeras et al., 2014; Villaseñor et al., 2015). This anomalous body has a slab-like geometry and most likely corresponds to subducted oceanic lithosphere, in the so-called western Mediterranean subduction system. This system is currently in its last evolutionary stage and does not seem to be presently active (e.g., Stich et al., 2006; Iribarren et al., 2007; Zitellini et al., 2009), although this remains the object of debate (see extensive revision by Gutscher et al., 2012). At the northern edge of this system a slab tearing process has been proposed (e.g., Faccenna et al., 2004; Duggen et al., 2004; Spakman and Wortel, 2004; Duggen et al., 2005; Govers and Wortel, 2005; García-Castellanos and Villaseñor, 2011; Mancilla et al., 2013; Chertova et al., 2014; Mancilla et al., 2015a; Mancilla et al., 2015b; Mancilla et al., 2018) and an associated vertical STEP fault has been imaged by P-wave Receiver Functions (RF) (Mancilla et al., 2015a; Mancilla et al., 2018). This tearing affects the eastern and central Betics (**Figure 1**), where it is shown as an abrupt change in lithospheric and crustal thickness across the STEP fault (**Figures 2**, **3**), while the slab seems to be connected to the surface further to the west (e.g. Spakman and Wortel, 2004; García-Castellanos and Villaseñor, 2011; Bezada et al., 2013; Mancilla et al., 2013; Spakman et al., 2018; Jiménez-Munt et al., 2019; Molina-Aguilera et al., 2019) (**Figure 1C**).

Different mechanisms have been proposed to explain the complex tectonic evolution of the area since the Miocene, the most popular being slab retreat (Lonergan and White, 1997; Faccenna et al., 2004; Vergès and Fernàndez, 2012; Chertova et al., 2014; van Hinsbergen et al., 2014). On the other hand, models proposing continental delamination, understood as the separation between the crust and lithospheric mantle (as originally proposed by Bird, 1978; Bird, 1979) are gaining popularity, either proposed as delamination alone (e.g., Seber et al., 1996; Calvert et al., 2000; Fadil et al., 2006; Valera et al., 2008; Baratin et al., 2016) or related to slab tearing (e.g., Duggen et al., 2003; Duggen et al., 2004; Duggen et al., 2005; Martínez-Martínez et al., 2006; Booth-Rea et al., 2007; Mancilla et al., 2013; Mancilla et al., 2015a; Heit et al., 2017). A detailed comparison between these conceptual models and the inferences from our modeling will be carried out in the Discussion section.

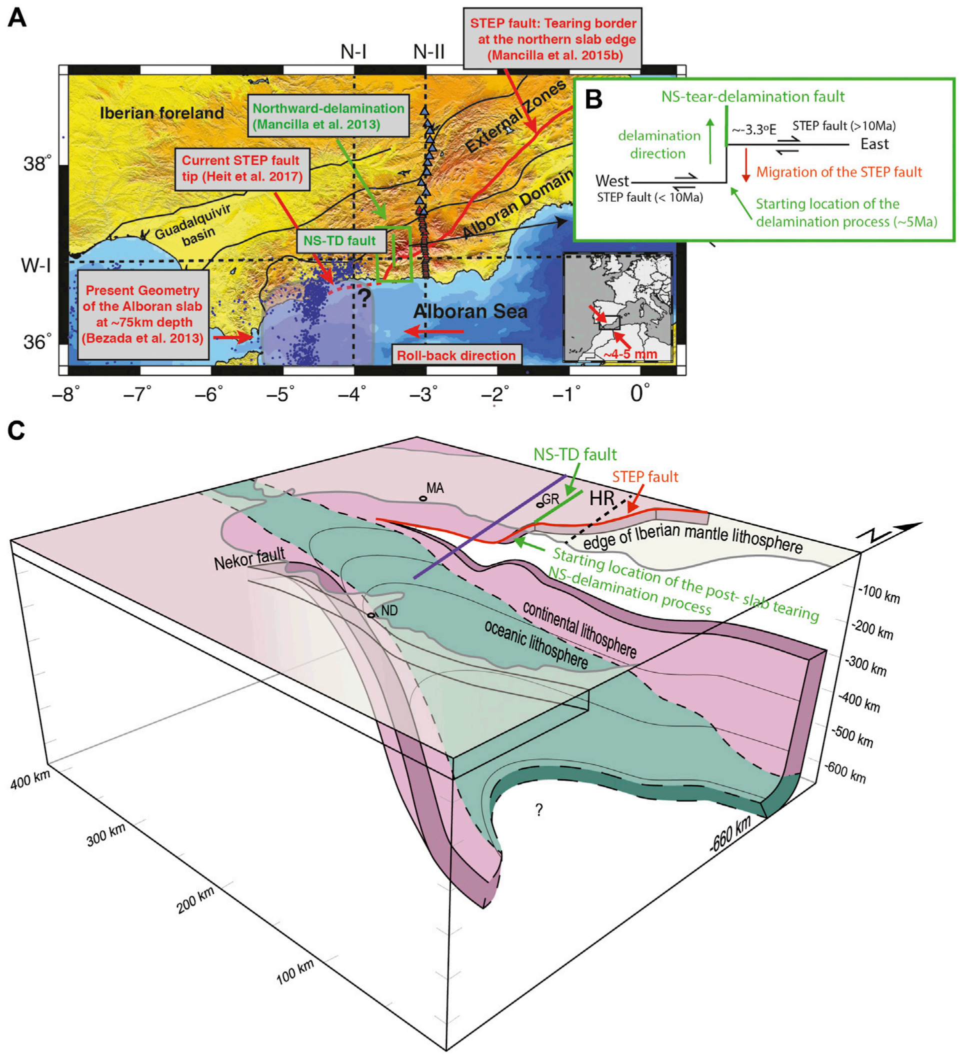

FIGURE 1 | (A) Topography map with the boundary of the main tectonic units of the Betic domain and foreland. The continuous red line marks the edge of the Iberian crust, i.e., the tearing border produced by a Subduction-Transform Edge Propagator (STEP) fault imaged by the P-receiver functions (Mancilla et al., 2015a) and the red dashed line indicates the presumably current tip position of this STEP fault (Heit et al., 2017). The green square marks the area investigated by this paper as prone for a delamination processes directed toward the north, perpendicular to the STEP fault. The purple transparent area delimits the positive velocity anomaly at 75 km depth described in the tomography study of Bezada et al. (2013) associated with the oceanic Alboran slab. Red triangles are the location of the first leg of the Hire seismic profile (~2 km inter-station distance, HIRE-I), blue triangles the second leg (~10 km inter-station distance, HIRE-II). Black dashed lines mark the locations of the P-wave receiver functions profiles of **Figure 2**: N-I (**Figure 2A**); N-II (**Figure 2B**) and W-I (**Figure 2C**). The inset map shows the collision direction of the Iberia and Africa plates. **(B)** Sketch of the relationship between the NS-tear delamination fault (TD-fault, green line), that allows the northwards migration of the delamination process, and the STEP fault that facilitates the slab rollback motion toward the west of the western Mediterranean subduction system. **(C)** Sketch of the proposed geometry by Mancilla et al. (2015b), of the underthrusted Iberian and Maghrebian lithospheres and their relation with the subducted oceanic slab observed by tomographic studies (Spakman and Wortel, 2004; Bezada et al., 2013; Villaseñor et al., 2015). Purple line marks the location of the generic modeled cross section (MA, Malaga; GR, Granada; ND, Nador; HR, Hire seismic profile A).

MODEL CONSTRAINTS FROM PRESENT-DAY LITHOSPHERIC SEISMIC STRUCTURE

The Betic-Rif belt is the result of the overthrusting of the Alboran domain onto the South Iberian and North Maghrebian passive continental paleomargins. The orogen was formed by the westward collision of the Alboran domain during the Miocene (e.g., Platt et al., 2003). A number of recent studies based on seismic receiver functions have mapped the geometry of this collision (**Figures 2**, **3**) and the STEP fault trace along the south Iberian Peninsula or south Iberia (red line in **Figure 1A**) revealing an abrupt east-west change in the underthrusted Iberian lithosphere beneath the Alboran domain at longitudes ~3.3°W (Mancilla et al., 2013; Mancilla et al., 2015a; **Figure 2C**). The location of this lateral change coincides with a migration toward the south of the STEP fault trace (**Figure 1B**). This change occurs in a very narrow area, suggesting that the underthrusting plate

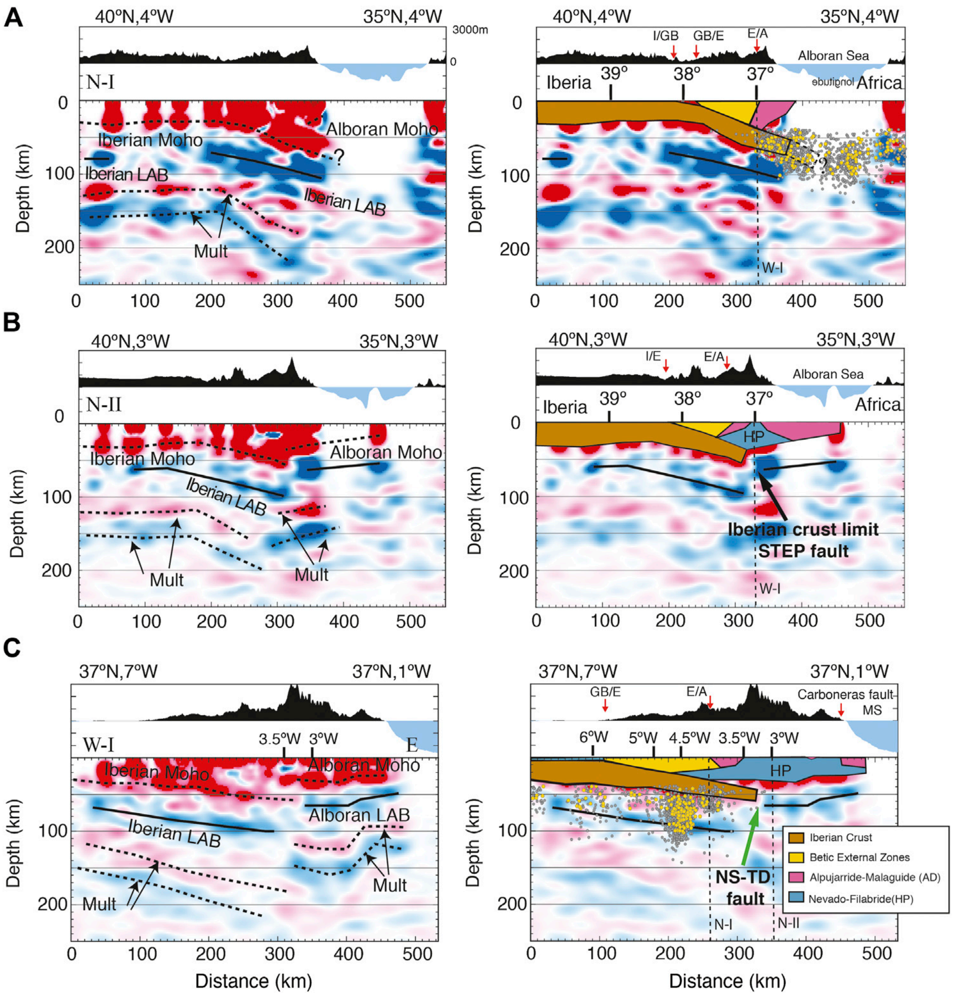

FIGURE 2 | Common conversion point images build with P-wave Receiver Functions (left panels) and their interpretation sketches (right panels). **(A,B)** are NS-cross-sections (N-I and N-2 see **Figure 1**) is WE-cross-section (W-I). In the stacked images, red colors (positive amplitudes) in a seismic discontinuity mean velocity increase with depth. The dashed black lines mark the inferred conversion depth of the Ps converted phase at the crustal-mantle boundary (the Moho discontinuity) and its first multiple reverberated phases generated at this discontinuity. Multiples (abbreviated Mult), although not migrated to their correct geometrical position, are useful to confirm the trend of the Moho discontinuity. Continuous black lines draw the Lithosphere-Asthenosphere boundary (LAB). At the top of each panel, we display the topography along the profile. Red arrows mark the contact, at the surface, between the different units (I, Iberian Massif; E, External zones; A, Alboran domain; GB, Guadalquivir basin). Common conversion point images modified from Mancilla and Diaz (2015). We plot the intermediate seismicity (depths >40 km; gray dots) for the ISC catalog together with the higher precision relocations of some of them from Santos-Bueno et al. (2019) (yellow dots). Vertical thin dashed lines are the crossing points with the other profiles in the figure.

may be broken by a N-S directed tear fault, at a longitude about 3.3°W (green line in **Figures 1**, **2C**). Since this fault enables the northwards progression of delamination in the central Betics, we term it "Tear-Delamination" fault (TD-fault).

East of the TD-fault, common conversion point images obtained from P-wave RF at a high density passive seismic profile (**Figure 1** for location) reveal that the underthrusting lithosphere of the South Iberian paleomargin ends with a sharp Moho and lithospheric step of ~17 and 40 km, respectively (**Figure 3**; Mancilla et al., 2018 for details). This abrupt ending is related to a near-vertical STEP fault tearing the slab and guiding its rollback motion toward the west (Mancilla et al., 2018).

On the other hand, west of the North-South TD (NS-TD) fault, the underthrusted Iberian lithosphere dips southwards (**Figure 2A**), with the dip angle increasing eastwards (see eastward deepening of seismic lithosphere-asthenosphere boundary in **Figure 2C**) so that it reaches depths close to the TD fault about 70 km deeper than under the Gibraltar Arc (Mancilla et al., 2013; Mancilla et al., 2015a). The southern location reached by the Iberian lithosphere west of the TD fault indicates a southward migration of the locus of the STEP fault (**Figure 1B**). This is supported by the localization of the intermediate seismicity (depths >40 km; gray and yellow dots, **Figures 2A,C**), which is interpreted as delineating the tip of the

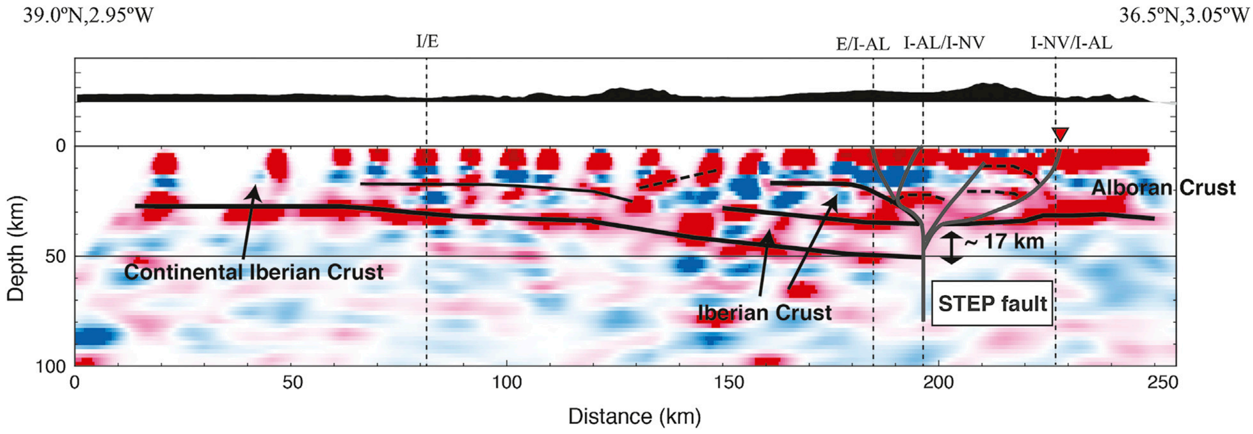

FIGURE 3 | Migrated Common conversion point images using P-wave receiver functions of the high density profile HIRE (triangles in **Figure 1A**) probing the crustal structure in central Betics. We overlap the images with our interpretations along the section: The crust-mantle boundary (Iberian and Alboran Moho, thick black lines), intracrustal converters (thin and dashed black lines) and the Subduction-Transform Edge Propagator fault and its continuation toward the surface as positive flower structure (gray lines). This image is a modification of the one published in Mancilla et al. (2018). For the details about the image construction and receiver function calculation see the source paper.

lateral slab tearing (Heit et al., 2017; Santos-Bueno et al., 2019), i.e., the currently active segment of the STEP fault.

Several lines of evidence suggest that northwards mantle delamination is likely occurring west of the TD fault (see Mancilla et al., 2013 for details). Among them, the fast mean uplift of 0.5 mm/yr during last <8 Ma (Azañón et al., 2015) that produces asymmetry in the topography between the western and eastern sides of Sierra Nevada mountains (different ~500 m in the highest altitude), together with the lack of correspondence between highest topography and thickest crust root, indicates that the topography could be partly supported by asthenospheric upwelling related to continental delamination (Mancilla et al., 2013; Mancilla et al., 2015a). GPS velocities and seismic deformation pattern also support this idea (Mancilla et al., 2013). The delaminated lithospheric mantle would peel off the crust and adopt a geometry consistent with the imaged southward dipping Iberian lithosphere in the central Betics (**Figure 2A**).

In this study we examine possible lithospheric configurations in the collisional contact between Iberian and Alboran domains that allow edge-delamination at the western side of the TD fault in central Betics after the tearing process caused by the westward propagation of the STEP fault.

METHODOLOGY

Fundamental Equations and Model Setup

Here we use the finite element open source code ASPECT 2.1 (Kronbirchler et al., 2012; Bangerth et al., 2019) to solve the coupled equations of conservation of mass, momentum and energy (**Eqs 1–3**) for a 2D vertical section of an incompressible fluid. We adopt the Boussinesq approximation, and therefore we assume that the density is constant in all the equations except for the buoyancy term (right hand term in **Eq. 2**) of the momentum equation. In addition, as the reference temperature is assumed to be constant, the adiabatic and shear heating are neglected in the energy equation. Then the equations of mass, momentum and energy adopt the following form:

$$\nabla \cdot u = 0 \tag{1}$$

$$-\nabla \cdot 2\,\mu\,\epsilon(u) + \nabla p = \rho\, g \tag{2}$$

$$\rho_0\, C_p\left(\frac{\partial T}{\partial t} + u \cdot \nabla T\right) - \nabla \cdot k \nabla T = \rho_0\, H \tag{3}$$

where, u is the velocity field, μ is the viscosity, $\varepsilon(u)$ is the strain rate tensor, p is the pressure, ρ is the density, ρ_0 is the reference density, g is the gravity acceleration, Cp is the specific heat, T is the temperature, k is the thermal conductivity, H is radiogenic heat production per unit mass. We neglect latent heat release due to phase transformation. We consider that the density satisfies the simple relationship $\rho = \rho_0\,(1 - \alpha\,(\mathrm{T} - \mathrm{T}_0))$, being α a small thermal expansion coefficient and ρ_0 the reference density that is attained at a temperature T_0. The Boussinesq approximation has great computational advantages as the algebraic systems of equations become much easier to solve. This is very useful particularly for a computationally demanding modeling as is the case of delamination incorporating a free surface on its top. This approximation is acceptable for the present modeling since we reproduce a relatively short-term evolution (<10 Myr) involving depths less than about 250 km, and therefore the range of variation of density with depth (pressure) is relatively small.

ASPECT has two particular advantages for modeling continental delamination: the adaptive mesh refinement (AMR) and the incorporation of a true free surface with stress-free boundary conditions on the top boundary (Rose et al., 2017). AMR allows for selective mesh refinement in areas of strong gradients in the material properties, while a coarser mesh can be used in areas with low velocities and/or smooth gradients of material properties. This feature allows robust modeling of high viscosity contrasts of >3–4 orders of

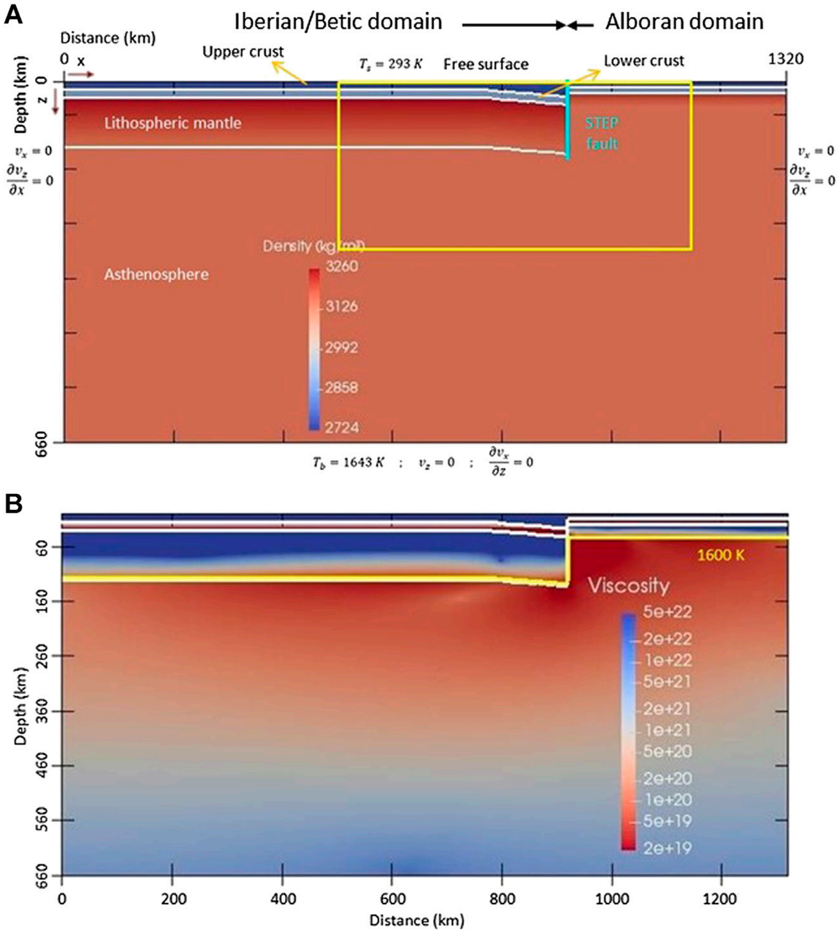

FIGURE 4 | Model setup for the Reference Model with the **(A)** initial density distribution and boundary conditions. The contour of the Iberian mantle lithosphere is shown for better understanding the evolution of delamination, albeit having the same composition and parameters as the asthenosphere and Alboran lithospheric mantle. **(B)** Initial viscosity distribution (units Pa s) and 1,600 K isotherm to show the initial lithospheric thickness.

magnitude on small length scales, as it is the case between the lower crust and upper lithospheric mantle. The free surface feature allows for self-consistent modeling of the surface dynamic response to mass redistribution during delamination. However, modeling free surfaces is a challenging problem (e.g., Kaus et al., 2010; Rose et al., 2017) and requires taking small time steps and the application of stabilization procedures to avoid instabilities in the free surface. We have performed a number of simulations to select the stabilization parameters giving a good compromise between stability and accuracy (see explanations in Bangerth et al., 2019). The modeled domain simulates a 2-D vertical section running N-S at a longitude of about 3.5°W (purple line in **Figure 1C**), with horizontal and vertical extents of 1,320 and 660 km, respectively (**Figure 4**). We checked that this size of the modeled domain is enough to prevent boundary effects. We will use the terms "Iberian" and "Alboran" to describe the simulations thereafter (**Figure 4**). Model parameters are compiled in **Table 1**. The initial setup simulates the initial contact of the thickened Iberian lithosphere under the central Betics and the thinned back-arc lithosphere of the Alboran Sea guided by the STEP fault. The model domain includes the upper and lower crusts, the lithospheric mantle and the asthenosphere, defined by different compositional fields. Although the parameters of the lithospheric mantle and asthenosphere are exactly the same (density differences just due to temperature variations), we have defined a specific body for the Betic lithospheric mantle to better track its evolution as it peels off the crust. We do not include in our modeling the deeper sinking slab since we assume that it was detached prior to delamination and therefore it has not any mechanical effect at shallower depths. The specific values of the initial thicknesses of the layers are based on a number of seismic receiver functions profiles reporting a 17 km step in the Moho depth between the Iberian and the Alboran crusts in the eastern Betics (Mancilla et al., 2015a; Mancilla et al., 2018). The geometric parameters (layer thicknesses) defining the crustal and lithospheric structure in the Iberian and Alboran domains are based on a number of geophysical modeling studies (e.g., Fullea et al., 2007; Fullea et al., 2010; Carballo et al., 2015; Mancilla and Diaz, 2015; Torné et al., 2015).

TABLE 1 | (A) . (B) Parameters considered for a wet-olivine rheology (Hirth and Koldstedt 2003) and feldspar (Bürgmann and Dresen, 2008).

A

Symbol	Meaning	Value
g	Acceleration of gravity	9.8 m s^{-2}
ρ_{uc}	Upper crust density	$2{,}750 \text{ kg m}^{-3}$
ρ_{lc}	Lower crust density	$2{,}900 \text{ kg m}^{-3}$
ρ_m	Mantle density	$3{,}300 \text{ kg m}^{-3}$
ρ_a	Asthenosphere density	$3{,}300 \text{ kg m}^{-3}$
T_0	Reference temperature	293 K
$h_{\text{uc,b}}$	Upper crust thickness, Iberia	15–27 km
$h_{\text{lc,b}}$	Lower crust thickness, Iberia	15 km
$h_{uc,a}$	Upper crust thickness, Alboran	10 km
$h_{lc,a}$	Lower crust thickness, Alboran	10 km
R	Gas constant	$8.31 \text{ J K}^{-1} \text{ mol}^{-1}$
T_s	Surface temperature	293 K
T_b	Bottom temperature	1,643 K
d	Grain size	10^{-2} m
σ_y	Yield stress (cohesion)	10^{20} Pa
c_p	Specific heat	$1{,}250 \text{ J kg}^{-1} \text{ K}^{-1}$
κ	Thermal diffusion	$0.8 \cdot 10^{-6} \text{ m}^2 \text{ s}^{-1}$
α	Thermal expansion coefficient	$3.5 \cdot 10^{-5} \text{ K}^{-1}$

B

Symbol	Meaning	Olivine (diffusion)	Olivine (dislocation)	Lower crust (diffusion)
A	Exponential prefactor	$4.7 \cdot 10^{-16} \text{ Pa m}^3 \text{ s}^{-1}$	$2.28 \cdot 10^{-18} \text{ Pa}^{-3.5} \text{ s}^{-1}$	$5 \cdot 10^{-19} \text{ Pa m}^7 \text{ s}^{-1}$
n	Stress exponent	1	3.5	1
m	Grain size exponent	3	—	7
E^*	Activation energy	335 kJ mol^{-1}	480 kJ mol^{-1}	170 kJ mol^{-1}
V^*	Activation volume	$4 \cdot 10^{-6} \text{ m}^3 \text{ mol}^{-1}$	$1.1 \cdot 10^{-5} \text{ m}^3 \text{ mol}^{-1}$	0

Previous studies on continental delamination introduce an increased reference density in the delaminating lithospheric mantle to force delamination initiation (e.g., Gögüs and Pysklywec 2008; Bajolet et al., 2012; Gögüs et al., 2016). Alternatively, a common assumption in delamination studies is that delamination develops in conjunction with, and in response to the negative buoyancy of a deep sinking slab (e.g., Duggen et al., 2003; Duggen et al., 2005; Faccenda et al., 2009; Göğüş et al., 2011; Ueda et al., 2012; Baratin et al., 2016). In contrast, in our post slab-tearing setup, slab pull does not act and the driving mechanism is the buoyancy forces arising from the lateral thermal contrast between the orogenic central Betic lithosphere and the thinned Alboran lithosphere. Slab detachment and related uplift occurring prior to delamination is attested by the pre-Messinian marine–continental transition in the Betic internal basins being presently at altitudes of about 1,000 m, with ages of marine to non-marine transition between 7.2 and 5.3 for the central Betics (Iribarren et al., 2009; see interpretation in terms of slab tearing by García-Castellanos and Villaseñor, 2011).

In this way we avoid additional forcing of the model setup to develop delamination. For the same reason, we do not introduce any asthenospheric channel or weak zone in the lithospheric mantle to enable asthenospheric upwelling and inflow into the lower crust, as it is commonly done in delamination models (e.g., Gögüs and Pysklywec, 2008; Valera et al., 2008; Valera et al., 2011; Bajolet et al., 2012; Gögüs et al., 2016; see revision in Göğüş and Ueda, 2018).

The initial temperature distribution is a conductive profile in the lithosphere, with a linear increase from 20°C at the surface to Tm = 1370°C at the base of the lithosphere. In the sub-lithospheric mantle we assume initial constant temperature of Tm (i.e., negligible adiabatic gradient). The temperature is kept at the initial values at the vertical and horizontal model boundaries. Mechanical boundary conditions are free slip at the lateral and bottom boundaries, and a true free-surface condition at the top boundary to account for topography evolution. We do not apply a lateral boundary condition accounting for Eurasia-Nubia convergence velocity because its north component (parallel to the modeled section) is very small (computed with MORVEL model by DeMets et al., 2011) and NW-SE Eurasia-Nubia convergence is most likely accommodated further to the south of the modeled generic section (e.g., Negredo et al., 2002; Cunha et al., 2012).

Rheological Setting

We adopt a visco-plastic rheology with a composite viscosity μ_{comp} given by a combination of diffusion and creep dislocation viscous flow laws:

$$\mu_{comp} = \left(\frac{1}{\mu_{disl}} + \frac{1}{\mu_{diff}} \right)^{-1}$$

where μ_{disl} and μ_{diff} represent dislocation and diffusion viscosities. Both viscosities can be expressed in the same form but with different parameters (e.g., Hirth and Kohlstedt, 2003; Billen and Hirth, 2007; Rodríguez-González et al., 2012; Rodríguez-González et al., 2014):

$$\mu_i = \frac{1}{2} A_i^{\frac{-1}{n_i}} d_i^{\frac{m_i}{n_i}} \dot{\epsilon}_{ii}^{\frac{1-n_i}{n_i}} exp\left(\frac{E_i + PV_i}{n_i RT}\right)$$

where the index i denotes the creep mechanism (dislocation or diffusion). A is the pre-exponential factor, d is the grain size, m is the grain size exponent, n is the stress exponent, $\dot{\epsilon}_{ii}$ is the square root of the deviatoric strain rate tensor second invariant, E is activation energy, V is activation volume, P is pressure, R is the gas constant and T is temperature. Therefore, in the diffusion viscosity case (μ_{diff}, n = 1, m ≠ 0) there is not dependence on the strain rate, while in the dislocation viscosity case (μ_{disl}, n > 1, m = 0) a power law dependence on the strain rate is in place. We have imposed maximum and minimum viscosity cut-offs of 10^{24} and 10^{19} Pa·s, respectively, although other values have been tested in different simulations as will be explained in the subsection *Sensitivity Study*. For the lithospheric mantle and asthenosphere we have adopted a rheology for wet olivine from Hirth and Koldstedt (2003). The parameters adopted for olivine (**Table 1**) give a composite viscosity of 10^{20} Pa·s at a depth z = 150 km for a strain rate of 10^{-15} s^{-1}. For the lower crust we consider a diffusion rheology for wet anorthite feldspar, with parameters from Bürgmann and Dresen (2008). For the upper crust we assume a constant composite viscosity equal to the maximum viscosity cutoff of each model.

The visco-plastic adopted approach takes into account both brittle (plastic) yielding and viscous deformation. Plasticity limits viscous stresses through a Von Mises yield criterion, with the yield stress fixed to the cohesion $\sigma_y = C$. When the viscous stress $2\mu\,\dot{\epsilon}_{ii}$ exceeds the yield stress, the viscosity is rescaled to the yield surface $\mu_y = \sigma_y/2\,\dot{\epsilon}_{ii}$ (e.g., Thieulot, 2011). The viscosity is then given by:

$$\mu = min\left\{\frac{\sigma_y}{2\dot{\epsilon}_{ii}}, \mu_{comp}\right\}$$

Table 1 lists the rheological parameters used for the different creep mechanism and compositional fields.

RESULTS

We have performed a large number of simulations (>50) testing the effects of varying the lithospheric structures at both sides of the STEP fault as well as the viscosity distribution. From this sensitivity study we have constrained the conditions controlling the occurrence or not of delamination, and the pace of delamination process when it occurs. Broadly speaking we can group our simulations into three clearly differentiated end-members attending to the pace of the delamination process and topographic evolution: i) Reference Model, ii) slow delamination, and iii) no delamination. The first end member ("Reference Model"), has been calibrated according to the structure and topography evolution of the delamination process proposed for the central Betics. We select a representative model for slowly evolving delamination in order to illustrate how delamination speed affects the surface response (topography and surface velocity). The main difference between the Reference Model and the slow model stands on a difference of 20 km for the thickness of the South Iberian lithospheric mantle. This difference will be shown to have a significant effect on the buoyancy forces triggering delamination. In the following we describe in detail two of the end member scenarios: Reference (**Figures 4–7**) and slow models (**Figures 9–11**).

Reference Model

The Reference Model assumes an initial LAB (Lithosphere-Asthenosphere Boundary) depth for the South Iberian margin of 120–132 km and reproduces a well-developed delamination process (**Figures 5**, **6**). The initial setup assumes an initial LAB depth for the Alboran Sea of 45 km, representing moderate back-arc thinning (stretching factor about two, assuming an initial LAB depth of 90 km). The maximum and minimum viscosity cutoffs are 5×10^{22} and 2×10^{19} Pa·s, respectively. These values represent a moderate stiffness of the lithospheric mantle and weak lower crust and asthenosphere. **Figure 5** shows the density and velocity field evolution as well as the topographic response; **Figure 6** shows the viscosity distribution evolution, and **Figure 7** shows the surface response along a simulation lasting 5.4 Ma. The lateral density contrast results in a negatively buoyant thick Iberian lithosphere. In contrast, the warm, low viscosity Alboran lithosphere creates a weak zone that channels asthenospheric upwelling and inflow along the base of the Iberian crust. Two clearly differentiated stages of evolution can be distinguished, as it is shown in the plot of maximum velocity *vs.* time (**Figure 8**). The first phase comprises the first ~3 Ma and is characterized by upward and leftward mantle flow sourced from the Alboran domain, adjacent to the vertical step. This flow is further enhanced by the viscosity reduction due to the high temperature and strain rate. The pressure difference forces the upwelling mantle into the Iberian lower crust, with maximum horizontal velocities of 2 cm/yr (**Figure 5A**).

The second phase is characterized by the acceleration of delamination (**Figures 5B,C**). The progression of the asthenospheric lateral intrusion generates crustal thickening in front of the delamination hinge, and crustal thinning behind it, removing completely the lower crust. As the area of the intruding mantle grows, the extent of unsupported (from above), negatively buoyant Iberian lithospheric mantle increases and starts sinking faster into the asthenosphere. This sinking continental slab pulls down the lower crust at the delamination hinge and the adjacent lithosphere, further accelerating the lateral spreading of delamination. The inflow velocity increases dramatically (**Figures 5C and 8**) and the system tends to become very unstable. As discussed in the analytical study by Bird (1979), two main competing effects determine whether the system is stable or unstable. First, the intruding asthenosphere cools down and develops a thermal boundary layer (high viscosity borders of the intruding mantle in **Figure 6A**), thus reducing the thickness of the low viscosity layer. Second, the sinking of the lithospheric mantle slab increases the thickness of this overlying weak layer. If "freezing" in the low viscosity layer dominates the system will be stable whereas if sinking and separation dominate the system will be very unstable.

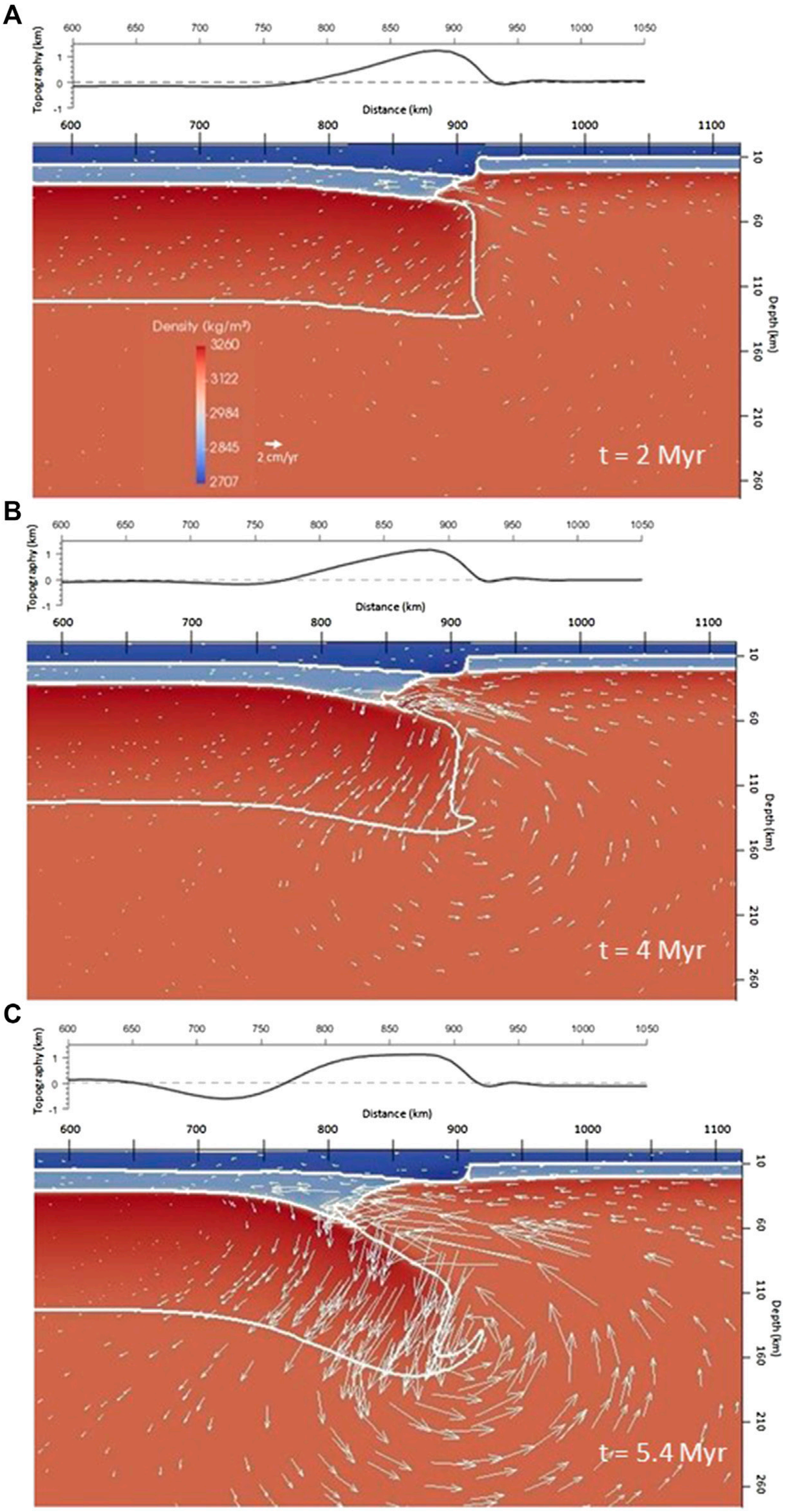

FIGURE 5 | Distribution of density and velocity field and topographic response at different times **(A)** 2, **(B)** 4, and **(C)** 5.4 Myr of the Reference Model.

At 5.4 Myr, the maximum crustal thickness (>50 km) has migrated about 106 km to the left since the beginning of the simulation. The descending lithospheric mantle slab peels away rapidly from the crust, and sinks into the mantle, in a similar fashion as a retreating slab subduction mechanism. The tip of the modeled Iberian lithospheric mantle slab reaches a depth of about

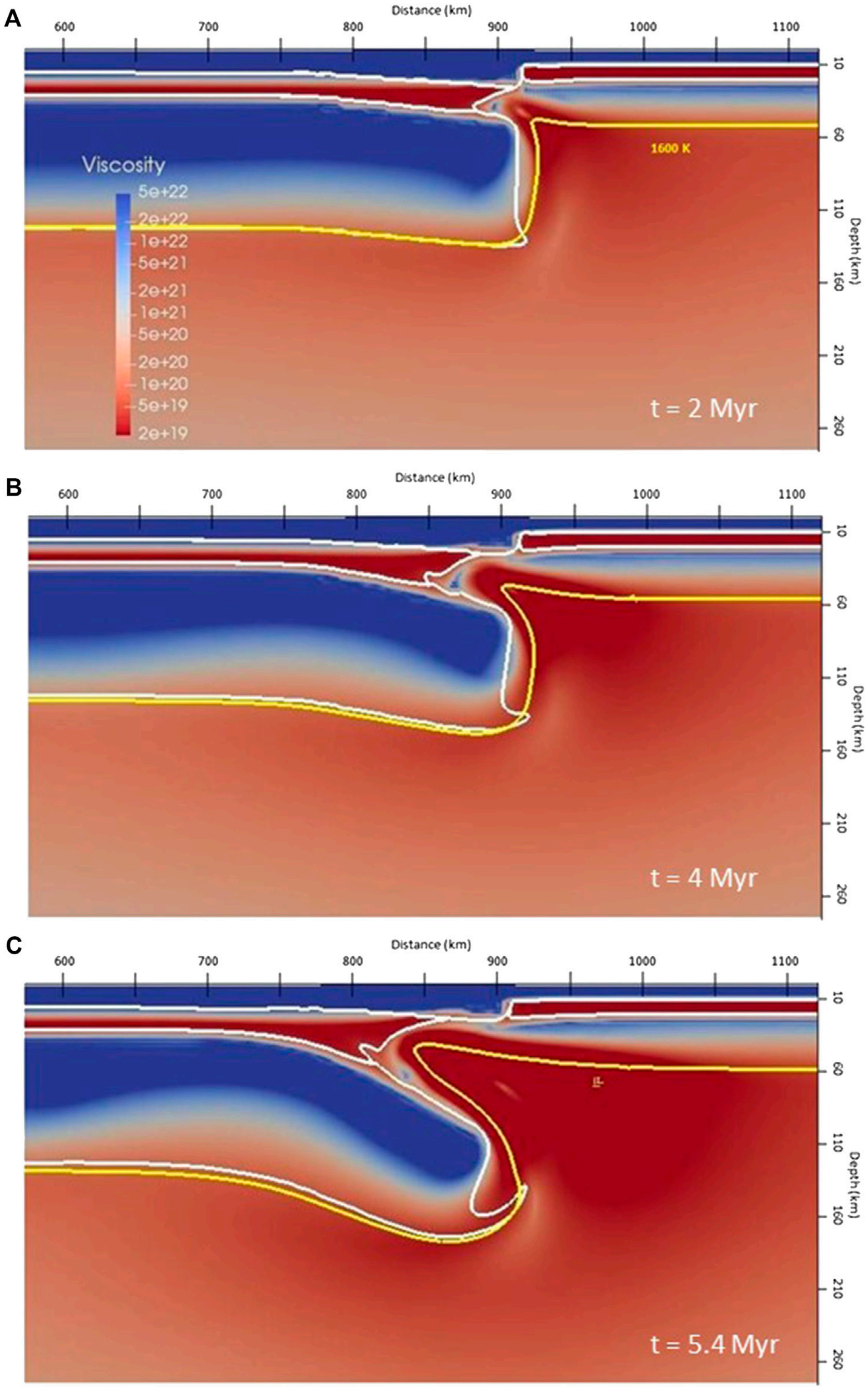

FIGURE 6 | Distribution of viscosity (logarithmic scale plot; Pa s units) and location of the 1,600 K isotherm at different times **(A)** 2, **(B)** 4, and **(C)** 5.4 Myr of the Reference Model.

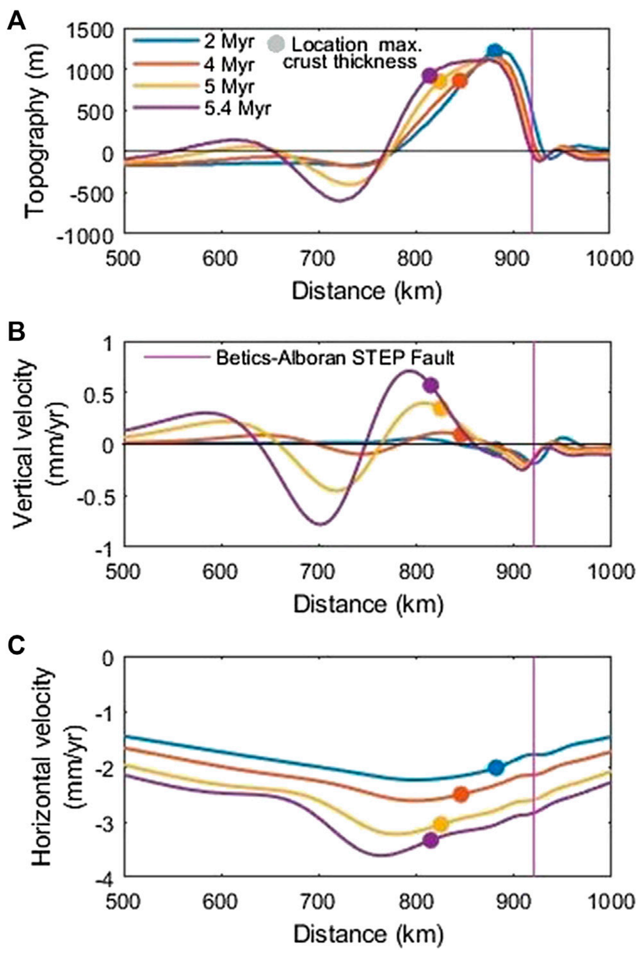

FIGURE 7 | (A) Topography, **(B)** vertical velocity, and **(C)** horizontal velocity of the free surface at different time steps of the Reference Model. The location of the maximum crustal thickness at each time step is also marked (colored dots) to facilitate the interpretation.

100 km, in line with the seismically mapped geometry of the Iberian dipping slab at longitudes 3.3°W (Mancilla et al., 2013; **Figure 12**).

Figure 7 shows the surface evolution of the Reference Model in terms of topography, and horizontal and vertical components of the velocity. The evolution of the model topography shows a characteristic migrating pattern of uplift/subsidence, following the direction of migration of delaminating lithospheric mantle and crustal thickening over the slab. During the first phase (represented by the t = 2 Myr line in **Figure 7**) the location of the maximum topography coincides with that of maximum crustal thickness. During the phase of enhanced asthenospheric inflow and slab sinking (represented by t = 4 and 5.4 Myr lines in **Figure 7**) the location of maximum crustal thickness is shifted by about 30 km. The region of high topography (>1 km) becomes wider and the maximum elevation values are maintained through the evolution time, so that a narrow high plain develops. Note that the crustal thickness above the zone of delamination is mostly <35 km, and therefore the high topography is sustained by the replacement of dense lithospheric mantle by warmer asthenosphere inflow. In contrast, a shallow basin is formed to the left of the delamination hinge (660 km < x < 770 km) as a consequence of the negatively buoyant sinking slab. Further to the right (770 km < x < 820 km), this downward pull is counteracted by isostatic uplift due to crustal thickening, which results in positive surface topography.

Surface uplift (positive vertical velocity in **Figure 7B**) occurs when crustal thickening and inflow of hot mantle dominate over the downward pull exerted by the sinking slab. The maximum uplift rate is ~0.7 mm/yr at 5.4 Myr and its location is shifted about ~20 km to the left from the location of maximum crustal thickening. The offset stems from the fact that maximum uplift rates correlate with the rate of crustal thickening rather than the crustal thickness itself. The leftward migration of high uplift rates is responsible for the progressive widening of the elevated area (**Figure 7A**). Similarly, the highest subsidence rate occurs to the left of the deepest point of the basin, consistently with it leftward migration, but without increasing its width.

This particular modeling setup generates a predominantly leftwards flow at shallow levels (**Figure 5**). As a consequence, the surface velocity is negative (left-directed; **Figure 7C**) with values increasing as delamination proceeds and a vigorous counterclockwise flow develops (**Figure 5C**). Maximum absolute values of ~3.5 mm/yr at x = 770 are attained at 5.4 Myr. There is extension to the right of this point and compression to the left, with maximum contraction rates (highest lateral gradient of horizontal velocity) between 680 and 760 km, thus in the area of basin formation.

Sensitivity Study

We have conducted a series of simulations to test the effect of viscosity cutoffs on the evolution of delamination. The variation

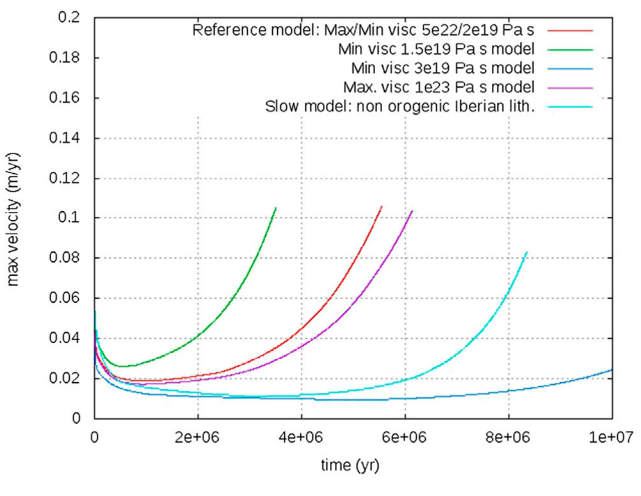

FIGURE 8 | Sensitivity study showing the evolution of maximum velocities of different simulations. Acceleration of maximum velocities indicate the transition from stable to unstable delamination. Only the viscosity cutoffs are varied with respect to the Reference Model (red line), except for the "Slow Model," which considers a 20 km thinner Iberian lithosphere and a minimum viscosity cutoff 10^{19} Pa·s.

of maximum velocity for different simulations is shown in **Figure 8**. This figure is useful to identify the transition from stable to unstable regimes. During the first phase of the Reference Model, intrusion along the lower Iberian crust proceeds steadily, with migration of the delamination hinge of 2–3 cm/yr. The transition to the unstable regime occurs as slab sinking and separation become dominant. This transition is characterized by a rapid increase in the maximum velocity (simulations are stopped when maximum velocities exceed ~10 cm/yr). When the minimum viscosity is reduced from 2×10^{19} Pa·s (Reference Model) to 1.5×10^{19} Pa·s delamination starts accelerating about 2 Myr before than for the Reference Model (green vs. red lines in **Figure 8**). When the minimum viscosity is increased to 3×10^{19} Pa·s, the delamination process does not take place (deep blue line in **Figure 8**). The transition to the unstable regime is only slightly delayed when the maximum viscosity is increased from 5×10^{22} Pa·s (Reference Model) to 10^{23} Pa·s (purple line in **Figure 8**). The stronger dependence on the minimum viscosity cutoff (reached at the lower crust and intruding asthenosphere) is consistent with the higher sensitivity of the slab sinking velocity to variations of lower crust viscosity ($\mu_{LC}{}^{-2/3}$) than to lithospheric mantle viscosity variations ($\mu_{LM}{}^{-1/3}$), found by Bird (1979). Additional simulations (not shown) were conducted by increasing the initial Alboran LAB depth from 45 to 50 km (keeping the same viscosity cutoffs as the Reference Model). Delamination does not occur in this case; the maximum velocity always decreases and cooling of the slowly intruding Alboran mantle hinders delamination and slab sinking. This is because the colder and stiffer Alboran lithospheric mantle resists flow around the upper corner of the Iberian lithospheric mantle and slows down the intrusion into the lower crust.

Baes et al. (2011) argued that the contrast resulting from STEP tearing may not be sharp. To investigate a more general case we have performed additional tests to evaluate the sensitivity to the width of the contrast. STEP faults dipping toward the continental margin, as considered in some simulations of the Baes et al. (2011) study and near the Plini-Strabo trenches (Özbakir et al., 2013), result in a reduction of buoyancy forces compared to the vertical STEP fault geometry, and do not lead to delamination (with the Reference model parameters). Vertical STEP faults maximize lateral density contrasts and are therefore the most favourable geometry for post-tearing delamination.

Slow Delamination Model

The second end member assumes a thinner Iberian lithosphere, with initial LAB depth for the South Iberian margin of 100–112 km, and predicts a slow evolution of delamination (**Figures 9–11**). If the viscosity cutoffs of the Reference Model are maintained, delamination simply does not develop, provided that the buoyancy forces are too weak to overcome viscous resistance. In the simulation shown in **Figures 9 and 10** (and light blue line in **Figure 8**), the minimum viscosity is reduced from 2×10^{19} Pa·s (Reference Model) to 10^{19} Pa·s. This simulation is characterized by the slow development of delamination and therefore a longer evolution time, 8.2 Myr, is allowed to reach a final configuration similar to the final stage of the Reference Model (same depth of ~100 km for the tip of the top of the slab in **Figures 5C and 9B**). **Figure 9A** shows the evolution at 5.4 Myr, the final time of the Reference Mode (**Figure 5C**), to enable a direct comparison of both end member models at the same times of evolution. Asthenosphere intrusion spreads into the Iberian lower crust at velocities <2 cm/yr during the first 6 Myr (**Figure 9A** and light blue line in **Figure 8**). As a consequence of this slower intrusion, the “chilled” viscous boundary of the intruding mantle is more developed than in the reference model (compare **Figures 6 and 10**). As described above, this “freezing” dominates over slab sinking and the delamination process is stable for a longer time. Maximum velocities only increase significantly during the last 2 Myr of evolution. At 8.2 Myr, the maximum crustal thickness is 45 km and its location has migrated 108 km to the left since the beginning of the simulation. In spite of the similar structure reached by both end member simulations albeit at different times, the surface response to delamination (**Figure 11**) is dramatically different, indicating the importance of dynamic topography in the faster Reference Model. No basin is created because the slower sinking of the delaminating lithospheric mantle makes conductive thermal equilibration with the surrounding mantle more effective and therefore the negative buoyancy of the sinking lithosphere is smaller. The maximum topography decreases with time by about 400 m, being always located in an area of relatively thin crust. The topographic subsidence indicates that the isostatic effect of crustal thinning predominates over the dynamic contribution from the slowly intruding warm mantle. Vertical velocities have small values (**Figure 11B**) as reflected by the slow evolution of the topography, except at the end of the simulation, when delamination accelerates. Similarly, the slow development of delamination results in very low (<0.8 mm/yr) horizontal velocities.

DISCUSSION

Here we have shown that, for some specific thermal and rheological conditions, the setup after slab tearing by means of a STEP fault is prone to generate continental delamination. This setup based on negatively buoyant lithosphere and adjacent weak material is present in a number of delamination models (e.g., Göğüs and Pysklywec, 2008; Valera et al., 2008; Valera et al., 2011; Bajolet et al., 2012; Valera et al., 2014; see Göğüs and Ueda, 2018 for a revision). In contrast to those earlier studies where delamination had to be enforced by imposing ad hoc initial conditions, here we explore the conditions under which delamination in the vicinity of STEP faults naturally occurs. In particular, we reproduce, without any external forcing, the formation of a “broad conduit” across the lithospheric mantle as originally described analytically by Bird (1979). We also demonstrate that under some particular thermal and rheological settings delamination evolves from a stable to a very unstable and fast evolving regime.

Inferences About Possible Delamination in the Central Betics

The predicted evolution of the Reference end member model is consistent with a number of observations for the central Betics. The final structure (**Figures 5C and 6C**) resembles the overall

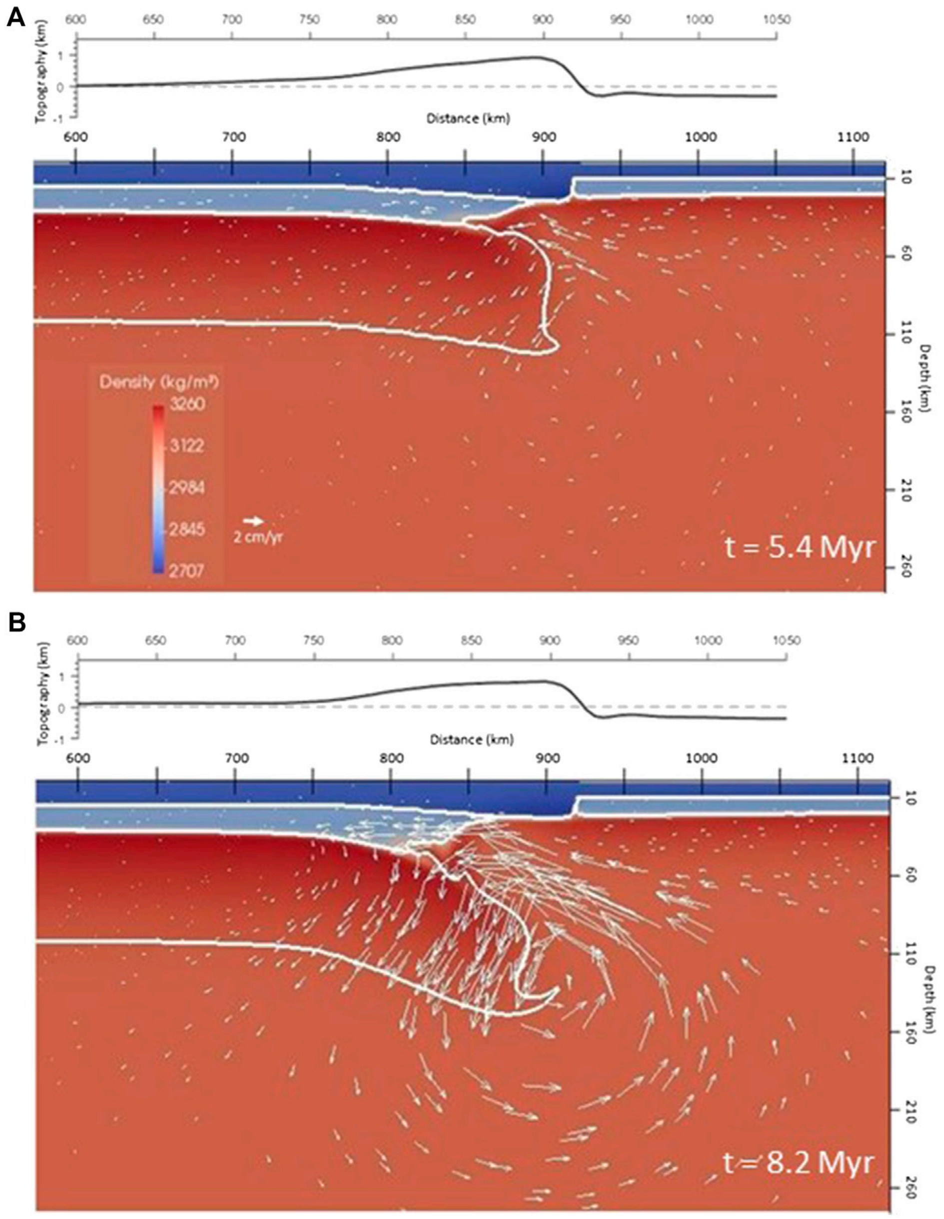

FIGURE 9 | Distribution of density and velocity field and topographic response at different times **(A)** 5.4 Myr (for comparison purposes with the final time of the Reference Model), **(B)** 8.2 Myr of the "Slow Model."

lithospheric structure mapped by RF studies in the area where ongoing delamination has been proposed (**Figure 12**), with a southwards dipping slab-like structure reaching a depth about 100 km about 100 km south of the area of maximum crustal thickness (Mancilla et al., 2013). The lack of isostatic correlation between the thickest crust and highest topography (Mancilla et al., 2013; Mancilla et al., 2015a; Mancilla et al., 2015b) is a dynamic feature properly reproduced by our modeling. Therefore, this model supports the hypothesis that the high topography in the central Betics is partly sustained by asthenospheric inflow during delamination. The evolving pattern of uplift/subsidence predicted by the Reference Model is consistent with the fact that the uplift in the western side of Sierra Nevada was accompanied by subsidence of the Granada Basin (except in its NE border), further to the northwest of Sierra Nevada, during the Late Pleistocene (Azañón et al., 2012; Azañón et al., 2015).

Duggen et al. (2003) and Duggen et al. (2005) proposed that the westward rollback of the oceanic lithosphere also peeled away portions of the lithospheric mantle from beneath the Iberian and African margins, and that this westward delamination of the lithospheric mantle would be consistent with the volcanism (location and composition) and the margins uplift that closed the Miocene gateways between the Atlantic Ocean and the

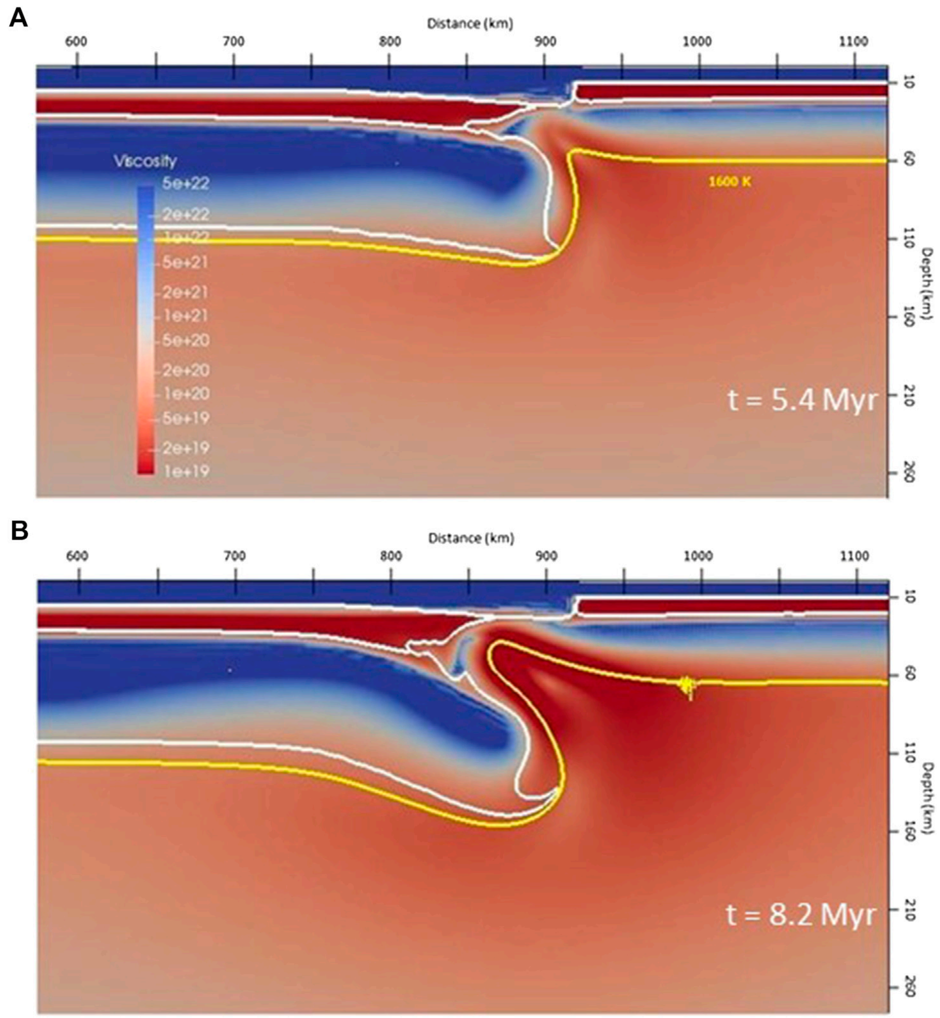

FIGURE 10 | Distribution of viscosity (logarithmic scale plot; Pa s units) and location of the 1,600 K isotherm at different times **(A)** 5.4 Myr (for comparison purposes with the final time of the Reference Model), **(B)** 8.2 Myr of the "Slow Model."

Mediterranean. Similarly, Martinez-Martinez et al. (2006) proposed that the westward migration of extensional loci was related to delamination and westward asthenospheric inflow under the southern Iberian margin. A number of RF studies show prominent steps not only in the LAB, but also in the Moho depth (Mancilla et al., 2013; Mancilla et al., 2015a; Mancilla et al., 2018); this fact contradicts the idea of a westward delamination of the lithospheric mantle beneath the margins, leaving an unperturbed crust. However, the observation of a large Moho step is not incompatible with the overall westward peeling of the lithospheric mantle beneath the Iberian margin accommodated by a westward propagating STEP fault, with this fault representing the vertical boundary of the mantle gap left by delamination (Baes et al., 2011). On the light of the present modeling we can add that this process most likely thinned the overlying crust at the back of the delamination hinge. The westward delamination proposed by Duggen et al. (2005) is compatible with our initial setup as long as the tearing migrated to a more southern location in the central Betics and then continued westwards. It could be then followed by the initiation of northward migrating delamination modeled in this study for the central Betics. Following our modeling, this post-tearing delamination would be favored by a margin lower crust thick enough to act as a mechanical weakness, enabling asthenospheric inflow and decoupling of the crust and lithospheric mantle. We suggest that these conditions were only met in the central Betics provided that the STEP fault, located further to the south compared to the eastern Betics (**Figure 1**), likely tore orogenic Betic lithosphere, with a thick and weak lower crust and a thick lithospheric mantle favoring its sinking into the asthenosphere.

Model Limitations

The geometry after slab tearing by means of a STEP fault is intrinsically three-dimensional and would therefore require a 3D modeling approach (e.g., Munch et al., 2020). Future efforts

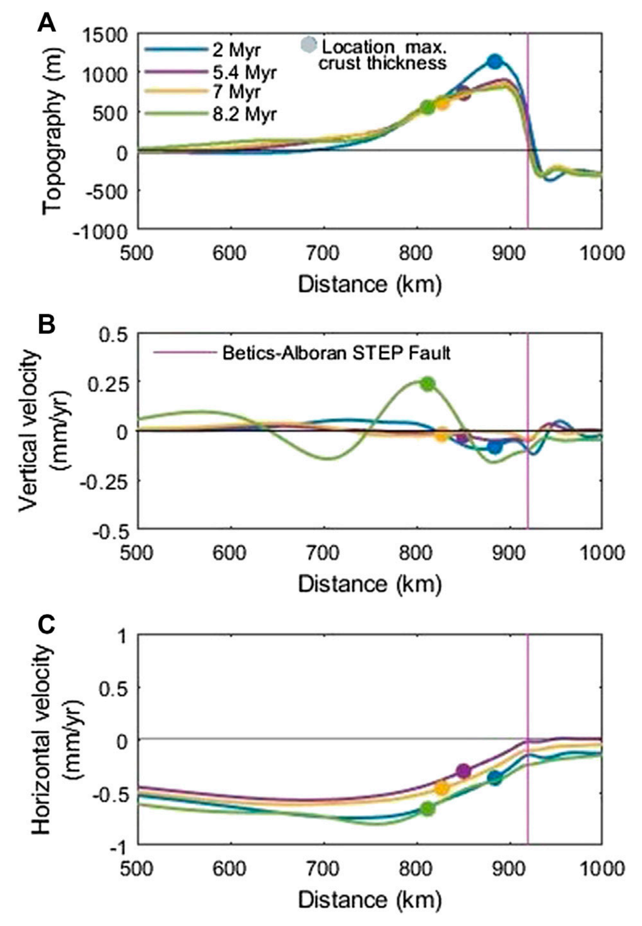

FIGURE 11 | (A) Topography, **(B)** vertical velocity, and **(C)** horizontal velocity of the free surface at different time steps of the Slow Model. The location of the maximum crustal thickness at each time step is also marked (colored dots) to facilitate the interpretation.

in the Betic-Rift system should move forward along this line to avoid limitations as for example the close location of generic modeled cross-section to the active tip of the STEP fault to the west and to the Tear-Delamination fault to the east (**Figure 1**). However, time evolving 3D delamination is a very challenging problem. A high resolution grid is required to account for sharp viscosity contrasts due to compositional variations and to high strain rates during asthenospheric inflow. Furthermore, the free surface boundary condition (required to quantify uplift/subsidence consistently) is computationally demanding as well, requiring small time steps to have a good accuracy. This could be avoided by using instantaneous 3D models (e.g., Negredo et al., 1999) albeit at the price of losing the transient characteristics of delamination, an essential component of this mechanism as illustrated in this work. Hence, inferences from instantaneous approaches, as in the delamination modeling for northern Morocco from Baratin et al. (2016), should be taken with caution.

No plastic weakening occurs during the simulations presented here as slab bending is quite low. However, plasticity should be accounted for in models of slab sinking across the entire upper mantle, where high bending stress associated with rollback of the lithospheric mantle slab can lead to breakoff (e.g., Ueda et al., 2012; Göğüs et al., 2016). This would be the case for past evolution of the Southeast Carpathians (Göğüs et al., 2016) or the Moroccan Atlas, where piecewise delamination of the continental lithosphere has been proposed (Bezada et al., 2014). Finally, it is worth stressing that this study is not intended to perform a detailed modeling of the recent evolution of the central Betics, given the mentioned limitations, but rather to show that first order characteristics like the pattern of uplift/subsidence and lithospheric structure are properly accounted for in this modeling of post-tearing northward delamination in the central Betics.

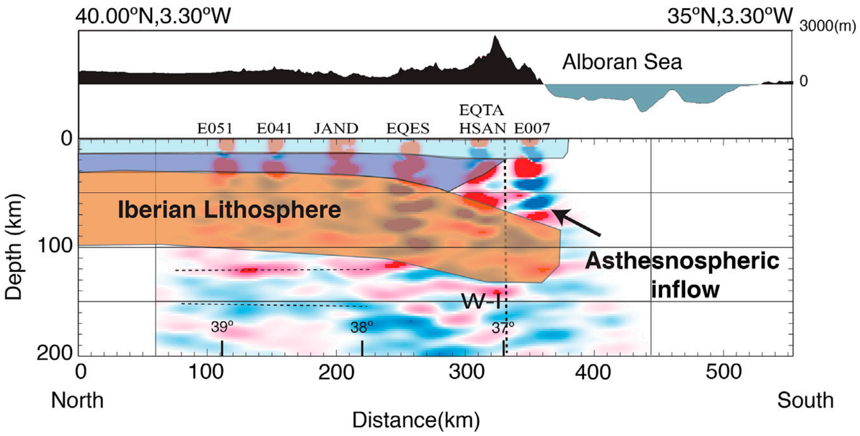

FIGURE 12 | Comparison of the common conversion point migration image of P-receiver function built using only the closest stations to the profile (modified from Figure 9 of Mancilla et al., 2015a) with the simulated structure of the Iberian lithosphere for the Reference Model at 5.4 Myr. At the top, we display the topography along the profile.

CONCLUSIONS

In this study we investigate the first order characteristics of continental edge delamination across STEP faults after slab tearing by means of geodynamic modeling. In doing so, we use as reference the STEP fault observed in the Betic orogeny taking advantage of the unprecedented resolution mapping of its lithospheric structure where edge delamination is proposed. The comparison with real observations is an essential component in a dynamic process very sensitive to relatively small variations in the thermal and rheological initial conditions.

The lateral contrast in lithospheric structure resulting from STEP faults provides necessary conditions for the development of continental delamination, namely: a strong density contrast between the orogenic and the back-arc lithospheres, a relatively thick and weak lower crust in the Iberian margin, and a thinned (warm and weak) back-arc lithosphere allowing for asthenospheric upwelling and inflow along the orogenic lower crust. The topographic response associated with delamination changes dramatically with the velocity of delamination. Fast delaminating models predict a progressive widening of the elevated area, due to the dynamic effect of asthenospheric inflow, and adjacent subsidence due to the downward pull of the sinking lithospheric mantle slab. In contrast, the maximum topography decreases with time and no basin is formed in slow delamination models. This topographic subsidence indicates that the isostatic effect of crustal thinning predominates over the dynamic effect of slowly intruding warm mantle. For other thermal and rheological setting delamination is not even triggered.

Predictions from the fast delamination end member model (Reference model) are consistent with a number of observations for the central Betics area where ongoing delamination has been proposed (e.g., Mancilla et al., 2013; Mancilla et al., 2015a; Heit et al., 2017); these features are the first order characteristics of the lithospheric structure, the offset between highest topography and thickest crust locations, and the observed topographic pattern of uplift in western Sierra Nevada, and subsidence in the Granada Basin. In summary, our results, bearing in mind the limitations imposed by the 2D assumption, are consistent with the hypothesis of present-day north-directed delamination in the central Betics.

DATA AVAILABILITY STATEMENT

The datasets generated for this study are available on request to the corresponding author.

AUTHOR CONTRIBUTIONS

AN and CC perform the numerical modelling; FdLM is responsible of the P-wave receiver function analysis and its interpretation; JM and JF contributed significantly to the interpretation. All authors participated in the discussions and contributed to the manuscript.

FUNDING

The present research has been funded by projects Spanish Ministry of Science projects PGC2018-095154-B-I00 (AN) and PID2019-109608GB-I00 (FM and JM). JF is supported by an Atracción Talento senior fellowship (2018-T1/AMB/11493) funded by Comunidad Autonoma de Madrid (Spain). This work has been done using the facilities of the Laboratory of Geodynamic Modelling from Geo3BCN-CSIC. We thank the Computational Infrastructure for Geodynamics (geodynamics.org) which is funded by the National Science Foundation under award EAR-0949446 and EAR-1550901 for supporting the development of ASPECT.

ACKNOWLEDGMENTS

We acknowledge constructive reviews by the two reviewers. Juliane Dannberg is kindly acknowledged for her support with ASPECT simulations. Figures were created with ParaView, Gnuplot, GMT, and Matlab environments.

REFERENCES

Azañón, J. M., Galve, J. P., Pérez-Peña, J. V., Giaconia, F., Carvajal, R., Booth-Rea, G., et al.(2015). Relief and drainage evolution during the exhumation of the Sierra Nevada (SE Spain): is denudation keeping pace with uplift? *Tectonophysics*, 663, 19–32. doi:10.1016/j.tecto.2015.06.015

Azañón, J. M., Pérez-Peña, J. V., Giaconia, F., Booth-Rea, G., Martínez-Martínez, J. M., and Rodríguez-Peces, M. J. (2012). Active tectonics in the central and eastern Betic Cordillera through morphotectonic analysis: the case of Sierra Nevada and Sierra Alhamilla. *J. Iber. Geol.* 38 (1), 225–238. doi:10.5209/rev_jige.2012.v38.n1.39214

Bürgmann, R., and Dresen, G. (2008). Rheology of the lower crust and upper mantle: evidence from rock mechanics, geodesy, and field observations. *Annu. Rev. Earth Planet Sci.* 36, 531–567. doi:10.1146/annurev.earth.36.031207.124326

Baes, M., Govers, R., and Wortel, R. (2011). Subduction initiation along the inherited weakness zone at the edge of a slab: insights from numerical models. *Geophys. J. Int.* 184 (3), 991–1008. doi:10.1111/j.1365-246X.2010.04896.x

Bajolet, F., Galeano, J., Funiciello, F., Moroni, M., Negredo, A. M., and Faccenna, C. (2012). Continental delamination: insights from laboratory models. *Geochem. Geophys. Geosyst.* 13, Q02009. doi:10.1029/2011GC003896

Bangerth, W., Dannberg, J., Gassmoeller, R., and Heister, T. (2019). ASPECT, April 29. ASPECT v2.0.1. *Zenodo*. doi:10.5281/zenodo.2653531

Baratin, L. M., Mazzotti, S., Chéry, J., Vernant, P., Tahayt, A., and Mourabit, T. (2016). Incipient mantle delamination, active tectonics and crustal thickening in Northern Morocco: insights from gravity data and numerical modeling. *Earth Planet Sci. Lett.* 454, 113–120. doi:10.1016/j.epsl.2016.08.041

Bezada, M. J., Humphreys, E. D., Davila, J. M., Carbonell, R., Harnafi, M., and Palomeras, I. (2014). Piecewise delamination of Moroccan lithosphere from beneath the Atlas mountains. *Geochem. Geophys. Geosyst.* 15, 975–985. doi:10.1002/2013GC005059

Bezada, M. J., Humphreys, E. D., Toomey, D. R., Harnafi, M., Davila, J. M., and Gallart, J. (2013). Evidence for slab rollback in westernmost Mediterranean from improved upper mantle imaging. *Earth Planet Sci. Lett.* 368, 51–60. doi:10.1016/j.epsl.2013.02.024

Billen, M., and Hirth, G. (2007). Rheologic controls on slab dynamics. *Geochem. Geophys. Geosyst.* 8, 1–24. doi:10.1029/2007gc001597

Bird, P. (1978). Initiation of intracontinental subduction in the Himalaya. *J. Geophys. Res. Solid Earth.* 83, 4975–4987. doi:10.1029/JB083iB10p04975

Bird, P. (1979). Continental delamination and the Colorado Plateau. *J. Geophys. Res. Solid Earth.* 84, 7561–7571. doi:10.1029/jb084ib13p07561

Booth-Rea, G., Ranero, C. R., Martínez-Martínez, J. M., and Grevemeyer, I. (2007). Crustal types and Tertiary tectonic evolution of the Alboran sea, western Mediterranean. *Geochem. Geophys. Geosyst.* 8, Q10005. doi:10.1029/2007gc001639

Calvert, A., Sandvol, E., Seber, D., Barazangi, M., Roecker, S., and Mourabit, T. (2000). Geodynamic evolution of the lithosphere and upper mantle beneath the Alboran region of the western Mediterranean: constraints from travel time tomography. *J. Geophys. Res. Solid Earth.* 105, 10871–10898. doi:10.1029/2000JB900024

Carballo, A., Fernàndez, M., Jiménez-Munt, I., Torne, M., Vergés, J., Melchiorre, M. , et al. (2015). From the north-Iberian margin to the Alboran basin: a lithosphere geo-transect across the Iberian plate. *Tectonophysics* 663, 399–418. doi:10.1016/j.tecto.2015.07.009

Chertova, M. V., Spakman, W., Geenen, T., van den Berg, A. P., and van Hinsberger, D. J. J. (2014). Underpinning tectonic reconstructions of the western Mediterranean region with dynamic slab evolution from 3-D numerical modeling. *J. Geophys. Res. Solid Earth.* 119, 5876–5902. doi:10.1002/2014jb011150

Cunha, T. A., Matias, L. M., Terrinha, P., Negredo, A. M., Rosas, F., and Fernandes, R. M. (2012). Neotectonics of the SW Iberia margin, Gulf of Cadiz and Alboran Sea: a reassessment including recent structural, seismic and geodetic data. *Geophys. J. Int.* 188, 850–872. doi:10.1111/j.1365-246X.2011.05328.x

DeMets, C., Gordon, R. G., and Argus, D. F. (2011). Geologically current plate motions. *Geophys. J. Int.* 187, 538. doi:10.1111/j.1365-246X.2011.05186.x

Duggen, S., Hoernle, K., van den Bogaard, P., and Garbe-Schönberg, D. (2005). Post-collisional transition from subduction- to intraplate-type magmatism in the westernmost Mediterranean: evidence for continental-edge delamination of subcontinental lithosphere. *J. Petrol.* 46, 1155–1201. doi:10.1093/petrology/egi013

Duggen, S., Hoernle, K., van den Bogaard, P., and Harris, C. (2004). Magmatic evolution of the Alboran region: the role of subduction in forming the western Mediterranean and causing the Messinian salinity crisis. *Earth Planet Sci. Lett.* 218, 91–108. doi:10.1016/s0012-821x(03)00632-0

Duggen, S., Hoernle, K., van den Bogaard, P., Rüpke, L., and Morgan, J. P. (2003). Deep roots of the Messinian salinity crisis. *Nature* 422, 602–606. doi:10.1038/nature01553

Faccenda, M., Minelli, G., and Gerya, T. V. (2009). Coupled and decoupled regimes of continental collision: numerical modeling. *Earth Planet Sci. Lett.* 278, 337–349. doi:10.1016/j.epsl.2008.12.021

Faccenna, C., Piromallo, C., Crespo-Blanc, A., Jolivet, L., and Rossetti, F. (2004). Lateral slab deformation and the origin of the western Mediterranean arcs. *Tectonics* 23, TC1012. doi:10.1029/2002tc001488

Fadil, A., Vernant, P., McClusky, S., Reilinger, R., Gomez, F., and Ben Sari, D. (2006). Active tectonics of the western Mediterranean: geodetic evidence for rollback of a delaminated subcontinental lithospheric slab beneath the Rif Mountains, Morocco. *Geology* 34 (7), 529–532. doi:10.1130/G22291.1

Fullea, J., Fernández, M., Alfonso, J. C., Vergés, J., and Zeyen, H. (2010). The structure and evolution of the lithosphere-asthenosphere boundary beneath the Atlantic-Mediterranean transition region. *Lithos* 120, 74–95. doi:10.1016/j.lithos.2010.03.003

Fullea, J., Fernández, M., Vergés, J., and Zeyen, H. (2007). A rapid method to map the crustal and lithospheric thickness using elevation, geoid anomaly and thermal analysis. Application to the Gibraltar Arc System, Atlas Mountains and adjacent zones. *Tectonophysics* 430, 97–117. doi:10.1016/j.tecto.2006.11.003

Göğüs, O. H., and Pysklywec, R. N. (2008). Near-surface diagnostics of dripping or delaminating lithosphere. *J. Geophys. Res.* 113, 1–11. doi:10.1029/2007jb005123

Göğüş, O. H., Pysklywec, R. N., Corbi, F., and Faccenna, C. (2011). The surface tectonics of mantle lithosphere delamination following ocean lithosphere subduction: insights from physical-scaled analogue experiments. *Geochem. Geophys. Geosyst.* 12, Q05004. doi:10.1029/2010GC003430

Göğüs, O. H., Pysklywec, R. N., and Faccenna, C. (2016). Postcollisional lithospheric evolution of the Southeast Carpathians: comparison of geodynamical models and observations. *Tectonics* 35, 1205–1224. doi:10.1002/2015tc004096

Göğüş, O. H., and Ueda, K. (2018). Peeling back the lithosphere: controlling parameters, surface expressions and the future directions in delamination modeling. *J. Geodyn.* 117, 21–40. doi:10.1016/j.jog.2018.03.003

García-Castellanos, D., and Villaseñor, A. (2011). Messinian salinity crisis regulated by competing tectonics and erosion at the Gibraltar Arc. *Nature* 480, 359–363. doi:10.1038/nature10651

Govers, R., and Wortel, M. J. R. (2005). Lithosphere tearing at {STEP} faults: response to edges of subduction zones. *Earth Planet Sci. Lett.* 236, 505–523. doi:10.1016/j.epsl.2005.03.022

Gutscher, M. A., Dominguez, S., Westbrook, G. K., Le Roy, P., Rosas, F., and Duarte, J. C. (2012). The Gibraltar subduction: a decade of new geophysical data. *Tectonophysics* 574, 72–91. doi:10.1016/j.tecto.2012.08.038

Gutscher, M. A., Malod, J., Rehault, J.-P., Contrucci, I., Klingelhoefer, F., Mendes-Victor, L., et al.(2002). Evidence for active subduction beneath Gibraltar. *Geology* 30, 1071–1074. doi:10.1130/0091-7613

Heit, B., Mancilla, F., Yuan, X., Morales, J., Stich, D., and Martín, R. (2017). Tearing of the mantle lithosphere along the intermediate-depth seismicity zone beneath the Gibraltar Arc: the onset of lithospheric delamination. *Geophys. Res. Lett.* 44, 4027–4035. doi:10.1002/2017GL073358

Hidas, K., Garrido, C. J., Booth-Rea, G., Marchesi, C., Bodinier, J.-L., Dautria, J.-M., et al.(2019). Lithosphere tearing along STEP faults and synkinematic formation of lherzolite and wehrlite in the shallow subcontinental mantle. *Solid Earth.* 10, 1099–1021. doi:10.5194/se-10-1099-2019

Hirth, G., and Kohlstedt, D. (2003). Rheology of the upper mantle and the mantle wedge: a view from the experimentalists. *Geophys. Monogr. Ser.* 138, 83–105. doi:10.1029/138gm06

Iribarren, L., Verges, J., Camurri, F., Fullea, J., and Fernàndez, M. (2007). The structure of the Atlantic–Mediterranean transition zone from the Alboran Sea to the Horseshoe Abyssal Plain (Iberia–Africa plate boundary). *Mar. Geol.* 243, 97–119. doi:10.1016/j.margeo.2007.05.011

Iribarren, L., Vergés, J., and Fernàndez, M. (2009). Sediment supply from the Betic–Rif orogen to basins through Neogene. *Tectonophysics* 475, 68–84. doi:10.1016/j.tecto.2008.11.029

Jiménez-Munt, I., and Negredo, A. M. (2003). Neotectonic modelling of the western part of the Africa/Eurasia plate boundary: from the Mid-Atlantic ridge to Algeria. *Earth Planet Sci. Lett.* 205, 257–271. doi:10.1016/s0012-821x(02)01045-2

Jiménez-Munt, I., Torne, M., Fernàndez, M., Vergés, J., Kumar, A., and Carballo, A. (2019). Deep seated density anomalies across the Iberia-Africa plate boundary and its topographic response. *J. Geophys. Res. Solid Earth.* 124, 13310–13332. doi:10.1029/2019JB018445

Kaus, B. J. P., Mühlhaus, H., and May, D. A (2010). A stabilization algorithm for geodynamic numerical simulations with a free surface. *Phys. Earth Planet. Inter.* 181, 12–20. doi:10.1016/j.pepi.2010.04.007

Kronbichler, M., Heister, T., and Bangerth, W. (2012). High accuracy mantle convection simulation through modern numerical methods. *Geophys. J. Int.* 191, 12–29. doi:10.1111/j.1365-246x.2012.05609.x

Levander, A., Bezada, M., Niu, F., Humphreys, E. D., Palomeras, I., and Thurner, S. M. (2014). Subduction-driven recycling of continental margin lithosphere. *Nature* 515, 253–256. doi:10.1038/nature13878

Lonergan, L., and White, N. (1997). Origin of the Betic-Rif mountain belt. *Tectonics* 16, 504–522. doi:10.1029/96tc03937

Mancilla, F. d. L., Booth-Rea, G., Stich, D., Pérez-Peña, J. V., Morales, J., Azañón, J. M., et al.(2015b). Slab rupture and delamination under the Betics and Rif constrained from receiver functions. *Tectonophysics* 663, 225–237. doi:10.1016/j.tecto.2015.06.028

Mancilla, F. d. L., and Diaz, J. (2015). High resolution Moho topography map beneath Iberia and Northern Morocco from receiver function analysis. *Tectonophysic* 663, 203–211. doi:10.1016/j.tecto.2015.06.017

Mancilla, F. d. L., Heit, B., Morales, J., Yuan, X., Stich, D., Molina-Aguilera, A., et al.(2018). A STEP fault in Central Betics, associated with lateral lithospheric tearing at the northern edge of the Gibraltar Arc subduction system. *Earth Planet Sci. Lett.* 486, 32–40. doi:10.1016/j.epsl.2018.01.008

Mancilla, F. d. L., Stich, D., Berrocoso, M., Martín, R., Morales, J., Fernandez-Ros, A., et al.(2013). Delamination in the Betic range: deep structure, seismicity and GPS motion. *Geology* 41, 307–310. doi:10.1130/g33733.1

Mancilla, F. d. L., Stich, D., Morales, J., Martín, R., Diaz, J., Pazos, A., et al.(2015a). Crustal thickness and images of the lithospheric discontinuities in the Gibraltar Arc and surrounding areas. *Geophys. J. Int.* 203, 1804–1820. doi:10.1093/gji/ggv390

Martínez-Martínez, J. M., Booth-Rea, G., Azañón, J. M., and Torcal, F. (2006). Active transfer fault zone linking a segmented extensional system (Betics, southern Spain): insight into heterogeneous extension driven by edge delamination. *Tectonophysics* 422, 159–173. doi:10.1016/j.tecto.2006.06.001

Molina-Aguilera, A., Mancilla, F. d. L., Morales, J., Stich, D., Yuan, X., and Heit, B. (2019). Connection between the Jurassic oceanic lithosphere of the Gulf of Cádiz and the Alboran slab imaged by Sp receiver functions. *Geology* 47, 227–230. doi:10.1130/g45654.1

Munch, J., Gerya, T., and Ueda, K. (2020). Oceanic crust recycling controlled by weakening at slab edges. *Nat. Commun.* 11, 2009. doi:10.1038/s41467-020-15750-7

Negredo, A. M., Bird, P., Sanz de Galdeano, C., and Buforn, E. (2002). Neotectonic modeling of the Ibero-Maghrebian región. *J. Geophys. Res. Solid Earth.* 107, B11. doi:10.1029/2001jb000743

Negredo, A. M., Sabadini, R., Bianco, G., and Fernández, M. (1999). Three-dimensional modelling of crustal motions caused by subduction and continental convergence in the central Mediterranean. *Geophys. J. Int.* 136, 261–274. doi:10.1046/j.1365-246x.1999.00726.x

Özbakır, A. D., Govers, R., and Fichtner, A. (2020). The Kefalonia transform fault: a step fault in the making. *Tectonophysics* 787, 228471. doi:10.1016/j.tecto.2020.22847

Özbakır, A. D., Şengör, A. M. C., Wortel, M. J. R., and Govers, R. (2013). The Pliny–Strabo trench region: a large shear zone resulting from slab tearing. *Earth Planet Sci. Lett.* 375, 188–195. doi:10.1016/j.epsl.2013.05.025

Palomeras, I., Thurner, S., Levander, A., Liu, K., Villasenor, A., and Carbonell, R. (2014). Finite-frequency Rayleigh wave tomography of the western Mediterranean: mapping its lithospheric structure. *Geochem. Geophys. Geosyst.* 15, 140–160. doi:10.1002/2013gc004861

Platt, J. P., Allerton, S., Kirker, A., Mandeville, C., Mayfield, A., and Platzman, E. S. (2003). The ultimate arc: differential displacement, oroclinal bending, and vertical axis rotation in the external Betic-Rif arc. *Tectonics* 22, 1017. doi:10.1029/2001tc001321

Rodríguez-González, J., Billen, M. I., and Negredo, A. M. (2014). Steady-state subduction and trench-parallel flow induced by overriding plate structure. *Earth Planet Sci. Lett.* 401, 227–235. doi:10.1016/j.epsl.2014.06.013

Rodríguez-González, J., Negredo, A. M., and Billen, M. I. (2012). The role of the overriding plate thermal state on slab dip variability and on the occurrence of flat subduction. *Geophys. Geochem. Geosyst.* 13, Q01002. doi:10.1029:/2011GC003859

Rose, I., Buffet, B., and Heister, T. (2017). Stability and accuracy of free surface time integrations in viscous flows. *Phys. Earth Planet. Int.* 262, 90–100. doi:10.1016/j.pepi.2016.11.007

Santos-Bueno, N., Fernández-García, C., Stich, D., Mancilla, F. d. L., Martín, R., and Molina-Aguilera, A. (2019). Focal mechanisms for subcrustal earthquakes beneath the Gibraltar Arc. *Geophys. Res. Lett.* 46, 2534–2543. doi:10.1029/2018GL081587

Seber, D., Barazangi, M., Ibenbrahin, A., and Demnati, A. (1996). Geophysical evidence for lithospheric delamination beneath the Alboran Sea and the Rif-Betic mountains. *Nature* 379, 785–790. doi:10.1038/379785a0

Spakman, W., Chertova, M. V., van den Berg, A., and van Hinsbergen, D. J. J. (2018). Puzzling features of western Mediterranean tectonics explained by slab dragging. *Nat. Geosci.* 11, 211–216. doi:10.1038/s41561-018-0066-z

Spakman, W., and Wortel, R. (2004). “A tomographic view on western Mediterranean geodynamics. The TRANSMED atlas,” in *The Mediterranean region from crust to mantle*, Berlin Heidelberg: Springer, 31–52. doi:10.1007/978-3-642-18919-72

Stich, D., Serpelloni, E., Mancilla, F., and Morales, J. (2006). Kinematics of the Iberia-Maghreb plate contact from seismic moment tensors and GPS observations. *Tectonophysics* 426, 295–317. doi:10.1016/j.tecto.2006.08.004

Thieulot, C. (2011). FANTOM: two- and three-dimensional numerical modelling of creeping flows for the solution of geological problems. *Phys. Earth Planet. Inter.* 188, 47–68. doi:10.1016/j.pepi.2011.06.011

Torne, M., Fernàndez, M., Vergés, J., Ayala, C., Salas, M.-C., Jimenez-Munt, I., et al. (2015). Crustal and mantle lithosphere structure from potential field and thermal analysis. *Tectonophysics*, 663, 419–433. doi:10.1016/j.tecto.2015.06.003

Ueda, K., Gerya, T. V., and Burg, J.-P. (2012). Delamination in collisional orogens: thermomechanical modelling. *J. Geophys. Res.* 117, B08202, doi:10.1029/2012JB009144

Valera, J. L., Negredo, A. M., Billen, M. I., and Jiménez-Munt, I. (2014). Lateral migration of a foundering high-density root: insights from numerical modeling applied to the southern Sierra Nevada. *Lithos* 198, 77–88. doi:10.1016/j.lithos.2013.08.021

Valera, J. L., Negredo, A. M., and Jiménez-Munt, I. (2011). Deep and near-surface consequences of root removal by asymmetric continental delamination. *Tectonophysics* 502, 257–265. doi:10.1016/j.tecto.2010.04.002

Valera, J. L., Negredo, A. M., and Villaseñor, A. (2008). Asymmetric delamination and convective removal numerical modeling: comparison with evolutionary models for the Alboran Sea region. *Pure Appl. Geophys.* 165, 1683–1706. doi:10.1007/s00024-008-0395-8

van Hinsbergen, D. J. J., Vissers, R. L. M., and Spakman, W. (2014). Origin and consequences of western Mediterranean subduction, rollback and slab segmentation. *Tectonics* 33, 393–419. doi:10.1002/2013tc003349

Vergés, J., and Fernández, M. (2012). Tethys-Atlantic interaction along the Iberia-Africa plate boundary: the Betic-Rif orogenic system. *Tectonophysics* 579, 144–172. doi:10.1016/j.tecto.2012.08.032

Villaseñor, A., Chevrot, S., Harnafi, M., Gallart, G., Pazos, A., and Serrano, I. (2015). Subduction and volcanism in the Iberia-North Africa collision zone from tomographic images of the upper mantle. *Tectonophysics* 663, 238–249. doi:10.1016/j.tecto.2015.08.042

Zitellini, N., Gracia, E., Matias, L., Terrinha, P., Abreu, M. A., and DeAlteriis, G. (2009). The quest for NW Africa–SW Eurasia plate boundary west of Gibraltar. *Earth Planet Sci. Lett.* 280, 13–50 doi:10.1016/j.epsl.2008.12.005

Conflict of Interest: The authors declare that the research was conducted in the absence of any commercial or financial relationships that could be construed as a potential conflict of interest.

frontiers
in Earth Science

REVIEW
published: 30 October 2020
doi: 10.3389/feart.2020.535879

Old/New Subduction Zone Paradigms as Seen From the Cascades

*William P. Leeman**

Department of Earth and Environmental Sciences, Rice University, Houston, TX, United States

This paper briefly reviews the magmatic manifestations of volcanic arcs and aspects of how such magmas form. Common concepts about "how subduction zones work" are reassessed—with particular emphasis on the atypical Cascades volcanic arc. This arc is associated with one of the warmest modern subduction zones, with accelerated slab dehydration and low flux of slab-derived fluids compared to most others. With minimized leverage of fluids, other aspects of arc magmatism become more evident. We see multiple distinct basaltic magma types, all represented by relatively primitive high-MgO end members that allow assessment of their conditions of formation. Dominant types include two distinct intraplate varieties: low-K tholeiite with similarities to mid-ocean ridge basalts and another variety with affinities to many ocean island basalts. In addition, there is a spectrum of more typical calcalkalic basalts that range to fairly alkali-rich compositions (absarokites) as well as high-Mg basaltic andesites. These magma types are variably present throughout much of the arc and all are present coevally in a transect paralleling the Columbia River. Their complex spatial distributions may in part reflect along-strike differences in tectonic controls and/or dynamics of mantle convective flow. The Cascades arc is relatively broad, with significant basaltic volcanism locally in frontal and back arc regions. Prominence of basaltic magmatism has emerged since the late Miocene, and may be related to changes in the regional tectonic regime over time. These mafic magmas provide energy to drive melting in the crust, and perhaps in the lithospheric mantle, that feeds the more prominent stratovolcanoes distributed along the arc axis. Thermobarometry of the most primitive basalts implies unusual relations between depth and composition, as well as conflicting views regarding melt generation. Some traditional interpretations concerning 1) the conditions of magma formation, 2) the role of subducting oceanic plates (±sediments) in forming volcanic arc magmas, and 3) the nature of magmatic source domains in general appear to be inconsistent with current observations to some degree. These topics are reviewed and their implications assessed regarding physical and tectonic aspects of subduction zones.

Keywords: subduction, magmatism, basalt, volcanic arc, thermobarometry, Cascades, lithosphere

Edited by:
Matthias Konrad-Schmolke,
University of Gothenburg, Sweden

Reviewed by:
Robert J. Stern,
The University of Texas at Dallas,
United States
Paul Wallace,
University of Oregon, United States

***Correspondence:**
William P. Leeman
leeman@rice.edu

Specialty section:
This article was submitted to
Petrology,
a section of the journal
Frontiers in Earth Science

Received: *17 February 2020*
Accepted: *02 September 2020*
Published: *30 October 2020*

Citation:
Leeman WP (2020) Old/New
Subduction Zone Paradigms as Seen
From the Cascades.
Front. Earth Sci. 8:535879.
doi: 10.3389/feart.2020.535879

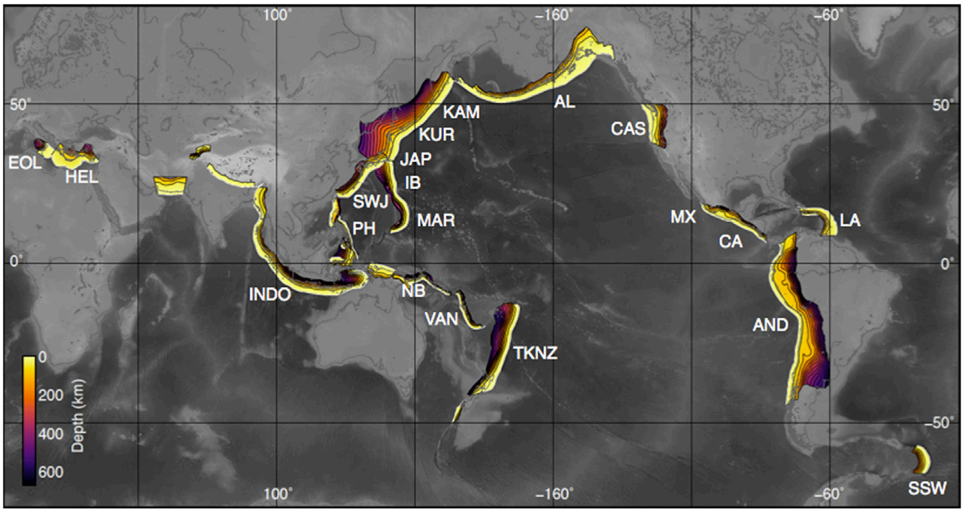

FIGURE 1 | Slab2 image showing global distribution of active subduction zones (Hayes et al., 2018). Contours indicate depth to slab surface and illustrate variations in slab geometry as defined by distributions of SZ seismicity. Major subduction zones are labeled as follows: Cascades (CAS), Aleutian (AL), Kamchatka (KAM), Kurile (KUR), Japan (JAP), Mariana (MAR), Izu-Bonin (IB), SW Japan (SWJ), Philippine (PH), New Britain (NB), Vanuatu (VAN), Tonga-Kermadec-New Zealand (TKNZ), Andes (AND), Central America (CA), Mexico (MX), Lesser Antilles (LA), South Sandwich (SSW), Indonesia (INDO), Hellenic (HEL), and Eolian (AOL) arcs. Continent-continent collision zones near India are not labeled.

INTRODUCTION

It is well established that there is a causative relationship between ongoing subduction processes and volcanic arc magmatism (cf. Gill, 1981; Stern, 2002; Tatsumi, 2005). A common paradigm has emerged in which addition of subducted materials (including ocean crust, sediments, and oceanic mantle) in various ways contributes to the formation of arc magmas and significantly influences their compositions. In detail, magmatic outcomes may be determined by compositional variations in subducted materials from place to place or over time, and by varied physical aspects of the subduction process itself. For example, ages of the subducting plate(s), rates of subduction, and other tectonic factors vary widely, resulting in quite different thermal conditions from one subduction zone (SZ) to another (cf. Syracuse et al., 2010; van Keken et al., 2011; Maunder et al., 2019). Likewise, the upper plate can be influential in many ways. The character of its crust and lithospheric mantle also vary considerably from place to place depending on their prior history, leading to dramatic differences between continental and oceanic settings.

The nature of arc magmatism exhibits wide latitude in variability both between and within individual volcanic arcs (cf. **Figure 1**, showing the global distribution of active subduction). This diversity complicates our understanding of the interrelationships between influential factors and specific details of arc magmatism. Much effort has been expended to understand individual arcs, and global coverage has expanded greatly in recent years, revealing many complexities and enigmas. This paper revisits some basic tenets regarding manifestations and causes of arc magmatism, with dominant focus on formation of primitive arc magmas and their implications regarding subduction processes overall. In assessing familiar paradigms, the Cascades volcanic arc is discussed in some detail because it offers unusual perspectives.

STATE OF THE ARC

Subduction-Related Magmatism: Chemical and Petrologic Properties

To begin, I briefly outline some common generalizations regarding arc magmatism:

(1) Global studies of arc volcanoes suggest that arc magmas are commonly of "calcalkalic" (or "CA") affinity (cf. Miyashiro, 1974; Le Maitre, 2002) and generally differ in important respects from typical magmas formed at mid-ocean ridge or oceanic island settings (so-called intraplate magmas). This dominant view (cf. Gill, 1981; Pearce, 1982) has often been invoked in assigning a tectonic setting to ancient igneous suites. But from today's perspective of more detailed and systematic analytic investigations, considerable diversity between individual arc volcanoes is apparent and there can be multiple, essentially contemporaneous, magmatic series present at both the intra-volcano and intra-arc scales. This is strongly evident in the Cascades (cf. Leeman et al., 1990; Bacon et al., 1997; Conrey et al., 1997; Leeman et al., 2005) and Trans-Mexican arcs (cf. Righter, 2000) and elsewhere to varying degree. A major challenge is to understand the causes and significance of such diversity.

(2) CA type lavas tend to have distinctive geochemical characteristics. Notably, many exhibit variable enrichments in large-ion lithophile elements (LILE; e.g., Ba, Sr, K, Rb, and Cs) and fluid-mobile elements (FME; e.g., B, Pb, As, and Sb)

whereas they are commonly depleted in high field-strength elements (HFSE; e.g., Nb, Ta, Zr, and Hf) relative to typical intraplate oceanic island basalts (OIB) and mid-ocean ridge basalts (MORB) (Sun and McDonough, 1989; Pearce and Peate, 1995; Leeman, 1996; Noll et al., 1996). These features are usually attributed to selective enrichment of arc magma sources by slab-derived LILE-enriched aqueous fluids or melts (cf. Pearce, 1982; McCulloch and Gamble, 1991; Plank, 2014). A link between FME enrichments and subducted slabs is convincingly demonstrated by strong correlations between B/Nb and similar ratios with enrichment of short-lived ^{10}Be in arc lavas (Morris et al., 1990). Slab-derived transfer agents (aqueous fluids, melts, or supercritical fluids) commonly are thought to be liberated during progressive heating and dehydration of hydrous minerals within subducting plates or incorporated in melts of slab components such as sediments or altered oceanic crust (cf. Walowski et al., 2016; Cerpa et al., 2018; Zheng, 2019). Our understanding of mass transfer processes in SZs is in a state of flux—so to speak.

(3) Tectonic and geophysical studies also demonstrate wide variance in factors that likely influence magmatism. For example, differences in age and geologic nature of upper and lower (i.e., subducting) plates, in convergence rates, etc., are predicted to produce significant differences in thermal conditions within subducting slabs. Such differences are assumed to affect the dehydration, metamorphic, and perhaps melting behavior of subducted materials, hence the character and compositions of any fluids or melts extracted therefrom (cf. Spandler and Pirard, 2013; Bebout and Penniston-Dorland, 2015). The full impact of these processes are unclear.

(4) It is commonly believed that andesitic lavas are dominantly erupted in many if not most volcanic arcs, and that they are essential building blocks for continental crust—that itself is estimated to be generally "andesitic" in composition (cf. Rudnick and Gao, 2003). The origins of andesitic magmas are widely debated as discussed below. Most fundamental is the question of what types of magmas are produced in subduction environments (and where), and how and to what extent are they modified during ascent. It is also unclear what proportion of available magma is erupted vs. intruded into the mantle or crust. Thus, another basic question: how representative of deep processes are the erupted volcanic products in any given place?

To address such questions, it is essential to understand in greater detail what factors control magmatic diversity in subduction settings. This need has promoted diverse investigations including: 1) systematic petrologic and geochemical studies of arc volcanic products at scales ranging from whole rocks to minerals to melt inclusions (MIs), 2) experimental studies of melting and crystallization of relevant materials, 3) development of suitable geochemical tracers to quantify involvement of particular materials proposed to contribute to forming or modifying arc magmas, 4) acquisition of geophysical data to image the physical properties of SZs and the nature of the crust and mantle beneath volcanic arcs, and 5) theoretical studies and models to simulate physical and chemical conditions in such settings. Many attempts have been made to define the dynamics of SZs, and to develop a global perspective of how they work.

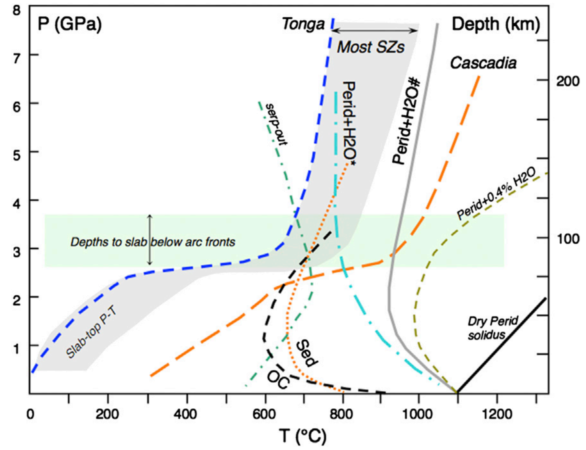

FIGURE 2 | Depth profiles of slab-surface temperature are shown for global subduction zones (gray shaded field for most) based on numerical models of Syracuse et al. (2010), assuming full coupling between slab and mantle to a depth of 80 km. Extrema are shown for the coolest (Tonga) and hottest (Cascadia) SZs. The upper stability limit of serpentine is shown by the "serp-out" curve (Ulmer and Trommsdorff, 1995), and wet-melting solidus curves are shown for oceanic crust ("OC"; Vielzeuf and Schmidt, 2001) and marine sediments ("Sed"; Poli and Schmidt, 2001; Hermann and Spandler, 2007). For wet-melting of mantle peridotite, two solidus curves are shown owing to unresolved controversy between Grove et al. (2012; lower T solidus*) and Green et al. (2014, higher T solidus#); both are substantially cooler than the dry peridotite solidus (~1,450°C at 100 km depth; Hirschmann, 2000). At sub-arc depths, the hot Cascadia slab is expected to have undergone significant dehydration. If water is present (e.g., from the slab interior), the ocean crust and sediment portions of the slab are likely to partially melt, as might deep parts of the overlying mantle wedge. At similar depths (ca. 100 km) beneath most other SZs, the slabs are likely to retain a significant part of their water inventory and in many cases be too cool to undergo partial melting. Whether or not the lowermost mantle wedge can produce hydrous melts depends on which wet-solidus curve is applicable, and on the manner in which slab-derived fluids or melts are transferred into the mantle wedge (cf. Cerpa et al., 2018).

GENERAL DISCUSSION OF ARC MAGMATISM

The Importance of Thermal Structure

A critical concensus is that thermal structures of SZ systems vary considerably worldwide and even along-strike in local areas (Syracuse et al., 2010). We can view them as a spectrum (**Figure 2**) ranging from cold to hot in terms of the predicted maximum slab-surface temperature at depths below the volcanic front (defined as the alignment of the most proximal volcanoes to the modern trench). This convenient reference temperature does not fully correspond to actual temperature distributions throughout the upper and subducting plates as these may be influenced by other factors. But it carries implications regarding the dehydration history of the subducting plate and, indirectly, the potential availability and nature of slab-derived fluids and likelihood of partial melting of the subducted slab. Such models can be tested against known metamorphic conditions in exhumed subduction complexes to evaluate how well they reproduce thermal conditions within subducting plates. Because predicted temperatures do not always closely reproduce estimates based on mineral assemblages or mineral thermometry (cf. Penniston-Dorland et al., 2015), it is clear that the physical and conceptual models can be improved. Similarly, temperature and pressure estimates based on volcanic rocks (cf. Lee et al., 2009; Perrin et al., 2016) can theoretically be used to constrain temperature distributions below volcanic arcs. At this point, there remain issues to resolve to improve such estimates (cf. Herzberg and Asimow, 2015; Matzen et al., 2017; Till, 2017). Most importantly, are the estimated conditions of melt equilibration with the mantle representative of the conditions at which melting occur, or simply points along much longer ascent paths? Also, how does the nature of the source (e.g., proportions of lherzolite vs. pyroxenite, overall fertility, etc.) affect actual melting, as well as the accuracy of estimates for melt equilibration conditions? Theoretical models provide some sense of the relative differences in the thermal structures between subduction systems, and these have been compared with compositional features of arc lavas (e.g., water content) to evaluate how they may be linked to temperature (cf. van Keken et al., 2011; Cooper et al., 2012; Ruscitto et al., 2012). They can also be compared with geophysical observations (e.g., Wannamaker et al., 2014; McGary et al., 2014) that are sensitive to thermal signatures for independent assessment of their validity.

One important insight is that a greater diversity of magma types is seen in hot arcs compared to cold arcs (cf. Leeman et al., 2005; Kimura et al., 2014). Also, a larger proportion of primitive basaltic lavas erupt in hot arcs compared to cold arcs (Schmidt and Jagoutz, 2017). Is this a consequence of lesser input of slab-derived fluids beneath hot arcs (cf. Ruscitto et al., 2012)? And does a stronger slab-fluid input beneath cooler arcs somehow dominate the production of particular magma types, or more strongly overprint the magma sources, and thereby skew the compositional distribution of erupted magmas? Conversely, does slab-melting play a more significant role where subducted slabs are anomalously hot (cf. Yogodzinski et al., 2015; Walowski et al., 2016)? Such factors potentially bias the estimated composition of magmas from one arc to another. For example, is the perceived dominance of hydrous magmas in arcs a consequence of the fact that most arcs are on the cooler side of the thermal spectrum? At the least, there must be varied magmatic responses to this range of thermal conditions.

How Well Do Magmas Represent Their Source?

Another possible bias relates to the fact that, in many arcs, primitive magmas with >7–8 wt% MgO are rare to absent whereas they are relatively common in some arcs, like the Cascades (cf. Schmidt and Jagoutz, 2017; Pitcher and Kent, 2019). This is an important issue, in that the nature of the upper plate (e.g., continental vs. oceanic) can influence the ascent of a given magma, and may determine whether or not it can actually reach the surface and erupt, or the degree to which it evolves from its initial composition. This hinders our ability to accurately assess the nature of the magma sources because lower-MgO magmas almost certainly have undergone significant degrees of magmatic differentiation and/or interaction with wall rocks (and possibly older stored magmas) during their ascent. Where magmas considered to be primitive do erupt, their calculated eruptive temperatures are generally high (Leeman et al., 2005; Schmidt and Jagoutz, 2017). Projected to realistic mantle equilibrium depths, they commonly approach or even exceed the dry solidus for typical mantle lithologies (see below). This observation implies that some primitive arc basaltic magmas form under lower H_2O water conditions, as opposed to the prevalent view that many/most are products of flux-melting and are water-rich (Cooper et al., 2012; Grove et al., 2012). The interplay of temperature and H_2O fundamentally controls mantle melting (cf. Portnyagin et al., 2007).

If this view is correct, it implies that the role of slab-derived fluids must be carefully assessed in terms of their effect on arc magma production. For example, if slab-derived fluids or melts are invoked to account for enrichment of LILE components in an arc magma source, this could occur over long time periods rather than in a single stage associated with the active generation of a given melt. In such cases, source modification could be a multi-stage process and not require large spikes of fluid to catalyze melt production. Importantly, the occurrence of intra-plate type magmas in arcs demonstrates that either 1) the mantle source domains cannot be pervasively modified by SC infiltration or 2) that multiple distinct source domains must be tapped—in which case, how are they distributed and how do the respective melts remain distinctive during extraction and migration? Finally, if source modification does occur over protracted time intervals, it is also possible that the fluids or melts involved could vary in composition over time.

A prime example of this point is the occurrence of so-called absarokite-shoshonite-banakite series lavas that are extremely enriched in K_2O and LILE. Such lavas are found in some modern arcs (e.g., Fiji-Vanuatu, Marianas, Cascades, Mexico), and also in extensional settings (e.g., Turkey, American Rocky Mountains). In Vanuatu and Fiji, these unusual lavas erupted during the rift stage of the Vitiaz arc, several Ma after the active peak of subduction (Peate et al., 1997; Leslie et al., 2009). In Anatolia, examples of such magmas occur in currently extensional settings, but that had experienced subduction in the past, and thus appear to involve mantle domains that could have been modified or "refertilized" long before (cf. Coban et al., 2019). Finally, such lavas associated with intra-arc rifting in the northern Mariana arc are interpreted to be melts of previously enriched upper mantle domains that experienced decompression melting at the onset of extension within the arc (Ishizuka et al., 2010). These examples are consistent with the idea that parts of the lithospheric (?) mantle can retain a cumulative record of prior subduction-related magmatism, and that rejuvenated melting of such domains can produce magmas having geochemical similarities to those in active subduction settings.

Influences From the Sub-Arc Crust and Mantle

Here, I briefly address the nature of the crust and mantle at depth. For mantle-derived magmas this could pertain to lithospheric mantle (i.e., in the case of SZs, a preserved remnant of the upper plate that has not been actively involved in mantle convection), or to deeper asthenospheric mantle that may be undergoing convective flow in association with subduction tectonics. Such mantle domains presumably impart a compositional signature on primitive arc magmas that reflects the time-integrated history of said domains.

The crustal section is likewise important in two significant ways. First, it comprises a potentially complex geologic section with which ascending or stored magmas can interact. Such interactions include assimilation, chemical reaction, and partial melting, each of which can modify the original composition of ascending magmas and thereby obscure their primary nature (e.g., type of mantle source). Second, the nature of the crustal section can influence magma ascent dynamics. Assuming that magma rise is driven primarily by its buoyancy relative to surrounding or overlying crustal rocks, efficiency of ascent is inversely related to overburden density. Ascent and eruption of basaltic magmas is inherently more efficient in oceanic settings where the crust on average is denser than the magma. Conversely, the comparatively lower average density of continental crust does not favor easy ascent of basaltic magmas, as they are prone to stagnate and intrude at depths (lower to middle crust?) where neutral buoyancy is attained. In the latter case, mantle-derived mafic magmas are likely to interact with crustal wallrocks (or earlier stored magmas) and more likely to undergo significant compositional modification due to magmatic differentiation and assimilation processes (cf. Annen et al., 2006). A seminal example of these relations is provided by the southern Chilean Andes (cf. Hildreth and Moorbath, 1988), where along-strike crustal thickness varies more than two-fold from >60 km in the north to ~30 km in the south. Notably, 1) Quaternary mafic volcanism is most pronounced in the south, whereas there are no true basaltic lavas in the north and 2) compositions of the most mafic lavas reflect progressively greater “crustal” input toward the north.

Intra-oceanic arcs (e.g., Tonga, Marianas, South Sandwich, western Aleutians) are built upon essentially oceanic basement that has a comparatively simple geologic history and restricted compositional range–similar to that produced at mid-ocean ridges. However, in such areas complications sometimes arise where oceanic plateaux are involved (e.g., near New Britain; Woodhead et al., 1998). Such basement is presumed to have formed in part over an upwelling mantle plume, and therefore presumably adds an additional OIB-like component. Moreover, later post-subduction magmatism may reactivate relict mantle wedge lithosphere (e.g., as in Fiji and some parts of the Izu arc). Remelting of such mantle has been proposed to explain the origin of certain alkalic lavas within these arcs (as noted above).

So What Is the Nature of Arc Magmas?

It is useful to reflect on what a volcanic arc actually is. Modern volcanic arcs are evident along plate margins inboard of active SZs, where usually oceanic lithospheric plates are being thrust beneath other oceanic or continental plates or fragments thereof. Volcanic arcs typically comprise a chain or belt of young volcanoes oriented more or less parallel to the strike of the SZ; in detail they can be more complex in structure. Overall, erupted products commonly comprise a compositional spectrum including basalt, andesite, and dacite ± rhyolite—often with a preponderance of intermediate composition products. Leeman (1983) observed that the median composition of arc lavas from global localities varied rather systematically with the thickness of the underlying arc crust; this observation is well confirmed by the current vastly larger global database (cf. Farner and Lee, 2017). Median SiO_2 content is lowest (dominantly basaltic) in oceanic arcs, and generally higher (andesitic or more evolved) in continental margin arcs. And, on an intra-arc scale, SiO_2 content and a variety of other compositional parameters of recent volcanoes clearly vary with crustal thickness. Analogous and more global studies (e.g., Plank and Langmuir, 1988) have repeatedly shown that crustal processes appear to exert strong control on the nature of erupted volcanic material.

Implicitly, there is a complementary, but generally inaccessible, intrusive component to arc volcanism (cf. DeBari and Greene, 2011; Kelemen and Behn, 2016; Mullen et al., 2018). Clearly, significant fractions of arc magma stagnate within the crust and gradually modify its overall composition as well as impact its thermal structure (cf. Karlstrom et al., 2015; Rees-Jones et al., 2018). There are myriad ways that ascending magmas can be modified by combinations of crystallization, mixing with other stored magmas or partial melts of crustal rocks, etc.—the mixing, assimilation, storage, and hybridization (MASH) process (cf. Murphy et al., 2000; Annen et al., 2006; Hildreth, 2007; Solano et al., 2012). These processes tend to obscure the compositions of primitive magmas formed deep in the mantle. Thus, many investigations have focused on what exactly is the nature of the most primitive magmas in volcanic arcs (cf. Schmidt and Jagoutz, 2017). This is extremely important because it bears on where and how parental arc magmas form as well as on the nature of their source rocks (see later discussion).

Do Andesites Rule?

Andesitic rocks are common in many volcanic arcs (especially continental ones), and have been considered characteristic of arc volcanism (e.g., Gill, 1981). Kelemen et al. (2003) summarize arguments favoring the origin of so-called “high-Mg andesites” (HMA, or adakites) as direct melts of mantle lithologies, and it is well known that hydrous melting of mafic compositions (e.g., subducted oceanic crust; Beard and Lofgren, 1991; Rapp and Watson, 1995; Grove et al., 2003; Sisson and Kelemen, 2018) can produce a variety of intermediate to silicic melts depending on water availability. However, the concept that andesitic magmas form by direct melting of ultramafic mantle is questionable for several reasons. First, although “andesitic” lavas and intrusive rocks happen to be common (Gómez-Tuana et al., 2013; Kent, 2013), the occurrence of natural andesitic magmas (actual liquids) is extremely rare (cf. Reubi and Blundy, 2009), as are quenched glasses (e.g., in the form of MIs in phenocryst minerals; Naumov et al., 1997; Zhu et al., 2013). In contrast, many investigations of andesitic rocks have shown them to be products of mixing between more mafic and more silicic liquids ± other crystalline components (cf. Anderson, 1976; Tatsumi, 2005; Humphreys et al., 2013; Kent, 2013; Sisson et al., 2014). An important example is (adakitic) HMA from near Mt. Shasta in the Cascade arc—considered to be a near-primary magma by Grove et al. (2002, 2003), or a mixture of mantle-derived basaltic andesite and high-Mg andesite (Ruscitto et al., 2011). These interpretations are questioned by Streck and Leeman (2018), who show this lava to be a hybrid mixture of basaltic and dacitic magmas plus ultramafic xenocrysts, and unlikely to be a direct mantle melt. Also, early views that a magmatic continuum can develop dominantly via fractional crystallization have now shifted to include the likelihood that there is an essentially bimodal distribution of mafic (basaltic) and silicic (dacitic-rhyolitic depending on the nature of the local arc crust) magma populations in most volcanic arcs, and that these to varied extent mix and interact with country rocks to form the observed spectrum of arc magmas (cf. Reubi and Blundy, 2009; Kent, 2013; Blum-Oeste and Wörner, 2016; Beier et al., 2017; Conway et al., 2020).

An increasingly prevalent view is that arc magmatism is driven primarily by ascent of mantle-derived basaltic magmas that 1) interact with pre-existing crustal rocks to form silicic partial melts (e.g., dacite, rhyolite), 2) undergo stagnation largely at crustal depths where mixing and contamination may occur, and 3) undergo fractional crystallization to produce mafic to ultramafic cumulate lenses during eventual solidification. To reconcile the "andesitic" nature of continental crust vs. the inferred basaltic nature of mantle inputs, it is necessary to remove large portions of the latter mafic cumulate component. This may be accomplished by delamination and foundering of lower crust segments containing relatively dense cumulate materials (cf. Kelemen et al., 2003; Tatsumi, 2005), or by "relamination" or underplating by new relatively evolved magmas (Kelemen and Behn, 2016).

The exact nature of mafic magmas in volcanic arcs may be to some extent masked by the effects of the pre-existing crust as a density filter. This is manifest by the skewness in magma compositions relative to crustal type and thickness noted above. A notable example is Mount St. Helens, in the Washington Cascades (cf. Smith and Leeman, 1993; Leeman and Smith, 2018). There, the prevalent erupted magmas are dacitic with subordinate andesite. Basaltic magmas of two distinct types have erupted only during a brief period (~300 years), but their presence is required over the 300 ka lifetime of the volcano as a mixing component to produce observed compositional trends in the more evolved intermediate composition rocks, and as a heat source to drive crustal level processes—including partial melting of crustal rocks and stabilization of shallow magma reservoirs.

Comments on Other Critical Factors—Oxygen and Water

How Oxidized Are Arc Magma Sources?

Many factors have been invoked to account for differences between arc vs. oceanic intraplate magma suites. Examples include the perceived roles of oxidation and/or water content, both of which are inferred to be generally greater in arc magma suites than in intraplate magmas. It is widely accepted that the calcalkalic (CA) magma series forms under relatively oxidizing conditions that promote crystallization of magnetite in addition to other liquidus phases (olivine, plagioclase, pyroxenes, etc.) so as to minimize Fe-enrichment in evolving magmas. Conversely, repression of magnetite as a crystallizing phase allows evolving magmas to generate a more iron-rich tholeiitic (TH) magma series. The presence of magnetite as a liquidus phase is widely attributed to whether redox conditions in the magma are 1) significantly above vs. 2) near or below the quartz-fayalite-magnetite (QFM) redox buffer (cf. Blatter et al., 2013). Notably, both magma series can be found in many volcanic arcs (e.g., Japan, Cascades). The CA series seemingly requires more oxidized conditions in the magmas that implicitly arise owing to inputs from subducted materials—notably sediment melts and aqueous fluids (cf. Kelley et al., 2010). However, considering redox sensitive indicators like V/Sc or Zn/Fe elemental ratios (Lee et al., 2005; Lee et al., 2010), it appears that at least the most primitive basalts in the CA series from the Cascades and several other arcs are no more oxidized than typical intraplate basalts (ocean islands, mid-ocean ridges) that have essentially no apparent subduction relationship. Thus, to the extent that CA compositional trends in arc lava suites actually can be replicated by mixing between basaltic and more evolved magmas (cf. Eichelberger et al., 2006), the inferred redox differences may be artifacts of processes that occur after formation of primary magmas—and thus may not necessarily reflect source differences. The stage at which arc magmas acquire their "oxidized signature" remains a topic of contention (cf. Kelley and Cottrell, 2009; Rowe et al., 2009; Walowski et al., 2015).

How Wet Are Arc Magma Sources?

Water contents are elevated in many arc lavas relative to most intraplate lavas of similar bulk composition (cf. Wallace, 2005; Zimmer et al., 2010; Ruscitto et al., 2012). This is usually attributed to high water contents in the magma sources, that in turn can be explained by influx of aqueous fluids or hydrous melts derived from water-rich subducted materials (cf. Schmidt and Poli, 1998; van Keken et al., 2011). In evaluating direct measurements of magmatic water content, it is noteworthy that the solubility of water in silicate melts is pressure and temperature dependent. This means that if ascending magmas become water-saturated, any further rise will result in partial losses of water vapor. Thus, the only potential direct record of water content is in MIs trapped at high pressures in phenocrystic minerals, olivine usually being the first to form in mafic magmas. The extent to which ascending magmas have outgassed prior to phenocryst formation is generally unknown. Also, many published water determinations are for olivine-hosted MIs that are variably evolved from primitive compositions, and often the host olivines are less magnesian than expected for mantle source compositions (i.e., ~Fo_{90} or higher). Thus, "reverse fractionation" corrections (e.g., addition of olivine) commonly are applied to the studied samples to approximate compositions of primary mantle melts. Measured water and incompatible element contents are thus diluted to some extent relative to the analyzed values (cf. Schmidt and Jagoutz, 2017). Adjusted MI water contents of ~4 wt% are typical for basaltic liquids from most arcs, and slightly lower (~3 wt%) for the Cascades arc (Ruscitto et al., 2012; Plank et al., 2013; Walowski et al., 2015). However, detailed studies of MIs from the Cascades suggest that measured water content varies systematically with magma type, and also may vary according to along-strike position in the arc; this is revisited later in the paper.

Implications of Water Contents and Scenarios for Melt Formation

A major question concerns the timing and place where arc magmas acquire their water (and other volatile) contents. Presumably, the water is largely derived from dehydration of subducted materials. In a flux-melting scenario (cf. Cooper et al., 2010), water released from subducting slabs lowers the mantle solidus and promotes hydrous melting at near-slab depths (≥~80 km). Such models are supported by the occurrence in some arc magmas (cf. discussion of the Tonga-Kermadec-New Zealand arc by Leeman et al., 2017) of short-lived radioisotopes (e.g., ^{10}Be; excess ^{238}U, ^{226}Ra) that must be recently added to arc magma sources, as well as fluid-mobile elements (FMEs; B, Pb, As, Sb, etc.), all of which are likely slab-derived to some degree. Grove and Till (2019) review such melting scenarios, and discuss how such magmas may evolve during ascent, first through an upward-increasing temperature gradient in the lower mantle wedge, then through an upward-decreasing gradient in the uppermost mantle. Clearly, such an ascent path provides myriad possibilities of magma modification including interaction with multiple mantle wall rocks (including previously stagnated melt columns or intrusive bodies).

An alternative scenario involves adiabatic melting of upwelling asthenospheric (?) mantle material, likely derived from back-arc regions (cf. Long et al., 2012; Turner and Langmuir, 2015; Perrin et al., 2018), but also potentially mantle rising through tears or holes in the subducting slab (cf. Ferrari et al., 2012; Mullen and Weis, 2013). In this case, the types of melts produced and overall melt productivity are influenced by heterogeneities in the upwelling mantle (cf. Turner et al., 2017) and by the thermal structure of the mantle wedge beneath a given arc (cf. Turner et al., 2016). A third potential source of some arc magmas, that may be decoupled from direct slab inputs, is lithospheric mantle. Such domains may have a complex history, including prior melting events and/or modifications from earlier fluid and melt infiltrations as noted above. Modeling by Rees-Jones et al. (2018) suggests that lithospheric mantle temperatures can be elevated by several hundred degrees at depths as shallow as 60 km in response to heat transfer by magma migration over extended time. Such mantle domains may contribute significantly to arc magma production, particularly in continental margin settings where the lithosphere is likely to be thick and have a distinctive composition (cf. Pearce, 1982).

Corresponding magmatic liquid temperatures calculated (Lee et al., 2009; Perrin et al., 2016) for many primitive arc basaltic magmas are at most about 100°C below solidus conditions for dry peridotite (e.g., ~1,450°C at 3.0 GPa; cf. Hirschmann, 2000). Estimated magma P–T conditions that fall below the dry solidus require the presence of some water in the magma source (cf. Katz et al., 2003; Green et al., 2014). The amount required depends on ΔT below the solidus (cf. Portnyagin et al., 2007). In contrast, where temperatures above the dry solidus are predicted, source H_2O content may be negligibly small. These relationships have not been widely incorporated into geodynamic models for SZs, but they potentially provide useful constraints on depths of primary melt generation. In flux-melting scenarios, where near-slab melts might initially form at temperatures below 900°C (cf. Grove et al., 2012), there must be significant heating and re-equilibration of the melt column to produce the erupted magmas (cf. Mallik et al., 2016), and this may occur as low temperature melts ascend through the inverted thermal gradient in the mantle wedge. This introduces considerable uncertainty regarding which initial parameters (including slab-derived tracers) the final melts actually retain vs. what are likely to be significant modifications during a tortuous ascent. It is uncertain what fraction of the near-slab melt actually persists relative to melt increments added in the process of reaching the highest estimated mantle equilibration temperatures (possibly ≥600°C heating based on thermobarometry cited above). Conversely, adiabatic melting also seems capable of reproducing the thermobarometric estimates, but leaves open the question of how such sources acquire the geochemical signatures attributed to SC inputs. And if non-convecting lithospheric mantle is a significant magma source, reactivated via intense rejuvenated magma flux from below, it is possible that slab geochemical signatures could be cumulative over time, and even partly related to earlier magmas in the rejuvenating pulse. Realistically, all of these general processes could be involved in arc magmatism. What is especially puzzling is how the observed diversity of magmas in some arcs can be produced, often in single volcanoes and for restricted intra-arc areas. Not only does this seem to dictate that there are significant small-scale heterogeneities in source domains, but that physical processes of magma segregation and ascent must operate on small spatial scales.

DIVERSITY OF ARC MAGMAS

Geochemical characteristics have been utilized in creative ways to address diversity of arc magmas as well as to identify unique features that can discriminate among potential contributions to their formation. Based on earlier discussion, such approaches are best applied to the most primitive lavas that are available–ideally basaltic lavas with ≥7–8 wt% MgO for which nominal equilibrium olivine composition approaches Fo_{90} or higher, which would imply that said magmas could have been in equilibrium with typical peridotitic or pyroxenitic mantle lithologies (cf. Leeman et al., 2005; Herzberg and Asimow, 2015). Where such primitive basalts are rare or absent (e.g., central Andes, portions of western Pacific arcs), primary source characteristics may not be faithfully retained in available samples. Schmidt and Jagoutz (2017) have attempted to assess variations in "primitive" arc magmas on a global scale; interestingly, from the enormous GEOROC volcanic arc database, only 938 samples from 30 arcs passed their filter—primarily that Mg#s are consistent with near-equilibration with mantle olivine compositions. They recognize at least six distinct magma types, two of which are varieties of mafic andesites, and observe that most arcs have more than one melt type—this is attributed to heterogeneity in the mantle wedge coupled with additional contributions of varied slab components. Below, I review in greater detail the diversity of primitive magmas in the Cascade arc, and note that the picture there is more complex.

More on Geochemical Discrimination

In assessing overall geochemistry, two fundamentally different groups of elements are considered: 1) those that are incompatible in dominant mineral phases in the mantle and in common phenocrysts in crystallizing magmas, and 2) all of the rest, for which magmatic relative abundances can be altered during melting or crystallization processes that involve physical separation of liquids, solid phases, and/or fluids. The highly incompatible elements (e.g., LILE, FME) are of greatest utility in assessing source compositions as their elemental ratios are expected to be little affected by either melt formation or crystallization processes during magma ascent. Of course, such ratios can be modified by open system processes such as assimilation of distinct country rocks or melts thereof, or by mixing with other distinct magma types. Theoretically, it can be expected that a primitive mantle-derived basaltic magma that ascended directly to the surface will retain an incompatible element record characteristic of its mantle source. Much the same is true regarding isotopic ratios of elements such as B, Sr, Nd, Pb, Hf, etc., that are unchanged by normal closed-system magmatic processes (cf. Ryan and Chauvel, 2014).

Locally, there are significant spatial variations in the geochemistry of arc basalts. For example, lavas from most cross-arc transects display increasing proportions of fluid-mobile elements approaching the arc front (trenchward), that are suggestive of progressively decreasing contributions of slab-derived fluids with increasing depth along the subducting slabs (Woodhead et al., 1993; Noll et al., 1996; Elliot et al., 1997; Tonarini et al., 2001). These trends are consistent with predicted fluxes of water released from progressively dehydrated slabs (van Keken et al., 2011). Similarly, along-strike variations in some arcs (e.g., Tonga-Kermadec-New Zealand; Leeman et al., 2017) appear to reflect lateral changes in overall slab thermal structure or volumes of subducted material corresponding to changes in age or convergence rate of the subducting plate.

Superimposed on such variations, is the surprising occurrence of two or more distinct basalt variants within local arc regions, and in some cases at a single volcanic center or stratovolcano (e.g., Reagan and Gill, 1989; Leeman et al., 1990; Bacon et al., 1997; Kimura et al., 2002; Leeman et al., 2005; Hickey-Vargas et al., 2016; Rawson et al., 2016; many others). Such examples imply that the sub-arc mantle cannot be considered to be compositionally homogeneous. An obvious question concerns the extent to which inherent heterogeneities in the sub-arc mantle can be masked or effectively overprinted by progressive infiltration of slab-derived fluids and/or melts. And, to what extent are such effects related to the thermal conditions (hence, dehydration history or melting) in local subducting slabs?

The Case for Looking at Hot, "Dry" End Member Volcanic Arcs

Slab-derived fluid contributions are expected to be greatest in cooler SZs typically associated with the majority of modern volcanic arcs. It has been proposed that slab-derived melt contributions might arise from diapiric upwelling of mélange material that then undergoes decompression melting, possibly enhanced by fluxing due to any entrained aqueous fluid (cf. Gerya and Stöckhert, 2006; Behn et al., 2011; Marschall and Schumacher, 2012; Codillo et al., 2018). Also, availability of slab-derived fluids is likely to be strongly enhanced in places where fracture zones in the downgoing plate are subducted (Singer et al., 1996; Peate et al., 1997; Manea et al., 2014; Singer et al., 2007; Cooper et al., 2020). In contrast, at relatively warm SZs (Cascades, southwest Japan, western Mexico) slab dehydration effects may occur at predominantly shallow depths, largely in the frontal arc region, such that slab fluid contributions beneath the main body and rear of the arc are likely minimal (cf. Harry and Green, 1999; Manea et al., 2005; Ferrari et al., 2012; Kimura et al., 2014). However, release of water from deep serpentinized parts of hot slabs could potentially trigger wet melting of altered oceanic crust or sediments (cf. van Keken et al., 2011; Yogodzinski et al., 2015; Sisson and Kelemen, 2018).

CASE STUDY—THE CASCADES VOLCANIC ARC

Overview of the Arc

From the perspective of subduction-related magmatism, it is useful to examine more closely the well-characterized Cascade arc of western North America (**Figure 1**). This ~1,300 km-long arc is an important end member example in that it is one of the warmest modern SZs. After an early compressive and accretionary history (Mesozoic to Eocene time; cf. Sigloch and Mihalynuk, 2017), subduction beneath the Pacific Northwest migrated westward to its present location following accretion of the Siletzia oceanic plateau (ca. 50 Ma; McCrory and Wilson, 2013; Wells et al., 2014). Remnants of the Siletzia terrane comprise much of the Oregon-Washington Coast Ranges, and pieces likely extend further east in the subsurface (cf. Bedrosian and Feucht, 2014; Gao and Shen, 2014). Some have proposed that the westward jump in subduction could have been triggered directly by impingement of a mantle plume on the PNW, that presumably produced the Siletzia and related oceanic volcanics,

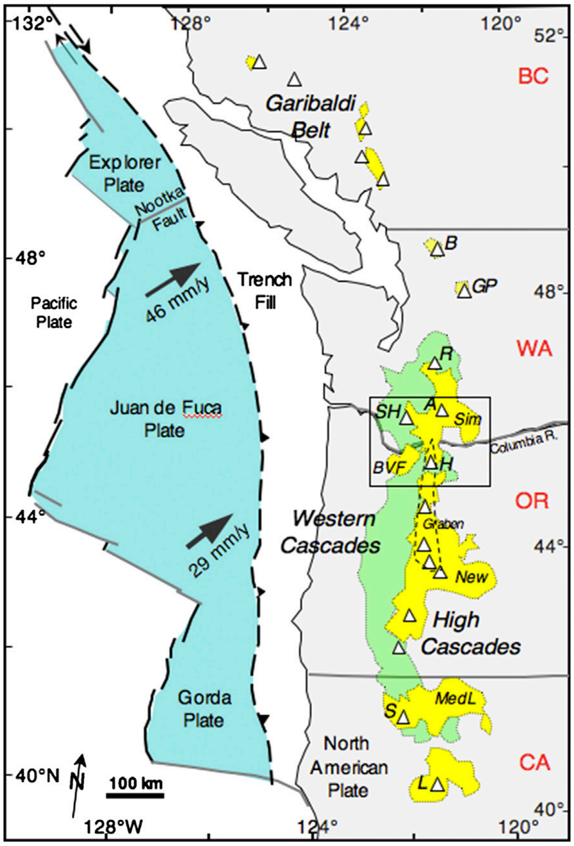

FIGURE 3 | General tectonic setting of the Cascade volcanic arc that spans from British Columbia through Washington and Oregon to northern California (after Mullen et al., 2017). Triangles indicate locations of prominent Quaternary stratovolcanoes; selected ones are identified as Mts. Baker (B), Glacier Peak (GP), Rainier (R), St. Helens (SH), Adams (A), Hood (H), Shasta (S), and Lassen (L). Large backarc volcanic fields are identified as Simcoe (Sim), Newberry (New), and Medicine Lake (MedL). Dashed field in Oregon is the High Cascades central graben. Also shown are general distributions of Pliocene-Recent High Cascades (yellow field) and Eocene-Miocene Western Cascades (green field) volcanic rocks (cf. Luedke and Smith, 1982). Large arrows show azimuth and velocity of subducting oceanic plates (dark green field) relative to North America. Selected inset rectangle is expanded in **Figure 4**.

and is now situated beneath Yellowstone (Stern and Dumitru, 2019). The ancestral Cascade arc was initiated by ca. 40–45 Ma (du Bray and John, 2013; du Bray et al., 2014), and has been intermittently active to the present. High convergence rates during early stages (Verplanck and Duncan, 1987) would have caused dehydration of the slab to persist well inboard of the trench compared to the present, thereby modifying the composition of the mantle wedge and accounting for initially high volcanic productivity. Over time, convergence rate has declined about four-fold resulting in warming of the slab, accelerated dehydration of subducted materials, release of slab-derived fluids predominantly beneath the forearc region, and diminished fluid flux beneath the modern volcanic arc and back-arc region (cf. Bostock et al., 2002; van Keken et al., 2011).

Because of better preservation and exposure, the Pliocene to Quaternary activity (<~5 Ma) has been investigated in greatest detail as summarized by Hildreth (2007). Cascadia is more complex than the standard paradigm for volcanic arcs. Owing to the curvature of the coastline, convergence is oblique along the US coast and nearly orthogonal along the British Columbia coast (**Figure 3**). Volcanic activity forms a narrow, near-linear belt in Canada with three major stratovolcano complexes and associated mafic monogenetic vent fields. Isolated centers of Mt. Baker and Glacier Peak extend the northern Cascades into Washington State. Following a gap of ~100 km in which there has been no Quaternary volcanic activity, the arc becomes more continuous and progressively broadens going from southern Washington, through Oregon, and into northern California. Oblique convergence resulted in fragmentation and clockwise rotation of tectonic blocks underlying the forearc and much of the southern Cascades in Oregon and California (Wells et al., 1998; McCaffrey et al., 2007; Wells and McCaffrey, 2013). This is accompanied by westward slab rollback beneath much of the US Cascades (cf. Humphreys and Coblentz, 2007; Long et al., 2012). Consequently, parts of the arc have been in a state of extension dating back to ~16 Ma in the south (Priest et al., 2012; Wells and McCaffrey, 2013), and ~7 Ma in central Oregon where a central graben initiated and has propagated as far north as southern Washington (Conrey et al., 1997). Also the large, dominantly basaltic, Simcoe, Newberry, and Medicine Lake lava fields developed immediately behind (east of) the main Cascades arc since late Pliocene time. High frequency mafic volcanism in these latter regions likely reflects increasingly more efficient transmissivity of basaltic magmas through the extending crust over time (cf. Hildreth, 2007; Porritt et al., 2011; Till et al., 2019).

The nature of the underlying crust varies along strike: accretionary Klamath terrane (Paleozoic-to-Cretaceous) in northern CA and southern OR, accreted Silezia oceanic terrane in northern OR-southern WA, and accretionary North Cascades terrane (Paleozoic-to-Paleocene) in northern WA and southern British Columbia (cf. Schmidt et al., 2008; Mullen et al., 2017). The northern and southern sectors have a more "continental" character whereas the central part of the arc is more mafic and denser. Presumably the associated lithospheric mantle domains differ as well and, together with the distinct crustal assemblages, may partly account for along-strike variations in the arc magmas. Several groups have investigated this possibility, focusing on relatively young and primitive basaltic lavas, with somewhat different outcomes (e.g., Schmidt et al., 2008; Mullen et al., 2017; Pitcher and Kent, 2019). It should be noted that these studies focus almost exclusively on mafic samples from lava fields and flank eruptions peripheral to the major stratovolcanoes (that are andesitic or more evolved in composition). All of the cited works find that the northern (Canadian) Cascades are distinctive in having dominantly intraplate OIB-like basalts accompanied by smaller proportions of CA type basalts. Mount Baker and Glacier Peak areas have few basaltic lavas but include some high-Mg andesites of CA type. In southern Washington, the Mt. Rainier area has few basalts, largely of CA type with minor LKT (cf. Reiners et al.,

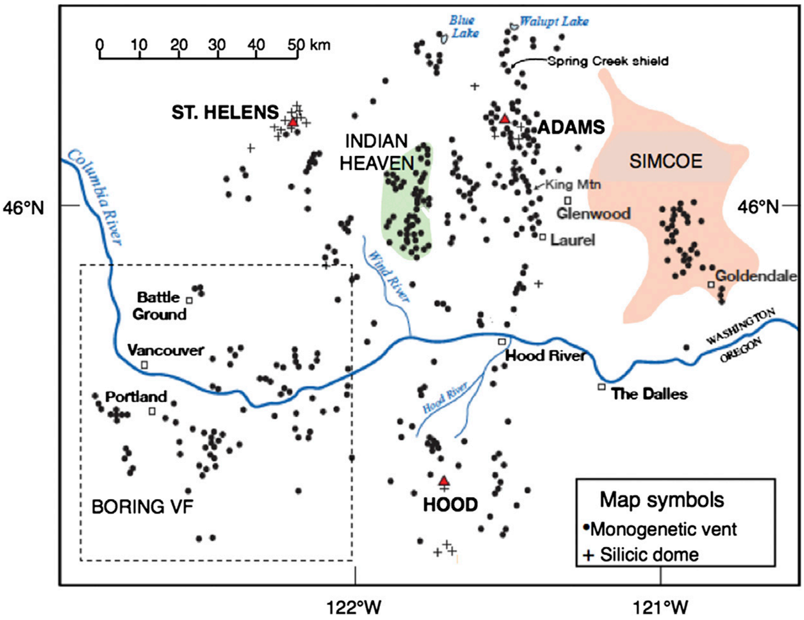

FIGURE 4 | Map of volcanic fields, monogenetic vents, and stratovolcano complexes (Mt. St. Helens, Adams, and Hood) in the Cascades Columbia Transect (CCT), near latitude 46°N (after Hildreth, 2007). Indian Heaven (green shading) and Simcoe (red shading) are coherent volcanic fields of dominantly mafic lavas. Dashed rectangle is location of Boring Volcanic Field, shown in more detail in **Figure 8**.

2000; Sisson et al., 2014). Beginning near Mount St. Helens and Mt. Adams, basaltic activity is increasingly prolific and quite diverse with abundant LKT and OIB-like lavas coupled with diverse CA type lavas including basalt, absarokite, and mafic basaltic andesite (see below).

Proceeding further south through Oregon, mafic products increase in proportion but are dominantly of CA and LKT types. Schmidt et al. (2008) proposed that the chemical variances define four distinct segments to the arc, whereas Pitcher and Kent (2019) subdivide the arc into six statistically distinct segments based on a much larger data set. An interesting outcome of their work is a tally of the proportions of each magma type found in each of their segments (see below). Both studies advocate subtle differences in the mantle sources for basalts along strike, with possible modifications in the nature and/or magnitude of slab-derived contributions (increasing toward the south; cf. Walowski et al., 2016). In contrast, Mullen et al. (2017) argue that primitive Cascade LKT and CA basalts are very similar with regard to their Sr-Nd-Hf and particularly Pb isotopic compositions, and propose that they could be derived from a common "background" mantle, modified by varied input from subducted sediments or oceanic crust to produce respective LKT and CA type sources. They consider that the "background" mantle was isotopically similar to the Juan de Fuca MORB source mantle, which poses the question of how such material is now accessible—presumably in the mantle wedge. They also propose the involvement of a distinct source of OIB-like character for dominant basalts of the Canadian sector and for the Simcoe backarc volcanic area, and attribute its presence to upwelling of asthenospheric mantle through tears in the subducting slab.

Curious Aspects of the Cascades Arc

The Cascades arc is unusual in that modern volcanism occurs in a wide arc-normal swath, including vents up to 90 km trenchward from the main volcanic axis. The southern part shares similarities with the Trans-Mexican Volcanic arc including oblique subduction and extensional tectonism. Except in the Canadian sector, there is no well-defined volcanic front but rather a broad distribution of vents that suggests magma availability beneath an extensive area. A good example is seen in a west-east transect proximal to the Columbia River near latitude 46°N (**Figure 4**; the Cascade Columbia Transect, or CCT, of Leeman et al., 2005). The vent distribution in this area is possibly influenced by oblique convergence (Hildreth, 2007; Fleck et al., 2014), and by northern reaches of the central graben, both of which may be facilitated by complex material flow in the underlying mantle. Representative lavas from this area have been described in detail (cf. Leeman et al., 1990; Conrey et al., 1997; Leeman et al., 2005; Jicha et al., 2009). Mafic lavas in this sector of the Cascades are more diverse than anywhere else in the arc, and often erupted from vents as close as a few km apart (cf. Hildreth, 2007). See **Supplementary Table S3** for typical data.

Small-Scale Diversity at Mount St. Helens—A Typical Example

Leeman and Smith (2018) describe two varieties of basaltic lavas erupted within a period of ≤300 years (~1,700–2,000 years BP) from flank and near-summit vents at Mount St. Helens (MSH) separated by only 3 km. These magmas were essentially contemporaneous and fed by close-spaced conduits, but show no evidence of interacting with one another. Both magmas are of

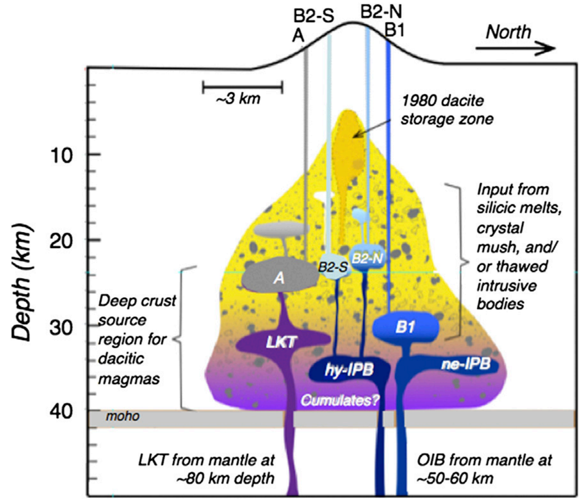

FIGURE 5 | Schematic cross-section showing inferred depth relations for crustal-level Mount St. Helens (MSH) magma reservoirs and plumbing system as described in Leeman and Smith (2018); note that horizontal scale is greatly expanded. In this case, depths are computed using the thermobarometer of Lee et al. (2009) and based on compositions of the most MgO-rich Cave basalt (LKT) and Castle Creek basalts (OIB-like) of both nepheline- and hypersthene-normative character. Reservoirs feeding these eruptions are, respectively, "A," "B1," and "B2-S"/"B2-N"—the latter for hy-normative lavas vented high on the south and north flanks of MSH. Multiple flows from these vents exhibit compositional variations due to mixing with andesitic material within the magmatic system. Diagram also shows implied feeder conduits to deeper mantle sources of the respective LKT and OIB-like primary magmas (below diagram). Additional shallower reservoirs are inferred to exist as ultimate sources for more evolved magmas at MSH; formation and storage depths of evolved dacitic magmas are discussed by Blatter et al. (2017).

intraplate type—slightly evolved LKT and OIB-like basalts with up to ~7% MgO, but very distinctive overall geochemistry. Their proximity raises interesting questions. Can they be formed by melting a common heterogeneous source domain, or must their sources be separated in space or depth? And, in either case, how do proximal magma streams retain their compositional uniqueness? Based on thermobarometry, it was concluded that these eruptions originated from distinct magma reservoirs located at depths near 24 and ~28 km, respectively, and that each originally segregated from mantle depths of ~80 and ~50–60 km. As a hint to the complexity of this system, **Figure 5** shows an interpretive view of the magma plumbing system beneath MSH. Depths to shallower magma reservoirs are also based on thermobarometry of more evolved basaltic and intermediate composition lavas, and on the work of Blatter et al. (2013, 2017) on the andesites and dacites. It is generally assumed that all Cascade stratovolcanoes are underlain by analogous complex systems of stacked magma reservoirs and conduits where opportunities for melting wall rocks and mixing of magmas likely abound (cf. Hildreth, 2007; Kent, 2013). It is surprising that discrete basaltic magma types largely survived the transit to the surface through such an obstacle course, although the MSH data do show that mixing occurred between the least-evolved basaltic end members and a component similar to MSH andesite (Leeman and Smith, 2018). Indeed, many of the CCT vents seen in **Figure 4** produced chemically diverse basalts that are more primitive than those at MSH (cf. Leeman et al., 2005; Pitcher and Kent, 2019).

Anomalous Forearc Magmatism of the Boring Volcanic Field

The diversity issue is further exemplified in the Boring Volcanic Field (BVF) situated in the Portland Basin and contiguous areas at the far western end of the CCT (see inset in **Figure 4**). The forearc BVF is dispersed over an area of ~4,000 km^2, of which ~500 km^2 is covered by volcanic rocks with a cumulate volume of ~10 km^3 erupted from at least 80 distinct monogenetic vents that were active in late Pliocene–Pleistocene time (Evarts et al., 2009; Evarts et al., 2017; Leeman et al., 2019). Over 100 distinct map units have been defined, many consisting of multiple flow units. Most of the field has been systematically sampled for chemical and paleomagnetic analyses, and many of the distinct volcanic map units have been dated by high-precision ^{40}Ar/^{39}Ar geochronology (Fleck et al., 2014; Hagstrum et al., 2017). Those from local vents range in age from ~2,700 to 50 ka; these are locally underlain or interfingered with numerous late Tertiary (3,600–1,400 ka) LKT flows that originated from vents just east of the Portland Basin, in the western High Cascades. There are minor equivalents further south in the western Cascades as young as 42 ka (Rowe and Tepley, 2016).

Description of Boring Volcanic Field Compositional Features

High-precision XRF analyses are available for 1,271 samples, and these data are used to assess magmatic diversity. Overall, the suite is relatively mafic (SiO_2 range: 47–60 wt%), and many of the basaltic lavas have greater than 7.5% MgO, ranging up to 10 wt% for some samples. All samples have been assigned to compositional groups, similar to those of Leeman et al. (2005); distinguishing criteria given in **Supplementary Table S4** are for high-MgO (>7.5 wt%) samples. Groups from the BVF are given a "B" prefix, whereas the slightly older LKTs are distinguished with a "T" prefix: specifically, low-K tholeiites (BLKT, 5%; TLKT, 14%), OIB-like lavas (BOIB, 12%), calcalkalic basalts (BCA, 37%), absarokites (BABS, 7%), and rocks with greater than 56% SiO_2 are classified as andesites (BAND, 9%); cited percentages indicate proportions of the total sample population. And finally, samples that did not precisely meet the classification criteria are simply called "transitional" (BTran, 15%). Many of the latter have affinity to one of the other groups, but are anomalous in some fashion and do not fall cleanly into one of the prescribed groups; it is suspected that many are products of mixing between two or more of the defined magma types. Key discriminants used to classify the entire population are: 1) LKTs have less than 0.5% K_2O; 2) OIBs have K_2O >0.5% as well as elevated Nb and Nb/Zr ratios; 3) both intraplate groups have low Ba- and Sr-enrichment relative to Ti, Zr, or Nb; 4) CA types are distinct in having strong enrichments of Ba and Sr; and 5) ABS types are more extremely enriched in K_2O, Ba, and Sr; all CA type samples with more than

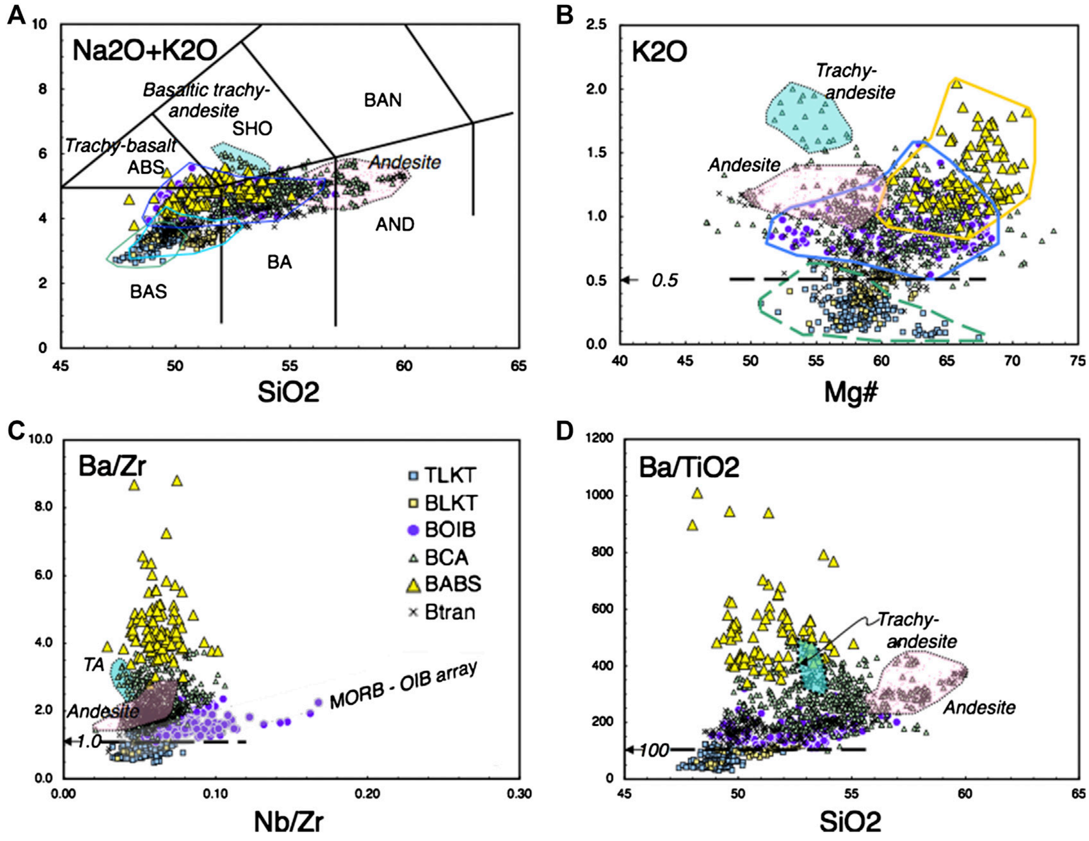

FIGURE 6 | Variation diagrams for lavas of the Boring Volcanic field (BVF) are based on XRF analyses of 1,271 samples (Leeman et al., 2005, Leeman et al., 2019); these show range in **(A)** SiO_2 vs. total alkalis, **(B)** Mg# (=Mg/[Mg + Fe], molar ratio) vs. K_2O, **(C)** Nb/Zr vs. Ba/Zr, and **(D)** SiO_2 vs. Ba/TiO_2. Symbols denote assigned magma type based on these and other discriminant diagrams. Fields in **(A)** are labeled to indicate compositional space for basalt (BAS), basaltic andesite (BA), andesite (AND), absarokite (ABS, or Trachy-basalt), shoshonite (SHO, or Basaltic trachy-andesite), and banakite (BAN) as referred to in text. Symbol key: age differences are denoted by prefix "T" for Pliocene (3.0–3.6 Ma) or "B" for Quaternary (<2.6 Ma); magma types include "low-K tholeiite" (LKT), "ocean island-like" (OIB), and "calcalkalic" (CA) basalts, and "absarokitic" (ABS), "andesitic" (AND), and "transitional" (Tran; mixtures or otherwise ill-defined) lavas. Dashed lines denote upper limit values for K_2O, Ba/Zr, and Ba/TiO_2 used to distinguish the LKT group.

500 ppm Ba are arbitrarily assigned to the ABS group (that now includes what Leeman et al., 2005, called high-K CA lavas.

Although details of the petrology and geochemistry of the BVF will be presented elsewhere, diagrams in **Figure 6** illustrate several unique aspects of the magma types with respect to their SiO_2 content and Mg# (values > 63 correspond to equilibrium olivine of ~Fo_{85} or higher, and are considered to be primitive). First, a plot of total alkalis ($Na_2O + K_2O$) vs. SiO_2, shows the general petrologic groupings to which samples are assigned. Although fields for the CA and OIB-like magma types overlap considerably in this diagram, the LKTs are systematically lower in alkalis. Some of the OIB-like and CA types with highest alkali content fall into either the absarokite (ABS) or shoshonite (SHO) field. In the other diagrams, the LKTs are again clearly distinguished, as are the OIB-like group with respect to their Nb-enrichment, and the ABS group forms a distinct cluster with respect to Ba/Zr and Ba/TiO_2 ratios.

Figure 7 illustrates Ba-, Sr-, and K- enrichment vs. both Mg# and wt% MgO. Primitive LKT types are readily distinguished from other magma types in all of these diagrams, albeit a few overstep the plotted discriminant lines as MgO content decreases below 7 wt%. OIB-like lavas are likewise distinguished from CA types by their low Ba/Nb ratios, and from the LKTs by their higher Sr/Y, Ba/TiO_2, and K_2O/TiO_2 ratios. Primitive ABS type lavas are clearly strongly enriched in Ba, Sr, and K_2O, but enrichments in these elements diminish with decreasing MgO content, and there is a possible continuum between ABS and the less enriched CA types. These patterns likely signify that some local mixing occurs between different magma types. However, clear compositional differences between most of the LKTs and the other groups implies their formation from distinctly lower K_2O and Ba sources. The OIB-like lavas also require a source with lower Ba as well as higher Nb than any of the CA type lavas. Finally, because many of the CA type lavas have higher MgO (many exceeding 9 wt%, and Mg#s ≥ 70) than the most mafic LKT or OIB-like lavas, it appears that they are derived from more refractory (i.e., relatively melt-depleted) sources; this is supported by the presence of magnesian olivine phenocrysts (up to Fo_{92}) in some of these samples (Smith and Leeman, 2005).

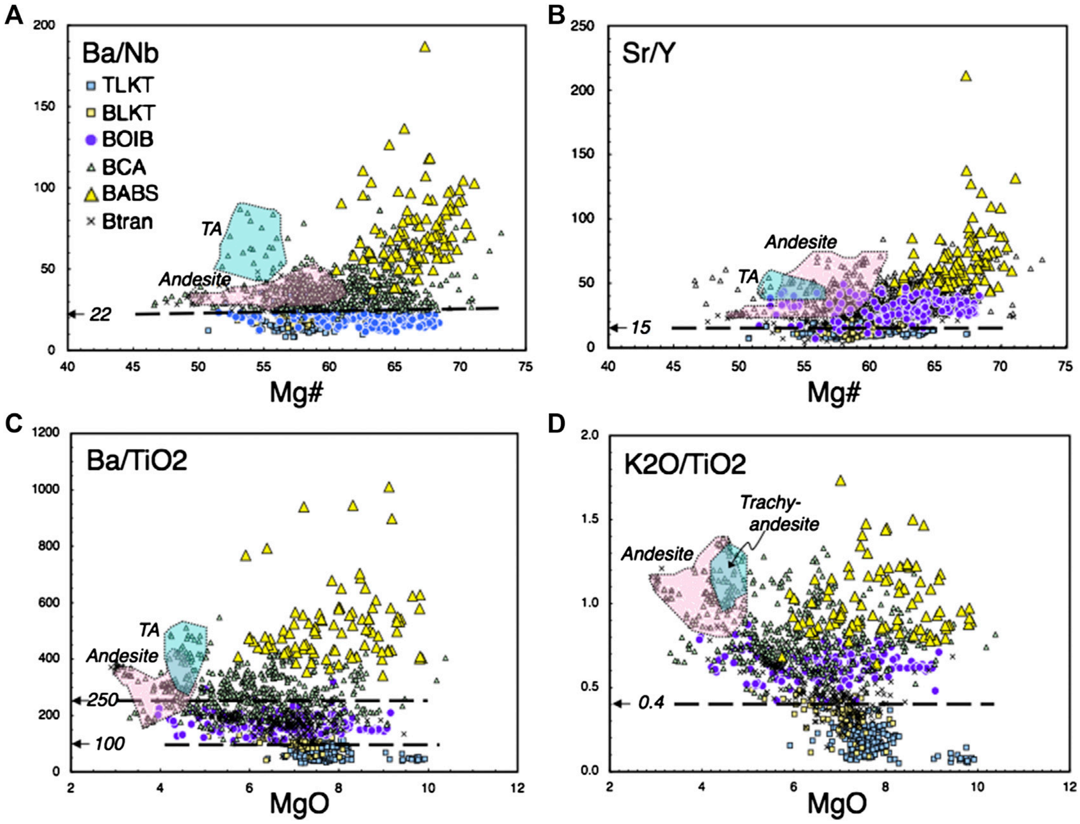

FIGURE 7 | Additional discriminant diagrams for BVF lavas; same key as in **Figure 6**. Ratios of Ba/Nb, Sr/Y, Ba/TiO_2, and K_2O/TiO_2 are plotted vs. Mg# or MgO wt%. Note that all chemical types include a significant number of "primitive" lavas with MgO > 8 wt%. Ba/Nb clearly distinguishes all intraplate lavas (both LKT and OIB-like) from those of CA affinity (CA and ABS types). Primitive LKT types are easily distinguished in all of these diagrams, albeit some overstep the plotted discriminant lines as MgO content decreases below 7 wt%. Primitive ABS type lavas are clearly strongly enriched in Ba, Sr, and K_2O, but enrichments in these elements diminish as MgO content decreases. Dashed lines indicate discriminant values for abscissa parameters in defining magma groups.

For purposes of this paper, the data set was further filtered to exclude evolved lavas by considering only samples with Mg# > 57 and MgO wt% > 8.0; lavas with as little as 7.48% MgO were included for the BLKT group to obtain a more representative population. Average compositions of these groups are presented in **Table 1** and are believed to approximate distinctive end member magma types that fed the BVF. It is inferred that such MgO-rich magmas ascended more or less directly from the underlying mantle.

Spatial and Temporal Distribution of Boring Volcanic Field Magma Types

The map distribution of BVF samples is provided in **Figure 8**, where plot symbols indicate magma type. The striking impression is that, despite some clustering, all magma types are dispersed across the entire Portland Basin as far west as the Portland Hills, some 90 km west of the main High Cascades axis (e.g., Mt. Hood). **Figure 9** shows the age and spatial distribution of the magma types, and again there is considerable overlap indicating that all types were generally available throughout the early history of the BVF. LKT magmas dominated the earliest stages, and last appeared at ~1,400 ka. Other magma types collectively have been dominant in the area since that time. It also appears that volcanism generally expanded westward over the lifespan of the field. This is particularly noticeable for the OIB-like lavas, with exception of a ca. 2,500 ka group in the southern Portland Basin. As at MSH, a fundamental question regards how these diverse magma types are produced, and where.

Where Do the Melts Come From?

In an attempt to answer this question, a thermobarometric approach was taken using primitive lavas of each distinct BVF magma type as well as representative samples from across the CCT. The methodology is described in the Supplementary Material, and uses basaltic samples with high MgO content (≥8 wt% for all groups except the less magnesian BLKT, for which 7.5 wt% was used as a cutoff) that are essentially olivine-phyric (ideally of ~Fo_{85} or higher), such that their compositions are closest to equilibrium with assumed mantle peridotite. As described by Leeman et al. (2005), the bulk compositions are corrected by incremental addition of equilibrium olivine until they approach final equilibrium with a target source Mg#. Calculations were done assuming that the magmas were only slightly more oxidized than the QFM redox

TABLE 1 | Averages ±SD for BVF primitive basaltic magma types.

Magma type	TLKT		BLKT		OIB		CA		ABS	
	Avg. (31)	SD	Avg. (8)	SD	Avg. (22)	SD	Avg. (49)	SD	Avg. (48)	SD
SiO_2	48.63	0.59	49.92	1.12	49.58	0.35	50.60	0.66	50.33	0.97
TiO_2	1.31	0.14	1.27	0.14	1.60	0.14	1.27	0.12	1.36	0.11
Al_2O_3	17.05	0.46	17.30	0.52	17.01	0.38	16.86	0.49	16.11	0.47
FeO*	11.38	0.67	10.84	0.71	9.11	0.32	8.72	0.67	8.61	0.60
MnO	0.18	0.01	0.18	0.01	0.16	0.01	0.15	0.01	0.15	0.01
MgO	8.78	0.80	7.70	0.24	8.61	0.35	8.48	0.51	8.81	0.55
CaO	9.54	0.42	9.40	0.50	9.11	0.31	9.24	0.48	9.48	0.53
Na_2O	2.83	0.16	2.96	0.14	3.43	0.21	3.33	0.27	3.31	0.28
K_2O	0.17	0.09	0.28	0.11	1.02	0.14	1.05	0.16	1.38	0.24
P_2O_5	0.13	0.02	0.14	0.02	0.37	0.05	0.30	0.03	0.46	0.11
Mg#	61.7	2.4	59.9	1.9	66.5	1.4	67.1	2.2	68.2	1.5
Ba/Nb	17.5	4.5	20.0	3.5	16.3	3.2	41.8	15.1	80.2	22.5
Ba/TiO_2	57	20	84	26	162	22	284	73	540	139
Ba/Zr	0.93	0.25	1.15	0.29	1.63	0.26	2.82	0.75	4.81	1.11
Nb/Zr	0.054	0.010	0.058	0.011	0.102	0.020	0.071	0.013	0.062	0.011
Sr/Y	11.2	1.8	11.9	2.7	29.1	4.6	46.1	15.4	74.6	29.9
Ba	75	28	105	26	260	45	355	74	736	217
Rb	1.5	1.3	2.2	1.8	11.7	2.6	9.9	4.0	11.8	4.0
Sr	269	29	334	40	660	84	882	188	1,480	382
Y	24.3	3.1	28.9	4.9	22.8	1.7	19.9	2.8	20.6	2.6
Zr	80	15	91	9	160	14	128	14	152	19
Nb	4.4	1.3	5.3	1.1	16.6	4.9	9.0	1.9	9.4	2.2
Ni	166	45	121	15	159	15	170	33	196	26
X-Fo	84.3	—	83.4	—	86.9	—	87.2	—	87.8	—
T1 (°C)	1,256	—	1,221	—	1,246	—	1,237	—	1,234	—
T2 (°C)	—	1,476	—	1,447	—	1,355	—	1,331	—	1,327
D2 (km)	—	79	—	67	—	54	—	45	—	47

*Averages ± SD for samples that meet the discrimination criteria in **Supplementary Table S4**. All Fe is reported as FeO*; analyses normalized to total 100%, volatile-free. X-Fo = calc. equilibrium olivine composition assuming X-fe3 = 0.15; T1 = "eruptive" temperature; T2 and D2 = segregation temperature and depth for Mg# 90 source. Key: labels same as in **Supplementary Table S4**.*

buffer (Smith and Leeman, 2005), assuming a value of 0.15 for the mole fraction of ferric iron. This value is consistent with actual olivine phenocrysts (typically ca. $Fo_{84–86}$ in LKTs, and higher for OIB-like and CA type lavas). It is also consistent with measured V/Sc and Zn/Fe ratios that in primitive CCT lavas overlap with values for magnesian intraplate basalts (cf. Lee et al., 2005, Lee et al., 2010). Detailed examples of recalculated "primary" melt compositions of representative CCT lava types are presented in **Supplementary Table S2**. Partial results are also shown in **Table 1** for the BVF average magma types. These are calculated on a water-free basis. However, inclusion of water (up to 3 wt%) lowers estimated temperatures by <30°C per wt% H_2O and has little effect on calculated pressures of equilibration (cf. Plank and Forsythe, 2016). Existing MI data for CCT lavas indicate that water contents are less than ~0.3 wt% for LKTs and about 2 wt% for the most water-rich CA and ABS lavas that have been studied (e.g., Rea et al., 2012). Also, because the fertility of actual magma sources is unknown, results were computed for a range of mantle Mg#s (90 all groups; also 91 and 92 for the more magnesian CA type magmas; see below). As a caveat, these calculations are based on melt equilibration with olivine + orthopyroxene-bearing mantle sources, but are applicable to lherzolitic sources (cf. **Supplementary Material**). Compositions of primitive LKTs are consistent with this assumption; compositions of many of the other magma types suggest possible fractionation of clinopyroxene or involvement of pyroxenitic sources (cf. Herzberg and Asimow, 2015; Lambart et al., 2016). Future work is needed to evaluate the effects of source variability on estimated segregation (i.e., final equilibration) depths and temperatures.

Figure 10 shows estimated final equilibration depths vs. longitudinal position for a number of representative CCT lavas, including several from the frontal arc BVF. These are near 65–80 km for the most primitive LKTs, decrease to ~50–60 km for primitive OIB-like basalts within the arc, and increase to ~100 km for some backarc Simcoe lavas. Note that P–T loci for these samples lie above the dry peridotite solidus (cf. **Figure 11**). If derived from a source with similar Mg#, primitive CA and ABS types appear to segregate from shallower depths (~45–60 km). Yet shallower depths obtained for mafic basaltic andesites are likely minimal values considering their comparatively evolved compositions. For example, at MSH, shallowing of calculated depths is correlated with increasing andesite component mixed into mafic lavas; this essentially lowers the Mg# of the mixture (Leeman et al., 2005; Leeman and Smith, 2018). Taken at face value, the relative depths are surprising in that the CA type magmas with the strongest "slab" influence appear to have equilibrated with mantle domains furthest above the subducting slab. Equilibration depths for the westernmost LKTs appear to be near or possibly below the seismically imaged slab (McCrory et al., 2012; Mann et al., 2019), but this may be an artifact because some originated from vents

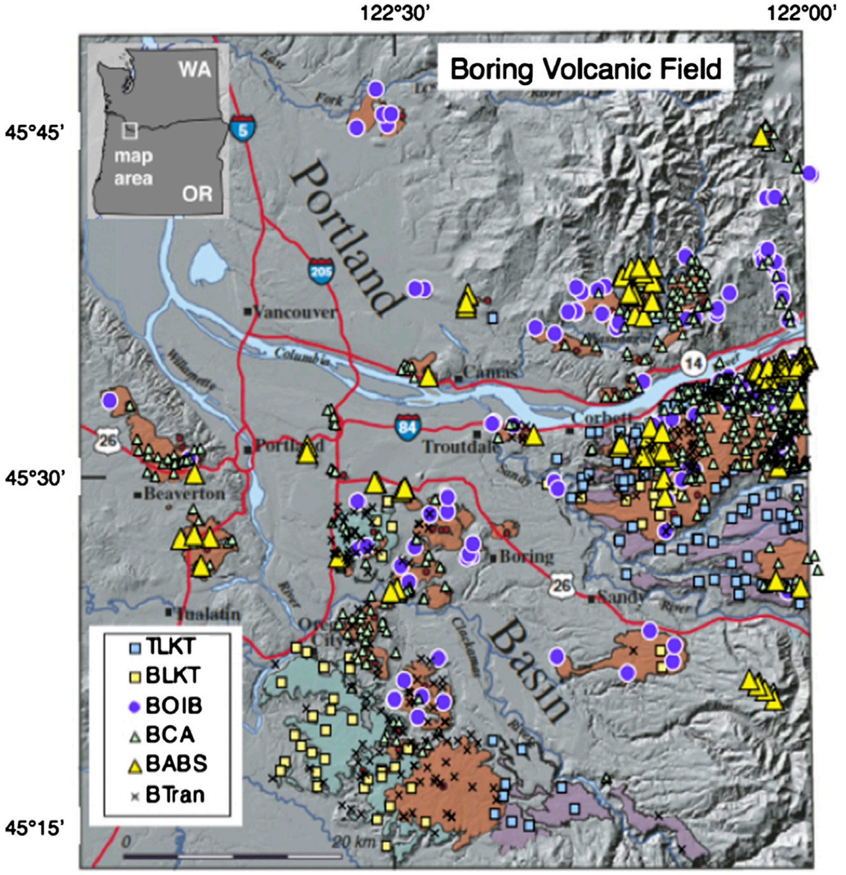

FIGURE 8 | Locations of analyzed samples within the Portland Basin forearc region of the Cascade arc (Leeman et al., 2019). Base map is from Evarts et al. (2009). Symbols denote chemical affinity for individual samples collected at those locations. Map colors show distribution of locally erupted volcanic rocks (in orange except for BLKT tholeiites (blue-green), and TLKT tholeiites (purple) from High Cascades vents east of the map area.

many kms to the east. In any case, LKT depths are considered most robust and leave little wiggle room to produce other magma types from greater depths within the mantle wedge.

Average primitive CA and ABS group lavas have high Mg#s consistent with equilibrium olivine compositions near Fo_{88}, and some individual lavas carry olivine phenocrysts of up to Fo_{92}. Depth estimates for both the CA and ABS averages increase on the order of 10–15 km for each 1% increase in source Mg#, placing them closer (possibly equivalent?) to segregation depths for some of the LKT/OIB magmas. Scenarios that bring the respective sources spatially closer carry the implication that the mantle source domain is heterogeneous, in which case production and effective separation of the respective distinct magma types becomes a challenge.

If the magmas ascend vertically from their source domains, this creates a spatial problem in getting LKT (and perhaps other) source material into the forearc part of the mantle wedge. Moreover, this region is interpreted to be extensively serpentinized and thus much cooler (e.g., <700°C) than the estimated magmatic temperatures, as verified by geophysical investigations in southern Washington (Brocher et al., 2003; Hansen et al., 2016; Abers et al., 2017). This problem is further compounded because even the eruptive temperatures (those calculated from uncorrected lava compositions) are above 1,200°C for each magma type (**Table 1**). This issue has been addressed in several geophysical studies proximal to MSH, and Hansen et al. (2016) propose that magmas feeding MSH migrate there from more easterly sources. However, this idea is difficult to reconcile with the demonstrated diversity of magmas erupted there and at points even further west (i.e., BVF).

The broad and persistent distribution of mafic magmatism in the BVF and nearby areas suggests that there has been sustained melt generation in the forearc region for ≥2.5 Ma. Its manifestation may be facilitated by tectonic factors related to oblique subduction. But the source of thermal energy to drive melt generation remains unclear. Two possibilities are that: 1) there is a disruption or tear in the subducting slab, that allows ascent and decompression melting of asthenospheric mantle to produce the OIB-like basalts; and 2) there is a broad upwelling of asthenospheric mantle from the backarc region that can melt, possibly producing LKT magmas (Sisson and Bronto, 1998; Elkins-Tanton et al., 2001; Lewis et al., 2001; Tamura et al., 2002). Ascent of the latter (or both) may provide sufficient heat to partially melt the shallower lithospheric mantle to produce CA

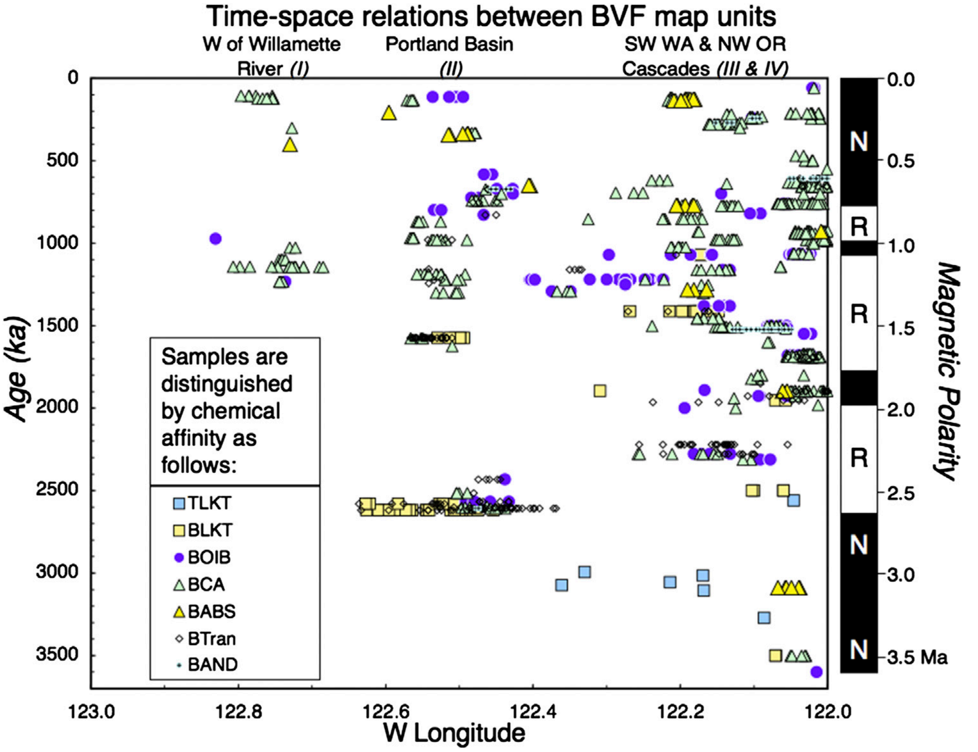

FIGURE 9 | Distribution of magma types over time in western sectors of the Cascades Columbia Transect (CCT) proximal to Portland Basin (Fleck et al., 2014; Hagstrum et al., 2017; Leeman et al., 2019). Local eruptions in the Portland Basin area initiated as early as ~2,600 ka and have continued intermittently to ~50 ka. LKT activity was restricted to the early history of the field, whereas other magma types erupted from the onset to the near-present.

type magmas. This scenario is consistent with the larger segregation depths and early arrival of LKT type magmas. Although Mann et al. (2019) find no break in the slab, there is tomographic evidence for thinning or a gap in the Farallon slab near latitude 46°N (Liu and Stegman, 2011; Porritt et al., 2011) and, more convincingly, evidence for a tear in the Juan de Fuca plate further south (Hawley and Allen, 2019). A similar "slab-tear" scenario has been proposed for the Canadian Cascades to explain the abundance of OIB-like basalts in that region (Mullen and Weis, 2015). There is also considerable evidence for mantle upwelling in the backarc (Currie et al., 2004; Long et al., 2012; Till et al., 2013; Gao and Shen, 2014) as well as under portions of the Cascades (Bodmer et al., 2018; Zhou et al., 2018).

It is interesting to compare such suggested upwelling with models proposed for mantle plumes. In Hawaii, evidence for compositional heterogeneities has been explained in terms of domains of relatively enriched material (e.g., pyroxenites) embedded within more refractory peridotitic mantle. The kinematic modeling of Hofmann and Farnetani (2013) suggests that, with large-scale convection or flow, such impurities can be effectively drawn into long string-like structures ("fibers") that may preferentially melt during ascent. At low degrees of melting the impurities dominate early melts that are relatively LILE-rich, whereas at high degrees of melting this component is diluted or depleted and melts become less enriched in incompatible elements. In the case of SZs, there is also the added factor that impurities can be in the form of slab-derived contributions, and these may have a more dominating effect in cooler systems as opposed to warm systems like the Cascades. Another possibility is that portions of lithospheric mantle, associated with blocks like the Siletzia oceanic plateau, are subducted and comprise "impurities" (or domains) of significant volume (cf. Schmandt and Humphreys, 2011). Such materials, if melted, would be expected to produce magmas of "oceanic" compositional character–as has been proposed by Straub et al. (2008) for the Mexican volcanic arc. It is clear that some Simcoe basalts have Pb isotopic compositions (Leeman et al., 1990; Mullen et al., 2017) that uniquely resemble such data for the Siletzia volcanics (Phillips et al., 2017) and are isotopically distinct from Pb in other Cascades magma types. At present, it remains a challenge to explain the diversity of the CCT magma array, not only regarding the nature and proportions of source components, but also how so many of the erupted basaltic lavas retain their distinct primitive compositions as they make their way toward the surface.

There is seismic and magnetotelluric evidence for the presence of warm domains both near the subducting slab and at Moho depths (~40 km), for example near the latitude of Mount Rainier (McGary et al., 2014), and in the deep crust beneath parts of the CCT (Hansen et al., 2016). Such evidence supports the presence of melt at depths consistent with the thermobarometry approach summarized above. However, the relatively small-scale diversity

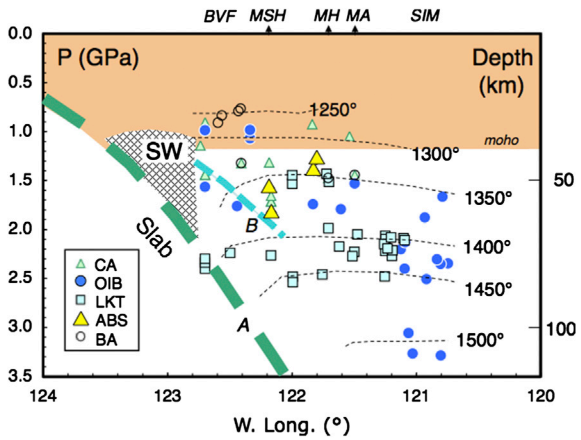

FIGURE 10 | Cross-section of the Cascadia subduction zone near latitude 46°N provides a broad view illustrating calculated segregation P–T relations for representative CCT lavas. The thermobarometry depicted is based on primitive magma compositions corrected by olivine addition to attain equilibrium with Fo_{90} mantle olivine (cf. Leeman et al., 2005; Lee et al., 2009; see Supplementary Material for details and **Supplementary Table S2** for example calculations). Sample points are positioned assuming vertical ascent to the actual sample localities, but westernmost LKTs likely vented tens of kms to the east; symbols denote magma type. Reference localities are Boring Volcanic Field (BVF), Mt. St. Helens (MSH), Hood (MH), and Adams (MA), and the Simcoe volcanic field (SIM). Temperature contours based on interpolation of calculated segregation temperatures suggest that the upper mantle is very warm in this region, approaching the dry peridotite solidus at depths near 80–90 km. These data suggest a tiered compositional structure with intraplate type magmas rising from systematically deeper levels than the calcalkalic magma types. "SW" is inferred serpentinized portion of the mantle wedge (after Bostock et al., 2002). Heavy green dashed lines indicate top of the subducting slab near this part of the arc from **(A)** Michaelson and Weaver (1986) and **(B)** Mann et al. (2019).

among the erupted basaltic magmas suggests that conduits and magma chambers must commonly be isolated at the scale of a few km as opposed to forming large homogenizing reservoirs.

What Controls the Distribution of Cascades Magmas?

At this point, it is useful to consider the geographic distribution of magma types in the Cascades. This approach has been used previously (e.g., Pearce et al., 2005) to investigate links between magma geochemistry and kinematic development of parts of the Marianas arc. Pitcher and Kent (2019) effectively have done this to some extent for the Cascades. They present their results in the form of averages of the magma types present in their six arc segments, weighted according to numerical proportions in each area. It is informative to simply look at the spatial distribution of the most primitive lavas. This obviously restricts the number of samples being considered, and may leave some spatial gaps, but does provide a general view of how distinct mantle sources are likely distributed at depth. This map (**Figure 12**) shows locations of samples screened as before for primitive character; also juxtaposed is another map from Hildreth (2007) showing tectonic elements in the same area. What stands out first is the concentration of OIB-like samples (and to lesser extent ABS samples) in the CCT traverse, but also in a southeast-trending belt that runs from the BVF area across the Oregon graben area toward the Newberry volcanic field and perhaps further east. Data are sparse for the latter trend, and there are few OIB-like samples in the far back-arc High Lava Plains (HLP) region. Compared with the tectonic map, this distribution shows a close correspondence with the boundary between extensional and transpressional regimes, and the concentration of OIB-like basalts roughly corresponds to the region impacted by the Siletzia accretion event. Also, the OIB-like lavas are less than ~5 Ma in age; older ones have not been recognized so far. Does their appearance record a significant tectonic transition?

A second feature that stands out is the distribution of LKT basalts. With very few exceptions, these are concentrated south of about 46°N latitude, are very common and widespread across the Cascades in southern Oregon and California, and similar lavas are common in the backarc regions (Newberry-HLP and Medicine Lake areas). This has been noted in previous surveys (cf. Till et al.,

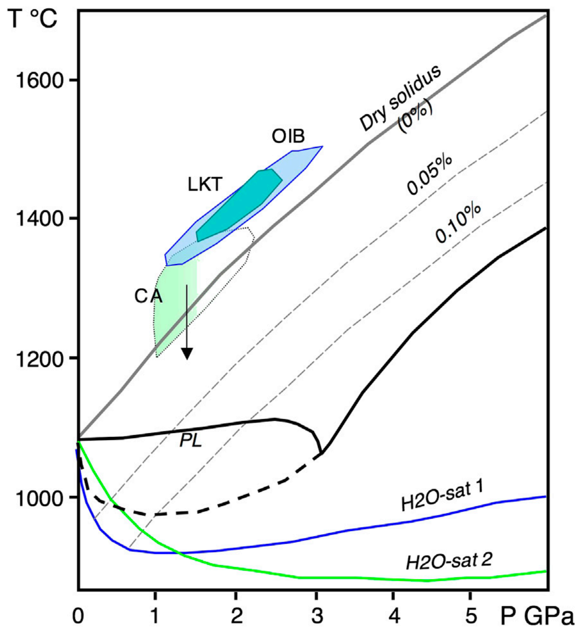

FIGURE 11 | Estimated P–T conditions for last equilibration of primitive Cascades basaltic lavas (from **Figure 10**) assuming lherzolitic mantle sources (Mg# = 90) for all. These are compared with representative mantle solidi curves. Gray lines are calculated peridotite solidi with 0, 0.05, and 0.10 wt% H_2O (Katz et al., 2003). Equivalent dry solidus of Hirschmann (2000) (for plot, see **Supplementary Table S2**) is slightly warmer than labeled "Dry solidus." Bold black line is experimental solidus for pargasite lherzolite (PL) with ~0.02% ppm H_2O; bold dashed and solid line at *p* above 3 GPa represent mantle vapor-saturated solidus (Green et al., 2014). Blue and green curves (H_2O-sat 1 and H_2O-sat 2), solidi for water-saturated peridotite (also see Fig. 2), are considered less realistic by Green et al. (2014). Cascades LKT and OIB lavas are consistent with essentially anhydrous sources. CA type melts with temperature adjustments (arrow) for up to 3 wt% H_2O, lie near or plot below the dry solidus—consistent with their formation from slightly hydrated sources. Alternative source models need to be evaluated further for these melts.

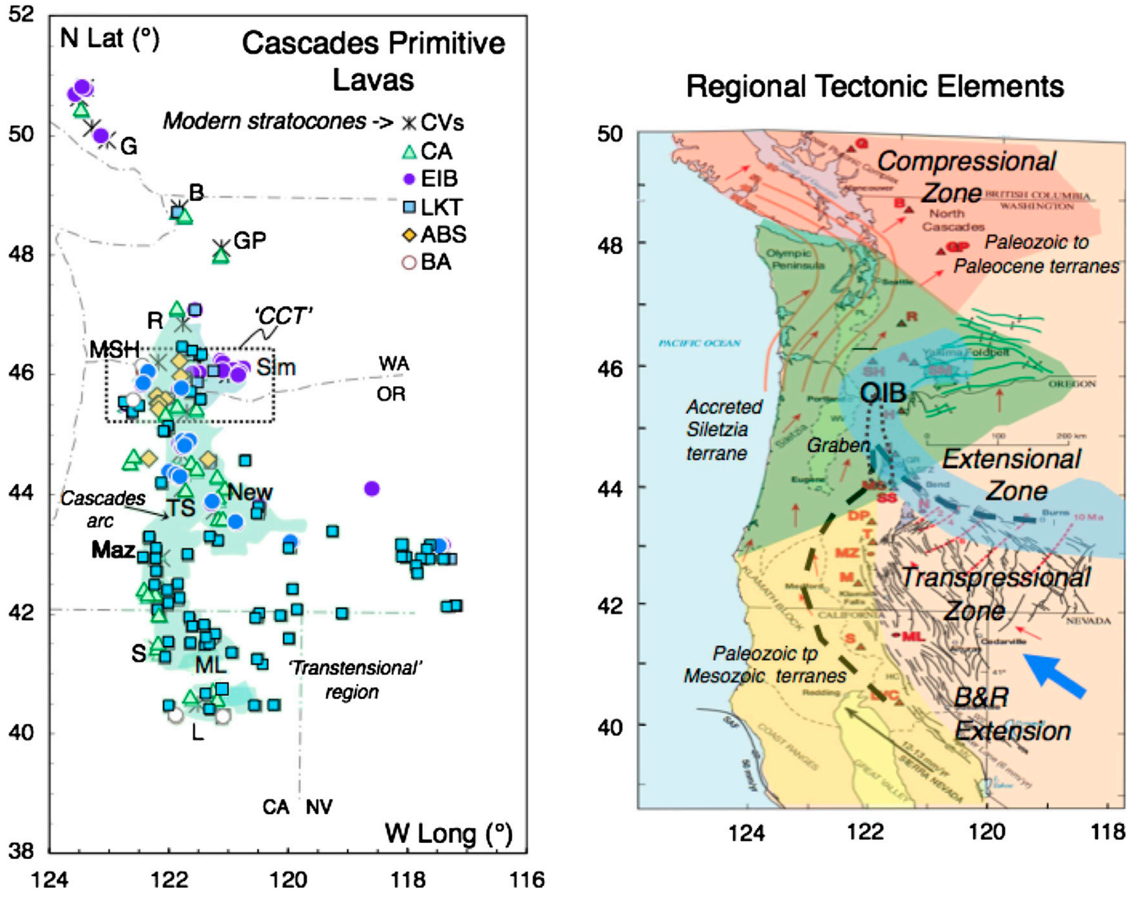

FIGURE 12 | (Left) Map showing locations of primitive Cascades basaltic lavas, with symbols denoting magma type. Only samples with Mg# > 60 and MgO > 7.5 wt% are plotted. Additional stratocones identified include Mts. Garibaldi (G), Mazama (Maz) and the Three Sisters (TS). The distribution of Pliocene-Recent Cascades volcanic rocks is shown in darker green shading, and a region of transtensional deformation (pale green shading) includes much of the southern Cascades as well as a broad High Lava Plains area behind the arc in southern Oregon; the distribution of LKT type basalts is concentrated in this area. **(Right)** Map (after Hildreth, 2007) shows tectonic elements in the Cascades and nearby areas, as well as along-strike differences in the nature of the underlying basement terranes (after Schmidt et al., 2008). These figures emphasize the restricted distribution of primitive OIB-like basalts. Those in Oregon-Washington are concentrated in the CCT swath near 46°N and in a diffuse array extending southeastward from the Portland area, following an inferred transition zone between dominantly transpressional (to the west) and extensional (to the east) tectonic regimes. Their close association with the region of the accreted Siletzia terrane may not be coincidental. Also note that the preponderance of LKT in the southern portions of the arc and backarc regions appears to be associated with extension that began propagating into the region (blue arrow) in late Miocene time (cf. Till et al., 2013).

2013), and it is clear that the LKT basalts are associated with areas that have been in extensional mode beginning in the late Miocene in the backarc regions, and propagating into the Cascades up to modern times. Pitcher and Kent (2019) estimate LKT proportions (of all samples in a given segment) to be approximately 25% for southern Washington, 20% for the Oregon graben area, and 50% for the southern Cascades, with similar proportions in the immediate backarc fields (Medicine Lake and Newberry).

Although few CA type basalts are plotted in **Figure 12** (only those with Mg# > 63), such lavas (including high-Mg basaltic andesites) comprise significant proportions in all but the Canadian segment; they dominate northern Washington, and comprise about half of the samples in more southerly segments (Pitcher and Kent, 2019). It has been suggested that CA and LKT magmas may be produced from a common source as a consequence of flux melting (i.e., degree of melting varies in response to the amount of aqueous fluid that is available; Reiners et al., 2000; Rowe et al., 2009). Considering the warmth of the Cascadia slab, it has also been proposed that primitive CA type lavas may form by flux/reaction between wedge peridotite and infiltrating hot-slab hydrous melts (Lassen region, Walowski et al., 2016; Mt. Baker and Glacier Peak, Sas et al., 2017). Rather than forming these different magma types by flux melting of a common source, Mullen et al. (2017) visualize them having distinct sources evolved from a common "background" depleted mantle (~MORB source) via different degrees of enrichment by slab-derived SC. Relative to LKTs, it is enigmatic that the higher Mg# CA types (presumably from more refractory sources) are most enriched in so-called slab-derived elements.

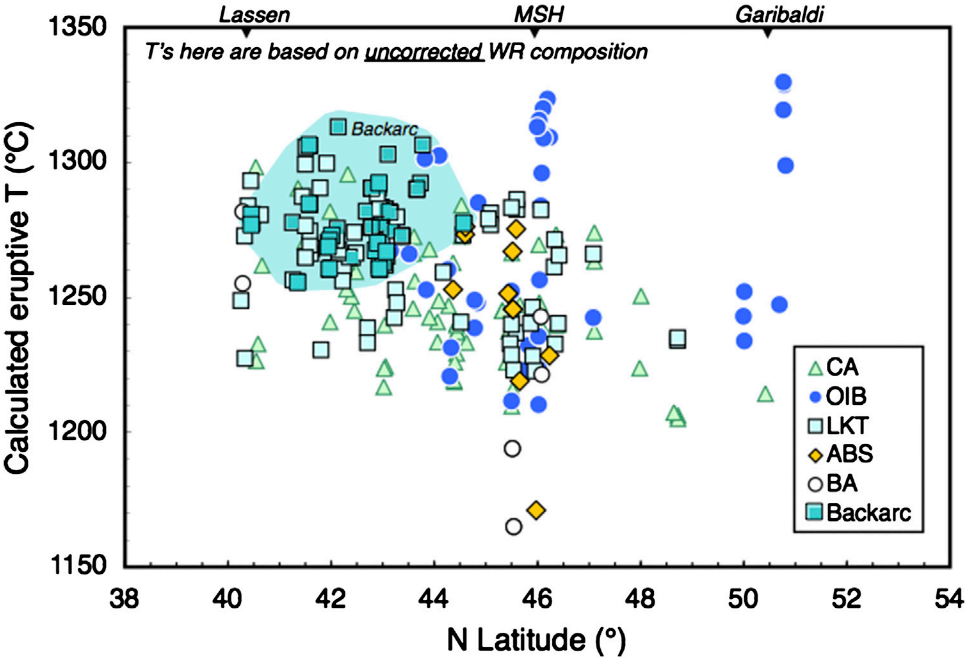

FIGURE 13 | Estimated eruptive temperatures for samples of primitive magma types along strike in the Cascade arc (cf. Leeman et al., 2005). Data for far backarc LKTs from the High Lava Plains in eastern Oregon (cf. Till et al., 2013) are superimposed for comparison (outlined in green field). Temperatures are calculated for lavas with MgO >7 wt% (see Supp**lementary Material** for details). Thermometry is most robust for the LKTs owing to their low water contents. Of significance is the general increase in magmatic temperatures for Cascades LKT going southward from southern Washington (Mt. St. Helens area) to northern California (Lassen area).

Another Look at Thermal Aspects of Magma Generation

Here, I compare calculated eruptive temperatures for primitive Cascades and representative backarc (HLP) basalts (**Figure 13**). Such estimates are based on uncorrected sample analyses using thermometry of Lee et al. (2009); where measured, water contents are <1 wt% for most LKTs and rarely exceed 3 wt% for other magma types (see earlier discussion). Relative to latitudinal position, there are several notable points. First, OIB-like basalts have maximal Ts in excess of 1,300°C, and a range of about 100°C, which is positively correlated with sample MgO content (~8–10 wt%), or increasing "primitiveness." Higher Ts would seem consistent with segregation of OIB-like magmas from deep mantle as it welled up through gaps in the subducting slabs. Second, Cascades LKTs exhibit a robust along-strike increase in T (also Mg#; cf. Leeman et al., 2005) going south from Washington to California. Essentially, the southern LKTs and those from the HLP are derived from more refractory mantle than those near the CCT. These two groups are associated with highly extensional areas accompanied by significant mantle upwelling due to slab rollback (cf. Long et al., 2012; Gao and Shen, 2014) and by opening of a tear or hole in the subducting Juan de Fuca plate beneath the southern Cascades (Hawley and Allen, 2019). There is also a southward increase in Ba content of LKTs (cf. Leeman et al., 2005) that may reflect higher contributions of slab-derived SC beneath the southern segment of the arc. If this implies greater influx of water or melt diapirs from the subducting slab, it might be expected to see this reflected in lowered magmatic temperatures—but this is not apparent. The mantle in this region was possibly depleted in magmaphile elements such that slab contributions have greater leverage there than further north, hence enrichments of Ba, etc. are proportionally larger (Borg et al., 1997; Borg et al., 2002). Also, segregation depths calculated for these LKTs are consistent with their formation near the dry mantle peridotite solidus (Hirschmann, 2000) at depths ca. 75 km. On an anhydrous basis, apparent Ts for primitive CA type basalts overlap those of the other groups. However, with corrections for up to 3 wt% H_2O (cf. Walowski et al., 2015), maximum Ts are close to 1,200°C. These Ts are well above water-saturated peridotite or pyroxenite solidi, yet below the dry mantle solidus–thus, consistent with slightly hydrated sources (cf. Katz et al., 2003). These conditions also seem consistent with flux-melting models involving hydrous silicic slab melts as proposed by Walowski et al., 2015). A plausible alternative scenario is that melt generation is primarily due to upwelling or reheating of mantle (asthenosphere or remobilized lithosphere) that had been enhanced previously by additions of Ba and other slab-derived components (Borg et al., 2002).

BASIC REFLECTIONS AND CONCLUSIONS

Current views on subduction-related magmatism are based on observations of diverse volcanic arcs that differ in significant

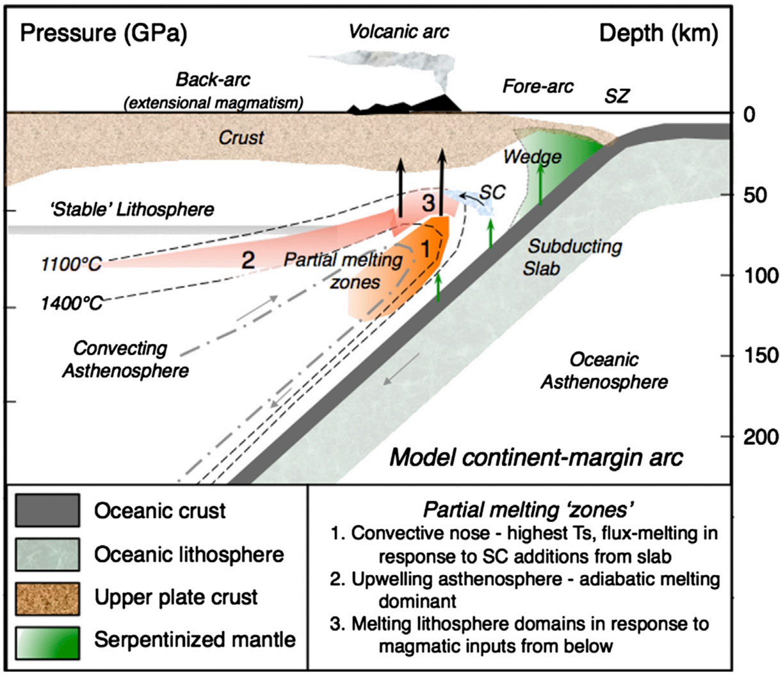

FIGURE 14 | Schematic cross-section of a generalized continental margin subduction zone showing important petrologic and geochemical domains. Boundary between non-convecting lithospheric mantle portion of the upper plate and the underlying convecting asthenospheric mantle is highly schematic. Light arrows rising from the subducting slab signify transfer of fluids and/or melts from slab to lower mantle wedge; in warm Cascadia the shallow wedge is considered to be strongly serpentinized due to shallow slab dehydration. A blue-shaded arrow symbolizes how subduction components (SC) may be distributed into the convecting mantle wedge (cf. Cerpa et al., 2018). This and the distribution of partial melts within the wedge are highly dependent upon many factors (cf. **Figure 2** of this paper). It is generally believed that many arc magmas are 1) generated within the mantle wedge partly in response to the catalytic effect of adding slab-derived water and/or melts, 2) enriched in other components that produce distinctive calcalkalic charateristics, and 3) modified by reactions with progressively warmer mantle as they rise, thus accounting for their elevated temperatures (cf. Grove et al., 2012). In the figure, location "1" signifies a likely position from which such magmas may ascend beneath arcs (bold vertical arrows). A second style of magmatism is related to decompression of convective limbs in the mantle wedge; e.g., region "2" in the figure. Such melts are formed and released over a broad backarc region and in the uppermost part of the ascending asthenospheric limb. If direct inputs of SC from the currently subducting slab are small to negligible, these melts are likely to resemble intraplate magmas (LKT and possibly OIB-like variants), depending upon the history and compositional structure of the convecting asthenosphere. It is probable that the transfer of heat (and possibly fluids) by magmas ascending from domains "1" and "2" will promote warming and partial melting of parts of the lithospheric mantle; e.g., region "3." Such melts could form by remelting earlier emplaced magmatic bodies as well as more refractory components of the old lithospheric mantle. Considering the unusually warm nature of the Cascadia SZ, involvement of slab-derived fluids is likely relatively small during Quaternary time, and appears unlikely to dominate the style of magma productivity in this arc. The smaller leverage of fluid-related processes may contribute to the apparent eminence of intraplate-like magmatism, to increased production of slab melting locally, and to generally high magmatic temperatures in primitive basaltic magmas—overall a higher involvement of adiabatic vs. aqueous flux melting. Conversely, in cooler SZs, greater influence of slab-derived fluids is likely to shift the magmatic spectrum toward the calcalkalic flavor.

ways. It is important to recognize fundamental processes that create suitable sources for arc magmas, but also consider that they have been operating over long periods of time and have cumulative effects such as storage of subduction signatures in static lithospheric mantle and crustal reservoirs. Very sparse data for early Cascades magmatism precludes definitive statements about its inception and early evolution. But the post-Miocene warm Cascades arc provides perspective on SZ processes where fluid contributions from the downgoing slab are relatively low. This is supported by generally low abundances of FMEs like boron (cf. Leeman et al., 2004; Manea et al., 2014) as well as the occurrence of numerous lavas with intraplate-like trace element contents. Warm slab temperatures are expected to promote melting of subducted oceanic crust or sediments, and high precision Sr-Nd-Pb-Hf isotopic data seem consistent with such contributions to many arc magmas (e.g., Cascades CA types and some LKTs; Mullen et al., 2017). The relative importance of these vs. lithosphere contributions is unresolved, but in cooler arcs (most SZs), larger inputs of slab-derived fluids may promote a dominance of CA type magmas. This in turn may mask (or simply overwhelm) melt productivity within the lithosphere. This leaves open questions regarding the timing and magnitude of slab contributions. For example, to what extent are observed subduction signatures in a given magma directly induced by coeval direct slab inputs vs. inherited from the shallow lithospheric mantle (i.e., recycling of older magmatic products)?

These concepts are incorporated into **Figure 14** that portrays a Cascadia-like continental margin SZ. Three general modes of magma formation are envisaged: [1] CA type magmas produced in response to SC additions to the deep mantle wedge, followed by ascent with modification; [2] LKT and possibly OIB-like magmas produced by decompression melting of asthenospheric mantle ascending from backarc regions or through torn slab; and [3] calcalkalic-like magmas produced by melting of lithospheric mantle (including earlier frozen-in magmatic contributions) in response to magma infusion from the other domains. In post-Miocene Cascadia, modes [2] and [3] have become increasingly assertive at the expense of mode [1], and vary in intensity along-strike in response to varied tectonic influences.

Other take away points that can be applicable elsewhere include the following:

(1) An important impetus driving overall arc magmatism is from ascending mafic magmas (largely basalt) that energize the whole system and instigate remelting of shallower mantle and crust. In most arcs, certainly continental ones, significant fractions of the basaltic magma produced never make it to the surface owing to impediments (zero buoyancy, structural compression, etc.) to their ascent. They provide an efficient mechanism to transfer heat and mass to shallower domains (uppermost mantle near Moho or lower crust). But to make continental crust from an arc, a large fraction of that intruded basalt ultimately must be removed (delamination?) to get the correct mass balance.

(2) Some primitive arc basalts are surprisingly hot! Cascade arc LKT and OIB-like magmas appear to have last equilibrated with mantle at conditions above the anhydrous peridotite solidus; their formation requires no slab-derived fluid, and they likely are products of decompression melting of ascending mantle in diapirs or convective flow. In contrast, primitive Cascade CA type magmas appear to be derived from more refractory sources and have predicted P–T equilibration conditions near or below the anhydrous mantle solidus; their formation is inferred to involve some degree of flux-melting, consistent with their relatively higher water contents.

(3) In general, many compositional features of arc magmas point to significant contributions of subducted materials in their formation and/or evolution. But it is often difficult to ascertain the processes or time-scales by which these additions occur. Selective enrichments of strongly fluid-mobile components point to influxes of aqueous fluids, whereas some components are more readily mobilized in melts. Which transport pathway is involved, and which components are transported may be strongly influenced by thermal regime. And, of course, there is considerable variability in what is being subducted, hence in the nature of slab-derived components.

(4) There is potential to use magma chemistry as a "monitor" of spatial-temporal processes operating in volcanic arcs. This is one of the few ways to obtain a direct signal for what is happening at depth. Coupled with geophysical and other means of probing the Earth's interior, it provides a broader base to interpret what is going on. In this regard, it is unsettling that there seems to be uncertainty as to where the magmas feeding Mount St. Helens actually come from!

AUTHOR CONTRIBUTIONS

The author confirms being the sole contributor of this work and has approved it for publication.

FUNDING

Portions of this work were funded by National Science Foundation in the form of research grants, most recently Grant No. 0003612.

ACKNOWLEDGMENTS

I especially thank Vlad Manea for his invitation to prepare this paper on a topic that I have considered for most of my career. I also thank numerous colleagues and associates who worked with me on past projects and contributed ideas and data. And as an impetus for this particular paper, I had the pleasure of working with Russ Evarts who really kick-started new studies of the Boring Volcanic Field, and provided access to much of the analytical data mentioned here. We lost Russ in 2017, and my goal is to formally see that his contributions see the light of day. Likewise, I have benefitted greatly from my association with Rick Conrey, Martin Streck, and Diane Smith—my Cascades coauthors and friends for many years. Finally, I thank Paul Wallace, Robert Stern, and Diane Smith for their contributions to helping me improve this paper.

SUPPLEMENTARY MATERIAL

The Supplementary Material for this article can be found online at: https://www.frontiersin.org/articles/10.3389/feart.2020.535879/full#supplementary-material

REFERENCES

Abers, G. A., van Keken, P. E., and Hacker, B. R. (2017). The cold and relatively dry nature of mantle forearcs in subduction zones. *Nat. Geosci.* 10 (5), 333–337. doi:10.1038/ngeo2922

Anderson, A. T. (1976). Magma mixing: petrological process and volcanological tool. *J. Volcanol. Geoth. Res.* 1, 3–33. doi:10.1016/0377-0273(76)90016-0

Annen, C., Blundy, J. D., and Sparks, R. S. J. (2006). The genesis of intermediate and silicic magmas in deep crustal hot zones. *J. Petrol.* 47, 505–539. doi:10.1093/petrology/egi084

Bacon, C. R., Bruggman, P. E., Christiansen, R. L., Clynne, M. A., Donnelly-Nolan, J. M., and Hildreth, W. (1997). Primitive magmas at five cascade volcanic fields: melts from hot, heterogeneous sub-arc mantle. *Can. Mineral.* 35, 397–423.

Beard, J. S., and Lofgren, G. E. (1991). Dehydration melting and water-saturated melting of basaltic and andesitic greenstones and amphibolites at 1, 3, and 6. 9 kb. *J. Petrol.* 32, 365–401. doi:10.1093/petrology/32.2.365

Bebout, G. E., and Penniston-Dorland, S. C. (2016). Fluid and mass transfer at subduction interfaces-the field metamorphic record. *Lithos.* 240–243, 228–258. doi:10.1016/j.lithos.2015.10.007

Bedrosian, P. A., and Feucht, D. W. (2014). Structure and tectonics of the northwestern United States from EarthScope USArray magnetotelluric data. *Earth Planet Sci. Lett.* 402, 275–289. doi:10.1016/j.epsl.2013.07.035

Behn, M. D., Kelemen, P. B., Hirth, G., Hacker, B. R., and Massonne, H.-J. (2011). Diapirs as the source of the sediment signature in arc lavas. *Nat. Geosci.* 4, 641–646. doi:10.1038/NGEO1214

Beier, C., Haase, K. M., Brandl, P. A., and Krumm, S. H. (2017). Primitive andesites from the Taupo Volcanic Zone formed by magma mixing. *Contrib. Mineral. Petrol.* 172, 33. doi:10.1007/s00410-017-1354-0

Blatter, D. L., Sisson, T. W., and Hankins, W. B. (2013). Crystallization of oxidized, moderately hydrous arc basalt at mid- to lower-crustal pressures: implications for andesite genesis. *Contrib. Mineral. Petrol.* 166, 861–886. doi:10.1007/s00410-013-0920-3.

Blatter, D. L., Sisson, T. W., and Hankins, W. B. (2017). Voluminous arc dacites as amphibole reaction-boundary liquids. *Contrib. Mineral. Petrol.* 172, 27. doi:10.1007/s00410-017-1340-6

Blum-Oeste, M., and Wörner, G. (2016). Central Andean magmatism can be constrained by three ubiquitous end-members. *Terra. Nova.* 28, 434–440. doi:10.1111/ter.12237

Bodmer, M., Toomey, D. R., Hooft, E. E. E., and Schmandt, B. (2018). Buoyant asthenosphere beneath Cascadia influences megathrust segmentation. *Geophys. Res. Lett.* 45, 6954–6962. doi:10.1029/2018GL078700

Borg, L. E., Blichert-Toft, J., and Clynne, M. (2002). Ancient and modern subduction zone contributions to the mantle sources of lavas from the Lassen region of California inferred from Lu-Hf isotopic systematics. *J. Petrol.* 43, 705–723. doi:10.1093/petrology/43.4.705

Borg, L. E., Clynne, M., and Bullen, T. (1997). The variable role of slab-derived fluids in the generation of a suite of primitive calc-alkaline lavas from the southernmost Cascades, California. *Can. Mineral.* 35, 425–452.

Bostock, M. G., Hyndman, R. D., Rondenay, S., and Peacock, S. M. (2002). An inverted continental Moho and serpentinization of the forearc mantle. *Nature.* 417, 536–538. doi:10.1038/417536a

Brocher, T. M., Parsons, T., Tréhu, A. M., Snelson, C. M., and Fisher, M. A. (2003). Seismic evidence for widespread serpentinized forearc upper mantle along the Cascadia margin. *Geology.* 31 (3), 267–270. doi:10.1130/0091-7613(2003)031<0267:SEFWSF>2.0.co;2

Cerpa, N. G., Wada, I., and Wilson, C. R. (2018). Effects of fluid influx, fluid viscosity, and fluid density on fluid migration in the mantle wedge and their implications for hydrous melting. *Geosphere.* 15, 1–23. doi:10.1130/GES01660.1

Çoban, H., Karsli, O., Caran, S., and Yilmaz, K. (2019). What processes control the genesis of absarokite to shoshonite-banakite series in an intracontinental setting, as revealed by geochemical and Sr-Nd-Pb isotope data of Karadağ Stratovolcano in Central Anatolia, Turkey. *Lithos.* 324–325, 609–625. doi:10.1016/j.lithos.2018.11.034

Codillo, E. A., Le Roux, V., and Marschall, H. R. (2018). Arc-like magmas generated by mélange-peridotite interaction in the mantle wedge. *Nat. Commun.* 9 (9), 2864. doi:10.1038/s41467-018-05313-2

Conrey, R. M., Sherrod, D. R., Hooper, P. R., and Swanson, D. A. (1997). Diverse primitive magmas in the Cascade Arc, northern Oregon and southern Washington. *Can. Mineral.* 35, 367–396.

Conway, C. E., Chamberlain, K. J., Harigane, Y., Morgan, D. J., and Wilson, C. J. N. (2020). Rapid assembly of high-Mg andesites and dacites by Magma mixing at a continental arc stratovolcano. *Geology*, 1033–1037. doi:10.1130/G47614.1

Cooper, G. F., Macpherson, C. G., Macpherson, C. G., Blundy, J. D., Maunder, B., Allen, R. W., et al. (2020). Variable water input controls evolution of the Lesser Antilles volcanic arc. *Nature.* 582 (7813), 525–529. doi:10.1038/s41586-020-2407-5

Cooper, L. B., Ruscitto, D. M., Plank, T., Wallace, P. J., Syracuse, E. M., and Manning, C. E. (2012). Global variations in H_2O/Ce: 1. Slab surface temperatures beneath volcanic arcs. *Geochem. Geophys. Geosyst.* 13. doi:10.1029/2011GC003902

Currie, C., Wang, K., Hyndman, R. D., and He, J. (2004). The thermal effects of steady-state slab-driven mantle flow above a subducting plate: the Cascadia subduction zone and backarc. *Earth Planet Sci. Lett.* 223, 35–48. doi:10.1016/j.epsl.2004.04.020

DeBari, S. M., and Greene, A. R. (2011). "Vertical stratification of composition, density, and inferred magmatic processes in exposed arc crustal sections." in *Arc-continent collision.* Berlin, Germany: Springer, 121–144. doi:10.1007/978-3-540-88558-0_5

du Bray, E. A., and John, D. A. (2013). Petrologic, tectonic, and metallogenic evolution of the Ancestral Cascades magmatic arc, Washington, Oregon, and northern California. *Geosphere.* 7, 1102–1133. doi:10.1130/GES00669.1

du Bray, E. A., John, D. A., and Cousens, B. L. (2014). Petrologic, tectonic, and metallogenic evolution of the southern segment of the ancestral Cascades magmatic arc, California and Nevada. *Geosphere.* 10, 1–39. doi:10.1130/GES00944.1

Eichelberger, J. C., Izbekov, P. E., and Browne, B. L. (2006). Bulk chemical trends at arc volcanoes are not liquid lines of descent. *Lithos.* 87, 135–154. doi:10.1016/j.lithos.2005.05.006

Elkins Tanton, L. T., Grove, T. L., and Donnelly-Nolan, J. (2001). Hot, shallow mantle melting under the Cascades volcanic arc. *Geology.* 29(7), 631–634. doi:10.1130/0091-7613(2001)029<0631:HSMMUT>2.0.co;2

Elliott, T., Plank, T., Zindler, A., White, W., and Bourdon, B. (1997). Element transport from slab to volcanic front at the Mariana arc. *J. Geophys. Res.* 102, 14991–15019. doi:10.1029/97JB00788

Evarts, R. C., Conrey, R. M., Fleck, R. J., and Hagstrum, J. T. (2009). "The boring volcanic field of the Portland-Vancouver area, Oregon and Washington: tectonically anomalous forearc volcanism in an urban setting." in *Volcanoes to vineyards: geologic field trips through the dynamic landscape of the Pacific Northwest.* Editors J. E. O'Connor, R. J. Dorsey, and I. P. Madin (Boulder, CO: Geological Society of America Field Guide), Vol. 15, 253–270.

Evarts, R. C., Conrey, R. M., Leeman, W. P., and Streck, M. J. (2017). *Insights into magmatic diversity in the Columbia Cascades Transect (CCT).* Portland, Oregon: International Association of Volcanology and Chemistry of the Earth's Interior General Session. , Abstract 1232.

Farner, M. J., and Lee, C.-T. A. (2017). Effects of crustal thickness on magmatic differentiation in subduction zone volcanism: a global study. *Earth Planet Sci. Lett.* 470, 96–107. doi:10.1016/j.epsl.207.04.025

Ferrari, L., Orozco-Esquivel, T., Manea, V., and Manea, M. (2012). The dynamic history of the Trans-Mexican Volcanic Belt and the Mexico subduction zone. *Tectonophysics.* 522–523, 122–149. doi:10.1016/j.tecto.2011.09.018

Fleck, R. J., Hagstrum, J. T., Calvert, A. T., Evarts, R. C., and Conrey, R. M. (2014). 40Ar/39Ar geochronology, paleomagnetism, and evolution of the Boring volcanic field, Oregon and Washington, USA. *Geosphere.* 10 (6): 1283–1314. doi:10.1130/GES00985.1

Gao, H., and Shen, Y. (2014). Upper mantle structure of the cascades from full-wave ambient noise tomography: evidence for 3D mantle upwelling in the back-arc. *Earth Planet Sci. Lett.* 390, 222–233. doi:10.1016/j.epsl/2014.01.012

Gerya, T., and Stöckhert, B. (2006). Two-dimensional numerical modeling of tectonic and metamorphic histories at active continental margins. *Int. J. Earth Sci.* 95, 250–274. doi:10.1007/s00531-005-0035-9

Gill, J. B. (1981). *Orogenic andesites and plate tectonics.* Berlin, Germany: Springer-Verlag, 392.

Gómez-Tuana, A., Straub, S. M., and Zellmer, G. F. (2013). "An introduction to orogenic andesites and crustal growth," in *Orogenic andesites and crustal growth.* Editors A. Gómez-Tuena, S. M. Straub, and G. F. Zellmer (London, UK: Geological Society of London Special Publication) Vol. 385, 1–13.

Green, D. H., Hibberson, W. O., Rosenthal, A., Kovács, I., Yaxley, G. M., Falloon, T. J., et al. (2014). Experimental study of the influence of water on melting and phase assemblages in the upper mantle. *J. Petrol.* 55, 2067–2096. doi:10.1093/petrology/egu050

Grove, T. L., Elkins-Tanton, L. T., Parman, S. W., Chatterjee, N., Muntener, O., and Gaetani, G. A. (2003). Fractional crystallization and mantle-melting controls on calc-alkaline differentiation trends. *Contrib. Mineral. Petrol.* 145, 515–533. doi:10.1007/s00410-003-0448-z

Grove, T. L., and Till, C. B. (2019). H2O-rich mantle melting near the slab-wedge interface. *Contrib. Mineral. Petrol.* 174, 80. doi:10.1007/s00410-019-1615-1

Grove, T. L., Till, C. B., and Krawczynski, M. J. (2012). The role of H_2O in subduction zone magmatism. *Annu. Rev. Earth Planet Sci.* 40, 413–439. doi:10.1146/annurev-earth-042711-105310

Grove, T., Parman, S., Bowring, S., Price, R., and Baker, M. (2002). The role of an H_2O-rich fluid component in the generation of primitive basaltic andesites and andesites from the Mt. Shasta region, N California. *Contrib. Mineral. Petrol.* 142, 375–396. doi:10.1007/s004100100299

Hagstrum, J. T., Fleck, R. J., Evarts, R. C., and Calvert, A. T. (2017). Paleomagnetism and 40Ar/39Ar geochronology of the Plio-Pleistocene Boring Volcanic Field: implications for the geomagnetic polarity time scale and paleosecular variation. *Phys. Earth Planet. Int.* 262, 101–115. doi:10.1016/j.pepi.2016.07.008

Hansen, S. M., Schmandt, B., Levander, A., Kiser, E., Vidale, J. E., Abers, G. A., et al. (2016). Seismic evidence for a cold serpentinized mantle wedge beneath Mount St Helens. *Nat. Commun.* 7, 1–6. doi:10.1038/ncomms13242.

Harry, D. L., and Green, N. L. (1999). Slab dehydration and basalt petrogenesis in subduction systems involving very young oceanic lithosphere. *Chem. Geol.* 160, 309–333. doi:10.1016/S0009-2541(99)00105-9

Hawley, W. B., and Allen, R. M. (2019). The fragmented death of the Farallon plate. *Geophys. Res. Lett.* 46, 7386–7394. doi:10.1029/2019GL083437

Hayes, G. P., Moore, G. L., Portner, D. E., Hearne, M., Flamme, H., Furtney, M., et al. (2018). Slab2, a comprehensive subduction zone geometry model. *Science.* 362, 58–61. doi:10.1126/science.aat4723

Hermann, J., and Spandler, C. J. (2007). Sediment melts at sub-arc depths: an experimental study. *J. Petrol.* 49 (4), 717–740. doi:10.1093/petrology/egm073

Herzberg, C., and Asimow, P. D. (2015). PRIMELT3 MEGA.XLSM software for primary magma calculation: peridotite primary magma MgO contents from the liquidus to the solidus. *Geochem. Geophys. Geosyst.* 16, 563–578. doi:10.1002/2014GC005631

Hickey-Vargas, R., Holbik, S., Tormey, D., Frey, F. A., and Moreno Roa, H. (2016). Basaltic rocks from the Andean Southern Volcanic Zone: insights from the comparison of along-strike and small-scale geochemical variations and their sources. *Lithos.* 258–259, 115–132. doi:10.1016/j.lithos.2016.04.014

Hildreth, W. (2007). Quaternary magmatism in the cascades – geologic perspectives. *U. S. Geol. Surv. Prof. Pap.* 174, 125.

Hildreth, W., and Moorbath, S. (1988). Crustal contributions to arc magmatism in the Andes of Central Chile. *Contrib. Mineral. Petrol.* 98, 455–489. doi:10.1007/BF00372365

Hirschmann, M. M. (2000). Mantle solidus: experimental constraints and the effects of peridotite composition. *Geochem. Geophys. Geosyst.* 1, 1042. doi:10.1029/2000GC000070

Hofmann, A. W., and Farnetani, C. G. (2013). Two views of Hawaiian plume structure. *Geochem. Geophys. Geosyst.* 14, 5308–5322. doi:10.1002/2013GC004942

Humphreys, E. D., and Coblentz, D. D. (2007). North American dynamics and western U.S. tectonics. *Rev. Geophys.* 45. doi:10.1029/2005RG000181

Humphreys, M. C. S., Edmonds, M., Plail, M., Barclay, J., Parkes, D., and Christopher, T. (2013). A new method to quantify the real supply of mafic components to a hybrid andesite. *Contrib. Mineral. Petrol.* 165, 191–215. doi:10.1007/s00410-012-0805-x

Ishizuka, O., Yuasa, M., Tamura, Y., Shukuno, H., Stern, R. J., Naka, J., et al. (2010). Migrating shoshonitic magmatism tracks Izu-Bonin-Mariana intra-oceanic arc rift propagation. *Earth Planet Sci. Lett.* 294, 111–122. doi:10.1016/j.epsl.2010.03.016

Jicha, B. R., Hart, G. L., Johnson, C. M., Hildreth, W., Beard, B. L., Shirey, S. B., et al. (2009). Isotopic and trace element constraints on the petrogenesis of lavas from the Mount Adams volcanic field, Washington. *Contrib. Mineral. Petrol.* 157, 189–207. doi:10.1007/s00410-008-0329-6

Karlstrom, L., Wright, H. M., and Bacon, C. R. (2015). The effect of pressurized magma chamber growth on melt migration and pre-caldera vent locations through time at Mount Mazama, Crater Lake, Oregon. *Earth Planet Sci. Lett.* 412, 209–219. doi:10.1016/j.epsl.2014.12.001

Katz, R. F., Spiegelman, M., and Langmuir, C. H. (2003). A new parameterization of hydrous mantle melting. *Geochem. Geophys. Geosyst.* 4 (9), 1073. doi:10.1029/2002GC000433

Kelemen, P. B., and Behn, M. D. (2016). Formation of lower continental crust by relamination of buoyant arc lavas and plutons. *Nat. Geosci.* 9, 197–205. doi:10.1038/NGEO2662

Kelemen, P. B., Hanghj, K., and Greene, A. R. (2003). One view of the geochemistry of subduction-related magmatic arcs, with an emphasis on primitive andesite and lower crust. *Treatise on Geochemistry.* 3, 593–659. doi:10.1016/B0-08-043751-6/03035-8

Kelley, K. A., and Cottrell, E. (2009). Water and the oxidation state of subduction zone magmas. *Science.* 325, 605–607. doi:10.1126/science.1174156

Kelley, K. A., Plank, T., Newman, S., Stolper, E. M., Grove, T. L., Parman, S., et al. (2010). Mantle melting as a function of water content beneath the Mariana arc. *J. Petrol.* 51, 1711–1738. doi:10.1093/petrology/egq036

Kent, A. J. R. (2013). "Preferential eruption of andesitic magmas: implications for volcanic magma fluxes at convergent margins." in: *Orogenic andesites and crustal growth.* Editors A. Gómez-Tuena, S. M. Straub, and G. F. Zellmer (London: Geological Society of London Special Publication) 385, 257–289. doi:10.1144/SP385.10

Kimura, J.-I., Gill, J. B., Kunikiyo, T., Osaka, I., Shimoshioiri, Y., Katakuse, M., et al. (2014). Diverse magmatic effects of subducting a hot slab in SW Japan: results from forward modeling. *Geochem. Geophys. Geosyst.* 15, 691–739. doi:10.1002/2013GC005132

Kimura, J.-I., Manton, W. I., Sun, C.-H., Iizumi, S., Yoshida, T., and Stern, R. J. (2002). Chemical diversity of the Ueno basalts, Central Japan: identification of mantle and crustal contributions to arc basalts. *J. Petrol.* 43, 1923–1946. doi:10.1093/petrology/43.10.1923

Lambart, S., Baker, M. B., and Stolper, E. M. (2016). The role of pyroxenite in basalt genesis: melt-PX, a melting parameterization for mantle pyroxenites between 0.9 and 5 GPa. *J. Geophys. Res. Solid Earth.* 121, 5708–5735. doi:10.1002/2015JB012762

Le Maitre, R. W. (2002). *Igneous rocks—a classification and glossary of terms.* 2nd Edn. Cambridge, England: Cambridge University Press, 236.

Lee, C.-T. A., Leeman, W. P., Canil, D., and Li, Z. A. (2005). Similar V/Sc systematics in MORB and arc basalts: implications for the oxygen fugacities of their mantle source regions. *J. Petrol.* 46, 2315–2336. doi:10.1093/petrology/egi056

Lee, C.-T. A., Luffi, P., Le Roux, V., Dasgupta, R., Albaréde, F., and Leeman, W. P. (2010). The redox state of arc mantle using Zn/Fe systematics. *Nature.* 468, 681–685. doi:10.1038/nature09617

Lee, C.-T. A., Luffi, P., Plank, T., Dalton, H., and Leeman, W. P. (2009). Constraints on the depths and temperatures of basaltic magma generation on Earth and other terrestrial planets using new thermobarometers for mafic magmas. *Earth Planet Sci. Lett.* 279, 20–33. doi:10.1016/j.epsl.2008.12.020

Leeman, W. P. (1983). The influence of crustal structure on compositions of subduction-related magmas. *J. Volcanol. Geoth. Res.* 18, 561–588. doi:10.1016/0377-0273(83)90026-4

Leeman, W. P. (1996). "Boron and other fluid-mobile elements in volcanic arc lavas: implications for subduction processes." in *Subduction: top to bottom. Geophysical Monograph series.* Editors G. E. Bebout, W. Scholl, H. Kirby, and P. Platt (Washington, DC: American Geophysical Union), Vol. 96, 269–276.

Leeman, W. P., Evarts, R. C., Conrey, R. M., and Streck, M. J. (2019). Magmatic diversity in the boring volcanic field, Portland Basin, Oregon and Washington: implications for subduction zone magmatism. *Geological Society of America Abstracts with Program.* 51, 33–3. doi:10.1130abs/2019CD-329545

Leeman, W. P., Lewis, J. F., Evarts, R. C., Conrey, R. M., and Streck, M. J. (2005). Petrologic constraints on the thermal structure of the Cascades arc. *J. Volcanol. Geoth. Res.* 140, 67–105. doi:10.1016/j.jvolgeores.2004.07.016

Leeman, W. P., and Smith, D. R. (2018). The role of magma mixing, identification of mafic magma inputs, and structure of the underlying magmatic system at Mount St. Helens. *American Mineralogy.* 103, 1925–1944. doi:10.2138/am-2018-6555

Leeman, W. P., Smith, D. R., Hildreth, W., Palacz, Z., and Rogers, N. (1990). Compositional diversity of Late Cenozoic basalts in a transect across the southern Washington Cascades: implications for subduction zone magmatism. *J. Geophys. Res.* 95, 19561–19582. doi:10.1029/JB095iB12p19561

Leeman, W. P., Tonarini, S., Chan, L. H., and Borg, L. E. (2004). Boron and lithium isotopic variations in a hot subduction zone-the southern Washington cascades. *Chem. Geol.* 212, 101–124. doi:10.1016/j.chemgeo.2004.08.010

Leeman, W. P., Turner, S. P., and Tonarini, S. (2017). Boron isotope variations in Tonga-Kermadec-New Zealand arc lavas: implications for origin of subduction components and mantle influences. *Geochem. Geophys. Geosyst.* 18, 1126–1162. doi:10.1002/2016GC006523

Leslie, R. A. J., Danyushevsky, L. V., Crawford, A. J., and Verbeeten, A. C. (2009). Primitive shoshonites from Fiji: geochemistry and source components. *Geochem. Geophys. Geosyst.* 10, 1–24. doi:10.1029/2008GC002326

Lewis, J. F., Leeman, W. P., and Evarts, R. C. (2001). Petrological constraints on the thermal structure of the southern Washington cascades. *EOS Trans. AGU.* 82 (47). Fall Meet. Suppl., Abstract V21C-0981.

Liu, L., and Stegman, D. R. (2011). Segmentation of the Farallon slab. *Earth Planet Sci. Lett.* 311 (1–2), 1–10. doi:10.1016/j.epsl.2011.09.027

Long, M. D., Till, C. B., Druken, K. A., Carlson, R. W., Wagner, L. S., Fouch, M. J., et al. (2012). Mantle dynamics beneath the Pacific Northwest and the generation of voluminous back-arc volcanism. *Geochem. Geophys. Geosyst.* 13. doi:10.1029/2012GC004189

Luedke, R. G., and Smith, R. L. (1982). Map showing distribution, composition, and age of late Cenozoic volcanic centers in Washington and Oregon. United States Geological Survey Miscellaneous Investigations Map I-1091-D, scale 1:1,000,000.

Mallik, A., Dasgupta, R., Tsuno, K., and Nelson, J. (2016). Effects of water, depth and temperature on partial melting of mantle-wedge fluxed by hydrous sediment-melt in subduction zones. *Geochem. Cosmochim. Acta.* 195, 226–243. doi:10.1016/j.gca.2016.08.018

Manea, V. C., Leeman, W. P., Gerya, T., Manea, M., and Zhu, G. (2014). Subduction of fracture zones controls mantle melting and geochemical signature above slabs. *Nat. Commun.* 5, 5095. doi:10.1038/ncomms6095

Manea, V. C., Manea, M., Kostoglodov, V., and Sewell, G. (2005). Thermo-mechanical model of the mantle wedge in Central Mexican subduction zone and a blob tracing approach for the magma transport. *Phys. Earth Planet. In.* 149, 165–186, doi:10.1016/j.pepi.2004.08.024.

Mann, M. E., Abers, G. A., Crosbie, K., Creager, K., Ulberg, C., Moran, S., et al. (2019). Imaging subduction beneath Mount St. Helens: implications for slab dehydration and magma transport. *Geophys. Res. Lett.* 46. doi:10.1029/2018GL081471

Marschall, H. R., and Schumacher, J. C. (2012). Arc magmas sourced from mélange diapirs in subduction zones. *Nat. Geosci.* 5 (12), 862–867. doi:10.1038/ngeo1634

Matzen, A. K., Wood, B. J., Baker, M. B., and Stolper, E. M. (2017). The roles of pyroxenite and peridotite in the mantle sources of oceanic basalts. *Nat. Geosci.* 10, 530–535. doi:10.1038/NGEO2968

Maunder, B., van Hunen, J., Bouilhol, P., and Magni, V. (2019). Modeling slab temperature: a reevaluation of the thermal parameter. *Geochem. Geophys. Geosyst.* 20. doi:10.1029/2018GC007641

McCaffrey, R., Qamar, A. I., King, R. W., Wells, R., Khazaradze, G., Williams, C. A., et al. (2007). Fault locking, block rotation and crustal deformation in the Pacific Northwest. *Geophys. J. Int.* 169, 1315–1340. doi:10.1111/j.1365-246X.2007.03371.x

McCrory, P. A., Blair, J. L., Waldhauser, F., and Oppenheimer, D. H. (2012). Juan de Fuca slab geometry and its relation to Wadati-Benioff zone seismicity. *J. Geophys. Res.* 117, B09306. doi:10.1029/2012JB009407

McCrory, P. A., and Wilson, D. S. (2013). A kinematic model for the formation of the Siletz-Crescent forearc terrane by capture of coherent fragments of the Farallon and Resurrection plates. *Tectonics.* 32, 718–736. doi:10.1002/tect.20045

McCulloch, M. T., and Gamble, J. A. (1991). Geochemical and geodynamical constraints on subduction zone magmatism. *Earth Planet Sci. Lett.* 102, 358–374. doi:10.1016/0012-821X(91)90029-H

McGary, R. S., Evans, R. L., Wannamaker, P. E., Elsenbeck, J., and Rondenay, S. (2014). Pathway from subducting slab to surface for melt and fluids beneath Mount Rainier. *Nature.* 511, 338–341. doi:10.1038/nature13493

Michaelson, C. A., and Weaver, C. S. (1986). Upper mantle structure from teleseismic Pwave arrivals in Washington and northern Oregon. *J. Geophys. Res.* 91, 2077–2094. doi:10.1029/JB091iB02p02077

Miyashiro, A. (1974). Volcanic rock series in island arcs and active continental margins. *Am. J. Sci.* 274. 321–355. doi:10.2475/ajs.274.4.321

Morris, J. D., Leeman, W. P., and Tera, F. (1990). The subducted component in island arc lavas: constraints from Be isotopes and B-Be systematics. *Nature.* 344, 31–36. doi:10.1038/344031a0

Mullen, E. K., Paquette, J.-L., Tepper, J. H., and McCallum, I. S. (2018). Temporal and spatial evolution of Northern Cascade Arc magmatism revealed by LA-ICP-MS U-Pb zircon dating. *Can. J. Earth Sci.* 55, 443–462. doi:10.1139/cjes-2017-0167

Mullen, E. K., and Weis, D. (2015). Evidence for trench-parallel mantle flow in the Northern Cascade Arc from basalt geochemistry. *Earth Planet Sci. Lett.* 414, 100–107. doi:10.1016/j.epsl.2015.01.010

Mullen, E. K., Weis, D., Marsh, N. B., and Martindale, M. (2017). Primitive arc magma diversity: new geochemical insights in the Cascade Arc. *Chem. Geol.* 448, 43–70. doi:10.1016/j.chemgeo.2016.11.006

Mullen, E. K., and Weis, D. (2013). Sr-Nd-Hf-Pb isotope and trace element evidence for the origin of alkalic basalts in the Garibaldi Belt, northern Cascade arc. *Geochem. Geophys. Geosyst.* 14, 3126–3155. doi:10.1002/ggge.20191

Murphy, M. D., Sparks, R. S. J., Barclay, J., Carroll, M. R., and Brewer, T. S. (2000). Remobilization of andesite magma by intrusion of mafic magma at the Soufriere Hills Volcano, Montserrat, West Indies. *J. Petrol.* 41, 21–42. doi:10.1093/petrology/41.1.21

Naumov, B. V., Kovalenko, V. I., Babansky, A. D., and Tolstykh, M. L. (1997). Genesis of andesites: evidence from studies of melt inclusions from minerals. *Petrology.* 5, 586–596.

Noll, P. D., Newsom, H. E., Leeman, W. P., and Ryan, J. G. (1996). The role of hydrothermal fluids in the production of subduction zone magmas: evidence from siderophile and chalcophile trace elements and boron. *Geochem. Cosmochim. Acta.* 60, 587–611. :doi:10.1016/0016-7037(95)00405-X.

Pearce, J. A. (1982). "Trace element characteristics of lavas from destructive plate boundaries." in *Andesites: orogenic andesites and related rocks.* Editor R. S. Thorpe (Chichester, UK: John Wiley), 525–548.

Pearce, J. A., and Peate, D. W. (1995). Tectonic implications of the composition of volcanic arc magmas. *Annu. Rev. Earth Planet Sci.* 23, 251–285. doi:10.1146/annurev.ea.23.050195.001343

Pearce, J. A., Stern, R. J., Bloomer, S. H., and Fryer, P. (2005). Geochemical mapping of the Mariana Arc-Basin system: implications for the nature and distribution of subduction components. *Geochem. Geophys. Geosyst.* 6, 1–27. doi:10.1029/2004GC000895

Peate, D. W., Pearce, J. A., Hawkesworth, C. J., Colley, H., Edwards, C. M. H., and Hirose, K. (1997). Geochemical variations in Vanuatu arc lavas: the role of subducted material and a variable mantle wedge composition. *J. Petrol.* 38, 1331–1358. doi:10.1093/petroj/38.10.1331

Penniston-Dorland, S. C., Kohn, M. J., and Manning, C. E. (2015). The global range of subduction zone thermal structures from exhumed blueschists and eclogites: rocks are hotter than models. *Earth Planet Sci. Lett.* 428, 243–254. doi:10.1016/j.epsl.2015.07.031

Perrin, A., Goes, S., Prytulak, J., Davies, D. R., Wilson, C., and Kramer, S. (2016). Reconciling mantle wedge thermal structure with arc lava thermobarometric determinations in oceanic subduction zones. *Geochem. Geophys. Geosyst.* 17, 4105–4127. doi:10.1002/2016GC006527

Perrin, A., Goes, S., Prytulak, J., Rondenay, S., and Davies, D. R. (2018). Mantle wedge temperatures and their potential relation to volcanic arc location. *Earth Planet Sci. Lett.* 501, 67–77. doi:10.1016/j.epsl.2018.08.011

Phillips, B. A., Kerr, A. C., Mullen, E. K., and Weis, D. (2017). Oceanic mafic magmatism in the Siletz terrane, NW North America: fragments of an Eocene oceanic plateau? *Lithos.* 274–275, 291–303. doi:10.1016/j.lithos.2017.01.005

Pitcher, B. W., and Kent, A. J. R. (2019). Statistics and segmentation: using Big Data to assess Cascades arc compositional variability. *Geochem. Cosmochim. Acta.* 265, 443–467. doi:10.1016/j.gca.2019.08.035

Plank, T., and Forsyth, D. W. (2016). Thermal structure and melting conditions in the mantle beneath the Basin and Range province from seismology and petrology. *Geochem. Geophys. Geosyst.* 17, 1312–1338. doi:10.1002/2015GC006205

Plank, T., Kelley, K. A., Zimmer, M. M., Hauri, E. H., and Wallace, P. J. (2013). Why do mafic arc magmas contain ~4 wt% water on average? *Earth Planet Sci. Lett.* 364, 168–179. doi:10.1016/j.epsl.2012.11.044

Plank, T., and Langmuir, C. H. (1988). An evaluation of the global variations in the major element chemistry of arc basalts. *Earth Planet Sci. Lett.* 90, 349–370. doi:10.1016/0012-821x(88)90135-5

Plank, T. (2014). "The chemical composition of subducting sediments." in *Treatise on geochemistry.* 2nd Edn. Amsterdam, Holland: Elsevier, Chap. 4.17, 607–629.

Poli, S., and Schmidt, M. W. (2002). Petrology of subducted slabs. *Annu. Rev. Earth Planet Sci.* 30, 207–235. doi:10.1146/annurev.earth.30.091201.140550

Porritt, R. W., Allen, R. M., Boyarko, D. C., and Brudzinski, M. R. (2011). Investigation of Cascadia segmentation with ambient noise tomography. *Earth Planet Sci. Lett.* 309, 67–76. doi:10.1016/j.epsl.2011.06.026

Portnyagin, M., Hoernle, K., Plechov, P., Mironov, N., and Khubunaya, S. (2007). Constraints on mantle melting and composition and nature of slab components in volcanic arcs from volatiles (H2O, S, Cl, F) and trace elements in melt inclusions from the Kamchatka Arc. *Earth Planet Sci. Lett.* 255, 53–69. doi:10.1016/j.epsl.2006.12.005

Priest, G. R., Hladky, F. R., Mertzman, S. A., Murray, R. B., and Wiley, T. J. (2013). Volcanic signature of basin and range extension on the shrinking Cascade arc, Klamath Falls-Keno area, *Oregon. J. Geophys. Res.* 118, 4013–4038. doi:10.1002/jgbr.50290.

Rapp, R. P., and Watson, E. B. (1995). Dehydration melting of metabasalt at 8-32 kbar: implications for continental growth and crust-mantle recycling. *J. Petrol.* 36, 891–931. doi:10.1093/petrology/36.4.891

Rawson, H., Keller, T., Fontijn, K., Pyle, D. M., Mather, T. A., Smith, V. C., et al. (2016). Compositional variability in mafic arc magmas over short spatial and temporal scales: evidence for the signature of mantle reactive melt channels. *Earth Planet Sci. Lett.* 456, 66–77. doi:10.1016/j.epsl.2016.09.056

Rea, J., Wallace, P. J., and Clynne, M. A. (2012). *Pre-eruptive volatile contents of mafic magmas from the 2.0–1.7 ka Castle Creek eruptive period.* Mount St. Helens, WA: EOS, American Geophysical Union, Fall Meeting. 2012, Abstract V53C-2853.

Reagan, M. K., and Gill, J. B. (1989). Coexisting calcalkaline and high-niobium basalts from Turrialba Volcano, Costa Rica: implications for residual titanates in arc magma sources. *J. Geophys. Res.* 94, 4619–4633. doi:10.1029/JB094iB04p04619

Rees Jones, D. W., Katz, R. F., Tian, M., and Rudge, J. F. (2018). Thermal impact of magmatism in subduction zones. *Earth Planet Sci. Lett.* 481, 73–79. doi:10.1016/j.epsl.2017.10.015

Reiners, P. W., Hammond, P. E., McKenna, J. M., and Duncan, R. A. (2000). Young basalts of the central Washington Cascades, flux melting of the mantle, and trace element signatures of primary arc magmas. *Contrib. Mineral. Petrol.* 138, 249–264. doi:10.1007/s004100050561

Reubi, O., and Blundy, J. (2009). A dearth of intermediate melts at subduction zone volcanoes and the petrogenesis of arc andesites. *Nature.* 461, 1269–1273. doi:10.1038/nature08510

Righter, K. (2000). A comparison of basaltic volcanism in the Cascades and western Mexico: compositional diversity in continental arcs. *Tectonophysics.* 318, 99–117. doi:10.1016/S0040-1951(99)00308-X

Rowe, M. C., Kent, A. J. R., and Nielsen, R. L. (2009). Subduction influence on oxygen fugacity and trace and volatile elements in basalts across the Cascade Volcanic Arc. *J. Petrol.* 50, 61–91. doi:10.1093/petrology/egn072

Rowe, M. C., and Tepley, F. J., III. (2016). Origin and petrogenetic implications of anomalous olivine from a Cascade forearc basalt. *Am. Mineral.* 101, 1807–1819. doi:10.2138/am-2016-5651

Rudnick, R. L., and Gao, S. (2003). Composition of the continental crust. *Treatise of Geochemistry.* 3, 1–64. doi:10.1016/B0-08-043751-6/03016-4

Ruscitto, D. M., Wallace, P. J., Cooper, L. B., and Plank, T. (2012). Global variations in H_2O/Ce: 2.Relationships to arc magma geochemistryand volatile fluxes. *Geochem. Geophys. Geosyst.* 13. doi:10.1029/2011GC003887.

Ruscitto, D. M., Wallace, P. J., and Kent, A. J. R. (2011). Revisiting the compositions and volatile contents of olivine-hosted melt inclusions from the Mount Shasta region: implications for the formation of high-Mg andesites. *Contrib. Mineral. Petrol.* 162, 109–132. doi:10.1007/s00410-010-0587-y

Ryan, J. G., and Chauvel, C. (2014). "The subdiction-zone filter and the impact of recycled material on the evolution of the mantle." in *Treatise on geochemistry.* 2nd Edn. Amsterdam, Holland: Elsevier, Chap. 3.13, 479–508.

Sas, M., DeBari, S. M., Clynne, M. A., and Rusk, B. G. (2017). Using mineral geochemistry to decipher slab, mantle, and crustal input in the generation of high-Mg andesites and basaltic andesites from the northern Cascade Arc. *Am. Mineral.* 102, 948–965. doi:10.2138/am-2017-5756

Schmandt, B., and Humphreys, E. (2011). Seismically imaged relict slab from the 55 Ma Siletzia accretion to the northwest United States. *Geology.* 39, 175–178. doi:10.1130/G31558.1

Schmidt, M. E., Grunder, A. L., and Rowe, M. C. (2008). Segmentation of the Cascade Arc as indicated by Sr and Nd isotopic variation among diverse primitive basalts. *Earth Planet Sci. Lett.* 266, 166–181. doi:10.1016/j.epsl.2007.11.013

Schmidt, M. W., and Jagoutz, O. (2017). The global systematics of primitive arc melts. *Geochem. Geophys. Geosyst.* 18, 2817–2854. doi:10.1002/2016GC006699

Schmidt, M. W., and Poli, S. (1998). Experimentally based water budgets for dehydrating slabs and consequences for arc magma generation. *Earth Planet Sci. Lett.* 163, 361–379. doi:10.1016/S0012-821X(98)00142-3

Sigloch, K., and Mihalynuk, M. G. (2017). Mantle and geological evidence for a late jurassic–cretaceous suture spanning north America. *Geol. Soc. Am. Bull.* 129, 1489–1520. doi:10.1130/B31529.1

Singer, B. S., Jicha, B. R., Leeman, W. P., Rogers, N. W., Thirlwall, M. F., Ryan, J., et al. (2007). Along-strike trace element and isotopic variation in Aleutian Island arc basalt: subduction melts sediments and dehydrates serpentine. *J. Geophys. Res.* 112, B06206. doi:10.1029/2006JB004897

Singer, B. S., Leeman, W. P., Thirlwall, M. W., and Rogers, N. W. (1996). "Does fracture zone subduction increase sediment flux and mantle melting in subduction zones? Trace element evidence from Aleutian arc basalts." in *Subduction top to bottom geophysical monograph series.* Editors G. E. Bebout, et al. (Washington, DC: American Geophysical Union), Vol. 96, 285–291.

Sisson, T. W., and Bronto, S. (1998). Evidence for pressure-release melting beneath magmatic arcs from basalt at Galunggung, Indonesia. *Nature.* 391, 883–886. doi:10.1038/36087

Sisson, T. W., and Kelemen, P. B. (2018). Near-solidus melts of MORB+4 wt% H_2O at 0.8-2.8 GPa applied to issues of subduction magmatism and continent formation. *Contrib. Mineral. Petrol.* 173:70. doi:10.1007/s00410-018-1494-x

Sisson, T. W., Salters, V. J. M., and Larson, P. B. (2014). Petrogenesis of Mount Rainier andesite: magma flux and geologic controls on the contrasting differentiation styles at stratovolcanoes of the southern Washington Cascades. *Geol. Soc. Am. Bull.* 126, 122–144. doi:10.1130/B30852.1

Smith, D. R., and Leeman, W. P. (1993). The origin of Mount St. Helens andesites. *J. Volcanol. Geoth. Res.* 55, 271–303. doi:10.1016/0377-0273(93)90042-P

Smith, D. R., and Leeman, W. P. (2005). Chromian spinel-olivine phase chemistry and the origin of primitive basalts of the southern Washington Cascades. *J. Volcanol. Geoth. Res.* 140, 49–66. doi:10.1016/j.jvolgeores.2004.07.015

Solano, J. M. S., Jackson, M. D., Sparks, R. S. J., Blundy, J. D., and Annen, C. (2012). Melt segregation in deep crustal hot zones: a mechanism for chemical differentiation, crustal assimilation and the formation of evolved magmas. *J. Petrol.* 53, 1999–2026. doi:10.1093/petrology/egs041

Spandler, C., and Pirard, C. (2013). Element recycling from subducting slabs to arc crust: a review. *Lithos.* 170–171, 208–223. doi:10.1016/j.lithos.2013.02.016

Stern, R. J. (2002). Subduction zones. *Rev. Geophys.* 40, 1012. doi:10.1029/2001RG000108

Stern, R. J., and Dumitru, T. A. (2019). Eocene initiation of the Cascadia subduction zone: a second example of plume-induced subduction initiation? *Geosphere.* 15, 1–23. doi:10.1130/GES02050.1

Straub, S. M., LaGatta, A. B., Martin-Del Pozzo, A. L., and Langmuir, C. H. (2008). Evidence from high-Ni olivines for a hybridized peridotite/pyroxenite source for orogenic andesites from the central Mexican Volcanic Belt. *Geochem. Geophys. Geosyst.* 9. doi:10.1029/2007GC001583

Streck, M. J., and Leeman, W. P. (2018). Petrology of "Mt. Shasta" high-magnesian andesite (HMA): a product of multi-stage crustal assembly. *American Mineralogy.* 103, 216–240. doi:10.2138/am-2018-6151

Sun, S.-S., and McDonough, W. F. (1989). "Chemical and isotopic systematics of oceanic basalts: implications for mantle composition and processes." in *Magmatism in the ocean basins.* Editors A. D. Saunders and M. J. Norry (London, UK: Geological Society Special Publication), Vol. 42, 313–345.

Syracuse, E. M., van Keken, P. E., and Abers, G. A. (2010). The global range of subduction zone thermal models. *Phys. Earth Planet. In.* 183, 73–90. doi:10.1016/j.pepi.2010.02.004

Tamura, Y., Tatsumi, Y., Zhao, D., Kido, Y., and Shukuno, H. (2002). Hot fingers in the mantle wedge: new insights into magma genesis in subduction zones. *Earth Planet Sci. Lett.* 197, 105–116. doi:10.1016/S0012-821X(02)00465-X.

Tatsumi, Y. (2005). The subduction factory: how it operates in the evolving Earth. *GSA Today (Geol. Soc. Am.)* 15, 4–10. doi:10.1130/1052-5173(2005)015[4:tsfhio]2.0.co;2

Till, C. B. (2017). A review and update of mantle thermobarometry of primitive arc magmas. *American Mineralogy.* 102, 931–947. doi:10.2138/am-2017-5783

Till, C. B., Grove, T. L., Carlson, R. W., Donnelly-Nolan, J. M., Fouch, M. J., Wagner, L. S., et al. (2013). Depths and temperatures of <10.5 Ma mantle melting and the lithosphere-asthenosphere boundary below southern Oregon and northern California. *Geochem. Geophys. Geosyst.* 14, 864–879. doi:10.1002/ggge.20070

Till, C. B., Kent, A. J. R., Abers, G. A., Janiszewski, H. A., Gaherty, J. B., and Pitcher, B. W. (2019). The causes of spatiotemporal variations in erupted fluxes and compositions along a volcanic arc. *Nat. Commun.* 10:1350. doi:10.1038/s41467-019-09113-0

Tonarini, S., Leeman, W. P., and Ferrara, G. (2001). Boron isotopic variations in lavas of the Aeolian volcanic arc, South Italy. *J. Volcanol. Geoth. Res.* 110, 155–170. doi:10.1016/S0377-0273(01)00203-7

Turner, S. J., and Langmuir, C. H. (2015). The global chemical systematics of arc front stratovolcanoes: evaluating the role of crustal processes. *Earth Planet Sci. Lett.* 422, 182–193. doi:10.1016/j.epsl.2015.03.056

Turner, S. J., Langmuir, C. H., Dungan, M. A., and Escrig, S. (2017). The importance of mantle wedge heterogeneity to subduction zone magmatism and the origin of EM1. *Earth Planet Sci. Lett.* 472, 216–228. doi:10.1016/j.epsl.2017.04.051

Turner, S. J., Langmuir, C. H., Katz, R. F., Dungan, M. A., and Escrig, S. (2016). Parental arc magma compositions dominantly controlled by mantle-wedge thermal structure. *Nat. Geosci.* 9, 772–776. doi:10.1038/ngeo2788

Ulmer, P., and Trommsdorff, V. (1995). Serpentine stability to mantle depths and subduction-related magmatism. *Science.* 268, 858–861. doi:10.1126/science.268.5212.858

van Keken, P. E., Hacker, B. R., Syracuse, E. M., and Abers, G. A. (2011). Subduction factory: 4. Depth-dependent flux of H2O from subducting slabs worldwide. *J. Geophys. Res.* 116, B01401. doi:10.1029/2010JB007922

Verplanck, E. P., and Duncan, R. A. (1987). Temporal variations in plate convergence and eruption rates in the western Cascades, Oregon. *Tectonics.* 6, 197–209. doi:10.1029/tc006i002p00197

Vielzeuf, D., and Schmidt, M. W. (2001). Melting relations in hydrous systems revisited: application to metapelites, metagreywackes and metabasalts. *Contrib. Mineral. Petrol.* 141, 251–267. doi:10.1007/s004100100237

Wallace, P. J. (2005). Volatiles in subduction zone magmas: concentrations and fluxes based on melt inclusion and volcanic gas data. *J. Volcanol. Geoth. Res.* 140, 217–240. doi:10.1016/j.jvolgeores.2004.07.023

Walowski, K. J., Wallace, P. J., Clynne, M. A., Rasmussen, D. J., and Weis, D. (2016). Slab melting and magma formation beneath the southern Cascade arc. *Earth Planet Sci. Lett.* 446, 100–112. doi:10.1016/j.epsl.2016.03.044

Walowski, K. J., Wallace, P. J., Hauri, E. H., Wada, I., and Clynne, M. A. (2015). Slab melting beneath the Cascade Arc driven by dehydration of altered oceanic peridotite. *Nat. Geosci.* 8, 404–408. doi:10.1038/NGEO2417

Wannamaker, P. E., Evans, R. L., Bedrosian, P. A., Unsworth, M. J., Maris, V., and McGary, R. S. (2014). Segmentation of plate coupling, fate of subduction fluids, and modes of arc magmatism in Cascadia, inferred from magnetotelluric resistivity. *Geochem. Geophys. Geosyst.* 15, 4230–4253. doi:10.1002/2014GC005509

Wells, R., Bukry, D., Friedman, R., Pyle, D., Duncan, R., Haeussler, P., et al. (2014). Geologic history of Siletzia, a large igneous province in the Oregon and Washington Coast Range: correlation to the geomagnetic polarity time scale and implications for a long-lived Yellowstone hotspot. *Geosphere.* 10, 692–719. doi:10.1130/GES01018.1

Wells, R. E., and McCaffrey, R. (2013). Steady rotation of the Cascade arc. *Geology* 41, 1027–1030. doi:10.1130/G34514.1

Wells, R. E., Weaver, C. S., and Blakely, R. J. (1998). Fore-arc migration in Cascadia and its neotectonic significance. *Geol.* 26, 759–762. doi:10.1130/0091-7613(1998)026<0759:famica>2.3.co;2

Woodhead, J. D., Eggins, S. M., and Johnson, R. W. (1998). Magma genesis in the New Britain island arc: further insights into melting and mass transfer processes. *J. Petrol.* 39, 1641–1668. doi:10.1093/petroj/39.9.1641

Woodhead, J., Eggins, S., and Gamble, J. (1993). High field strength and transition element systematics in island arc and back-arc basin basalts: evidence for multi-phase melt extraction and a depleted mantle wedge. *Earth Planet Sci. Lett.* 114, 491–504. doi:10.1016/0012-821X(93)90078-N

Yogodzinski, G. M., Brown, S. T., Kelemen, P. B., Vervoort, J. D., Portnyagin, M., Sims, K. W. W., et al. (2015). The role of subducted basalt in the source of island arc magmas: evidence from seafloor lavas of the Western Aleutians. *J. Petrol.* 56, 441–492. doi:10.1093/petrology/egv006

Zheng, Y.-F. (2019). Subduction zone geochemistry. *Geoscience Frontiers.* 10, 1223–1254. doi:10.1016/j.gsf.2019.02.003

Zhou, Q., Liu, L., and Hu, J. (2018). Western US volcanism due to intruding oceanic mantle driven by ancient Farallon slabs. *Nat. Geosci.* 11(1), 70–76. doi:10.1038/s41561-017-0035-y

Zhu, M.-S., Miao, L.-C., and Yang, S.-H. (2013). Genesis and evolution of subduction-zone andesites: evidence from melt inclusions. *Int. Geol. Rev.* 55, 1179–1190. doi:10.1080/00206814.2013.767527

Zimmer, M. M., Plank, T., Hauri, E. H., Yogodzinski, G. M., Stelling, P., Larsen, J., et al. (2010). The role of water in generating the calc-alkaline trend: new volatile data for Aleutian magmas and a new tholeiitic index. *J. Petrol.* 51, 2411–2444. doi:10.1093/petrology/egq062

Conflict of Interest: The author declares that the research was conducted in the absence of any commercial or financial relationships that could be constructed as a potential conflict of interest.

Advantages of publishing in Frontiers

OPEN ACCESS
Articles are free to read
for greatest visibility
and readership

FAST PUBLICATION
Around 90 days
from submission
to decision

HIGH QUALITY PEER-REVIEW
Rigorous, collaborative,
and constructive
peer-review

TRANSPARENT PEER-REVIEW
Editors and reviewers
acknowledged by name
on published articles

Frontiers
Avenue du Tribunal-Fédéral 34
1005 Lausanne | Switzerland

Visit us: www.frontiersin.org
Contact us: info@frontiersin.org | +41 21 510 17 00

REPRODUCIBILITY OF RESEARCH
Support open data
and methods to enhance
research reproducibility

DIGITAL PUBLISHING
Articles designed
for optimal readership
across devices

FOLLOW US
@frontiersin

IMPACT METRICS
Advanced article metrics
track visibility across
digital media

EXTENSIVE PROMOTION
Marketing
and promotion
of impactful research

LOOP RESEARCH NETWORK
Our network
increases your
article's readership